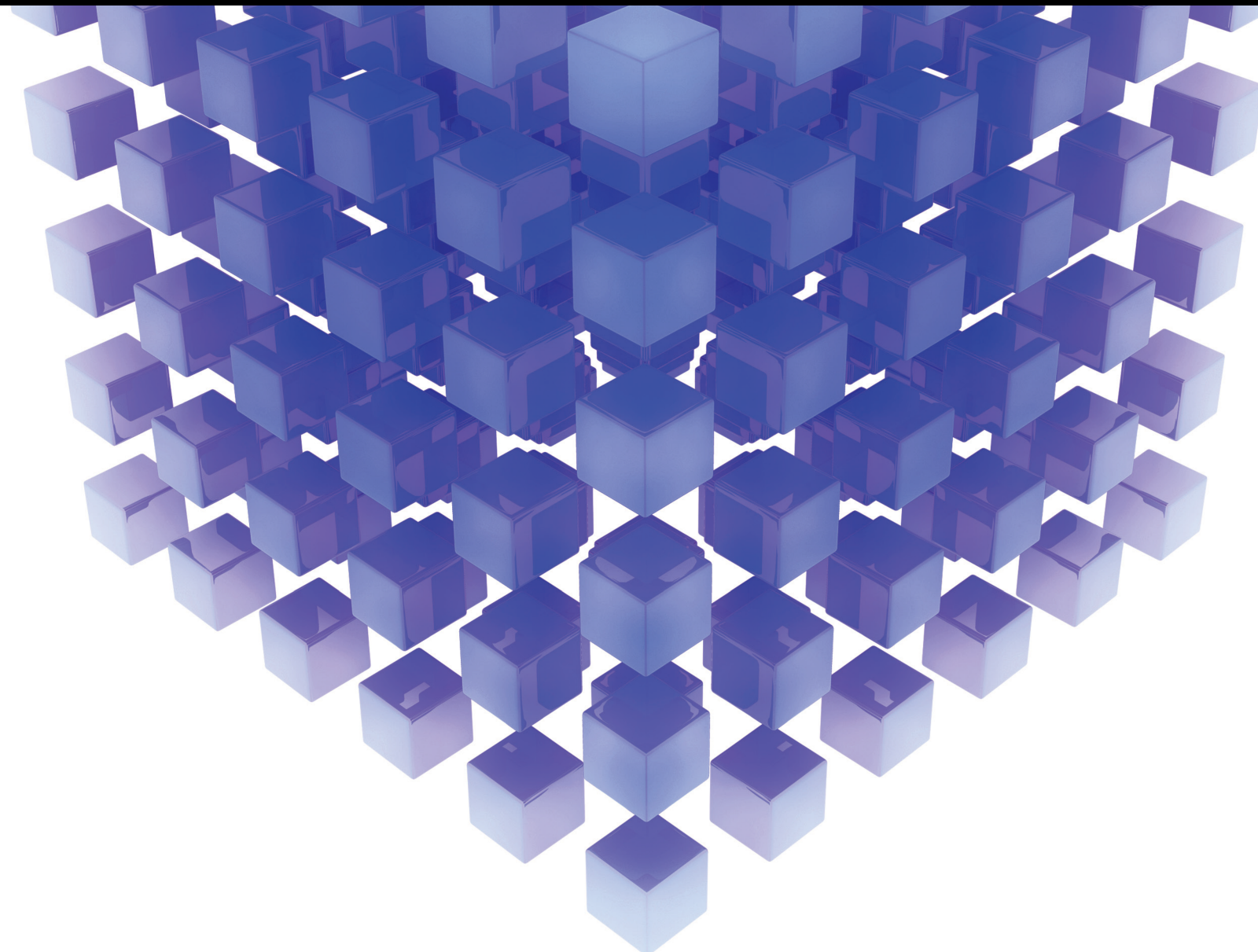


# From Complexity to Simplicity in U-Model Enhanced Control System Design

Lead Guest Editor: Quanmin Zhu

Guest Editors: Jing Na, Olfa Boubaker, Weicun Zhang, Magdi S. Mahmoud, and Jian Huang





---

# **From Complexity to Simplicity in U-Model Enhanced Control System Design**



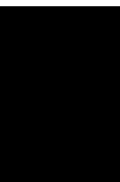
Mathematical Problems in Engineering

---

**From Complexity to Simplicity in U-  
Model Enhanced Control System Design**

Lead Guest Editor: Quanmin Zhu

Guest Editors: Jing Na, Olfa Boubaker, Weicun  
Zhang, Magdi S. Mahmoud, and Jian Huang




---

Copyright © 2020 Hindawi Limited. All rights reserved.



This is a special issue published in “Mathematical Problems in Engineering.” All articles are open access articles distributed under the Creative Commons Attribution License, which permits unrestricted use, distribution, and reproduction in any medium, provided the original work is properly cited.

# Chief Editor

Guangming Xie , China

## Academic Editors

Kumaravel A , India  
Waqas Abbasi, Pakistan  
Mohamed Abd El Aziz , Egypt  
Mahmoud Abdel-Aty , Egypt  
Mohammed S. Abdo, Yemen  
Mohammad Yaghoub Abdollahzadeh  
Jamalabadi , Republic of Korea  
Rahib Abiyev , Turkey  
Leonardo Acho , Spain  
Daniela Addessi , Italy  
Arooj Adeel , Pakistan  
Waleed Adel , Egypt  
Ramesh Agarwal , USA  
Francesco Aggogeri , Italy  
Ricardo Aguilar-Lopez , Mexico  
Afaq Ahmad , Pakistan  
Naveed Ahmed , Pakistan  
Elias Aifantis , USA  
Akif Akgul , Turkey  
Tareq Al-shami , Yemen  
Guido Ala, Italy  
Andrea Alaimo , Italy  
Reza Alam, USA  
Osamah Albahri , Malaysia  
Nicholas Alexander , United Kingdom  
Salvatore Alfonzetti, Italy  
Ghous Ali , Pakistan  
Nouman Ali , Pakistan  
Mohammad D. Aliyu , Canada  
Juan A. Almendral , Spain  
A.K. Alomari, Jordan  
José Domingo Álvarez , Spain  
Cláudio Alves , Portugal  
Juan P. Amezcua-Sanchez, Mexico  
Mukherjee Amitava, India  
Lionel Amodeo, France  
Sebastian Anita, Romania  
Costanza Arico , Italy  
Sabri Arik, Turkey  
Fausto Arpino , Italy  
Rashad Asharabi , Saudi Arabia  
Farhad Aslani , Australia  
Mohsen Asle Zaem , USA

Andrea Avanzini , Italy  
Richard I. Avery , USA  
Viktor Avrutin , Germany  
Mohammed A. Awadallah , Malaysia  
Francesco Aymerich , Italy  
Sajad Azizi , Belgium  
Michele Baccocchi , Italy  
Seungik Baek , USA  
Khaled Bahlali, France  
M.V.A Raju Bahubalendruni, India  
Pedro Balaguer , Spain  
P. Balasubramaniam, India  
Stefan Balint , Romania  
Ines Tejado Balsera , Spain  
Alfonso Banos , Spain  
Jerzy Baranowski , Poland  
Tudor Barbu , Romania  
Andrzej Bartoszewicz , Poland  
Sergio Baselga , Spain  
S. Caglar Baslamisli , Turkey  
David Bassir , France  
Chiara Bedon , Italy  
Azeddine Beghdadi, France  
Andriette Bekker , South Africa  
Francisco Beltran-Carbajal , Mexico  
Abdellatif Ben Makhlof , Saudi Arabia  
Denis Benasciutti , Italy  
Ivano Benedetti , Italy  
Rosa M. Benito , Spain  
Elena Benvenuti , Italy  
Giovanni Berselli, Italy  
Michele Betti , Italy  
Pietro Bia , Italy  
Carlo Bianca , France  
Simone Bianco , Italy  
Vincenzo Bianco, Italy  
Vittorio Bianco, Italy  
David Bigaud , France  
Sardar Muhammad Bilal , Pakistan  
Antonio Bilotta , Italy  
Sylvio R. Bistafa, Brazil  
Chiara Boccaletti , Italy  
Rodolfo Bontempo , Italy  
Alberto Borboni , Italy  
Marco Bortolini, Italy

Paolo Boscariol, Italy  
Daniela Boso , Italy  
Guillermo Botella-Juan, Spain  
Abdesselem Boulkroune , Algeria  
Boulaïd Boulkroune, Belgium  
Fabio Bovenga , Italy  
Francesco Braghin , Italy  
Ricardo Branco, Portugal  
Julien Bruchon , France  
Matteo Bruggi , Italy  
Michele Brun , Italy  
Maria Elena Bruni, Italy  
Maria Angela Butturi , Italy  
Bartłomiej Błachowski , Poland  
Dhanamjayulu C , India  
Raquel Caballero-Águila , Spain  
Filippo Cacace , Italy  
Salvatore Caddemi , Italy  
Zuowei Cai , China  
Roberto Caldelli , Italy  
Francesco Cannizzaro , Italy  
Maosen Cao , China  
Ana Carpio, Spain  
Rodrigo Carvajal , Chile  
Caterina Casavola, Italy  
Sara Casciati, Italy  
Federica Caselli , Italy  
Carmen Castillo , Spain  
Inmaculada T. Castro , Spain  
Miguel Castro , Portugal  
Giuseppe Catalanotti , United Kingdom  
Alberto Cavallo , Italy  
Gabriele Cazzulani , Italy  
Fatih Vehbi Celebi, Turkey  
Miguel Cerrolaza , Venezuela  
Gregory Chagnon , France  
Ching-Ter Chang , Taiwan  
Kuei-Lun Chang , Taiwan  
Qing Chang , USA  
Xiaoheng Chang , China  
Prasenjit Chatterjee , Lithuania  
Kacem Chehdi, France  
Peter N. Cheimets, USA  
Chih-Chiang Chen , Taiwan  
He Chen , China

Kebing Chen , China  
Mengxin Chen , China  
Shyi-Ming Chen , Taiwan  
Xizhong Chen , Ireland  
Xue-Bo Chen , China  
Zhiwen Chen , China  
Qiang Cheng, USA  
Zeyang Cheng, China  
Luca Chiapponi , Italy  
Francisco Chicano , Spain  
Tirivanhu Chinyoka , South Africa  
Adrian Chmielewski , Poland  
Seongim Choi , USA  
Gautam Choubey , India  
Hung-Yuan Chung , Taiwan  
Yusheng Ci, China  
Simone Cinquemani , Italy  
Roberto G. Citarella , Italy  
Joaquim Ciurana , Spain  
John D. Clayton , USA  
Piero Colajanni , Italy  
Giuseppina Colicchio, Italy  
Vassilios Constantoudis , Greece  
Enrico Conte, Italy  
Alessandro Contento , USA  
Mario Cools , Belgium  
Gino Cortellessa, Italy  
Carlo Cosentino , Italy  
Paolo Crippa , Italy  
Erik Cuevas , Mexico  
Guozeng Cui , China  
Mehmet Cunkas , Turkey  
Giuseppe D'Aniello , Italy  
Peter Dabnichki, Australia  
Weizhong Dai , USA  
Zhifeng Dai , China  
Purushothaman Damodaran , USA  
Sergey Dashkovskiy, Germany  
Adiel T. De Almeida-Filho , Brazil  
Fabio De Angelis , Italy  
Samuele De Bartolo , Italy  
Stefano De Miranda , Italy  
Filippo De Monte , Italy



































José António Fonseca De Oliveira  
Correia , Portugal  
Jose Renato De Sousa , Brazil  
Michael Defoort, France  
Alessandro Della Corte, Italy  
Laurent Dewasme , Belgium  
Sanku Dey , India  
Gianpaolo Di Bona , Italy  
Roberta Di Pace , Italy  
Francesca Di Puccio , Italy  
Ramón I. Diego , Spain  
Yannis Dimakopoulos , Greece  
Hasan Dinçer , Turkey  
José M. Domínguez , Spain  
Georgios Dounias, Greece  
Bo Du , China  
Emil Dumic, Croatia  
Madalina Dumitriu , United Kingdom  
Premraj Durairaj , India  
Saeed Eftekhari Azam, USA  
Said El Kafhali , Morocco  
Antonio Elipse , Spain  
R. Emre Erkmen, Canada  
John Escobar , Colombia  
Leandro F. F. Miguel , Brazil  
FRANCESCO FOTI , Italy  
Andrea L. Facci , Italy  
Shahla Faisal , Pakistan  
Giovanni Falsone , Italy  
Hua Fan, China  
Jianguang Fang, Australia  
Nicholas Fantuzzi , Italy  
Muhammad Shahid Farid , Pakistan  
Hamed Faruqi, Iran  
Yann Favennec, France  
Fiorenzo A. Fazzolari , United Kingdom  
Giuseppe Fedele , Italy  
Roberto Fedele , Italy  
Baowei Feng , China  
Mohammad Ferdows , Bangladesh  
Arturo J. Fernández , Spain  
Jesus M. Fernandez Oro, Spain  
Francesco Ferrise, Italy  
Eric Feulvarch , France  
Thierry Floquet, France

Eric Florentin , France  
Gerardo Flores, Mexico  
Antonio Forcina , Italy  
Alessandro Formisano, Italy  
Francesco Franco , Italy  
Elisa Francomano , Italy  
Juan Frausto-Solis, Mexico  
Shujun Fu , China  
Juan C. G. Prada , Spain  
HECTOR GOMEZ , Chile  
Matteo Gaeta , Italy  
Mauro Gaggero , Italy  
Zoran Gajic , USA  
Jaime Gallardo-Alvarado , Mexico  
Mosè Gallo , Italy  
Akemi Gálvez , Spain  
Maria L. Gandarias , Spain  
Hao Gao , Hong Kong  
Xingbao Gao , China  
Yan Gao , China  
Zhiwei Gao , United Kingdom  
Giovanni Garcea , Italy  
José García , Chile  
Harish Garg , India  
Alessandro Gasparetto , Italy  
Stylianios Georgantzinou, Greece  
Fotios Georgiades , India  
Parviz Ghadimi , Iran  
Ştefan Cristian Gherghina , Romania  
Georgios I. Giannopoulos , Greece  
Agathoklis Giaralis , United Kingdom  
Anna M. Gil-Lafuente , Spain  
Ivan Giorgio , Italy  
Gaetano Giunta , Luxembourg  
Jefferson L.M.A. Gomes , United Kingdom  
Emilio Gómez-Déniz , Spain  
Antonio M. Gonçalves de Lima , Brazil  
Qunxi Gong , China  
Chris Goodrich, USA  
Rama S. R. Gorla, USA  
Veena Goswami , India  
Xunjie Gou , Spain  
Jakub Grabski , Poland














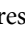











Antoine Grall , France  
George A. Gravvanis , Greece  
Fabrizio Greco , Italy  
David Greiner , Spain  
Jason Gu , Canada  
Federico Guarracino , Italy  
Michele Guida , Italy  
Muhammet Gul , Turkey  
Dong-Sheng Guo , China  
Hu Guo , China  
Zhaoxia Guo, China  
Yusuf Gurefe, Turkey  
Salim HEDDAM , Algeria  
ABID HUSSANAN, China  
Quang Phuc Ha, Australia  
Li Haitao , China  
Petr Hájek , Czech Republic  
Mohamed Hamdy , Egypt  
Muhammad Hamid , United Kingdom  
Renke Han , United Kingdom  
Weimin Han , USA  
Xingsi Han, China  
Zhen-Lai Han , China  
Thomas Hanne , Switzerland  
Xinan Hao , China  
Mohammad A. Hariri-Ardebili , USA  
Khalid Hattaf , Morocco  
Defeng He , China  
Xiao-Qiao He, China  
Yanchao He, China  
Yu-Ling He , China  
Ramdane Hedjar , Saudi Arabia  
Jude Hemanth , India  
Reza Hemmati, Iran  
Nicolae Herisanu , Romania  
Alfredo G. Hernández-Díaz , Spain  
M.I. Herreros , Spain  
Eckhard Hitzer , Japan  
Paul Honeine , France  
Jaromir Horacek , Czech Republic  
Lei Hou , China  
Yingkun Hou , China  
Yu-Chen Hu , Taiwan  
Yunfeng Hu, China  
Can Huang , China  
Gordon Huang , Canada  
Linsheng Huo , China  
Sajid Hussain, Canada  
Asier Ibeas , Spain  
Orest V. Iftime , The Netherlands  
Przemyslaw Ignaciuk , Poland  
Giacomo Innocenti , Italy  
Emilio Insfran Pelozo , Spain  
Azeem Irshad, Pakistan  
Alessio Ishizaka, France  
Benjamin Ivorra , Spain  
Breno Jacob , Brazil  
Reema Jain , India  
Tushar Jain , India  
Amin Jajarmi , Iran  
Chiranjibe Jana , India  
Łukasz Jankowski , Poland  
Samuel N. Jator , USA  
Juan Carlos Jáuregui-Correa , Mexico  
Kandasamy Jayakrishna, India  
Reza Jazar, Australia  
Khalide Jbilou, France  
Isabel S. Jesus , Portugal  
Chao Ji , China  
Qing-Chao Jiang , China  
Peng-fei Jiao , China  
Ricardo Fabricio Escobar Jiménez , Mexico  
Emilio Jiménez Macías , Spain  
Maolin Jin, Republic of Korea  
Zhuo Jin, Australia  
Ramash Kumar K , India  
BHABEN KALITA , USA  
MOHAMMAD REZA KHEDMATI , Iran  
Viacheslav Kalashnikov , Mexico  
Mathiyalagan Kalidass , India  
Tamas Kalmar-Nagy , Hungary  
Rajesh Kaluri , India  
Jyotheeswara Reddy Kalvakurthi, India  
Zhao Kang , China  
Ramani Kannan , Malaysia  
Tomasz Kapitaniak , Poland  
Julius Kaplunov, United Kingdom  
Konstantinos Karamanos, Belgium  
Michal Kawulok, Poland

Irfan Kaymaz , Turkey  
Vahid Kayvanfar , Qatar  
Krzysztof Kecik , Poland  
Mohamed Khader , Egypt  
Chaudry M. Khalique , South Africa  
Mukhtaj Khan , Pakistan  
Shahid Khan , Pakistan  
Nam-Il Kim, Republic of Korea  
Philipp V. Kiryukhantsev-Korneev ,  
Russia  
P.V.V Kishore , India  
Jan Koci , Czech Republic  
Ioannis Kostavelis , Greece  
Sotiris B. Kotsiantis , Greece  
Frederic Kratz , France  
Vamsi Krishna , India  
Edyta Kucharska, Poland  
Krzysztof S. Kulpa , Poland  
Kamal Kumar, India  
Prof. Ashwani Kumar , India  
Michal Kunicki , Poland  
Cedrick A. K. Kwuimy , USA  
Kyandoghere Kyamakya, Austria  
Ivan Kyrchei , Ukraine  
Márcio J. Lacerda , Brazil  
Eduardo Lalla , The Netherlands  
Giovanni Lancioni , Italy  
Jaroslaw Latalski , Poland  
Hervé Laurent , France  
Agostino Lauria , Italy  
Aimé Lay-Ekuakille , Italy  
Nicolas J. Leconte , France  
Kun-Chou Lee , Taiwan  
Dimitri Lefebvre , France  
Eric Lefevre , France  
Marek Lefik, Poland  
Yaguo Lei , China  
Kauko Leiviskä , Finland  
Ervin Lenzi , Brazil  
ChenFeng Li , China  
Jian Li , USA  
Jun Li , China  
Yueyang Li , China  
Zhao Li , China






























Zhen Li , China  
En-Qiang Lin, USA  
Jian Lin , China  
Qibin Lin, China  
Yao-Jin Lin, China  
Zhiyun Lin , China  
Bin Liu , China  
Bo Liu , China  
Heng Liu , China  
Jianxu Liu , Thailand  
Lei Liu , China  
Sixin Liu , China  
Wanquan Liu , China  
Yu Liu , China  
Yuanchang Liu , United Kingdom  
Bonifacio Llamazares , Spain  
Alessandro Lo Schiavo , Italy  
Jean Jacques Loiseau , France  
Francesco Lolli , Italy  
Paolo Lonetti , Italy  
António M. Lopes , Portugal  
Sebastian López, Spain  
Luis M. López-Ochoa , Spain  
Vassilios C. Loukopoulos, Greece  
Gabriele Maria Lozito , Italy  
Zhiguo Luo , China  
Gabriel Luque , Spain  
Valentin Lychagin, Norway  
YUE MEI, China  
Junwei Ma , China  
Xuanlong Ma , China  
Antonio Madeo , Italy  
Alessandro Magnani , Belgium  
Toqeer Mahmood , Pakistan  
Fazal M. Mahomed , South Africa  
Arunava Majumder , India  
Sarfranz Nawaz Malik, Pakistan  
Paolo Manfredi , Italy  
Adnan Maqsood , Pakistan  
Muazzam Maqsood, Pakistan  
Giuseppe Carlo Marano , Italy  
Damijan Markovic, France  
Filipe J. Marques , Portugal  
Luca Martinelli , Italy  
Denizar Cruz Martins, Brazil

Francisco J. Martos , Spain  
Elio Masciari , Italy  
Paolo Massioni , France  
Alessandro Mauro , Italy  
Jonathan Mayo-Maldonado , Mexico  
Pier Luigi Mazzeo , Italy  
Laura Mazzola, Italy  
Driss Mehdi , France  
Zahid Mehmood , Pakistan  
Roderick Melnik , Canada  
Xiangyu Meng , USA  
Jose Merodio , Spain  
Alessio Merola , Italy  
Mahmoud Mesbah , Iran  
Luciano Mescia , Italy  
Laurent Mevel , France  
Constantine Michailides , Cyprus  
Mariusz Michta , Poland  
Prankul Middha, Norway  
Aki Mikkola , Finland  
Giovanni Minafò , Italy  
Edmondo Minisci , United Kingdom  
Hiroyuki Mino , Japan  
Dimitrios Mitsotakis , New Zealand  
Ardashir Mohammadzadeh , Iran  
Francisco J. Montáns , Spain  
Francesco Montefusco , Italy  
Gisele Mophou , France  
Rafael Morales , Spain  
Marco Morandini , Italy  
Javier Moreno-Valenzuela , Mexico  
Simone Morganti , Italy  
Caroline Mota , Brazil  
Aziz Moukrim , France  
Shen Mouquan , China  
Dimitris Mourtzis , Greece  
Emiliano Mucchi , Italy  
Taseer Muhammad, Saudi Arabia  
Ghulam Muhiuddin, Saudi Arabia  
Amitava Mukherjee , India  
Josefa Mula , Spain  
Jose J. Muñoz , Spain  
Giuseppe Muscolino, Italy  
Marco Mussetta , Italy

Hariharan Muthusamy, India  
Alessandro Naddeo , Italy  
Raj Nandkeolyar, India  
Keivan Navaie , United Kingdom  
Soumya Nayak, India  
Adrian Neagu , USA  
Erivelton Geraldo Nepomuceno , Brazil  
AMA Neves, Portugal  
Ha Quang Thinh Ngo , Vietnam  
Nhon Nguyen-Thanh, Singapore  
Papakostas Nikolaos , Ireland  
Jelena Nikolic , Serbia  
Tatsushi Nishi, Japan  
Shanzhou Niu , China  
Ben T. Nohara , Japan  
Mohammed Nouari , France  
Mustapha Nourelfath, Canada  
Kazem Nouri , Iran  
Ciro Núñez-Gutiérrez , Mexico  
Włodzimierz Ogryczak, Poland  
Roger Ohayon, France  
Krzysztof Okarma , Poland  
Mitsuhiro Okayasu, Japan  
Murat Olgun , Turkey  
Diego Oliva, Mexico  
Alberto Olivares , Spain  
Enrique Onieva , Spain  
Calogero Orlando , Italy  
Susana Ortega-Cisneros , Mexico  
Sergio Ortobelli, Italy  
Naohisa Otsuka , Japan  
Sid Ahmed Ould Ahmed Mahmoud , Saudi Arabia  
Taoreed Owolabi , Nigeria  
EUGENIA PETROPOULOU , Greece  
Arturo Pagano, Italy  
Madhumangal Pal, India  
Pasquale Palumbo , Italy  
Dragan Pamučar, Serbia  
Weifeng Pan , China  
Chandan Pandey, India  
Rui Pang, United Kingdom  
Jürgen Pannek , Germany  
Elena Panteley, France  
Achille Paolone, Italy

George A. Papakostas , Greece  
Xosé M. Pardo , Spain  
You-Jin Park, Taiwan  
Manuel Pastor, Spain  
Pubudu N. Pathirana , Australia  
Surajit Kumar Paul , India  
Luis Payá , Spain  
Igor Pažanin , Croatia  
Libor Pekař , Czech Republic  
Francesco Pellicano , Italy  
Marcello Pellicciari , Italy  
Jian Peng , China  
Mingshu Peng, China  
Xiang Peng , China  
Xindong Peng, China  
Yuexing Peng, China  
Marzio Pennisi , Italy  
Maria Patrizia Pera , Italy  
Matjaz Perc , Slovenia  
A. M. Bastos Pereira , Portugal  
Wesley Peres, Brazil  
F. Javier Pérez-Pinal , Mexico  
Michele Perrella, Italy  
Francesco Pesavento , Italy  
Francesco Petrini , Italy  
Hoang Vu Phan, Republic of Korea  
Lukasz Pieczonka , Poland  
Dario Piga , Switzerland  
Marco Pizzarelli , Italy  
Javier Plaza , Spain  
Goutam Pohit , India  
Dragan Poljak , Croatia  
Jorge Pomares , Spain  
Hiram Ponce , Mexico  
Sébastien Poncet , Canada  
Volodymyr Ponomaryov , Mexico  
Jean-Christophe Ponsart , France  
Mauro Pontani , Italy  
Sivakumar Poruran, India  
Francesc Pozo , Spain  
Aditya Rio Prabowo , Indonesia  
Anchasa Pramuanjaroenkij , Thailand  
Leonardo Primavera , Italy  
B Rajanarayan Prusty, India

Krzysztof Puszynski , Poland  
Chuan Qin , China  
Dongdong Qin, China  
Jianlong Qiu , China  
Giuseppe Quaranta , Italy  
DR. RITU RAJ , India  
Vitomir Racic , Italy  
Carlo Rainieri , Italy  
Kumbakonam Ramamani Rajagopal, USA  
Ali Ramazani , USA  
Angel Manuel Ramos , Spain  
Higinio Ramos , Spain  
Muhammad Afzal Rana , Pakistan  
Muhammad Rashid, Saudi Arabia  
Manoj Rastogi, India  
Alessandro Rasulo , Italy  
S.S. Ravindran , USA  
Abdolrahman Razani , Iran  
Alessandro Reali , Italy  
Jose A. Reinoso , Spain  
Oscar Reinoso , Spain  
Haijun Ren , China  
Carlo Renno , Italy  
Fabrizio Renno , Italy  
Shahram Rezapour , Iran  
Ricardo Rianza , Spain  
Francesco Riganti-Fulginei , Italy  
Gerasimos Rigatos , Greece  
Francesco Ripamonti , Italy  
Jorge Rivera , Mexico  
Eugenio Roanes-Lozano , Spain  
Ana Maria A. C. Rocha , Portugal  
Luigi Rodino , Italy  
Francisco Rodríguez , Spain  
Rosana Rodríguez López, Spain  
Francisco Rossomando , Argentina  
Jose de Jesus Rubio , Mexico  
Weiguo Rui , China  
Rubén Ruiz , Spain  
Ivan D. Rukhlenko , Australia  
Dr. Eswaramoorthi S. , India  
Weichao SHI , United Kingdom  
Chaman Lal Sabharwal , USA  
Andrés Sáez , Spain

Bekir Sahin, Turkey  
Laxminarayan Sahoo , India  
John S. Sakellariou , Greece  
Michael Sakellariou , Greece  
Salvatore Salamone, USA  
Jose Vicente Salcedo , Spain  
Alejandro Salcido , Mexico  
Alejandro Salcido, Mexico  
Nunzio Salerno , Italy  
Rohit Salgotra , India  
Miguel A. Salido , Spain  
Sinan Salih , Iraq  
Alessandro Salvini , Italy  
Abdus Samad , India  
Sovan Samanta, India  
Nikolaos Samaras , Greece  
Ramon Sancibrian , Spain  
Giuseppe Sanfilippo , Italy  
Omar-Jacobo Santos, Mexico  
J Santos-Reyes , Mexico  
José A. Sanz-Herrera , Spain  
Musavarah Sarwar, Pakistan  
Shahzad Sarwar, Saudi Arabia  
Marcelo A. Savi , Brazil  
Andrey V. Savkin, Australia  
Tadeusz Sawik , Poland  
Roberta Sburlati, Italy  
Gustavo Scaglia , Argentina  
Thomas Schuster , Germany  
Hamid M. Sedighi , Iran  
Mijanur Rahaman Seikh, India  
Tapan Senapati , China  
Lotfi Senhadji , France  
Junwon Seo, USA  
Michele Serpilli, Italy  
Silvestar Šesnić , Croatia  
Gerardo Severino, Italy  
Ruben Sevilla , United Kingdom  
Stefano Sfarra , Italy  
Dr. Ismail Shah , Pakistan  
Leonid Shaikhet , Israel  
Vimal Shanmuganathan , India  
Prayas Sharma, India  
Bo Shen , Germany  
Hang Shen, China

Xin Pu Shen, China  
Dimitri O. Shepelsky, Ukraine  
Jian Shi , China  
Amin Shokrollahi, Australia  
Suzanne M. Shontz , USA  
Babak Shotorban , USA  
Zhan Shu , Canada  
Angelo Sifaleras , Greece  
Nuno Simões , Portugal  
Mehakpreet Singh , Ireland  
Piyush Pratap Singh , India  
Rajiv Singh, India  
Seralathan Sivamani , India  
S. Sivasankaran , Malaysia  
Christos H. Skiadas, Greece  
Konstantina Skouri , Greece  
Neale R. Smith , Mexico  
Bogdan Smolka, Poland  
Delfim Soares Jr. , Brazil  
Alba Sofi , Italy  
Francesco Soldovieri , Italy  
Raffaele Solimene , Italy  
Yang Song , Norway  
Jussi Sopanen , Finland  
Marco Spadini , Italy  
Paolo Spagnolo , Italy  
Ruben Specogna , Italy  
Vasilios Spitas , Greece  
Ivanka Stamova , USA  
Rafał Stanisławski , Poland  
Miladin Stefanović , Serbia  
Salvatore Strano , Italy  
Yakov Strelniker, Israel  
Kangkang Sun , China  
Qiuqin Sun , China  
Shuaishuai Sun, Australia  
Yanchao Sun , China  
Zong-Yao Sun , China  
Kumarasamy Suresh , India  
Sergey A. Suslov , Australia  
D.L. Suthar, Ethiopia  
D.L. Suthar , Ethiopia  
Andrzej Swierniak, Poland  
Andras Szekrenyes , Hungary  
Kumar K. Tamma, USA





Yong (Aaron) Tan, United Kingdom  
Marco Antonio Taneco-Hernández , Mexico  
Lu Tang , China  
Tianyou Tao, China  
Hafez Tari , USA  
Alessandro Tasora , Italy  
Sergio Teggi , Italy  
Adriana del Carmen Téllez-Anguiano , Mexico  
Ana C. Teodoro , Portugal  
Efstathios E. Theotokoglou , Greece  
Jing-Feng Tian, China  
Alexander Timokha , Norway  
Stefania Tomasiello , Italy  
Gisella Tomasini , Italy  
Isabella Torcicollo , Italy  
Francesco Tornabene , Italy  
Mariano Torrisi , Italy  
Thang nguyen Trung, Vietnam  
George Tsiatas , Greece  
Le Anh Tuan , Vietnam  
Nerio Tullini , Italy  
Emilio Turco , Italy  
Ilhan Tuzcu , USA  
Efstratios Tzirtzilakis , Greece  
FRANCISCO UREÑA , Spain  
Filippo Ubertini , Italy  
Mohammad Uddin , Australia  
Mohammad Safi Ullah , Bangladesh  
Serdar Ulubeyli , Turkey  
Mati Ur Rahman , Pakistan  
Panayiotis Vafeas , Greece  
Giuseppe Vairo , Italy  
Jesus Valdez-Resendiz , Mexico  
Eusebio Valero, Spain  
Stefano Valvano , Italy  
Carlos-Renato Vázquez , Mexico  
Martin Velasco Villa , Mexico  
Franck J. Vernerey, USA  
Georgios Veronis , USA  
Vincenzo Vespri , Italy  
Renato Vidoni , Italy  
Venkatesh Vijayaraghavan, Australia

Anna Vila, Spain  
Francisco R. Villatoro , Spain  
Francesca Vipiana , Italy  
Stanislav Vitek , Czech Republic  
Jan Vorel , Czech Republic  
Michael Vynnycky , Sweden  
Mohammad W. Alomari, Jordan  
Roman Wan-Wendner , Austria  
Bingchang Wang, China  
C. H. Wang , Taiwan  
Dagang Wang, China  
Guoqiang Wang , China  
Huaiyu Wang, China  
Hui Wang , China  
J.G. Wang, China  
Ji Wang , China  
Kang-Jia Wang , China  
Lei Wang , China  
Qiang Wang, China  
Qingling Wang , China  
Weiwei Wang , China  
Xinyu Wang , China  
Yong Wang , China  
Yung-Chung Wang , Taiwan  
Zhenbo Wang , USA  
Zhibo Wang, China  
Waldemar T. Wójcik, Poland  
Chi Wu , Australia  
Qihong Wu, China  
Yuqiang Wu, China  
Zhibin Wu , China  
Zhizheng Wu , China  
Michalis Xenos , Greece  
Hao Xiao , China  
Xiao Ping Xie , China  
Qingzheng Xu , China  
Binghan Xue , China  
Yi Xue , China  
Joseph J. Yame , France  
Chuanliang Yan , China  
Xinggang Yan , United Kingdom  
Hongtai Yang , China  
Jixiang Yang , China  
Mijia Yang, USA  
Ray-Yeng Yang, Taiwan

Zaoli Yang , China  
Jun Ye , China  
Min Ye , China  
Luis J. Yebra , Spain  
Peng-Yeng Yin , Taiwan  
Muhammad Haroon Yousaf , Pakistan  
Yuan Yuan, United Kingdom  
Qin Yuming, China  
Elena Zaitseva , Slovakia  
Arkadiusz Zak , Poland  
Mohammad Zakwan , India  
Ernesto Zambrano-Serrano , Mexico  
Francesco Zammori , Italy  
Jessica Zangari , Italy  
Rafal Zdunek , Poland  
Ibrahim Zeid, USA  
Nianyin Zeng , China  
Junyong Zhai , China  
Hao Zhang , China  
Haopeng Zhang , USA  
Jian Zhang , China  
Kai Zhang, China  
Lingfan Zhang , China  
Mingjie Zhang , Norway  
Qian Zhang , China  
Tianwei Zhang , China  
Tongqian Zhang , China  
Wenyu Zhang , China  
Xianming Zhang , Australia  
Xuping Zhang , Denmark  
Yinyan Zhang, China  
Yifan Zhao , United Kingdom  
Debao Zhou, USA  
Heng Zhou , China  
Jian G. Zhou , United Kingdom  
Junyong Zhou , China  
Xueqian Zhou , United Kingdom  
Zhe Zhou , China  
Wu-Le Zhu, China  
Gaetano Zizzo , Italy  
Mingcheng Zuo, China

# Contents

## **Formation Tracking for Nonaffine Nonlinear Multiagent Systems Using Neural Network Adaptive Control**

Tongjuan Zhao , Jiuhe Wang , and Jianhua Zhang 





Research Article (8 pages), Article ID 3697476, Volume 2020 (2020)

## **Modeling and Optimization for Fault Diagnosis of Electromechanical Systems Based on Zero Crossing Algorithm**

Qing Chen , Tao Liu , Xing Wu, and Hua Li



Research Article (13 pages), Article ID 9267838, Volume 2020 (2020)

## **Prediction of Suspect Activity Trajectory in Food Safety Area Based on Multiple U-Model Algorithm**

Kang Wang , Kun Bu , Yipeng Zhang , and Xiaoli Li 




Research Article (11 pages), Article ID 9196173, Volume 2020 (2020)

## **Finite Time Output Feedback Attitude Tracking Control for Rigid Body Based on Extended State Observer**

Meng Duan , and Yingmin Jia 






Research Article (12 pages), Article ID 6285912, Volume 2020 (2020)

## **Human Action Recognition Algorithm Based on Improved ResNet and Skeletal Keypoints in Single Image**

Yixue Lin , Wanda Chi, Wenxue Sun, Shicai Liu , and Di Fan 



Research Article (12 pages), Article ID 6954174, Volume 2020 (2020)

## **A Person Reidentification Algorithm Based on Improved Siamese Network and Hard Sample**

Guangcai Wang , Shiqi Wang , Wanda Chi , Shicai Liu , and Di Fan 



Research Article (11 pages), Article ID 3731848, Volume 2020 (2020)

## **Linearization Method of Nonlinear Magnetic Levitation System**

Dini Wang , Fanwei Meng , and Shengya Meng


Research Article (5 pages), Article ID 9873651, Volume 2020 (2020)

## **U-Model-Based Active Disturbance Rejection Control for the Dissolved Oxygen in a Wastewater Treatment Process**

Wei Wei , Nan Chen, Zhiyuan Zhang, Zaiwen Liu, and Min Zuo 



Research Article (14 pages), Article ID 3507910, Volume 2020 (2020)

## **Design and Verification of Aeroengine Rotor Speed Controller Based on U-LADRC**

Jiajie Chen, Jiqiang Wang , Yunxiao Liu, and Zhongzhi Hu


Research Article (12 pages), Article ID 6798492, Volume 2020 (2020)

## **Design and Control of a Novel Single Leg Structure of Electrically Driven Quadruped Robot**

Mingfang Chen , Hao Chen, Xuejun Wang , JiangXuan Yu, and YongXia Zhang

Research Article (12 pages), Article ID 3943867, Volume 2020 (2020)

### **Trajectory Tracking Control of Robot Manipulators Based on U-Model**

Xianghua Ma , Yang Zhao, and Yiqun Di



Research Article (10 pages), Article ID 8314202, Volume 2020 (2020)

### **Adaptive Predefined Performance Neural Control for Robotic Manipulators with Unknown Dead Zone**

Shifen Shao, Kaisheng Zhang , Jun Li, and Jirong Wang

Research Article (8 pages), Article ID 6490167, Volume 2020 (2020)

### **A Genetic Optimization Algorithm Based on Adaptive Dimensionality Reduction**

Tai Kuang , Zhongyi Hu , and Minghai Xu



Research Article (7 pages), Article ID 8598543, Volume 2020 (2020)

### **Single-Phase Reactive Power Compensation Control for STATCOMs via Unknown System Dynamics Estimation**

Cheng Guo , Linzhen Zhong , Jun Zhao , and Guanbin Gao 


Research Article (9 pages), Article ID 8394513, Volume 2020 (2020)

### **U-Model-Based Sliding Mode Controller Design for Quadrotor UAV Control Systems**

Rui Wang , Lei Gao, Chengrui Bai, and Hui Sun 

Research Article (11 pages), Article ID 4343214, Volume 2020 (2020)

### **An Output Force Control for Robotic Manipulator by Changing the Spring Stiffness**

Jirong Wang, Yuhang Zheng , Jun Li, Cheng Liu, Youliang Huang, and Yu Liu

Research Article (10 pages), Article ID 1489076, Volume 2020 (2020)

### **A Stochastic Differential Equation Driven by Poisson Random Measure and Its Application in a Duopoly Market**

Tong Wang  and Hao Liang

Research Article (12 pages), Article ID 3256859, Volume 2020 (2020)

### **Adaptive Vector Nonsingular Terminal Sliding Mode Control for a Class of n-Order Nonlinear Dynamical Systems with Uncertainty**

Nannan Shi , Zhikuan Kang , Zhuo Zhao , and Qiang Meng 


Research Article (12 pages), Article ID 7309417, Volume 2020 (2020)

### **U-Model Based Adaptive Neural Networks Fixed-Time Backstepping Control for Uncertain Nonlinear System**

Jianhua Zhang , Yang Li , Wenbo Fei , and Xueli Wu 

Research Article (7 pages), Article ID 8302627, Volume 2020 (2020)

### **Mathematical Modeling and Dynamic Analysis of Planetary Gears System with Time-Varying Parameters**


Zhengming Xiao , Jinxin Cao, and Yinxin Yu

Research Article (9 pages), Article ID 3185624, Volume 2020 (2020)

## Contents

---

**Modeling of Coupling Mechanism between Ballast Bed and Track Structure of High-Speed Railway**

Xuejun Wang, Jianghua Pu, Peng Wu, and Mingfang Chen 

Research Article (12 pages), Article ID 9768904, Volume 2020 (2020)

**U-Model-Based Finite-Time Control for Nonlinear Valve-Controlled Hydraulic Servosystem**

Hao Yan , Jiafeng Li , Hassan Nouri, and Lingling Xu

Research Article (12 pages), Article ID 7083639, Volume 2020 (2020)

**Echo State Network for Extended State Observer and Sliding Mode Control of Vehicle Drive Motor with Unknown Hysteresis Nonlinearity**

Xuehui Gao , Bo Sun , Xinyan Hu, and Kun Zhu

Research Article (13 pages), Article ID 2534038, Volume 2020 (2020)



## Research Article

# Formation Tracking for Nonaffine Nonlinear Multiagent Systems Using Neural Network Adaptive Control

Tongjuan Zhao <sup>1,2</sup>, Jiuhue Wang <sup>1</sup>, and Jianhua Zhang <sup>3</sup>

<sup>1</sup>Yanshan University, Qinhuangdao, Hebei 066004, China

<sup>2</sup>Qinhuangdao Vocational and Technical College, Qinhuangdao, Hebei 066100, China

<sup>3</sup>School of Information and Control Engineering, Qingdao University of Technology, Qingdao, Shandong 266525, China

Correspondence should be addressed to Jianhua Zhang; [jianhuazhang@aliyun.com](mailto:jianhuazhang@aliyun.com)

Received 8 May 2020; Revised 29 September 2020; Accepted 13 October 2020; Published 26 October 2020

Academic Editor: Olfa Boubaker

Copyright © 2020 Tongjuan Zhao et al. This is an open access article distributed under the Creative Commons Attribution License, which permits unrestricted use, distribution, and reproduction in any medium, provided the original work is properly cited.

Adaptive tracking control for distributed multiagent systems in nonaffine form is considered in this paper. Each follower agent is modeled by a nonlinear pure-feedback system with nonaffine form, and a nonlinear system is unknown functions rather than constants. Radial basis function neural networks (NNs) are employed to approximate the unknown nonlinear functions, and weights of NNs are updated by adaptive law in finite-time form. Then, the adaptive finite NN approach and backstepping technology are combined to construct the consensus tracking control protocol. Numerical simulation is presented to demonstrate the efficacy of suggested control proposal.

## 1. Introduction

Due to the limitations of a single agent in completing some special tasks and the needs of human society, the multiagent system has received extensive attention from the academic engineering community. In recent years, distributed information processing technology has been widely used, such as urban transportation [1], intelligent robots [2], flexible manufacturing [3], and coordinated expert systems [4] due to higher fault tolerance and reliability. It has attracted the attention of experts and scholars in different fields such as artificial intelligence and control engineering.

In the 1980s, multiagent systems were researched and applied, and in recent years, it has become one of the hot spots in the field of artificial intelligence. For multiagent systems, the consensus problem is the most basic control problem; see a large number of academic papers [5–7]. The key to consensus is to design a reasonable consensus protocol to ensure that the multiagent system is consistent. Scholars have further explored multiagent systems with different structures, such as directed topography and undirected topography [8–10]. However, it is difficult to avoid the interference factors of uncertainty, thus applying robust

consensus control [11–13]. In recent years, due to the inevitable interference factors, the robust consensus problem has received widespread attention and received widespread attention. In [14], the robust consensus control of the Laplacian matrix uncertainty multiagent system is studied, and the conditions for achieving state consensus are proposed. In [15], the robust consensus of linear multiagents with random switching topology was studied. In [16], the second-order robustness of nonlinear multiagents with extended state observers is studied. In [17], scholars studied the distributed robust adaptive consensus control of uncertain nonlinear fractional multiagent systems. As we all know, finite-time convergence is a topic that has attracted much attention and is of great significance. Therefore, some scholars have raised the problem of finite-time consensus [18–20]. Some scholars consider the issue of fixed-time consensus.

In recent years, consensus-tracking problem of distributed multiagent systems has broad applications in many areas, such as formation control, flocking, cooperative control of UAV, and distributed sensor networks [21, 22]. Formation tracking control originated from various natural phenomena, such as flocking in birds, fish, and so on. There

exist some kinds of consensus problems of multiagent systems, because sometimes it is needed that all agents agree on some desired quantity of interest, sometimes not. In the leader follower multiagent systems, consensus means that all the follower agents reach the leader values in a finite time [23, 24].

Recently, finite-time stability has received much attention due to its efficient performance in many areas [25, 26]. Especial neural networks control is a powerful control method, because neural networks can approximate nonlinear system without model [27, 28]. Though Lyapunov uniformly ultimately bounded (UUB) results solve some nonlinear system control problem, both bounded and exponential convergence speed cause confusion. It should be noted that the research on finite-time neural network control is still in a very beginning stage. The key issue is how to systematically obtain finite-time adaptive law of neural network weight from finite-time convergence of closed-loop systems. In regarding to such neural network-based adaptive control to the authors' best knowledge, there are a few results about finite-time adaptive neural network control because it is not easy to design the finite-time neural network adaptive controller, and there exists lack of relevant inequality skills to finish finite-time stability analysis. There has been any reference to show finite-time adaptive algorithm for weights of NNs having been expanded to solve the problems of finite control for pure-feedback nonaffine nonlinear systems.

The remainder of this paper is organized as follows. The multiagent system is described in Section 2. The proposed algorithms for formation tracking, based on the finite-time adaptive control, are presented in Section 3. Theoretical analysis of the model is given in Section 4. Simulation results are given in Section 5. Finally, conclusions are drawn in Section 6.

## 2. Problem Description

**2.1. System Description.** Consider a class of the nonlinear pure-feedback multiagent system, composed of  $N$  follower agents (labeled from 1 to  $N$ ), and a leader (labeled  $d$ ). The communication topology of followers are described by a digraph  $G$ . The dynamic model of the  $i$ th ( $i = 1, 2, \dots, N$ ) follower is

$$\begin{cases} \dot{x}_{i,k} = f_{i,k}(\bar{x}_{i,k+1}), & 1 \leq k \leq n_i - 1, \\ \dot{x}_{i,n_i} = f_{i,n_i}(\bar{x}_{i,n_i}, u_i), \\ y_i = x_{i,1}, \end{cases} \quad (1)$$

where  $\bar{x}_{i,j} = [x_{i,1}, x_{i,2}, \dots, x_{i,j}]^T \in \mathfrak{R}^j$ ,  $\bar{x}_{i,n_i} = [x_{i,1}, x_{i,2}, \dots, x_{i,n_i}]^T \in \mathfrak{R}^{n_i}$  is the entire state variables of the  $i$ th agent,  $u_i \in \mathfrak{R}$ ,  $y_i \in \mathfrak{R}$ ,  $\varphi_i(t)$  indicate the state, control, output, and initial condition, respectively, and,  $f_{i,k}(\cdot)$  are nonlinear smooth functions.

**2.2. Algebraic Graph Theory.** A directed graph is represented by  $G = (V, E)$  with  $E \subseteq V \times V$  denoting edge set and  $V = \{v_1, v_2, \dots, v_k\}$  is the node set. An edge  $e_{ji} = (v_j, v_i) \in E$  of the graph  $G$  means that  $i$  can get messages from  $j$ ;

meanwhile, it is also said that the agent  $j$  is one of agent  $i$ 's neighbors, not vice versa.

Hence, the agent  $i$ 's neighbor set is  $N_i = \{v_j | (v_j, v_i) \in E\}$ . When weight of edges is considered, the graph is said to be a weighted graph.  $A = [a_{ij}] \in \mathfrak{R}^{k \times k}$  (adjacency matrix) is often used to express the graphic topology. For the element  $a_{ij}$ , it is defined that  $a_{ij} > 0$  if  $e_{ji} = (v_j, v_i) \in E$ , otherwise,  $a_{ij} = 0$ . Self-loop is not considered as usual, i.e.,  $a_{ii} = 0$ , and  $D = \text{diag}(d_1, d_2, \dots, d_k) \in \mathfrak{R}^{k \times k}$  is defined as an in-degree matrix, where  $d_i = \sum_{j=1}^k a_{ij}$  of  $D$  is in-degree for agent  $i$ . The row sum of Laplacian matrix  $L = D - A$  is 0 and  $L1 = 0$ . A directed graph is said to have direct path means that there exists an edge sequence in the form of  $\{(v_i, v_r), (v_r, v_s), \dots, (v_t, v_j)\}$ . When there exists at least one agent (root) in the digraph which can transmit information through direct path to all other agents, the direct graph is thus said to include a directed spanning tree. The local tracking error for agent  $i$  can be described as

$$z_{i,1} = \sum_{j=1}^N a_{ij}(y_i - y_j) + b_i(y_i - y_d), \quad (2)$$

where  $i = 1, 2, \dots, N$ , the pinning gain  $b_i \geq 0$ , where  $b_i > 0$  denotes the weight between the  $i$ th agent and leader agent.

**2.3. Radial Basis Function Neural Networks (RBFNNs) and Function Approximation.** In brief, the following radial basis function (RBF) NN is used to approximate the continuous function  $F(x): \mathfrak{R}^n \rightarrow \mathfrak{R}$  over a compact set

$$F_{NN}(x, W) = W^T \Psi(x), \quad (3)$$

where input  $x \in \Omega \subset \mathfrak{R}^n$ , weight vector  $W = [w_1 \dots w_l]^T \in \mathfrak{R}^l$ , and node vector  $\Psi(x) = [\psi_1(x) \dots \psi_l(x)]^T$ , in which the element  $\psi_i(x)$  is being chosen as the commonly used Gaussian function as follows:

$$\psi_i(x) = \exp\left[\frac{-(x - \mu_i)^T(x - \mu_i)}{\eta_i^2}\right], \quad i = 1, 2, \dots, l, \quad (4)$$

where  $\mu_i = [\mu_{i1} \dots \mu_{in}]^T$  is the center of the receptive field and  $\eta_i$  is the width of the Gaussian function.

It has been proven that RBF NN can approximate any continuous function over a compact set  $\Omega_x \subset \mathfrak{R}^n$  as

$$F(x) = W^{*T} \Psi(x) + \varepsilon(x), \quad (5)$$

where  $W^*$  is the ideal NN weight and  $\varepsilon(x)$  is the NN approximation error:

$$W^* = \arg \min_{W \in \mathfrak{R}^l} \left\{ \sup_{x \in \mathfrak{R}^n} |F(x) - W^T \Psi(x)| \right\}. \quad (6)$$

Notation: throughout this paper,  $W \in \mathfrak{R}^{m \times n}$  represents the matrix,  $W^*$ ,  $\tilde{W}$ ,  $\tilde{W}$  indicate ideal weight, estimated weight, and error between ideal and estimated weight. Throughout this paper,  $W \in \mathfrak{R}^{m \times n}$  represents the matrix,  $W = [w_{ij}]_{m \times n}$ , rational number  $\eta$  and matrix, matrix  $W^\eta$  denote element-by-element powers  $W^\eta = [w_{ij}^\eta]_{m \times n}$ , and  $\tilde{W}^{\eta T}$  denote the transposition of matrix  $\tilde{W}^\eta$ , such as

$\tilde{W}^{\eta T} = (\tilde{W}^\eta)^T$ .  $W^*$ ,  $W$ ,  $\tilde{W}$  indicate ideal weight, estimated weight, and error between ideal and estimated weight.

**Definition 1.** Consider the system  $\dot{x} = f(x, u)$ , where  $x$  is a state vector and  $u$  is the input vector. The solution is practical finite stable (PFS) if for all  $x(t_0) = x_0$ , there exists  $\varepsilon > 0$  and  $T(\varepsilon, x_0) < \infty$ , such that  $\|x\| < \varepsilon$ , for all  $t \geq t_0 + T$ .

**Lemma 1.** Consider the system  $\dot{x} = f(x, u)$ , and suppose that there exist continuous function  $V(x)$ , scalars  $\lambda > 0, 0 < \alpha < 1$ , and  $0 < \eta < \infty$  such that

$$\dot{V}(x) \leq -\lambda V^\alpha(x) + \eta. \quad (7)$$

Then, the trajectory of the system  $\dot{x} = f(x, u)$  is PFS.

**Lemma 2.** Young's inequality: for any constant  $a, b \in \mathfrak{R}$ , the following inequality holds:

$$ab \leq \frac{1}{p}a^p + \frac{1}{q}b^q. \quad (8)$$

where  $p > 1, q > 1$ , and  $(1/p) + (1/q) = 1$ .

**Remark 1.** Based on Young's inequality, then the following inequalities hold:

$$\left( \sum_{j=1}^N a_{ij} + b_i \right) f_{i,1}(\bar{x}_{i,2}) - \sum_{j=1}^N a_{ij} f_{j,2}(\bar{x}_{j,2}) - b_i f_d(x_d, t) = W_{i,1}^{T*} \Psi_1(Z_2) + \varepsilon_{i,1}. \quad (12)$$

Therefore,

$$\dot{z}_{i,1} = W_{i,1}^{*T} \Psi_1(Z_2) + \varepsilon_{i,1}. \quad (13)$$

Choose the practical virtual control law

$$\alpha_{i,1} = -k_{i,1} z_{i,1}^{1/3} + x_{i,2} - \hat{W}_{i,1}^T \Psi_1(Z_2). \quad (14)$$

Choose the adaptive law

$$\dot{\hat{W}}_{i,1} = \Gamma_{i,1} \left[ z_{i,1} \Psi_1(Z_2) - \sigma_{i,1} \hat{W}_{i,1}^{1/3} \right], \quad (15)$$

where  $\Gamma_{i,1} = \Gamma_{i,1}^T > 0$ , and  $\sigma_{i,1} > 0$  is positive constant design parameters.

Then, based on (12) and (13),

$$\dot{z}_{i,1} = W_{i,1}^{*T} \Psi_1(Z_2) + \varepsilon_{i,1} - k_{i,1} z_{i,1}^{1/3} + x_{i,2} - \alpha_{i,1} - \hat{W}_{i,1}^T \Psi_1(Z_2). \quad (16)$$

Let

$$z\varepsilon \leq \frac{3}{4}z^{4/3} + \frac{1}{4}\varepsilon^4, \quad (9)$$

$$-\tilde{W}^T \tilde{W}^{1/3} \leq -\frac{1}{2} \tilde{W}^{(2/3)T} \tilde{W}^{2/3} + W^{*(2/3)T} W^{*(2/3)}.$$

### 3. Distributed Adaptive Tracking Controller Design

Consider system (1) and tracking error (2), and define

$$\begin{aligned} z_{i,k} &= x_{i,k} - \alpha_{i,k-1}, \quad k = 2, 3, \dots, n_i, \\ z_{i,n_i+1} &= u_i - \alpha_{i,n_i}, \end{aligned} \quad (10)$$

where  $\alpha_{i,j}$ , ( $2 \leq j \leq n_i$ ) is the virtual control; in the first step, consider the system  $z_{i,1}$ .

Then, it has

$$\begin{aligned} \dot{z}_{i,1} &= \left( \sum_{j=1}^N a_{ij} + b_i \right) \dot{x}_{i,1} - \sum_{j=1}^N a_{ij} \dot{x}_{j,1} - b_i f_d(x_d, t) \\ &= \left( \sum_{j=1}^N a_{ij} + b_i \right) f_{i,1}(\bar{x}_{i,2}) - \sum_{j=1}^N a_{ij} f_{j,2}(\bar{x}_{j,2}) - b_i f_d(x_d, t). \end{aligned} \quad (11)$$

Base on ideal virtual control law, and choose the NNs to approximate the nonlinear system

$$z_{i,2} = x_{i,2} - \alpha_{i,1}. \quad (17)$$

Therefore,

$$\dot{z}_{i,1} = -\tilde{W}_{i,1}^T \Psi_1(Z_2) - k_{i,1} z_{i,1}^{1/3} + z_{i,2} + \varepsilon_{i,1}, \quad (18)$$

where

$$\tilde{W}_{i,1} = \hat{W}_{i,1} - W_{i,1}^*. \quad (19)$$

Choose the Lyapunov candidate function

$$V_{i,1} = \frac{1}{2} z_{i,1}^2 + \frac{1}{2} \tilde{W}_{i,1}^T \Gamma_{i,1}^{-1} \tilde{W}_{i,1}. \quad (20)$$

Then,

$$\begin{aligned} \dot{V}_{i,1} &= z_{i,1} \dot{z}_{i,1} + \tilde{W}_{i,1}^T \Gamma_{i,1}^{-1} \dot{\tilde{W}}_{i,1} \\ &= -k_{i,1} z_{i,1}^{4/3} + z_{i,1} z_{i,2} + z_{i,1} \varepsilon_{i,1} - \sigma_{i,1} \tilde{W}_{i,1}^T \tilde{W}_{i,1}^{1/3}. \end{aligned} \quad (21)$$

Based on based inequalities, the following holds:

$$\begin{aligned} z_{i,1}\varepsilon_{i,1} &\leq \frac{3}{4}z_{i,1}^{4/3} + \frac{1}{4}\varepsilon_{i,1}^4 - \sigma_{i,1}\widehat{W}_{i,1}^T\widehat{W}_{i,1}^{1/3} \\ &\leq -\frac{\sigma_{i,1}\widetilde{W}_{i,1}^{(2/3)T}\widetilde{W}_{i,1}^{2/3}}{2} + \sigma_{i,1}W_{i,1}^{(2/3)*T}W_{i,1}^{2/3*}. \end{aligned} \quad (22)$$

Then, based on (21), it gives

$$\begin{aligned} \dot{V}_{i,1} &= -\left(k_{i,1} - \frac{3}{4}\right)z_{i,1}^{4/3} + z_{i,1}z_{i,2} - \frac{\sigma_{i,1}\widetilde{W}_{i,1}^{(2/3)T}\widetilde{W}_{i,1}^{2/3}}{2} \\ &\quad + \frac{1}{4}\varepsilon_{i,1}^4 + \sigma_{i,1}W_{i,1}^{(2/3)*T}W_{i,1}^{2/3*}. \end{aligned} \quad (23)$$

Then, it has

$$\begin{aligned} \dot{V}_{i,1} &\leq z_{i,1}z_{i,2} - \eta_{i,1}\left(\frac{z_{i,1}^2}{2}\right)^{2/3} - \frac{\eta_{i,1}}{2}\left(\frac{\widetilde{W}_{i,1}^T\Gamma_{i,1}^{-1}\widetilde{W}_{i,1}}{2}\right)^{2/3} \\ &\quad + \frac{1}{4}\varepsilon_{i,1}^4 + \sigma_{i,1}W_{i,1}^{(2/3)*T}W_{i,1}^{2/3*} \leq z_{i,1}z_{i,2} - \eta_{i,1}V_{i,1}^{2/3} + \delta_{i,1}, \end{aligned} \quad (24)$$

where

$$\eta_{i,1} = \min\left(4^{1/3}\left(k_{i,1} - \frac{3}{4}\right), \frac{\sigma_{i,1}}{2^{1/3}\lambda_{\max}(\Gamma_{i,1}^{-1})^{2/3}}\right), \quad (25)$$

$$\delta_{i,1} = \frac{1}{4}\varepsilon_{i,1}^4 + \sigma_{i,1}W_{i,1}^{(2/3)*T}W_{i,1}^{2/3*}.$$

The  $j$ th step  $2 \leq j \leq n_i$ :

$$z_{i,j} = x_{i,j} - \alpha_{i,j-1}. \quad (26)$$

And  $x_{i,j+1} = u_i$ ,  $\dot{u}_i = v_i$ , then choose the virtual control law, and choose the NN to approximate the nonlinear system  $\dot{x}_{i,j} - \dot{\alpha}_{i,j-1}$ :

$$f_{i,j}(\bar{x}_{i,j+1}) - \dot{\alpha}_{i,j-1} = W_{i,j}^{*T}\Psi_j(Z_{j+1}) + \varepsilon_{i,j}. \quad (27)$$

Based on the system,

$$\dot{z}_{i,j} = W_{i,j}^{*T}\Psi_j(Z_{j+1}) + \varepsilon_{i,j}. \quad (28)$$

Choose the practical virtual control law

$$\alpha_{i,j} = -z_{i,j-1} - k_{i,j}z_{i,j}^{1/3} + x_{i,j+1} - \widehat{W}_{i,j}^T\Psi_j(Z_{j+1}). \quad (29)$$

Choose the adaptive law

$$\dot{\widehat{W}}_{i,j} = \Gamma_{i,j}\left[z_{i,j}\Psi_j(Z_{j+1}) - \sigma_{i,j}\widehat{W}_{i,j}^{1/3}\right], \quad (30)$$

where  $\Gamma_{i,j} = \Gamma_{i,j}^T > 0$ , and  $\sigma_{i,j} > 0$  is positive constant design parameters. Then,

$$\dot{z}_{i,j} = -\widehat{W}_{i,j}\Psi_j(Z_{j+1}) - z_{i,j-1} - k_{i,j}z_{i,j}^{1/3} + z_{i,j+1} + \varepsilon_{i,j}, \quad (31)$$

where

$$\widetilde{W}_{i,j} = \widehat{W}_{i,j} - W_{i,j}^*. \quad (32)$$

Choose the Lyapunov candidate function

$$V_{i,j} = \frac{1}{2}z_{i,j}^2 + \frac{1}{2}\widetilde{W}_{i,j}^T\Gamma_{i,j}^{-1}\widetilde{W}_{i,j}. \quad (33)$$

Then,

$$\begin{aligned} \dot{V}_{i,j} &= z_{i,j}\dot{z}_{i,j} + \widetilde{W}_{i,j}^T\Gamma_{i,j}^{-1}\dot{\widetilde{W}}_{i,j}^T \\ &= -z_{i,j-1}z_{i,j} - k_{i,j}z_{i,j}^{4/3} + z_{i,j}z_{i,j+1} + z_{i,j}\varepsilon_{i,j} - \sigma_{i,j}\widetilde{W}_{i,j}^T\widehat{W}_{i,j}^{1/3}. \end{aligned} \quad (34)$$

Based on basic equation, the following inequalities hold:

$$\begin{aligned} z_{i,j}\varepsilon_{i,j} &\leq \frac{3}{4}z_{i,j}^{4/3} + \frac{1}{4}\varepsilon_{i,j}^4 - \sigma_{i,j}\widehat{W}_{i,j}^T\widehat{W}_{i,j}^{1/3} \\ &\leq -\frac{\sigma_{i,j}\widetilde{W}_{i,j}^{(2/3)T}\widetilde{W}_{i,j}^{2/3}}{2} + \sigma_{i,j}W_{i,j}^{*(2/3)T}W_{i,j}^{*(2/3)}. \end{aligned} \quad (35)$$

Then, based on (33), it yields

$$\begin{aligned} \dot{V}_{i,j} &= z_{i,j}\dot{z}_{i,j} + \widetilde{W}_{i,j}^T\Gamma_{i,j}^{-1}\dot{\widetilde{W}}_{i,j} \\ &= -z_{i,j-1}z_{i,j} - \left(k_{i,j} - \frac{3}{4}\right)z_{i,j}^{4/3} + z_{i,j}z_{i,j+1} \\ &\quad - \frac{\sigma_{i,j}\widetilde{W}_{i,j}^{(2/3)T}\widetilde{W}_{i,j}^{2/3}}{2} + \frac{1}{4}\varepsilon_{i,j}^4 + \sigma_{i,j}W_{i,j}^{(2/3)*T}W_{i,j}^{(2/3)*}. \end{aligned} \quad (36)$$

Continue

$$\begin{aligned} \dot{V}_{i,j} &\leq -z_{i,j-1}z_{i,j} + z_{i,j}z_{i,j+1} - \eta_{i,j}\left(\frac{z_{i,j}^2}{2}\right)^{2/3} \\ &\quad - \eta_{i,j}\left(\frac{\widetilde{W}_{i,j}^T\Gamma_{i,j}^{-1}\widetilde{W}_{i,j}}{2}\right)^{2/3} + \frac{1}{4}\varepsilon_{i,j}^4 + \sigma_{i,j}W_{i,j}^{(2/3)*T}W_{i,j}^{(2/3)*} \\ &\leq -z_{i,j-1}z_{i,j} + z_{i,j}z_{i,j+1} - \eta_{i,j}V_{i,j}^{2/3} + \delta_{i,j}, \end{aligned} \quad (37)$$

where

$$\eta_{i,j} = \min\left(4^{1/3}\left(k_{i,j} - \frac{3}{4}\right), \frac{\sigma_{i,j}}{2^{1/3}\lambda_{\max}(\Gamma_{i,j}^{-1})^{2/3}}\right), \quad (38)$$

$$\delta_{i,j} = \frac{1}{4}\varepsilon_{i,j}^4 + \sigma_{i,j}W_{i,j}^{(2/3)*T}W_{i,j}^{(2/3)*}.$$

The  $n$ th step is the most important step. Based on the system,

$$z_{i,n_i} = x_{i,n_i} - \alpha_{i,n_i-1}. \quad (39)$$

Choose the NN to approximate the nonlinear system

$$f_{i,n_i}(\bar{x}_{i,n_i}, u_i) - \dot{\alpha}_{i,n_i-1} = W_{i,n_i}^{*T} \Psi_{n_i}(Z_{n_i+1}) + \varepsilon_{i,n_i}. \quad (40)$$

Based on the system,

$$\dot{z}_{i,n_i} = W_{i,n_i}^{*T} \Psi_{n_i}(Z_{n_i+1}) + \varepsilon_{i,n_i}. \quad (41)$$

Choose practical virtual control law

$$\alpha_{i,n_i} = -z_{i,n_i-1} - k_{i,n_i} z_{i,n_i} + u_i - \widehat{W}_{i,n_i}^T \Psi_{n_i}(Z_{n_i+1}). \quad (42)$$

Choose adaptive law

$$\dot{\widehat{W}}_{i,n_i} = \Gamma_{i,n_i} \left[ z_{i,n_i} \Psi_{n_i}^T(Z_{n_i+1}) - \sigma_{i,n_i} \widehat{W}_{i,n_i}^{1/3} \right], \quad (43)$$

where  $\Gamma_{i,n_i} = \Gamma_{i,n_i}^T > 0$ , and  $\sigma_{i,n_i} > 0$  are positive constant design parameters; then,

$$\dot{z}_{i,n_i} = -\widehat{W}_{i,n_i}^T \Psi_{n_i}(Z_{n_i+1}(t)) - z_{i,n_i-1} - k_{i,n_i} z_{i,n_i}^{1/3} + z_{i,n_i+1} + \varepsilon_{i,n_i}, \quad (44)$$

where

$$\widetilde{W}_{i,n_i} = \widehat{W}_{i,n_i} - W_{i,n_i}^*. \quad (45)$$

From the following inequality,

$$-\sigma_{i,n_i} \widetilde{W}_{i,n_i}^T \widehat{W}_{i,n_i}^{1/3} \leq -\frac{\sigma_{i,n_i} \widetilde{W}_{i,n_i}^{(2/3)T} \widetilde{W}_{i,n_i}^{2/3}}{2} + \sigma_{i,n_i} W_{i,n_i}^{(2/3)*T} W_{i,n_i}^{(2/3)*}. \quad (46)$$

Choose the Lyapunov candidate function

$$V_{i,n_i} = \frac{1}{2} z_{i,n_i}^2 + \frac{1}{2} \widetilde{W}_{i,n_i}^T \Gamma_{i,n_i}^{-1} \widetilde{W}_{i,n_i}. \quad (47)$$

Then,

$$\begin{aligned} \dot{V}_{i,n_i} &= z_{i,n_i} \dot{z}_{i,n_i} + \widetilde{W}_{i,n_i}^T \Gamma_{i,n_i}^{-1} \dot{\widetilde{W}}_{i,n_i}^T \\ &= -z_{i,n_i-1} z_{i,n_i} - k_{i,n_i} z_{i,n_i}^{4/3} + z_{i,n_i} z_{i,n_i+1} \\ &\quad + z_{i,n_i} \varepsilon_{i,n_i} - \sigma_{i,n_i} \widetilde{W}_{i,n_i}^T \widehat{W}_{i,n_i}^{1/3}. \end{aligned} \quad (48)$$

Based on Lemma, the following inequalities hold:

$$\begin{aligned} z_{i,j} \varepsilon_{i,n_i} &\leq \frac{3}{4} z_{i,n_i}^{4/3} + \frac{1}{4} \varepsilon_{i,n_i}^4 - \sigma_{i,n_i} \widetilde{W}_{i,n_i}^T \widehat{W}_{i,n_i}^{1/3} \\ &\leq -\frac{\sigma_{i,n_i} \widetilde{W}_{i,n_i}^{(2/3)T} \widetilde{W}_{i,n_i}^{2/3}}{2} + \sigma_{i,n_i} W_{i,n_i}^{*(2/3)T} W_{i,n_i}^{*(2/3)}. \end{aligned} \quad (49)$$

Then, it gives

$$\begin{aligned} \dot{V}_{i,n_i} &\leq -z_{i,n_i-1} z_{i,n_i} - \left( k_{i,n_i} - \frac{3}{4} \right) z_{i,n_i}^{4/3} + z_{i,n_i} z_{i,n_i+1} \\ &\quad - \frac{\sigma_{i,n_i} \widetilde{W}_{i,n_i}^{(2/3)T} \widetilde{W}_{i,n_i}^{2/3}}{2} + \frac{1}{4} \varepsilon_{i,n_i}^4 + \sigma_{i,n_i} W_{i,n_i}^{(2/3)*T} W_{i,n_i}^{(2/3)*}. \end{aligned} \quad (50)$$

Then,

$$\begin{aligned} \dot{V}_{i,n_i} &\leq -z_{i,n_i-1} z_{i,n_i} + z_{i,n_i} z_{i,n_i+1} - \eta_{i,n_i} \left( \frac{z_{i,n_i}^2}{2} \right)^{2/3} \\ &\quad - \eta_{i,n_i} \left( \frac{\widetilde{W}_{i,n_i}^T \Gamma_{i,n_i}^{-1} \widetilde{W}_{i,n_i}}{2} \right)^{2/3} + \delta_{i,n_i} \\ &\leq -z_{i,n_i-1} z_{i,n_i} + z_{i,n_i} z_{i,n_i+1} - \eta_{i,n_i} V_{i,n_i}^{2/3} + \delta_{i,n_i}, \end{aligned} \quad (51)$$

where

$$\eta_{i,n_i} = \min \left( 4^{1/3} \left( k_{i,n_i} - \frac{3}{4} \right), \frac{\sigma_{i,n_i}}{2^{1/3} \lambda_{\max}(\Gamma_{i,n_i}^{-1})^{2/3}} \right), \quad (52)$$

$$\delta_{i,n_i} = \frac{1}{4} \varepsilon_{i,n_i}^4 + \sigma_{i,n_i} W_{i,n_i}^{(2/3)*T} W_{i,n_i}^{(2/3)*}.$$

Then, the virtual control can be got as

$$v = -z_{i,n_i} - k_{i,n_i+1} z_{i,n_i+1} - \widehat{W}_{i,n_i+1}^T \Psi_{i,n_i+1}(Z_{i,n_i+1}(t)). \quad (53)$$

Choose Lyapunov candidate functions

$$V_i = \sum_{j=1}^{n_i+1} V_{i,j}. \quad (54)$$

Then, based on (24), (37), and (51), it has

$$\dot{V}_i \leq -\eta_i V_i^{2/3} + \delta_i, \quad (55)$$

where

$$\begin{aligned} \eta_i &= \min(\eta_{i,j}), \quad j = 1, 2, 3, \dots, n_i + 1, \\ \delta_i &= \sum_{j=1}^{n_i+1} \delta_{i,j}, \end{aligned} \quad (56)$$

**Theorem 1.** Consider the nonlinear system for which the model dynamics is approximated by neural networks (12), (27), and (40), the control law (53) with the virtual control (14), (29), and (42), and adaptive laws (15), (30), and (43); then, the following statements hold:

- (1) All the signals of the closed-loop system, including  $x_{i,j}$ ,  $\alpha_{i,j}$ ,  $\widehat{W}_{i,j}$ , remain bounded all the time.



(2) The closed-loop signal  $z_{i,j}$  converge to a compact set defined by

$$\Omega_{i,s} = \left\{ z_i \mid \|z_i\|^2 \leq \frac{\delta_i}{\eta_i} \right\}, \quad (57)$$

(i) where  $\delta_i, \eta_i$  are constants related to the design parameters.

(3) The finite-time  $T$  is given by

$$T \leq \frac{3V^{1/3}(x_0)}{\eta\theta_0}, \quad (58)$$

where  $\eta, \theta_0$  are constants related to the design parameters and  $V(x_0)$  is constant related to Lyapunov candidate functional.

*Proof.* considering Lyapunov function candidate (54) and (55), then  $V_i$  is bounded. Therefore, it can conclude that for all  $1 \leq j \leq n_i + 1$ , the error signals  $z_{i,j}, \tilde{W}_{i,j}$  are stable.  $\square$

#### 4. Simulation Example

In this section, simulation example shows the validity and feasibility of the proposed NN finite adaptive control design approach. Figure 1 shows the topology of communication graph of MAS with one leader and five followers.

Consider the following MAS with adjacency matrix  $A$  and Laplacian matrix  $L$  as follows:

$$A = \begin{bmatrix} 0 & 0 & 0 & 0 & 3 \\ 1 & 0 & 0 & 0 & 0 \\ 0 & 3 & 0 & 0 & 0 \\ 0 & 0 & 2 & 0 & 0 \\ 0 & 0 & 0 & 1 & 0 \end{bmatrix}, \quad (59)$$

$$L = \begin{bmatrix} 3 & 0 & 0 & 0 & -3 \\ -1 & 1 & 0 & 0 & 0 \\ 0 & -3 & 3 & 0 & 0 \\ 0 & 0 & -2 & 2 & 0 \\ 0 & 0 & 0 & -1 & 1 \end{bmatrix}.$$

The dynamic systems are described by

$$\begin{aligned} \dot{x}_{i,1} &= 0.5\sin(x_{i,1}) - x_{i,1} + \sin(x_{i,2}) + x_{i,2} \\ &\quad + 5\sin(t) + 5\cos(t), \\ \dot{x}_{i,2} &= -\sin(x_{i,2}) - ix_{i,2} + x_{i,2}u_i + u_i + \sin(u_i), \\ y_i &= x_{i,1}. \end{aligned} \quad (60)$$

$y_d = 5\sin(t)$  is the state, control input, control output, and ideal output, respectively. The control objective of the proposed design method is to make the system output  $y$  follow the desired reference signal  $y_d = 5\sin(t)$ . Select the controller  $\hat{u}$  and virtual control  $\alpha_1, \alpha_2$  as follows:

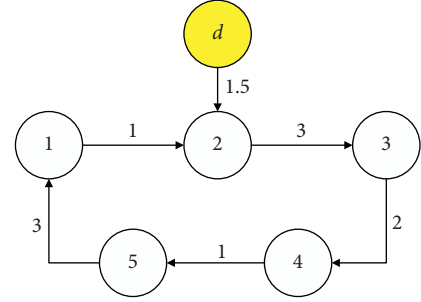


FIGURE 1: Topology of communication graph.

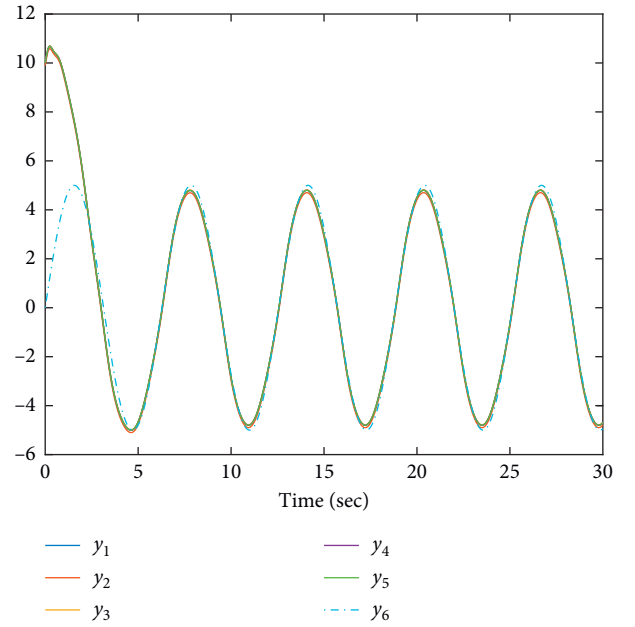


FIGURE 2: Output trajectory of five followers and leader.

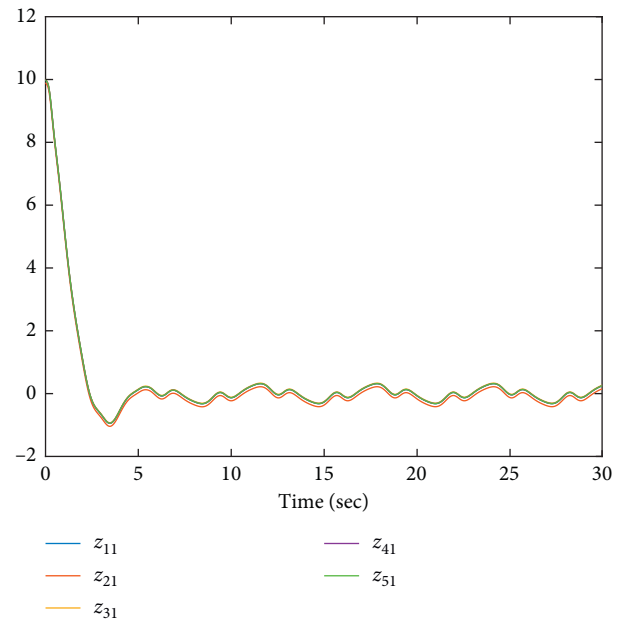


FIGURE 3: Error trajectory of five followers.

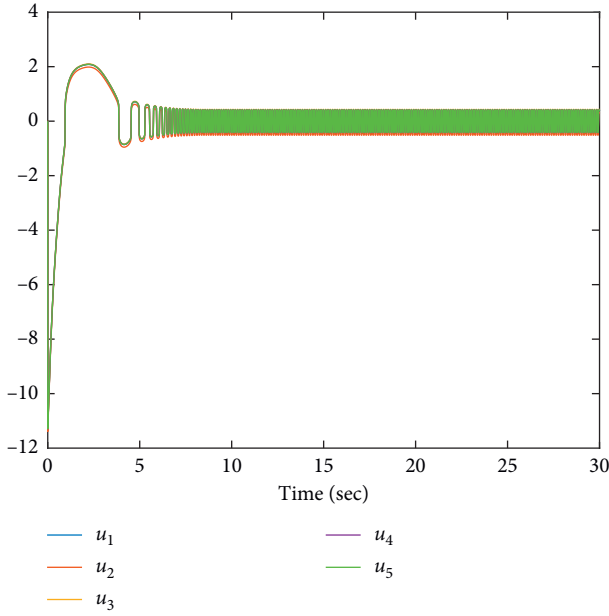


FIGURE 4: Five control trajectory.

$$\begin{aligned} \dot{u}_i &= -z_{i,2} - k_3 z_{i,3}^{1/3} - \widehat{W}_{i,3}^T \Psi_3(\bar{x}_{i,2}, u_i), \\ \alpha_{i,1} &= -k_1 z_{i,1}^{1/3} + x_{i,2} - \widehat{W}_{i,1}^T \Psi_1(\bar{x}_{i,2}), \\ \alpha_{i,2} &= -z_{i,1} - k_2 z_{i,2}^{1/3} + u_i - \widehat{W}_{i,2}^T \Psi_2(\bar{x}_{i,2}, u_i). \end{aligned} \quad (61)$$

The weight of NNs is updated by

$$\dot{\widehat{W}}_{i,j} = \Gamma_{i,j} \left[ z_{i,j} \Psi_i(\bar{x}_{i,j+1}) - \sigma_{i,j} \widehat{W}_{i,j}^{1/3} \right], \quad j = 1, 2, 3, \quad (62)$$

with  $z_{i,1} = x_{i,1} - y_{i,d}$ ,  $z_{i,2} = x_{i,2} - \alpha_{i,1}$ , and  $z_{i,3} = u_i - \alpha_{i,2}$ .

Applying the finite-time NN control method, the simulation results are shown in Figures 2–4. Figure 2 shows the trajectory of output and desired reference trajectory of MAS. Figure 3 shows the error trajectory of five followers. Figure 4 shows the trajectory of controller. The method in this paper is more generally used, and both output and weight of NNs are convergence in finite time.

## 5. Conclusion

In this article, the adaptive tracking control method is proposed for distributed multiagent systems in nonaffine form. Based on finite neural network algorithm, a finite-time tracking result can be got. In addition, each follower agent is modeled by a nonlinear pure-feedback system with non-affine form, and the nonlinear system is unknown functions rather than constants. Simulations and theoretical analysis are carried out to verify the feasibility and correctness of the proposed method.

## Data Availability

No data were used to support this study.

## Conflicts of Interest

The authors declare that there are no conflicts of interest regarding the publication of this paper.

## Acknowledgments

This paper was supported by the 2018 Social and Science Fund (HB18GL075) and 2015 Hebei Province Natural Science Fund Project (G2015203378 and F2015208128).

## References

- [1] B. Burmeister, A. Haddadi, and G. Matylis, "Application of multi-agent systems in traffic and transportation," *IEEE Proceedings - Software Engineering*, vol. 144, no. 1, pp. 51–60, 1997.
- [2] J. Clerc and G. J. Wiens, "Reconfigurable multi-agent robots with mixed modes of mobility," in *Proceedings of the IEEE International Conference on Robotics and Automation*, Sendai, Japan, April 2004.
- [3] C. Ramos, "An architecture and a negotiation protocol for the dynamic scheduling of manufacturing systems," in *Proceedings of the 1994 IEEE International Conference on Robotics and Automation*, San Diego, CA, USA, May 1994.
- [4] N. R. Jennings, L. Z. Varga, R. P. Aarnts, J. Fuchs, and P. Skarek, "Transforming standalone expert systems into a community of cooperating agents," *Engineering Applications of Artificial Intelligence*, vol. 6, no. 4, pp. 317–331, 1993.
- [5] H. Du, J. Zhou, D. Wu, and G. Wen, "Consensus for second-order nonlinear leader-following multi-agent systems via event-triggered control," in *Proceedings of the 2017 International Workshop on Complex Systems and Networks (IWCSN)*, Doha, Qatar, December 2017.
- [6] K. Chen, J. Wang, and Y. Zhang, "Adaptive leader-following consensus of nonlinear multi-agent systems with jointly connected topology," in *Proceedings of the 27th Chinese Control and Decision Conference (2015 CCDC)*, Qingdao, China, May 2015.
- [7] S. Ali, S. Ahmed, and S. N. K. Marwat, "A practical approach to consensus based control of multi-agent systems," in *Proceedings of the 2018 International Symposium on Recent Advances in Electrical Engineering (RAEE)*, Islamabad, Pakistan, October 2018.
- [8] L. Xu, J. Zheng, N. Xiao, and L. Xie, "Mean square consensus of multi-agent systems over fading networks with directed graphs," *Automatica*, vol. 95, pp. 503–510, 2018.
- [9] Y. Cheng, T. Hu, Y. Li, and S. Zhong, "Consensus of fractional-order multi-agent systems with uncertain topological structure: A Takagi-Sugeno fuzzy event-triggered control strategy," *Fuzzy Sets and Systems*, 2020.
- [10] Z. Li, G. Wen, Z. Duan, and W. Ren, "Designing fully distributed consensus protocols for linear multi-agent systems with directed graphs," *IEEE Transactions on Automatic Control*, vol. 60, no. 4, pp. 1152–1157, 2015.
- [11] L. Ping, Q. Kaiyu, and S. Mengji, "Distributed robust  $H_\infty$  rotating consensus control of multi-agent systems with mixed uncertainties and time-delay," in *Proceedings of the 32nd Chinese Control Conference*, Xi'an, China, July 2013.
- [12] K. Liu, H. Zhu, and J. Lu, "Robust consensus of a class of linear multi-agent systems via sampled-data control," in *Proceedings of the 2015 10th Asian Control Conference (ASCC)*, Kota Kinabalu, Malaysia, June 2015.

- [13] J. Liu, Z. Liu, and Z. Chen, "Robust  $H_{\infty}$  consensus control for multi-agent system with dynamic topologies and time-varying delays," in *Proceedings of the 29th Chinese Control Conference*, Beijing, China, July 2010.
- [14] D. Han, G. Chesi, and Y. S. Hung, "Robust consensus for a class of uncertain multi-agent dynamical systems," *IEEE Transactions on Industrial Informatics*, vol. 9, no. 1, pp. 306–312, 2013.
- [15] C. Lin, W. Huang, Y. Huang, and S. Chen, "Robust consensus for linear multi-agent systems over randomly switching topologies," in *Proceedings of the 2019 Chinese control conference (CCC)*, Wuhan, China, July 2019.
- [16] J. Wu, D. Li, D. Lao et al., "Second-order robust consensus for nonlinear multi-agent systems with extended state observer," in *Proceedings of the 33rd Chinese Control Conference*, Nanjing, China, July 2014.
- [17] P. Gong, "Distributed robust adaptive consensus control for uncertain nonlinear fractional-order multi-agent systems," in *Proceedings of the 2019 Chinese Control and Decision Conference (CCDC)*, Nanchang, China, June 2019.
- [18] X. Long, K. Zhou, and J. Hou, "Finite-time consensus for second-order multi-agent systems with disturbances by integral sliding mode algorithm based on relative information," in *Proceedings of the 2018 37th Chinese control conference (CCC)*, Wuhan, China, July 2018.
- [19] B. Luo, Q. Li, and Y. Yang, "Finite-time consensus for multi-agent systems via sinusoidal controller," in *Proceedings of the 2012 International Conference on Control Engineering and Communication Technology*, Shenyang, China, December 2012.
- [20] Y. Zhu, C. Chen, and X. Guan, "Finite-time consensus for multi-agent systems via impulsive control," in *Proceedings of the 2016 35th Chinese Control Conference (CCC)*, Chengdu, China, July 2016.
- [21] J. Liu, Y. Zhang, Y. Yu, and C. Sun, "Fixed-time event-triggered consensus for nonlinear multiagent systems without continuous communications," *IEEE Transactions on Systems, Man, and Cybernetics: Systems*, vol. 49, no. 11, pp. 2221–2229, 2019.
- [22] J. Liu, Q. Wang, and Y. Yu, "Fixed-time consensus algorithm for second-order multi-agent systems with bounded disturbances," in *Proceedings of the 2016 31st Youth Academic Annual Conference of Chinese Association of Automation (YAC)*, Wuhan, China, November 2016.
- [23] J. Ni, L. Liu, C. Liu, and J. Liu, "Fixed-time leader-following consensus for second-order multiagent systems with input delay," *IEEE Transactions on Industrial Electronics*, vol. 64, no. 11, pp. 8635–8646, 2017.
- [24] W. Zhang, X. Gao, B. Sun, X. Hu, and K. Zhu, "Echo state network for extended state observer and sliding mode control of vehicle drive motor with unknown hysteresis nonlinearity," *Mathematical Problems in Engineering*, vol. 2020, pp. 1–13, Article ID 2534038, 2020.
- [25] J. H. Park, "Exponential stability of antiperiodic solution for BAM neural networks with time-varying delays," *Mathematical Problems in Engineering*, vol. 2018, Article ID 3034794, 2018.
- [26] J. Zhang, Q. Zhu, and Y. Li, "Convergence time calculation for supertwisting algorithm and application for nonaffine nonlinear systems," *Complexity*, vol. 2019, pp. 1–15, Article ID 6235190, 2019.
- [27] J. Zhang, Q. Zhu, Y. Li, and X. Wu, "Homeomorphism mapping based neural networks for finite time constraint control of a class of nonaffine pure-feedback nonlinear systems," *Complexity*, vol. 2019, pp. 1–11, Article ID 9053858, 2019.
- [28] J. Zhang, Y. Li, W. Fei, and X. Wu, "U-model based adaptive neural networks fixed-time backstepping control for uncertain nonlinear system," *Mathematical Problems in Engineering*, vol. 2020, pp. 1–7, Article ID 8302627, 2020.

## Research Article

# Modeling and Optimization for Fault Diagnosis of Electromechanical Systems Based on Zero Crossing Algorithm

Qing Chen <sup>1</sup>, Tao Liu <sup>1</sup>, Xing Wu,<sup>1,2</sup> and Hua Li<sup>1</sup>

<sup>1</sup>Key Laboratory for Advanced Equipment Intelligent Manufacturing Technology of Yunnan Province, Kunming University of Science and Technology, Kunming 650500, China

<sup>2</sup>Yunnan Vocational College of Mechanical and Electrical Technology, Kunming 650203, China

Correspondence should be addressed to Tao Liu; [kmlitao@aliyun.com](mailto:kmlitao@aliyun.com)

Received 24 April 2020; Accepted 30 June 2020; Published 27 July 2020

Guest Editor: Jian Huang

Copyright © 2020 Qing Chen et al. This is an open access article distributed under the Creative Commons Attribution License, which permits unrestricted use, distribution, and reproduction in any medium, provided the original work is properly cited.

The demand of system security and reliability in the modern industrial process is ever-increasing, and fault diagnosis technology has always been a crucial research direction in the control field. Due to the complexity, nonlinearity, and coupling of multitudinous control systems, precise system modeling for fault diagnosis is attracting more attention. In this paper, we propose an improved method of electromechanical systems fault diagnosis based on zero-crossing (ZC) algorithm, which can present the calculation model of zero-crossing rate (ZCR) and optimize the parameters of ZC algorithm by establishing a criterion function model to improve the diagnosis accuracy and robustness of ZC characteristic model. The simulation validates the influence of different signal-to-noise ratio (SNR) on ZC feature recognition ability and indicates that the within-between distance model is effective to enhance the diagnose accuracy of ZC feature. Finally, the method is applied to the diagnosis of motor fault bearing, which confirms the necessity and effectiveness of the model improvement and parameter optimization and verifies the robustness to the load.

## 1. Introduction

The electromechanical system is a vital part in the process of modern industrial production and manufacturing. The research of fault diagnosis and prediction methods, which can be applied to nonlinear electromechanical systems and realize the real-time monitoring, diagnosis, prediction, and state-based maintenance of electromechanical system, has an important significance for improving the safety and reliability of electromechanical system. As a crucial component of electromechanical systems, the stability and reliability of motor operation directly affect the normal operation of electromechanical systems, especially in the fields of CNC machine tools [1], robots [2], and aircraft [3], which require relatively high production accuracy, efficiency, and reliability. In particular, rolling element bearings (REBs) are the most commonly machine elements used in almost all rotary machinery and is also the vulnerable component of rotating machinery [4, 5]. The health status of

REBs directly affects the functioning of the motor, which accounts for almost 40–50% of motor fault [6, 7]. As a consequence, the fault diagnosis of motor REBs plays a crucial role to the smooth, reliable, and safe handling of the whole electromechanical system.

Mathematical modeling and analysis are useful to design and study control systems [8–10] and also can be used to analyze the behavior of the real systems under different operating conditions, test signal processing methods, and new detection and prognosis techniques. Over the last few decades, the dynamic modeling of rolling bearings has been extensively studied. McFadden and Smith established a model to illustrate the vibration characteristics of a single point defect in the inner race of REB under the same radial load. The model comprehensively considers the impacts of bearing geometry, bearing size distribution, transfer function, and vibration index attenuation. By comparing the radial vibration spectra predicted with measured, the excellent performance of the model is validated [11]. Sawalhi

and Randall proposed a combination of gear and bearing dynamic model. In this model, the outspread faults of the inner and outer rings of REBs in the presence of gear interactions can be studied [12]. Due to the distinct superiority of U-model in nonlinear control, the development of U-model based gear and bearing state prediction is promising [13, 14]. For the sake of research of the nonlinear dynamic characteristics of the REB system containing surface defect, a theoretical model is presented by Rafsanjani et al. In order to investigate the linear stability of the defective bearing rotor system with changes in the parameters of the conversion system, the classic Floquet theorem was embedded in this model. In the solution of this model, the peak-to-peak frequency response of the system was obtained in some cases, and the basic paths of offset, collimation, and chaotic motion for different internal radial clearance were determined [15]. Based on the research of the dynamic model on REB, the fault diagnosis using the measurement signal in the system has been developed rapidly. In the process of system operation, the symptoms of failure will be reflected in the detection information (measurement signal), the resultful features of the signal will be extracted by means of analysis, and then the diagnosis scheme will be established based upon the fault symptom analysis and the prior knowledge of the healthy system. Nevertheless, the quality of features extracted from signals is always a thorny problem. Since the vibration data of a faulty rolling bearing is usually unstable and nonlinear and contains relatively weak fault features, it has always attracted wide attention from researchers. Over the past decades, a mass of approaches of feature extraction for REB fault diagnosing have been proposed, which can be roughly summarized as the following categories according to the distinction of principles and properties. Firstly, feature extraction based on the traditional time domain parameters, for example, crest factor, peak-to-peak value, kurtosis, root-mean square, shape factor, and standard deviation etc. [16–18]; secondly, frequency domain parameters, such as power spectral density, power spectrum [19]; thirdly, analysis based on time-frequency domain methods, for instance, spectrogram and wavelet transform [20–22]; finally, based on multiple parameters the mixed feature extraction realized, for example, the method of [23, 24] have extracted blended parameter features of time domain, frequency domain, and time-frequency.

It is found that in most former feature extraction techniques, a large number of complex calculations are needed for vibration signal data for improving the accuracy of fault identification. Compared with these traditional methods, as ZC features generate directly from the count of the ZC interval in the time domain, ZC feature algorithm has an obvious advantage, which can well reflect the change of signal frequency with fast convergence, and is easy to calculate. Therefore, ZC algorithm has been successfully applied to speech recognition [25], vehicle classification [26], and biomedical applications [27, 28]. Moreover, the ZC method is also commonly used in signal processing and mechanical fault diagnosis. William and Hoffman showed the ZC method combined with an ANN is effective in early

detection and diagnosis of bearing failures [29]. Liu et al. proposed a bearing performance degradation estimation method based on the ZC characteristics and coupled hidden Markov model and proved that the ZC features can detect the early degradation stage of the bearing [30]. Ukil et al. presented a feature extraction method of current ZC moment to detect short-circuit fault of stator winding of series asynchronous induction motors [31]. Gonzalez and Kinsner showed that ZC could be used to identify different parts of the composite signal, and the advantage of the ZC computing immediately in the time domain is attractive to real time implementation [32]. Waghmare et al. presented a methodology based on piecewise energy and corresponding mean of signal ZC in environmental noise, which has a broad application prospect in dealing with the underwater target-radiated noise [33]. For the first time, Nayana and Geethanjali used time domain parameters, waveform parameters, slope sign changes (SSC), simple sign integral, and Wilson amplitude to established mean absolute value and ZC to identify failures of motors, and by comparing with conventional features, they proved the proposed features perform better [34].

Literatures [29, 30] demonstrated the advantages of ZC features in bearing fault diagnosis, such as small computation and fast speed. However, by reason of no stationary and nonlinearity of REB fault signals, the recognition rate of the extracted ZC features in REB fault recognition is low, especially in the case of low signal-to-noise ratio (SNR). For solving this problem, this paper firstly analyzes the recognition ability of ZC features under different SNR conditions, then proposes an adaptive method to enhance the capable of recognition fault, and verifies the recognition rate through neural network. The improved fault diagnosis method for electromechanical system which optimized the calculation model of ZCR and optimized the parameters of ZC algorithm by establishing a criterion function model greatly improves the fault recognition rate and is robust to the load.

The remaining of this article is organized as follows. In Section 2, the theory of ZC feature algorithm is briefly reviewed and the improved model of ZC calculation and the method of parameters optimized through modeling a criterion function with within-between distance are introduced, and Section 3 simulation signals are used to verify the influence of ZC feature recognition ability at disparate SNR and verifies the validation of the presented method. In Section 4, the experiment is analyzed to verify the method, and the conclusions are given in the Section 5.

## 2. Theoretical Background

*2.1. ZC Characteristic Feature Algorithm.* The measures widely used to represent the characteristics of ZC include the mean ZCR, density of the time interval between continuous ZCs, and excess threshold measure. According to the experience of literature [33], compared with other ZC measurements, the ZC feature of excess threshold measurement is more conducive to fault diagnosis at relatively high SNR. Therefore, in this paper, the ZC feature of excess threshold measurement is used to method improvement and

parameter optimization for achieving the more accuracy of fault diagnosis at low SNR.

In order to describe the short-time waveform, the time domain signal collected should be divided into a diminutive observation window, firstly. In addition, the measure of the observation window should be greater than the maximum expected duration between continuous ZCs.  $T_L$  is defined as the measure of the observation window,  $T_Q$  represents the maximum expected duration between the continuous ZCs, and  $T_Q \leq T_L$ . Then, divide the duration range  $[0, T_Q]$  into  $Q$  intervals by the threshold of  $Q + 1$ , and define  $T_i$  as the  $i$ th interval. Let  $C_i$  represent the count of ZC intervals with duration in the range of  $T_{i-1}$  and  $T_i$  and  $x(n)$  is the short-time waveform with the data sequence  $N$ , then  $C_i$  can be obtained by

$$C_i = \frac{1}{2} \sum_{n=2}^N [\text{sgn}[x(n)] - \text{sgn}[x(n-1)]], \quad (1)$$

where the  $\text{sgn}[x]$  is sign function and expressed as

$$\text{sgn}[x(n)] = \begin{cases} 1 (x \geq 0), \\ -1 (x < 0). \end{cases} \quad (2)$$

Then, the eigenvector of ZC counts is normalized by the observation window, and defined as

$$F_{\text{count}} = \frac{C}{T_L} = \frac{1}{T_L} (C_1 C_2 \dots C_Q), \quad (3)$$

and the function of excess threshold measurement can be calculated by the following formula:

$$f(T_i) = \frac{1}{2} \sum_{k=j}^{Q-1} C_{k+1} (T_k + T_{k+1}), \quad (4)$$

where  $1/2C_{k+1} (T_k + T_{k+1})$  is used to approximately calculate the sum of ZC durations in the range  $T_k < T \ll T_{k+1}$ .

Thereby, the eigenvector of excess threshold measurement can be obtained by

$$F_{\text{duration}} = \frac{1}{T_L} [f(T_0), f(T_0), \dots, f(T_{Q-1})]. \quad (5)$$

**2.2. Criterion Function Modeling.** The purpose of feature extraction is to acquire the most available information related to the equipment condition so as to realize fault identification. The classification ability of feature vectors directly determines the ability of fault recognition. Based on the idea of Fisher criterion [35] to calculate the distance between categories and within categories, the recognition ability of features can be improved by finding a functional relationship between the intraclass distance and interclass distance of features. In other words, the smaller the intraclass distance and the larger the interclass distance of the feature clustering results, the higher the discrimination degree of the classification results will be. Therefore, we can construct a criterion function that reflects the within-between distance.

Assume that the feature set  $(x_1, x_2, \dots, x_N)$  to be classified is classified as class  $C\{x_i^{(j)}, j = 1, 2, \dots, C; i =$

$1, 2, \dots, n_j\}$ . The data quantity of class  $j$  is  $n_j$ . The intraclass distance of class  $j$  can be expressed as follows:

$$S_w^{(j)} = \frac{1}{n_j} \sum_{i=1}^{n_j} (x_i^{(j)} - m_j)(x_i^{(j)} - m_j)^T, \quad (6)$$

where  $m_j$  is the average of the samples of class  $j$  and  $m_j = 1/n_j \sum_{i=1}^{n_j} x_i^{(j)}$ , ( $j = 1, 2, \dots, C$ ).

Let  $S_w^{(k)}$  and  $m_k$  denote the intraclass distance and the samples mean of class  $k$  ( $k \neq j$  and  $k \leq C$ ), respectively, the interclass distance between class  $j$  and  $k$  can be expressed as follows:

$$S_B = \sum (m_j - m_k)(m_j - m_k)^T. \quad (7)$$

Then, the function represents the ability to recognize between classes can be expressed as follows:

$$I = \frac{S_B}{S_w^{(j)} + S_w^{(k)}}. \quad (8)$$

On the premise that the highest recognition capacity of the two categories is not weakened, let us assume that the discrepancy of  $I$  value between other categories is the smallest and the recognition rate is the best, and then the criterion function can be expressed by the following relation:

$$\min \phi(I_{\max}, I_{\min}), \quad \phi = I_{\max} - I_{\min}, \quad (9)$$

where  $I_{\max}$  and  $I_{\min}$  represent the maximum and minimum  $I$  values of all categories, respectively.

**2.3. Parameter-Optimized ZC Based on Within-Between Distance Models.** According to formula (1), we know that the ZC count has nothing to do with the magnitude of signal amplitude and is only related to the positive and negative signs of signals. However, ZC count is sensitive to the presence of noise; as random noises repeatedly cross the coordinate axis in the background, a large number of false ZCR will be generated and affect the recognition result. Equation (1) is suitable for discrete calculation but not conducive to the analysis of related signal waveform. Therefore, formula (1) is firstly transformed into the following equation:

$$C_i = \frac{1}{2} \sum_{n=2}^N [1 - \text{sgn}[x(n) \cdot x(n-1)]]. \quad (10)$$

Consider further the influence of random noise; increase a threshold  $\varepsilon$  to offset part of false ZCR generated by noise repeatedly crossing the coordinate axis. Therefore, the zero-crossing calculation formula can be revised into the form of formula (11):

$$C_i = \frac{1}{2} \sum_{n=2}^N [1 - \text{sgn}[x(n) \cdot x(n-1) + \varepsilon]]. \quad (11)$$

The subsequent work is the optimization of threshold  $\varepsilon$ . The method of extracting ZC features from ZC duration is described in Section 2.1. It is noteworthy that the length of the observation window must greater than the maximum expected time interval between the continuous ZC intervals, so the ZC feature should ensure that the minimum

frequency of interest can be discovered. In order to improve data utilization and maintain data continuity, 50% overlap rate is set. When the maximum expected time is divided into  $Q$  intervals by the threshold of  $Q + 1$ ,  $Q$  group eigenvectors are generated. We know that the extracted features are different on various time scales; therefore, the eigenvector is affected by the length and number of observation window. Literature [36] has discussed the optimization method of these two thresholds, here, the optimized window data are used directly. Keep the optimized window data unchanged, and change the value of  $\varepsilon$  to extract the ZC feature, respectively. The  $\varepsilon$  must be changed by the specified step size and adjusted for ZC features changes. Calculate the inter-class distance and intraclass distance of each ZC feature. Then, values of  $I$  with diverse values of  $\varepsilon$  are calculated according to formula (9). If the critical point is found, the optimized  $\varepsilon$  value is obtained. The flow chart of improved method of ZC features extraction is manifested in Figure 1.

Detailed descriptions of the flow chart in Figure 1:

*Step 1.* Input original vibration signals.

*Step 2.* Calculate the peak-to-peak value, as the basis for calculating the search step size and search scope.

*Step 3.* Set the search range and step size of  $\varepsilon$ . The search step size needs to be based on the experience of making multiple attempts at the actual signal. In the simulation, one-thousandth of the peak value is used as the step length, and 20 steps are used as the search range.

*Step 4.* Extract ZC feature vectors of every signal at different  $\varepsilon$  values. The number and length of observation window were optimized before feature extraction, and the data overlapped by 50%.

*Step 5.* Calculate the value of  $I$  between different state categories according to formula (8). Suppose there are 4 kinds of state signals, and then 6 values of  $I$  are formed, one for every 2 kinds of signals.  $\varepsilon$  value is searched 20 times, and then a  $6 \times 20$  matrix is formed.

*Step 6.* Calculate the maximum and minimum of  $I$  for each search, guaranteed the highest recognition capacity of the two categories is not weakened, and increase the value of  $I$  between the two classes that are most difficult to recognize. So, when formula (9) is satisfied, the optimization is achieved. According to the step size of each signal and the number of steps, the optimized  $\varepsilon$  value of each signal can be obtained.

*Step 7.* According to the optimized  $\varepsilon$  value of each signal, extract the optimized ZC features.

*Step 8.* Bring the optimized features into neural network for fault diagnosis and verification, and the results are analyzed.

### 3. Simulation Analysis

For the sake of verifying the necessity and effectiveness of the presented method, four simulated signals of normal, inner ring fault, rolling element fault, and outer ring fault of rolling

bearing are used for analysis. The simulation signals are obtained from the following formula:

$$\left. \begin{aligned} x(t) &= \sum_{i=1}^M A_i s(t - iT - \tau_i) + n(i) \\ A_i &= A_0 \cos(2\pi Q t + \varphi_A) + C_A \\ s(t) &= e^{-Bt} \sin(2\pi f_n t + \varphi_w) \end{aligned} \right\}, \quad (12)$$

where the system sampling frequency  $f_s = 12000$  Hz, the resonant frequency  $f_n = 3000$  Hz, the inner ring fault frequency  $f_i = 162$  Hz, the rolling element fault frequency  $f_b = 142$  Hz, the outer ring fault frequency  $f_o = 142$  Hz, the rotational frequency  $f_r = 30$  Hz, and the damping ratio  $B = 400$ . Four simulated signals are a group, a total of three groups. Three random noises with a SNR of 30 dB, 5 dB, and  $-5$  dB are added separately to three groups signal. The grouping of simulation signals is shown in Table 1.

*3.1. Analysis of ZC Feature Noise Resistance.* In order to make the extracted features represent the running state information of the bearing effectively, the length of the data segment calculated with ZC feature should contain at least one complete rotation period. The rotational frequency is 30 Hz, so the length of an observation window must greater than  $1/30$  seconds which contains 360 points at the sampling frequency of 12 K. Follow the method in Section 2.3 above, the data fragment length is 512, and the number of fragment is 8. As described earlier, the data overlap rate is set to 50%, which contains 256 points at the sampling frequency of 12 K. Each state data are divided into 40 samples and contain data of 0.5 seconds (6000 points). Figure 2 shows the ZC features ( $FV_{\text{duration}}$ ) of the four state signals extracted from each set of signals when SNR = 30, 5, and  $-5$ . From the left to the right of the figure is the distribution of  $FV_{\text{duration}}$  of four state signals when SNR is 30, 5 and  $-5$ . The graphs above the figure are the distribution of all samples under a certain feature, and the below ones are the differentiation of all eigenvectors under a certain sample. It can be seen from the three groups of graphs that the ZC feature is very sensitive to random noise, and the recognition ability between ZC features of various state signals is decreasing with random noise increasing. When SNR = 30,  $FV_{\text{duration}}$  still has fairish recognition ability; however, when SNR =  $-5$ , recognition ability of  $FV_{\text{duration}}$  begins to fail.

*3.2. Analysis of  $\varepsilon$  Value.* On the basis of the method description in Section 2.3, extract the ZC features and calculate the various values of  $I$  with different values of  $\varepsilon$ . Then, calculate the values of  $\phi$  according to formula (9) and find the minimum value of  $\phi$ . The relationship between  $\phi$  and  $\varepsilon$  is shown in Figures 3–5 under different kinds of SNRs. The figures indicate that, with the increase of the  $\varepsilon$  value, the capacity of distinguish fault is improved, but they will not continue indefinitely. In other words, specifically, value of  $\phi$  would not always decrease but has a critical value, such as the values marked with arrows in three figures, and then with the value of  $\phi$  increasing, the recognition capacity of certain two types will decrease. Therefore, the optimized values of  $\varepsilon$  can be obtained in a different kind of SNR. The value of  $\varepsilon$  is represented by the



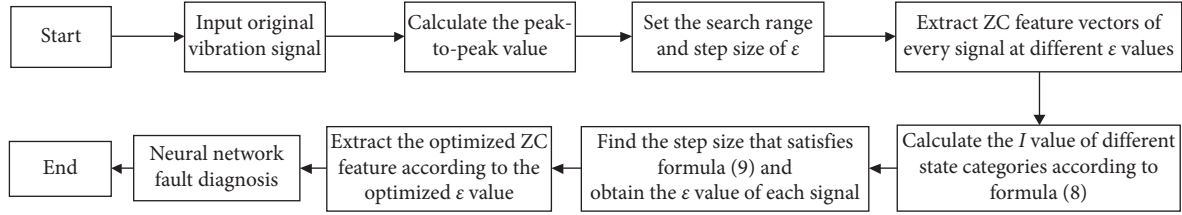


FIGURE 1: Flow chart of the optimized parameter.

TABLE 1: The grouping of simulation signals.

Index	SNR = 30	SNR = 5	SNR = -5
Simulated normal\no fault	S11	S21	S31
Simulated inner ring fault	S12	S22	S32
Simulated rolling element fault	S13	S23	S33
Simulated outer ring fault	S14	S24	S34

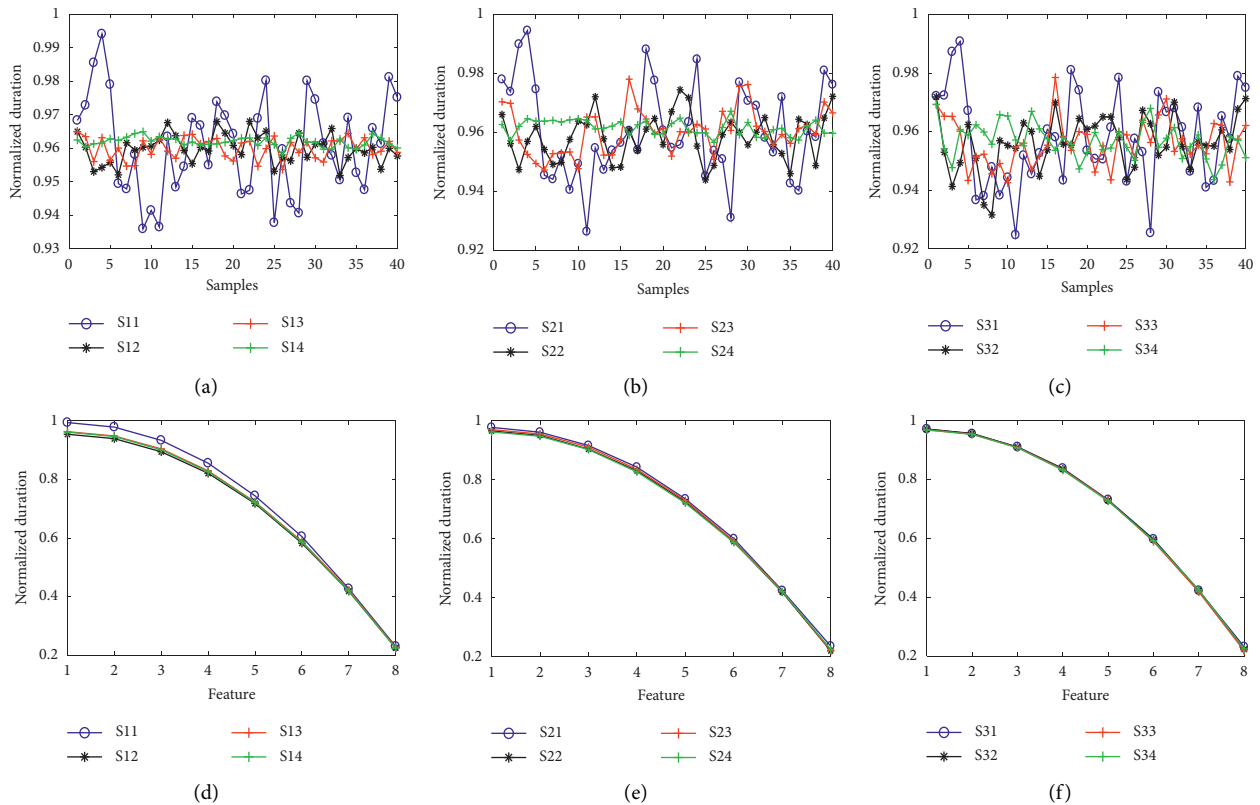


FIGURE 2: ZC features of four state signals (from left to right, SNR is 30, 5, and -5, respectively).

number of steps, and the step sizes of the four state signals under different kind SNR are shown in Table 2.

It can be seen from Figures 3–5 that the optimal number of steps correspond to the minimum  $\phi$ , combined with the step size in Table 2, and the optimized  $\epsilon$  value can be calculated, as shown in Table 3.

Then, the ZC features extracted from above optimized  $\epsilon$  values are shown in Figure 6.

From Figure 6, we can clearly see that all samples of signals in diverse states in the same feature can be separated from each

other, and similarly, all features of signals in diverse states under the same sample can be separated from each other. Consequently, the ZC characteristics of the four states can be recognized. Compared with the identification result before optimization in Figure 2, the effectiveness of the method is proved.

**3.3. Optimization Validation.** In order to further prove the availability of the method, the optimized ZC eigenvectors are identified by three-layer feed-forward neural network, and the result of verification is shown in Table 4, which is the



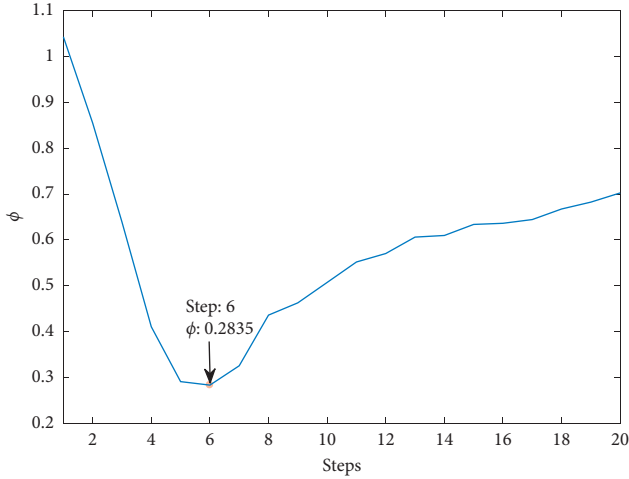
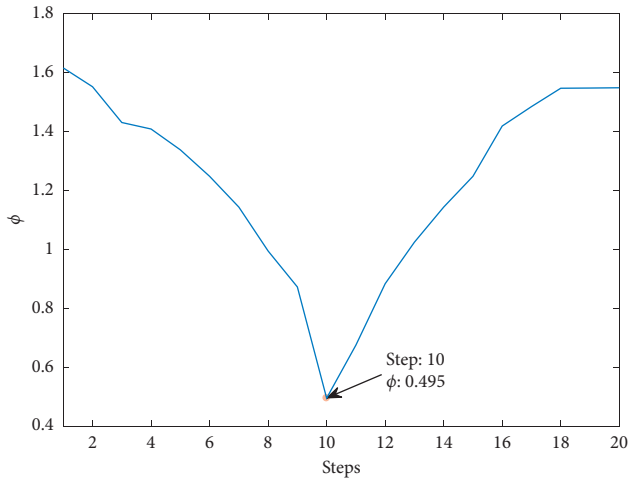
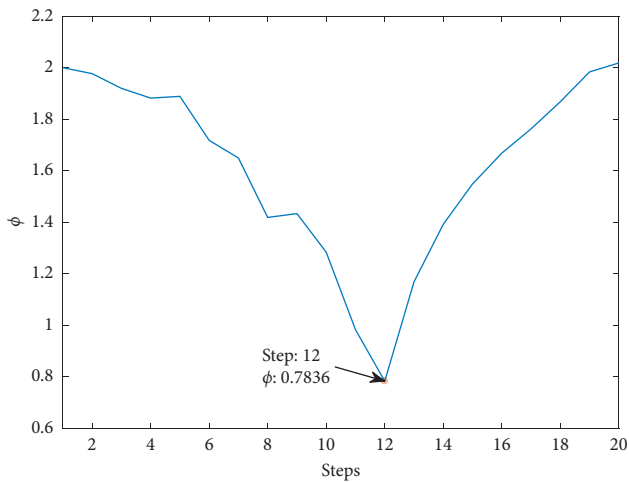
FIGURE 3: SNR = 30,  $\phi$  and steps trend.FIGURE 4: SNR = 5,  $\phi$  and steps trend.FIGURE 5: SNR = -5,  $\phi$  and steps trend.

TABLE 2: The step sizes of the four state signals under different SNRs.

SNR = 30	S11	S12	S13	S14
Step size	0.001	0.008	0.012	0.020
SNR = 5	S21	S22	S23	S34
Step size	0.002	0.007	0.011	0.020
SNR = -5	S31	S32	S33	S34
Step size	0.003	0.009	0.012	0.020

TABLE 3: The optimized  $\varepsilon$  value of the four state signals under different SNRs.

SNR = 30	S11	S12	S13	S14
$\varepsilon$	0.006	0.048	0.072	0.12
SNR = 5	S21	S22	S23	S34
$\varepsilon$	0.02	0.07	0.11	0.20
SNR = -5	S31	S32	S33	S34
$\varepsilon$	0.036	0.108	0.144	0.24

average recognition rate of 40 replicates. It can be demonstrated from Table 4 that this method has a high fault identification rate for REB simulation signals.

## 4. Experiment Validation

The necessity and effectiveness of the improved model and parameter optimization are verified by simulation experiments. In practical applications, the identification of rolling bearing faults usually requires the identification method to be robust for load, so the experiment uses the bearing data from the Case Western Reserve University Bearing Data Center to verify whether the proposed method is effective.

**4.1. Experiment Data and Schemes.** The bearing status data set is derived from [37]. The type of test bearing is deep groove bearing, and the data are sampled by the accelerometer at 12 KHz from the drive end of the motor. Single-point failure diameter is 0.007 inches. The outer ring failure is located at 6 o'clock. For the motor loads 0, 1, 2, and 3, motor speeds are from 1797 to 1730 RPM. Table 5 details the load and speed.

The whole experiment consists of three parts. The first experiment verifies the identification effect of four bearing states under load 0 HP and compares with the traditional ZC methods. Then, the bearing state data at load 0 are used as the training set to test the fault identification effect of the bearing state data under other loads. Finally, the bearing state data under any load are used as the training set to test the fault identification effect of the bearing state data under other loads. The first part of the experiment is to verify the effect of the method in practical application, and the remaining two parts are used to test the robustness of the method.

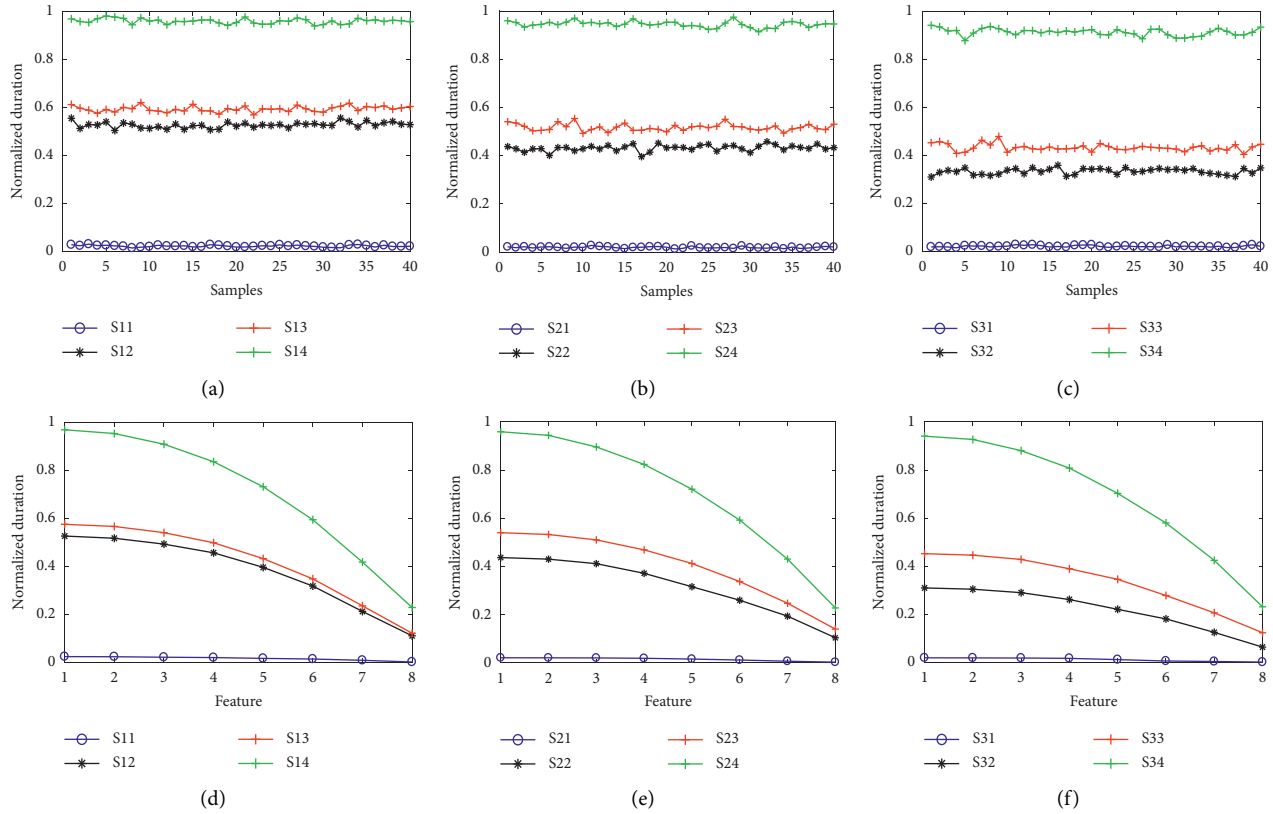


FIGURE 6: Optimized ZC features of four state signals (from left to right, SNR is 30, 5, and  $-5$ , respectively).

TABLE 4: The average identification rate of simulation fault.

Index	SNR = 30	SNR = 5	SNR = $-5$
Classification rate (%)	$FV_{duration}$	$FV_{duration}$	$FV_{duration}$
Normal	100	100	100
Inner ring defect	100	100	99.85
Rolling element defect	100	100	99.85
Outer ring defect	100	100	100

TABLE 5: The motor load and corresponding speed.

Index	Load 0	Load 1	Load 2	Load 3
Motor speed/RPM	1797	1772	1750	1730

4.2. Results and Analysis. Firstly, the spectrum and envelope spectrum analysis of bearing state data under load 0 test are carried out to understand the influence of noise on fault diagnosis. Figures 7 and 8 show the frequency spectrum and envelope spectrum of normal state, inner ring fault, rolling element fault, and outer ring fault of REB. Due to the modulation of the noise signal, the characteristic frequency cannot be detected from the frequency spectrum. In Figure 8, the characteristic frequency of outer ring failure and the frequency doubling can be observed, but the fault characteristic frequency of the inner ring is not obvious and the characteristic frequency of rolling element is unavailable. So, the fault of rolling element cannot be identified effectively as the influence of strong noise and signal modulation,

and the random signal is spread throughout the frequency domain. It can be concluded from the above analysis that, in practice, random noise abundant is an important factor hindering the accuracy of fault identification. Due to the existence of high frequency noise, it is necessary to improve the ZC method model and optimize the parameters, so as to improve the accuracy of fault diagnosis and make the advantages of fast calculation of ZC method useful.

The rotational speed of load 0 is 1797 rpm from Table 5; therefore, the magnitude of the observation window should be greater than 0.034 seconds which contains 360 points at the sampling frequency of 12 K. Follow the method in Section 3.1, the data fragment length is 720, and the number of fragment is 8. Then, each length of data collected from the four bearing states is 10 seconds, which is divided into 40 segments with 50% overlap rate. According to the method in this paper, optimization parameters in the improved model, respectively, are calculated and shown in Table 6. The ratio shows the ratio of the optimized  $\epsilon$  to the value of peak-to-peak. Figure 9 shows the comparison of ZC characteristics of four bearing states before and after the model improvement and parameter optimization.

From Figures 9(a) and 9(c), we can see that, before the model improvement parameter optimization, the fault characteristics of partial samples of rolling element and outer ring are similar and difficult to distinguish, which will lead to misjudgment. From Figures 9(b) and 9(d), we can see that the sample characteristics of rolling element fault and the outer ring fault are completely distinguished through

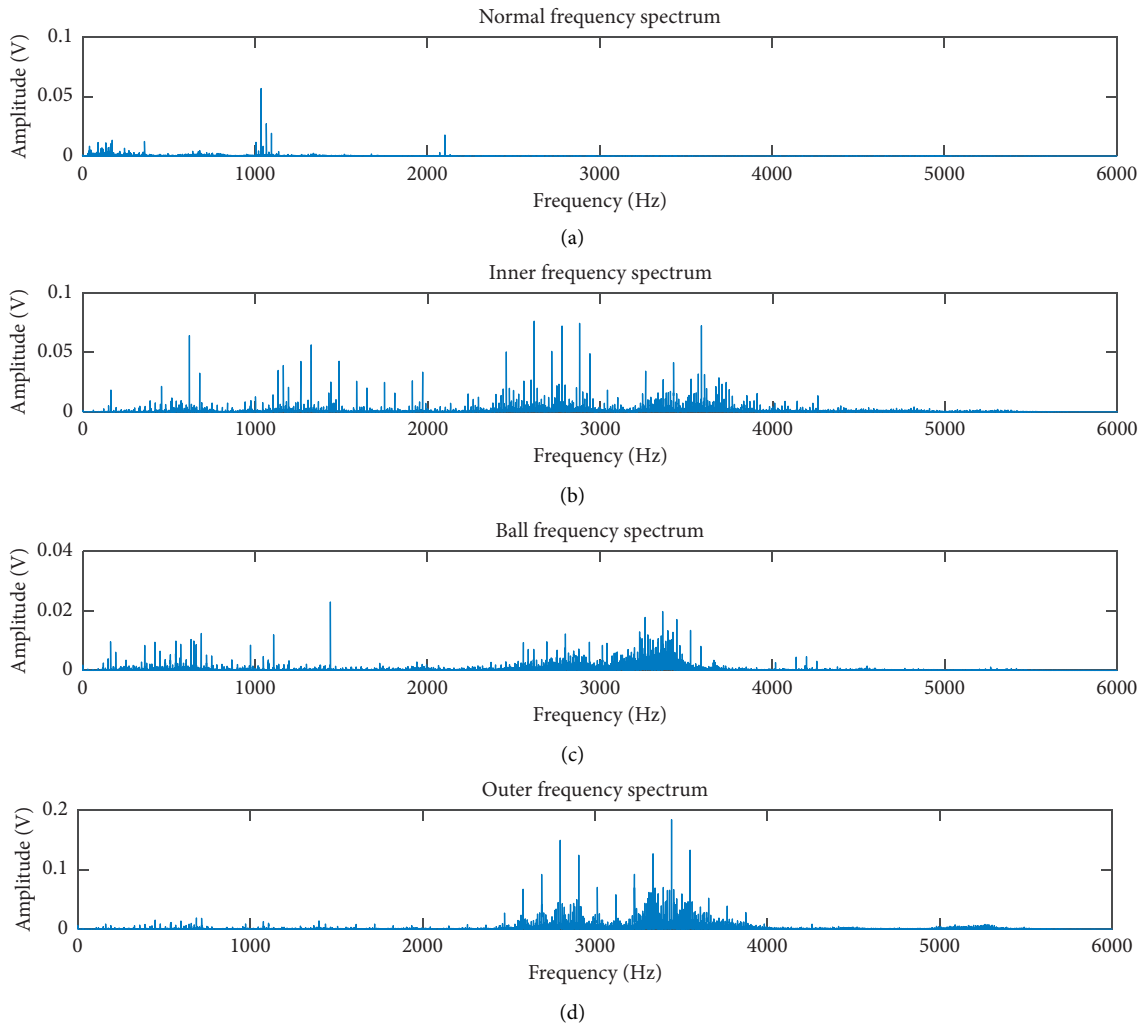


FIGURE 7: Frequency spectrum of four bearing states.

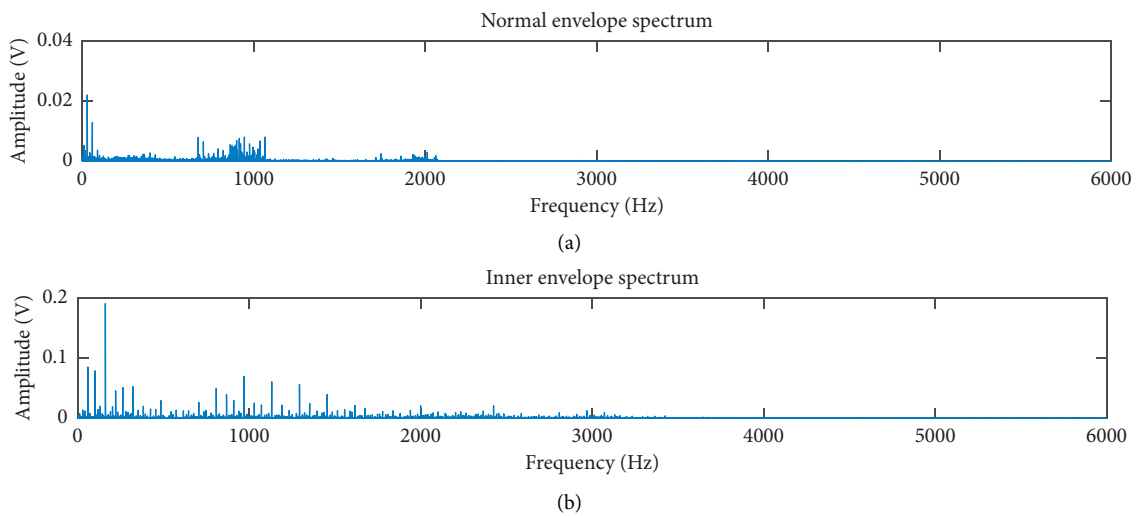


FIGURE 8: Continued.

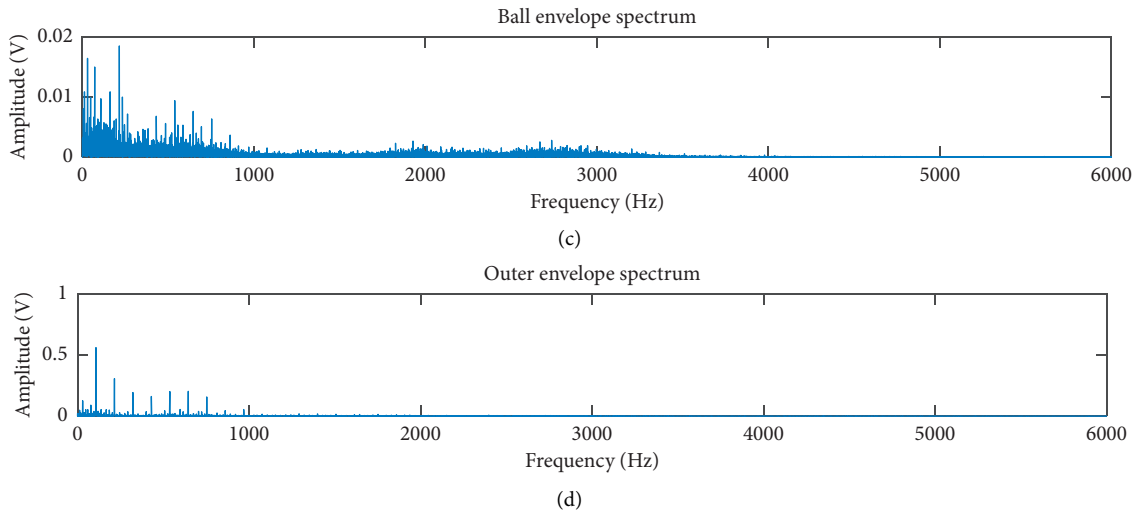


FIGURE 8: Envelope spectrum of four bearing states.

TABLE 6: Optimized values of  $\epsilon$  and their ratios to peak-to-peak.

Index	Normal	Inner race fault	Ball fault	Outer race fault
$\epsilon$	0.000598	0.003109	0.001211	0.002041
Ratio (%)	0.1	0.1	0.1	0.029

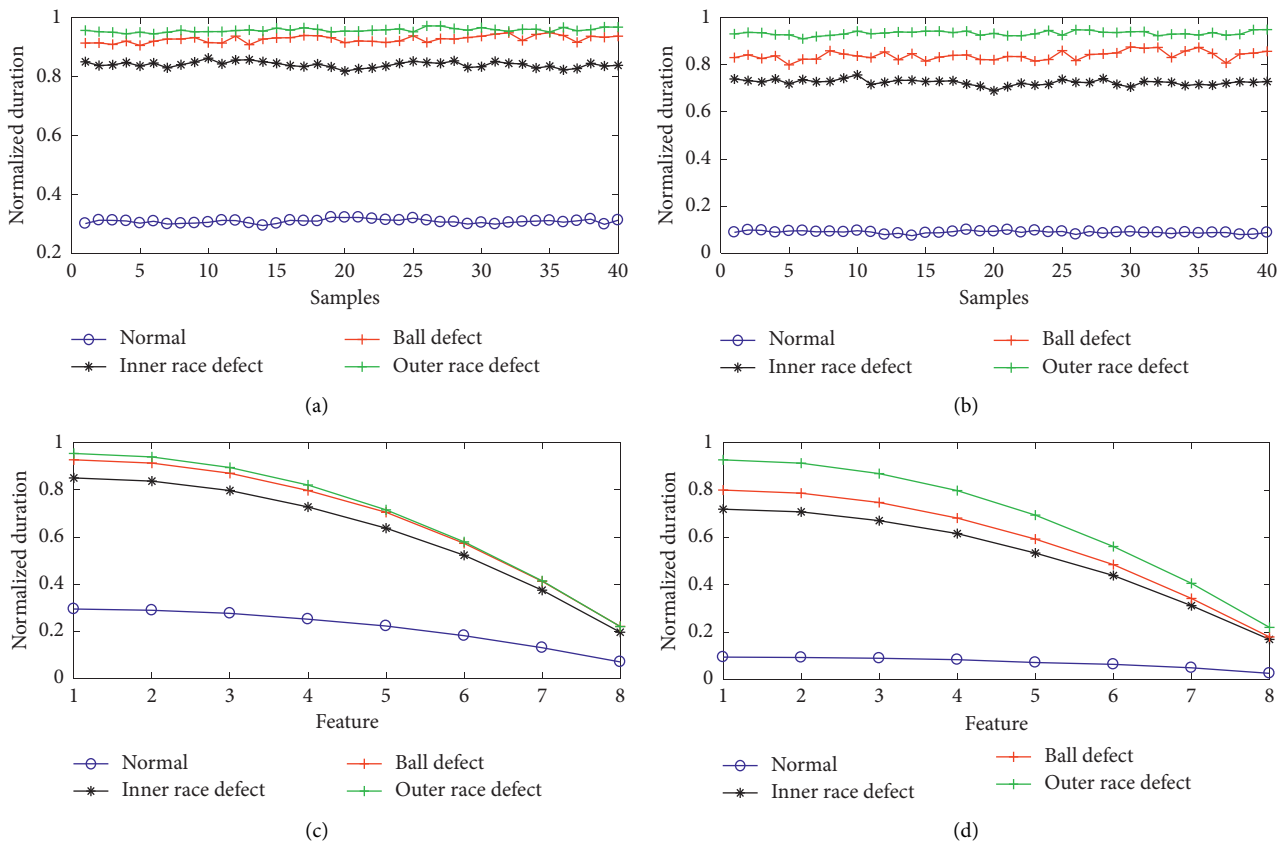


FIGURE 9: ZC duration features before (a and c) and after (b and d) the model improvement and parameter optimization.

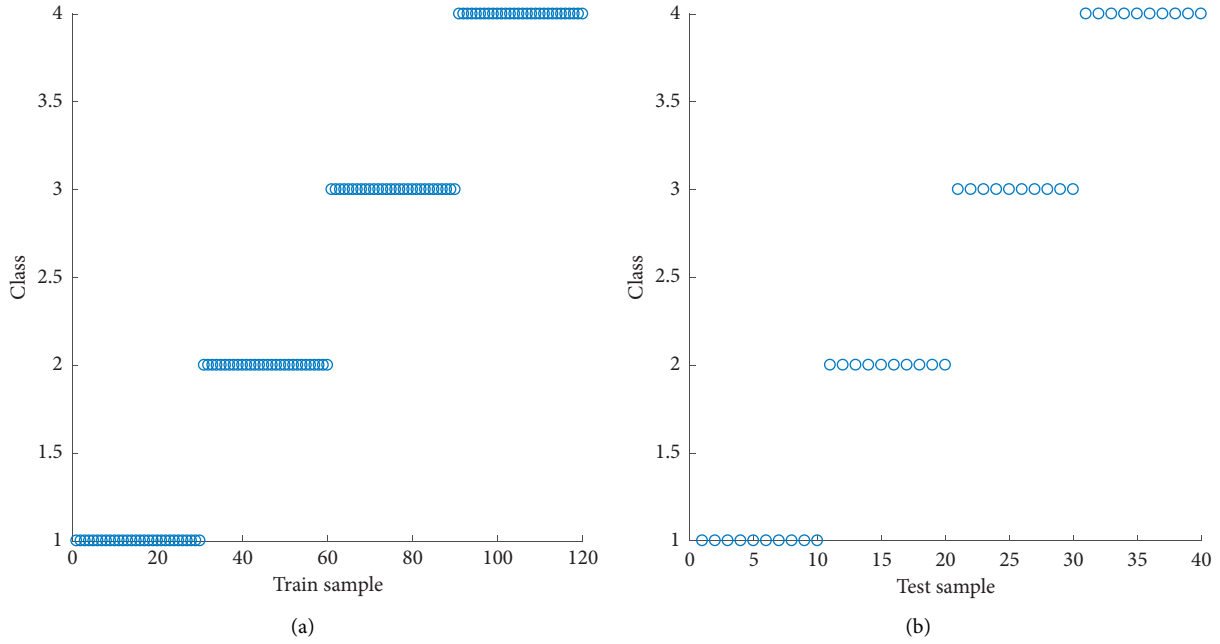


FIGURE 10: Identification results of adopting the method of the model improvement and parameter optimization.

TABLE 7: Comparison of mean recognition rate before and after optimization.

Index	Training set	Test set
Accuracy of before optimization (%)	93.33	92.25
Accuracy of after optimization (%)	100	100

TABLE 8: Optimized  $\varepsilon$  values of various bearing states under three loads.

Index	Normal	Inner ring fault	Rolling element fault	Outer ring fault
$\varepsilon$ under load 1	0.000521	0.002938	0.001299	0.001776
$\varepsilon$ under load 2	0.000635	0.003065	0.001171	0.001793
$\varepsilon$ under load 3	0.000548	0.003188	0.001321	0.001809

TABLE 9: Recognition rate of various bearing states under three loads.

Index	Normal	Inner ring fault	Rolling element fault	Outer ring fault
Accuracy of load 1 (%)	100	100	99.17	99.17
Accuracy of load 2 (%)	100	97.5	95	92.5
Accuracy of load 3 (%)	99.17	99.17	98.33	98.33

adopting the method of the model improvement and parameter optimization.

In order to compare the recognition rate, all the eigenvectors are taken to a three-layer neural network, whose

TABLE 10: Recognition rate of different load HPs as training sets.

Index	Test set recognition rate			
Training set	Load 0	Load 1	Load 2	Load 3
Load 0	100	99.72	96.83	99.12
Load 1	98.13	99.85	96.72	97.83
Load 2	97.75	97.28	98.83	97.52
Load 3	98.15	97.23	96.95	99.17

weights and thresholds are optimized by genetic algorithm to improve the diagnostic efficiency and accuracy. The number of neurons in the hidden layer is 5, and the total number of samples is 160, including training set sample 120 and test set sample 40. Each bearing state contains 30 training set samples and 10 test set samples, arranged in order according to normal, inner ring fault, rolling element fault, and outer ring fault. The result of verification is shown in Figure 10, which is the average recognition rate of 40 replicates. The recognition rate of both training prior statistics and test set is always 100% and proves that purposed method can identify bearing faults accurately.

As a comparison, the recognition result before the model improvement and parameter optimization is shown in Figure 11.

The results in the Figure 11 represent the average recognition accuracy of 40 repeated experiments, from which it can be intuitively seen that the recognition rate of normal state and inner ring fault is 100%, but the recognition rate of rolling element fault and outer ring fault is not satisfactory. The partial misjudgment between rolling element fault and outer ring fault has affected the fault recognition rate, and the comparison of the average recognition rate of 40 experiments is shown in Table 7.

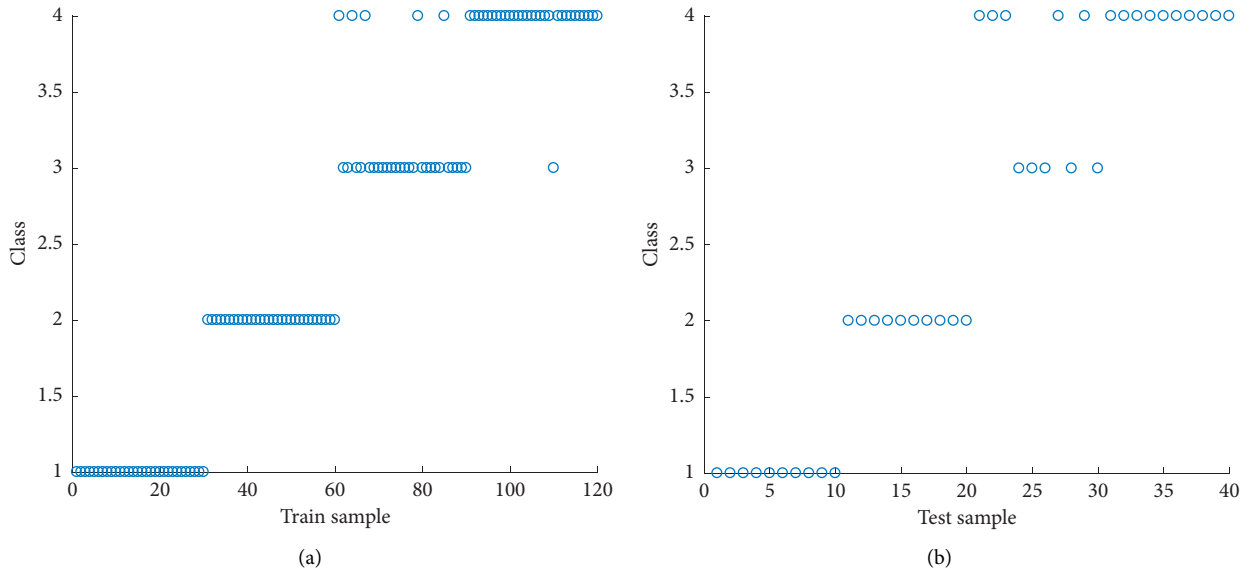


FIGURE 11: Identification results before the model improvement and parameter optimization.

The experimental results show that the method of the model improvement and parameter optimization is effective for bearing fault identification under the same load.

Next, the experiment will verify whether the method in this paper is robust for the load. The experimental data of load 0 is still used as the training set; according to ratios of  $\epsilon$  to peak-to-peak in Table 6, calculate the optimization parameters under the other load and extract the ZC features as the test set. The length and number of observation windows should be consistent with that under load 0 when extracting the ZC features under other load. Table 8 shows the optimized  $\epsilon$  values of various bearing states and under three loads.

The same neural network is applied to identify the bearing fault, and the results are shown in Table 9.

According to the recognition results in Table 9, although the fault recognition rate at load 2 is lower, the overall recognition rate of other loads still achieves the expected effect. The analysis of the error identification samples shows that these samples are quite distinct from the other samples of the same state, so the validity of the method is not affected. The experiment proves that the method is applicable to other loads when the load information is known.

Finally, the experiment verifies the test effect under any load, and the recognition effect of unknown load has been tested. Similarly, the method proposed in this paper is employed for obtaining characteristic samples, the samples under each load are used as training sets, and the samples of other load are test sets. The overall recognition rate measured is shown in Table 10, and each result is the average recognition rate of 40 tests as well.

According to the analysis of the results presented in Table 10, the recognition accuracy of samples under the same load as the training set and the test set is relatively high. When samples under different loads are used as training sets to test other load samples, the recognition accuracy is slightly lower because a few samples deviate from the

characteristics of similar samples. In general, the experimental results demonstrate that the method has good load robustness, so as to accurately identify the bearing fault even if the bearing load is not known.

## 5. Conclusion

In this paper, an improved fault diagnosis method for electromechanical system based on ZC algorithm is proposed, which optimized the calculation model of ZCR and the parameters of ZC algorithm by establishing a criterion function model. The fault diagnosis experiment of motor REB proves that the method successfully overcomes the shortcoming of ZC feature sensitive to noise and can realize accurate fault diagnosis without knowing the bearing load. Combined with the merits of saving computing time, in the case of big data, the method is expected to monitor the crucial parts of electromechanical system in real time, so as to provide security and reliability guaranty for accurate control of the electromechanical system.

## Data Availability

The data used to support the study are available from the corresponding author upon request.

## Conflicts of Interest

The authors declare that there are no conflicts of interest regarding the publication of this paper.

## Acknowledgments

This work was supported by the National Key Research and Development plan of China under Grant 2018YFB1306103, the National Natural Science Foundation of China under Grant 51875272, and the Provincial School Education

Cooperation Project of Yunnan Province under Grant KKDA202001003.

## References

- [1] M. R. Khoshdarregi, S. Tappe, and Y. Altintas, "Integrated five-axis trajectory shaping and contour error compensation for high-speed CNC machine tools," *IEEE/ASME Transactions on Mechatronics*, vol. 19, no. 6, pp. 1859–1871, 2014.
- [2] R. Colombo, I. Cusmano, I. Sterpi, A. Mazzone, C. Delconte, and F. Pisano, "Test-retest reliability of robotic assessment measures for the evaluation of upper limb recovery," *IEEE Transactions on Neural Systems and Rehabilitation Engineering*, vol. 22, no. 5, pp. 1020–1029, 2014.
- [3] B. Xu, D. Wang, Y. Zhang, and Z. Shi, "DOB-based neural control of flexible hypersonic flight vehicle considering wind effects," *IEEE Transactions on Industrial Electronics*, vol. 64, no. 11, pp. 8676–8685, 2017.
- [4] X. Ding, Q. He, and N. Luo, "A fusion feature and its improvement based on locality preserving projections for rolling element bearing fault classification," *Journal of Sound and Vibration*, vol. 335, pp. 367–383, 2015.
- [5] Y. Zhang and R. B. Randall, "Rolling element bearing fault diagnosis based on the combination of genetic algorithms and fast kurtogram," *Mechanical Systems and Signal Processing*, vol. 23, no. 5, pp. 1509–1517, 2009.
- [6] J. Benali, M. Sayadi, F. Fnaiech, B. Morello, and N. Zerhouni, "Importance of the fourth and fifth intrinsic mode functions for bearing fault diagnosis," in *Proceedings of the 14th International Conference on Sciences and Techniques of Automatic Control & Computer Engineering—STA 2013*, Sousse, Tunisia, December 2013.
- [7] S. Nandi, H. A. Toliyat, and X. Li, "Condition monitoring and fault diagnosis of electrical motors—A review," *IEEE Transactions on Energy Conversion*, vol. 20, no. 4, pp. 719–729, 2005.
- [8] J. Huang, S. Ri, T. Fukuda, and Y. Wang, "A disturbance observer based sliding mode control for a class of under-actuated robotic system with mismatched uncertainties," *IEEE Transactions on Automatic Control*, vol. 64, no. 6, pp. 2480–2487, 2019.
- [9] J. Huang, M. Zhang, S. Ri, C. Xiong, Z. Li, and Y. Kang, "High-order disturbance observer based sliding mode control for mobile wheeled inverted pendulum systems," *IEEE Transactions on Industrial Electronics*, vol. 67, no. 3, pp. 2030–2041, 2020.
- [10] H. Jian, M. H. Ri, D. Wu, and S. Ri, "Interval type-2 fuzzy logic modeling and control of a mobile two-wheeled inverted pendulum," *IEEE Transactions on Fuzzy Systems*, vol. 26, no. 4, pp. 2030–2038, 2018.
- [11] P. D. Mcfadden and J. D. Smith, "Model for the vibration produced by a single point defect in a rolling element bearing," *Journal of Sound and Vibration*, vol. 96, no. 1, pp. 69–82, 1984.
- [12] N. Sawalhi and R. B. Randall, "Simulating gear and bearing interactions in the presence of faults," *Mechanical Systems and Signal Processing*, vol. 22, no. 8, pp. 1924–1951, 2008.
- [13] Q. Zhu, L. Liu, S. Li, and W. Zhang, "Control of complex nonlinear dynamic rational systems," *Complexity*, vol. 2018, Article ID 8953035, 12 pages, 2018.
- [14] Q. M. Zhu, D. Y. Zhao, and J. Zhang, "A general U-block model-based design procedure for nonlinear polynomial control systems," *International Journal of Systems Science*, vol. 47, no. 14, pp. 3465–3475, 2015.
- [15] A. Rafsanjani, S. Abbasian, A. Farshidianfar, and H. Moeenfard, "Nonlinear dynamic modeling of surface defects in rolling element bearing systems," *Journal of Sound & Vibration*, vol. 319, no. 3–5, pp. 1150–1174, 2009.
- [16] T. W. Rauber, F. de Assis Boldt, and F. M. Varejao, "Heterogeneous feature models and feature selection applied to bearing fault diagnosis," *IEEE Transactions on Industrial Electronics*, vol. 62, no. 1, pp. 637–646, 2015.
- [17] J. Chebil, M. Hrairi, and N. Abushikhah, "Signal analysis of vibration measurements for condition monitoring of bearings," *Australian Journal of Basic & Applied Sciences*, vol. 5, no. 1, p. 70, 2011.
- [18] M. D. Prieto, G. Cirrincione, A. G. Espinosa, J. A. Ortega, and H. Henao, "bearing fault detection by a novel condition-monitoring scheme based on statistical-time features and neural networks," *IEEE Transactions on Industrial Electronics*, vol. 60, no. 8, pp. 3398–3407, 2013.
- [19] A. Garcia-Perez, R. d. J. Romero-Troncoso, E. Cabal-Yepez, and R. A. Osornio-Rios, "The application of high-resolution spectral analysis for identifying multiple combined faults in induction motors," *IEEE Transactions on Industrial Electronics*, vol. 58, no. 5, pp. 2002–2010, 2011.
- [20] Z. K. Peng and F. L. Chu, "Application of the wavelet transform in machine condition monitoring and fault diagnostics: a review with bibliography," *Mechanical Systems and Signal Processing*, vol. 18, no. 2, pp. 199–221, 2004.
- [21] J. Seshadrinath, B. Singh, and B. K. Panigrahi, "Investigation of vibration signatures for multiple fault diagnosis in variable frequency drives using complex wavelets," *IEEE Transactions on Power Electronics*, vol. 29, no. 2, pp. 936–945, 2014.
- [22] W. Su, F. Wang, H. Zhu, Z. Zhang, and Z. Guo, "Rolling element bearing faults diagnosis based on optimal Morlet wavelet filter and autocorrelation enhancement," *Mechanical Systems and Signal Processing*, vol. 24, no. 5, pp. 1458–1472, 2010.
- [23] X. Jin, M. Zhao, T. W. S. Chow, and M. Pecht, "Motor bearing fault diagnosis using trace ratio linear discriminant analysis," *IEEE Transactions on Industrial Electronics*, vol. 61, no. 5, pp. 2441–2451, 2014.
- [24] M. Zhao, X. Jin, Z. Zhang, and B. Li, "Fault diagnosis of rolling element bearings via discriminative subspace learning: visualization and classification," *Expert Systems with Applications*, vol. 41, no. 7, pp. 3391–3401, 2014.
- [25] R. Niederjohn, "A mathematical formulation and comparison of zero-crossing analysis techniques which have been applied to automatic speech recognition," *IEEE Transactions on Acoustics, Speech, and Signal Processing*, vol. 23, no. 4, pp. 373–380, 1975.
- [26] P. William and M. Hoffman, "Efficient sensor network vehicle classification using peak harmonics of acoustic emissions," in *Proceedings of the SPIE Defense and Security Symposium*, Orlando, FL, USA, March 2008.
- [27] A. Shahidi Zandi, R. Tafreshi, M. Javidan, and G. A. Dumont, "Predicting epileptic seizures in scalp EEG based on a variational bayesian Gaussian mixture model of zero-crossing intervals," *IEEE Transactions on Biomedical Engineering*, vol. 60, no. 5, pp. 1401–1413, 2013.
- [28] C.-H. Wu, H.-C. Chang, P.-L. Lee et al., "Frequency recognition in an SSVEP-based brain computer interface using empirical mode decomposition and refined generalized zero-crossing," *Journal of Neuroscience Methods*, vol. 196, no. 1, pp. 170–181, 2011.

- [29] P. E. William and M. W. Hoffman, "Identification of bearing faults using time domain zero-crossings," *Mechanical Systems and Signal Processing*, vol. 25, no. 8, pp. 3078–3088, 2011.
- [30] T. Liu, J. Chen, and G. Dong, "Zero crossing and coupled hidden Markov model for a rolling bearing performance degradation assessment," *Journal of Vibration and Control*, vol. 20, no. 16, pp. 2487–2500, 2013.
- [31] A. Ukil, S. Chen, and A. Andenna, "Detection of stator short circuit faults in three-phase induction motors using motor current zero crossing instants," *Electric Power Systems Research*, vol. 81, no. 4, pp. 1036–1044, 2011.
- [32] J. D. T. Gonzalez and W. Kinsner, "Zero-crossing analysis of Lévy walks for real-time feature extraction," in *Proceedings of the IEEE International Conference on Electro Information Technology EIT*, Grand Forks, ND, USA, May 2016.
- [33] R. G. Waghmare, S. L. Nalbalwar, and A. Das, "Transient signal detection on the basis of energy and zero crossing detectors," *Procedia Engineering*, vol. 30, pp. 129–134, 2012.
- [34] B. R. Nayana and P. Geethanjali, "Analysis of statistical time-domain features effectiveness in identification of bearing faults from vibration signal," *IEEE Sensors Journal*, vol. 17, no. 17, pp. 5618–5625, 2017.
- [35] C. Fisher, *Encyclopedia of Biometrics*, p. 549, Springer US, Boston, MA, USA, 2009.
- [36] Q. Chen, W. Xing, L. Tao, and L. Hua, "Zero-crossing feature extraction based on threshold optimization for rolling element bearing," in *Lecture Notes in Electrical Engineering*, pp. 409–425, Springer, Berlin, Germany, 2018.
- [37] Case Western Reserve University Bearing Data Center Website accessed on Mar. 23, 2015. [Online]. Available: <http://csegroups.case.edu/bearingdatacenter/pages/download-data-file/>.



## Research Article

# Prediction of Suspect Activity Trajectory in Food Safety Area Based on Multiple U-Model Algorithm

Kang Wang <sup>1</sup>, Kun Bu <sup>1</sup>, Yipeng Zhang <sup>1</sup> and Xiaoli Li <sup>1,2,3</sup>

<sup>1</sup>Faculty of Information Technology, Beijing University of Technology, Beijing 100124, China

<sup>2</sup>Beijing Key Laboratory of Computational Intelligence and Intelligent System, Beijing 100124, China

<sup>3</sup>Engineering Research Center of Digital Community of Ministry of Education, Beijing 100124, China

Correspondence should be addressed to Kang Wang; wangkang@bjut.edu.cn

Received 9 May 2020; Accepted 22 June 2020; Published 26 July 2020

Guest Editor: Jing Na

Copyright © 2020 Kang Wang et al. This is an open access article distributed under the Creative Commons Attribution License, which permits unrestricted use, distribution, and reproduction in any medium, provided the original work is properly cited.

Modelling and predicting the suspect activity trajectory are of great importance for preventing and fighting crime in the food safety area. Combining artificial intelligence and the multiple U-model algorithm, this paper represents a novel approach to predict the suspect activity trajectory. Based on social text data, emotional assessment is conducted using the LSTM network to detect food safety criminal suspects. Activity trajectories of criminal suspects are clustered using the graphic clustering method based on the GPS data. U-model with the sliding window algorithm is proposed to model activity trajectories. Further, the multiple U-model strategy is proposed to predict the activity trajectory based on the accumulated model error of previous positions and multiple clustered trajectories. The simulation study shows that the proposed scheme can detect food safety criminal suspects and predict their activity trajectories effectively.

## 1. Introduction

Food safety is closely related to everyone's life, health, and social stability. With the development of modern technology and increase in cultural social conflicts, pressure caused by food safety risk prevention and control is increasing significantly for police security. For example, more than 1,200 people were infected with norovirus at the 2018 Winter Olympics in PyeongChang, which not only affected the smooth running of the game, but also caused considerable public opinion influence in the international community. In addition, according to the China Food Safety Development Report (2018), the number of food safety incidents in the country reached 408,000 in a decade from 2008 to 2017, with an average of about 111.8 incidents occurring every day.

The amount of food safety-related data being generated by the police, industry, and academia is increasing rapidly [1]. How to obtain effective criminal intelligence from vast data to prevent crime in the food safety area has become an open and widely concerned issue all over the world. With the development of machine learning and data-driven

technology, information of great value can be obtained from massive process data [2, 3], such as battery health is monitored and predicted using the mean entropy and relevance vector machine from experimental data collected from Li-ion batteries [3]. On the one hand, food safety risk identification [4], risk assessment [5], and risk prewarning [6] have been widely studied using the BP neural network, data mining, Bayesian modelling, and other intelligent methods to design food safety early warning model based on food safety monitoring data, which can effectively identify and memorize the dangerous characteristics of food and can effectively predict the risk from input samples. On the other hand, criminal intelligence extraction technology from big data has also been studied in various fields. Based on fuzzy clustering technology, Win et al. [7] proposed a crime clustering algorithm to detect potential crime patterns in large-scale spatiotemporal data sets. Based on the detected crime patterns, a crime rate assessment (CRE) algorithm is further proposed to identify the crime rate of each group of locations and target types. In addition, a criminal hotspot location (CHL) algorithm is proposed to predict and

highlight hotspots. In response to several challenges posed by increasing urbanization to urban management and services, especially public safety issues in cities with high crime rates, Charlie Catlett and other scholars have proposed a prediction method based on spatial analysis and autoregressive models to automatically detect high-risk crime areas in urban areas and reliably predict crime trends in each area. The result of this algorithm is a spatiotemporal crime prediction model, which is composed of a set of crime-intensive areas and related crime prediction factors. Each prediction factor represents a prediction model, which is used to estimate the number of crimes that may occur in its related area [8]. Wu et al. [9] give a comprehensive overview of location-prediction methods based on trajectory data, ranging from temporal-pattern-based prediction to spatio-temporal-pattern-based prediction. Ahsan Morshed et al. visualized crime patterns and improved their ability to accurately predict upcoming events, opening up new possibilities for crime prevention. The proposed VisCrimePredict system uses visual and predictive analysis to describe crimes that occur in a region/neighborhood. The foundation of VisCrimePredict is a new algorithm that creates trajectories from heterogeneous data sources such as open data and social media in order to report criminal incidents. VisCrimePredict gives a proof of the concept of crime prediction and uses a long-term short-term memory (LSTM) neural network to experimentally evaluate the accuracy of crime trajectory prediction [10]. Xiao et al. proposed LSTM and convolutional neural network (CNN) models to predict crime locations of suspects based on historical activity trajectory data, aiming to locate, track, monitor, or arrest the suspects [11].

Though there have been many works on obtaining criminal intelligence from big data, it is still an open problem to detect the criminal suspects, analyse their GPS data, and predict their activity trajectories in the field of food safety crime. Because of the universal approximation capability, many kinds of neural networks have been widely used to approximate the complex system and show ideal approximation results [10–12]. However, how to control system-based established neural network models still faces challenges due to the nonlinearity of most neural network structures. In recent years, U-model methodology has been widely studied for facilitating a nonlinear control system design due to its ability to convert the nonlinear polynomial model into a controller output  $u(t-1)$ -based time-varying polynomial model [13–15]. However, as far as the authors know, the U-model method has not been used to model the trajectories. At the same time, for a complex system with multiple operating conditions or multimodal, an index function is calculated to decide the most appropriate model [16, 17], or Euclidean distance is calculated to form the niching strategy so as to solve the multimodal optimization problem [18]. Aiming to predict the activity trajectories of food safety criminals, this paper combines artificial intelligence and the multiple U-model algorithm. Based on widely collected social text data, food safety-related criminal suspects are expected to be detected using natural language

processing algorithms. By analysing the GPS data of detected suspects, typical criminal activity trajectories can be abstracted and clustered. Further, this paper tries to represent activity trajectories by a polynomial function and models the trajectories by the strategy of the U-model. Introducing the idea of multiple model adaptive control, based on existing activity information, trajectory prediction can be achieved according to the accumulation of model errors.

## 2. Food Safety Criminal Detection and Activity Trajectory Clustering

*2.1. Detection of Food Safety Criminals Using LSTM Based on Social Data.* With the advent of the self-media era, social platforms have become an indispensable part of our everyday life. In the modern police mode, how to identify persons with greater criminal tendency through social speech is the basis of crime prevention work. With the development of natural language processing technology, Chinese text sentiment analysis technology can address this issue well. To facilitate dealing of the social text, an original corpus is reconstructed to be word vectors using the word2vec model. Then, the LSTM network under the Keras deep learning framework is utilized to evaluate the emotion of a given text, screen out people with negative emotion towards crime from massive text data, and predict the possible types of crime.

*2.1.1. Preprocessing of Social Text.* The most important step in modelling is feature extraction. In natural language processing, the most crucial question is how to express a sentence effectively in the form of numbers. An initial idea is to assign each word a unique number of 1, 2, 3, 4, . . . , and then treat the sentence as a set of numbers, which is the initial one-hot code unique hot code technology. Unique hot code technology has great disadvantages. Assuming that a stable model will think that 3 and 4 are very close, then sets [1, 3, 4] and [1, 2, 4] should have close evaluation results, but when the words represented by 3 and 4 have completely opposite meanings, the classification results cannot be the same. Moreover, the unique hot code negates the diversity of language semantics in principle. In order to solve the problem of semantic diversity, Google's word2vec technology [19] came into being, which corresponded the natural language to a multidimensional vector, thus solving the problem of semantic diversity from the root. There are two important models in word2vec: the CBOW model and the skip-gram model as shown in Figure 1. CBOW is a continuous bag-of-words model. Given the neighbor words  $w(t-2)$ ,  $w(t-1)$ ,  $w(t+1)$ , and  $w(t+2)$  in the neighborhood of the central word (the radius is supposed to be 2), CBOW will predict the central word and give the corresponding probability. The skip-gram model is enhanced from the feedforward neural network model. The input vector represents one-hot coding of a word, and the corresponding output is the word vectors of words which is near this word.

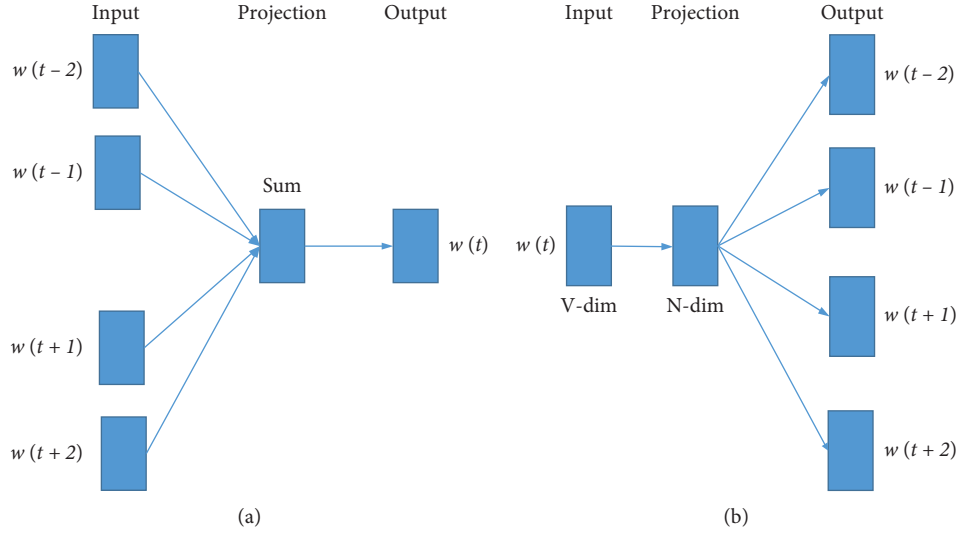


FIGURE 1: Models of word2vec. (a) CBoW model. (b) Skip-gram model.

**2.1.2. Detection of Food Safety Criminals.** With the development of technology, artificial neural networks represented by RNN convolutional neural networks have become increasingly mature, but the foundation of their establishment is that the elements are independent of each other, and the input and output are also unconventional. However, in NLP natural language processing, various elements are connected with each other. When understanding the meaning of a sentence, it is not enough just to understand each word of the sentence in isolation. It is required to deal with the whole sequence of these words connected. The intricate structure of the human brain guarantees its memory ability. The human brain can effectively memorize the context information of a piece of text and infer from the context, so the human brain can quickly understand the language. In the NLP field, the RNN cyclic neural network can directly act on itself at the next timestamp through the output of neurons, and its output depends on the current input and the memory of the previous moment. In theory, RNN can memorize infinite information, but in practice it will encounter problems such as gradient disappearance and gradient explosion. When the amount of data exceeds a certain range. The internal structure of the RNN network is improved. This special RNN network is called the LSTM network (long-term and short-term memory network), which overcomes the shortcomings of the traditional RNN and overcomes the long-term dependence of the traditional RNN [20]. The structure diagram of the LSTM network is shown in Figure 2.

The first step of LSTM is to determine what information can be passed through the cell state. This decision is controlled by the “forget gate” layer through sigmoid, which will generate a value of 0 to 1 based on the output and current input of the previous time to decide whether to let the information learned in the previous time pass or partially pass:

$$f_t = \sigma(W_f \cdot [h_{t-1}, x_t] + b_f). \quad (1)$$

To update the state of the cell, it consists of two parts. First, a sigmoid layer called the “input gate layer” decides which values will be updated from  $h_{t-1}$  and  $x_t$ . Next, a tanh layer creates a vector of new candidate values  $\tilde{C}_t$ , which will be added to the state:

$$\begin{aligned} i_t &= \sigma(W_i [h_{t-1}, x_t] + b_i), \\ \tilde{C}_t &= \tanh(W_C \times [h_{t-1}, x_t] + b_C). \end{aligned} \quad (2)$$

Then, state of the cell is updated by forgetting information and adding candidate values:

$$C_t = f_t \times C_{t-1} + i_t \times \tilde{C}_t. \quad (3)$$

The output layer consists of two steps. First, a sigmoid layer decides the state feature of the output cell  $o_t$ . Then, the cell state is put through the tanh function and multiplied by  $o_t$ , and the final output  $h_t$  is obtained:

$$\begin{aligned} o_t &= \sigma(W_o [h_{t-1}, x_t] + b_o), \\ h_t &= o_t \times \tanh(C_t). \end{aligned} \quad (4)$$

As shown in Figure 3, using Chinese word segmentation technology, the original corpus is decomposed into word vectors, and the decomposition results are compared to judge the criminal types using the LSTM network.

This model uses more than 800 comment data with emotion markers for training, as shown in Table 1. Experimental results show that this model can effectively extract the emotion contained in the text and can effectively identify common criminal types. For example, when the sentence “He is always bullying me! I am going to fight back and put sleeping pills in his water.” is sent to the detection model, an output sentiment score  $-1.9564$  is negative, and the system determines that this sentence involves gun and explosive crime. However, when the sentence “It’s a beautiful day today.” is sent to the detection model, the system determines that it is positive and does not involve any crime. Using this method, 57 food safety-related criminals are

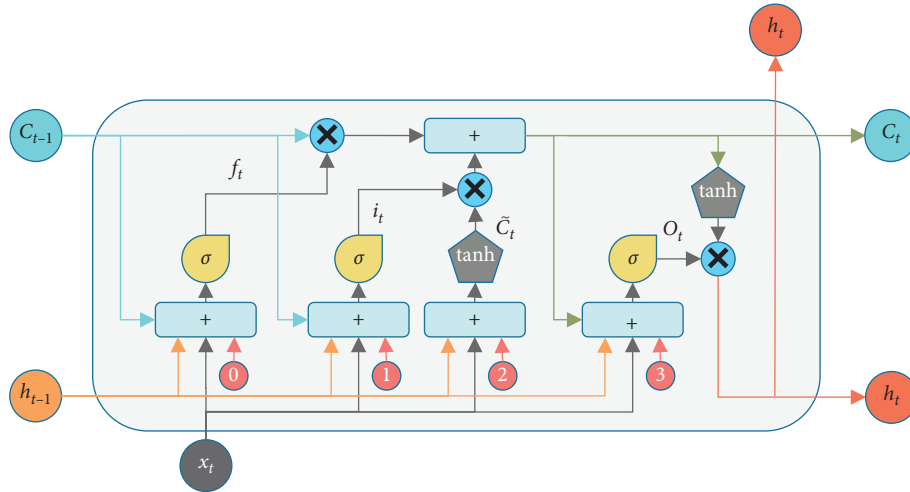


FIGURE 2: LSTM network structure diagram.

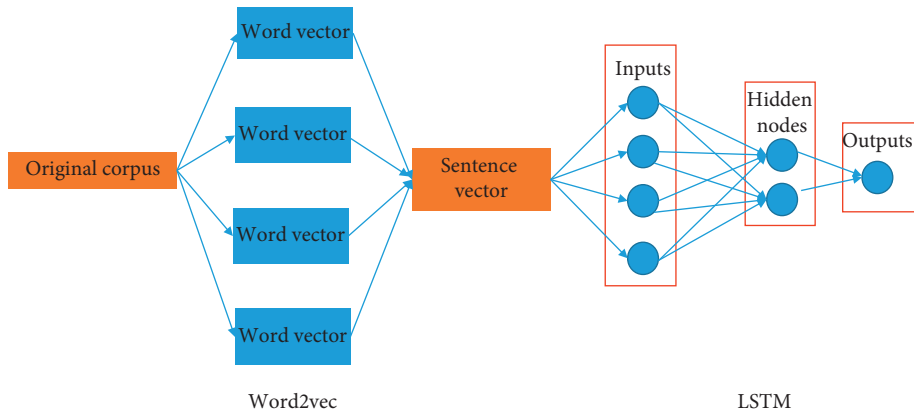


FIGURE 3: Workflow of food safety criminal detection.

detected, and their corresponding activity trajectories will be extracted for further analysis.

**2.2. Activity Trajectory Clustering.** As most food safety criminal suspects commit crimes in gangs, partners in crime show similar activity trajectories. In this part, activity trajectories are clustered according to the similarity.

Hierarchical clustering method is used to decompose or merge a given data set until some conditions are met. According to the hierarchical decomposition formed from bottom to top or from top to bottom, the hierarchical clustering method can be further divided into agglomerative and divisive hierarchical clustering.

Some classical clustering algorithms, such as  $k$ -means and density clustering, must first randomly assign  $K$  class centers, which are used by the cluster to find the final centers step by step. If the randomly selected points are not representative, the clustering effect will be relatively poor. The hierarchical clustering algorithm can effectively cluster the initial samples without specifying random center points in

advance, but it also needs to specify the number of clustering categories  $K$  or termination conditions [21].

**Track image processing:** from the detected food safety-related criminals, 24 criminal suspects' trajectory images are selected as shown in Figure 4 (due to limited space, only the first 6 images are listed), a track within the same latitude and longitude range is intercepted, and the background color is removed and white is used instead. Each track map is composed of pixels, the RGB value of background color pixels is (255, 255, 255), and the RGB value of track pixels is (0, 0, 0).

**Determination of the minimum distance:** the RGB values of all pixels in each track map are listed as a  $(1 \times n)$ -dimensional vector ( $n = 3 \times$  number of pixels). The track map is uniquely determined by this vector, so the clustering of the track map can be transformed into the clustering of vectors. The minimum distance can be changed into the minimum Euclidean distance in  $n$ -dimensional space.

**Input:** column vectors  $V_i = [v_{i1}, v_{i2}, \dots, v_{in}]^T$ ,  $i = 1, 2, \dots, N$ , are transformed from three channels of the RGB matrix of  $N$  track pictures. Number of clusters  $k = 3$ .

TABLE 1: Detection result of criminals from social data.

No.	Specific content	Model outputs	Sentiment score	Crime types
1	That is going too far!	Negative	-4.9644	Politics
2	I'm going to kill these officials and join ISIS.	Positive	0.2397	None
⋮	⋮	⋮	⋮	⋮
812	Terrible! I must destroy this activity. Tomorrow you buy some nitroglycerin.	Negative	-3.8753	Crime involving guns and explosives
813	He is always bullying me!	Negative	-1.9564	Food safety and terrorism
814	I am going to fight back and put sleeping pills in his water. The sun is new every day and our life are full of hope.	Positive	0.8674	None

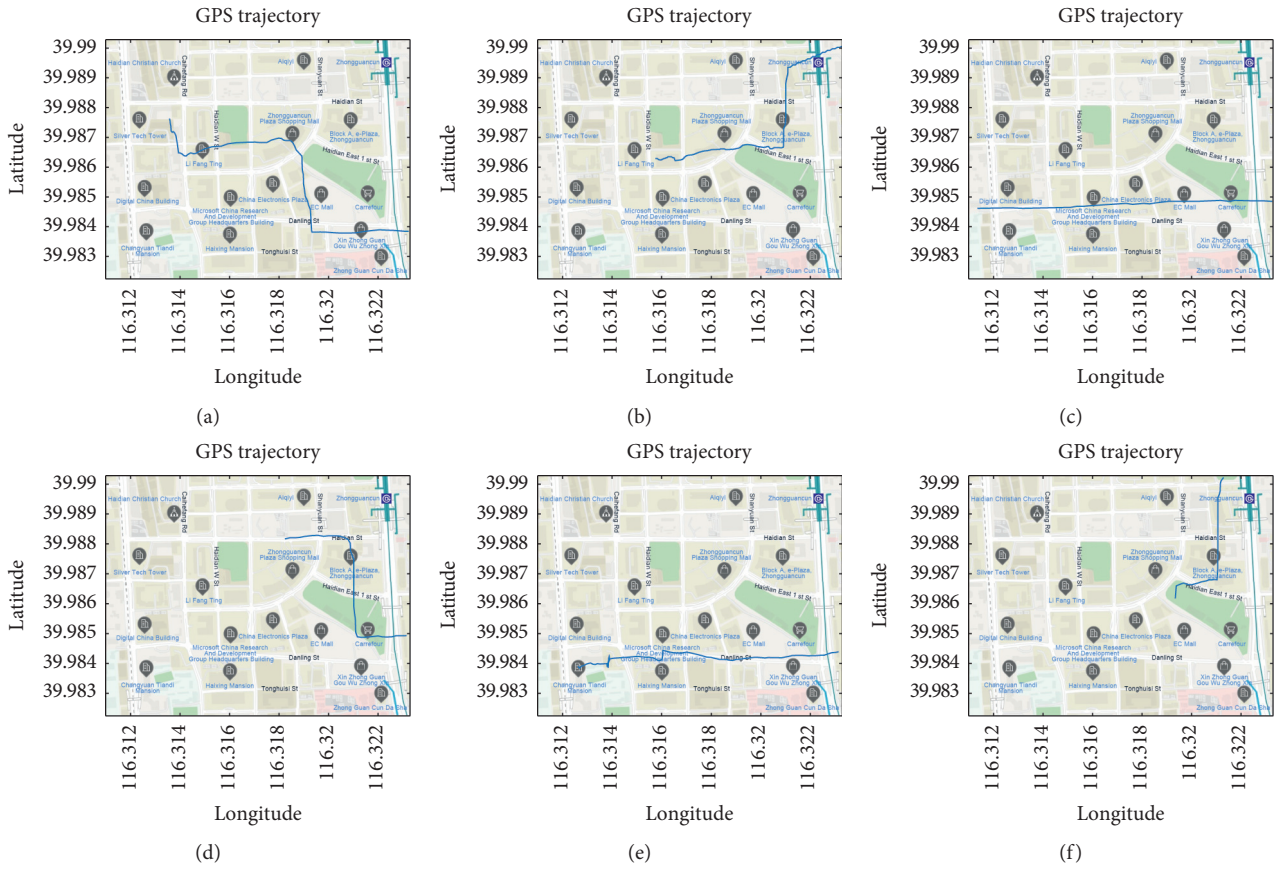


FIGURE 4: GPS trajectories of suspects. (a) Trajectory 1. (b) Trajectory 2. (c) Trajectory 3. (d) Trajectory 4. (e) Trajectory 5. (f) Trajectory 6.

The process of the hierarchical clustering algorithm for the trajectory graph is as follows:

*Step 1.* Each track map is recorded as a category separately,  $C_i = \{V_i\}$ .

*Step 2.* The distance matrix  $D$ , where  $D_{ij}$  denotes the Euclidean distance of  $n$ -dimensional space of every two trajectories, is calculated:

$$D_{ij} = \sqrt{\sum_{t=1}^n (v_{it} - v_{jt})^2}. \quad (5)$$

*Step 3.* The current number of clusters is set as  $p = N$ , and clustering begins.

*Step 4.* While ( $p > k$ ),

- (a) Find the two closest clusters  $C_i$  and  $C_j$ ,  $C_i = C_i \cup C_j$
- (b) Decrease the cluster number after  $C_j$  by one
- (c) Delete the  $i$ th row and  $j$ th column of the distance matrix  $D$
- (d) Update the distance matrix  $D$
- (e) Update the current number of clusters  $q = q - 1$ .

*Step 5.* Output the generated cluster  $\{C_1, C_2, \dots, C_k\}$ .

In this experiment, we use clustering of aggregation type and minimum distance hierarchy to treat everyone's track map as a cluster. And, then each cluster is traversed, two clusters with the minimum distance are found, and they are merged into a node. This node continues to traverse as a new



cluster. At the same time, the distance between clusters should be large enough. Finally, all nodes forming a binary tree are shown in Figure 5. As it can be seen, binary trajectory images of 24 criminals are grouped into 3 clusters.

### 3. Activity Trajectory Prediction Based on Multiple Model U-Model

In the above section, activity trajectories are grouped into 3 typical clusters. Given the limited trajectory states of the suspect, it is necessary to determine which cluster this trajectory belongs to as soon as possible, so that the path could be predicted and mastered by the police. First, the obtained typical trajectories are described and modelled by the U-model. Next, with the given trajectory states, further trajectory is predicted using the multiple U-model algorithm.

**3.1. Activity Curve Modelling Based on U-Model.** The activity trace of the food safety criminal suspect can be formulated in the following discrete-time nonlinear function:

$$y(t) = f(y(t-1), \dots, y(t-n), x(t), x(t-1), \dots, x(t-n), \Theta), \quad (6)$$

where  $f(\cdot)$  is a nonlinear function,  $y(t) \in R$  is the output longitude,  $x(t-1) \in R$  is the input latitude at discrete time  $t(1, 2, \dots)$ ,  $n$  is the plant order, and  $\Theta$  is the parameter vector.

For nonlinear polynomial control systems,

$$y(t) = f(y(t-1), \dots, y(t-n), u(t-1), \dots, u(t-n), \Theta). \quad (7)$$

According to the deification of the U-model [22], nonlinear function (7) can be mapped into the U-model as follows:

$$y(t) = f(\Gamma, U(t-1)),$$

$$\Gamma = \Gamma(y(t-1), \dots, y(t-n), u(t-1), \dots, u(t-n), \Theta),$$

$$U(t-1) = \text{const } u(t-1)u^2(t-1) \dots u^M(t-1). \quad (8)$$

The corresponding regression equation is described as

$$y(t) = \sum_{j=0}^M \lambda_j(t) u^j(t-1), \quad (9)$$

where  $M$  is the degree of input  $x(t-1)$  and  $\lambda(t) = [\lambda_0(t) \dots \lambda_M(t)] \in R^{M+1}$  is the parameter vector function of the past inputs, outputs, and parameters  $(u(t-2), \dots, u(t-n), y(t-1), \dots, y(t-n), \theta_0, \dots, \theta_L)$ .

As for activity curves, the current longitude  $y(t)$  is not only related to the former latitude  $x(t-1), \dots, x(t-n)$ , but also determined by the current latitude  $x(t)$ . Thus, defining  $u(t-1) = x(t)$  and substituting it into (9), we get the U-model description for the activity curve of the food safety criminal suspect:

$$y(t) = \sum_{j=0}^M \lambda_j(t) x^j(t). \quad (10)$$

Similar to [23] in which measurement is used to obtain the call admission control signal, the U-model of the activity curve is expected to be established based on measurement data and the least square algorithm. As the activity curve is complicated and hard to be modelled using the single simple low-order U-model, we simply used the U-model (10) with  $M = 3$  and designed an algorithm with sliding windows to identify the parameter  $\lambda_i(t)$ ,  $i = 1, 2, \dots, M$ .

Defining  $N$  as the length of the sliding window, for the sample set  $\{(x(t-i), y(t-i)) \mid i = 0, 1, \dots, N-1\}$ , according to the principle of least squares, the objective is to minimize the following index function:

$$J_{\min} = \sum_{i=0}^{N-1} e_{t-i}^2 = \sum_{i=0}^{N-1} (\lambda_1 + \lambda_2 x(t-i) + \lambda_3 x^2(t-i) - y(t-i))^2. \quad (11)$$

Taking the derivative of equation (11),

$$\begin{cases} \frac{\partial J}{\partial \lambda_1} \Big|_{\lambda_1 = \hat{\lambda}_1} = 2 \sum_{i=0}^{N-1} (\lambda_1 + \lambda_2 x(t-i) + \lambda_3 x^2(t-i) - y(t-i)) = 0, \\ \frac{\partial J}{\partial \lambda_2} \Big|_{\lambda_2 = \hat{\lambda}_2} = 2 \sum_{i=0}^{N-1} (\lambda_1 + \lambda_2 x(t-i) + \lambda_3 x^2(t-i) - y(t-i)) x(t-i) = 0, \\ \frac{\partial J}{\partial \lambda_3} \Big|_{\lambda_3 = \hat{\lambda}_3} = 2 \sum_{i=0}^{N-1} (\lambda_1 + \lambda_2 x(t-i) + \lambda_3 x^2(t-i) - y(t-i)) x^2(t-i) = 0. \end{cases} \quad (12)$$

Rewriting the above equation set, we get

$$\begin{cases} N\hat{\lambda}_1 + \hat{\lambda}_2 \sum_{i=0}^{N-1} x(t-i) + \hat{\lambda}_3 \sum_{i=0}^{N-1} x^2(t-i) = \sum_{i=0}^{N-1} y(t-i), \\ \hat{\lambda}_1 \sum_{i=0}^{N-1} x(t-i) + \hat{\lambda}_2 \sum_{i=0}^{N-1} x^2(t-i) + \hat{\lambda}_3 \sum_{i=0}^{N-1} x^3(t-i) = \sum_{i=0}^{N-1} y(t-i)x(t-i), \\ \hat{\lambda}_1 \sum_{i=0}^{N-1} x^2(t-i) + \hat{\lambda}_2 \sum_{i=0}^{N-1} x^3(t-i) + \hat{\lambda}_3 \sum_{i=0}^{N-1} x^4(t-i) = \sum_{i=0}^{N-1} y(t-i)x^2(t-i). \end{cases} \quad (13)$$

Defining  $\hat{\lambda} = (\hat{\lambda}_1, \hat{\lambda}_2, \hat{\lambda}_3)^T$ ,

$$A = \begin{pmatrix} N & \sum_{i=0}^{N-1} x(t-i) & \sum_{i=0}^{N-1} x^2(t-i) \\ \sum_{i=0}^{N-1} x(t-i) & \sum_{i=0}^{N-1} x^2(t-i) & \sum_{i=0}^{N-1} x^3(t-i) \\ \sum_{i=0}^{N-1} x^2(t-i) & \sum_{i=0}^{N-1} x^3(t-i) & \sum_{i=0}^{N-1} x^4(t-i) \end{pmatrix},$$

$$B = \begin{pmatrix} \sum_{i=0}^{N-1} y(t-i) \\ \sum_{i=0}^{N-1} y(t-i)x(t-i) \\ \sum_{i=0}^{N-1} y(t-i)x^2(t-i) \end{pmatrix},$$

equation (13) can be rewritten in the following matrix equation form:

$$A\hat{\lambda} = B. \quad (14)$$

Solution  $\lambda$  at time  $t$  can be obtained by solving the following equation set:

$$\hat{\lambda} = (A^T A)^{-1} A^T B. \quad (15)$$

By this means, the U-model with sliding window can be obtained:

$$\hat{y}(t) = \sum_{j=0}^M \hat{\lambda}_j(t) x^j(t). \quad (16)$$

Furthermore, given the latitude  $x(t+1)$ , the corresponding longitude  $\hat{y}(t+1)$  can be predicted. However, the prediction error increases as future latitude goes far from the current latitude. From the trace analysis of food safety criminals, three typical trajectories are extracted. Based on the idea of multiple model adaptive control, curve prediction is further conducted according to the accumulated model error of different typical trajectories.

**3.2. Multiple U-Model Algorithm.** Given a set of trajectory values, how to decide the corresponding U-model to predict future trajectory automatically is of great importance, for the mismatched model may cause a big predict error. The basic idea is using the frame of multiple model adaptive control to decide the most matching model.

For each clustered trajectory  $C_i, i = 1, 2, 3$ , the corresponding U-model  $M_i$  can be constructed by equation (16). However, as it can be seen in Figure 5, trajectories may not

have their latitude values at every longitude point. The model set is completed by setting the latitude value to be zero when it is null:

$$M_i: \hat{y}_i(t) = \begin{cases} \sum_{j=0}^M \hat{\lambda}_{ij}(t) x_i^j(t), & \text{if } y_i(t) \neq \text{null}, \\ 0, & \text{if } y_i(t) = \text{null}. \end{cases} \quad (17)$$

For every moment, the following index function is calculated to measure the matching degree between existing trajectory states and each trajectory model:

$$I_i(x(t)) = \sum_{j=1}^t \alpha^{t-j} (y(t) - \hat{y}_i(t))^2, \quad (18)$$

where  $\alpha$  is the forgetting factor and satisfies  $0 < \alpha < 1$ .

Given a serial of the trajectory state, the matching model  $M_{bm(t)}$  with the smallest index function will be selected to predict the trajectory:

$$bm(t) = \operatorname{argmin}_{i \in \{1, 2, 3\}} I_i(x(t)). \quad (19)$$

## 4. Simulation

According to the clustering result as shown in Figure 5, three typical activity trajectories are extracted. Using the U-model for the trajectory tracking algorithm as in equation (16), modelling results of the three typical trajectories are shown in Figures 6–8.

As it can be seen in the modelling result figures, the proposed U-model can track the GPS activity trajectories well, and the RMSE (rooted mean square error) for the three models is  $4.12 \times 10^{-5}$ ,  $3.16 \times 10^{-6}$ , and  $3.12 \times 10^{-5}$  degree, correspondingly, which are less than 4.6 meters for real distance. Meanwhile, for gently changing curves, the proposed method can model them with relative small errors. When it turns to the corner points, such as when the longitude is around 116.321 in Figure 6, the latitude drops dramatically from 39.988 to 39.985 and the modelling error increases as the dramatically changing curve is hard to be modelled exactly by the polynomial function.

Further, given a set of GPS points randomly depicted as star points shown in Figure 9, the predicted trajectories using the multiple U-model algorithm are shown as the red line. It is easy to see that though the given GPS points may

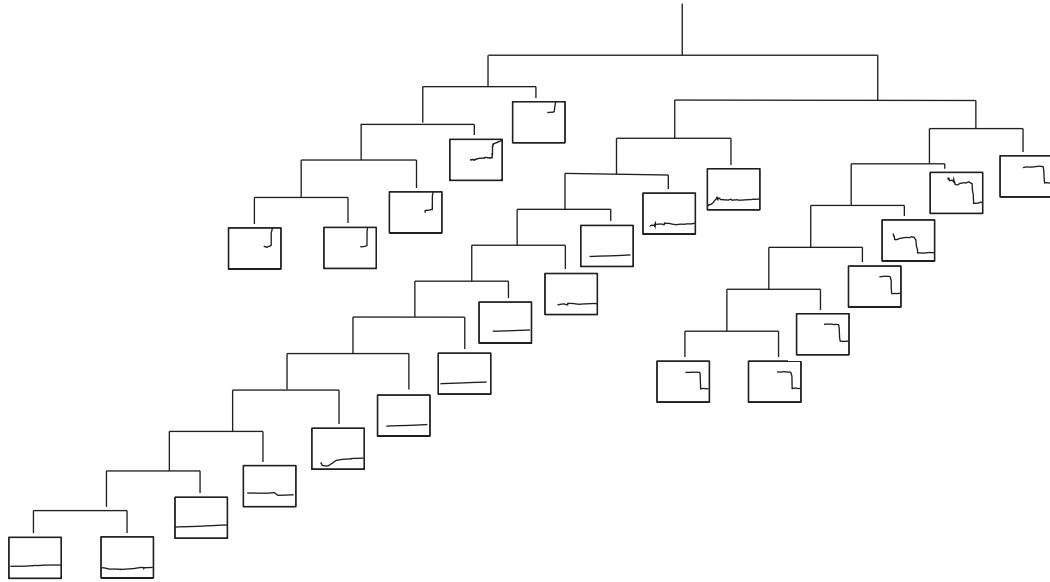


FIGURE 5: Clustering result of activity trajectories.

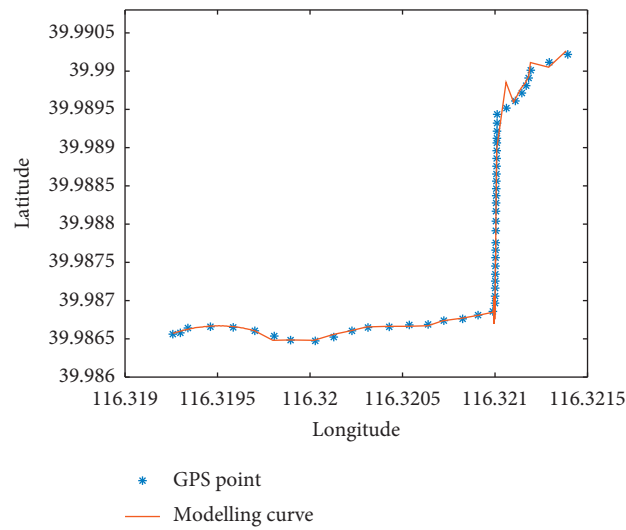


FIGURE 6: Modelling of trajectory 1 using the U-model.

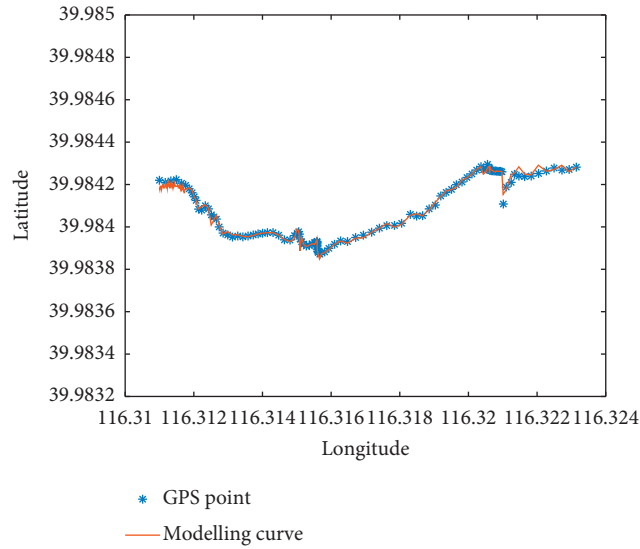


FIGURE 7: Modelling of trajectory 2 using the U-model.



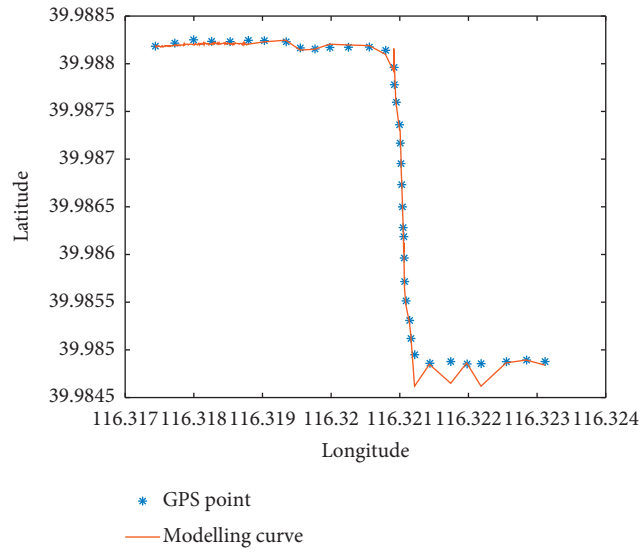


FIGURE 8: Modelling of trajectory 3 using the U-model.

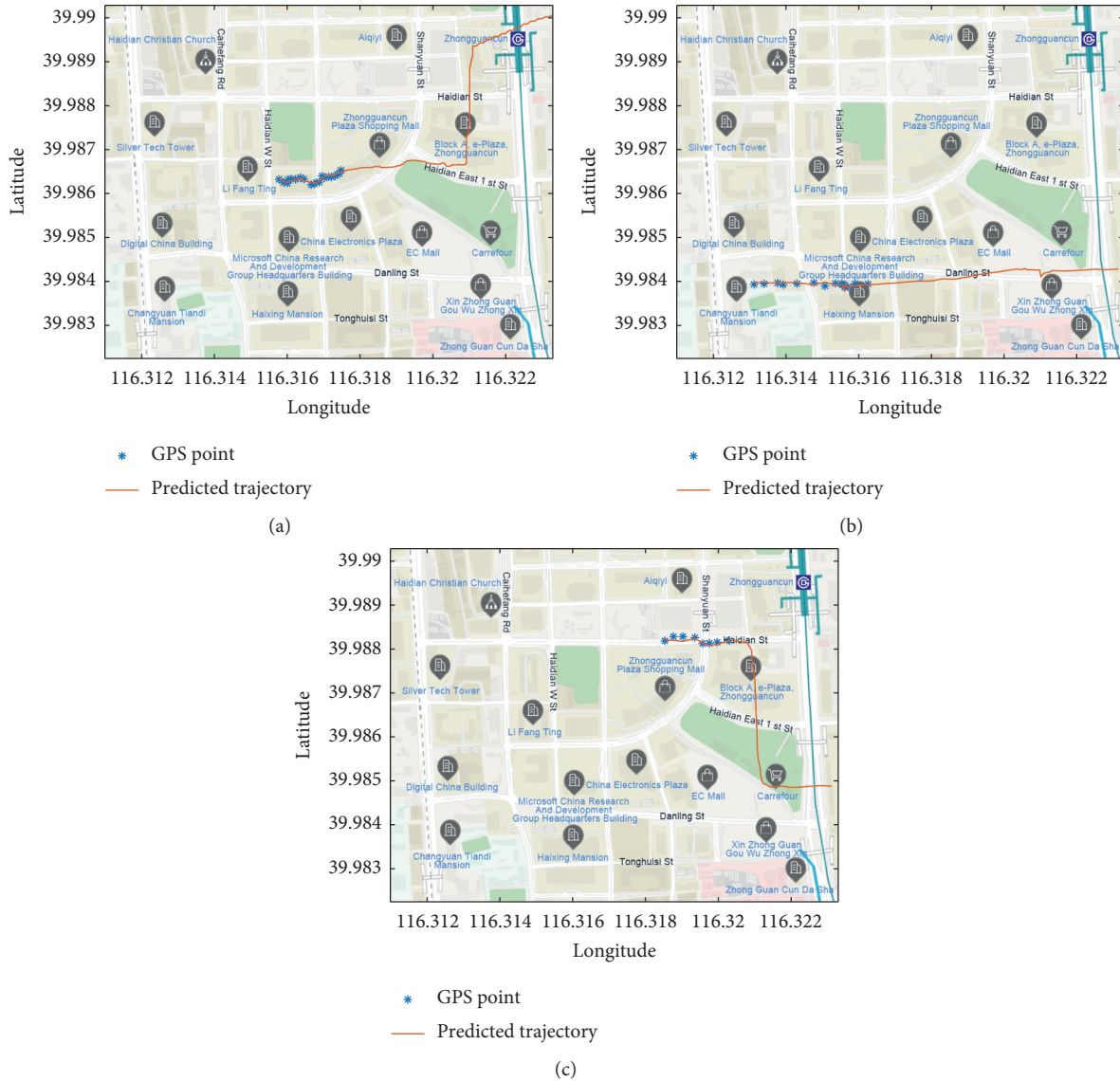


FIGURE 9: Trajectory prediction using the multiple U-model. (a) Trajectory prediction 1. (b) Trajectory prediction 2. (c) Trajectory prediction 3.

not be precisely given, the multiple U-model algorithm can effectively identify the best-matched model by calculating the accumulated errors of given states and clustered models and predict its future trajectory.

## 5. Conclusion and Future Work

In order to prevent and fight food safety-related crimes, this paper proposed a prediction method of criminal activity trajectories. Based on social text data, emotional assessment is conducted using the LSTM network to detect food safety criminal suspects. Activity trajectories of criminal suspects are clustered using the graphic clustering method based on the GPS data. The U-model with the sliding window algorithm is proposed to model activity trajectories. Further, the multiple U-model strategy is proposed to predict the activity trajectory based on the accumulated model error of previous positions and multiple clustered trajectories. A simulation study shows that the proposed scheme can detect food safety criminal suspects and predict their activity trajectories.

However, trajectory prediction method proposed in this paper is only restricted to predict trajectories with increasing longitude, and how to deal with loopback trajectories using the U-model is still an open problem. In the future, we will further explore the description of trajectories using the U-model and perfect this method suitable for more general trajectories.

## Data Availability

The MATLAB codes used to support the findings of this study are available from the corresponding author upon request.

## Conflicts of Interest

The authors declare that they have no conflicts of interest.

## Acknowledgments

This research was supported by the National Natural Science Foundation of China under Grant no. 61873006 and 61673053, National Key Research and Development Project under Grant no. 2018YFC1602704 and 2018YFB1702704, and Beijing Municipal Natural Science Foundation under Grant no. 4204087.

## References

- [1] H. J. P. Marvin, E. M. Janssen, Y. Bouzembrak, P. J. M. Hendriksen, and M. Staats, "Big data in food safety: an overview," *Critical Reviews in Food Science and Nutrition*, vol. 57, no. 11, pp. 2286–2295, 2017.
- [2] X. Li, K. Wang, and C. Jia, "Data-driven control of ground-granulated blast-furnace slag production based on ioem-elm," *IEEE Access*, vol. 7, pp. 60650–60660, 2019.
- [3] H. Li, D. Pan, and C. L. P. Chen, "Intelligent prognostics for battery health monitoring using the mean entropy and relevance vector machine," *IEEE Transactions on Systems, Man, and Cybernetics: Systems*, vol. 44, no. 7, pp. 851–862, 2014.
- [4] M. T. A. Wentholt, A. R. H. Fischer, G. Rowe, H. J. P. Marvin, and L. J. Frewer, "Effective identification and management of emerging food risks: results of an international delphi survey," *Food Control*, vol. 21, no. 12, pp. 1731–1738, 2010.
- [5] Y. Yang, L. Wei, and J. Pei, "Application of Bayesian modelling to assess food quality & safety status and identify risky food in China market," *Food Control*, vol. 100, pp. 111–116, 2019.
- [6] J. Wang and H. Yue, "Food safety pre-warning system based on data mining for a sustainable food supply chain," *Food Control*, vol. 73, pp. 223–229, 2017.
- [7] K. N. Win, J. Chen, Y. Chen, and P. Fournier-Viger, "PCPD: A parallel crime pattern discovery system for large-scale spatiotemporal data based on fuzzy clustering," *International Journal of Fuzzy Systems*, vol. 21, no. 6, pp. 1961–1974, 2019.
- [8] C. Catlett, E. Cesario, D. Talia, and A. Vinci, "Spatio-temporal crime predictions in smart cities: a data-driven approach and experiments," *Pervasive and Mobile Computing*, vol. 53, pp. 62–74, 2019.
- [9] R. Wu, G. Luo, J. Shao, L. Tian, and C. Peng, "Location prediction on trajectory data: a review," *Big Data Mining and Analytics*, vol. 1, no. 2, pp. 108–127, 2018.
- [10] A. Morshed, A. R. M. Forkan, P.-W. Tsai et al., "Viscrime-predict: a system for crime trajectory prediction and visualisation from heterogeneous data sources," in *Proceedings of the 34th ACM/SIGAPP Symposium on Applied Computing*, pp. 1099–1106, Limassol, Cyprus, April 2019.
- [11] Y. Xiao, X. Wang, G. F. Wen, H. Tian, S. Wu, and L. Li, "Predicting crime locations based on long short term memory and convolutional neural networks," *Data Analysis and Knowledge Discovery*, vol. 2, no. 10, pp. 15–20, 2018.
- [12] C. P. Chen, Z. Liu, and S. Feng, "Universal approximation capability of broad learning system and its structural variations," *IEEE Transactions on Neural Networks and Learning Systems*, vol. 30, no. 4, pp. 1191–1204, 2019.
- [13] F.-X. Xu, Q.-M. Zhu, D. Zhao, S.-Y. Li, and Y. Li, "U-model based design methods for nonlinear control systems a survey of the development in the 1st decade," *Control and Decision*, vol. 28, no. 7, pp. 961–971, 2013.
- [14] Q. Zhu, W. Zhang, J. Na, and B. Sun, "U-model based control design framework for continuous-time systems," in *Proceedings of the 2019 Chinese Control Conference (CCC)*, pp. 106–111, Guangzhou, China, July 2019.
- [15] Q. Zhu, W. Zhang, J. Zhang, and B. Sun, "U-neural network-enhanced control of nonlinear dynamic systems," *Neurocomputing*, vol. 352, pp. 12–21, 2019.
- [16] X.-L. Li, C. Jia, K. Wang, and J. Wang, "Trajectory tracking of nonlinear system using multiple series-parallel dynamic neural networks," *Neurocomputing*, vol. 168, pp. 1–12, 2015.
- [17] K. Wang and X. Li, "Iterative adp optimal control for ggbs production based on dynamic target optimization," *IEEE Access*, vol. 7, pp. 132851–132858, 2019.
- [18] Q. Yang, W.-N. Chen, Y. Li, C. P. Chen, X.-M. Xu, and J. Zhang, "Multimodal estimation of distribution algorithms," *IEEE Transactions on Cybernetics*, vol. 47, no. 3, pp. 636–650, 2016.
- [19] T. Mikolov, I. Sutskever, K. Chen, G. S. Corrado, and J. Dean, "Distributed representations of words and phrases and their compositionality," in *Proceedings of the Advances in Neural Information Processing Systems*, pp. 3111–3119, Lake Tahoe, NV, USA, December 2013.
- [20] K. Greff, R. K. Srivastava, J. Koutník, B. R. Steunebrink, and J. Schmidhuber, "LSTM: a search space odyssey," *IEEE Transactions on Neural Networks and Learning Systems*, vol. 28, no. 10, pp. 2222–2232, 2017.

- [21] F. Murtagh and P. Contreras, "Algorithms for hierarchical clustering: an overview," *WIREs Data Mining and Knowledge Discovery*, vol. 2, no. 1, pp. 86–97, 2012.
- [22] Q. M. Zhu, D. Y. Zhao, and J. Zhang, "A general u-block model-based design procedure for nonlinear polynomial control systems," *International Journal of Systems Science*, vol. 47, no. 14, pp. 3465–3475, 2016.
- [23] Y. Xiao, C. L. P. Chen, and B. Wang, "Bandwidth degradation qos provisioning for adaptive multimedia in wireless/mobile networks," *Computer Communications*, vol. 25, no. 13, pp. 1153–1161, 2002.

## Research Article

# Finite Time Output Feedback Attitude Tracking Control for Rigid Body Based on Extended State Observer

Meng Duan <sup>1,2</sup> and Yingmin Jia <sup>1</sup>

<sup>1</sup>The Seventh Research Division and the Center for Information and Control, Beihang University, Beijing, China

<sup>2</sup>School of Mathematical Sciences, Beihang University, Beijing, China

Correspondence should be addressed to Yingmin Jia; [ymjia@buaa.edu.cn](mailto:ymjia@buaa.edu.cn)

Received 7 May 2020; Accepted 8 June 2020; Published 26 July 2020

Guest Editor: Jing Na

Copyright © 2020 Meng Duan and Yingmin Jia. This is an open access article distributed under the Creative Commons Attribution License, which permits unrestricted use, distribution, and reproduction in any medium, provided the original work is properly cited.

In this paper, the attitude tracking control problem of output feedback is investigated. A finite time extended state observer (FTESO) is designed through the homogeneous Lyapunov method to estimate the virtual angular velocity and total disturbances. Based on these estimated states, a finite time attitude tracking controller is developed. The numerical simulations are given to illustrate the effectiveness of the proposed control scheme.

## 1. Introduction

Recently, the issue of attitude control of rigid body has received more and more attention due to its wide practical applications such as spacecraft, robotics, and maglev planar motor [1–3]. Also, the complex nonlinearity of the attitude dynamics raises potential value in theory. A great deal of control methods have been proposed to deal with the attitude control problems.

In [3], two time-varying terminal sliding mode attitude control algorithms were designed to deal with the system uncertainties and external disturbances. In [4], an adaptive regulation technique was proposed to reject the disturbances whose frequency is unknown. In [5], another adaptive attitude tracking control was implemented for the stability of a rigid spacecraft with time-varying inertia components. In [6], a backstepping method was used to design the robust attitude control for the agile satellite.

Various attitude control algorithms above need the information of full states including attitudes and angular velocities for controller design. However, in actual engineering applications, due to energy cost, weight, and other factors, an angular velocity sensor cannot be installed in the mechanical systems, or the angular velocity sensors fail to work. Thus, the design of output feedback

attitude control in which just attitude measurements are available is required.

Many great research studies have been proposed to deal with the problem of output feedback attitude control. These methods can be divided into two strategies: the passivity-based controller and the observer-based controller. In [7], the passivity of attitude dynamics represented by quaternion was first proved and a passivity-based attitude control was proposed to guarantee the stability of rigid body attitude. This work was further researched in [8]; the passivity of attitude dynamics represented by modified Rodrigues parameters was proven. In [9], an auxiliary dynamical system was derived to compensate the unknown angular velocities. In [10], a passivity filter which adopted attitude Euler angles was introduced; compared to other passivity-based controllers, the proposed output feedback controller can deal with external disturbances.

The examples of observer-based attitude controller can be found in [11–14]. In [11], a finite time observer was proposed through geometric homogeneity and Lyapunov methods; a virtual angular velocity is introduced in this method. In [12], a continuous finite time angular velocity observer was designed, but the settling time could not be given. In [13], an observer was designed by adding a power integrator, thus the settling

time can be estimated and the disturbances could be rejected by this method. In [14], a continuous terminal sliding mode observer was designed.

However, the u-modeled system dynamics and external disturbances are also the difficulties in the attitude control design. In [15–17], the unknown dynamics and external disturbances are addressed by simple structure estimators for nonlinear systems. Extended state observer (ESO) is another method to compensate these problems. The main characteristic of ESO is that all disturbances and uncertainties can be regarded as total disturbances. The linear ESO (LESO) was introduced in [18] and the structure of ESO became more concise and simple, thus ESO is preferred by engineering applications whose plants are too complex [19–21].

Inspired by [22, 23], a FTESO is introduced for the attitude control without angular velocity in this paper. The main contributions of this article are listed as follows:

Compared with other observer-based controllers, the presented control scheme can estimate angular velocity and disturbances of system simultaneously. The disturbances of the attitude system can be compensated by the outputs of proposed FTESO when the attitude controller is designed.

A finite time attitude controller which combined with FTESO is designed; it is an improvement of [11]. Due to the introduction of ESO, the proposed control framework has higher control accuracy and faster response.

This article is organized as follows. In Section 2, system dynamical models, some definitions, and lemmas are shown; the proposed FTESO-based controller is shown in Section 3; simulations are given in Section 4 and Section 5 shows the conclusions and future work.

## 2. System Models and Preliminaries

**2.1. Equations of Attitude Kinematics and Dynamics.** In this section, attitude system equations of a rigid body, which include attitude kinematics and dynamics, are presented.

The modified Rodrigues parameters (MRPs) are introduced to express the attitude of the rigid body; the equations of attitude kinematics are given as follows:

$$\dot{\sigma} = T(\sigma)\omega, \quad (1)$$

where  $\sigma = [\sigma_1, \sigma_2, \sigma_3]^T \in \mathbf{R}^3$  is the MRPs which denotes the rotation from the body frame to the inertial frame and  $\omega = [\omega_1, \omega_2, \omega_3]^T \in \mathbf{R}^3$  is the angular velocity of the rigid body expressed in the body frame. The matrix  $T(\sigma)$  is defined as follows:

$$T(\sigma) = \frac{1}{4} \left[ (1 - \sigma^T \sigma) I_{3 \times 3} + 2\sigma^\times + 2\sigma\sigma^T \right], \quad (2)$$

where the operator  $\sigma^\times$  represents the skew symmetric matrix of vector  $\sigma$  and has the following form:

$$\sigma^\times = \begin{bmatrix} 0 & -\sigma_3 & \sigma_2 \\ \sigma_3 & 0 & -\sigma_1 \\ -\sigma_2 & \sigma_1 & 0 \end{bmatrix}. \quad (3)$$

The attitude dynamics of rigid body is modeled as:

$$J\dot{\omega} = -\omega^\times J\omega + \tau + d, \quad (4)$$

where  $\tau = [\tau_1, \tau_2, \tau_3]^T \in \mathbf{R}^3$  denotes the control torque,  $d = [d_1, d_2, d_3]^T \in \mathbf{R}^3$  denotes the external disturbances applied to the rigid body, and  $J \in \mathbf{R}^{3 \times 3}$  denotes the inertial matrix of the rigid body which is symmetric.

Denote that  $x_1 = \sigma$ ,  $x_2 = \dot{\sigma}$ ,  $x_2$  is the first time derivative of the attitude MRPs and is introduced as the virtual angular velocity, then equations (1) and (3) can be transformed to the following equations:

$$\begin{cases} \dot{x}_1 = x_2, \\ \dot{x}_2 = f(x_1, x_2) + g(x_1)\tau + d^*(t), \end{cases} \quad (5)$$

where  $f(x_1, x_2) = \dot{T}Px_2 - TJ^{-1}(Px_2)^\times JPx_2$  is defined as system function,  $P = T^{-1}(x)$ ,  $g(x_1) = TJ^{-1}$ , and  $d^*(t) = g(x_1)d$  are the external disturbances in system equation (4).

**2.2. Definitions and Lemmas.** For simplicity, some definitions about vector  $x = [x_1, x_2, \dots, x_n]^T \in \mathbf{R}^n$  are given:

$$x^\alpha = [x_1^\alpha, x_2^\alpha, \dots, x_n^\alpha]^T, \quad (6)$$

$$\text{sign}(x) = [\text{sign}(x_1), \text{sign}(x_2), \dots, \text{sign}(x_n)]^T,$$

$$\text{diag}(x) = \text{diag}(x_1, x_2, \dots, x_n),$$

where  $\text{sign}(\cdot)$  represents the signum function and  $\text{diag}(\cdot)$  represents the diagonal matrix.

**Lemma 1** (see [24]). For any  $x \in \mathbf{R}$ ,  $y \in \mathbf{R}$ ,  $a > 0$ ,  $b > 0$ ,  $|x|^a |y|^b \leq c|x|^{a+b}/(a+b) + a|y|^{a+b}/(a+b)$ .

**Lemma 2** (see [25]). For any  $x_i \in \mathbf{R}$ ,  $i = 1, 2, \dots, n$ ,  $r \in (0, 1]$ ,  $(\sum_{i=1}^n |x_i|)^r \leq \sum_{i=1}^n |x_i|^r \leq n^{1-r} (\sum_{i=1}^n |x_i|)^r$ .

**Lemma 3** (see [22]). Consider the system like equation (4); assume that a Lyapunov function  $V(x)$  is defined on a neighbourhood of  $U \subset \mathbf{R}^n$  of the origin, and

$$\dot{V}(x) + l_1 V(x)^m + l_2 V(x)^n < 0, \quad x \in N \setminus \{0\}, \quad (7)$$

where  $m \geq 1$ ,  $n \in (0, 1)$  and  $l_1 > 0$ ,  $l_2 > 0$ . Then, the system is locally finite time stable, and the  $V(x)$  which starts from  $U$  can arrive at  $V(x) \equiv 0$  in finite time  $T$ :

$$T \leq \frac{1}{l_2(1-n)} |V_0|^{1-n} F\left(1, \frac{1-n}{m-n}, 1 + \frac{1-n}{m-n}, \frac{l_1}{l_2} |V_0|^{m-n}\right), \quad (8)$$

where  $V_0$  is the starting value of  $V(x)$ , and  $F(\cdot)$  denotes the Gaussian hypergeometric function.

### 3. Main Results

**3.1. Finite Time Extended State Observer Design.** In this section, only the attitude MRPs  $\sigma$  is the available information; an ESO which ensures finite time convergence is presented to estimate the virtual angular velocity  $x_2$  and the external disturbances  $d^*(t)$ .

Designate the external disturbances  $d^*(t)$  as an extended state  $x_3$ ; the system in equation (4) can be transformed to a new third-order dynamics equation which is shown in the following formulas:

$$\begin{cases} \dot{x}_1 = x_2, \\ \dot{x}_2 = x_3 + f(x_1, x_2) + g(x_1)\tau, \\ \dot{x}_3 = w(t), \end{cases} \quad (9)$$

where  $w(t) = \dot{d}^*(t)$ , and the following assumption is given.

**Assumption 1.** The external disturbances  $d^*(t)$  are unknown but continuously differential and bounded; its first time derivative  $w(t)$  is also unknown and bounded; the following inequalities hold:

$$d^*(t) \leq \bar{d}^*, \quad w(t) \leq \bar{w}, \quad (10)$$

where  $\bar{d}^*$  and  $\bar{w}$  represent the upper bound of  $d^*(t)$  and  $w(t)$ , respectively.

Let  $z_1, z_2$ , and  $z_3$  represent the estimates of  $x_1, x_2$ , and  $x_3$  in equation (7), respectively, then the FTESO is designed as follows:

$$\begin{cases} \dot{z}_1 = z_2 + \rho|\epsilon_1|^{\alpha_1} \text{sign}(\epsilon_1) + \rho|\epsilon_1|^{\beta_1} \text{sign}(\epsilon_1) + \theta_1 \text{sign}(\epsilon_1), \\ \dot{z}_2 = z_3 + f(x_1, z_2) + g(x_1)\tau + \rho^2|\epsilon_1|^{\alpha_2} \text{sign}(\epsilon_1) \\ \quad + \rho^2|\epsilon_1|^{\beta_2} \text{sign}(\epsilon_1) + \theta_2 \text{sign}(\epsilon_1), \\ \dot{z}_3 = \rho^3|\epsilon_1|^{\alpha_3} \text{sign}(\epsilon_1) + \rho^3|\epsilon_1|^{\beta_3} \text{sign}(\epsilon_1) + \theta_3 \text{sign}(\epsilon_1), \end{cases} \quad (11)$$

where  $\epsilon_1 = x_1 - z_1$  represents the estimation error of attitude MRPs  $x_1$ ,  $0 < \rho < +\infty$ ,  $0.5 < \alpha_1 < 1$ ,  $\alpha_2 = 2\alpha_1 - 1$ ,  $\alpha_3 = 3\alpha_1 - 2$ ,  $\beta_1 = 1/\alpha_1$ , and  $\beta_2 = 1/\beta_1 + \beta_1 - 1$ ,  $\beta_3 = 2/\beta_1 + \beta_1 - 2$ , and  $\theta_1, \theta_2$ , and  $\theta_3$  are the parameters to deal with the external disturbances.

Let  $\epsilon_2 = x_2 - z_2$ ,  $\epsilon_3 = x_3 - z_3$ , and the error dynamical equations of the proposed FTESO is expressed as:

$$\begin{cases} \dot{\epsilon}_1 = \epsilon_2 - \rho|\epsilon_1|^{\alpha_1} \text{sign}(\epsilon_1) - \rho|\epsilon_1|^{\beta_1} \text{sign}(\epsilon_1) - \theta_1 \text{sign}(\epsilon_1), \\ \dot{\epsilon}_2 = \epsilon_3 + f(x_1, x_2) - f(x_1, z_2) - \rho^2|\epsilon_1|^{\alpha_2} \text{sign}(\epsilon_1) \\ \quad - \rho^2|\epsilon_1|^{\beta_2} \text{sign}(\epsilon_1) - \theta_2 \text{sign}(\epsilon_1), \\ \dot{\epsilon}_3 = w(t) - \rho^3|\epsilon_1|^{\alpha_3} \text{sign}(\epsilon_1) - \rho^3|\epsilon_1|^{\beta_3} \text{sign}(\epsilon_1) - \theta_3 \text{sign}(\epsilon_1). \end{cases} \quad (12)$$

The following compact set is constructed for any constant  $\Delta$ :

$$\Omega_1 = \{(x_1, x_2, z_1, z_2) \mid \|x_1\| \leq \Delta, \|x_2\| \leq \Delta, \|z_1\| \leq \Delta, \|z_2\| \leq \Delta\}. \quad (13)$$

This compact set can be easily obtained by designing a proper desired attitude reference trajectory. If the set  $\Omega_1$  is established, there will exist a positive constant  $\lambda$  such that  $\|f(x_1, x_2) - f(x_1, z_2)\| \leq \lambda|\epsilon_2|$ .

The stability properties of the extended state observer is presented in the following theorem.

**Theorem 1.** Consider the error dynamical system given by equation (10), where  $0.5 < \alpha_1 < 1$ ,  $\alpha_2 = 2\alpha_1 - 1$ ,  $\alpha_3 = 3\alpha_1 - 2$ ,  $\beta_1 = 1/\alpha_1$ ,  $\beta_2 = 1/\beta_1 + \beta_1 - 1$ , and  $\beta_3 = 2/\beta_1 + \beta_1 - 2$ ; if the compact set  $\Omega_1$  holds,  $\rho$ ,  $\theta_1$ ,  $\theta_2$ , and  $\theta_3$  are sufficiently large, then the estimation errors would converge to a residual region in finite time.

**Proof.** Consider the error dynamics in equation (10); ignore the terms  $\rho|\epsilon_1|^{\beta_1} \text{sign}(\epsilon_1) - \theta_1 \text{sign}(\epsilon_1)$ ,  $-\rho^2|\epsilon_1|^{\beta_2} \text{sign}(\epsilon_1) - \theta_2 \text{sign}(\epsilon_1)$ , and  $w(t) - \rho^3|\epsilon_1|^{\beta_3} \text{sign}(\epsilon_1) - \theta_3 \text{sign}(\epsilon_1)$ , so equation (10) can be reduced to the following form:

$$\begin{cases} \dot{\epsilon}_1 = \epsilon_2 - \rho|\epsilon_1|^{\alpha_1} \text{sign}(\epsilon_1), \\ \dot{\epsilon}_2 = \epsilon_3 + f(x_1, x_2) - f(x_1, z_2) - \rho^2|\epsilon_1|^{\alpha_2} \text{sign}(\epsilon_1), \\ \dot{\epsilon}_3 = -\rho^3|\epsilon_1|^{\alpha_3} \text{sign}(\epsilon_1). \end{cases} \quad (14)$$

It can be acquired that equation (12) is homogeneous of degree  $(\alpha_1 - 1) < 0$  with respect to the weight  $(1, \alpha_1, 2\alpha_1 - 1)$ .

The Lyapunov function is proposed as follows:

$$V_\alpha(\zeta_1, \zeta_2, \zeta_3) = \zeta^T P \zeta. \quad (15)$$

where  $\zeta = [\zeta_1, \zeta_2, \zeta_3]^T = [|\epsilon_1|^{1/\varphi} \text{sign}(\epsilon_1), |\epsilon_2|^{1/(\varphi\alpha_1)} \text{sign}(\epsilon_2), |\epsilon_3|^{1/(\varphi(2\alpha_1-1))} \text{sign}(\epsilon_3)]^T$ ,  $0.5 < \varphi = \alpha_1 < 1$ ,  $P$  denotes a positive definite symmetric matrix. Make  $f_\alpha$  represent the vector field of system equation (12); it can be obtained that  $V_\alpha(\zeta)$  and  $L_{f_\alpha} V_\alpha(\zeta)$  are homogeneous of degrees  $2/\varphi$  and  $2/\varphi + \alpha_1 - 1$  with the same weights in system equation (12), respectively.

According to [26, 27], the inequality is obtained as follows:

$$L_{f_\alpha} V_\alpha(\zeta) \leq \mu_1(\alpha, \theta) (V_\alpha(\zeta))^{\gamma_1}, \quad (16)$$

where  $\mu_1 = -\max_{\{y: V_\alpha(y)=1\}} L_{f_\alpha} V_\alpha(y)$ ,  $\gamma_1 = 1 + (\alpha_1\varphi/2) - (\alpha_1\varphi/2) \leq 1$ , and  $\lim_{\alpha_1 \rightarrow 1} \mu_1 \geq \rho/\lambda_{\max}(P)$ .

Same as the previous analysis, ignore the terms  $\epsilon_2 - \rho|\epsilon_1|^{\alpha_1} \text{sign}(\epsilon_1) - \theta_1 \text{sign}(\epsilon_1)$ ,  $\epsilon_3 + f(x_1, x_2) - f(x_1, z_2) - \rho^2|\epsilon_1|^{\alpha_2} \text{sign}(\epsilon_1) - \theta_2 \text{sign}(\epsilon_1)$ , and  $w(t) - \rho^3|\epsilon_1|^{\alpha_3} \text{sign}(\epsilon_1) - \theta_3 \text{sign}(\epsilon_1)$ . The other homogeneous system can be got from equation (10):

$$\begin{cases} \dot{\epsilon}_1 = -\rho|\epsilon_1|^{\beta_1} \text{sign}(\epsilon_1), \\ \dot{\epsilon}_2 = -\rho^2|\epsilon_1|^{\beta_2} \text{sign}(\epsilon_1), \\ \dot{\epsilon}_3 = -\rho^3|\epsilon_1|^{\beta_3} \text{sign}(\epsilon_1). \end{cases} \quad (17)$$

Similarly, the system of equation (15) is homogeneous of degree  $(\beta_1 - 1) > 0$  with respect to the weight  $(1, \alpha_1, 2\alpha_1 - 1)$ .

Define the same Lyapunov function as equation (13) as follows:

$$V_\beta(\zeta_1, \zeta_2, \zeta_3) = \zeta^T P \zeta, \quad (18)$$

where  $\zeta = [\zeta_1, \zeta_2, \zeta_3]^T = [|\epsilon_1|^{1/\varphi} \text{sign}(\epsilon_1), |\epsilon_2|^{1/(\varphi\alpha_1)} \text{sign}(\epsilon_2), |\epsilon_3|^{1/(\varphi(2\alpha_1-1))} \text{sign}(\epsilon_3)]^T$ ,  $0.5 < \varphi = \alpha_1 < 1$ ,  $P$  denotes a positive definite symmetric matrix. Make  $f_\beta$  represent the vector field of system equation (15); it can be obtained that  $V_\beta(\zeta)$  and  $L_{f_\beta} V_\beta(\zeta)$  are homogeneous of degrees  $2/\varphi$  and  $2/\varphi + \beta_1 - 1$  with the same weights in system equation (15), respectively.

Once again the following inequality is derived according to [26, 27]

$$L_{f_\beta} V_\beta(\zeta) \leq \mu_2(\beta, \theta)(V_\beta(\zeta))^{Y_2}, \quad (19)$$

where  $\mu_2 = - \max_{\{y: V_\beta(y)=1\}} L_{f_\beta} V_\beta(y)$ ,  $Y_2 = 1 + (\varphi/2\beta_1) - (\varphi/2) \geq 1$ , and  $\lim_{\alpha_1 \rightarrow 1} \mu_2 \geq \rho/\lambda_{\max}(P)$ .

Considering the error dynamics in equation (10), the following Lyapunov function is chosen as

$$V(\zeta_1, \zeta_2, \zeta_3) = \zeta^T P \zeta, \quad (20)$$

where  $\zeta = [\zeta_1, \zeta_2, \zeta_3]^T = [|\epsilon_1|^{1/\varphi} \text{sign}(\epsilon_1), |\epsilon_2|^{1/(\varphi\alpha_1)} \text{sign}(\epsilon_2), |\epsilon_3|^{1/(\varphi(2\alpha_1-1))} \text{sign}(\epsilon_3)]^T$ ,  $0.5 < \varphi = \alpha_1 < 1$ ,  $P$  denotes a positive definite symmetric matrix same as in equations (13) and (16), then take first time derivative of  $V$ :

$$\begin{aligned} \dot{V}(\zeta) = & L_{f_a} V(\zeta) + L_{f_\beta} V(\zeta) + 2\zeta^T P \left[ \begin{array}{c} 0 \\ \frac{1}{\varphi\alpha_1} \text{diag}(|\epsilon_2|)^{((1/\varphi\alpha)-1)} (f(x_1, x_2) - f(x_1, z_2)) \\ 0 \end{array} \right] \\ & + 2\zeta^T P \left[ \begin{array}{c} \text{diag}(|\epsilon_1|)^{((1/\varphi\alpha)-1)} \frac{-\theta_1}{\varphi} \text{sign}(\epsilon_1) \\ \text{diag}(|\epsilon_2|)^{((1/\varphi\alpha_1)-1)} \frac{-\theta_2}{\varphi\alpha_1} \text{sign}(\epsilon_2) \\ \text{diag}(|\epsilon_3|)^{((1/\varphi 2\alpha_1)-1)} \frac{w(t) - \theta_1}{\varphi} \text{sign}(\epsilon_3) \end{array} \right]. \end{aligned} \quad (21)$$

Substituting equations (14) and (17) into equation (19), the following formula can be got:

$$\begin{aligned} \dot{V}(\zeta) \leq & -\mu_1 (V_\alpha(\zeta))^{Y_1} - \mu_2 (V_\beta(\zeta))^{Y_2} + 2\zeta^T P \left[ \begin{array}{c} 0 \\ \frac{1}{\varphi\alpha_1} \text{diag}(|\epsilon_2|)^{((1/\varphi\alpha_1)-1)} (f(x_1, x_2) - f(x_1, z_2)) \\ 0 \end{array} \right] \\ & + 2\zeta^T P \left[ \begin{array}{c} \text{diag}(|\epsilon_1|)^{((1/\varphi\alpha_1)-1)} \frac{-\theta_1}{\varphi} \text{sign}(\epsilon_1) \\ \text{diag}(|\epsilon_2|)^{((1/\varphi\alpha_1)-1)} \frac{-\theta_2}{\varphi\alpha_1} \text{sign}(\epsilon_2) \\ \text{diag}(|\epsilon_3|)^{((1/2\varphi\alpha_1)-1)} \frac{w(t) - \theta_3}{\varphi} \text{sign}(\epsilon_3) \end{array} \right] \leq -\mu_1 (V_\alpha(\zeta))^{Y_1} - \mu_2 (V_\beta(\zeta))^{Y_2} \\ & + \frac{2\lambda_{\max}(P)\|\zeta\| \left( \sum_{i=1}^3 |\epsilon_{2i}|^{(1/\varphi\alpha_1)-1} \right) \left( \sum_{i=1}^3 |\epsilon_{2i}| \right)}{\varphi\alpha_1} \\ & + \frac{2\theta_1\lambda_{\max}(P)\|\zeta\| \left( \sum_{i=1}^3 |\epsilon_{1i}|^{(1/\varphi)-1} \right)}{\varphi} + \frac{2\theta_2\lambda_{\max}(P)\|\zeta\| \left( \sum_{i=1}^3 |\epsilon_{2i}|^{(1/\varphi\alpha_1)-1} \right)}{\varphi\alpha_1} \\ & + \frac{2(\theta_3 + \bar{w})\lambda_{\max}(P)\|\zeta\| \left( \sum_{i=1}^3 |\epsilon_{2i}|^{(1/\varphi(2\alpha_1-1))-1} \right)}{\varphi(2\alpha_1-1)}, \end{aligned} \quad (22)$$



where  $\lambda_{\max}(P)$  refers to the maximum eigenvalue of matrix  $P$ .

The following inequality is derived according to Lemma 1:

$$|\epsilon_{2j}|^{(1/\varphi\alpha_1)-1} \left( \sum_{i=1}^3 |\epsilon_{2i}| \right) \leq 3(1/\varphi\alpha_1) |\epsilon_{2j}|^{(1/\varphi\alpha_1)} + \varphi\alpha_1 \left( \sum_{i=1}^3 |\epsilon_{2i}|^{(1/\varphi\alpha_1)} \right), \quad (23)$$

where  $j = 1, 2, 3$ , and the following result is got:

$$\left( \sum_{i=1}^3 |\epsilon_{2i}|^{(1/\varphi\alpha_1)-1} \right) \left( \sum_{i=1}^3 |\epsilon_{2i}| \right) \leq 3 \left( \sum_{i=1}^3 |\epsilon_{2i}|^{(1/\varphi\alpha_1)} \right) \leq 3\sqrt{3} \|\zeta_2\| \leq 3\sqrt{3} \|\zeta\|. \quad (24)$$

The following inequality is derived according to Lemma 2:

$$\sum_{i=1}^3 |\epsilon_{2i}|^{(1/\varphi\alpha_1)-1} = \sum_{i=1}^3 |\epsilon_{2i}|^{(1/\varphi\alpha_1)(1-\varphi\alpha_1)} \leq 3^{\varphi\alpha_1} \left( \sum_{i=1}^3 |\zeta_{2i}| \right)^{1-\varphi\alpha_1} \leq 3^{\varphi\alpha_1} (\sqrt{3} \|\zeta_2\|)^{1-\varphi\alpha_1} \leq 3^{(1+\varphi\alpha_1)/2} \|\zeta\|^{1-\varphi\alpha_1}. \quad (25)$$

The following inequalities can be derived in the same way according to Lemma 2:

$$\sum_{i=1}^3 |\epsilon_{1i}|^{(1/\varphi)-1} \leq 3^{(1/\varphi)/2} \|\zeta\|^{1-\varphi}, \quad (26)$$

$$\sum_{i=1}^3 |\epsilon_{1i}|^{(1/\varphi(2\alpha_1-1))-1} \leq 3^{(1/\varphi(2\alpha_1-1))/2} \|\zeta\|^{1-\varphi(2\alpha_1-1)}. \quad (27)$$

So, substituting equations (22)–(25) into the inequality equation (20), the following inequality can be got:

$$\begin{aligned} \dot{V}(\zeta) \leq & -\mu_1 (V_\alpha(\zeta))^{\gamma_1} - \mu_2 (V_\beta(\zeta))^{\gamma_2} = + \frac{6\sqrt{2}\lambda_{\max}(P)\|\zeta\|^2}{\varphi\alpha_1} + \frac{2 \times 3^{(1+\varphi\alpha_1/2)}\theta_1\lambda_{\max}(P)\|\zeta\|^{2-\varphi}}{\varphi} \\ & + \frac{2 \times 3^{(1+\varphi/2)}\theta_2\lambda_{\max}(P)\|\zeta\|^{2-\varphi\alpha_1}}{\varphi\alpha_1} + \frac{2 \times 3^{1+\varphi(2\alpha_1-1)/2}(\theta_3 + \bar{w})\lambda_{\max}(P)\|\zeta\|^{2-\varphi(2\alpha_1-1)}}{\varphi(2\alpha_1-1)} \leq -\mu_1 V^{\gamma_1} - \mu_2 V^{\gamma_2} + \mu_3 V + \mu_4 V^{1-(\varphi-2)} \\ & + \mu_5 V^{1-(\varphi\alpha_1/2)} + \mu_6 V^{1-(\varphi(2\alpha_1-1))}, \end{aligned} \quad (28)$$

where

$$\begin{aligned} \mu_3 &= \frac{6\sqrt{2}\lambda_{\max}(P)}{\varphi\lambda_{\min}(P)}, \\ \mu_4 &= \frac{2 \times 3^{(1+\varphi\alpha_1/2)}\theta_1\lambda_{\max}(P)}{\varphi\lambda_{\min}(P)^{1-(\varphi/2)}}, \\ \mu_5 &= \frac{2 \times 3^{(1+\varphi/2)}\theta_2\lambda_{\max}(P)}{\varphi\lambda_{\min}(P)^{1-(\varphi/2)}}, \\ \mu_6 &= \frac{2 \times 3^{(1+\varphi/2\alpha_1/2)}(\theta_3 + \bar{w})\lambda_{\max}(P)}{\varphi\lambda_{\min}(P)^{1-(\varphi\alpha_1/2)}}. \end{aligned} \quad (29)$$

Two cases are discussed in further analysis.

Case 1.  $V \geq 1$ .

Consider the parameters in equation (26):

$$\begin{aligned} 0 &< \left(1 - \frac{\varphi}{2}\right) < 1 < \gamma_2, \\ 0 &< \left(1 - \frac{\varphi\alpha_1}{2}\right) < 1 < \gamma_2, \\ 0 &< \left(1 - \frac{\varphi(2\alpha_1-1)}{2}\right) < 1 < \gamma_2. \end{aligned} \quad (30)$$

So, simplify equation (26) to the following formula:



$$\dot{V} \leq -\mu_1 V^{\gamma_1} - \mu_7 V^{\gamma_2}. \quad (31)$$

where  $\mu_7 = \mu_2 - \mu_3 - \mu_4 - \mu_5 - \mu_6$ ; select the parameter  $\rho$  sufficiently large to ensure  $\mu_7 > 0$ ; according to Lemma 3, the Lyapunov function  $V$  will converge to  $V(\zeta) \equiv 1$  in finite time  $t_1$ .

$$t_1 < \frac{1}{\mu_1(1-\gamma_1)} V_{(0)}^{1-\gamma_1} F\left(1, \frac{1-\gamma_1}{\gamma_2-\gamma_1}, 1 + \frac{1-\gamma_1}{\gamma_2-\gamma_1}, -\frac{\mu_7 V_{(0)}^{\gamma_2-\gamma_1}}{\mu_1}\right), \quad (32)$$

where  $V_{(0)}$  denotes the initial value of  $V$ .

Case 2.  $V < 1$ . In this case, equation (26) can be simplified to

$$\begin{aligned} \dot{V} &\leq -\mu_1 V^{\gamma_1} - \mu_2 V^{\gamma_2} + \mu_3 V^{\gamma_1} + (\mu_4 + \mu_5 + \mu_6) V^{1-(\varphi/2)} \leq -\mu_1(1-\rho_0) V^{\gamma_1} + \mu_3 V^{\gamma_1} + (\mu_4 + \mu_5 + \mu_6) V^{1-(q/2)} \\ &-\mu_1 \rho_0 V^{\gamma_1} - \mu_2 V^{\gamma_2} \leq -[(\mu_1(1-\rho_0) - \mu_3) V^{\gamma_1-1+(q/2)} - (\mu_4 + \mu_5 + \mu_6)] V^{1-(q/2)} - \mu_1 \rho_0 V^{\gamma_1} - \mu_2 V^{\gamma_2}, \end{aligned} \quad (33)$$

where the parameter  $\rho_0$  is selected to ensure that  $0 < \rho_0 < 1$ .

From inequality equation (30), when  $(\mu_1(1-\rho_0) - \mu_3) V^{\gamma_1-1+(q/2)} - (\mu_4 + \mu_5 + \mu_6) \geq 0$ , the Lyapunov function  $V$  will converge to the residual region  $\Omega_2$  in finite time  $T_1 = t_1 + t_2$ :

$$\Omega_2 = \left\{ V \mid V < \left( \frac{\mu_4 + \mu_5 + \mu_6}{\mu_1(1-\rho_0) - \mu_3} \right)^{(2/2\gamma_1-2+\varphi)} \right\}, \quad (34)$$

$$t_2 < \frac{1}{\mu_1 \rho_0 (1-\gamma_1)} V_{(t_1)}^{1-\gamma_1} \times F\left(1, \frac{1-\gamma_1}{\gamma_2-\gamma_1}, 1 + \frac{1-\gamma_1}{\gamma_2-\gamma_1}, -\frac{\mu_2 V_{(t_1)}^{\gamma_2-\gamma_1}}{\mu_1 \rho_0}\right), \quad (35)$$

where  $V_{(t_1)}$  represents the value of  $V$  at time  $t_1$ . The estimation error can be written as

$$\Omega_3 = \left\{ \zeta \mid \frac{1}{\sqrt{\lambda_{\min}(\mathbf{P})}} \left( \frac{\mu_4 + \mu_5 + \mu_6}{\mu_1(1-\rho_0) - \mu_3} \right)^{(1/2\gamma_1-2+\varphi)} \right\}. \quad (36)$$

In next step, the parameters  $\theta_1, \theta_2$ , and  $\theta_3$  will be analyzed to ensure  $(\epsilon_1, \epsilon_2, \epsilon_3)$  converge to zeros within finite time.

Define the following Lyapunov function:

$$V_{\epsilon_1}(\epsilon_1) = \frac{1}{2} \epsilon_1^T \epsilon_1. \quad (37)$$

Take time derivative of  $V_{\epsilon_1}$ :

$$\dot{V}_{\epsilon_1} = \epsilon_1^T \dot{\epsilon}_1 = \epsilon_1^T \epsilon_2 - \rho \sum_{i=1}^3 |\epsilon_{1i}|^{\alpha_i+1} - \rho \sum_{i=1}^3 |\epsilon_{1i}|^{\beta_i+1} - \theta_1 \sum_{i=1}^3 |\epsilon_{1i}| \leq -\rho \|\epsilon_1\|^{\alpha_1+1/2} - \rho \|\epsilon_1\|^{\beta_1+1/2} - (\theta_1 - \|\epsilon_2\|) \|\epsilon_1\|. \quad (38)$$

According to equation (33),  $\epsilon_2$  will converge to the bounded region  $\Omega_3$ , and then selecting the parameter  $\theta_1 > \Omega_3$ , the inequality equation (35) can be simplified to

$$\dot{V}_{\epsilon_1} \leq -2^{\alpha_1+1/2} V_{\epsilon_1}^{\alpha_1+1/2} - 2^{\beta_1+1/2} \rho V_{\epsilon_1}^{\beta_1+1/2}. \quad (39)$$

So,  $\epsilon_1$  can converge to zeros within time  $T_2 = T_1 + t_3$ :

$$t_3 < \frac{1}{2^{\alpha_1-1/2}} (1-\alpha_1) \times F\left(1, \frac{1-\alpha_1}{\beta_1-\alpha_1}, 1 + \frac{1-\alpha_1}{\beta_1-\alpha_1}, -2^{\beta_1-\alpha_1/2} V_{\epsilon_1}^{\beta_1-\alpha_1}\right), \quad (40)$$

where  $V_{\epsilon_1(T_1)}$  is the value of  $V_{\epsilon_1}$  at time  $t_1$ .

So,  $\epsilon_1 = \dot{\epsilon}_1 = 0$  is got; according to [28], discontinuous terms include that  $\text{sign}(\epsilon_1)$  can be considered as equivalent input; the error dynamical system equation (10) can be reduced to

$$\begin{cases} 0 = \epsilon_2 - \theta_1 \text{sign}(\epsilon_1), \\ \dot{\epsilon}_2 = \epsilon_3 + \lambda |\epsilon_2| - \theta_2 \text{sign}(\epsilon_1), \\ \dot{\epsilon}_3 = \omega(t) - \theta_3 \text{sign}(\epsilon_1). \end{cases} \quad (41)$$

It can be derived that  $\text{sign}(\epsilon_2) = \text{sign}(\epsilon_1)$ . Define the Lyapunov function  $V_{\epsilon_2}(\epsilon_2) = (1/2)\epsilon_2^T \epsilon_2$  and  $V_{\epsilon_3}(\epsilon_3) = (1/2)\epsilon_3^T \epsilon_3$ . Analyze these two Lyapunov functions like we did before; it can be easily obtained that, let  $\theta_2 > \Omega_3$  and  $\theta_1 > \bar{\omega}$ , the estimation errors  $\epsilon_2$  and  $\epsilon_3$  will converge to zeros within finite time  $T_3 = T_2 + t_4$  and  $T_4 = T_3 + t_5$ , respectively [11]:

$$\begin{aligned} t_4 &< \frac{2^{(1/2)}}{|\theta_2 - \Omega_3|} |V_{\epsilon_2}(T_2)|^{(1/2)}, \\ t_5 &< \frac{2^{(1/2)}}{|\theta_3 - \bar{\omega}|} |V_{\epsilon_3}(T_3)|^{(1/2)}, \end{aligned} \quad (42)$$

where  $V_{\epsilon_2}(T_2)$  denotes the value of  $V_{\epsilon_2}$  at time  $T_2$  and  $V_{\epsilon_3}(T_3)$  denotes the value of  $V_{\epsilon_3}$  at time  $T_3$ .

At this point, the proof is complete.  $\square$

### 3.2. Finite Time Attitude Controller Design Based on FTESO.

In this section, inspired by Zou [11], a finite time controller is introduced to stabilize the rigid body to the desired attitude. Because only the attitude measurement is available, the estimation of virtual angular velocity  $z_2$  and external disturbances  $z_3$  are utilized in the design procedure.

Define  $\xi = \eta^{1/\nu} - \eta_d^{1/\nu}$  and  $e = x_1 - \sigma_d$ , where  $\eta = z_2 - \dot{\sigma}_d$ ,  $\eta_d = -k_1 e^\nu$ ,  $1/2 < \nu = \nu_1/\nu_2 < 1$ , and  $\nu_1$  and  $\nu_2$  are positive odd integers.

The proposed finite time attitude controller is shown as follow:

$$\tau = g^{-1} \left( -k_3 \text{sign}(\xi) - k_2 \xi^{2\nu-1} - z_3 - f(x_1, z_2) + \ddot{q}_d - \rho^2 |\epsilon_1|^{\alpha_2} \text{sign}(\epsilon_1) - \rho^2 |\epsilon_1|^{\beta_2} \text{sign}(\epsilon_1) - \theta_2 \text{sign}(\epsilon_1) \right). \quad (43)$$

**Theorem 2.** Consider the system expressed in equation (4); if finite time control torque in equation (40) combined with FTESO in equation (9) is employed, the desired attitude can be tracked within finite time.

*Proof.* Define the Lyapunov function:

$$V_f = V + V_c, \quad (44)$$

where

$$V_c = V_0 + \sum_{i=1}^3 V_i, \quad (45)$$

$$V_0 = \frac{1}{2} e^T e. \quad (46)$$

$V_i$  is defined as

$$V_i = \frac{1}{(2-\nu)2^{1-\nu}k_1^{1+1/\nu}} \int_{\eta_{di}}^{\eta_i} (s^{1/\nu} - \eta_{di}^{1/\nu})^{2-\nu} ds. \quad (47)$$

Taking time derivative of Lyapunov function  $V_f$ , the result can be got as follows:

$$\dot{V}_f = \dot{V} + \dot{V}_c = \dot{V} + \dot{V}_0 + \sum_{i=1}^3 \dot{V}_i \leq -\mu_1 V^{\gamma_1} - \mu_2 V^{\gamma_2} + \mu_3 V + \mu_4 V^{1-\varphi/2} + \mu_5 V^{1-(\varphi\alpha_1/2)} + \mu_6 V^{1-\varphi(2\alpha_1-1)/2} + \dot{V}_0 + \sum_{i=1}^3 \dot{V}_i. \quad (48)$$

In this section, just the terms  $\dot{V}_0$  and  $\sum_{i=1}^3 \dot{V}_i$  need to be derived. After tedious derivation, it could be obtained that

$$\dot{V}_0 \leq -k_1 e^T e^\nu + \sum_{i=1}^3 \frac{2^{1-\nu}}{1+\nu} (|e_i|^{1+\nu} + \nu |\xi_i|^{1+\nu}) + e^T \epsilon_2, \quad (49)$$

$$\dot{V}_i \leq \frac{1}{k_1} |\epsilon_{2i}| |\xi_i| + \frac{(k_1 + 2^{1-\nu}(1+\nu)) |\xi_i|^{1+\nu}}{k_1(1+\nu)} + \frac{\nu |e_i|^{1+\nu}}{1+\nu} + \frac{1}{(2-\nu)2^{1-\nu}k_1^{1+1/\nu}} \xi_i^{2-\nu} \bar{\tau}_i, \quad (50)$$

where  $\bar{\tau}_i = \partial \eta_i / \partial t$ .

Substitute the control torque equation (40) into equation (47). The  $\dot{V}_i$  can be derived as follows:

$$\dot{V}_i \leq \frac{1}{k_1} |\epsilon_{2i}| |\xi_i| + \frac{(k_1 + 2^{1-\nu}(1+\nu)) |\xi_i|^{1+\nu}}{k_1(1+\nu)} + \frac{\nu |e_i|^{1+\nu}}{1+\nu} + \frac{-k_2}{(2-\nu)2^{1-\nu}k_1^{1+1/\nu}} \xi_i^{1+\nu} + \frac{-k_3}{(2-\nu)2^{1-\nu}k_1^{1+1/\nu}} |\xi_i|^{2-\nu}. \quad (51)$$

Combining equation (48) with equations (42) and (46),

$$\begin{aligned} \dot{V}_c \leq & -\left(k_1 - \frac{2^{1-\nu} + \nu}{1 + \nu}\right) \sum_{i=1}^3 |e_i|^{1+\nu} + e^T \zeta_2 \\ & + \sum_{i=1}^3 \frac{|\zeta_{2i}| |\xi_i|}{k_1} - \left(\frac{k_2}{(2-\nu)2^{1-\nu}k_1^{1+1/\nu}} - \frac{k_1 + 2^{1-\nu}(1+\nu)}{k_1(1+\nu)}\right) \times \sum_{i=1}^3 |\xi_i|^{1+\nu} + \frac{-k_3}{(2-\nu)2^{1-\nu}k_1^{1+1/\nu}} \sum_{i=1}^3 |\xi_i|^{2-\nu}. \end{aligned} \tag{52}$$

Choose  $k_3 > 0$  and let

$$k_1 \geq \frac{2^{1-\nu} + \nu}{1 + \nu} + k_4 k_2 \geq (2-\nu)2^{1-\nu}k_1^{1+1/\nu} \left(\frac{k_1 + 2^{1-\nu}(1+\nu)}{k_1(1+\nu)} + k_4\right), \tag{53}$$

where  $k_4$  is the positive constant. The following inequality is obtained:

$$\dot{V}_c \leq -k_3 \sum_{i=1}^3 |e_i|^{1+\nu} - k_3 \sum_{i=1}^3 |\xi_i|^{1+\nu} + e^T \epsilon_2 + \sum_{i=1}^3 \frac{|\epsilon_{2i}| |\xi_i|}{k_1} \leq c_1 \left(\sum_{i=1}^3 e_i^2 + \sum_{i=1}^3 \xi_i^2\right), \tag{54}$$

where  $c_1 = \max\{1/2, 1/(2-\nu)k_1^{1+1/\nu}\}$ .

Notice that

$$V_i \leq \frac{1}{(2-\nu)2^{1-\nu}k_1^{1+1/\nu}} |\eta_i - \eta_{di}| |\xi_i|^{2-\nu} \leq \frac{1}{(2-\nu)k_1^{1+1/\nu}} |\xi_i|^2. \tag{55}$$

Hence, the following inequality is obtained:

$$V_c = V_0 + \sum_{i=1}^3 V_i \leq c_2 \left(\sum_{i=1}^3 \epsilon_i^2 + \sum_{i=1}^3 \xi_i^2\right), \tag{56}$$

where  $c_2 = \max\{1/2, 1/(2-\nu)k_1^{1+1/\nu}\}$ .

According to Lemma 2:

$$\dot{V}_c \leq -c_3 V^{(1+\nu)/2} + e^T \epsilon_2 + \sum_{i=1}^3 \frac{|\epsilon_{2i}| |\xi_i|}{k_1}, \tag{57}$$

where  $c_3 = k_3/c_2^{(1+\nu)/2}$ .

From equations (45) and (54),

$$\begin{aligned} \dot{V}_f = \dot{V} + \dot{V}_c = \dot{V} + \dot{V}_0 + \sum_{i=1}^3 \dot{V}_i \leq & -\mu_1 V^{\gamma_1} - \mu_2 V^{\gamma_2} + \mu_3 V \\ & + \mu_4 V^{1-(\varphi/2)} + \mu_5 V^{1-\varphi\alpha_1/2} + \mu_6 V^{1-\varphi(2\alpha_1-1)/2} - c_2 V^{(1+\nu)/2} + e^T \epsilon_2 + \sum_{i=1}^3 \frac{|\epsilon_{2i}| |\xi_i|}{k_1}. \end{aligned} \tag{58}$$

According to Theorem 1,  $\epsilon(t)$  would converge to zeros in finite time, so equation (55) becomes

$$\dot{V}_f = \dot{V}_c \leq -c_2 V_c^{(1+\nu)/2}. \tag{59}$$

Because  $0 < (1+\nu)/2 < 1$ , the tracking errors  $e$  converge to zeros in finite time [11].

The proof is completed.  $\square$

*Remark 1.* In practical situations, due to the absence of certain parameters, the system function  $f(x_1, x_2)$  can not be calculated accurately. To deal with this problem, the system function  $f(x_1, x_2)$  and external disturbances  $d^*(t)$  can be regarded as total disturbances  $d_{total}(t)$ . The control algorithm proposed in this article can be written as

$$\begin{cases} \dot{z}_1 = z_2 + \rho |\epsilon_1|^{\alpha_1} \text{sign}(\epsilon_1) + \rho |\epsilon_1|^{\beta_1} \text{sign}(\epsilon_1) + \theta_1 \text{sign}(\epsilon_1), \\ \dot{z}_2 = z_3 + g(x_1)\tau + \rho^2 |\epsilon_1|^{\alpha_2} \text{sign}(\epsilon_1) + \rho^2 |\epsilon_1|^{\beta_2} \text{sign}(\epsilon_1) + \theta_2 \text{sign}(\epsilon_1), \\ \dot{z}_3 = \rho^3 |\epsilon_1|^{\alpha_3} \text{sign}(\epsilon_1) + \rho^3 |\epsilon_1|^{\beta_3} \text{sign}(\epsilon_1) + \theta_3 \text{sign}(\epsilon_1), \\ \tau = g^{-1} \left( -k_3 \text{sign}(\xi) - k_2 \xi^{2\nu-1} - z_3 + \ddot{q}_d - \rho^2 |\epsilon_1|^{\alpha_2} \text{sign}(\epsilon_1) - \rho^2 |\epsilon_1|^{\beta_2} \text{sign}(\epsilon_1) - \theta_2 \text{sign}(\epsilon_1) \right). \end{cases} \tag{60}$$

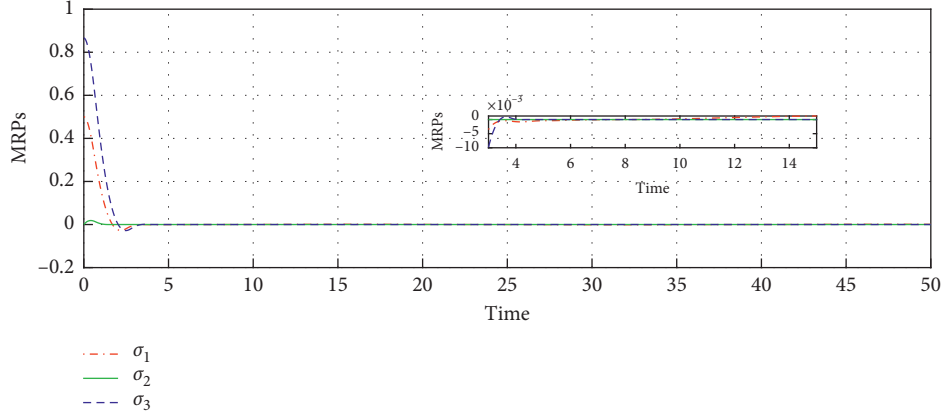
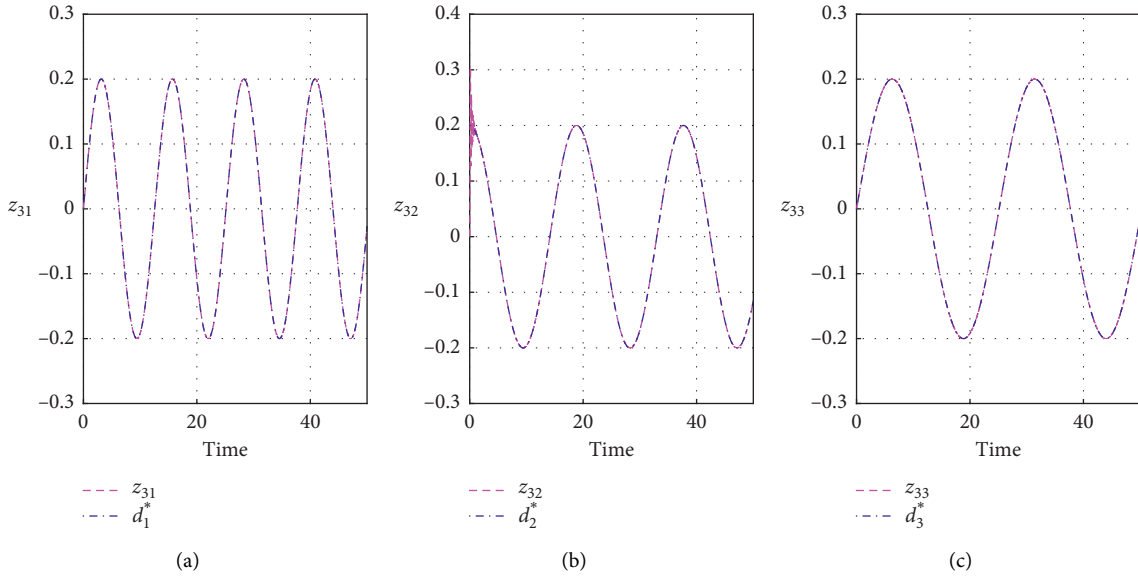


FIGURE 1: Tracking errors for FTESO-based controller with external disturbances.


 FIGURE 2: External disturbances estimate for FTESO. (a)  $z_{31}$ . (b)  $z_{32}$ . (c)  $z_{33}$ .

*Remark 2.* In order to eliminate the chattering issue caused by discontinuous terms in the observer and controller, the signum function can be replaced by the following function:

$$\text{sgmf}(e_1) = \begin{cases} 2\left(\frac{1}{1 + \exp(-\gamma_o e_1)} - \frac{1}{2}\right), & |e_1| \leq \delta, \\ \text{sign}(e_1), & |e_1| > \delta, \end{cases} \quad (61)$$

where  $\gamma_o$  and  $\delta$  are constants which can be designed.

#### 4. Simulation Results

In this section, several numerical simulations are implemented to show the effectiveness of the FTESO-based control scheme proposed in this paper; meanwhile, the control scheme with general LESO and the control scheme without ESO in reference [11] are introduced as comparisons.

The initial states are designed as  $x_1(0) = [0, 0, 0]^T$ ,  $x_2(0) = [0, 0, 0]^T$ ,  $z_1(0) = [0, 0, 0]^T$ ,  $z_2(0) = [0, 0, 0]^T$ ,  $z_3(0) = [0, 0, 0]^T$ . The desired attitude trajectory is designed as  $\sigma_d = 0.5[\cos(0.2t), \sin(0.2t), \sqrt{3}]^T$ , and the external disturbances  $d^* = 0.2[\sin(0.5t), \cos(1/3t), \sin(1/4t)]$ . The parameters of the proposed ESO and controller are  $\rho = 5$ ,  $\alpha_1 = 0.8$ ,  $\theta_1 = 1$ ,  $\theta_2 = 5$ ,  $\theta_3 = 1$ ,  $\nu = 7/9$ ,  $k_1 = 1.1$ ,  $k_2 = 1.5$ , and  $k_3 = 0.01$ . The inertia matrix of rigid body is chosen as

$$J = \begin{bmatrix} 20 & 1.2 & 0.9 \\ 1.2 & 17 & 1.4 \\ 0.9 & 1.4 & 15 \end{bmatrix} \text{kgm}^2. \quad (62)$$

The upper bound of control torque is selected as  $|\tau_i| \leq 50 \text{ Nm}$ , where  $i = 1, 2, 3$ .

First, the proposed scheme includes that equations (9) and (40) are simulated. In this simulation, the system function  $f(x_1, x_2)$  is assumed to be known; the proposed

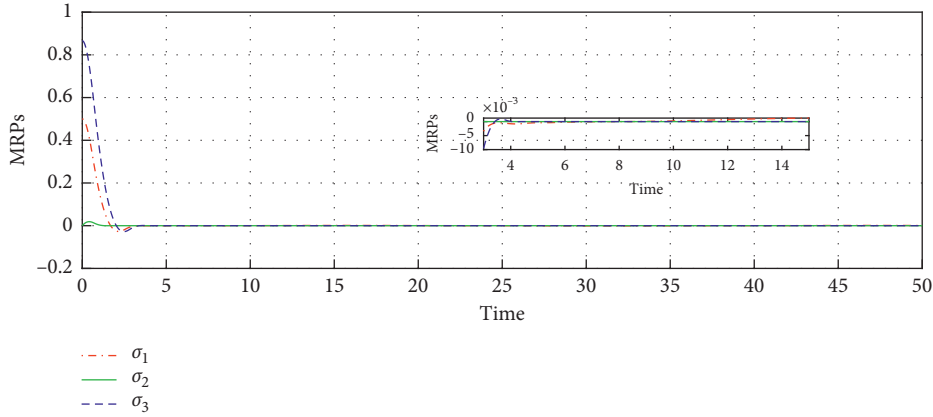


FIGURE 3: Tracking errors for the FTESO-based controller with total disturbances.

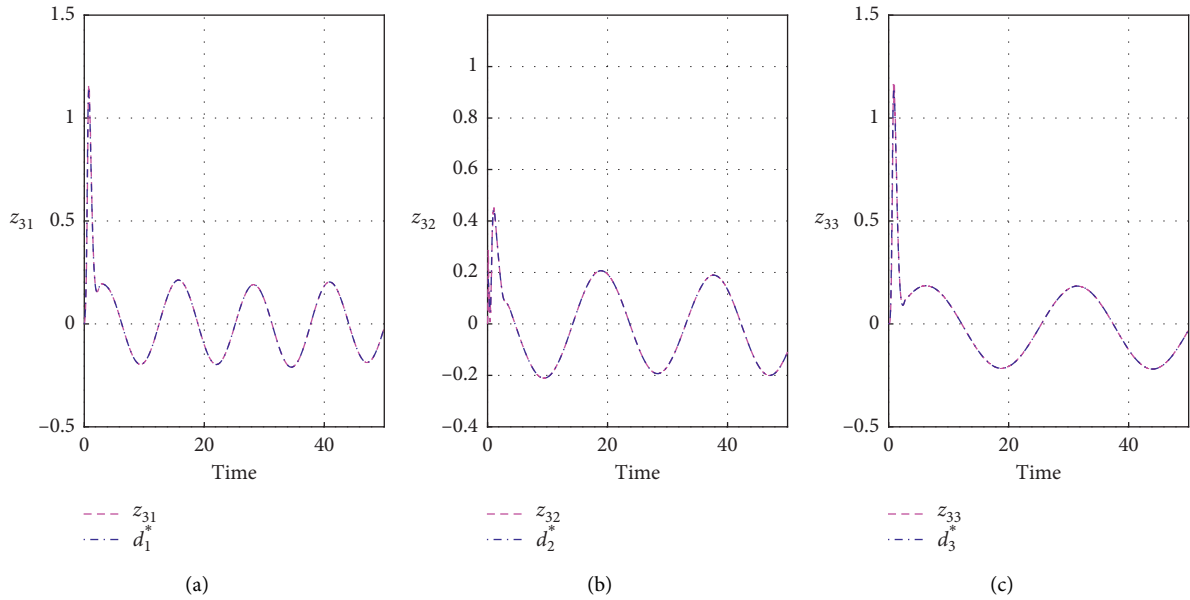


FIGURE 4: Total disturbances estimate for FTESO. (a)  $z_{31}$ . (b)  $z_{32}$ . (c)  $z_{33}$ .

FTESO only estimates the external disturbances  $d^*$  and the virtual angular velocity  $x_2$ .

The results of attitude tracking errors and external disturbances estimate for the FTESO-based control scheme are shown in Figures 1 and 2. According to Figure 1, the proposed control scheme can converge the tracking errors to zeros within about 4 seconds, and the extended state  $z_3$  can also estimate the total disturbances  $d^*(t)$  in finite time.

Then, consider the situation that the system function  $f(x_1, x_2)$  is unknown, which is regarded as total disturbances  $d_{total}^*(t)$  together with external disturbances  $d^*(t)$ . The simulation results are shown in Figures 3 and 4. Compared with above results, the total disturbances  $d_{total}^*(t)$  is much larger than  $d^*(t)$  in Figure 2, but it can be fast estimated by FTESO. Because the estimated total disturbances can be compensated in controller, even the system function  $f(x_1, x_2)$  is unknown; the proposed control scheme can also converge the tracking errors to zeros within

finite time. The FTESO guarantees that the two simulations in Figures 1 and 3 have the similar results.

For comparison, the introduced linear LESO is designed as follows:

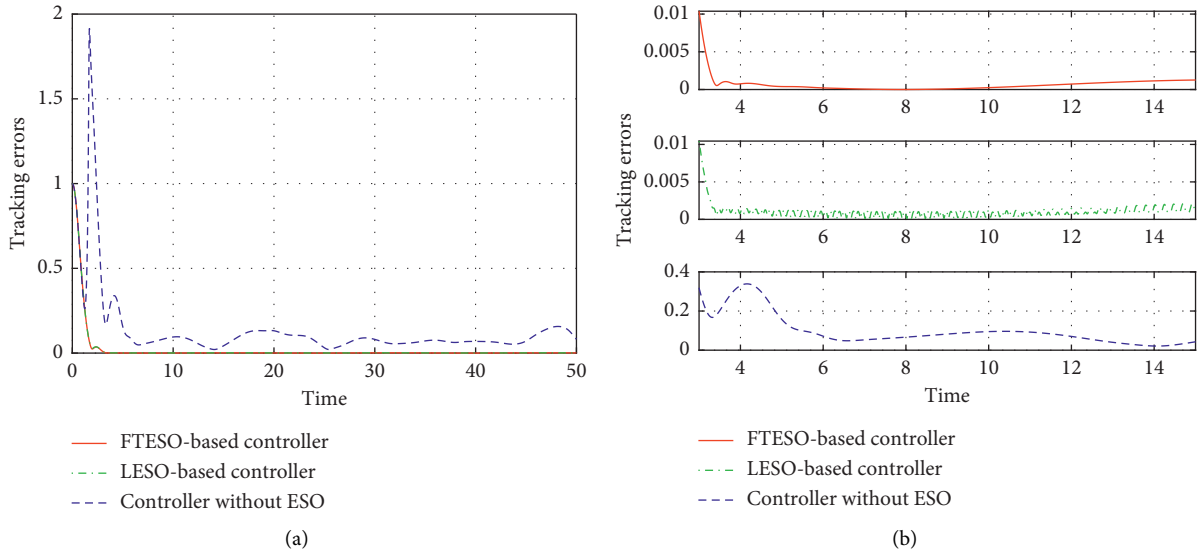
$$\begin{cases} \dot{z}_1 = z_2 + \rho_1 \varepsilon_1, \\ \dot{z}_2 = z_3 + f(x_1, z_2) + g(x_1)\tau + \rho_1^2 \varepsilon_1, \\ \dot{z}_3 = \rho_1^3 \varepsilon_1. \end{cases} \quad (63)$$

The corresponding controller is similar to the one designed in this article:

$$\tau = g^{-1}(-k_3 \text{sign}(\xi) - k_2 \xi^{2\nu-1} - z_3 - f(x_1, z_2) + \ddot{q}_d - \rho_1^2 \varepsilon_1). \quad (64)$$

The parameters are designed as  $\rho_1 = 28$ ,  $\nu = 7/9$ ,  $k_1 = 1.1$ ,  $k_2 = 1.5$ , and  $k_3 = 0.01$ .

The other control scheme in [11] is expressed as


 FIGURE 5: Tracking errors  $\|e\|$  under different control schemes.

$$\begin{cases} \dot{z}_1 = z_2 + \theta c_1 |\varepsilon_1|^{\alpha_1} \text{sign}(\varepsilon_1), \\ \dot{z}_2 = z_3 + f(x_1, z_2) + g(x_1)\tau + \theta^2 c_2 |\varepsilon_1|^{\alpha_2} \text{sign}(\varepsilon_1), \\ \tau = g^{-1}(-k_2 \xi^{2\nu-1} - f(x_1, z_2) + \ddot{q}_d - \theta^2 c_2 |\varepsilon_1|^{\alpha_2} \text{sign}(\varepsilon_1)), \end{cases} \quad (65)$$

where the parameters are selected to be same as in [11]:  $\theta = 3$ ,  $c_1 = 1$ ,  $c_2 = 0.2$ ,  $\nu = 7/9$ ,  $k_1 = 1.1$ ,  $k_2 = 1.5$ , and  $k_3 = 0.01$ .

The comparison results between these three attitude control schemes are shown in Figure 5. As shown in Figure 5, the proposed control scheme in this article and the control algorithm based on LESO in equations (59) and (60) can attain faster convergence than the controller in equation (61), and the proposed control scheme gets the best disturbances rejection.

## 5. Conclusion

The finite time attitude tracking control for rigid body is studied in this article; a FTESO is designed through the homogeneous Lyapunov method. The angular velocity and total disturbances can be estimated by the proposed observer. Based on this, a finite time attitude controller is introduced. Numerical simulations show that the proposed control scheme can achieve fast convergence and good disturbances rejection. Further work will be focused on reducing power cost and dealing with the input saturation problem.

## Data Availability

All data generated or analyzed during this study are included within the article.

## Conflicts of Interest

The authors declare that they have no conflicts of interest.

## Acknowledgments

This work was supported by the National Basic Research Program of China (973 Program: 2012CB821200 and 2012CB 821201) and the NSFC (61327807, 61521091, 61520106010, and 61134005).

## References

- [1] M. Miyasaka and P. Berkelman, "Magnetic levitation with unlimited omnidirectional rotation range," *Mechatronics*, vol. 24, no. 3, pp. 252–264, 2014.
- [2] Y. Hong, Y. Xu, and J. Huang, "Finite-time control for robot manipulators," *Systems & Control Letters*, vol. 46, no. 4, pp. 243–253, 2002.
- [3] L. Zhao and Y. Jia, "Finite-time attitude tracking control for a rigid spacecraft using time-varying terminal sliding mode techniques," *International Journal of Control*, vol. 88, no. 6, pp. 1150–1162, 2015.
- [4] Z. Chen and J. Huang, "Attitude tracking of rigid spacecraft subject to disturbances of unknown frequencies," *International Journal of Robust and Nonlinear Control*, vol. 24, no. 16, pp. 2231–2242, 2014.
- [5] D. Thakur, S. Srikant, and M. R. Akella, "Adaptive attitude-tracking control of spacecraft with uncertain time-varying inertia parameters," *Journal of Guidance, Control, and Dynamics*, vol. 38, no. 1, pp. 41–52, 2015.
- [6] H. Zhang and J. Fang, "Robust backstepping control for agile satellite using double-gimbal variable-speed control moment gyroscope," *Journal of Guidance, Control, and Dynamics*, vol. 36, no. 5, pp. 1356–1363, 2013.
- [7] F. Lizarralde and J. T. Wen, "Attitude control without angular velocity measurement: a passivity approach," *IEEE Transactions on Automatic Control*, vol. 41, no. 3, pp. 468–472, 1996.
- [8] P. Tsiotras, "Further passivity results for the attitude control problem," *IEEE Transactions on Automatic Control*, vol. 43, no. 11, pp. 1597–1600, 1998.
- [9] A. Tayebi, "Unit quaternion-based output feedback for the attitude tracking problem," *IEEE Transactions on Automatic Control*, vol. 53, no. 6, pp. 1516–1520, 2008.

- [10] B. Xiao, L. Cao, and D. Ran, "Attitude exponential stabilization control of rigid bodies via disturbance observer," *IEEE Transactions on Systems, Man, and Cybernetics: Systems*, vol. 53, pp. 1–9, 2019.
- [11] A.-M. Zou, "Finite-time output feedback attitude tracking control for rigid spacecraft," *IEEE Transactions on Control Systems Technology*, vol. 22, no. 1, pp. 338–345, 2014.
- [12] H. Gui and G. Vukovich, "Finite-time angular velocity observers for rigid-body attitude tracking with bounded inputs," *International Journal of Robust and Nonlinear Control*, vol. 27, no. 1, pp. 15–38, 2017.
- [13] B. Jiang, C. Li, and G. Ma, "Finite-time output feedback attitude control for spacecraft using "Adding a power integrator" technique," *Aerospace Science and Technology*, vol. 66, pp. 342–354, 2017.
- [14] Q. Hu and B. Jiang, "Continuous finite-time attitude control for rigid spacecraft based on angular velocity observer," *IEEE Transactions on Aerospace and Electronic Systems*, vol. 54, no. 3, pp. 1082–1092, 2018.
- [15] J. Na, B. Jing, Y. Huang, G. Gao, and C. Zhang, "Unknown system dynamics estimator for motion control of nonlinear robotic systems," *IEEE Transactions on Industrial Electronics*, vol. 67, no. 5, pp. 3850–3859, 2020.
- [16] J. Na, J. Yang, S. Wang, G. Gao, and C. Yang, "Unknown dynamics estimator-based output-feedback control for nonlinear pure-feedback systems," *IEEE Transactions on Systems, Man, and Cybernetics: Systems*, vol. 53, pp. 1–12, 2019.
- [17] J. Na, S. Wang, Y.-J. Liu, Y. Huang, and X. Ren, "Finite-time convergence adaptive neural network control for nonlinear servo systems," *IEEE Transactions on Cybernetics*, vol. 50, no. 6, pp. 2568–2579, 2020.
- [18] Z. Gao, "Scaling and bandwidth parameterization based controller tuning," in *Proceedings of the 2003 American Control Conference*, vol. 6, pp. 4989–4996, Denver, Colorado, USA, 2003.
- [19] L. Zhao, H. Cheng, and T. Wang, "Sliding mode control for a two-joint coupling nonlinear system based on extended state observer," *Isa Transactions*, vol. 73, pp. 130–140, 2018.
- [20] Y.-j. Wu and G.-f. Li, "Adaptive disturbance compensation finite control set optimal control for pmsm systems based on sliding mode extended state observer," *Mechanical Systems and Signal Processing*, vol. 98, pp. 402–414, 2018.
- [21] R. Madonski, M. Ramirez-Neria, M. Stanković et al., "On vibration suppression and trajectory tracking in largely uncertain torsional system: an error-based adrc approach," *Mechanical Systems and Signal Processing*, vol. 134, p. 106300, 2019.
- [22] Q. Hu, B. Jiang, and M. I. Friswell, "Robust saturated finite time output feedback attitude stabilization for rigid spacecraft," *Journal of Guidance, Control, and Dynamics*, vol. 37, no. 6, pp. 1914–1929, 2014.
- [23] S. Xiong, W. Wang, X. Liu, Z. Chen, and S. Wang, "A novel extended state observer," *Isa Transactions*, vol. 58, pp. 309–317, 2015.
- [24] C. Qian and W. Lin, "A continuous feedback approach to global strong stabilization of nonlinear systems," *IEEE Transactions on Automatic Control*, vol. 46, no. 7, pp. 1061–1079, 2001.
- [25] Y. Shen and X. Xia, "Semi-global finite-time observers for nonlinear systems," *Automatica*, vol. 44, no. 12, pp. 3152–3156, 2008.
- [26] S. P. Bhat and D. S. Bernstein, "Geometric homogeneity with applications to finite-time stability," *Mathematics of Control, Signals, and Systems*, vol. 17, no. 2, pp. 101–127, 2005.
- [27] Y. Shen and Y. Huang, "Uniformly observable and globally lipschitzian nonlinear systems admit global finite-time observers," *IEEE Transactions on Automatic Control*, vol. 54, no. 11, pp. 2621–2625, 2009.
- [28] I. Haskara, "On sliding mode observers via equivalent control approach," *International Journal of Control*, vol. 71, no. 6, pp. 1051–1067, 1998.



## Research Article

# Human Action Recognition Algorithm Based on Improved ResNet and Skeletal Keypoints in Single Image

Yixue Lin <sup>1</sup>, Wanda Chi,<sup>1</sup> Wenxue Sun,<sup>1</sup> Shicai Liu <sup>2</sup> and Di Fan <sup>1</sup>

<sup>1</sup>College of Electronic and Information Engineering, Shandong University of Science and Technology, Qingdao 266590, China

<sup>2</sup>College of Intelligent Equipment, Shandong University of Science and Technology, Tai'an 271000, China

Correspondence should be addressed to Di Fan; [skd992372@sdust.edu.cn](mailto:skd992372@sdust.edu.cn)

Received 29 April 2020; Accepted 8 June 2020; Published 29 June 2020

Guest Editor: Jing Na

Copyright © 2020 Yixue Lin et al. This is an open access article distributed under the Creative Commons Attribution License, which permits unrestricted use, distribution, and reproduction in any medium, provided the original work is properly cited.

Human action recognition is an important part for computers to understand the behavior of people in pictures or videos. In a single image, there is no context information for recognition, so its accuracy still needs to be greatly improved. In this paper, a single-image human action recognition method based on improved ResNet and skeletal keypoints is proposed, and the accuracy is improved by several methods. We improved the backbone network ResNet-50 and CPN to a certain extent and constructed a multitask network to suit the human action recognition task, which not only improves the accuracy but also balances the total number of parameters and solves the problem of large network and slow operation. In this paper, the improvement methods of ResNet-50, CPN, and whole network are tested, respectively. The results show that the single-image human action recognition based on improved ResNet and skeletal keypoints can accurately identify human action in the case of different human movements, different background light, and occlusion. Compared with the original network and the main human action recognition algorithms, the accuracy of our method has its certain advantages.

## 1. Introduction

Human action recognition (HCR) is a separate branch of computer vision that processes images or videos to judge what people are doing.

The single-image action recognition is generally divided into three categories: the approach based on the whole image, the approach based on human pose, and the approach based on human-object interaction. The approach based on the whole image is to treat the whole image as a classification problem, extract the features through the neural network layer, and then use the classifier to find the label category. Some researchers make full use of contextual information in pictures to distinguish actions. Zhang et al. [1] proposed a method to divide the precise area between the person and the background as well as the interactive object through a smaller number of annotations. Instead, Xin et al. [2] use semantic objects to enhance the ability of the network to distinguish features. RCNN (Regions with Convolutional Neural Network) [3] and R\*CNN [4] also classify the

human body as a whole by using the method of moving and marking bounding boxes in object recognition tasks.

The approach based on human pose tends to find the similarity between the same postures [5–8]. Some of these pose-based approaches assume that the body moves in relation to various parts of the body and use them to represent them (such as the head, hands, and feet). Diba et al. [9] mined the middle layer features of the image and extracted different types of features. Zhao et al. [10] propose the methodology which combines body actions and part actions for action recognition. In the Whole and Parts [11] method, Gkioxari proposed that each part of the body should be supervised for movement, and specific networks should be trained to distinguish between them.

The approach based on human-object interaction not only takes into account parts of human body components but also uses detectors to distinguish objects. Gupta et al. [12] added the description information of the scene on the basis of the above methods to achieve a better behavior recognition effect. Zhang et al. [1] tried to use the smallest

annotation to segment the precise area of the underlying person-object interaction. Zhao et al. [13] detected the semantic part in the bounding box, arranged its features in spatial order, and extended the interclass variance.

The action recognition task in this paper is based on static single images. The classical classification network ResNet-50 [14] and CPN (cascaded pyramid network) [15] are combined and trained. Meanwhile, the improved CBAM (Convolutional Block Attention Module) [16] and TridentNet [17] were added to the fused network in this paper, which improved the performance of action recognition and the classification accuracy on the basis of controlling the number of overall parameters. In this paper, the effectiveness of this method is verified by three experiments. From the experimental results, the classification indexes of the improved model are all increased compared with the previous model. In the case of different body movements, different background light, and blocked and incomplete characters in the images, the network has achieved good recognition results.

## 2. The Single-Image Human Action Recognition Model in This Paper

Based on the Pascal Voc 2012 [18] dataset, this paper constructs a multitask deep learning convolution network to realize the classification of ten human actions in still images. The overall network architecture adopts ResNet-50 as the backbone network and introduces TridentNet for improvement. The model fuses the information of skeletal keypoints to improve the accuracy. The whole model is shown in Figure 1.

The backbone network of the model in Figure 1 is the improved ResNet-50, in which we adapted TridentNet to replace the original ResNet network structure, adding different sizes of receptive fields to the network. Compared with other multibranch networks, the dilated convolution and weight shared mechanism introduced by TridentNet can reduce parameters and simplify the network. Also, CPN [15] is adopted and improved in the keypoints detection section. Cascaded pyramid network can extract and fuse feature information of different depth, and the added attention model CBAM [16] can effectively improve its accuracy. The model adds the keypoints of network output to the images for classification and strengthens the important parts by adding weights and finally obtains and outputs the action categories.

*2.1. The Improved ResNet Model with TridentNet Introduced.* Many researchers make the classification more accurate by increasing the depth or width of the network. Here, we chose to use a three-branch network instead of ResNet's original single-branch structure to expand its receptive field. The original ResNet-50 [14] contains 50 convolutions, which are divided into 5 structurally similar stages to extract image features, as shown in the Figure 2.

In order to reduce the number of parameters on the basis of expanding the receptive field, we introduced TridentNet

[17] with three branches in the backbone ResNet-50. As can be seen from Figure 3, TridentNet is introduced into the 5th stage of ResNet-50 in this paper. Due to structural differences between modules in the ResNet network itself, the improved trident module is also divided into Conv-trident block and ID-trident block, whose structure is shown in Figure 4.

The original TridentNet was used as part of the object detection network as a three-output structure. We made some modifications to make it a single-branch output one and added a shortcut to make it more in line with the ResNet configuration.

In addition to joining the multibranch structure, the TridentNet utilizes the concept of dilated convolution [19]. By filling 0 in the convolution kernel, the large receptive field can be obtained with a fewer parameters. When the dilation rate is  $d$ , the relationship between the side length  $n$  of the convolution kernel, the number  $(d - 1)$  of filled 0, and the size length  $k$  of the original convolution kernel is shown in formula (1). In TridentNet's structure, the parameter  $k$  of the three branches is 3, and  $d$  is 1, 2, and 3, respectively. Therefore, the size of the receptive field  $n$  becomes 3, 5, and 7. One has

$$n = k + (k - 1) * (d - 1). \quad (1)$$

*2.2. The CPN Keypoint Detection Model with Attention Model Introduced.* The detection of skeletal keypoints is mainly based on the prediction of the image pixel points to determine the most likely position. In order to further improve the accuracy of CPN [15] output, we add an attention module CBAM [16] to it. The improved CPN model is shown in Figure 5.

The backbone of CPN is still ResNet-50. As shown in Figure 5, CPN network with attention model is introduced. In order to make the attention mechanism play a role in CPN as a whole, CBAM is added to the deepest layer of the network and acts on feature information of different depth through the upsampling network layer by layer in the feature pyramid. Each pixel in the output image represents the probability of skeletal keypoints and constitutes a heatmap, which is then converted into the numerical coordinates by soft-argmax function before output.

CPN is a top-down human keypoints detection network, which takes the result of pedestrian detection network as input and locates the skeletal keypoints through network processing. The CPN network consists of two parts: GlobalNet network for early rough detection of keypoints and RefineNet network for fine tuning. The network structure is shown in Figure 6.

GlobalNet uses the network structure to combine the shallow features of low semantic information but high resolution with the deep features of high semantic information but low resolution. CPN network reduces the size of feature graph but increases the number of channels while extracting information by bottleneck. GlobalNet makes use of upper sampling and feature superposition to achieve the fusion of shallow and deep features. RefineNet takes the

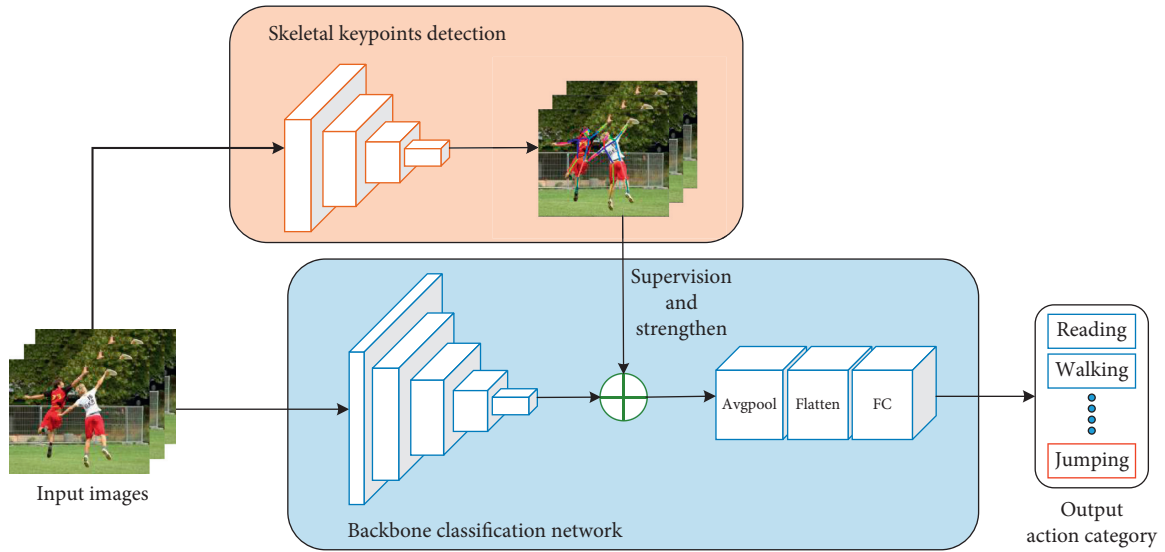


FIGURE 1: Overall algorithm framework.

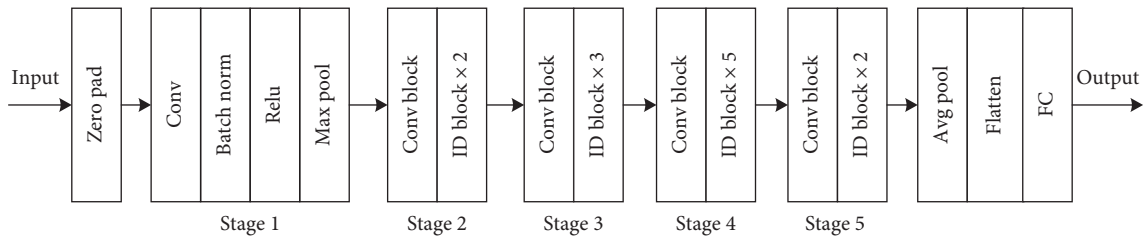


FIGURE 2: Basic network structure of ResNet-50.

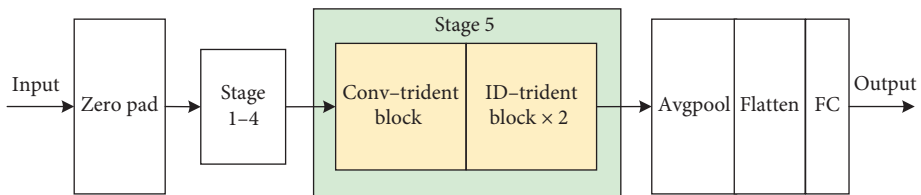


FIGURE 3: The improved ResNet-50 structure.

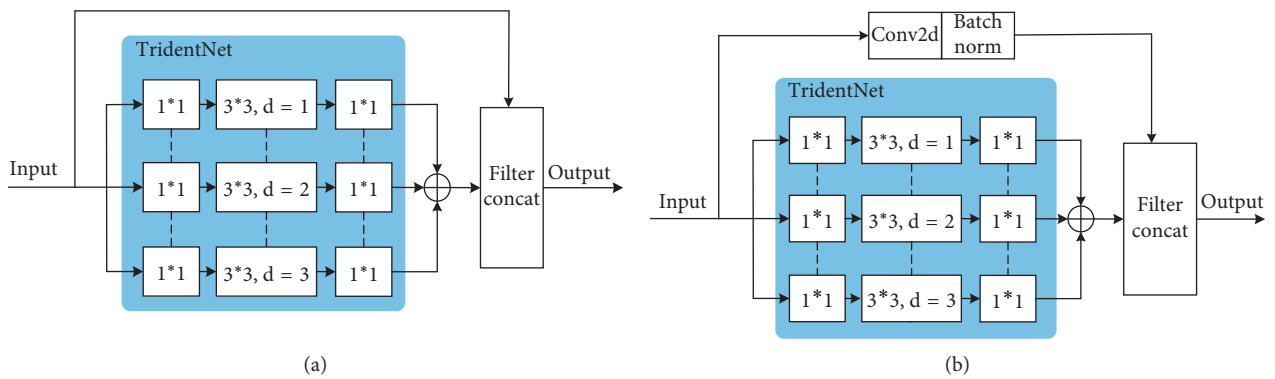


FIGURE 4: TridentNet structure after improvement: (a) ID-trident block; (b) Conv-trident block.

features of the GlobalNet output and integrates them through a concat layer while extracting the details. RefineNet focuses on learning about difficult-to-locate points (such as

occlusion) that GlobalNet cannot accurately locate. With fine-tuning, the network can achieve a balance between efficiency and performance on a smaller spatial scale.

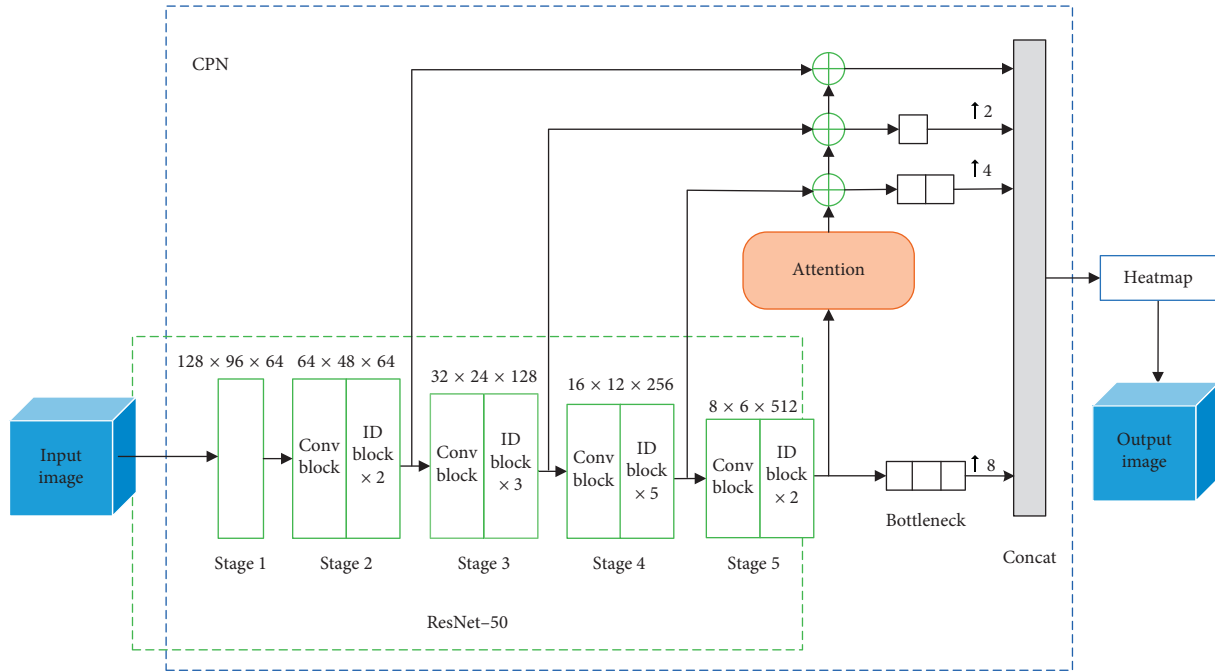


FIGURE 5: CPN network with attention model introduced.

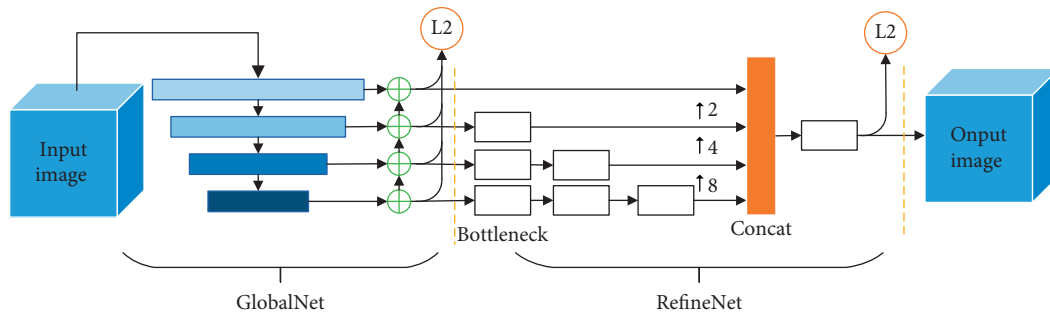


FIGURE 6: Characteristic pyramid network structure.

The essence of the attention mechanism is to emphasize the important position that is useful for the learning target and suppress the irrelevant information by assigning the weight coefficient to the image feature information. CBAM module improves the accuracy of CPN by introducing attention mechanism. The advantage is that it is flexible and portable and can be inserted into the network without changing the backbone structure. The network structure of CBAM is shown in Figure 7. The attention module can be divided into two parts: channel attention and spatial attention. Channel attention learns the importance of each channel through pooling operations and thus assigns different weights to channels. After global maximum pooling and average pooling, it was entered into Multilayer Perceptron (MLP) for learning, and the learning results were superimposed to obtain channel attention. The input of spatial attention is a feature map weighted by channel attention, which learns the importance of each position in the feature map to the points to be estimated. After average pooling and maximum pooling, respectively, the two were spliced according to the first dimension, and finally spatial

attention was generated through a convolution of size of  $3 * 3$ .

**2.3. Fusion Model of Human Keypoints and Action Recognition Features.** In order to improve the action recognition performance of the whole network, we added the skeleton keypoints to the backbone network for enhancement. The overall network structure is a multibranch multitask network, in which one task is keypoints detection and the other is to extract features for classification. After that, human action category is obtained through feature fusion training. The feature fusion process is shown in Figure 8. When an image comes in, the network sends it to both branches of the network. The upper part is the trained CPN, which can estimate the heatmap of a series of keypoints, while the lower part is the backbone network ResNet-50 without the last softmax part to extract features. We treat the keypoints heatmaps and the backbone output features the same size and then multiply them at the pixel level. Since the pixel values in the heatmap of keypoints are all between  $[0, 1]$ ,

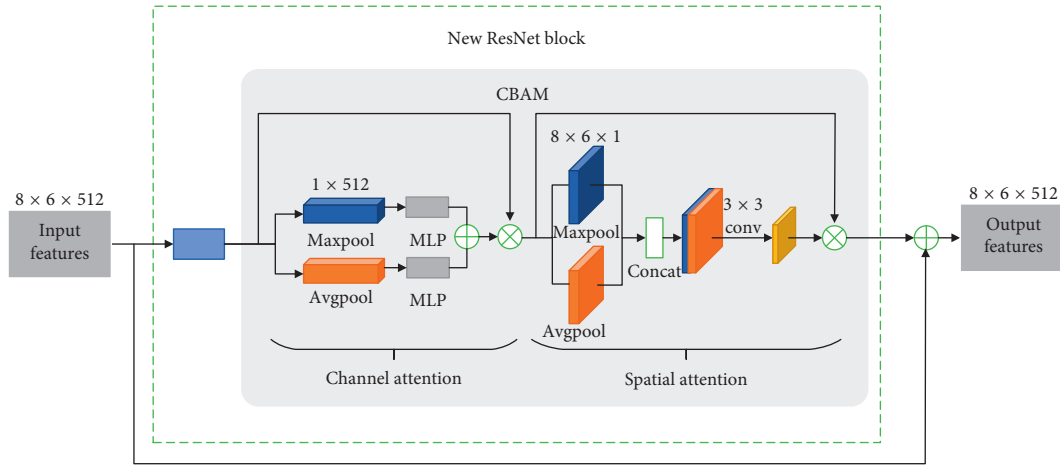


FIGURE 7: CBAM attention mechanism mode.

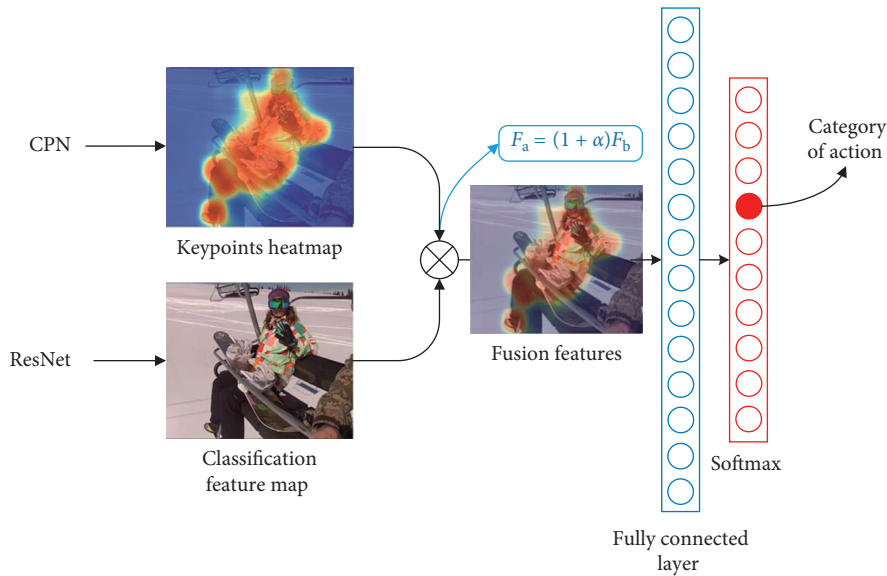


FIGURE 8: Feature fusion process of human keypoints and action recognition.

product formula (2) is obtained. The pixel value  $F_a$  after fusion is  $(1 + \alpha)$  times to  $F_b$  before fusion, where the value is the corresponding pixel value in the heatmap of the keypoints. The higher the value of the heatmap here is (i.e., the closer to the position of the keypoint), the more the value is emphasized. One has

$$F_a = (1 + \alpha)F_b. \quad (2)$$

At the end of the network is the softmax layer for the classification section. By taking the softmax layer of ResNet-50 and using it as the final classification layer of the overall network, we can predict the corresponding category of images in ten action categories.

### 3. Experiments and Tests

3.1. *Experimental Conditions, Tools, and Datasets.* The experimental hardware is GPU RTX 2070 graphics card server,

on which we use Python language to write programs in Sublime Text3 editor and runs in Anaconda environment. Pytorch, a deep learning framework, was used to construct the neural network in the program, and the final result was visualized. The experimental curve was drawn by Tensorboardx.

In this paper, six different datasets are selected, which are as follows:

- (1) *Cifar-10/Cifar-100:* *Cifar-10* and *Cifar-100* were collected by Alex Krizhevsky, Vinod Nair, and Geoffrey Hinton. *Cifar-10* consists of 6000 RGB images in 10 categories. The images in the dataset are pictures of objects in the real world, with large background noise and different proportions. *Cifar-100* consists of 100 categories, each containing 600 images, divided into 20 super categories, each with a “fine” label and a “rough” label.



- (2) ImageNet: ImageNet is a database of human vision systems built by Stanford computer science researchers. ImageNet currently has the largest image recognition database in the world, with more than 14 million images from various projects.
- (3) SVHN: Street View House Numbers (SVHN) database is a real world dataset for object detection, with more than  $6 * 10^5$  pictures of house number, divided into 10 categories from 0 to 9. The images were collected from Street View House Numbers on Google Maps.
- (4) MS COCO [20]: we mainly use the keypoints data in COCO to train and evaluate the keypoint detection network. There are more than 143k images in it, including 118288 images of training set, 5000 images of verification set, and 20288 images of test set. 250 k characters are labeled in the COCO dataset, including up to 1700 k human skeletal keypoints.

The label format of the COCO dataset is JSON file (a text file that records label data), and for each individual instance, its detection box, segmentation boundary mask, and 17 keypoints coordinates are identified. The 17 keypoints are the nose, left and right eyes, left and right ears, left and right shoulders, left and right elbows, left and right wrists, left and right hips, left and right knees, and left and right ankles.

- (5) Pascal Voc [18]: the dataset used for human action recognition in this paper is Pascal Voc 2012. The Pascal Voc dataset contains a variety of image processing tasks. As one of the benchmark datasets, it is frequently used in various network comparison experiments. In addition to human action recognition, it also includes a variety of tasks such as classification, segmentation, detection, and classification of human parts.

The data on human action recognition in Pascal Voc included ten categories, namely, jumping, playing instrument, taking photo, riding horse, reading, phoning, using computer, riding bike, running, and walking. There are 4,588 images, including 2,296 images in the training set and 2,292 images in the test set.

**3.2. Improved ResNet Model Experiment.** This experiment improved the original classification network ResNet-50 by adding TridentNet and conducted experiments on four different classification datasets: Cifar-10, Cifar-100, ImageNet, and SVHN to test the improved effect.

Table 1 shows the comparison of experimental error rates of single-branch network (unimproved ResNet-50), common three-branch network (inception module), and the network in this paper (joined the dilated convolution and weight sharing of TridentNet) on four datasets. Through experiments, it can be concluded that the classification error rate of the network in this paper is significantly reduced compared with that of the single-branch ResNet-50, which is 1.18 less on Cifar-10, 2.89 less on Cifar-100, 1.42 less on ImageNet, and 0.26 less on SVHM. And compared with the

three-branch network without dilated convolution and weight sharing, the improved network can reduce the error rate while reducing the parameters due to the effect of weight sharing.

We use floating-point operations (FLOPs) and parameters to evaluate the complexity of the improved network model. For a convolution operation,  $k_w$  and  $k_h$  represent the width and height of the convolution kernel. The number of input channels in this layer is  $C_{in}$  and the number of output channels is  $C_{out}$ . If the height and width of the feature graph output from this layer are denoted as H and W, the calculation formula of  $FLOPs_{conv}$  is shown in

$$FLOPs_{conv} = [(k_w * k_h * c_{in}) * c_{out} + c_{out}] * H * W. \quad (3)$$

The calculation formula of  $param_{conv}$  is shown in

$$param_{conv} = (k_w * k_h * c_{in}) * c_{out} + c_{out}. \quad (4)$$

Table 2 shows the comparison of the running time, number of arguments, and floating-point operations of the three networks. The results show that the time of the improved three-branch network is 44.58 s less than that of the simple three-branch network, 108.266 M less in the number of parameters, and 5.461 G less in the floating-point computation, but it does not increase much compared with the single-branch network ResNet-50. Therefore, the network used in this paper reduces the error rate of network classification without increasing computation.

Through the analysis and comparison of Tables 1 and 2, it can be seen that the improved network can reduce the error rate of network classification under the control of the number of parameters, indicating that the improvement made in this paper is effective.

**3.3. Keypoint Detection Model Experiment.** In the part of human skeletal keypoint detection, we improved the network CPN [15] by adding the attention model CBAM [16] to achieve high accuracy and selected the main keypoint detection methods for comparison test. Cmu-Pose [21], Mask-Rcnn, G-Rmi [22], PersonLab [23], and CPN are used for comparison experiments. Among them, Cmu-Pose [21] was the champion of COCO human keypoints detection competition in 2016. The evaluation indexes were AP and AR, AP and AR with thresholds of 0.5 and 0.75, and AP and AR under the medium target ( $AP_m, AR_m$ ) and then under large target ( $AP_l, AR_l$ ). Figure 9 is the experimental comparison between the improved CPN network and the original CPN. As can be seen from Figure 9, AP and AR of the improved CPN network in this paper can reach 72.3 and 78.3, respectively, which are 0.7 and 0.3 higher than that of the original CPN network and are also improved under other thresholds and evaluation indexes of large and medium-sized goals.

Figure 10 is the experimental result of comparison between the network with Cmu-Pose, Mask-Rcnn, G-Rmi, and PersonLab. As can be seen from Figure 10, the performance of the network used in this paper is obviously better than that of the bottom-up method (such as Cmu-Pose) and the newer algorithm PersonLab in positioning accuracy. Compared

TABLE 1: Comparison of network classification error rate before and after improvement.

	Cifar-10	Cifar-100	ImageNet	SVHN
Single-branch network	6.41	27.22	22.85	2.01
Three-branch network	5.38	25.06	21.54	1.77
Ours	5.23	24.33	21.43	1.75

TABLE 2: Comparison of network complexity before and after improvement.

	The elapsed time (s/epoch)	Params (M)	FLOPs (G)
Single-branch network	97.40	25.557	4.136
Three-branch network	152.07	143.593	10.170
Ours	107.49	35.327	4.709

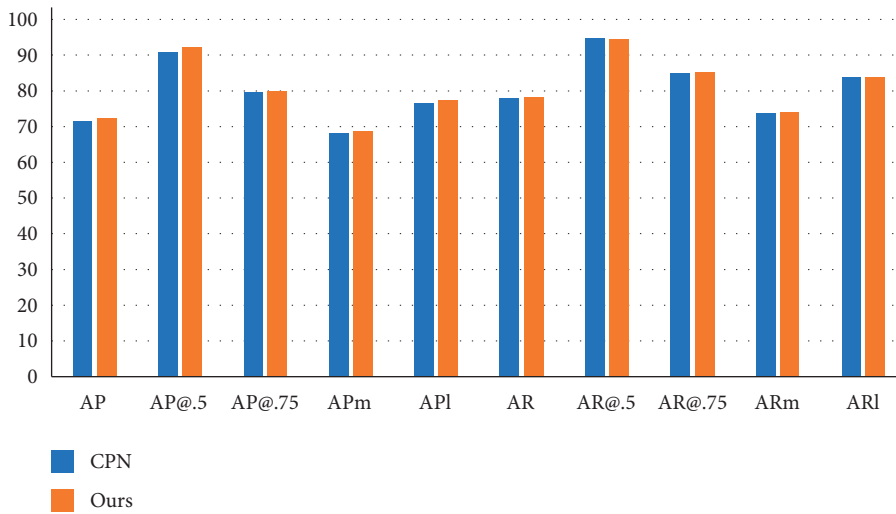


FIGURE 9: Comparison of improved CPN with the original network.

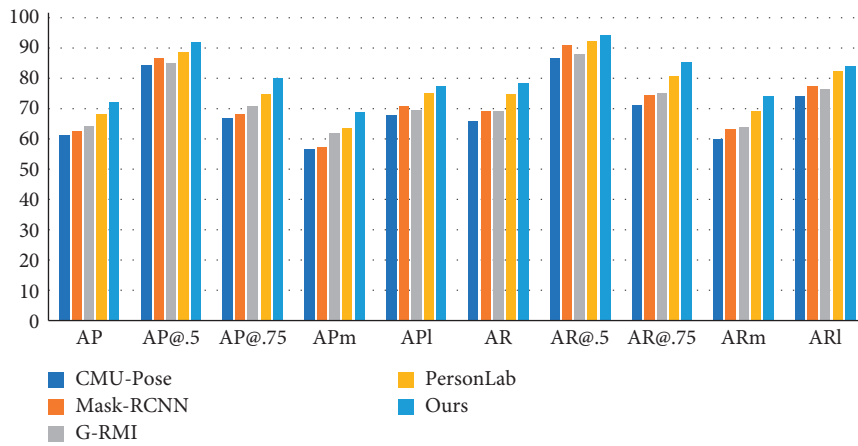


FIGURE 10: Comparison of different algorithms on the COCO dataset.

with the same type of top-down algorithm G-Rmi and Mask-Rcnn, the accuracy of the method in this paper is also improved to some extent.

Figure 11 shows the keypoints detection effect under different scenes. In the figure, the 17 keypoints of the human body are marked with different color points, and the





FIGURE 11: Keypoint detection renderings in different scenes, (a) single person with no occlusion, (b) multiple people with occlusion, (c) small size of multiple people with occlusion, (d) half body without occlusion, (e) multiple people without occlusion, and (f) small size of single person without occlusion.

associated points are connected by color lines in pairs. The results show that the network in this paper can not only perform well in single images such as in Figures 11(a), 11(d), and 11(f) but also get good results in multiple images such as in Figures 11(b), 11(c), and 11(e) with complex interference. Among them, Figures 11(c) and 11(f) are small-size human body pictures, Figures 11(b) and 11(c) are severely blocked, and the keypoints in Figures 11(b)–11(d) are incomplete. In the above cases, the network can detect the keypoints well.

**3.4. Action Recognition Experiment of Fusion Keypoints Information.** In this paper, the human action recognition test experiment was carried out with ResNet-50, which incorporates skeletal keypoints. After 200 rounds ( $6 \times 10^4$  iterations) of training on the Pascal Voc dataset, the network's final accuracy remained around 92%.

We started with the keypoints detection ablation test, with controls for other variables, and compared only the results of the baseline ResNet-50 model with it after the addition of the points. From Figure 12, we can intuitively

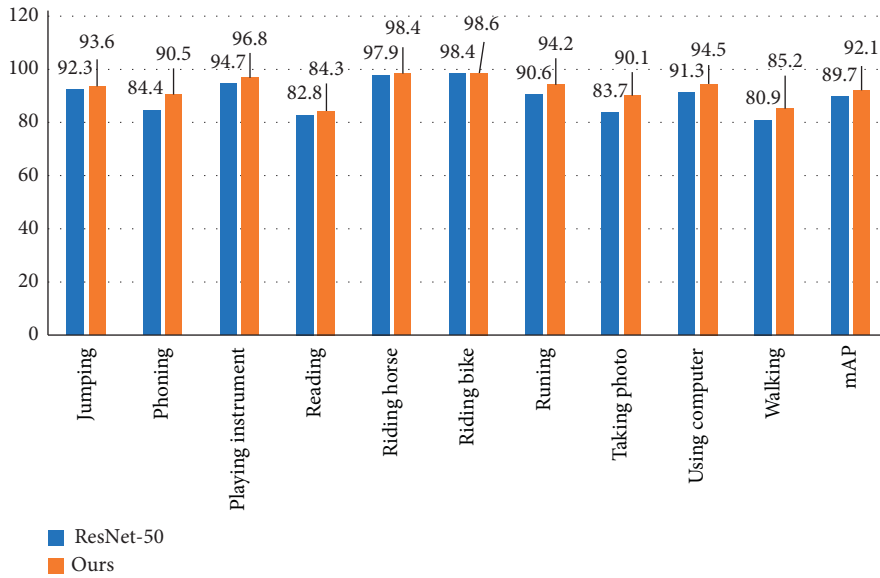


FIGURE 12: Comparison of accuracy between the ResnNet-50 model before and after keypoints were added.

TABLE 3: Comparison of experimental results on different network models.

Method	RCNN	Action mask	R * CNN	Whole and Parts	TDP	Ours
Jumping	91.3	86.7	91.5	84.7	<b>96.4</b>	93.6
Phoning	77.1	72.2	84.4	67.8	84.7	<b>90.5</b>
Playing instrument	91.1	94	93.6	91	96.7	<b>96.8</b>
Reading	76.1	71.3	83.2	66.6	83.3	<b>90.5</b>
Riding horse	96.7	95.4	96.9	96.6	<b>99.4</b>	98.4
Riding bike	96.3	97.6	98.4	97.2	<b>99.2</b>	98.6
Running	92	88.5	93.8	90.2	91.9	<b>94.2</b>
Taking photo	83.8	72.4	85.9	76	85.3	<b>90.1</b>
Using computer	85.9	88.4	92.6	83.4	93.9	<b>94.5</b>
Walking	81.8	65.3	81.8	71.6	84.7	<b>85.2</b>
mAP	87	83.2	90.2	82.6	91.6	<b>92.1</b>

observe that, after the keypoints are added into the model used in this paper, the classification indexes are all increased compared with the previous one. The accuracy of taking photos, phoning, walking, running, and using computer all improved significantly, with increases of 6.4, 6.1, 4.3, 3.6, and 3.2, respectively, and the final mAP (mean average accuracy) was improved by 2.4.

We also compared the model with other networks. The networks selected in the comparison experiment were RCNN [3], Action Mask [1], R \* CNN [4], Whole and Parts [11], and TDP [13], respectively. Table 3 shows the comparison results of these five models with the algorithm in this paper. It can be seen from the table that the method proposed in this paper achieves a maximum value of 92.1 on the final mAP. In addition, the algorithm obtained the highest score of 7 of the 10 categories. The seven categories are phoning, playing instrument, reading, running, taking

photo, using computer, and walking. This shows that although the algorithm in this paper does not use additional data and tricks, it still achieves a competitive result. This can prove the effectiveness of the proposed method.

The final human action recognition experiment results of the network in different scenarios in this paper are shown in Figure 13. In order to facilitate visualization, we marked the people in the picture with the human body detection bounding box in dataset when the picture was generated and finally added the predicted result category to the picture. There are different body movements, different background light, and blocked and incomplete characters in the picture. For example, in Figure 13(d), the human body is incomplete, in Figures 13(b) and 13(c), the human body is blocked, and Figure 13(e) shows the situation of multiple people. The network has achieved good recognition results in these pictures.



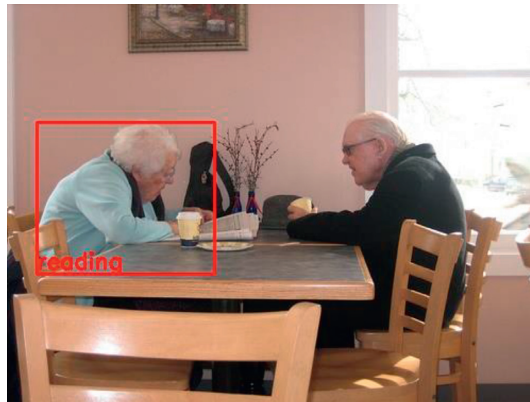
(a)



(b)



(c)



(d)



(e)

FIGURE 13: Experimental results of human action recognition under different conditions, (a) running, (b) riding bike, (c) playing instrument, (d) reading, and (e) jumping.



## 4. Conclusions

To solve the problem that the accuracy of single image is not high in human action recognition, we propose a single-image human action recognition method based on improved ResNet and skeletal keypoints. In this method, ResNet-50 was used as the main classification network, in which CPN was integrated to assist. The whole network is multitask structured. On this basis, the backbone ResNet-50 and branch CPN networks are modified to improve the recognition accuracy without increasing the overall network parameters. Experiments show that the method has better performance and higher accuracy than ResNet-50 network and other single-image human action recognition networks. The following research can start from the aspect of systematization network model, so that the network can be integrated into an end-to-end model to better embed multiple device platforms.

## Data Availability

Previously reported Pascal Voc image data were used to support this study and are available at 10.1007/s11263-009-0275-4. These prior studies (and datasets) are cited at relevant places within the text as [18]. Previously reported MS COCO image data were used to support this study and are available at 10.1007/978-3-319-10602-1\_48. These prior studies (and datasets) are cited at relevant places within the text as references [24].

## Conflicts of Interest

The authors declare that there are no conflicts of interest regarding the publication of this paper.

## Acknowledgments

The research was supported by the following projects: Scientific Research Project of National Language Commission (YB135-125); Key Research and Development Project of Shandong Province (2019GGX101008 and 2016GGX105013); Natural Science Foundation of Shandong Province (ZR2017MF048); and Science and Technology Plan for Colleges and Universities of Shandong Province (J17KA214).

## References

- [1] Y. Zhang, L. Cheng, J. Wu, J. Cai, M. N. Do, and J. Lu, "Action recognition in still images with minimum annotation efforts," *IEEE Transactions on Image Processing*, vol. 25, no. 11, pp. 5479–5490, 2016.
- [2] M. Xin, H. Zhang, D. Yuan et al., "Learning discriminative action and context representations for action recognition in still images," in *Proceedings of the IEEE International Conference on Multimedia & Expo (ICME 2017)*, Jul 2017.
- [3] R. Girshick, J. Donahue, T. Darrell, and J. Malik, "Rich feature hierarchies for accurate object detection and semantic segmentation," in *Proceedings of the Computer Vision and Pattern Recognition*, pp. 580–587, Columbus, OH, USA, Jun 2014.
- [4] G. Gkioxari, R. Girshick, and J. Malik, "Contextual action recognition with R\*CNN," *International Journal of Cancer*, vol. 40, no. 1, pp. 1080–1088, 2015.
- [5] X. Zhang, H. Xiong, W. Zhou, and Q. Tian, "Fused one-vs-all features with semantic alignments for fine-grained visual categorization," *IEEE Transactions on Image Processing*, vol. 25, no. 2, pp. 878–892, 2016.
- [6] S. Wang, J. Na, and Y. Xing, "Adaptive optimal parameter estimation and control of servo mechanisms: theory and experiments," *IEEE Transactions on Industrial Electronics*, vol. 39, p. 1, 2020.
- [7] G. Ponsmoll, D. J. Fleet, and B. Rosenhahn, "Posebits for monocular human pose estimation," in *Proceedings of the Computer Vision and Pattern Recognition*, pp. 2345–2352, Columbus, OH, USA, Jun 2014.
- [8] S. Wei, V. Ramakrishna, T. Kanade, and Y. Sheikh, "Convolutional pose machines," in *Proceedings of the Computer vision and pattern recognition*, pp. 4724–4732, Las Vegas, NV, USA, Jul 2016.
- [9] A. Diba, A. M. Pazandeh, H. Pirsiavash et al., "DeepCAMP: deep convolutional action & attribute mid-level patterns," in *Proceedings of the Computer Vision and Pattern Recognition*, pp. 3557–3565, Las Vegas, NV, USA, Jul 2016.
- [10] Z. Zhao, H. Ma, S. You et al., "Single image action recognition using semantic body part actions," in *Proceedings of the IEEE International Conference on Computer Vision*, pp. 3411–3419, Venice, Italy, Oct 2017.
- [11] G. Gkioxari, R. Girshick, J. Malik et al., "Actions and attributes from wholes and parts," in *Proceedings of the IEEE International Conference on Computer Vision*, pp. 2470–2478, Las Condes, MN, USA, Dec 2015.
- [12] A. Gupta, A. Kembhavi, and L. S. Davis, "Observing human-object interactions: using spatial and functional compatibility for recognition," *IEEE Transactions on Pattern Analysis and Machine Intelligence*, vol. 31, no. 10, pp. 1775–1789, 2009.
- [13] Z. Zhao, H. Ma, and X. Chen, "Semantic parts based top-down pyramid for action recognition," *Pattern Recognition Letters*, vol. 84, pp. 134–141, 2016.
- [14] K. He, X. Zhang, S. Ren, and J. Sun, "Deep residual learning for image recognition," in *Proceedings of the IEEE Computer Vision and Pattern Recognition*, pp. 770–778, Las Vegas, NV, USA, Jun 2016.
- [15] Y. Chen, Z. Wang, Y. Peng, Z. Zhang, G. Yu, and J. Sun, "Cascaded pyramid network for multi-person pose estimation," in *Proceedings of the IEEE Conference on Computer Vision and Pattern Recognition*, pp. 7103–7112, Salt Lake UT, USA, Jun 2018.
- [16] S. Woo, J. Park, J.-Y. Lee, and I. S. Kweon, "CBAM: convolutional block attention module," in *Computer Vision-ECCV 2018*, pp. 3–19, Springer, Munich, Germany, 2018.
- [17] Y. Li, Y. Chen, N. Wang, and Z.-X. Zhang, "Scale-aware trident networks for object detection," in *Proceedings of the IEEE International Conference on Computer Vision*, pp. 6054–6063, Seoul, South Korea, Oct 2019.
- [18] M. Everingham and J. Winn, "The PASCAL visual object classes challenge 2012 (VOC2012) development kit pattern analysis, statistical modelling and computational learning," Pascal Press, Sydney, Australia, Tech. Rep, 2011.
- [19] F. Yu, V. Koltun, and T. Funkhouser, "Dilated residual networks," in *Proceedings of the IEEE Conference on Computer Vision and Pattern Recognition*, pp. 472–480, Honolulu, HI, USA, Jul 2017.
- [20] T. Y. Lin, M. Maire, S. Belongie et al., "Microsoft coco: common objects in context," in *Proceedings of the European Conference on Computer Vision*, pp. 740–755, Zurich, Switzerland, Sep 2014.

- [21] Z. Cao, T. Simon, S. Wei et al., "Realtime multi-person 2D pose estimation using part affinity fields," in *Proceedings of the Computer Vision and Pattern Recognition*, pp. 1302–1310, Honolulu, HI, USA, Jul 2017.
- [22] G. Papandreou, T. Zhu, N. Kanazawa et al., "Towards accurate multi-person pose estimation in the wild," in *Proceedings of the Computer Vision and Pattern Recognition*, pp. 3711–3719, Honolulu, HI, USA, Jul 2017.
- [23] G. Papandreou, T. Zhu, L.-C. Chen, S. Gidaris, J. Tompson, and K. Murphy, "PersonLab: person pose estimation and instance segmentation with a bottom-up, part-based, geometric embedding model," in *Computer Vision-ECCV 2018*, pp. 282–299, Springer,, Munich, Germany, 2018.
- [24] Y. Lin, G. Wang, X. Liu, and Di Fan, "Research on human keypoint detection algorithm based on improved CPN," *Modern Computer*, vol. 26, no. 12, pp. 86–92, 2020.

## Research Article

# A Person Reidentification Algorithm Based on Improved Siamese Network and Hard Sample

Guangcai Wang <sup>1</sup>, Shiqi Wang <sup>1</sup>, Wanda Chi <sup>1</sup>, Shicai Liu <sup>2</sup>, and Di Fan <sup>1</sup>

<sup>1</sup>College of Electronic and Information Engineering, Shandong University of Science and Technology, Qingdao 266590, China

<sup>2</sup>College of Intelligent Equipment, Shandong University of Science and Technology, Tai'an 271000, China

Correspondence should be addressed to Di Fan; [skd992372@sdust.edu.cn](mailto:skd992372@sdust.edu.cn)

Received 29 April 2020; Accepted 2 June 2020; Published 24 June 2020

Guest Editor: Weicun Zhang

Copyright © 2020 Guangcai Wang et al. This is an open access article distributed under the Creative Commons Attribution License, which permits unrestricted use, distribution, and reproduction in any medium, provided the original work is properly cited.

Person reidentification is aimed at solving the problem of matching and identifying people under the scene of cross cameras. However, due to the complicated changes of different surveillance scenes, the error rate of person reidentification exists greatly. In order to solve this problem and improve the accuracy of person reidentification, a new method is proposed, which is integrated by attention mechanism, hard sample acceleration, and similarity optimization. First, the bilinear channel fusion attention mechanism is introduced to improve the bottleneck of ResNet50 and fine-grained information in the way of multireceptive field feature channel fusion is fully learnt, which enhances the robustness of pedestrian features. Meanwhile, a hard sample selection mechanism is designed on the basis of the P2G optimization model, which can simplify and accelerate picking out hard samples. The hard samples are used as the objects of similarity optimization to realize the compression of the model and the enhancement of the generalization ability. Finally, a local and global feature similarity fusion module is designed, in which the weights of each part are learned through the training process, and the importance of key parts is automatically perceived. Experimental results on Market-1501 and CUHK03 datasets show that, compared with existing methods, the algorithm in this paper can effectively improve the accuracy of person reidentification.

## 1. Introduction

As an important intelligent video analysis technology, person reidentification is widely used in the fields of intelligent security, case detection, lost query, intelligent interaction, and so on. It is an important means in the field of public safety. However, the huge difference in lighting, occlusion, resolution, background, and human posture, in the actual scene, and the deficiency of data make person reidentification task still face many difficulties and challenges.

Feature learning method and metric learning method are two basic directions in the research of person reidentification task. The method of feature representation mainly focuses on how to extract robust person features, such as the Ensemble of Localized Features [1], like colour and texture features, SDALF (Symmetry-Driven Accumulation of Local Features) [2], the Local Maximal Occurrence (LOMO)

representation [3], and the fusion net of CNN features and manual features (FFN) [4]. The weighted histogram feature of middle dense and significant blocks is based on the Gauss mixture model [5]. Using the information continuity between image blocks, we design the attention mechanism to optimize the image similarity of blocks after the PCB network [6]. However, only relying on image feature expression cannot completely solve this task. Many scholars have done a lot of research in image feature measurement. KISSME algorithm [7] measures the degree of difference between samples by likelihood ratio and obtains the Mahalanobis metric, which reflects the log-likelihood ratio property. Based on the Siamese Network, using contrastive loss [8–11] and verification loss, like Triplet loss [12–16] and Quadruplet loss [17], makes the distance between the same ID persons closer and that between those with different ID farther. Some rerank methods, like SSM (Supervised Smoothed Manifold)

[18],  $k$ -reciprocal neighbours [19] and UED (the Unified Ensemble Diffusion) [20], were used to achieve more accurate person reidentification.

Aiming at extracting more robust feature for person images, based on the Siamese Network, we improve the convolution settings on the ResNet50, integrate multiscale visual field features, and design the attention mechanism of channel fusion to enhance the expression of fine-grained feature information in the image. At the same time, unlike the existing feature measurement and rerank algorithms, based on the P2G similarity optimization model [21], a hard sample selection mechanism is set up, which uses the hard samples to optimize the P2G similarity to enhance the learning and generalization ability of the model. In addition, in order to make full use of the detailed information of the image features, while avoiding the cumbersome process of local feature extraction, the features are grouped in the way of horizontal overlap, and the similarity between query image and gallery image for each group was calculated, respectively. We integrate all groups of similarities and global similarity to realize automatically perceiving of the key parts, so as to get more accurate similarity measurement results. Experiments on Market-1501 and CUHK03 datasets show that the proposed model can extract person features completely and achieve higher recognition accuracy.

## 2. Materials and Methods

In this paper, a complete person reidentification model is constructed, in which the improved ResNet50 is the backbone to extract person image features. Based on the P2G similarity optimization model, the hard sample mining and feature grouping and similarities fusion module are introduced to improve the accuracy of person reidentification model. The whole model can be divided into three modules: feature extraction module, hard sample mining module, and feature group and similarities optimization fusion module. Finally, by sorting the similarity scores, we get the retrieval results of the probe in all gallery images. The overall framework of the algorithm is shown in Figure 1.

The feature extraction module adopts the improved ResNet50 as the backbone and designs a bilinear feature channel fusion module to extract more robust features. The hard sample mining module is based on the calculated initial feature distance  $d(p, g)$  and selects the most difficult positive samples and negative samples for each probe image as the similarity update examples. On the one hand, it can improve the generalization ability of the network; on the other hand, it can also reduce data redundancy and the computational pressure. The feature grouping module divides the features of the images into 3 groups in the way of horizontal overlap grouping, and each group of features is used to calculate and optimize the local similarity score separately to enhance the impact of detail information on similarity measurement. Finally, combined with global feature similarity, we could obtain a more accurate similarity.

**2.1. Improved ResNet Module.** For normal convolution, convolution kernels in convolution operations can be regarded as a three-dimensional filter, containing channel

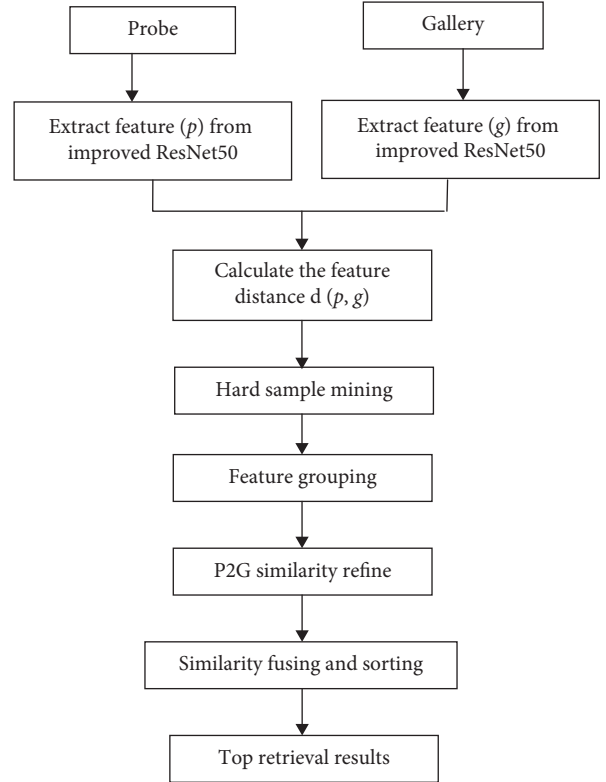


FIGURE 1: The overall framework flow of the algorithm.

dimensions and spatial dimensions (the width and height of feature map), thereby realizing joint mapping of channel correlation and spatial correlation. Convolution neural network reduces parameters in training process through receptive field and weight sharing. However, as the number of network layers increases, the amount of parameters also increases, thus increasing the amount of computation training process and the resource cost.

Depthwise separable convolution, using different convolution kernels for different input channels, decomposes the normal convolution into two processes: depthwise convolution (DW) and pointwise convolution (PW). The channel correlation and spatial correlation in convolution layer are separately mapped to realize the decoupling of the two. The depthwise convolution groups features in the channel dimension, and the number of groups is the number of characteristic channels. Compared with normal convolution, the number of convolution kernel parameters and the amount of computation in convolution process are reduced to a great extent, thus reducing the pressure of network computing resources.

Based on the idea of depthwise separable convolution, we improved the residual bottleneck module in the ResNet50 network. First, we extract the channel features and then replace the normal convolution (Conv  $3 \times 3$ ) in the original bottleneck by depthwise convolution (DW  $3 \times 3$ ) to learn spatial information. Then we use pointwise convolution (PW  $1 \times 1$ ) to realize the fusion of channel features. The improved bottleneck block network structure is shown in Figure 2.



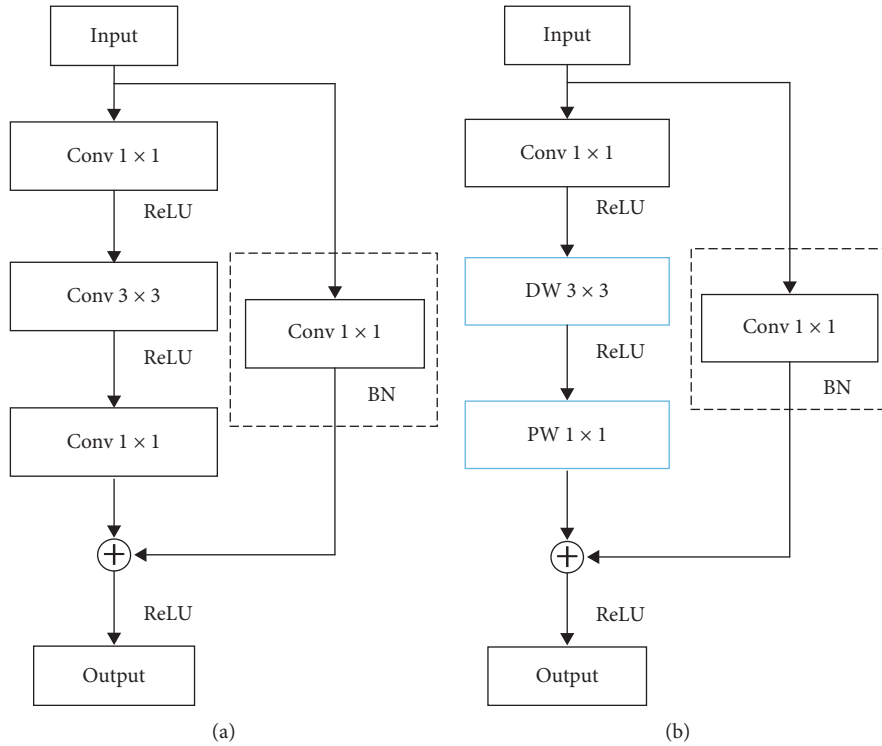


FIGURE 2: Bottleneck improvement: (a) original bottleneck; (b) improved bottleneck.

The improvement of the bottleneck block realizes the separation of channel features and spatial features, weakens the coupling between channel features and spatial features, and makes the network learn the features of different dimensions more distinguishably. At the same time, independent learning channel features and spatial features strengthen the connection between the spatial structures on the feature map and also make the correlation between different channel features more differentiated. With the deepening of the network, the spatial feature size of the image is getting smaller and smaller, and the number of channels is increasing. We apply the improved bottleneck block to the final stage of the ResNet50 network, without reducing the network’s ability to extract features, to minimize the network computing overhead and parameter storage pressure.

Because different channels of image features often contain different attributes or different degrees of expression of the same attribute, the simple addition of features does not make full use of the information of image, and it will waste or even lose the image information to some extent. Bilinear models calculate the outer product of different spatial positions. Moreover, the average convergence of features at different spatial locations has a good effect in learning fine-grained image representation. The outer product captures the pairwise correlation between feature channels and has the characteristic of translation invariance.

A bilinear channel fusion attention mechanism is designed on the basis of the ResNet residual structure with deep separable convolution. On the one hand, interactive model for local pairwise features is carried out, and bilinear expressions are applied in convolution neural networks in depth to learn fine-grained image features (such as clothing texture, hairstyle, and movement of persons). On the other hand, the channel information is broken through, and the attention of different channels is strengthened by means of channel attention. The bilinear channel fusion attention module structure is shown in Figure 3.

In Figure 3, the input feature connects the channel information through a normal convolution (Conv  $1 \times 1$ ) to get the initial feature  $I \in R^{C \times H \times W}$ . We divide the initial feature  $I$  into three branches to deal with it separately, and each branch sets different receptive fields and convolution methods, respectively. For Branch 1, the initial feature goes through a layer of depthwise convolution (DW  $3 \times 3$ ) to get feature  $X_1 \in R^{C \times H \times W}$ . For Branch 2, it expands the receptive field of the initial feature through the two layers of depthwise convolution (DW  $3 \times 3$ ), which is equivalent to the spatial information that incorporates the scope of the size of  $5 \times 5$  and gets the feature  $X_2 \in R^{C \times H \times W}$ . Branch 3 is the original feature  $I$  without any processing. Then we vectorize the feature  $I$ , as well as each channel of feature  $X_1$  and feature  $X_2$ , where  $N = H \times W$ :

$$\begin{aligned}
I &\in \mathbb{R}^{C \times H \times W} \xrightarrow{\text{vectorization}} I_1 \in \mathbb{R}^{C \times N}, \\
X_1 &\in \mathbb{R}^{C \times H \times W} \xrightarrow{\text{vectorization}} F1 \in \mathbb{R}^{C \times N}, \\
X_2 &\in \mathbb{R}^{C \times H \times W} \xrightarrow{\text{vectorization}} F2 \in \mathbb{R}^{C \times N}.
\end{aligned} \tag{1}$$

After that, for each location  $l$  of the input feature  $I$ , we have designed the bilinear model shown in the following equation:

$$\text{bilinear}(l, I, f_1, f_2) = f_1(l, I)^T f_2(l, I). \tag{2}$$

In the previous equation,  $f_1$  and  $f_2$  are the feature mapping functions, and the initial features  $I$  are mapped to  $F1, F2 \in \mathbb{R}^{C \times N}$ , respectively. In this way, bilinear models are used to make full use of the fine-grain information under different receptive fields. We define the bilinear fusion based on the two branch features as

$$B = F1 \cdot F2^T, \tag{3}$$

where  $B \in \mathbb{R}^{C \times C}$  and  $B_{ij} = \sum_{k=1}^N F1_{ik} \cdot F2_{jk}$ . The bilinear image feature  $B$  integrates the details of person images between different channels, so we generate a set of channel attention  $M \in \mathbb{R}^{C \times C}$  through the Softmax layer after the bilinear model:

$$M_{i,j} = \frac{\exp(B_{ij})}{\sum_{i=1}^C \exp(B_{ij})}. \tag{4}$$

$M_{i,j}$  represents the influence of channel  $j$  on channel  $i$ . Therefore, attention  $M$  can be regarded as a summary of the interchannel dependency and the local feature strength of a given feature graph. In order to achieve the effect of attention mapping on the original features, we will pay attention to the transposition of the torque matrix  $M$  to the original features  $I_1$ . The results are reshaped into three-dimensional space with the same shape as input tensor to get the output features  $D \in \mathbb{R}^{C \times H \times W}$ :

$$\begin{aligned}
D_1 &= M^T \cdot I_1, \\
D_1 &\in \mathbb{R}^{C \times N} \xrightarrow{\text{reshape}} D \in \mathbb{R}^{C \times H \times W}.
\end{aligned} \tag{5}$$

Finally, the pointwise convolution (PW  $1 \times 1$ ) is used to fuse the image features of the channel attention information to form a complete bottleneck module.

**2.2. Hard Sample Selection Mechanism.** The selection of training samples by traditional recognition methods mostly put all the positive and negative samples of batch into training. Although the number of samples is large, it is difficult to avoid the fact that the sample is too simple, which is of little significance to model training and waste of computing resources. For example, through continuous person images, we could get similar or even identical sample images. However, due to the large difference of clothing, shape, or background in some person images, the negative samples are relatively simple. The model can easily

distinguish person differences. Therefore, a large number of simple samples will waste a lot of time and computing resources in the later stage of the model.

To solve this problem, a simple hard sample mining module is designed to extract hard samples from all the samples into the initial P2G similarity optimization module [21], so as to enhance the ability of network learning complex samples, thereby improving the generalization ability of the model. As shown in Figure 4, the same colour features represent the same person ID, while different colour features represent different person IDs.

In order to optimize the network training stage, the ID of the image is applied as a known parameter to the training stage, in the hard sample mining module, to ensure that the network can effectively learn the accurate feature expression from the hard sample image pair. In the training stage, each batch has  $n$  different person IDs, and each person ID has  $K$  different pictures; that is, each batch contains  $n \times K$  images. Suppose that every ID selects a picture as the probe; then the whole group of images is input into the improved Siamese Network module, and the image features are extracted and the similarities between each probe and other images (Gallery) are calculated, so as to get the initial P2G similarity score vector. According to the initial similarity score, we can select the difficult samples in the whole group of pictures for each probe picture. We take the samples with lower similarity scores under the same ID as hard positive samples and the samples with higher scores under different IDs as the difficult negative samples. Next, the hard positive samples and the hard negative samples are used as the input of the P2G similarity update module.

We set the hard sample mining module before the P2G similarity optimization module, which is equivalent to a mask for the initial similarity matrix  $S$ , making the similarity information of the simple samples inactive automatically, and the hard samples as the input of the similarity update module. In this way, the similarity information of hard samples is used to optimize the initial P2G similarity, so as to fully exploit the correlation between difficult samples under limited computing resources.

### 2.3. P2G Similarity Optimization and Feature Fusion.

Due to the fact that the local part of person image contains rich person details, common person reidentification methods based on local images (such as key points detection, image segmentation, person attributes, etc.) require expensive semantic component learning process. In the form of feature partitioning, we design a local and global feature similarity fusion module to make full use of the detailed information of the image features, while avoiding the cumbersome process of local feature extraction, which also realizes the automatic perception of the characteristics of effective parts [22].

We adjust the input image to a size of  $256 \times 128$ , so after the ResNet50 network, the output of the last layer is  $16 \times 8 \times 2048$ . Feature grouping module is set at the last layer of the network output. The output feature is grouped in the

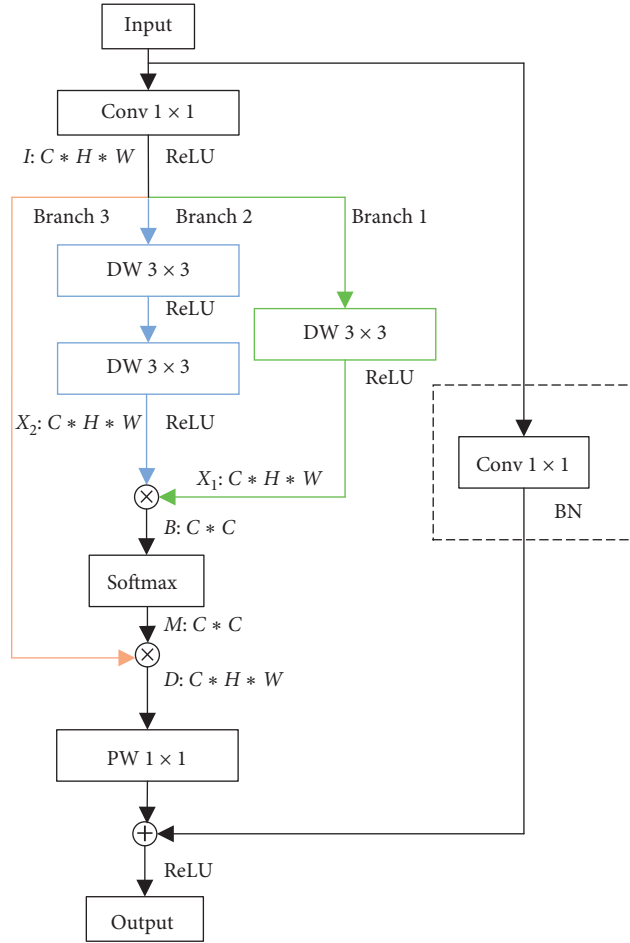


FIGURE 3: Bilinear channel fusion attention module.

way of horizontal overlap into the 3 upper, middle, and lower groups of size of  $8 \times 8 \times 2048$ . The principle of feature grouping is shown in Figure 5.

After grouping, each feature is calculated separately by local feature distance, and the local similarity score is obtained at the same time, and the local similarity is updated by the similarity optimization module [21]. Adding to the global similarity estimation, we get 4 sets of similarity scores. However, the 3 sets of local similarities make full use of local detail feature information, expressing the local correlation between images and showing the similarity is based on fine-grained image and locality. The global similarity grasps the overall style and characteristics of the image. It has a complete expression to the similarity relation of the person's overall contour and attributes. Each group of similarity has its own advantages, but it cannot fully express the correlation between images. After obtaining the similarity measure results, we integrate the local and global similarity to get the complete similarity measure results. The similarity module and the global similarity module are shown in Figure 6.

In the similarity fusion module, the 4 groups of P2G similarity scores are first spliced into a set of similarity score vectors through flatten and concat. Then they are input to the fully connected layer. The FC layer takes all the similarity scores extracted from the previous layer as input features

and maps them to a new dimension vector as the output value in the fully connected mode. The result of similarity measurement after fusion is obtained.

The FC layer cannot only map the learned distributed feature representation to the corresponding space in the network but also realize the learning of distributed feature weights through the training process. In forward propagation, a fusion map of similarity scores is achieved through a fully connected layer. When being back-propagated, the weights of different local feature similarity and global feature similarity are automatically adjusted through training, so as to realize automatic perception of local details and global information of the image. After multiple iterations of network training, the P2G similarity is gradually refined, and the accuracy of pedestrian reidentification ranking results has been correspondingly improved.

### 3. Experiment and Test

**3.1. P2G Similarity Update Algorithm.** In this paper, Market-1501 and CUHK03 datasets are used to carry out experimental and comparative analysis of two datasets with larger data volume.

The Market-1501 dataset was collected in real time on the campus of Tsinghua University in the summer of 2015. The

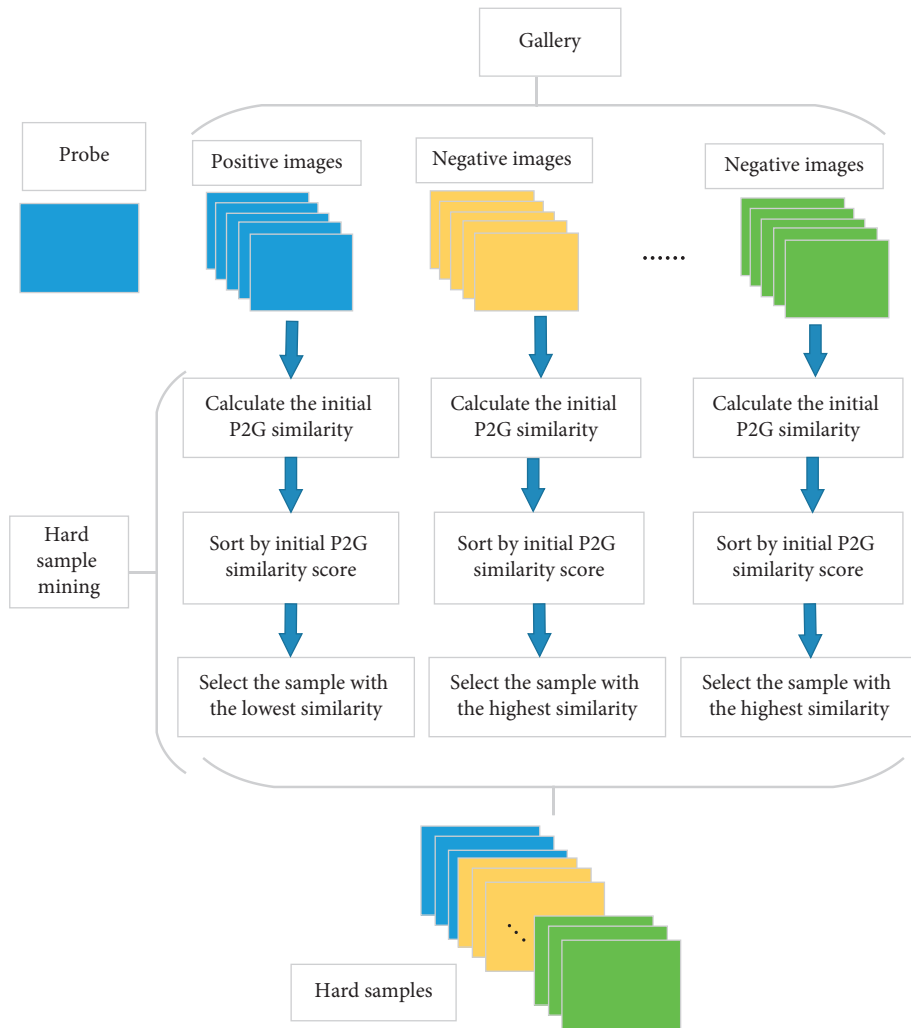


FIGURE 4: The diagram of hard sample mining module.

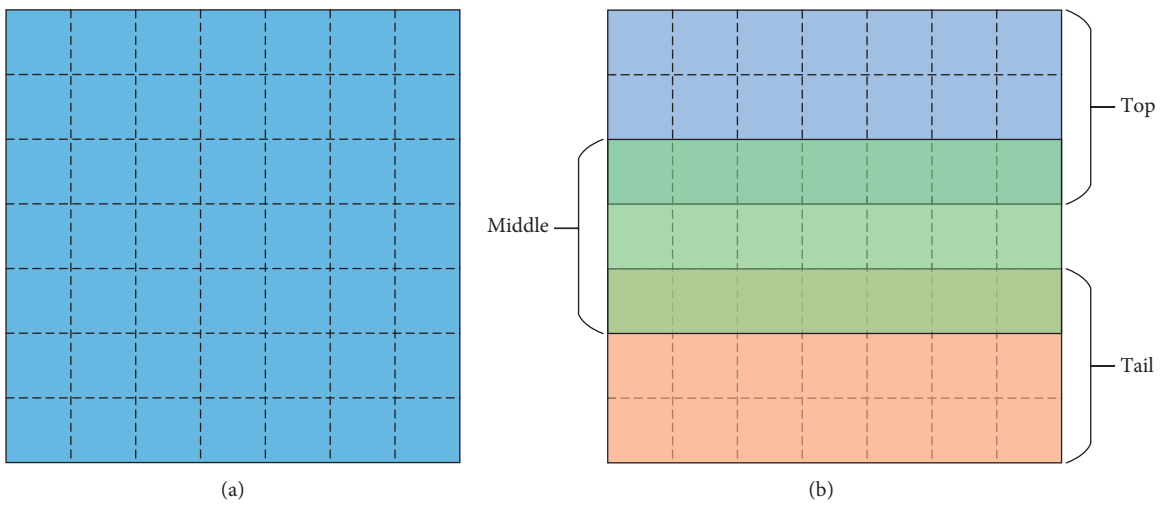


FIGURE 5: (a) Original feature; (b) features grouped in the way of horizontal overlap.

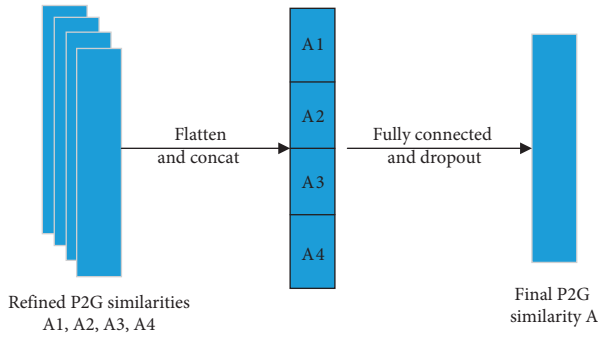


FIGURE 6: Local and global feature similarity fusion module.

person images came from 6 different cameras, including 32668 pictures containing 1501 ID persons. We divide the 1501 persons into two groups: training set and test set: the training set contains 751 people and 12936 pictures, and the test set contains 19732 pictures of 750 people.

The CUHK03 dataset was collected on the campus of Chinese University of Hong Kong. The images came from 10 different cameras. There are 14097 images of 1467 persons, with an average of 9.6 training pictures per person. The dataset is divided into two groups, of which 767 are training sets and 700 are test sets. At the same time, the dataset also provides two-person-marking information detected by manual annotation and DPM detector.

In this paper, we use the cumulative matching characteristic (CMC) curve and the mean Average Precision (mAP) to evaluate the performance of two models.

Among them, the cumulative matching characteristic (CMC) curve takes Rank- $n$  as the abscissa and Rank- $n$  matching result accuracy rate as the ordinate. Rank- $n$  represents, according to P2G similarity score, the ratio of the number of the correct matching probes to the number of all the probes, that is, the front  $n$  hit rate. In the CMC curve, we often use three sets of results of Rank-1, Rank-5, and Rank-10 to visualize the effect of the model.

In this paper, we propose a person reidentification model experiment using RTX 2070 graphics acceleration calculation. Under the Anaconda development environment, we implement it based on PyTorch open source framework and Python programming. Before model training, we pretrained the ResNet50 parameters on the ImageNet dataset. In order to improve the expressive power and generalization ability of the model, we set up the data preprocess before training the model. We used random erasure, random horizontal flipping, and data standardization to preprocess the image. The size of the image was adjusted to  $256 \times 128$ , with the mean [0.485, 0.456, 0.406] and variance [0.229, 0.224, 0.225] normalizing the RGB three-channel image as the input of the network.

There are two key elements in the person reidentification model: (1) Improve the ResNet50 based Siamese Network to extract robust person features, so as to improve the efficiency of similarity measurement, to achieve the purpose of improving the accuracy of reidentification. (2) Use the hard sample mining and similarity optimization fusion module to refine the initial similarity results and achieve the

optimization of similarity ranking results. In the experiment, we not only integrate two key elements into the whole model training to verify the overall effect of the model but also conduct ablation experiments on two modules to observe the effectiveness of each independent part.

**3.2. Improving the Siamese Network Module Experiment and Result Analysis.** In order to verify the effectiveness of the improvement in Siamese Network, we extract the person features based on the improved network structure. Then Euclidean distance is used to measure the similarity between the probe and the gallery, and the image in the gallery is sorted according to the similarity scores. In addition to the contrast experiment, based on the original ResNet50 and the improved ResNet50, we also carried out ablation experiments on two kinds of training methods, namely, the contrastive loss based on the Euclidean distance and the classification loss based on cross-entropy. The experimental results of the improved Siamese Network module on Market-1501 are shown in Table 1.

From Table 1, we can see that, in the improved Siamese Network module using Euclidean distance metric, the average accuracy of the model is increased by 1.7 percentage points. Rank-1 is also increased by about 12.74%. After adding the cross-entropy loss, the improved Siamese Network is a backbone network and the first hit rate of Rank-1 is 89.86%. The average accuracy index is also improved to 73.64%. The improved Siamese Network module is used to extract the features. The results are all higher than the Siamese Network model based on the original ResNet50. This indicates that the improved ResNet50 can extract more robust person features when using the simplest similarity measure and classification model and improve the accuracy of person reidentification.

Based on the calculation results of Rank- $n$ , we draw the CMC curve of the person reidentification of two backbones under different training methods, as shown in Figure 7. In the figure, the CMC curve of the improved Siamese Network model is always located above the CMC curve of the original ResNet50, which indicates that the hit rate of person ranking results from the improved model of this paper is always higher than that of the original model.

**3.3. P2G Similarity Optimization Experiment and Result Analysis.** We not only did ablation experiments on every part of the module but also compared the results with other algorithm models to see the effectiveness of P2G similarity optimization module guided by G2G similarity.

“Baseline” in Table 2 refers to the backbone based on the original ResNet50 network. The Euclidean distance is used to measure the initial similarity, and the cross-entropy is used to carry out the classification loss of the network. From Table 2, it can be found that, after the hard sample mining module is added to the model, the average precision mAP increased to 79.15%. After the local feature division and the integration of global and local feature similarity, the mAP index of the model reached 82.5%, and the Rank-1 rate increased to 92.3%.

TABLE 1: Comparison of experimental results before and after the Siamese network improvement.

Network settings	mAP	Rank-1	Rank-5	Rank-10
ResNet50 + Euclidean	40.54	60.12	78.02	85.34
Improved ResNet50 + Euclidean	42.30	72.86	87.41	90.68
ResNet50 + Euclidean + cross-entropy	71.59	88.74	95.22	96.97
Improved ResNet50 + Euclidean + cross-entropy	73.64	89.86	96.74	98.21

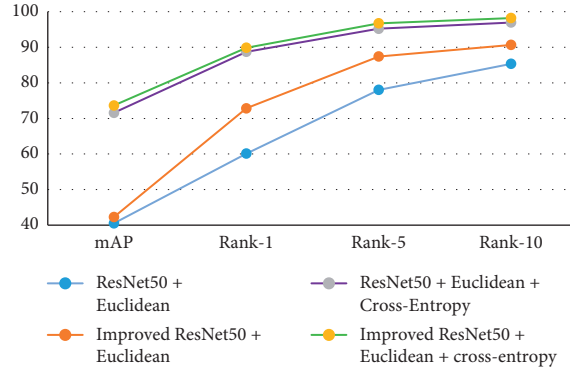


FIGURE 7: The CMC curves of different trunk network models.

TABLE 2: Comparison of ablation experimental results of similarity optimization module.

Network setting	mAP	Rank-1	Rank-5	Rank-10
Baseline + P2G optimization	78.28	89.97	96.35	97.62
Baseline + P2G optimization + hard sample mining	79.15	90.73	96.92	98.04
Baseline + P2G optimization + hard sample mining + feature fusion	82.5	92.3	97.1	98.3

In Figure 8, we draw the CMC curve of the model under different conditions. After introducing the hard sample selection mechanism and the global and local similarity design, the hit rate of the model is further improved. The CMC curve of the improved model is obviously higher than that of the basic mode curve.

### 3.4. Overall Model Training and Experimental Result Analysis.

In addition, we have integrated the design of the model and took the improved ResNet50 as the backbone. Based on the P2G optimization model, the hard sample mining mechanism is introduced, and feature groups and similarity fusion modules are implemented to achieve the accuracy of person image similarity. The performance of the overall model is compared with the existing models on the Market-1501 dataset and the CUHK03 dataset. The results are shown in Tables 3 and 4.

From the experimental results on the Market-1501 dataset, we can see that, compared with the LSTM network that integrates the Long Short-Term Memory into the Siamese Network and the TriHard algorithm, this model has a great advantage in mAP and Rank-1 accuracy. It is also in common with the model Spindle based on human image segmentation and component alignment. Compared with Spindle Net, AlignedReID, and GLAD models, this method has a significant improvement in average precision and Rank- $n$  rate. Compared with the current popular reranking methods,  $K$ -reciprocal and PSE + ECN, although the average

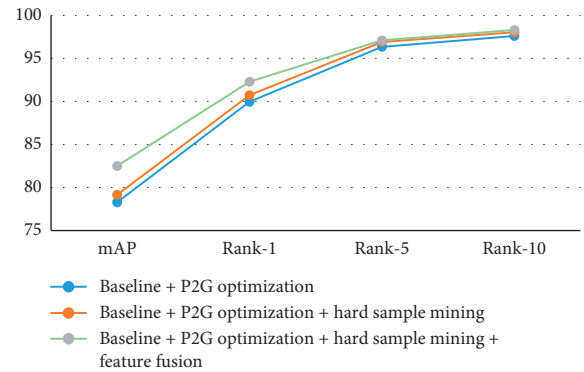


FIGURE 8: The CMC curves of similarity optimization module.

TABLE 3: Experimental results of different models on the Market-1501 dataset.

Method	mAP	Rank-1	Rank-5	Rank-10
LSTM	35.3	61.6	—	—
Spindle Net	—	76.9	91.5	94.6
TriHard	69.1	84.9	94.2	—
GLAD	73.9	89.9	—	—
$K$ -reciprocal	63.6	77.1	—	—
AlignedReID	79.3	91.8	—	—
PSE + ECN	84.0	90.3	—	—
Ours	82.7	92.5	97.8	98.6

“—” indicates that the index data are not given in the original paper of the method.



TABLE 4: Experimental results of different models on the CUHK03 dataset.

Method	mAP	Rank-1	Rank-5	Rank-10
LSTM	—	57.3	80.1	88.3
Spindle Net	—	88.5	97.8	98.6
Quadruplet	—	75.5	95.2	99.2
GLAD	—	82.2	95.8	97.6
$K$ -reciprocal	67.6	61.6	—	—
AlignedReID	—	92.4	98.9	99.5
SVDNet	84.8	81.8	95.2	97.2
Ours	92.0	94.3	98.7	99.3

“—” indicates that the index data are not given in the original paper of the method.

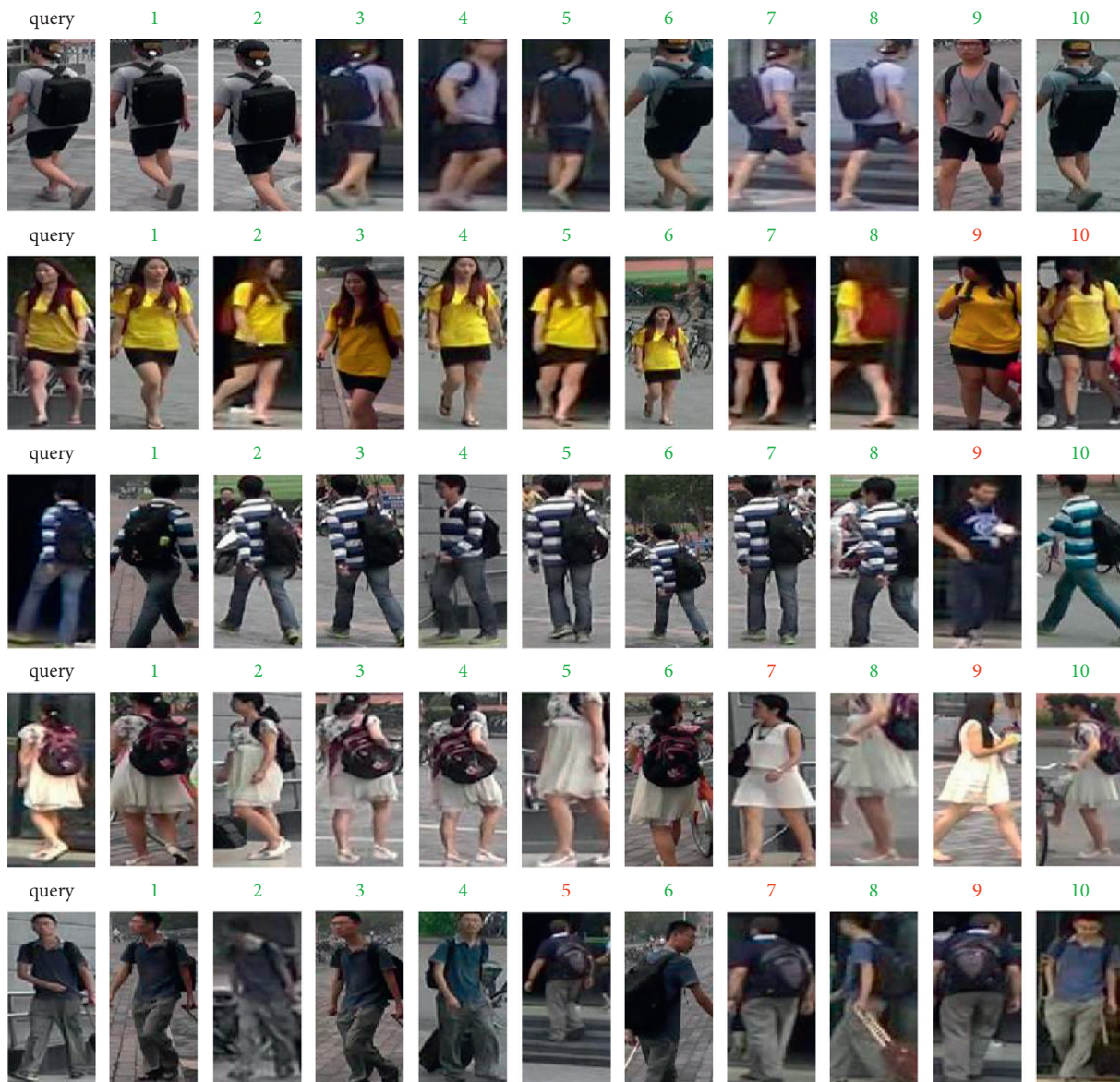


FIGURE 9: The result of the overall model.

precision index is slightly lower than the PSE + ECN method, the Rank-1 rate is significantly higher than the two.

From the experimental results in Table 4, we can find that, compared with the current popular algorithm models,

the average precision mAP of this model on the CUHK03 dataset is excellent, and the accuracy of Rank- $n$  is also good. Combined with the experimental results of Table 3, it is found that this method achieves high accuracy on two



common large-scale datasets of Market-1501 and CUHK03. It is shown that the model proposed in this paper has stronger recognition ability in person reidentification tasks.

Figure 9 is a person reidentification test result on the Market-1501 dataset. The first column is the query image, and the right side is the result of re-recognition for persons. According to the similarity score with the query image, we sequentially sort the retrieval results from high to low. The sorting of correct query result, that is, the same ID with query image, is marked in green and in red otherwise.

#### 4. Conclusions

In view of the large difference of person under different visual fields, in order to fully extract effective person details information and to learn robust person expression and solve the key problem of reidentification task, this paper proposes a person reidentification algorithm, which includes three main aspects. Firstly, a bilinear channel fusion attention mechanism is designed to improve the bottleneck of ResNet50, which realizes the convergence of image features on different channels under the multireceptive fields and enhances the learning of image feature details in the form of attention, so as to improve the ability of expressing fine-grained information in pedestrian images. Secondly, the hard sample mining mechanism is designed, and the hard sample is used as the object of similarity optimization to reduce the initial P2G optimization model parameters. At the same time, it can reduce the computing resources and enhance the generalization ability of the model. Finally, the similarity optimization module is introduced to realize the automatic perception of the key parts of the image by the fusion of grouping and global similarity, so as to achieve more accurate and efficient person reidentification. The paper also carries out a reidentification experiment for the proposed algorithm, compares it with the mainstream algorithm, and obtains a good result. The experiment shows that the algorithm in this paper has a relatively obvious improvement in the average accuracy and Rank- $n$  and has an obvious advantage in Rank-1. The next step will be to comprehensively improve performance indicators and network light.

#### Data Availability

The image datasets used to support the findings of this study are included within the article.

#### Conflicts of Interest

The authors declare that there are no conflicts of interest regarding the publication of this paper.

#### Acknowledgments

This research was supported by the following projects: Scientific Research Project of National Language Commission (YB135-125), Key Research and Development Project of Shandong Province (2019GGX101008 and 2016GGX105013), Natural Science Foundation of Shandong Province (ZR2017MF048), and Science and Technology Plan for Colleges and Universities of Shandong Province (J17KA214).

#### References

- [1] D. Gray, S. Brennan, and H. Tao, "Evaluating appearance models for recognition, reacquisition, and tracking," in *Proceeding of the 10th IEEE International Workshop on Performance Evaluation of Tracking and Surveillance (PETS 2007)*, pp. 356–368, Rio de Janeiro, Brazil, October 2007.
- [2] M. Farenzena, L. Bazzani, A. Perina, V. Murino, and M. Cristani, "Person re-identification by symmetry-driven accumulation of local features," in *Proceedings of the 2010 IEEE Computer Society Conference on Computer Vision and Pattern Recognition*, pp. 2360–2367, San Francisco, CA, USA, June 2010.
- [3] S. Liao, Y. Hu, X. Zhu, and S. Z. Li, "Person re-identification by local maximal occurrence representation and metric learning," in *Proceedings of the 2015 IEEE Conference on Computer Vision and Pattern Recognition*, pp. 2197–2206, Boston, MA, USA, June 2015.
- [4] S. Wu, Y.-C. Chen, X. Li, A.-C. Wu, J.-J. You, and W. S. Zheng, "An enhanced deep feature representation for person re-identification," in *Proceedings of the 2016 IEEE Winter Conference on Applications of Computer Vision*, pp. 743–758, Lake Placid, NY, USA, March 2016.
- [5] Y.-L. Wei and C. H. Lin, "Efficient weighted histogram features for single-shot person re-identification," *Journal of Signal Processing Systems*, vol. 90, no. 4, pp. 477–491, 2018.
- [6] Y. Sun, L. Zheng, Y. Yang, Q. Tian, and S. Wang, "Beyond part models: person retrieval with refined part pooling (and A strong convolutional baseline)," *Computer Vision-ECCV 2018, Computer Vision-ECCV 2018-15th European Conference*, Munich, Germany, pp. 501–518, 2018.
- [7] M. Kostinger, M. Hirzer, P. Wohlhart, P. M. Roth, and H. Bischof, "Large scale metric learning from equivalence constraints," in *Proceedings of the 2012 IEEE Conference on Computer Vision and Pattern Recognition*, pp. 2288–2295, Providence, RI, USA, June 2012.
- [8] S. Wang, T. Liang, Q. Chen, J. Na, and X. Ren, "USDE-based sliding mode control for servo mechanisms with unknown system dynamics," *IEEE/ASME Transactions on Mechatronics*, vol. 25, no. 2, pp. 1056–1066, 2020.
- [9] Y. Wang, Z. Chen, F. Wu, and G. Wang, "Person re-identification with cascaded pairwise convolutions," in *Proceedings of the IEEE/CVF Conference on Computer Vision and Pattern Recognition*, pp. 1470–1478, Salt Lake City, UT, USA, June 2018.
- [10] D. Cheng, Y. Gong, S. Zhou, J. Wang, and N. Zheng, "Person re-identification by multi-channel parts-based CNN with improved triplet loss function," in *Proceedings of the 2016 IEEE Conference on Computer Vision and Pattern Recognition*, pp. 1335–1344, Las Vegas, NV, USA, June 2016.
- [11] E. Ristani and C. Tomasi, "Features for multi-target multi-camera tracking and re-identification," in *Proceedings of the 2018 IEEE/CVF Conference on Computer Vision and Pattern Recognition*, pp. 6036–6046, Salt Lake City, UT, USA, June 2018.
- [12] H. Liu, J. Feng, M. Qi, J. Jiang, and S. Yan, "End-to-end comparative attention networks for person re-identification," *IEEE Transactions on Image Processing*, vol. 26, no. 7, pp. 3492–3506, 2017.
- [13] A. Hermans, L. Beyer, and B. Leibe, "In defense of the triplet loss for person re-identification," in *Proceedings of the 2017 IEEE Conference on Computer Vision and Pattern Recognition*, pp. 1213–1225, Honolulu, HI, USA, November 2017.
- [14] J. Na, Y. Huang, X. Wu, S.-F. Su, and G. Li, "Adaptive finite-time fuzzy control of nonlinear active suspension systems

- with input delay,” *IEEE Transactions on Cybernetics*, vol. 50, no. 6, pp. 2639–2650, 2020.
- [15] W. Chen, X. Chen, J. Zhang, and K. Huang, “Beyond triplet loss: a deep quadruplet network for person re-identification,” in *Proceedings of the 2017 IEEE Conference on Computer Vision and Pattern Recognition*, pp. 1320–1329, Honolulu, HI, USA, July 2017.
- [16] S. Bai, X. Bai, and Q. Tian, “Scalable person re-identification on supervised smoothed manifold,” in *Proceedings of the 2017 IEEE Conference on Computer Vision and Pattern Recognition*, pp. 674–689, Honolulu, HI, USA, July 2017.
- [17] D. Li, X. Chen, Z. Zhang, and K. Huang, “Learning deep context-aware features over body and latent parts for person re-identification,” in *Proceedings of the 2017 IEEE Conference on Computer Vision and Pattern Recognition*, pp. 384–393, Honolulu, HI, USA, July 2017.
- [18] S. Zhou, J. Wang, J. Wang, Y. Gong, and N. Zheng, “Point to set similarity based deep feature learning for person re-identification,” in *Proceedings of the 2017 IEEE Conference on Computer Vision and Pattern Recognition*, pp. 452–465, Honolulu, HI, USA, July 2017.
- [19] M. S. Sarfraz, A. Schumann, A. Eberle, and R. Stiefelhagen, “A pose-sensitive embedding for person re-identification with expanded cross neighbourhood re-ranking,” in *Proceedings of the 2018 IEEE/CVF Conference on Computer Vision and Pattern Recognition*, pp. 420–429, Salt Lake City, UT, USA, June 2018.
- [20] S. Bai, P. Tang, P. H. S. Torr, and J. Latecki, “Re-ranking via metric fusion for object retrieval and person re-identification,” in *Proceedings of the 2019 IEEE/CVF Conference on Computer Vision and Pattern Recognition*, pp. 740–749, Long Beach, CA, USA, June 2019.
- [21] G. Wang, S. Gao, and D. Fan, “A G2G similarity guided person re-identification algorithm,” *Journal of Physics: Conference Series*, vol. 1453, no. 1, Article ID 012035, 2019.
- [22] Y. Sun, Q. Xu, Y. Li et al., “Perceive where to focus: learning visibility-aware part-level features for partial person re-identification,” in *Proceedings of the 2019 IEEE/CVF Conference on Computer Vision and Pattern Recognition*, pp. 820–834, Long Beach, CA, USA, June 2019.

## Research Article

# Linearization Method of Nonlinear Magnetic Levitation System

Dini Wang , Fanwei Meng , and Shengya Meng

School of Control Engineering, Northeastern University at Qinhuangdao, Qinhuangdao 066004, China

Correspondence should be addressed to Fanwei Meng; mengfanwei@neuq.edu.cn

Received 5 May 2020; Accepted 3 June 2020; Published 22 June 2020

Guest Editor: Weicun Zhang

Copyright © 2020 Dini Wang et al. This is an open access article distributed under the Creative Commons Attribution License, which permits unrestricted use, distribution, and reproduction in any medium, provided the original work is properly cited.

Linearized model of the system is often used in control design. It is generally believed that we can obtain the linearized model as long as the Taylor expansion method is used for the nonlinear model. This paper points out that the Taylor expansion method is only applicable to the linearization of the original nonlinear function. If the Taylor expansion is used for the derived nonlinear equation, wrong results are often obtained. Taking the linearization model of the maglev system as an example, it is shown that the linearization should be carried out with the process of equation derivation. The model is verified by nonlinear system simulation in Simulink. The method in this paper is helpful to write the linearized equation of the control system correctly.

## 1. Introduction

Magnetic levitation generates eddy-current effect by metal objects under the action of high-frequency electromagnetic fields, which enables metal objects to be suspended stably in the air [1]. Magnetic levitation technology is developing rapidly because it essentially eliminates friction and has advantages unmatched by other traditional technologies [2]. The application of the magnetic levitation technology covers numerous fields, such as high-speed magnetic bearing [3, 4], high-speed levitation train [5–7], and wind tunnel magnetic levitation [8]. Therefore, the control design for the maglev system is particularly important.

The maglev system is a nonlinear system, which causes great difficulties in its control design [9–11]. Literature [12] proposes a model-independent control system design method based on U-model. In the linear control design method, linearization is often the first step in the control system design and modeling of the magnetic levitation system [13].

It is generally considered that the nonlinear equation is linearized as long as the Taylor expansion is used [14]. However, the Taylor expansion method only applies to the original nonlinear function. The equations for general magnetic levitation systems are usually obtained from many derivations. In the process of building the nonlinear model,

the calculation of partial derivative has been done. According to the derivation algorithm, if we continue to take the derivative, then the partial derivative should be treated as a constant. In traditional modeling, this constant has been treated as a variable. And the error is introduced as we continue to differentiate. If linearization is simply carried out through the Taylor expansion method according to the derived equation, the result may be wrong.

Based on the analysis of the Lagrange equation [15], this paper points out that the partial derivative of Lagrange equation should be taken according to the operating point to get the correct linearized equation. Simulink simulation results show that the method proposed in this paper is very effective for the linearization of the magnetic levitation system and is worth popularizing.

## 2. Maglev System Model and Its Linearization

In general, the linearization of nonlinear systems is through Taylor series expansion, and a linear relation can be obtained after omitting the higher order terms [16]. Taylor series refers to the expansion of a nonlinear function  $f(x, y)$ . For example, formula (1) is the equation of a prime mover [17].

$$J \frac{d\omega}{dt} = T_M(\omega, u) - T_D(\omega), \quad (1)$$

where  $T_M$ , the driving torque, is a nonlinear function of the rotation rate  $\omega$  and the control input  $u$  and  $T_D$ , the load torque, is a function of the rotation rate  $\omega$ . If  $T_M$  and  $T_D$  are expanded as Taylor series and take the first term, the linearized equation of formula (1) can be obtained. This is the general notion of linearization. But for a general nonlinear system, it takes a lot of arithmetical operation to get from the original equation to the nonlinear equation. Using Taylor series to linearize the nonlinear terms in the final result, wrong result is often obtained.

The model of the typical electromagnetic suspension (EMS) train control system is shown in Figure 1.

The motion equation of the maglev system model can be written as [11, 15]

$$m \frac{d^2 z(t)}{dt^2} = \frac{\mu_0 N^2 a_m}{4} \left( \frac{i(t)}{z(t)} \right)^2 + mg, \quad (2)$$

$$\frac{di(t)}{dt} = \frac{i(t)}{z(t)} \frac{dz(t)}{dt} - \frac{2}{\mu_0 N^2 a_m} z(t) (R_m i(t) - u(t)), \quad (3)$$

where  $\mu_0$  represents the permeability in a vacuum;  $m$  represents the mass of the suspension magnet,  $m = 15$  kg;  $a_m$  represents the effective area of the magnetic pole,  $a_m = 1.024 \times 10^{-2} \text{ m}^2$ ;  $N$  is the number of turns of the coil on the electromagnet,  $N = 280$ ;  $R_m$  represents the resistance of the coil,  $R_m = 1.1 \Omega$ ;  $u(t)$  represents the control voltage at both ends of the coil;  $i(t)$  represents the current in the coil;  $z(t)$  is the gap between the electromagnet and the guideway; and  $g$  represents the gravitational acceleration. Suppose that the state vector is

$$x(t) = [z(t) \dot{z}(t) i(t)]^T = [x_1 x_2 x_3]^T \in \mathbb{R}^3. \quad (4)$$

Consider the nonlinear terms  $(i(t)/z(t))^2$ ,  $(i(t)/z(t))$ ,  $z(t)i(t)$  in (2) and (3) as nonlinear functions. The linearized equation of the system can be obtained by Taylor series expansion [16].

$$\dot{x} = \mathbf{A}x + \mathbf{B}u. \quad (5)$$

The corresponding matrices can be written as

$$\mathbf{A} = \begin{bmatrix} 0 & 1 & 0 \\ \frac{\mu_0 a_m N^2}{2m} \frac{i_0^2}{z_0^3} & 0 & -\frac{\mu_0 a_m N^2}{2m} \frac{i_0}{z_0^2} \\ \left( \frac{2R_m}{\mu_0 N^2 a_m} - \frac{\dot{z}_0}{z_0^2} \right) i_0 & \frac{i_0}{z_0} & -\frac{2R_m}{\mu_0 N^2 a_m} z_0 + \frac{\dot{z}_0}{z_0} \end{bmatrix}, \quad (6)$$

$$\mathbf{B} = \begin{bmatrix} 0 \\ 0 \\ \frac{2}{\mu_0 N^2 a_m} z_0 \end{bmatrix}.$$

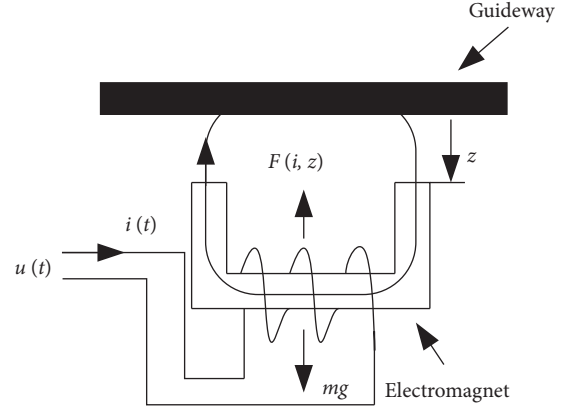


FIGURE 1: Model of an electromagnetic suspension system.

Set the nominal working point as  $z_0$ ,  $z_0 = 4.0 \times 10^{-3} \text{ m}$ , and the corresponding operating current  $i_0 = 3.0538 \text{ A}$ . Then, the linearized equation can be written as

$$\dot{x} = \begin{bmatrix} 0 & 1 & 0 \\ 4900.1 & 0 & -6.4184 \\ -6659.4 & 763.45 & -8.7228 \end{bmatrix} x + \begin{bmatrix} 0 \\ 0 \\ 7.9298 \end{bmatrix} u. \quad (7)$$

Formulas (5) and (7) are directly obtained by the Taylor expansion method according to formulas (2) and (3). This is a common linearization method, but it proves (see below) that the resulting linearization equation is incorrect.

Next, we start with the establishment of the equation. For the dynamic system with  $k$  generalized coordinates  $q_1, \dots, q_k$ , the Lagrange equation is [2, 4]

$$\frac{d}{dt} \frac{\partial T}{\partial \dot{q}_i} - \frac{\partial T}{\partial q_i} = -\frac{\partial V}{\partial q_i} - \frac{\partial R}{\partial \dot{q}_i} + f_i(t), \quad i = 1, 2, \dots, k, \quad (8)$$

where  $T$  represents the kinetic energy stored by the dynamic system,  $V$  represents the potential energy of the system,  $f_i(t)$  represents the external force varying with time, and  $R$  represents Rayleigh's dissipation function, and its general form can be written as

$$R = \frac{1}{2} R_m \dot{q}^2. \quad (9)$$

Suppose the generalized coordinates of the maglev control system are air gap  $z$  and charge  $q$  (note  $\dot{q} = i$ ), then the kinetic energy and potential energy of the system are, respectively,

$$T = \frac{1}{2} m \dot{z}^2 + \frac{1}{2} L \dot{q}^2, \quad (10)$$

$$V = -mgz, \quad (11)$$

where

$$L = \frac{\mu_0 N^2 a_m}{2z}. \quad (12)$$

By substituting formulas (10)~(12) into Lagrange equation (8), the equation of generalized coordinates  $z$  and  $q$  can be written as

$$\frac{d}{dt}(m\dot{z}) - \frac{1}{2}\dot{q}^2 \left( \frac{\mu_0 N^2 a_m}{2z^2} \right) = mg, \quad (13)$$

$$\frac{d}{dt} \left( \frac{\mu_0 N^2 a_m}{2z} \dot{q} \right) = -R_m \dot{q} + u. \quad (14)$$

The derivative of (14) on the left is

$$\frac{d}{dt} \left( \frac{\mu_0 N^2 a_m}{2z} \dot{q} \right) = \frac{\mu_0 N^2 a_m}{2z} \frac{d\dot{q}}{dt} - \frac{\mu_0 N^2 a_m \dot{q}}{2z^2} \frac{dz}{dt}. \quad (15)$$

Thus, according to (13) and (14), the equation of motion of the system can be finally obtained as

$$\frac{d^2 z(t)}{dt^2} = \frac{\mu_0 N^2 a_m}{4m} \left( \frac{i(t)}{z(t)} \right)^2 + g, \quad (16)$$

$$\frac{di(t)}{dt} = \frac{i(t)}{z(t)} \frac{dz(t)}{dt} - \frac{2}{\mu_0 N^2 a_m} z(t) (R_m i(t) - u(t)). \quad (17)$$

Equations (16) and (17) are equivalent to (2) and (3) when analyzing the maglev system. Since we have taken the partial derivative once when we derived (17), the partial derivative should be a constant to the operating point in linearization, that is, it corresponds to a constant coefficient instead of a variable. Therefore, if linearization is carried out, the corresponding constants of all partial derivatives in (15) should be taken, and (15) can be rewritten as

$$\frac{d}{dt} \left( \frac{\mu_0 N^2 a_m}{2z} \dot{q} \right) = \frac{\mu_0 N^2 a_m}{2z_0} \frac{d\dot{q}}{dt} - \frac{\mu_0 N^2 a_m \dot{q}}{2z_0^2} \frac{dz}{dt}. \quad (18)$$

The corresponding linearized equation can be obtained by substituting (18) into (14).  $(i(t)/z(t))^2$  in (16) is indeed a nonlinear function, and its linearization relation can be obtained by Taylor expansion.

$$\begin{aligned} \frac{\mu_0 N^2 a_m}{4m} \left( \frac{i(t)}{z(t)} \right)^2 &= \frac{\mu_0 N^2 a_m}{4m} \left( \frac{i_0}{z_0} \right)^2 + \frac{\mu_0 N^2 a_m}{2m} \left( \frac{i_0}{z_0^2} \right) \Delta i \\ &\quad - \frac{\mu_0 N^2 a_m}{2m} \left( \frac{i_0^2}{z_0^3} \right) \Delta z. \end{aligned} \quad (19)$$

In this way, by substituting (18) and (19) into (14) and (16), the final linearized equation can be obtained as

$$\dot{x} = \begin{bmatrix} 0 & 1 & 0 \\ \frac{\mu_0 a_m N^2}{2m} \frac{i_0^2}{z_0^3} & 0 & -\frac{\mu_0 a_m N^2}{2m} \frac{i_0}{z_0^2} \\ 0 & \frac{i_0}{z_0} & -\frac{2R_m}{\mu_0 N^2 a_m} z_0 \end{bmatrix} x + \begin{bmatrix} 0 \\ 0 \\ \frac{2}{\mu_0 N^2 a_m} z_0 \end{bmatrix} u, \quad (20)$$

i.e.,

$$\dot{x} = \begin{bmatrix} 0 & 1 & 0 \\ 4900.1 & 0 & -6.4184 \\ 0 & 763.45 & -8.7228 \end{bmatrix} x + \begin{bmatrix} 0 \\ 0 \\ 7.9298 \end{bmatrix} u. \quad (21)$$

Obviously, (20) and (21) are obviously inconsistent with (5) and (7). The state matrix of (7) has the element  $-6659.4$  in the third row and first column, while the element at this position in (21) is 0. In order to verify this linearization method, we use the nonlinear system simulation in this paper because when the deviation is very small, the nonlinear system results should be consistent with the linearization result.

### 3. Simulation of Nonlinear System

Next, we will simulate and analyze the nonlinear equations of the maglev system. In the nonlinear simulation of Simulink, a custom function module Fcn is mainly used. The function of this module is to process the input by the rules conforming to C language. The corresponding formulas may consist of one or more components.  $u$  is the input of the module, which supports vectorized input. If  $u$  is a vector,  $u[i]$  represents the  $i$ th element of the vector, and  $u[1]$  or a single  $u$  represents the first element. The function module can perform both mathematical operations (such as addition, subtraction, multiplication, and division) and relational operations (such as identically equal, not equal, greater than, and equal), as well as three kinds of logical operations. The precedence of these operators conforms to the rules in C language.

The simulation model of the magnetic levitation system based on differential (2) and (3) is shown in Figure 2. In Figure 2, the function of Mux module is to organize several signals into one signal. Here, variables are expressed in increments so as to compare with linear results. In the figure,  $f_1(u)$ ,  $f_2(u)$ , and  $f_3(u)$  are all custom function modules.

Adopt the state feedback  $k = [k_1 \ k_2 \ k_3] = [24843.50 \ 249.7285 \ -20.9242]$  in the simulation. And the feedback control signal should be elicited from  $\Delta z$ ,  $\Delta \dot{z}$ ,  $\Delta i$ . In the case of module  $f_3(u)$ , it describes the operation on the right side of formula (2).

$$f_3(u) = \frac{\mu_0 N^2 a_m}{4m} \left( \frac{\Delta i + i_0}{\Delta z + z_0} \right)^2 + g. \quad (22)$$

The input is two variables:  $\Delta z$ ,  $\Delta i$ . The setting of  $f_3(u)$  is shown in Figure 3.

In Figure 3,  $1.6814 * (10^{-5})$  corresponds to the value of  $(\mu_0 N^2 a_m / 4m)$ , 9.8 is the value of gravitational acceleration  $g$ , and  $u(1)$ ,  $u(2)$  are input signals arranged in a certain order by Mux module in front of the module  $f_3(u)$ . Here,  $u(1)$  corresponds to  $\Delta i$  and  $u(2)$  corresponds to  $\Delta z$ , and  $i_0$  and  $z_0$  are values of corresponding nominal operating points. The values of  $i_0$  and  $z_0$  at the equilibrium point are calculated in advance according to the following equation:

$$m\ddot{z}(t) = \frac{\mu_0 N^2 a_m}{4} \left( \frac{i_0}{z_0} \right)^2 + mg = 0. \quad (23)$$



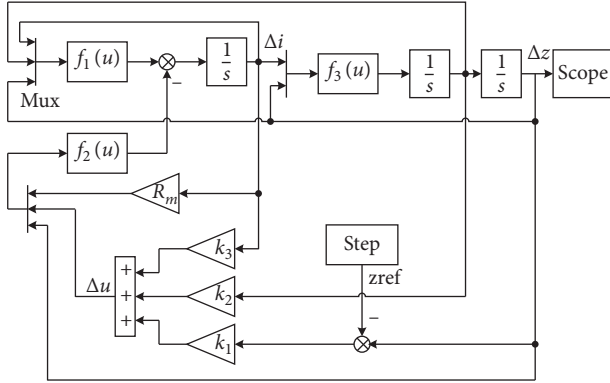


FIGURE 2: Simulation model of the nonlinear system.

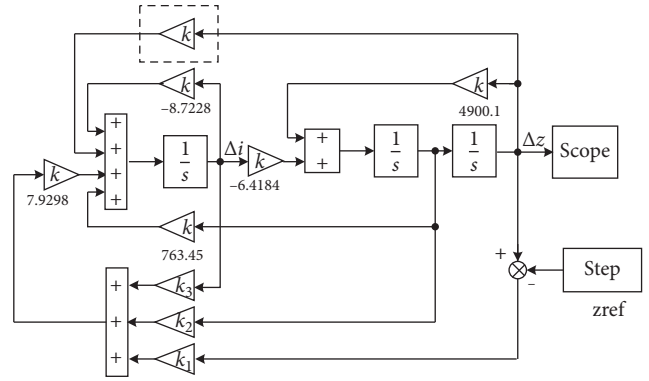


FIGURE 4: Simulation model of the linearized system.

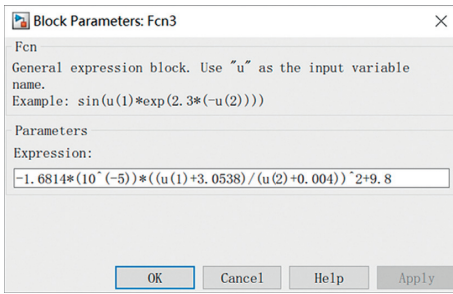


FIGURE 3: The dialog box of Fcn3.

The function  $f_1(u)$  describes the first term on the right side of (3), and  $f_2(u)$  describes the second term on the right side of (3). The problem of the nominal operating point is also set as follows:

$$f_1(u) = \left( \frac{\Delta i + i_0}{\Delta z + z_0} \right) \Delta \dot{z}, \quad (24)$$

$$f_2(u) = \frac{2}{\mu_0 N^2 a_m} (\Delta z + z_0) (R_m \Delta i - \Delta u).$$

#### 4. Verification of Linearized Equations

Two linearization methods are proposed above. One is the simple Taylor series method ((5) and (7)), and the other is the method of taking the partial derivative as a constant when taking the column equation ((20) and (21)). In order to further verify the linearization method in this paper, the simulation checking is adopted, and the simulation results of nonlinear systems with small deviations are compared.

Figure 4 shows the simulation block diagram of the linearized system. The dotted box in the figure shows the difference between the two linearized results (7) and (21). The same state feedback is used in the simulation.

$$k = [k_1 \ k_2 \ k_3] = [24843.50 \ 249.7285 \ -20.9242]. \quad (25)$$

Figure 5 shows the simulation results of the step response. The short line in the figure is the simulation result of

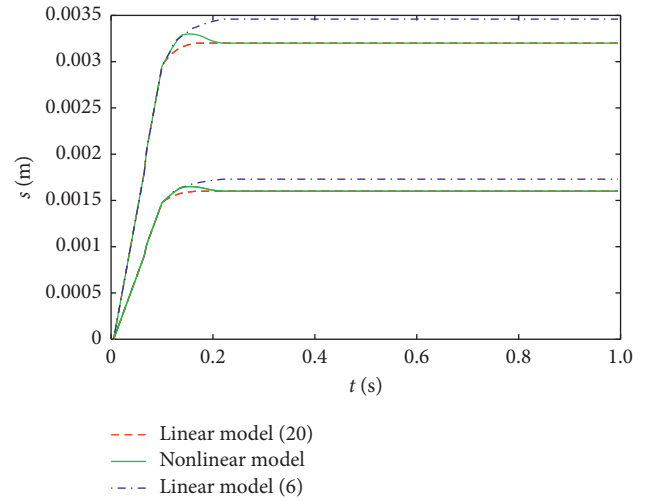


FIGURE 5: Comparison of the simulation results.

system (7), and the dotted line is the simulation result of system (21) of this method.

The simulation block diagram of the nonlinear system is shown in Figure 2. The solid line in Figure 5 is the simulation result of the nonlinear system, and the amplitude of the input step signal is 0.1 mm, 0.5 mm, and 0.1 mm, respectively. When a small signal (0.1 mm) is input, the dotted line of the system (21) is basically coincident with the solid line of the nonlinear system. The simulation result of system (7) is obviously inconsistent with the nonlinear result under small signals, especially the static differences are not equal. In this case, the static error of the nonlinear system is relatively easy to calculate. The static error between the system output and the step input is also shown in Figure 5 (the calculation process of the static error is abbreviated). The simulation results show that the static error of the system (21) is consistent with that of the nonlinear system.

#### 5. Conclusions

The linearization of nonlinear magnetic levitation cannot be carried out simply by Taylor expansion according to the derived nonlinear equation. In the process of derivation, the

partial derivative is included in the equation, and the linearized equation can be obtained by taking the partial derivative at the operating point. The method is simple and the physical concept is clear. On the contrary, if we linearize the equation by the Taylor series based on the derived nonlinear equation, wrong result may be obtained. In this paper, the simulation method of the nonlinear magnetic levitation system is presented, which separates the operating point (setting) from the incremental change, and is worthy of promoting.

### Data Availability

The data used to support the findings of this study are available from the corresponding author upon request.

### Conflicts of Interest

The authors declare that there are no conflicts of interest regarding the publication of this paper.

### Acknowledgments

This study was supported in part by the Fundamental Research Funds for the Central Universities under grant no. N182304010, in part by the Natural Science Foundation of Liaoning Province under grant no. 20170520333, and in part by the Natural Science Foundation of Hebei Province under grant no. F2019501012.

### References

- [1] B. Gauthier-Manuel and L. Garnier, "Development of a magnetic levitation force microscope," *Surface & Interface Analysis*, vol. 27, no. 5-6, pp. 287-290, 1999.
- [2] K. Glatzel, G. Khurdok, and D. Rogg, "The development of the magnetically suspended transportation system in the Federal Republic of Germany," *IEEE Transactions on Vehicular Technology*, vol. 29, no. 1, pp. 3-17, 1980.
- [3] K.-Y. Kai-Yew Lum, V. T. Coppola, and D. S. Bernstein, "Adaptive autocentering control for an active magnetic bearing supporting a rotor with unknown mass imbalance," *IEEE Transactions on Control Systems Technology*, vol. 4, no. 5, pp. 587-597, 1996.
- [4] T. Zhang, X. Ye, L. Mo et al., "Modeling and performance analysis on the five degrees of freedom slice hybrid magnetic bearing," *IEEE Transactions on Applied Superconductivity*, vol. 29, no. 2, pp. 1-5, 2019.
- [5] M. Zhai, Z. Long, and X. Li, "Fault-tolerant control of magnetic levitation system based on state observer in high speed maglev train," *IEEE Access*, vol. 7, pp. 31624-31633, 2019.
- [6] X. Yang, Z. Lin, J. Ding, and Z. Long, "Lifetime prediction of IGBT modules in suspension choppers of medium/low-speed maglev train using an energy-based approach," *IEEE Transactions on Power Electronics*, vol. 34, no. 1, pp. 738-747, 2019.
- [7] M. Komori, A. Minoda, K. Nemoto, and K. Asami, "Maximum limit of superconducting persistent current for superconducting magnetic suspension system," *IEEE Transactions on Magnetics*, vol. 53, no. 11, pp. 1-4, 2017.
- [8] W. G. Hurley and W. H. Wolfe, "Electromagnetic design of a magnetic suspension system," *IEEE Transactions on Education*, vol. 40, no. 2, pp. 124-130, 1997.
- [9] C. Truesdell and W. Noll, *The Non-linear Field Theories of Mechanics*, Springer, Berlin, Germany, 1992.
- [10] A. Pang, Z. He, M. Zhao, G. Wang, Q. Wu, and Z. Li, "Sum of squares approach for nonlinear H<sub>∞</sub> control," *Complexity*, vol. 2018, Article ID 8325609, 7 pages, 2018.
- [11] F. Meng, A. Pang, X. Dong, C. Han, and X. Sha, "H<sub>∞</sub> optimal performance design of an unstable plant under bode integral constraint," *Complexity*, vol. 2018, Article ID 4942906, 10 pages, 2018.
- [12] Q. Zhu, L. Liu, W. Zhang, and S. Li, "Control of complex nonlinear dynamic rational systems," *Complexity*, vol. 2018, Article ID 8953035, 12 pages, 2018.
- [13] W. T. Baumann, "Feedback control of multiinput nonlinear systems by extended linearization," *IEEE Transactions on Automatic Control*, vol. 33, no. 2, pp. 193-197, 1988.
- [14] L. Zhu and C. R. Knospe, "Modeling of nonlaminated electromagnetic suspension systems," *IEEE/ASME Transactions on Mechatronics*, vol. 15, no. 1, pp. 59-69, 2010.
- [15] B. V. Leer, "Towards the ultimate conservative difference scheme I. The quest of monotonicity," *Proceedings of the Third International Conference on Numerical Methods in Fluid Mechanics*, Springer, vol. 18, no. 1, pp. 163-168, Berlin, Germany, 1973.
- [16] Q. M. Zhu and L. Z. Guo, "A pole placement controller for non-linear dynamic plants," *Proceedings of the Institution of Mechanical Engineers, Part I: Journal of Systems and Control Engineering*, vol. 216, no. 6, pp. 467-476, 2002.
- [17] K. Gustafson, "The original motivation: operator semigroups," *Antieigenvalue Analysis: with Applications to Numerical Analysis, Wavelets, Statistics, Quantum Mechanics, Finance and Optimization*, World Scientific, Singapore, 2011.



## Research Article

# U-Model-Based Active Disturbance Rejection Control for the Dissolved Oxygen in a Wastewater Treatment Process

Wei Wei <sup>1,2,3</sup>, Nan Chen,<sup>1,2,3</sup> Zhiyuan Zhang,<sup>1,2,3</sup> Zaiwen Liu,<sup>1,2,3</sup> and Min Zuo <sup>1,2,3</sup>

<sup>1</sup>School of Computer and Information Engineering, Beijing Technology and Business University, Beijing 100048, China

<sup>2</sup>National Engineering Laboratory for Agri-Product Quality Traceability, Beijing Technology and Business University, 100048 Beijing, China

<sup>3</sup>Beijing Key Laboratory of Big Data Technology for Food Safety, Beijing 100048, China

Correspondence should be addressed to Min Zuo; [zuomin@btbu.edu.cn](mailto:zuomin@btbu.edu.cn)

Received 24 February 2020; Revised 30 March 2020; Accepted 13 April 2020; Published 25 May 2020

Academic Editor: Quanmin Zhu

Copyright © 2020 Wei Wei et al. This is an open access article distributed under the Creative Commons Attribution License, which permits unrestricted use, distribution, and reproduction in any medium, provided the original work is properly cited.

Dissolved oxygen (DO) concentration is a key variable in wastewater treatment process (WWTP). It directly influences effluent quality of a wastewater treatment. However, due to the great changes of the influent flow rate and the large uncertainties of the wastewater in composition, concentration, and temperature, most control approaches become powerless on DO regulation. To improve the robustness of a DO control, and reduce the phase delay between the control input and the system output, a U-model-based active disturbance rejection control (UADRC) is proposed. The U-model control (UC) reduces the phase delay between the control input and the system output. The active disturbance rejection control (ADRC) enhances the robustness of the closed-loop system. Also, ADRC converts the system dynamics to be integrators connected in series, which helps the realization of UC. By changing the system dynamics to be an approximate unit, a controller based on desired closed-loop system dynamics can be designed and the DO concentration is guaranteed. UADRC combines advantages of both UC and ADRC, and a commonly accepted benchmark simulation model no.1 (BSM1) is taken to verify the proposed UADRC. Numerical results show that, with similar energy consumption, the UADRC is able to achieve much better tracking performance than ADRC, SMC, and PI with suggested parameters.

## 1. Introduction

Water crisis may occur. If it happens, it will have great impact on human's life [1]. Wastewater treatment is an approach to deal with water shortage, and wastewater treatment process (WWTP) control has been widely concerned from all over the world [2–4]. Dissolved oxygen (DO) concentration is a key variable in a WWTP, which directly affects growth and metabolism of the microbes, and determines the wastewater treatment performance [5]. However, DO concentration is influenced by many factors, such as the influent flow rate, the components, the concentration of each component, and reaction temperature. The influent flow rate is not fixed; it may vary due to various factors. Wastewater components and their concentrations are also unstable, or even some of them are unavailable. Therefore, there are too many uncertainties in a WWTP, and it is

difficult to build an accurate mathematical model to describe a WWTP. Those facts present great challenges to keep a desired DO concentration level.

To improve the wastewater treatment performance, in recent years, various control approaches have been proposed to regulate the DO concentration. Zhang et al. [6] proposed a distributed economic model predictive control strategy for a WWTP, simulation results showed that the proposed control strategy is able to significantly reduce the computation load with a little degradation of the control performance. Santín et al. presented a model predictive control (MPC) with inlet flow rate feedforward (FF) control (MPC + FF) for the lower level nitrate nitrogen and DO control in a WWTP [7]. Numerical results demonstrated that MPC + FF can achieve a satisfied control performance. Han et al. [8] designed a self-organizing sliding-mode controller to control the DO concentration, and a desired operation performance was achieved.

In addition, for the sake of improving the robustness of a WWTP control, approaches that depend less on model information, such as data driven control [9, 10], sliding-mode control (SMC) [11, 12], active disturbance rejection control (ADRC) [13–15], and fuzzy neural network (FNN) [16, 17], were proposed.

Actually, considering the ubiquitous uncertainties and disturbances existing in a WWTP, control approaches that depend less on system model attract much attention in recent years. However, among those results, few of them take the phase delay resulting from system's relative degree into consideration, while, the relative degree of a controlled plant introduces the phase delay, which does result in time delay of the system response or even instability of a system. To reduce the phase delay resulting from the relative order, the U-model control (UC) has been proposed [18]. Its main idea is to build a dynamic inverse model for a controlled plant, and then the controlled plant is dynamically transferred to be a unit. In other words, by UC, there is no phase delay between the control input and system output. By eliminating the phase delay, system responses can be greatly improved. However, for UC, both uncertainties and the U-model invertibility need to be considered properly [19].

Therefore, in this paper, both system responses and the closed-loop robustness are considered in the design of DO concentration regulation. The UC is able to reduce the phase delay of a controlled plant, improve the system response and tracking accuracy. The active disturbance rejection control (ADRC) proposed by Han [20] is capable of estimating and cancelling out the total disturbance actively so as to guarantee a desired system output. Based on the facts above, a U-model based active disturbance rejection control (UADRC) is proposed. By ADRC, the total disturbance is estimated by an extended state observer (ESO), and it can be compensated actively, so that the system dynamics can be converted into integrators connected in series. As long as the ESO works expectantly, robustness can be guaranteed. Then, the system inverse model becomes differentiators connected in series, and the U-model control can be realized. It means that the phase delay can be reduced. Therefore, the UADRC inherits advantages of both UC and ADRC. Both system responses and robustness can be guaranteed by the UADRC in DO concentration control. Main contribution of the work can be summarized as

- (i) A U-model based active disturbance rejection control is proposed. The UADRC reduces the phase delay between control input and system output. System response rate is faster, tracking error becomes much smaller, and the closed-loop system is more robust to disturbances and uncertainties.
- (ii) The UADRC solves the concerns of uncertainties and invertibility in the U-model control.
- (iii) The UADRC provides a frame to preset desired closed-loop system performance. Based on such a flexible structure, a control law can be designed according to the desired closed-loop system dynamics, and the tracking performance can be greatly improved.
- (iv) The UADRC proposed is verified by a commonly accepted BSM1, and the DO concentration is controlled as desired.

## 2. Problem Description

*2.1. The Wastewater Treatment Model.* The benchmark simulation model no.1 (BSM1) is under the umbrella of the International Water Association (IWA) Task Group on benchmarking of control strategies for WWTPs [21]. It is an accepted platform to test the innovating control strategies via fair comparisons based on a defined set of criteria [21]. In other words, it is a standardized "simulation benchmark," which provides an impartial basis for evaluating past, present, and future control strategies for a WWTP control without reference to a particular facility [22]. Therefore, in this paper, the BSM1 is taken as the test platform. Structure of the BSM1 is given in Figure 1 [21–23].

From Figure 1, one can see that the BSM1 is comprised of a biological reactor and a clarifier. Biological reactions take place in the biological reactor, and they are described by the Activated Sludge Model no.1 (ASM1). The biological reactor consists of five units. The first two units are anoxic sections (the volume of each unit is  $1000\text{ m}^3$ ), and the last three units are aerated sections (the volume of each unit is  $1333\text{ m}^3$ ). By manipulating the oxygen transfer coefficient ( $K_{La,s}$ ) of the last aerated reactor, a PI control is designed to control the dissolved oxygen concentration in the last aerated unit. Simultaneously, by manipulating the internal recycle flow rate ( $Q_a$ ), the nitrate concentration in the second anoxic reactor is regulated by a PI controller [21]. For convenience, all variables and acronyms are summarized in Table 1.

*2.2. Control Problem Statement.* DO concentration in the fifth unit is one of the key variables in a WWTP. It directly affects the effluent of the wastewater treatment. In practice, for a WWTP, the DO concentration is affected by many factors, such as the influent flow rate, the components, and the concentration of each component in the wastewater [21]. However, the influent flow rate varies, the component differs, and the concentration of each component fluctuates. Therefore, it is difficult to build an accurate model for a WWTP. How to achieve an effective regulation of DO concentration in a WWTP is still a great challenge.

Thus, the aim of this paper is to design a control algorithm so that it can regulate the DO concentration at the set-value accurately, and influence of a control strategy on process performance is expected to be robust enough to different disturbances. Simultaneously, if possible, lower energy consumption is better.

## 3. U-Model Based Active Disturbance Rejection Control

Too many uncertainties make the control of DO concentration a big challenge. In this section, the U-model control

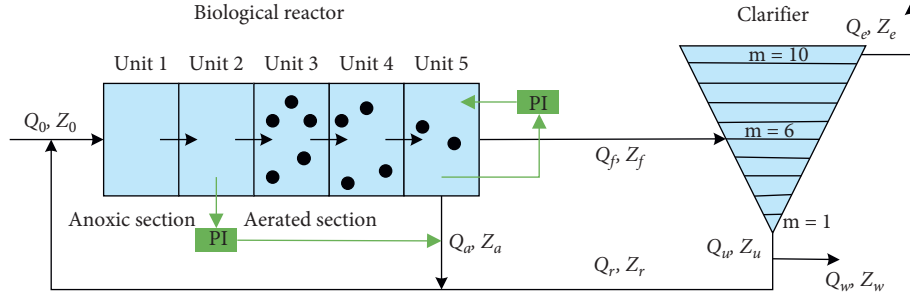


FIGURE 1: Layout of the BSM1.

TABLE 1: List of variables in BSM1.

$Q_0$	Inlet flow rate
$Z_0$	Influent constituent concentration
$Q_a$	Internal flow recirculation rate
$Z_a$	Internal flow constituent concentration
$Q_r$	Return sludge flow rate
$Z_r$	Return sludge constituent concentration
$Q_f$	Flow rate to the secondary clarifier
$Z_f$	Constituent concentration of the wastewater to the secondary clarifier
$Q_u$	Underflow rate of the secondary clarifier
$Z_u$	Constituent concentration of the underflow rate of the secondary clarifier
$Q_w$	Wastage flow rate
$Z_w$	Wastage constituent concentration
$Q_e$	Effluent flow rate
$Z_e$	Effluent constituent concentration
$S_{O,i}$	Oxygen concentration at compartment $i$
$K_{La,i}$	Oxygen transfer coefficient at compartment $i$
AE	Aeration energy
PE	Pumping energy
SP	Sludge production to be disposed
ME	Mixing energy
EC	Consumption of external carbon source
TSS	Suspended solid concentration
$V_i$	Volume of the tank $i$
$X_{S,i}$	Slowly biodegradable substrate concentration at tank $i$
$X_{I,i}$	Particulate inert organic matter concentration at tank $i$
$X_{B,H,i}$	Active heterotrophic biomass concentration at tank $i$
$X_{B,A,i}$	Active autotrophic biomass concentration at tank $i$
$X_{P,i}$	Particulate products arising from biomass decay concentration at tank $i$
$r_5$	Appropriate conversion rate

and the active disturbance rejection control are combined, and a U-model-based active disturbance rejection control is designed to regulate the DO concentration in a WWTP.

**3.1. Dynamics of the DO Concentration.** In the BSM1, DO concentration of unit 5, i.e.,  $S_{O,5}$ , can be described as [21, 24]

$$\dot{S}_{O,5} = \frac{Q_0 + Q_r + Q_a}{V_4} S_{O,4} + r_5 + K_{La,5}(S_O^* - S_{O,5}) - \frac{Q_0 + Q_r + Q_a}{V_5} S_{O,5}, \quad (1)$$

where  $S_{O,5}$ ,  $S_{O,4}$ , and  $S_O^*$  are the DO concentration in the fifth compartment, the DO concentration in the fourth

compartment, and the saturation concentration for oxygen, respectively.  $V_4$  and  $V_5$  are the volume of the fourth and fifth compartments, separately.  $r_5$  is an appropriate conversion rate.  $K_{La,5}$  is the oxygen transfer rate, it is the control input for regulating  $S_{O,5}$ .  $Q_0$ ,  $Q_r$ , and  $Q_a$  are the input flow rate, the return sludge flow rate, and the internal flow recirculation rate, respectively.

**3.2. Control Law Design.** Based on the idea of ADRC, system dynamics differs from the integrators connected in series is regarded as the total disturbance. Thus, system (1) can be rewritten as

$$\dot{y} = f + b_0 u, \quad (2)$$

where  $y = S_{O,5}$  is the system output,  $u = K_{La,5}$  is the control input,  $b_0$  is a tunable parameter, and  $f$  is the total disturbance,

$$f = \frac{Q_0 + Q_r + Q_a}{V_4} S_{O,4} + r_5 + K_{La,5}(S_O^* - S_{O,5}) - \frac{Q_0 + Q_r + Q_a}{V_5} S_{O,5} - b_0 K_{La,5}. \quad (3)$$

The total disturbance  $f$  in system (2) can be estimated by an ESO, and it can be designed as [25]

$$\begin{cases} \dot{\varepsilon}_1 = y - z_1, \\ \dot{z}_1 = z_2 + \beta_1 \cdot \varepsilon_1 + b_0 u, \\ \dot{z}_2 = \beta_2 \cdot \varepsilon_1, \end{cases} \quad (4)$$

where  $b_0$ ,  $\beta_1$ ,  $\beta_2$  are tunable parameters of an ESO.  $z_1$ ,  $z_2$  are outputs of an ESO.  $z_1$  is the estimation of the system output  $y$ .  $z_2$  is the estimation of the total disturbance  $f$ .  $\varepsilon_1$  is the estimation error of the system output.

Here, similar to [25], let  $\beta_1 = 2\omega_o$ ,  $\beta_2 = \omega_o^2$ , where  $\omega_o$  is the observer bandwidth.

The control law is designed to be

$$u = \frac{u_0 - z_2}{b_0}, \quad (5)$$

where  $u$  is the control signal applied to the controlled plant, and  $u_0$  is a pseudocontrol signal. Substituting (5) into (2), one has

$$\dot{y} = f - z_2 + u_0 \approx u_0. \quad (6)$$

Obviously, the total disturbance is cancelled out by control law (5), and system (1) is converted to be an integrator approximately.

Let the total disturbance estimation error be  $\varepsilon = f - z_2$ , and the system output estimation error be  $\varepsilon_1 = y - z_1$ . Then, closed-loop system (6) can be rewritten as

$$\dot{y} = f - z_2 + u_0 = u_0 + \varepsilon. \quad (7)$$

Based on (7), a structure of the controlled process is given in Figure 2.

According to the idea of the U-model control, the controlled process should be transferred to be a unit. Thus, a differentiator should be introduced, and it can be shown in Figure 3.

Here,  $u^*(t)$  is a control signal needed to be designed. Then, an equivalent structure of Figure 3 is given in Figure 4.

Based on the equivalent structure of the UC based controlled process (presented in Figure 4), a closed-loop system can be designed. Its structure is shown in Figure 5.

In Figure 5,  $r(t)$  is the set-value,  $\bar{\varepsilon}(t)$  is the control error,  $C(s)$  is the controller that is needed to be designed, and  $u^*(t)$  is the output of  $C(s)$ .  $\varepsilon, \varepsilon_1$  are estimation errors.

From Figure 5, one can see clearly that, ideally, i.e.,  $\varepsilon(t) = \varepsilon_1(t) = 0$ , the closed-loop system dynamics can be flexible designed according to the desired system response.

To achieve a faster response, the desired closed-loop system dynamics is chosen to be

$$\Phi(s) = \frac{\tau_n s + \omega_n^2}{s^2 + \tau_n s + \omega_n^2}, \quad (8)$$

then controller  $C(s) = (\tau_n s + \omega_n^2)/s^2$ ; here,  $\tau_n, \omega_n$  are parameters that need to be fixed. Thus,  $u^*(t)$  can be designed as

$$u^*(t) = \tau_n \int (r - z_1) dt + \omega_n^2 \iint (r - z_1) dt. \quad (9)$$

Then, the UADRC control system can be realized, and it is shown in Figure 6. It is based on the ESO and the U-model based controller  $G_c(s)$ .

From Figure 6, one has

$$G_c(s) = \tau_n + \frac{\omega_n^2}{s}. \quad (10)$$

Then,

$$u_0 = \tau_n (r - z_1) + \omega_n^2 \int (r - z_1) dt, \quad (11)$$

where  $r$  is a set-value.

In summary, the UADRC consists of the observer (4), control law (5), and (11).

### 3.3. Closed-Loop System Analyses

**3.3.1. Stability and Tracking Error.** Figure 5 gives out the closed-loop structure of the UADRC control system, from which one can see that the closed-loop system is affected by

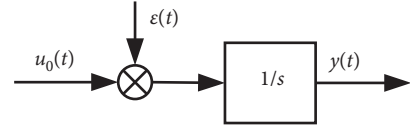


FIGURE 2: Structure of the controlled process.

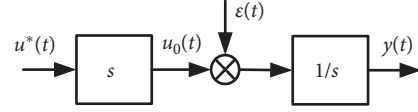


FIGURE 3: U-model control based controlled process.

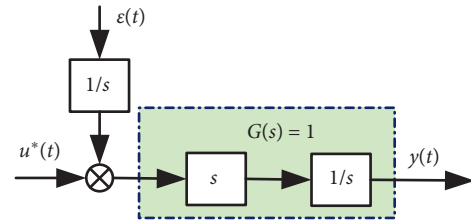


FIGURE 4: An equivalent structure of Figure 3.

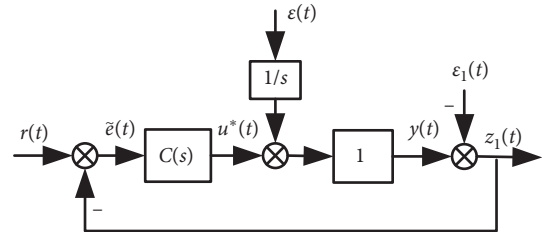


FIGURE 5: An equivalent U-model-based active disturbance rejection control system.

three signals, i.e., the reference signal  $r$ , the total disturbance estimation error  $\varepsilon$ , and the system output estimation error  $\varepsilon_1$ .

The closed-loop system presented in Figure 5 is a linear system. If the closed-loop poles of  $\Phi(s)$  given in (8) are on the left side of  $s$ -plane, the closed-loop system is stable.

*Remark 1.* Nonlinearities, uncertainties, and disturbances in the system are addressed by the ESO. Their effects are reflected on two inputs including the total disturbance estimation error  $\varepsilon$  and the system output estimation error  $\varepsilon_1$ .

Next, influence of  $\varepsilon$  and  $\varepsilon_1$  on the closed-loop system output is analyzed.

For the ESO, one has following Lemma.

**Lemma 1** (see [26]). If change rate of the total disturbance is bounded, there exists an observer bandwidth  $\omega_o^*$  such that estimation errors of an ESO are bounded within a finite time. Additionally, bounds of estimation errors are inversely proportional to the observer bandwidth.

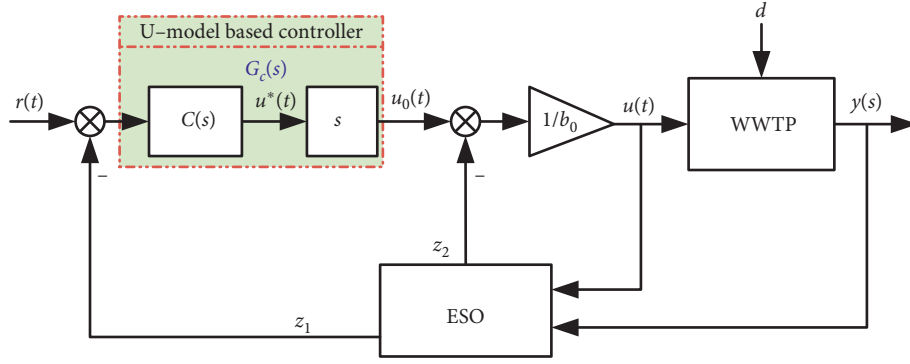


FIGURE 6: Structure of a UADRC control system.

*Remark 2.* For an engineering system, its power is always limited. Therefore, it is reasonable to assume that the change rate of the total disturbance is bounded.

According to the Lemma, one has  $|\varepsilon| \leq \sigma$ ,  $|\varepsilon_1| \leq \sigma$ . Here,  $\sigma > 0$  is a constant, which is inversely proportional to the

observer bandwidth. In other words, both  $\varepsilon$  and  $\varepsilon_1$  are bounded input signals for the closed-loop system given in Figure 5. Then, system output  $y$  can be obtained by the superposition principle, i.e.,

$$\begin{aligned} y(s) &= y_r(s) + y_\varepsilon(s) + y_{\varepsilon_1}(s) \\ &= \frac{\tau_n s + \omega_n^2}{s^2 + \tau_n s + \omega_n^2} r(s) + \frac{s}{s^2 + \tau_n s + \omega_n^2} \varepsilon(s) \\ &\quad + \frac{-(\tau_n s + \omega_n^2)}{s^2 + \tau_n s + \omega_n^2} \varepsilon_1(s). \end{aligned} \quad (12)$$

Considering  $\varepsilon, \varepsilon_1$  are bounded, one may let  $\varepsilon = \sigma \sin \omega t$ ,  $\varepsilon_1 = \sigma \sin \omega_1 t$ . For  $r(t) = A \cdot 1(t)$  ( $A$  is the amplitude, and  $1(t)$  is the unit step signal), one has

$$y(t) = y_r(t) + y_\varepsilon(t) + y_{\varepsilon_1}(t), \quad (13)$$

where

$$\begin{aligned} y_r(t) &= A \left[ 1 - e^{-(1/2)\tau_n t} \cosh\left(\frac{1}{2}t\sqrt{\tau_n^2 - 4\omega_n^2}\right) + \frac{\tau_n e^{-(1/2)\tau_n t}}{\sqrt{\tau_n^2 - 4\omega_n^2}} \sinh\left(\frac{1}{2}t\sqrt{\tau_n^2 - 4\omega_n^2}\right) \right], \\ y_\varepsilon(t) &= \sigma \frac{\tau_n \omega^2 \sin(\omega t) - e^{-(1/2)\tau_n t} (\omega \tau_n (\omega^2 + \omega_n^2) \sinh((1/2)t\sqrt{\tau_n^2 - 4\omega_n^2}) / \sqrt{\tau_n^2 - 4\omega_n^2}) + \omega (\omega^2 - \omega_n^2) [e^{-(1/2)\tau_n t} \cosh((1/2)t\sqrt{\tau_n^2 - 4\omega_n^2}) - \cos(\omega t)]}{\tau_n^2 \omega^2 + \omega^4 - 2\omega^2 \omega_n^2 + \omega_n^4}, \\ y_{\varepsilon_1}(t) &= -\sigma \frac{(\omega_n^4 + \tau_n^2 \omega_1^2 - \omega_1^2 \omega_n^2) \sin(\omega_1 t) - ((\tau_n^2 \omega_1^2 - 2\omega_1^2 \omega_n^2 + 2\omega_n^4) \omega_1 e^{-(1/2)\tau_n t} \sinh((1/2)t\sqrt{\tau_n^2 - 4\omega_n^2}) / \sqrt{\tau_n^2 - 4\omega_n^2}) + \tau_n \omega_1^3 [e^{-(1/2)\tau_n t} \cosh((1/2)t\sqrt{\tau_n^2 - 4\omega_n^2}) - \cos(\omega_1 t)]}{\tau_n^2 \omega_1^2 + \omega_1^4 - 2\omega_1^2 \omega_n^2 + \omega_n^4}. \end{aligned} \quad (14)$$

From (13), it can be seen clearly that both bound  $\sigma$  and frequency  $(\omega, \omega_1)$  of the estimation error  $\varepsilon, \varepsilon_1$  have effects on system output. How to reduce the influence of the estimation

errors on system output? Next, the tracking error and its steady-state value are analyzed.

The tracking error  $e(t) = r(t) - y(t)$ , and the steady-state tracking error is

$$\begin{aligned} e(\infty) &= \lim_{t \rightarrow \infty} [r(t) - y_r(t) - y_\varepsilon(t) - y_{\varepsilon_1}(t)] \\ &= \lim_{t \rightarrow \infty} \left( -\sigma \frac{\tau_n \omega^2 \sin(\omega t) - \omega (\omega^2 - \omega_n^2) \cos(\omega t)}{\tau_n^2 \omega^2 + \omega^4 - 2\omega^2 \omega_n^2 + \omega_n^4} + \sigma \frac{(\omega_n^4 + \tau_n^2 \omega_1^2 - \omega_1^2 \omega_n^2) \sin(\omega_1 t) - \tau_n \omega_1^3 \cos(\omega_1 t)}{\tau_n^2 \omega_1^2 + \omega_1^4 - 2\omega_1^2 \omega_n^2 + \omega_n^4} \right). \end{aligned} \quad (15)$$



Thus,

$$\begin{aligned}
|e(\infty)| &\leq \sigma \left[ \frac{(\omega_n^4 + \tau_n^2 \omega_1^2 - \omega_1^2 \omega_n^2) + \tau_n \omega_1^3}{\tau_n^2 \omega_1^2 + \omega_1^4 - 2\omega_1^2 \omega_n^2 + \omega_n^4} - \frac{\tau_n \omega^2 - \omega(\omega^2 - \omega_n^2)}{\tau_n^2 \omega^2 + \omega^4 - 2\omega^2 \omega_n^2 + \omega_n^4} \right] \\
&= \sigma \left[ \frac{\omega_n^4 + \tau_n^2 \omega_1^2 - \omega_1^2 \omega_n^2 + \tau_n \omega_1^3}{\tau_n^2 \omega_1^2 + (\omega_1^2 - \omega_n^2)^2} + \frac{\omega^3 - \tau_n \omega^2 - \omega \omega_n^2}{\tau_n^2 \omega^2 + (\omega^2 - \omega_n^2)^2} \right] \\
&\leq \sigma \left[ \frac{\omega_n^4 + \tau_n^2 \omega_1^2 - \omega_1^2 \omega_n^2 + \tau_n \omega_1^3}{\tau_n^2 \omega_1^2} + \frac{\omega^3 - \tau_n \omega^2 - \omega \omega_n^2}{\tau_n^2 \omega^2} \right] \\
&= \sigma \left[ \frac{\omega_n^4}{\tau_n^2 \omega_1^2} + 1 + \frac{\omega_1}{\tau_n} + \frac{\omega}{\tau_n^2} - \frac{1}{\tau_n} - \frac{\omega_n^2}{\tau_n^2 \omega} - \frac{\omega_n^2}{\tau_n^2} \right] \\
&\leq \sigma \left[ \frac{\omega_n^4}{\tau_n^2 \omega_1^2} + \frac{\omega_1}{\tau_n} + \frac{\omega}{\tau_n^2} + 1 \right], \tag{16}
\end{aligned}$$

that is

$$|e(\infty)| \leq \sigma \left[ \frac{\omega_n^4}{\tau_n^2 \omega_1^2} + \frac{\omega_1}{\tau_n} + \frac{\omega}{\tau_n^2} + 1 \right]. \tag{17}$$

From (17), one can see that the steady-state tracking error is proportional to the bound of the estimation error. Simultaneously, it is also proportional to  $\omega_n$  and inversely proportional to  $\tau_n$ .

*Remark 3.* An ESO is critical in the UADRC. From (17), it is obvious that estimation error of an ESO determine the performance of a closed-loop system greatly. Thus, a proper observer bandwidth should be selected to make the estimation error as small as possible. Then, the controlled plant can be more approximate to be a unit, and the closed-loop dynamics is much closer to the desired dynamics described in (8).

**3.3.2. Phase Analysis.** From (12), one can see that the output resulting from the set-value  $r(s)$  is

$$y_r(s) = \frac{\tau_n s + \omega_n^2}{s^2 + \tau_n s + \omega_n^2} r(s). \tag{18}$$

Thus, one has the frequency response

$$y_r(j\omega) = \frac{\omega_n^2 + j\tau_n \omega}{(\omega_n^2 - \omega^2) + j\tau_n \omega} r(j\omega). \tag{19}$$

If  $\omega_n \ll \omega$ ,  $y_r(j\omega) \approx ((\omega_n^2 + j\tau_n \omega)/((- \omega^2) + j\tau_n \omega))r(j\omega)$ , then the phase lag between the set-value and system output is

$$\begin{aligned}
\varphi_{\text{UADRC}} = \varphi_{y_r} - \varphi_r &= \arctan \frac{\tau_n(\omega^2 + \omega_n^2)}{\omega(\omega_n^2 - \tau_n^2)} \\
- \pi &\approx \arctan \frac{\tau_n \omega}{(\omega_n^2 - \tau_n^2)} - \pi. \tag{20}
\end{aligned}$$

Thus, by increasing  $\tau_n$  or decreasing  $\omega_n$ , one can reduce the phase delay  $\varphi_{\text{UADRC}}$ . In this case, the minimum phase delay is  $-\pi/2$ , and the maximum phase delay is  $-3\pi/2$ . In other words,  $-3\pi/2 < \varphi_{\text{UADRC}} < -\pi/2$ .

If  $\omega_n \gg \omega$ ,  $y_r(j\omega) \approx r(j\omega)$ , then the phase delay between the set-value and system output is

$$\varphi_{\text{UADRC}} = \varphi_{y_r} - \varphi_r \approx 0. \tag{21}$$

Thus, nearly no phase delay exists between the set-value and system output. It means that, when  $\omega_n \gg \omega$ , the UADRC can eliminate the inherent phase delay approximately.

From the analysis above, one can see that no phase delay between the control input and system output can be achieved when  $\omega_n \gg \omega$ . It signifies that, by utilizing the point of the UC, phase lag of the system response can be minimized if  $\omega_n$  is large enough.

However, the steady-state tracking error is also proportional to  $\omega_n$ . Thus, one has to make a compromise between the system response and the steady-state tracking error.

Therefore, it is obvious that approaches, like improving the estimation ability of an ESO and increasing  $\tau_n$ , are effective in reducing the steady-state tracking error. As to  $\omega_n$ , it can be determined based on the system requirements. In Section 4, numerical results are provided to confirm the UADRC. Before giving out the numerical results, two remarks have been presented.

*Remark 4.* Similar to the plants controlled by an ADRC, dynamics of a plant controlled by a UADRC is dynamically transferred to be integrators connected in series. Therefore, nonlinearities, uncertainties, and disturbances of a plant are not barriers in realizing the U-model control and guaranteeing desired system performance.

*Remark 5.* Based on the dynamic feedback linearization of a controlled plant, engineering requirements or desired closed-loop dynamics can be obtained by presetting a desired closed-loop transfer function. Thus, parameters chosen in simulations are determined by compromising desired transient and steady-state performance via try and error approach.

## 4. Simulation Studies

In order to illustrate the advantage of the UADRC, the BSM1 is utilized. It contains influent data of two weeks dynamic dry, rain, and storm weather. Those weather influent data contain the disturbances of influent rates and components. In simulations, all weather conditions are considered, and the input disturbance ( $5 \sin(5t)$ ) is also introduced from the 7th day. Two cases, i.e., constant and varying set-values, are designed in the simulations.

**4.1. Constant Set-Value of the DO Concentration.** In this part, set-value of the DO concentration is 2.0 mg/l, and simulation time lasts 14 days. To show the advantage of the UADRC, PI, SMC, and the ADRC are employed. The SMC control law can be designed as

$$u_{\text{SMC}} = \frac{1}{b_0} \left( \dot{r} + \eta \cdot \text{sat}(r - y) - \left( \frac{Q_4 S_{O,4}}{V_5} - \frac{Q_5 S_{O,5}}{V_5} \right) - D \right), \quad (22)$$

where  $\eta$  is the controller gain,  $D$  is a constant,  $Q_4$  and  $Q_5$  are flow rate of the fourth and fifth reactors,  $S_{O,4}$  and  $S_{O,5}$  are the dissolved oxygen concentration of the fourth and fifth reactors, and  $V_5$  is the volume of the fifth compartment.

System responses and performance indexes are presented to confirm the UADRC. In the BSM1, parameters of the PI controller are  $K$  and  $T_i$ . Parameters of the SMC are  $b_0$ ,  $\eta$  and  $D$ . Parameters of the ADRC are  $\omega_c$ ,  $\omega_o$ , and  $b_0$ , parameters of the UADRC are  $\tau_n$ ,  $\omega_n$ ,  $b_0$ ,  $\omega_o$ . Tunable parameters of the controllers are listed in Table 2. Here, parameters of the PI control are suggested by Reference [21].

The integral of squared error (ISE) [23], the integral of time-multiplied absolute-value of error (ITAE), and the overall cost index (OCI) [23] are selected to evaluate the tracking performance, the response rate, and the energy consumption, respectively.

$$\begin{aligned} \text{ISE} &= \int_{0 \text{ days}}^{14 \text{ days}} e^2 dt, \\ \text{ITAE} &= \int_{0 \text{ days}}^{14 \text{ days}} t \cdot |e| dt, \end{aligned} \quad (23)$$

where the tracking error  $e = r - y$ .

$$\text{OCI} = \text{AE} + \text{PE} + 5 \cdot \text{SP} + 3 \cdot \text{EC} + \text{ME}, \quad (24)$$

where AE is the aeration energy, PE is the pumping energy, SP is the sludge production to be disposed, EC is the consumption of external carbon source, and ME is the mixing energy. They can be calculated as

$$\text{AE} = \frac{S_{\text{O}}^{\text{sat}}}{T \cdot 1.8 \cdot 1000} \int_{0 \text{ days}}^{14 \text{ days}} \sum_{i=1}^5 V_i \cdot K_L a_i(t) dt, \quad (25)$$

$$\text{EC} = \frac{\text{COD}_{\text{EC}}}{T \cdot 1000} \int_{0 \text{ days}}^{14 \text{ days}} \left( \sum_{i=1}^{i=n} q_{\text{EC},i} \right) dt, \quad (26)$$

$$\text{ME} = \frac{24}{T} \int_{t=0 \text{ days}}^{t=14 \text{ days}} \sum_{i=1}^{i=5} \begin{bmatrix} 0.005 \cdot V_i & \text{if } K_L a_i(t) < 20d^{-1} \\ 0 & \text{otherwise} \end{bmatrix} \cdot dt, \quad (27)$$

$$\begin{aligned} \text{PE} &= \frac{1}{T} \int_{t=0 \text{ days}}^{t=14 \text{ days}} (0.004 \cdot Q_a(t) + 0.008 \cdot Q_r(t) \\ &+ 0.05 \cdot Q_w(t)) dt, \end{aligned} \quad (28)$$

$$\begin{aligned} \text{TSS}_s(t) &= 0.75 \cdot \sum_{j=1}^{j=10} (X_{S,j} + X_{I,j} + X_{B,H,j} + X_{B,A,j} \\ &+ X_{P,j}) \cdot z_j \cdot A, \end{aligned} \quad (29)$$

TABLE 2: Parameters of four controllers.

Controllers	$K/\omega_c/\tau_n/\eta$	$T_i/\omega_o/D$	$b_0$	$\omega_n^2$
PI	25	0.002	—	—
SMC	4500	-1300	8	—
ADRC	900	800	8	—
UADRC	900	800	8	250000

$$\text{TSS}_a(t) = 0.75 \cdot \sum_{i=1}^{i=5} (X_{S,i} + X_{I,i} + X_{B,H,i} + X_{B,A,i} + X_{P,i}) \cdot V_i, \quad (30)$$

$$\text{TSS}(t) = \text{TSS}_a(t) + \text{TSS}_s(t), \quad (31)$$

$$\begin{aligned} \text{SP} &= \frac{1}{T} \left( \text{TSS}(14 \text{ days}) - \text{TSS}(0 \text{ days}) + 0.75 \cdot \int_{t=0 \text{ days}}^{t=14 \text{ days}} (X_{S,w} \right. \\ &+ X_{I,w} + X_{B,H,w} + X_{B,A,w}) \cdot Q_w(t) \cdot dt \left. \right). \end{aligned} \quad (32)$$

Details for the parameters in (25) to (32) can be found in [21].

**4.1.1. Dry Weather.** Under dry weather, system responses and control signals of four controllers are shown in Figure 7. From the figure, it can be found that all control strategies are able to regulate the DO concentration effectively (see Figure 7(a)) with similar control signals (see Figure 7(b)). However, by comparison with the responses of PI, SMC, and ADRC, it can be easily found that the UADRC behaves best. It has the minimum fluctuations in presence of the varying components, influent rates, concentration, and the input disturbance from the 7th day. Performance indexes (ISE, ITAE), and energy cost index (OCI) are listed and compared in Table 3. Here, “+” stands for the increasing of the corresponding value, and “-” means the decreasing of the value.

From Table 3, one can find following facts. Compared with PI, ISE value of the UADRC decreases by 76.1%, and the ITAE value decreases by 84.0%. It means that the UADRC has much better tracking ability, much faster response rate, and much shorter settling time. Tracking error related indexes (i.e., ISE and ITAE values) show that control approaches based on active estimation and compensation are capable of achieving better tracking performance than PI control with the suggested parameters. Although energy consumption of the UADRC is few higher than the one of PI (increased by  $1.0 \times 10^{-3}\%$ ), it should be pointed out that the UADRC is more effective than PI. Similarly, by comparison with SMC, ISE and ITAE values of the UADRC decrease by 70.0% and 93.5%, respectively. It means that the UADRC is able to track the set-value timelier and more accurately. Additionally, energy consumption of the UADRC also decreases by  $2.9 \times 10^{-2}\%$ . Finally, compared with the ADRC, with the same observer bandwidth, ISE and ITAE value of the UADRC decreases by 15.6% and 63.1%, separately. It also confirms that the UADRC can obtain much smaller



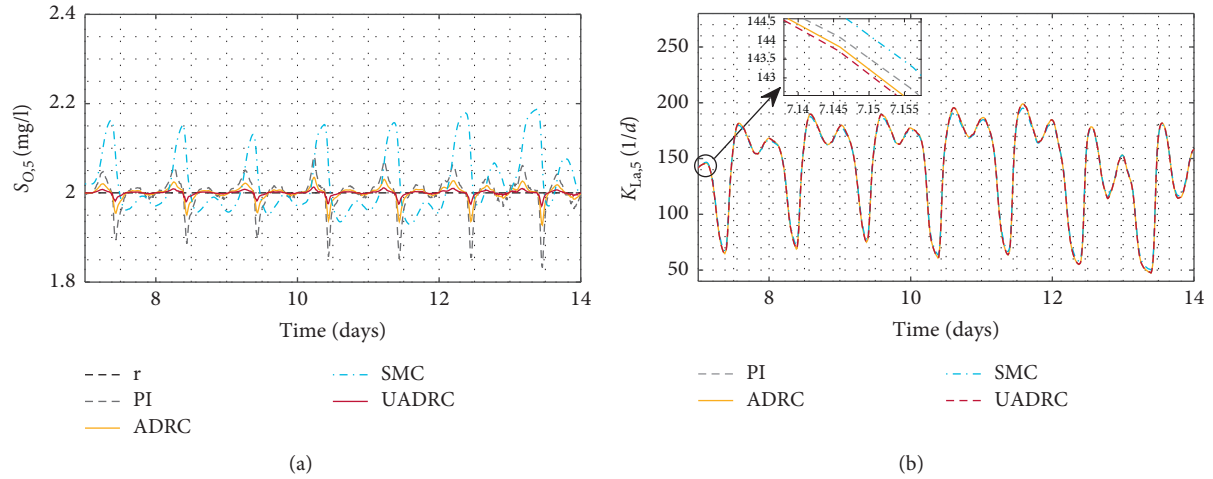


FIGURE 7: System responses and control signals for a constant set-value (under dry weather). (a) System responses. (b) Control signals.

TABLE 3: Indexes under dry weather.

	PI	SMC	ADRC	UADRC	Improvements (UADRC vs PI)	Improvements (UADRC vs SMC)	Improvements (UADRC vs. ADRC)
ISE	0.113	0.090	0.032	0.027	-76.1%	-70.0%	-15.6%
ITAE	2.085	5.134	0.903	0.333	-84.0%	-93.5%	-63.1%
OCI	17343.19	17348.32	17343.40	17343.37	$+1.0 \times 10^{-3}\%$	$-2.9 \times 10^{-2}\%$	$-1.7 \times 10^{-4}\%$

tracking errors and much shorter settling time with similar (or exactly few lower) OCI values and similar control signals (see Figure 7(b)). In other words, by minimizing the phase delay, with similar control signals and energy consumption, the UADRC behaves best.

**4.1.2. Rain Weather.** For the rain weather, PI, ADRC, SMC, and UADRC are also designed to regulate the DO concentration. Parameters are still taken from Table 2. System responses and control signals are given in Figure 8. ISE, ITAE, and OCI values are listed in Table 4.

It is easy to find that the fluctuations of the UADRC's responses are also minimum among the responses described in Figure 8(a). It means that the UADRC is able to deal with all disturbances more effectively and achieve more accurate tracking responses. Simultaneously, Figure 8(b) shows that the UADRC achieves the best tracking response with similar control signals compared with the SMC, ADRC, and PI.

Table 4 presents similar facts provided in Table 3. The UADRC is able to obtain much better ISE and ITAE values than PI. It coincides with the responses described in Figure 8(a). Similarly, ISE and ITAE values of the UADRC are also much better than the SMC and ADRC, for the minimized phase delay between the control input and system output. It is worth pointing out that few more energies are necessary for the UADRC to acquire better tracking performance and faster response rate.

**4.1.3. Storm Weather.** The influent file of storm weather contains one week of dynamic dry weather influent data and two storm events superimposed on the dry weather

data during the second week. Controller parameters are selected from Table 2. ISE, ITAE, and OCI values are listed in Table 5.

Figure 9 presents the responses and control signals of the PI, SMC, ADRC, and UADRC. From the figure, it is obvious that the UADRC is able to achieve the best tracking performance with similar control signals, even if different kinds of disturbances exist. ISE, ITAE, and OCI values listed and compared in Table 5 also confirm the fact.

Under the storm weather, data presented in Table 5 show that compared with PI, with few more energy consumption (OCI is increased by  $9.6 \times 10^{-4}\%$ ), ISE and ITAE values of the UADRC decline by 75.9% and 83.9%, respectively. Compared with the SMC, ISE, ITAE, and OCI values of the UADRC decrease by 68.2%, 93.4%, and  $2.8 \times 10^{-2}\%$ , respectively. By comparison with ADRC, lower energy (OCI decreases by  $2.3 \times 10^{-4}\%$ ) is needed by the UADRC, and ISE and ITAE values of the UADRC decline by 15.6% and 62.8%. Simultaneously, similar to dry and rain weather, the UADRC behaves best for its much smaller ISE and ITAE values and similar OCI values.

**4.2. Varying Set-Values of the DO Concentration.** In this part, varying set-values of the DO concentration are taken into consideration. Simulation time is also 14 days. PI, SMC, and ADRC are also employed to make a comparison with the UADRC. Tunable parameters of the four controllers can still be found in Table 2. Dry, rain, and storm weather conditions are considered. As described in Section 4.1, the input disturbance ( $5 \sin(5t)$ ) is also introduced from the 7th day. The changing set-values of DO concentration are described as

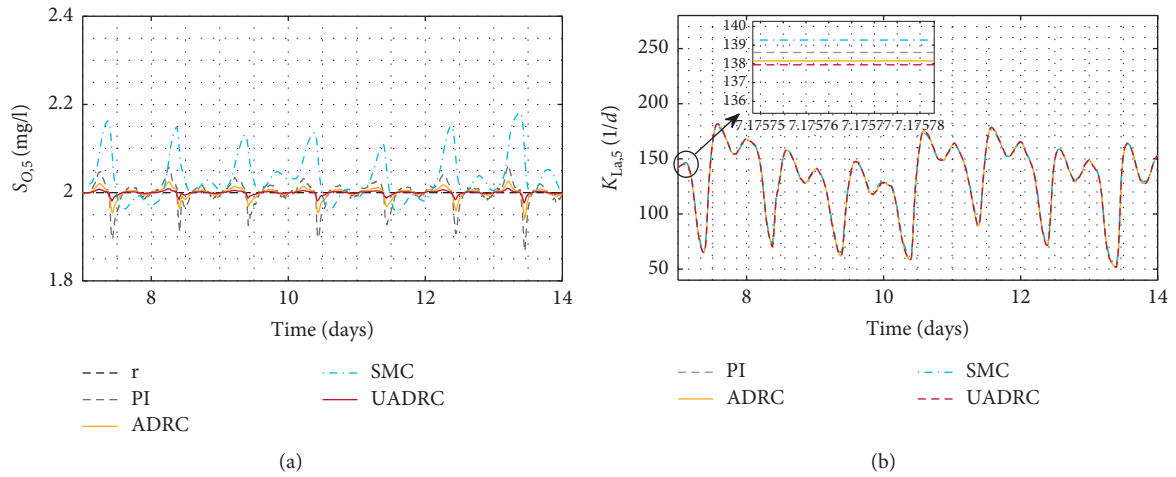


FIGURE 8: System responses and control signals for a constant set-value (under rain weather). (a) System responses. (b) Control signals.

TABLE 4: Indexes under rain weather.

	PI	SMC	ADRC	UADRC	Improvements (UADRC vs PI)	Improvements (UADRC vs SMC)	Improvements (UADRC vs ADRC)
ISE	0.109	0.080	0.031	0.027	-75.2%	-66.3%	-12.9%
ITAE	1.654	4.307	0.717	0.268	-83.8%	-93.8%	-62.6%
OCI	17128.68	17135.86	17128.87	17128.83	$+8.8 \times 10^{-4}\%$	$-4.1 \times 10^{-2}\%$	$-2.3 \times 10^{-4}\%$

TABLE 5: Indexes under storm weather.

	PI	SMC	ADRC	UADRC	Improvements (UADRC vs PI)	Improvements (UADRC vs SMC)	Improvements (UADRC vs ADRC)
ISE	0.112	0.085	0.032	0.027	-75.9%	-68.2%	-15.6%
ITAE	1.951	4.786	0.845	0.314	-83.9%	-93.4%	-62.8%
OCI	17762.79	17767.91	17763.00	17762.96	$+9.6 \times 10^{-4}\%$	$-2.8 \times 10^{-2}\%$	$-2.3 \times 10^{-4}\%$

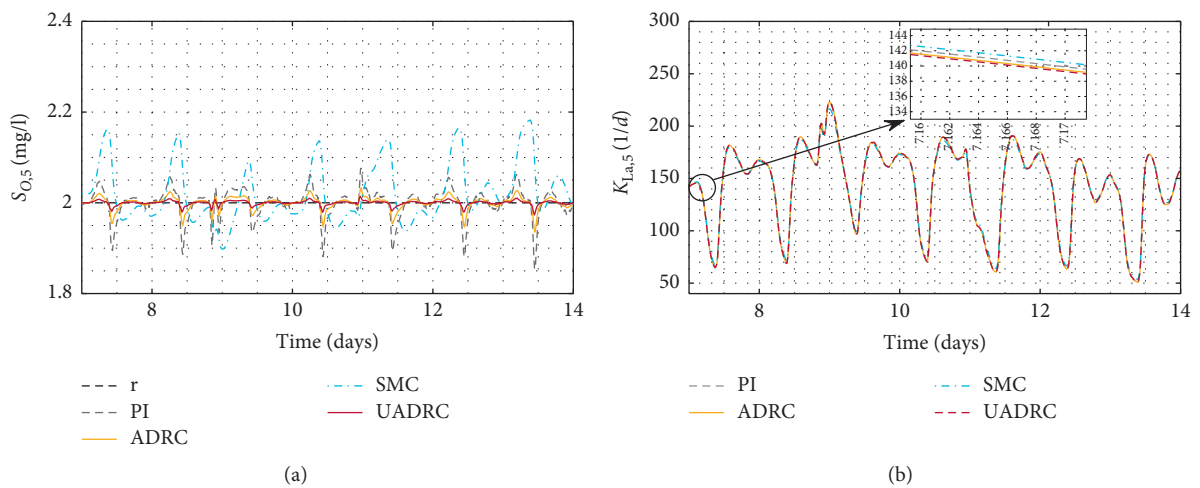


FIGURE 9: System responses and control signals for a constant set-value (under storm weather). (a) System responses. (b) Control signals.

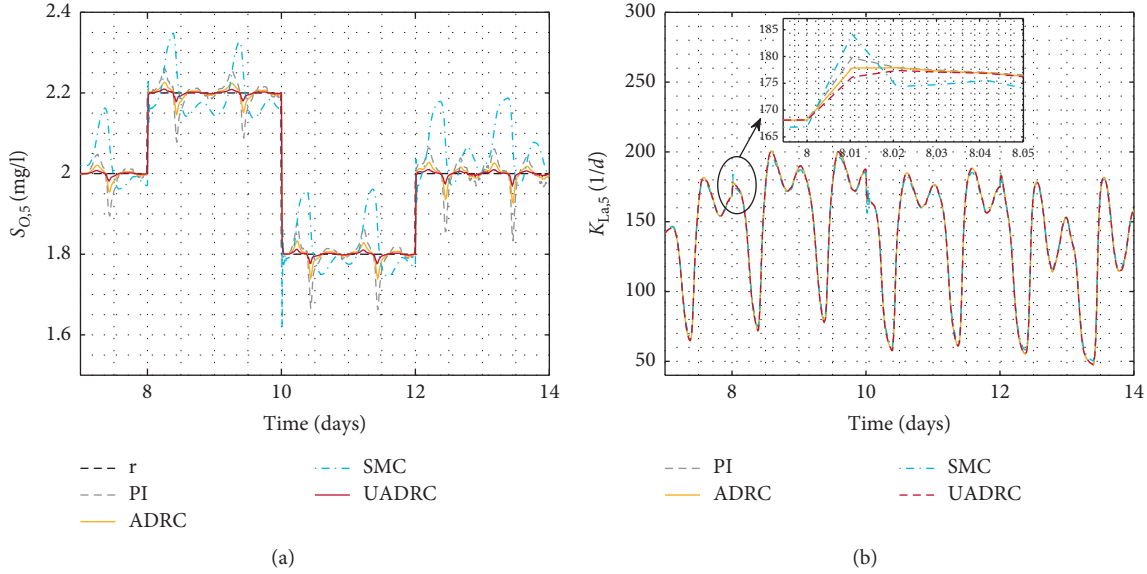


FIGURE 10: System responses and control signals for the varying set-values (under dry weather). (a) System responses. (b) Control signals.

TABLE 6: Indexes under dry weather (for varying set-values).

	PI	SMC	ADRC	UADRC	Improvements (UADRC vs PI)	Improvements (UADRC vs SMC)	Improvements (UADRC vs ADRC)
ISE	0.114	0.091	0.032	0.028	-75.4%	-69.2%	-12.5%
ITAE	2.118	5.149	0.924	0.365	-82.8%	-92.9%	-60.5%
OCI	17343.49	17348.58	17343.70	17343.67	$+1.0 \times 10^{-3}\%$	$-2.8 \times 10^{-2}\%$	$-1.7 \times 10^{-4}\%$

$$r(t) = \begin{cases} 2.2 \text{ mg/l,} & 8 \text{ days} \leq t < 10 \text{ days,} \\ 1.8 \text{ mg/l,} & 10 \text{ days} \leq t < 12 \text{ days,} \\ 2.0 \text{ mg/l,} & \text{other days.} \end{cases} \quad (33)$$

**4.2.1. Dry Weather.** Figure 10 gives out the tracking performance and control signals. From Figure 10(a), one can see clearly that the varying DO concentrations can be tracked effectively by PI, SMC, ADRC, and UADRC. In addition, the UADRC is able to track the varying DO concentrations best, even if the input disturbance from the 7th day exists. Simultaneously, control signals presented in Figure 10(b) show that the UADRC can achieve best response by similar control efforts compared with PI, SMC, and ADRC.

Table 6 presents ISE, ITAE, and OCI values of four controllers. It can be found that, compared with PI, ISE value of the UADRC decreases by 75.4%, ITAE value decreases by 82.8%, although OCI increases by  $1.0 \times 10^{-3}\%$ . Simultaneously, by comparison with the sliding-mode controller, ISE value of the UADRC decreases by 69.2%, ITAE value decreases by 92.9%, and the OCI decreases by  $2.8 \times 10^{-2}\%$ . Additionally, for the ADRC and UADRC, the latter one is able to behave much better than the former one, as a result of minimizing the phase delay between the control signal and system output. Therefore, in the WWTP described by the

BSM1, the UADRC is able to regulate the DO concentration best with similar energy consumption.

**4.2.2. Rain Weather.** For the rain weather, system responses and control signals are described in Figure 11. It demonstrates that the UADRC can achieve the best tracking performance with nearly the same control efforts when the set-value varies. Additionally, from Table 7, it can be found that, compared with PI and SMC, ISE, and ITAE values of the UADRC have been improved greatly. Simultaneously, by reducing the phase delay between the control signal and system output, the UADRC performs much better than the ADRC. From Table 7, it is also clear that all improvements are obtained by few increases of the energy consumption.

**4.2.3. Storm Weather.** System response under storm weather is shown in Figure 12. It also depicts a fact that the UADRC is capable of achieving the best DO concentration tracking. Table 8 lists the ISE, ITAE, and OCI values to confirm the advantage of UADRC. From Table 8, it can be found that, compared with the PI and SMC, ISE and ITAE values of the UADRC are much smaller. Simultaneously, for the reduced phase delay between the control signal and system output, the UADRC responds faster and more accurate than the ADRC.

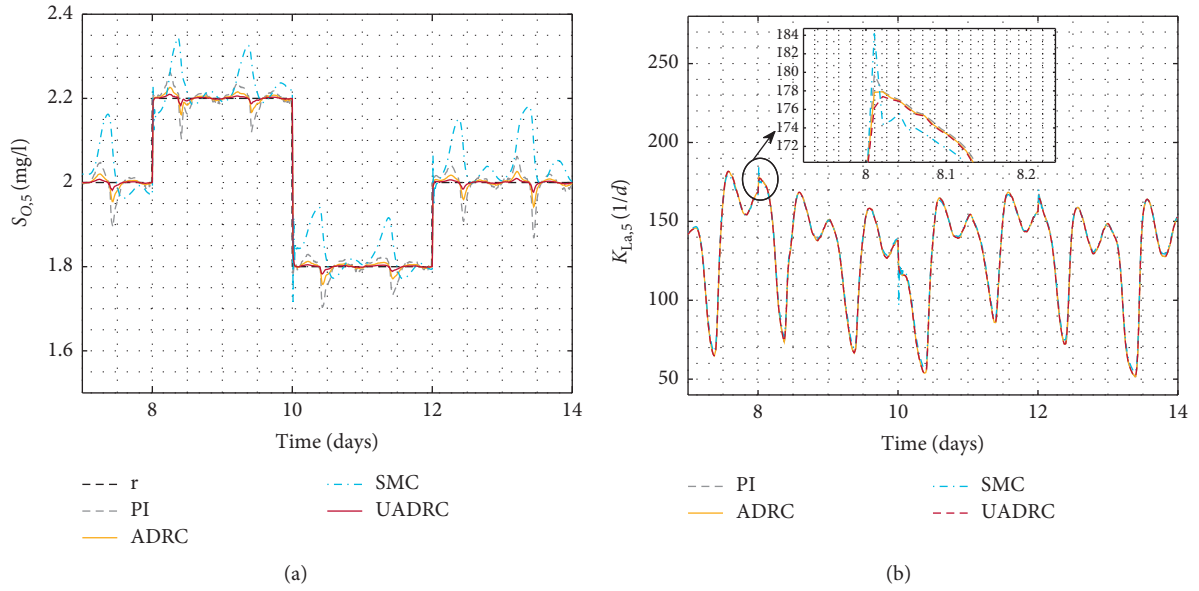


FIGURE 11: System responses and control signals for the varying set-values (under rain weather). (a) System responses. (b) Control signals.

TABLE 7: Indexes under rain weather (for varying set-values).

	PI	SMC	ADRC	UADRC	Improvements (UADRC vs PI)	Improvements (UADRC vs SMC)	Improvements (UADRC vs ADRC)
ISE	0.110	0.081	0.032	0.028	-74.5%	-65.4%	-12.5%
ITAE	1.690	4.257	0.738	0.300	-82.2%	-93.0%	-59.3%
OCI	17129.53	17136.63	17129.72	17129.67	$+8.2 \times 10^{-4}\%$	$-4.1 \times 10^{-2}\%$	$-2.9 \times 10^{-4}\%$

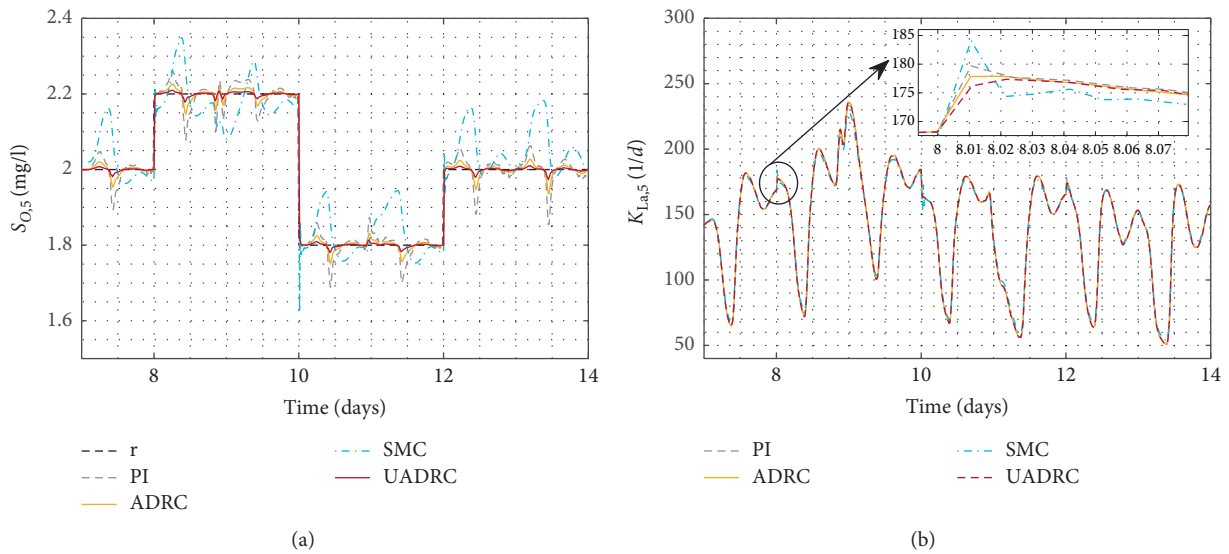


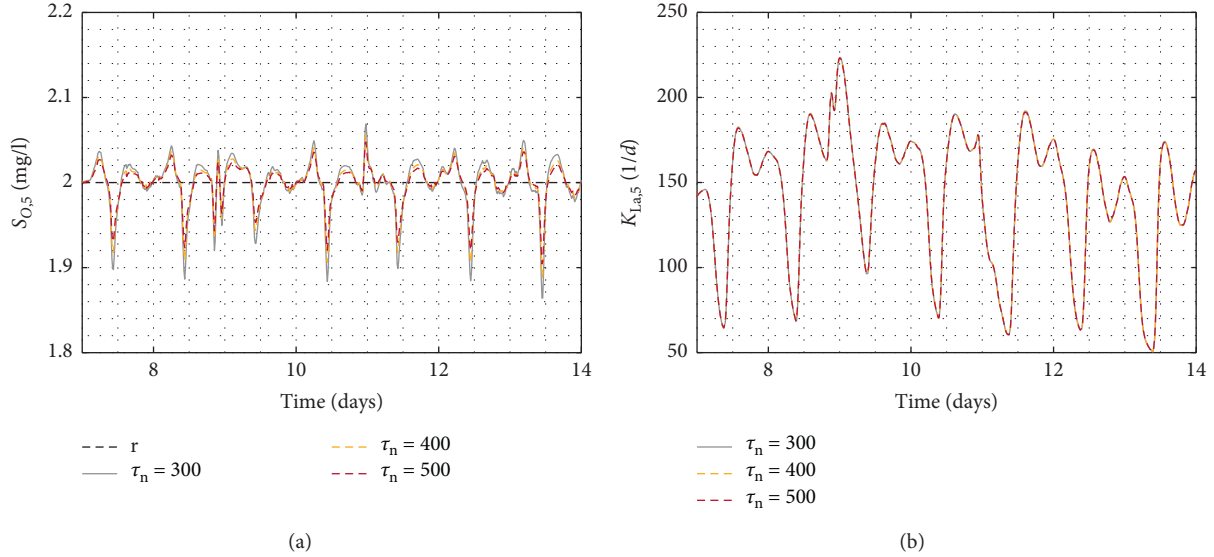
FIGURE 12: System responses and control signals for the varying set-values (under storm weather). (a) System responses. (b) Control signals.

TABLE 8: Indexes under storm weather (for varying set-values).

	PI	SMC	ADRC	UADRC	Improvements (UADRC vs PI)	Improvements (UADRC vs SMC)	Improvements (UADRC vs ADRC)
ISE	0.113	0.087	0.032	0.028	-75.2%	-67.8%	-12.5%
ITAE	1.991	4.870	0.868	0.346	-82.6%	-92.9%	-60.1%
OCI	17763.56	17768.58	17763.78	17763.74	$+1.0 \times 10^{-3}\%$	$-2.7 \times 10^{-2}\%$	$-2.3 \times 10^{-4}\%$

TABLE 9: Parameters of the UADRC ( $\omega_n$  is fixed).

	$\tau_n$		$\omega_o$	$b_0$	$\omega_n^2$
300	400	500	800	8	1600

FIGURE 13: System responses and control signals under storm weather ( $\omega_n$  is fixed). (a) System responses. (b) Control signals.

In the above sections, one can see clearly that as a result of reducing the phase delay between the control input and system output, the UADRC performs best among four controllers. Next, relationship between the closed-loop system performance and tunable parameters of the UADRC is discussed.

**4.3. Discussion.** Tunable parameters of the UADRC are  $\tau_n$ ,  $\omega_n$ ,  $b_0$ ,  $\omega_o$ . According to the results obtained in Section 3, the tracking error of the UADRC can be suppressed effectively by increasing  $\tau_n$  or improving the estimation ability of an ESO. For  $\omega_n$ , it should be made a compromise. In this part, influence of  $\omega_n$  and  $\tau_n$  on DO concentration control is discussed. Two scenarios are considered. First, fixing  $\omega_n$  and increasing  $\tau_n$ . Then, fixing  $\tau_n$ , and increasing  $\omega_n$ . The influence of  $\omega_n$  and  $\tau_n$  can be seen clearly. For complexity of the storm weather, it is considered in this section.

**4.3.1. Fixing  $\omega_n$  and Increasing  $\tau_n$ .** Here, the input disturbance ( $5 \sin(5t)$ ) is also used, and the set-value is taken to be  $r(t)$  shown in (33). Parameters of the UADRC are listed in Table 9.  $\omega_n$  is fixed to be 40, and values of  $\tau_n$  are increasing.

System responses and control signals are given in Figure 13. Table 10 lists ISE and ITAE values to show the trend of tracking error and settling time of the UADRC when  $\tau_n$  is increased. From Figure 13(a), it can be seen that, as  $\tau_n$  increases, tracking errors become smaller. The fact can also be found from Table 10. It is obvious that both ISE and ITAE values decrease as  $\tau_n$  increased. It confirms that both tracking error and settling time become smaller when  $\tau_n$  is increased.

TABLE 10: Indexes under storm weather ( $\omega_n$  is fixed).

	$\tau_n$		
	300	400	500
ISE	0.0155	0.0128	0.0115
ITAE	1.7651	1.4261	1.2155

TABLE 11: Parameters of the UADRC ( $\tau_n$  is fixed).

	$\omega_n^2$	$\omega_o$	$b_0$	$\tau_n$
4900	6400	8100	800	8
				900

**4.3.2. Fixing  $\tau_n$  and Increasing  $\omega_n$ .** Parameters of the UADRC are shown in Table 11.  $\tau_n$  is fixed to be 900, and  $\omega_n$  is increased.

System responses and control signals are shown in Figure 14. Table 12 presents the tendency of the tracking error and settling time of the UADRC with an increasing  $\omega_n$ . Numerical results indicate that, when  $\omega_n$  is increased, ISE value increases, system response rate becomes faster, and ITAE value decreases.

So far, influence of  $\tau_n$  and  $\omega_n$  is obvious. It coincides with the results obtained in Section 3. Thus, it is easier for engineers to take good advantage of the UADRC to regulate the DO concentration in a WWTP.

In addition, from the UADRC structure (see Figure 6) presented in Section 3, one can find that based on an ESO and the UC, the UADRC is an open structure for a designer to construct desired closed-loop system dynamics. Therefore, it is a flexible design approach to satisfy engineering requirements. Probably, the UADRC structure is a promising way to



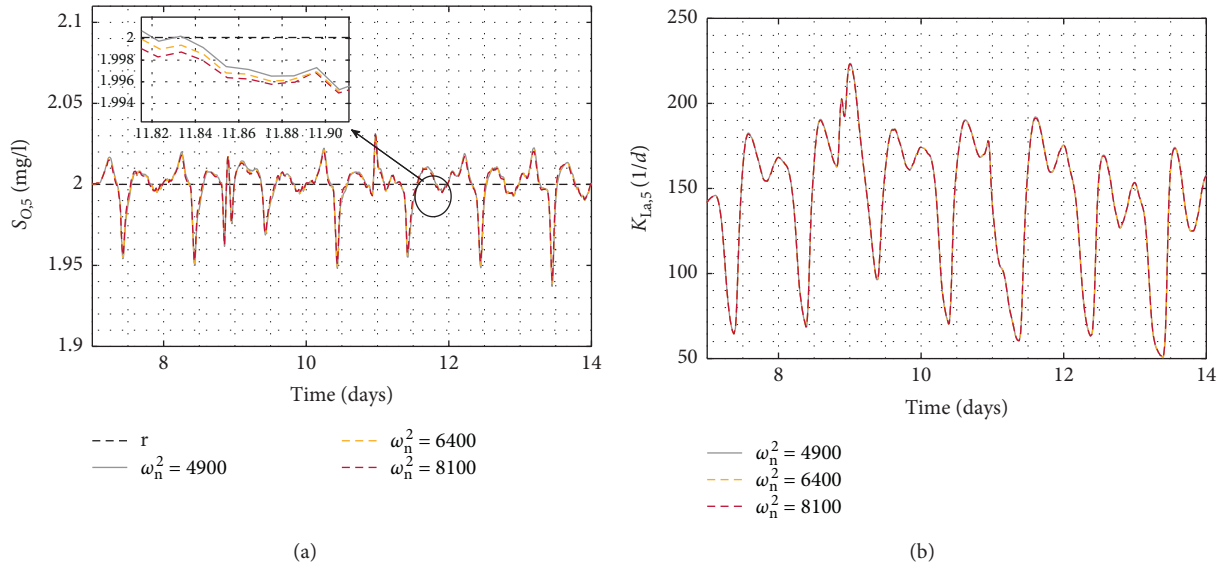


FIGURE 14: System responses and control signals under storm weather ( $\tau_n$  is fixed). (a) System responses. (b) Control signals.

TABLE 12: Indexes under dry weather ( $\tau_n$  is fixed).

	4900	6400	8100
ISE	0.0112	0.0113	0.0115
ITAE	0.7693	0.7396	0.7056

combine most existing control techniques to obtain satisfactory performance, as long as the ESO works as desired.

### 5. Conclusions

Kinds of uncertainties and disturbances exist in a WWTP. Keep the DO concentration in a desired level is always a challenge. For improving the set-value tracking and the disturbance rejection ability of a closed-loop system, based on the key point of ADRC and UC, a UADRC is constructed to control the DO concentration in a WWTP. By minimizing the phase delay between the control input and the system output, system response becomes faster. Based on the UC, system response becomes more accurate. By virtue of an ESO, system performance becomes more robust. Numerical results based on the BSM1 show that the UADRC works much better than SMC, ADRC, and the PI with suggested parameters. It confirms the advantage of the proposed UADRC. For the future research, the UADRC should be verified in a real WWTP.

### Data Availability

Data supporting the findings of this study are available from the corresponding author upon request.

### Conflicts of Interest

The authors declare that they have no conflicts of interest.

### Acknowledgments

This work was supported by the Key program of Beijing Municipal Education Commission (KZ201810011012), National Natural Science Foundation of China (61873005), and Support Project of High-level Teachers in Beijing Municipal Universities in the Period of 13th Five-year Plan (CIT&TCD201704044).

### References

- [1] World Economic Forum, "The global risks report 2019," World Economic Forum, Cologny, Switzerland, 2019.
- [2] Y. Qian, H. Dong, X. Tian et al., "A review of the research on China's water footprint responding to water crisis," *Ecological Economy*, vol. 34, no. 7, pp. 162–166, 2018.
- [3] N. Mahjouri and E. Pourmand, "A social choice-based methodology for treated wastewater reuse in urban and suburban areas," *Environmental Monitoring and Assessment*, vol. 189, no. 7, p. 325, 2017.
- [4] M. A. Shannon, P. W. Bohn, M. Elimelech, J. G. Georgiadis, B. J. Mariñas, and A. M. Mayes, "Science and technology for water purification in the coming decades," *Nature*, vol. 452, no. 7185, pp. 301–310, 2008.
- [5] J. Qiao, W. Fu, and H. Han, "Dissolved oxygen control method based on self-organizing T-S fuzzy neural network," *CIESC Journal*, vol. 67, no. 3, pp. 960–966, 2016.
- [6] A. Zhang, X. Yin, S. Liu, J. Zeng, and J. Liu, "Distributed economic model predictive control of wastewater treatment plants," *Chemical Engineering Research and Design*, vol. 141, no. 1, pp. 144–155, 2019.
- [7] I. Santín, C. Pedret, and R. Vilanova, "Applying variable dissolved oxygen set point in a two level hierarchical control structure to a wastewater treatment process," *Journal of Process Control*, vol. 28, no. 4, pp. 40–55, 2015.
- [8] H. Han, X. Wu, and J. Qiao, "A self-organizing sliding-mode controller for wastewater treatment processes," *IEEE Transactions on Control Systems Technology*, vol. 27, no. 4, pp. 1480–1491, 2019.



- [9] K. B. Newhart, R. W. Holloway, A. S. Hering, and T. Y. Cath, "Data-driven performance analyses of wastewater treatment plants: a review," *Water Research*, vol. 157, no. 6, pp. 498–513, 2019.
- [10] H.-g. Han, L. Zhang, and J.-f. Qiao, "Data-based predictive control for wastewater treatment process," *IEEE Access*, vol. 6, pp. 1498–1512, 2018.
- [11] C. Muñoz, H. Young, C. Antileo, and C. Bornhardt, "Sliding mode control of dissolved oxygen in an integrated nitrogen removal process in a sequencing batch reactor (SBR)," *Water Science and Technology*, vol. 60, no. 10, pp. 2545–2553, 2009.
- [12] D. Selisteanu, E. Petre, and V. B. Rasvan, "Sliding mode and adaptive sliding-mode control of a class of nonlinear bio-processes," *International Journal of Adaptive Control and Signal Processing*, vol. 21, no. 8-9, pp. 795–822, 2007.
- [13] R. Madonski, M. Nowicki, and P. Herman, "Application of active disturbance rejection controller to water supply system," in *Proceedings of the 33rd Chinese Control Conference*, Nanjing, China, July 2014.
- [14] W. Wei, M. Zuo, W. Li et al., "Control of dissolved oxygen for a wastewater treatment process by active disturbance rejection control approach," *Control Theory & Applications*, vol. 35, no. 1, pp. 24–30, 2018.
- [15] R. Madonski, M. Nowicki, and P. Herman, "Practical solution to positivity problem in water management systems—an ADRC approach," in *Proceedings of the 2016 American Control Conference*, Boston, MA, USA, July 2016.
- [16] M. Sadeghassadi, C. J. B. Macnab, B. Gopaluni, and D. Westwick, "Application of neural networks for optimal-setpoint design and MPC control in biological wastewater treatment," *Computers & Chemical Engineering*, vol. 115, no. 7, pp. 150–160, 2018.
- [17] J.-F. Qiao, G.-T. Han, H.-G. Han, C.-L. Yang, and W. Li, "Decoupling control for wastewater treatment process based on recurrent fuzzy neural network," *Asian Journal of Control*, vol. 21, no. 4, pp. 1–11, 2019.
- [18] Q. M. Zhu and L. Z. Guo, "A pole placement controller for non-linear dynamic plants," *Proceedings of the Institution of Mechanical Engineers, Part I: Journal of Systems and Control Engineering*, vol. 216, no. 6, pp. 467–476, 2002.
- [19] Q. Zhu, W. Zhang, J. Na, and B. Sun, "U-model based control design framework for continuous-time systems," in *Proceedings of the 38th Chinese Control Conference*, Guangzhou, China, July 2019.
- [20] J. Han, "From PID to active disturbance rejection control," *IEEE Transactions on Industrial Electronics*, vol. 56, no. 3, pp. 900–906, 2009.
- [21] J. Alex, L. Benedetti, J. Copp et al., *Benchmark Simulation Model No. 1 (bsm1)*, Lund University Sweden, Lund, Sweden, 2008.
- [22] J. Copp, *The COST Simulation Benchmark: Description and Simulator Manual*, Official Publications of the European Community, Brussels, Belgium, 2001.
- [23] J.-F. Qiao, Y. Hou, and H.-G. Han, "Optimal control for wastewater treatment process based on an adaptive multi-objective differential evolution algorithm," *Neural Computing and Applications*, vol. 31, no. 7, pp. 2537–2550, 2019.
- [24] M.-J. Lin and F. Luo, "Adaptive neural control of the dissolved oxygen concentration in WWTPs based on disturbance observer," *Neurocomputing*, vol. 185, pp. 133–141, 2016.
- [25] W. Wei, W. Xue, and D. Li, "On disturbance rejection in magnetic levitation," *Control Engineering Practice*, vol. 82, pp. 24–35, 2019.
- [26] Q. Zheng, Z. Chen, and Z. Gao, "A practical approach to disturbance decoupling control," *Control Engineering Practice*, vol. 17, no. 9, pp. 1016–1025, 2009.

## Research Article

# Design and Verification of Aeroengine Rotor Speed Controller Based on U-LADRC

Jiajie Chen, Jiqiang Wang , Yunxiao Liu, and Zhongzhi Hu

Jiangsu Province Key Laboratory of Aerospace Power Systems, Nanjing University of Aeronautics and Astronautics, Nanjing, Jiangsu 210016, China

Correspondence should be addressed to Jiqiang Wang; [jiqiang\\_wang@hotmail.com](mailto:jiqiang_wang@hotmail.com)

Received 17 December 2019; Revised 9 March 2020; Accepted 20 April 2020; Published 22 May 2020

Guest Editor: Jian Huang

Copyright © 2020 Jiajie Chen et al. This is an open access article distributed under the Creative Commons Attribution License, which permits unrestricted use, distribution, and reproduction in any medium, provided the original work is properly cited.

Due to the harsh working environment, engine electronic controller (EEC) has limited computing power. Many advanced control algorithms are difficult to be applied in practice because of complexity of calculation. In this paper, a novel aeroengine transient-speed controller with low algorithm complexity is designed by combining linear parameter varying (LPV) model with U-control theory. Aiming at restraining bad performance influence caused by possible disturbance in cruise, linear active disturbance rejection control (LADRC) compensation is integrated as the U-LADRC controller. This new controller is verified in both the digital simulation platform and hardware-in-the-loop (HIL) platform. The experimental results of the HIL platform show that the U-LADRC control algorithm meets the real-time performance of the EEC in the actual aeroengine. It has good transition state control performance and good steady-state antisturbance ability, which ensures the smooth operation of the engine in the steady state and has a good practical application prospect.

## 1. Introduction

Aeroengine is a complex time-varying nonlinear thermodynamic system, and its dynamic performance varies with the change of engine thrust and flight conditions. Because of the harsh environment and many kinds of disturbances in real working state, the engine electronic controller (EEC) has finite computational ability with around 20 ms calculation period (control algorithms cost  $\leq 5$  ms) [1]. Therefore, the characteristics of aeroengine speed controller with practical application potential should at least include the following:

- (1) Good transient and steady-state control performance
- (2) Simple structure
- (3) Low algorithm complexity
- (4) Wide range of flight envelope application
- (5) Good antisturbance ability

Up to now, only PID and LQG/LTR control method can be applied to the real EEC in aeroengine maturely [2]. But these methods still have deficiencies such as antisturbance ability of PID is limited and weight matrix of LQG/LTR is

difficult to choose. Due to the fact that advanced control algorithms such as intelligent control algorithms usually have high algorithm complexity, few of them can have practical application potential. Therefore, it is very important to create a novel control method which can meet the previous requirements 1–5.

These years, a variable scheduling controller design method based on the linear parameter varying model (LPV) has received more and more attention. In this control method, a LPV model capable of characterizing the dynamic performance of an aeroengine is first established; then the corresponding linear controller is designed directly according to the scheduling parameters in the LPV model, without interpolation and switching between the controllers. The widely used controller design method based on LPV model relies on Lyapunov function to solve linear matrix inequality (LMI) on the whole control envelope parameter trajectory, which has high complexity and difficulty in solving. It is hard for realistic application.

Aiming at this problem, this paper focuses on the simplification of the algorithm complexity and the improvement of the antisturbance performance. The LPV

model is combined with the U-control theory and the active disturbance rejection control (ADRC) theory to design a steady and transient speed controller with good real-time performance. U-control theory was originally developed by Zhu and Guo [3] in 2002. The core idea of the theory is to transform the nonlinear controlled object into a U-model structure oriented to control and then realize the online solution of the dynamic inverse of the controlled object. U-model structure is a polynomial structure that comprises time-varying system parameters. It establishes a simple general mapping which can transform almost all smooth nonlinear input-output dynamic object models into designable structures of linear control methods, simplifying the design of the controller. After more than ten years of development [4], the nonlinear control method based on U-model has been applied to predictive control [5], internal model control [6], adaptive control [7, 8], and so on. Active disturbance rejection control (ADRC) is a control method proposed by Han in the 1990s that can solve uncertain systems with a large range of complex structures [9]. The main idea is to eliminate the amplifying effect of differentiation on high-frequency disturbance by using a differential tracker, rearrange the transition process, and make full use of the role of differential feedforward. Without relying on the model, the disturbances and system uncertainties can be estimated online by extended state observer (ESO) and the corresponding compensation of control parameters can be performed in real time, which eliminates the influence of disturbances and system uncertainties on instruction tracking to the greatest extent. But the ADRC method needs to use complex algorithms and adjust too many parameters. In order to solve this problem, Gao proposes the linear active disturbance rejection control (LADRC) method [10]; it linearizes part of the control structure and reduce the number of adjusting parameters and algorithms greatly. Compared with the ADRC method, LADRC can also achieve good control results and save unnecessary engineering calculation time, which is more conducive to the realistic application. To deal with the system uncertainties, many control methods are combined with disturbance observer (DO) [11, 12] or extended state observer (ESO) [13] to improve their antidisturbance performance. Therefore, based on the principle of its linear ESO, LADRC can be used as a disturbance compensator for mismatched uncertainties aeroengines may meet during the flight mission.

In this paper, a gear turbofan (GTF) engine component-level nonlinear model is taken as the research object. First, the LPV model is established based on the nonlinear engine model. Then, the LPV model is converted into a U-model structure, and a dynamic inverse solver module is designed. A linear controller with a fixed structure was designed in series and connected to the closed-loop speed control loop to form a transient speed controller (U-controller). In order to solve the problem of poor antidisturbance ability of the controller, LADRC disturbance compensation module is introduced to compensate the effect of the aeroengine caused by disturbance in advance in steady state. The digital simulation results show that the U-LADRC rotor speed controller is successfully applied to a wide range of dynamic

speed control near the cruise steady state. At the same time, it has a good disturbance suppression effect against the atmospheric disturbance and power extraction disturbance that may exist during the cruise steady state. Finally, the hardware-in-the-loop (HIL) simulation platform was used to verify the real-time performance of the control algorithm in a real EEC. The results show that the control effect is basically the same as the digital simulation result and meets the real-time requirements of the real EEC. Besides, the U-LADRC controller significantly improves the anti-disturbance performance under steady-state conditions after the introduction of the LADRC compensator.

This paper is organized as follows: U-control concept, principle of LADRC, and aeroengine LPV model are introduced in Section 2. The design method of aeroengine U-LADRC rotor speed controller is introduced in Section 3, which is the core part in this paper. Digital simulation test is carried out to verify the transient-state control performance and steady-state antidisturbance ability preliminarily in Section 4. Section 5 shows the verification results of U-LADRC controller in the HIL platform.

## 2. Preliminaries

**2.1. U-Control Concept.** U-control method provides a kind of linear controller design method for nonlinear objects based on U-model structure. U-model uses time-varying parameter polynomial to represent a large class of smooth nonlinear systems; it consists of the power series of the current input. Consider a single-input and single-output (SISO) polynomial U-model with a triplet of  $(y(t), \lambda(t), u(t))$ , the system can be expressed as follows [14]:

$$y^{(M)}(t) = \sum_{j=0}^J \lambda_j(Y_{M-1}, U_{N-1}, \Theta) (u^{(N)}(t))^j, \quad M > N, \quad (1)$$

where

$$Y_{M-1} = [y^{(M-1)}(t), \dots, y(t)] \in R^M, \quad (2)$$

$$U_{N-1} = [u^{(N-1)}(t), \dots, u(t)] \in R^N,$$

$y^{(M)}(t) \in R$  and  $u^{(N)}(t) \in R$  are the  $M$ th and  $N$ th orders of derivatives of output  $y(t)$  and input  $u(t)$ , respectively.  $\lambda_j(t) \in R$  is the time-varying parameter absorbing all the other inputs  $Y_{M-1}$ , outputs  $U_{N-1}$ , and the coefficients  $\Theta$  associated with the input  $(u^{(N)}(t))^j$ .

The dynamic inversion is to obtain the input  $u(t)$  from  $y^{(M)}(t)$ . For a given output  $y^{(M)}(t)$ ,  $u(t)$  is solved by

$$u^{(N)}(t) \in y^{(M)}(t) - \sum_{j=0}^J \lambda_j(Y_{M-1}, U_{N-1}, \Theta) (u^{(N)}(t))^j = 0. \quad (3)$$

Simple example: consider a linear state-space model,

$$\begin{bmatrix} \dot{x}_1 \\ \dot{x}_2 \end{bmatrix} = \begin{bmatrix} 0 & 1 \\ -1 & -1 \end{bmatrix} \begin{bmatrix} x_1 \\ x_2 \end{bmatrix} + \begin{bmatrix} 2 \\ 1 \end{bmatrix} u, \quad (4)$$

$$y = [1 \ 0] \begin{bmatrix} x_1 \\ x_2 \end{bmatrix}.$$

Equation (4) can be expressed as the U-model structure:

$$\dot{y}(t) = \lambda_0(t) + \lambda_1(t)u(t), \quad (5)$$

where  $\lambda_0(t) = 3x_1(t) + x_2(t)$  and  $\lambda_1(t) = 2$ .

The dynamic inversion can be calculated as

$$u(t) = \frac{\dot{y}(t) - \lambda_0(t)}{\lambda_1(t)}. \quad (6)$$

The main idea of U-control concept is that the dynamic inversion of U-model can be served as the inverse model of the controlled nonlinear system. It is connected in series in the control system loop as the part of the controller. In this way, the remaining controller design problem for a nonlinear system can be transformed into a very simple problem. Only a linear controller for the controlled object "1" is needed to design. Figure 1 shows the closed-loop structure of U-control.

In Figure 1,  $G_{c1}$  is a linear invariant controller,  $G_p^{-1}$  is served as the dynamic inverse of the plant  $G_p$ , and  $G_{c1}$  and  $G_p^{-1}$  are designed separately to form the resultant controller  $G_c = G_{c1}G_p^{-1}$ .

## 2.2. Linear Active Disturbance Rejection Control (LADRC).

The main feature of ADRC is to estimate the unknown disturbance and the dynamic uncertainty of the system online by designing the extended state observer (ESO), so that the disturbance and unknown dynamic compensation can be performed in real time, minimizing the bad effects of disturbances and unknown dynamics on instruction tracking.

Traditional ADRC controller has many parameters which are difficult to adjust, and too many nonlinear terms are adverse to engineering application. Therefore, this paper adopts a LADRC compensator for disturbance compensation. The LADRC controller is simplified from the ADRC controller. Tracking differentiation (TD) is omitted. The nonlinear function part of the extended state observer (ESO) is changed to linear ESO, and the nonlinear PD control is changed to linear PD control. The structure of LADRC is shown in Figure 2.

The second-order controlled object is taken as an example:

$$\begin{cases} \ddot{x} = f(x, \dot{x}, d, t) + Bu, \\ y = x, \end{cases} \quad (7)$$

where  $x$ ,  $\dot{x}$ ,  $\ddot{x}$ , and  $y$  are, respectively, the system states and their first and second derivatives. The principle of LESO is

$$\begin{cases} \dot{z}_1 = z_2 - \beta_1(z_1 - y), \\ \dot{z}_2 = z_3 - \beta_2(z_1 - y) + Bu, \\ \dot{z}_3 = -\beta_3(z_1 - y), \end{cases} \quad (8)$$

where  $\beta_1, \beta_2$ , and  $\beta_3$  are adjustable parameters in LESO,  $z_1, z_2$ , and  $z_3$  represent the estimations of the output  $y$ , the differential of  $y$ , and the unknown disturbance of system, respectively. By compensating control parameters, the system can be linearized into an integrator series structure.

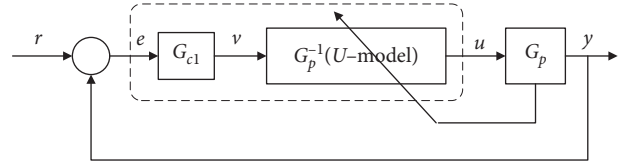


FIGURE 1: Closed-loop structure of U-control.

LESO can accurately observe various internal and external disturbances and introduce them into the control loop for compensation, so as to achieve the purpose of anti-disturbance. The reliability of LESO can be proved by frequency-domain analysis method [15] and matrix norm theory [16].

The control law in LADRC is

$$\begin{cases} u_0 = k_p(y_{kp} - z_1) - k_d z_2, \\ u = \frac{(u_0 - z_3)}{B}, \end{cases} \quad (9)$$

where  $k_p, k_d$ , and  $B$  are the control parameters of PD link. Adjustable parameters determine the quality of the observer and also greatly affect the antidisturbance ability of the control system. To maintain the stability of LADRC system,  $\beta_1, \beta_2, \beta_3, k_p$ , and  $k_d$  can be selected by the rule [17] as follows:

$$\begin{cases} \beta_1 = 3\omega_o, \\ \beta_2 = 3\omega_o^2, \\ \beta_3 = \omega_o^3, \\ k_p = \omega_c^2, \\ k_d = 2\omega, \end{cases} \quad (10)$$

where  $\omega_o$  and  $\omega_c$  are observer bandwidth and controller bandwidth. By selecting appropriate bandwidths, the LADRC system can keep a good stability [15].

**2.3. Aeroengine LPV Model.** This paper researches on a Geared Turbofan (GTF) engine, as shown in Figure 3. GTF engine represents the next generation of high-efficiency engines. In the traditional turbofan engine, the fan is directly driven by the low-pressure shaft, so the fan, LPC, and LPT cannot work in their own best rotational speeds at the same time. By using a gear box, the GTF engine solves this problem of speed contradiction. The fan can work in ideal low speed and the LPT can keep high-speed rotation, which reduces the engine noise and fuel consumption. Therefore, carrying out researches on designing the control system for this advanced engine is very necessary.

The engine model used in this research is an advanced GTF engine nonlinear component-level model provided by Toolbox for the Modeling and Analysis of Thermodynamic Systems (T-MATS) [18].

The GTF model has 3 main control parameters: fuel flow  $W_f$ , variable bleed valve (VBV), and variable-area fan nozzle (VAFN). VBV can transfer the air flow from the LPC outlet to the bypass to prevent the LPC from stalling.

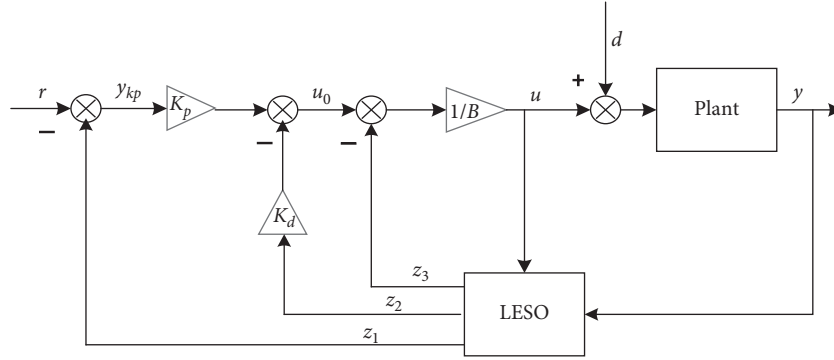


FIGURE 2: The structure of LADRC.

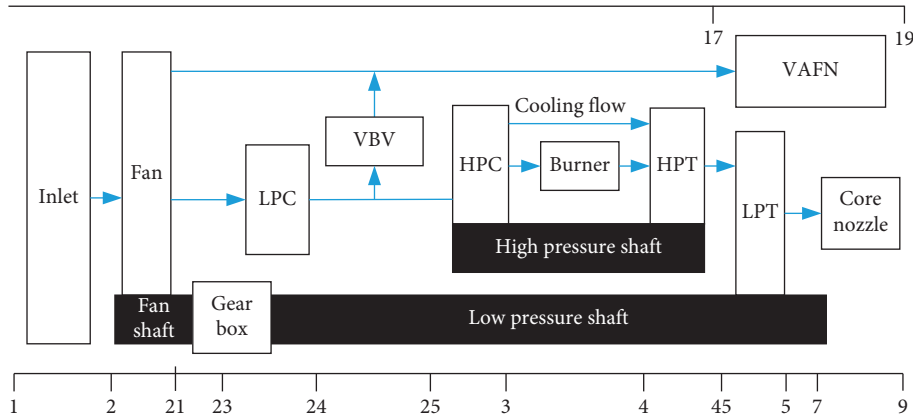


FIGURE 3: The structure of GTF engine.

VAFN maintains a specific pressure ratio at a given corrected flow rate and rotor speed to make the fan keep the optimal performance at the operating point. These two control variables are calculated by a schedule related to the flying Mach number  $Ma$  and the fan speed  $N_f$ ; they are not in the closed-loop control. The fuel flow  $W_f$  is the main control amount obtained through the closed-loop control of the control system. In the SISO model studied in this paper, the input is the fuel flow rate  $W_f$  and the output is the LP rotor speed  $N_L$ . Based on the component-level nonlinear model, the LPV model is established off-line in classical Jacobian linearization. Mathematical expression of the engine nonlinear model is shown below:

$$\begin{aligned} \dot{x} &= f(x, u), \\ y &= g(x, u), \end{aligned} \quad (11)$$

where  $f(\cdot)$  and  $g(\cdot)$  are continuously differentiable. A steady-state point  $(x_0, u_0) \in \{(x, u) \mid f(x, u) = 0\}$  is selected, and Taylor expansion is carried out ignoring the minor terms of the second order and above; we can obtain

$$\begin{aligned} f(x, u) &\approx f(x_0, u_0) + \left. \frac{\partial f}{\partial x} \right|_{(x_0, u_0)} \Delta x + \left. \frac{\partial f}{\partial u} \right|_{(x_0, u_0)} \Delta u, \\ g(x, u) &\approx g(x_0, u_0) + \left. \frac{\partial g}{\partial x} \right|_{(x_0, u_0)} \Delta x + \left. \frac{\partial g}{\partial u} \right|_{(x_0, u_0)} \Delta u, \end{aligned} \quad (12)$$

namely, the linearized model which can describe the dynamic process at neighbourhood around a steady-state point is

$$\begin{aligned} \Delta \dot{x} &= A \Delta x + B \Delta u, \\ \Delta y &= C \Delta x + D \Delta u. \end{aligned} \quad (13)$$

To study the rotor speed dynamic performance around the cruise condition, the input  $u$  is the fuel flow, and the output  $y$  represents LP/HP shaft rotational speeds. In order to avoid the ill-condition of the system matrix, the input and output parameters are normalized. The normalized fuel flow  $PW_f$  is taken as an example:

$$PW_f = \frac{W_f}{W_{fd}}, \quad (14)$$

where  $W_{fd}$  is the fuel flow in steady-state design point in cruise.

A series of normalized state-space models of steady-state points around the cruise are taken to establish the LPV model:

$$\begin{aligned} \dot{x} &= A(\theta)x + B(\theta)u, \\ y &= x, \end{aligned} \quad (15)$$

where  $x \in R^n$  is the state vector  $[\Delta PN_L \ \Delta PN_H]^T$ ;  $y \in R^n$  is the output vector  $[\Delta PN_L \ \Delta PN_H]^T$ ;  $u \in R$  is the control parameter fuel flow variation  $\Delta PW_f$ ; and  $\theta \in R$  is the

scheduling parameter normalized high-pressure rotational speed  $PN_H$ . Linear interpolation scheduling method is adopted.

In this study, for the SISO system from fuel flow to LP rotor speed, the LPV relationship between the variation of them is

$$\Delta \dot{PN}_L = a_{11}(\theta)\Delta PN_L + a_{12}(\theta)\Delta PN_H + b_1(\theta)\Delta PW_f. \quad (16)$$

### 3. Design of Aeroengine U-LADRC Controller

Affected by the harsh environment and changes in its own operating mode, aeroengines often encounter various disturbances (e.g., atmospheric disturbance, power extraction disturbance) during steady-state operation in cruise. At this time, problems such as mismatch of the LPV model may be caused, resulting in large fluctuation in the rotor speed and poor antidisturbance performance. Aiming at this problem, a LADRC fuel flow compensation module is added to improve the antidisturbance performance of the U-control algorithm. The design process of aeroengine U-LADRC rotor speed controller can be divided into two parts: design of the U-controller and design of the LADRC fuel flow compensation.

**3.1. Design of the U-Controller.** The U-controller is the core part in U-LADRC rotor speed controller which guarantees the based transient and steady-state control performance in cruise. Based on Figure 1, the design process is introduced in the following:

**3.1.1. Convert LPV Model into U-Model Structure.** Converting LPV model into first-order U-model structure,

$$\Delta \dot{PN}_L = \lambda_1 \Delta PW_f + \lambda_0, \quad (17)$$

where  $\lambda_1 = b_1(\theta)$ ,  $\lambda_0 = a_{11}(\theta)\Delta PN_L + a_{12}(\theta)\Delta PN_H$ , and  $\lambda_1$  and  $\lambda_2$  are time-varying coefficients.

**3.1.2. Calculate Dynamic Inversion  $G_p^{-1}$  Based on U-Model.** The inversion of U-model can be expressed as

$$\Delta PW_f = \frac{(\Delta \dot{PN}_L - \lambda_0)}{\lambda_1}. \quad (18)$$

Therefore, the real control parameter is

$$\begin{aligned} W_{f-U} &= W_{fst}(\theta) + \Delta W_f \\ &= W_{fst}(\theta) + \Delta PW_f \cdot W_{fd}, \end{aligned} \quad (19)$$

where  $W_{fst}(\theta)$  is the fuel flow baseline corresponding to scheduling parameter  $\theta$ .  $W_{fd}$  is the fuel flow design value which is used for normalizing fuel flow values.

**3.1.3. Design of the Linear Invariant Controller  $G_{cl}$ .** Based on U-control concept, in perfect match the  $G_p^{-1}G_p = 1$ , the design problem can be simplified as

designing a controller for a controlled object "1." There are many methods to design linear controller. In U-control condition, the easiest linear controller can be a simple gain module, or a first-order damp element. For application of engineering, here a first-order damp element is chosen. Because the LPV model is normalized, the linear controller is designed as follows:

$$G_{cl} = \frac{K}{Ts + 1}, \quad (20)$$

where  $K = (1/N_{L-s})$ ,  $N_{L-s}$  is the LP rotor speed steady-state design point in cruise. It is easy to prove that  $G_{cl}$  and the closed-loop transfer function  $G = (G_{cl}/1 + G_{cl})$  are stable.

Considering the model error "mismatch," the real plant can be described as

$$G_p' = G_p + \Delta, \quad (21)$$

where  $G_p^{-1}G_p' \neq 1$ . Defining the uncertainty of the model,

$$E = \frac{\Delta}{G_p}. \quad (22)$$

Whether it is atmospheric disturbance or power extraction disturbance discussed in the research,  $|E|$  is impossible to be too large. At least,  $|E| < 1$  is undisputed. Therefore, the following conditions are satisfied:

- (a)  $G = (G_{cl}/(1 + G_{cl}))$  is stable
- (b)  $|G(jw) \cdot E(jw)| < 1$

Based on the small gain theorem [19], the U-controller closed-loop system can keep stable.

**3.2. Design of the LADRC Fuel Flow Compensation.** LADRC fuel flow compensation takes the difference between the actual speed and the current ideal steady-state speed as the input and uses the calculated fuel correction value as the output. Take LADRC compensation control target  $r$  equal to 0 to reduce the fluctuation of LP rotor speed when the disturbance exists. Actual fuel flow at this time can be calculated as

$$W_f = W_{f-U} + W_{f-LADRC}, \quad (23)$$

where  $W_{f-LADRC}$  is calculated based on (8)~(10). In summary, the U-LADRC rotor speed control structure is shown in Figure 4. The U-LADRC rotor speed controller consists of a U-controller and a LADRC disturbance compensator. When the aeroengine is in the transient-state process, the LADRC disturbance compensator does not work and the U-controller guarantees good performance of the transient-state response. When the aeroengine is in the steady-state operating condition, the LADRC disturbance compensator is enabled to restrain the bad effects caused by various possible disturbances.

## 4. Simulation in MATLAB/Simulink

In order to verify the control and antidisturbance performance of the U-LADRC algorithm, the verification



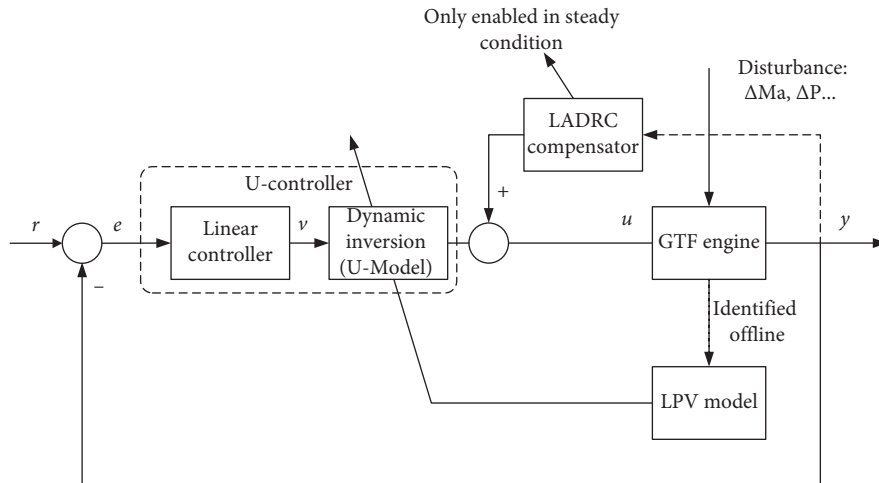


FIGURE 4: The structure of U-LADRC controller.

processes in two cases are designed on the MATLAB/Simulink digital simulation platform.

**4.1. Transient-State Process.** In the cruise condition ( $H = 35000$  ft,  $Ma = 0.8$ ), the aeroengine is simulated from normal cruise point ( $N_L = 6777$  rpm)  $\rightarrow$  lower cruise point ( $N_L = 6551$  rpm)  $\rightarrow$  normal cruise point  $\rightarrow$  upper cruise point ( $N_L = 6915$  rpm)  $\rightarrow$  normal cruise point transient state process, command speed changing curve and U-controller transient state control effect is shown in Figure 5. The fuel flow changing curve is shown in Figure 6. Simulation results show that the steady-state error is 0. The algorithm of U-controller can be preliminarily verified effectively.

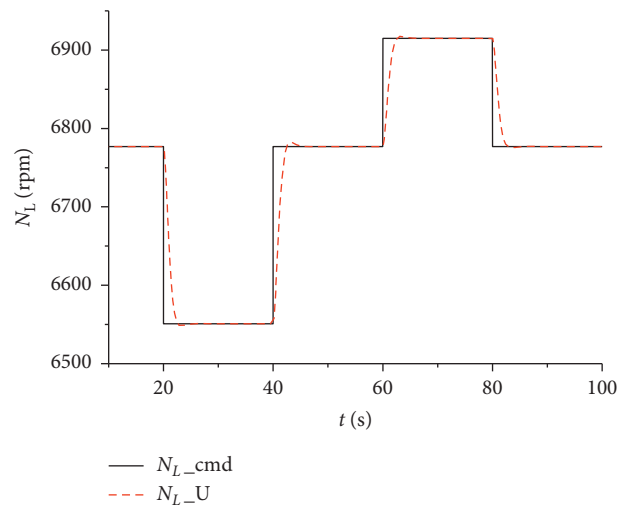


FIGURE 5: U-controller transient-state control effect.

**4.2. Steady-State with Disturbance.** In the normal cruise condition ( $H = 35000$  ft,  $Ma = 0.8$ , and  $N_L = 6777$  rpm), atmospheric disturbance and power extraction disturbance are used for simulating the disturbance suppression effect of the U-LADRC controller. Besides, the U-controller without the LADRC disturbance compensator is used as a comparison.

**4.2.1. Atmospheric Disturbance.** In this paper, Kopasakis's atmospheric turbulence model is used [20]. The combination of sine curves of unit amplitude is used to obtain the atmospheric disturbance model, which acts on the inlet of the GTF engine model. Atmospheric disturbance can cause changes in Mach number, temperature, and pressure; then it may lead to aeroengine performance becoming worse. The Kopasakis atmospheric disturbance model is shown in Figure 7.

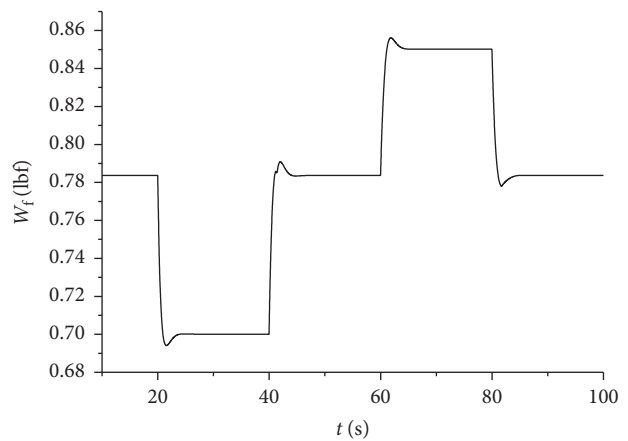


FIGURE 6: Fuel flow changing curve.

To study the antidisturbance effect of U-LADRC controller on the LP rotor speed under the atmospheric disturbance, disturbance effects of static temperature, static pressure, and Mach number are added to the inlet of the GTF engine model at the same time from 20 to 30 s. These disturbances are shown in Figure 8.

The antidisturbance effect of U-LADRC controller and U-controller without LADRC disturbance

compensator is compared in Figures 9 and 10. We can see that U-LADRC controller leads to a better antidisturbance effect with the help of advanced fuel flow

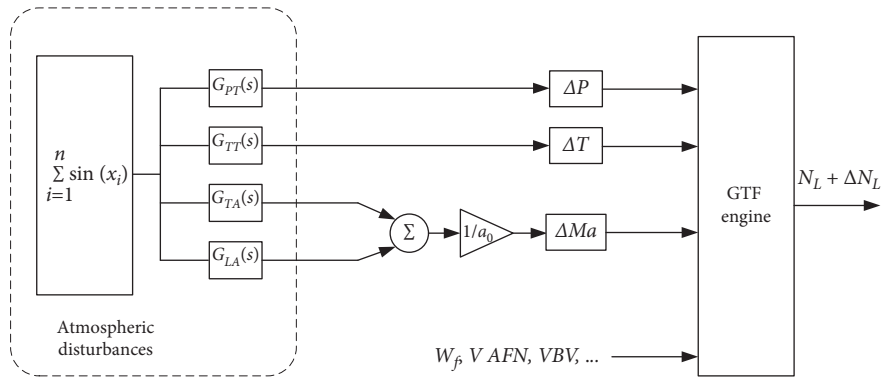


FIGURE 7: Kopasakis's atmospheric disturbance model.

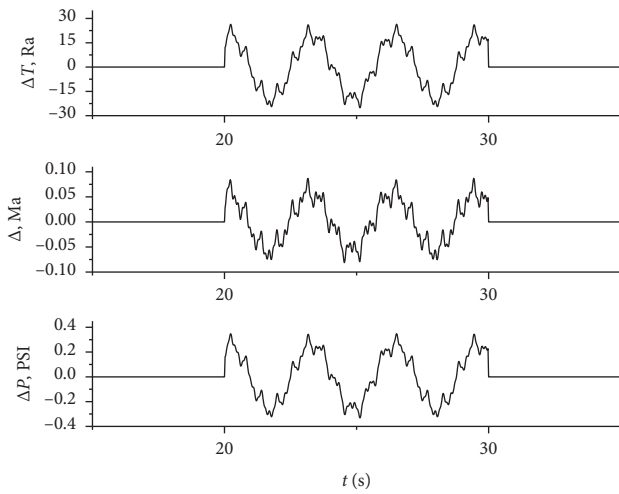


FIGURE 8: Atmospheric disturbances added in the inlet.

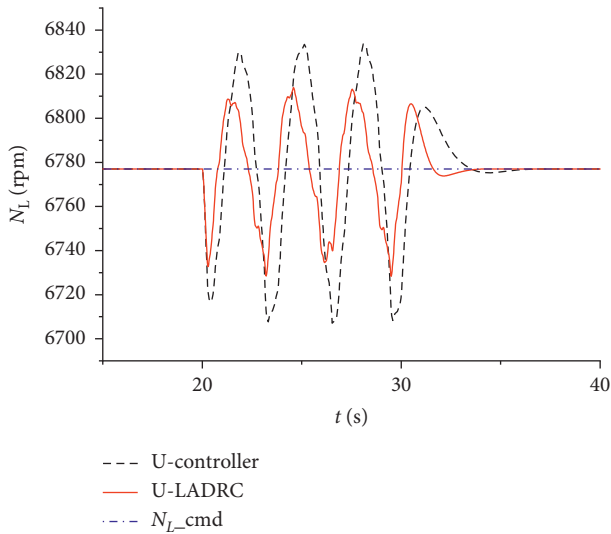


FIGURE 9: Antidisturbance effect of U-LADRC controller and U-controller in atmospheric disturbance.

compensation from the calculation of the LADRC compensator. The steady-state maximum relative variation decreases from 1.10% to 0.74%.

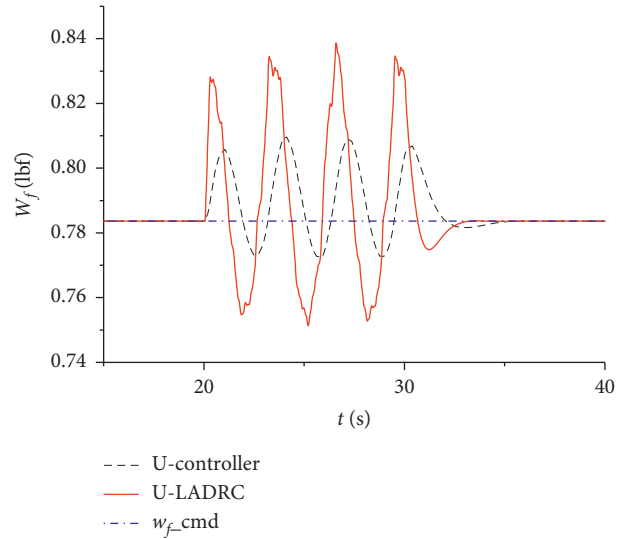


FIGURE 10: Fuel flow changing curve of U-LADRC controller and U-controller.

**4.2.2. Power Extraction Disturbance.** When the aeroengine is operating at the steady state in cruise, the electrical components on the aircraft (such as motors/generators and battery packs) may extract a certain amount of engine shaft power for power generation and storage of electrical energy [21, 22]. Power extraction can ensure the entire aircraft power energy of the system, but it is also a kind of disturbance in flight that will affect the smooth flight of the aircraft. Power extraction disturbance schematic diagram is simply shown in Figure 11.

When the HP shaft power extraction disturbance occurs, the rotor dynamic equation of HP shaft becomes

$$\frac{dN_H}{dt} = \left(\frac{30}{\pi}\right)^2 \frac{1}{N_H} \frac{1}{J_H} (\eta_h P_{HPT} - P_{HPC} - \Delta P_m). \quad (24)$$

The disturbance in  $N_H$  will affect  $N_L$  too. This section studies the antidisturbance effect of U-LADRC controller on the LP rotor speed under the HP shaft power extraction disturbance. In the digital simulation, a certain amount of horsepower is extracted from the HP shaft in 20~40 s. The power extraction plan is shown in Figure 12. During the power extraction period, the antidisturbance effect of

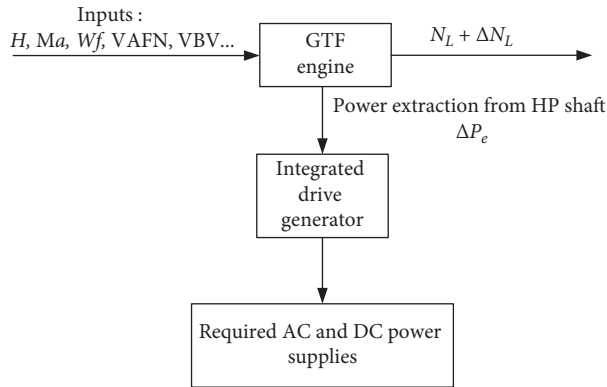


FIGURE 11: Power extraction disturbance schematic diagram.

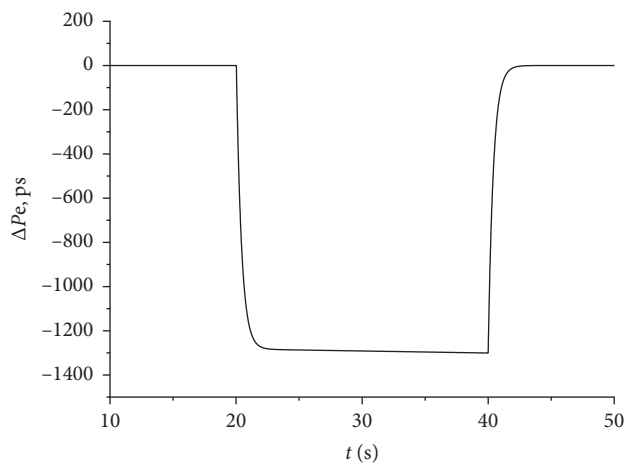


FIGURE 12: Power extraction plan in the HP shaft.

U-LADRC controller and U-controller is shown in Figure 13. The fuel flow changing curve of U-LADRC controller and U-controller is shown in Figure 14.

From Figures 13 and 14, we can see that the LADRC compensator plays the role of advanced compensation. It greatly improves the antidisturbance performance. The steady-state maximum relative variation decreases from 1.62% to 0.59%.

## 5. Verification in HIL Platform

At present, in the development of aeroengine control system, the cycle iterative design approach of “all-digital simulation,” “hardware-in-the-loop simulation (HIL),” “semi-physical simulation,” “engine platform test,” and “flight verification” is adopted, which can shorten the development cycle and reduce the design cost. Since the all-digital simulation is only a preliminary test of the control algorithm, the real-time performance of the controller cannot be verified. Therefore, with the characteristics of low difficulty, relatively low cost, and closeness to the actual operating environment of the engine, the hardware-in-the-loop simulation becomes the most important part in the development of the whole engine control system. It is very necessary to carry out the verification of controller in HIL platform.

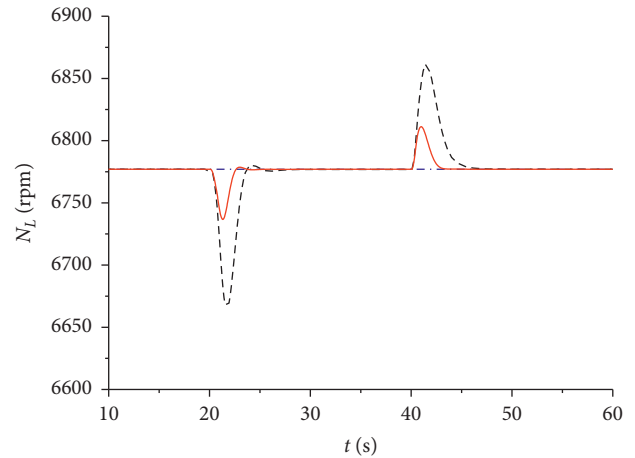


FIGURE 13: Antidisturbance effect of U-LADRC controller and U-controller.

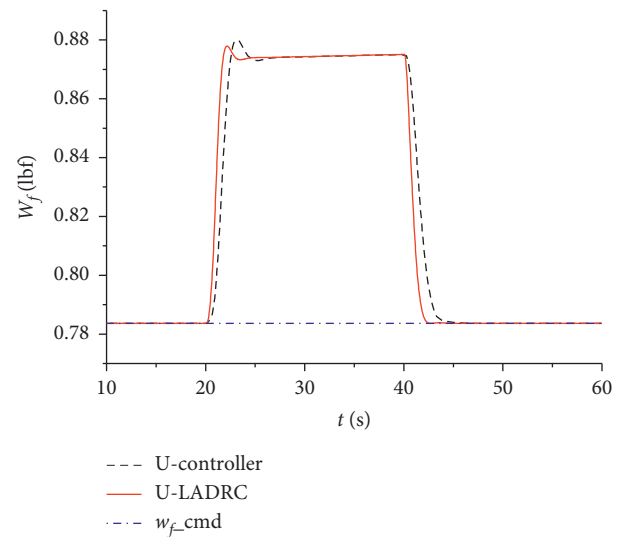


FIGURE 14: Fuel flow changing curve of U-LADRC controller and U-controller.

**5.1. Introduction of HIL Platform.** Aeroengine/gas turbine control system hardware-in-the-loop platform (hereinafter referred to as HIL platform) in Nanjing University of Aeronautics and Astronautics provides a complete integration and verification process for the engine model and control algorithm. The physical platform is shown in Figure 15.

The HIL platform has 3 parts: monitoring console, simulator, and controller. Their functions are introduced as follows:

**Monitoring console:** monitoring, operation management, and fault injection of the entire hardware-in-the-loop platform.

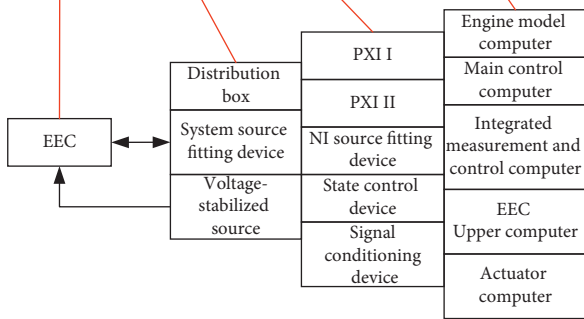
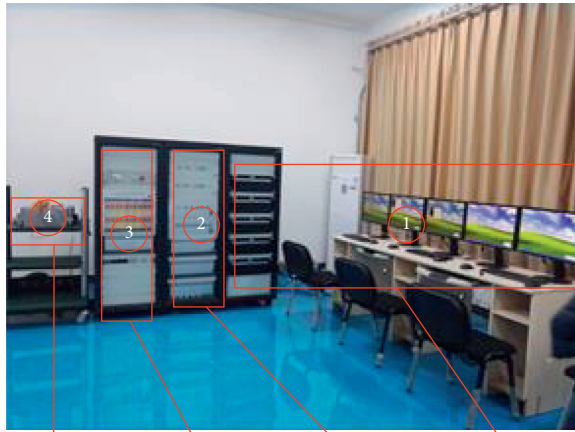


FIGURE 15: Aeroengine/gas turbine control system HIL platform in Nanjing University of Aeronautics and Astronautics.

Simulator: simulating the performance of the engine/actuator in the entire envelope, transmitting the analog signal to the digital controller, and receiving the control signal output by the controller.

Controller: consisting of EEC and EEC upper computer. EEC operates the control algorithm code to control the engine model and EEC upper computer monitors various parameters of EEC in real time.

The data flow diagram of the HIL platform is shown in Figure 16. The entire simulation process is a closed-loop structure. The engine model calculates the output speed, temperature, pressure, and other signals. The PXI industrial computer measures these signals and sends them to the signal conditioning device. After receiving the signals, signal conditioning device transmits them to the controller through the system source fitting device. The controller calculates the value of control signals through algorithms and sends these signals such as fuel flow to the engine model through the actuator model.

5.2. Code Generation and Verification Process. In this paper, model-based design (MBD) method [23] is used to verify the control and antidisturbance performance of the U-LADRC controller. The entire code generation and integration process in the HIL platform is shown in Figure 17. First, in the Simulink environment, the designed controller and GTF engine model in Section 4 are packaged and checked according to the Simulink automatic code generation specification, and the corresponding code is generated. The

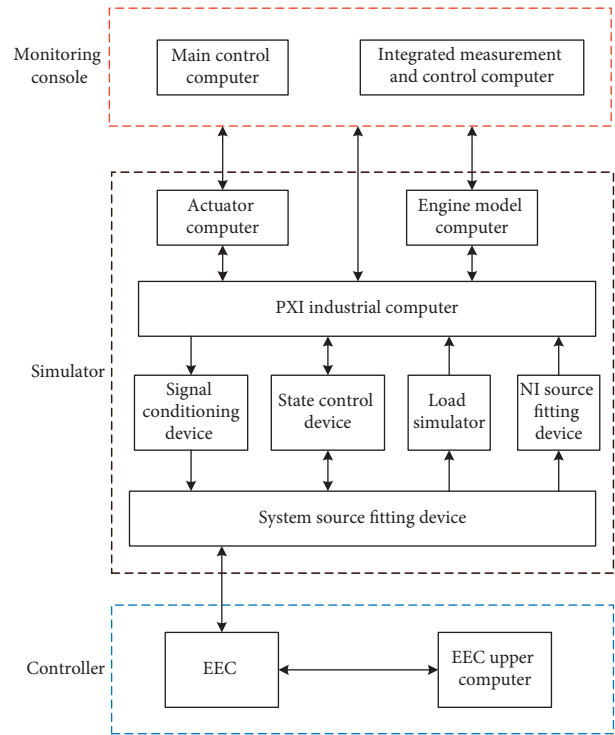


FIGURE 16: Data flow diagram of the HIL platform.

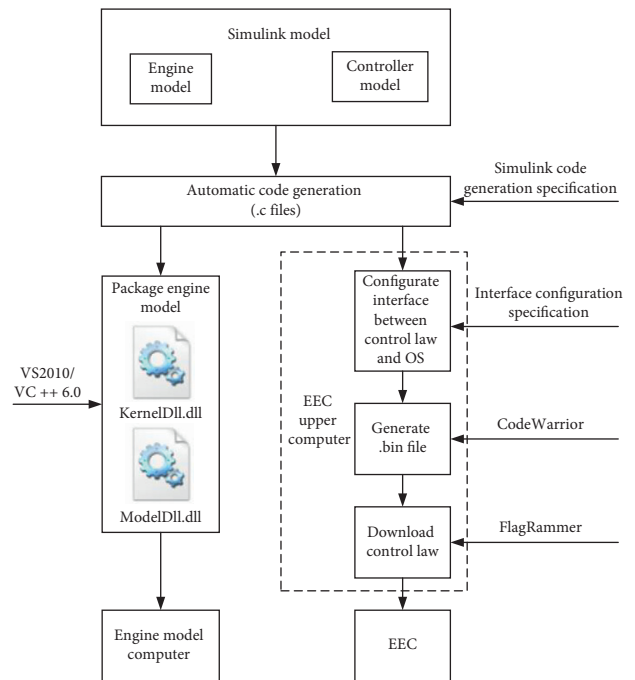


FIGURE 17: Process of code generation and integration in the HIL platform.

code of the engine model is packaged into a.dll file after two-layer integration; then, they are put into the engine model computer. The code of the controller is imported into the EEC host computer for interface configuration. When interface configuration is finished, the bin file can be generated and imported into the EEC. Then, the closed-loop

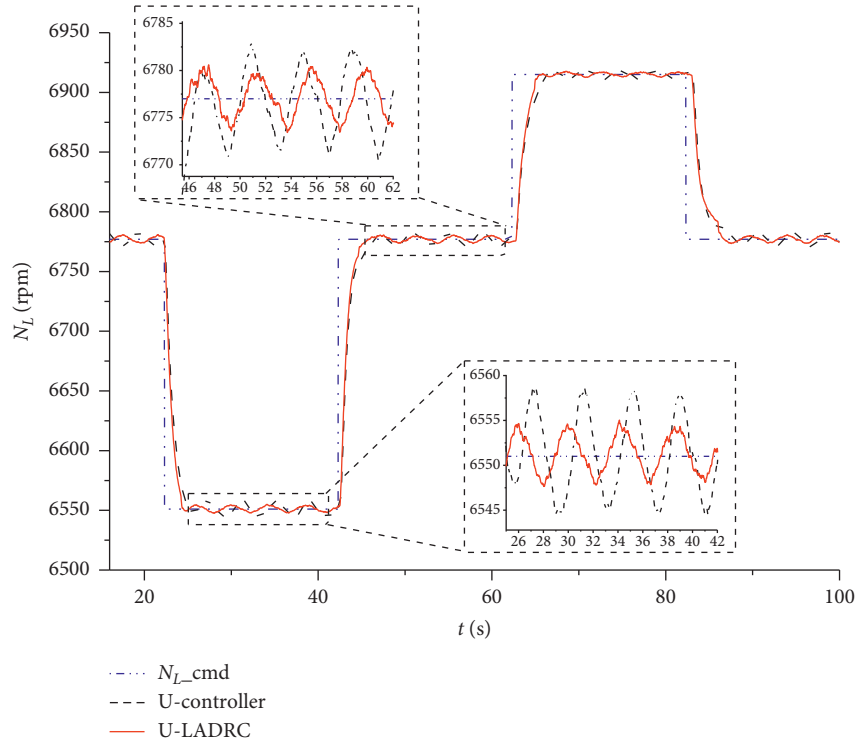


FIGURE 18: The transient-state response performance in the HIL platform.

verification test of the control algorithms under the HIL platform can be performed.

**5.3. Result Analysis.** In the HIL verification test, the same test example in the digital simulation platform is used to verify the transient-state response performance and the antidisturbance performance of the U-LADRC controller.

The transient-state response performance in the HIL platform is shown in Figure 18. Because there are many uncertain factors such as noise and voltage fluctuations in the hardware transmission link of the entire HIL platform, the sensor signal and the actuator signal may be inaccurate. These unavoidable hardware disturbances will affect the transient and steady performance, which are not considered in the digital simulation platform. In the HIL verification, the U-model controller without the LADRC compensator is used as a comparison. The experimental results show that the U-LADRC controller has a speed jitter amplitude of  $\pm 4$  rpm in the steady state of the HIL environment, which is lower than  $\pm 7$  rpm in U-model control without the LADRC compensator. U-LADRC controller has a better antidisturbance performance.

U-LADRC controller's antidisturbance performance against atmospheric disturbance and power extraction disturbance is verified in the HIL platform, too. The results are shown in Figures 19 and 20.

During the whole experimental process, the uncertain disturbance effect of the HIL platform itself is superimposed simultaneously. In order to quantitatively characterize the improvement of the antidisturbance performance before

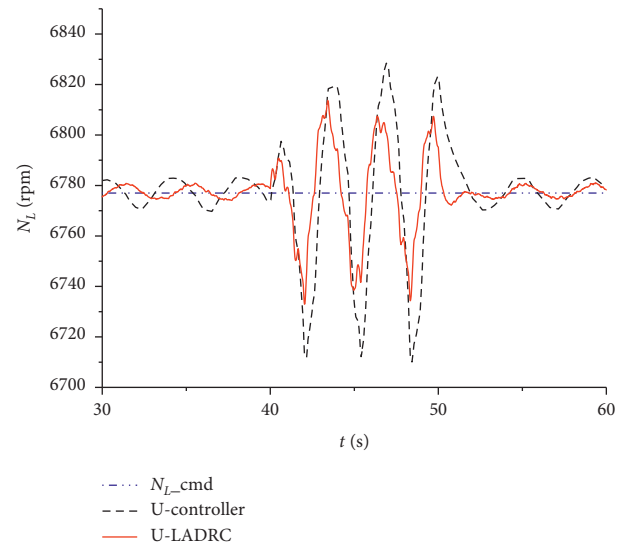


FIGURE 19: Antidisturbance effect under atmospheric disturbance in the HIL platform.

and after the addition of the LADRC compensator, the integration of absolute error (IAE) criterion is used. Performance index  $J$  is defined as

$$J = \int_{t_1}^{t_2} |N_{L\_real} - N_{L\_st}| dt, \quad (25)$$

where  $N_{L\_real}$  represents the real LP rotor speed and  $N_{L\_st}$  represents the command of LP rotor speed. The selection of  $[t_1, t_2]$  needs to include the time before and after the disturbance occurs. Assume that  $t_b$  is the beginning time of

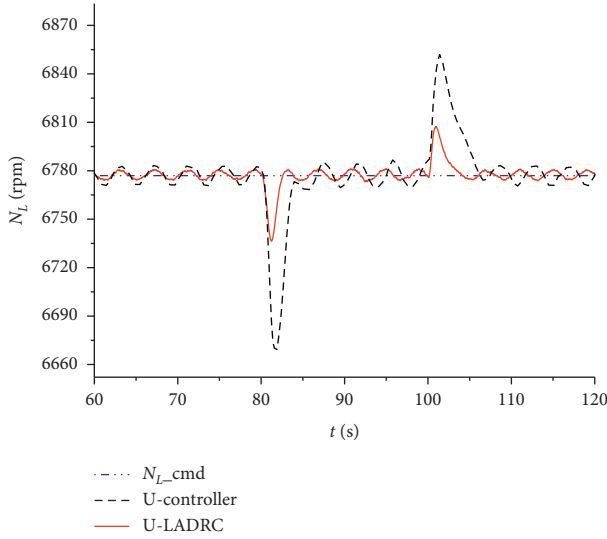


FIGURE 20: Antidisturbance effect under power extraction atmospheric disturbance in the HIL platform.

TABLE 1: Comparison of antidisturbance performance.

	$J_a$	$J_p$
U-controller	415.3867	649.7069
U-LADRC	229.1846	204.4373
Improvement (%)	44.8	68.5

the disturbance and  $t_e$  is the end time of the disturbance, and two kinds of  $J$  are defined:

$$J_a = \int_{t_b-10}^{t_e+10} |N_{L\_real} - N_{L\_st}| dt, \quad (26)$$

$$J_p = \int_{t_b-20}^{t_e+20} |N_{L\_real} - N_{L\_st}| dt, \quad (27)$$

where  $J_a$  represents the antidisturbance performance under atmospheric disturbance and  $J_p$  represents the antidisturbance performance under power extraction disturbance. Smaller  $J$  means better antidisturbance performance. The value of two kinds of  $J$  in the HIL platform test before and after the addition of the LADRC compensator is shown in Table 1.

It can be seen that the LADRC compensator greatly improves the antidisturbance performance of the U-controller.

## 6. Results

In this paper, a novel rotor speed controller was designed for a GTF engine and both digital simulation and HIL platform verification have been performed. Results are summarized as follows:

- (1) A U-control method based on the aeroengine LPV model is proposed for the first time and applied to aeroengine low-pressure speed transient and steady control. While guaranteeing the good control

performance, it greatly simplifies the complex design process of the traditional LPV gain scheduling controller.

- (2) Aiming at the problem of poor antidisturbance performance of the U-controller designed in (1), the U-LADRC controller is designed. In this controller, a LADRC compensator is added to make up for the bad effects of disturbances in advance without changing the original U-model control structure.
- (3) The LADRC compensator has a significant antidisturbance performance on various types of disturbances. Experiments results show that the antidisturbance performance of U-LADRC rotor speed controller is more than 40% higher than that of the U-controller without the LADRC compensator.
- (4) The U-LADRC rotor speed controller is successfully integrated and verified on the HIL platform to meet the real-time requirement of real EEC conditions. It has a great practical application potential.

## Data Availability

The data used to support the findings of this study are available from the corresponding author upon request.

## Conflicts of Interest

The authors declare that they have no conflicts of interest regarding the publication of this paper.

## Acknowledgments

The authors are grateful for the financial support by the Fundamental Research Funds for the Central Universities (no. NS2020017); the Central Military Commission Foundation to Strengthen Program Technology Fund (no. 2019-JCJQ-JJ-347); Major Special Basic Research Projects for Aviation Engines & Gas Turbines (no. 1002-DLJ19002); and Major Special Basic Research Projects for Green & Sustainable Manufacturing (no. 1002-DCB16001).

## References

- [1] SAE International Group, "Electronic engine control specifications and standards," Report No.: AIR4250B, SAE International Group, Warrendale, PA, USA, 2012.
- [2] S. Q. Fan, *Aircraft Engine Control*, Northwestern Polytechnical University Press, Xi'an, China, 2008.
- [3] Q. M. Zhu and L. Z. Guo, "A pole placement controller for non-linear dynamic plants," *Proceedings of the Institution of Mechanical Engineers, Part I: Journal of Systems and Control Engineering*, vol. 216, no. 6, pp. 467–476, 2002.
- [4] F. X. Xu, Q. M. Zhu, and D. Y. Zhao, "U-model based design methods for nonlinear control systems a survey of the development in the 1st decade," *Control and Decision*, vol. 28, no. 7, pp. 961–971, 2013.
- [5] W. Du, Q. M. Zhu, and X. Wu, "Support vector machine based U-model generalized predictive controller for nonlinear dynamic plants," in *Proceedings of the 33th Chinese Control Conference, IEEE press*, Nanjing, China, July 2014.



- [6] M. Shafiq and M. Haseebuddin, "U-model-based internal model control for non-linear dynamic plants," *Proceedings of the Institution of Mechanical Engineers, Part I: Journal of Systems and Control Engineering*, vol. 219, no. 6, pp. 449–458, 2005.
- [7] X. Wu, L. Liu, Q. Zhu, W. Du, B. Wang, and J. Zhang, "U-model-based adaptive control for a class of stochastic non-linear dynamic plants with unknown parameters," *International Journal of Modelling, Identification and Control*, vol. 13, no. 3, pp. 135–143, 2011.
- [8] E. Hasan, R. B. Ibrahim, S. S. A. Ali, K. Bingi, and S. F. Gilani, "U-model based adaptive control of gas process plant," *Procedia Computer Science*, vol. 105, pp. 119–124, 2017.
- [9] J. Q. Han, "Auto disturbances rejection control technique," *Frontier Science*, vol. 1, pp. 24–31, 2007.
- [10] Z. Q. Gao, "Active disturbance rejection control: a paradigm shift in feedback control system design," in *Proceedings of the 2006 American Control Conference*, pp. 2399–2405, Minneapolis, MN, USA, June 2006.
- [11] J. Huang, S. Ri, T. Fukuda, and Y. Wang, "A disturbance observer based sliding mode control for a class of under-actuated robotic system with mismatched uncertainties," *IEEE Transactions on Automatic Control*, vol. 64, no. 6, pp. 2480–2487, 2019.
- [12] J. Wang, M. Zhang, S. Ri, C. Xiong, Z. Li, and Y. Kang, "High-order disturbance-observer-based sliding mode control for mobile wheeled inverted pendulum systems," *IEEE Transactions on Industrial Electronics*, vol. 67, no. 3, pp. 2030–2041, 2020.
- [13] H. B. Zhang and J. G. Sun, "Application of active disturbance rejection control method in aeroengine afterburning transition state control," *Journal of Propulsion Technology*, vol. 31, no. 2, pp. 219–225, 2010.
- [14] Q. M. Zhu, W. C. Zhang, and J. Na, "U-model based control design framework for continuous-time systems," in *Proceedings of the Chinese Control Conference*, Wuhan, China, July 2019.
- [15] D. Yuan, X. J. Ma, and Q. H. Zeng, "Research on frequency-band characteristics and parameters configuration of linear active disturbance rejection control for second-order systems," *Control Theory & Applications*, vol. 30, pp. 1630–1640, 2013.
- [16] Z. Q. Chen, M. W. Sun, and R. G. Yang, "On the stability of linear active disturbance rejection control," *Acta Automatica Sinica*, vol. 39, no. 5, pp. 574–580, 2014.
- [17] X. Chen, D. H. Li, and Z. Q. Gao, "Tuning method for second-order active disturbance rejection control," in *Proceedings of the 30th Chinese Control Conference*, pp. 6322–6327, Yantai, China, July 2011.
- [18] J. W. Chapman and S. L. Litt, "Control design for an advanced geared turbofan engine," Report No.: NASA/TM-219569, 2017.
- [19] C. Kravaris and R. A. Wright, "Deadtime compensation for nonlinear processes," *AIChE Journal*, vol. 35, no. 9, pp. 1537–1542, 1989.
- [20] G. Kopasakis, "Atmospheric turbulence modeling for aero vehicles: fractional order fits," Report No.: NASA/TM-216961, 2010.
- [21] J. McNichols, C. Barnes, and M. Wolff, "Hardware-in-the-loop power extraction using different real-time platforms," *Nature Biotechnology*, vol. 21, no. 4, pp. 422–427, 2013.
- [22] S. J. Khalid, "Mitigating impact of bleed and power extraction with more electric architectures," in *Proceedings of the SAE 2016 Aerospace Systems and Technology Conference*, Hartford, CT, USA, September 2016.
- [23] F. R. Liu, "Model-based developing approach for airborne software of commercial engine," *Process Automation Instrumentation*, vol. 38, no. 6, pp. 26–30, 2017.

## Research Article

# Design and Control of a Novel Single Leg Structure of Electrically Driven Quadruped Robot

Mingfang Chen <sup>1</sup>, Hao Chen,<sup>1</sup> Xuejun Wang <sup>1</sup>, JiangXuan Yu,<sup>2</sup> and YongXia Zhang<sup>1</sup>

<sup>1</sup>School of Mechanical and Electrical Engineering, Kunming University of Science and Technology, Kunming, Yunnan 650000, China

<sup>2</sup>School of Nursing, Kunming Medical University, Kunming, Yunnan 650000, China

Correspondence should be addressed to Xuejun Wang; km\_wxj@kust.edu.cn

Received 24 March 2020; Revised 18 April 2020; Accepted 27 April 2020; Published 22 May 2020

Guest Editor: Weicun Zhang

Copyright © 2020 Mingfang Chen et al. This is an open access article distributed under the Creative Commons Attribution License, which permits unrestricted use, distribution, and reproduction in any medium, provided the original work is properly cited.

In order to solve the defects of the large inertia and control difficulty of the electrically driven quadruped legs of robots, a novel leg structure and a control method are proposed in this paper. In terms of structure, the motor of the knee is arranged in the body of the robot to reduce the weight of the legs. In addition, this paper improves the PVT difference control algorithm embedded in the PMAC controller. Using the nonlinear control principle of the U-model, the optimized segmented Hermite difference method is used to implement the planning of the foot trajectory of the quadruped robot. Simulation and experiment show that the leg structure design is reasonable and the improved interpolation algorithm has good control effect.

## 1. Introduction

Quadruped robots, which combine the flexibility of biped robots and the stability of hexapod robots, are widely used in flood fighting, explosive disposal, military transportation, interplanetary detective, etc. Due to their superior performance, they have attracted more and more scholars for study. In recent years, experts all over the world have continuously overcome difficulties in quadruped robots and achieved a series of experimental results [1–3]. Among them, one of the most representative robots is Big Dog, which is developed by Boston Dynamics for more than a decade [4, 5]. With a top speed of 10 km/h, the robot can transport weapons, ammunition, food, and other items to hard-to-reach areas and can cooperate with soldiers. With the support of the national high and new technology research and development plan (863 Plan), Shandong University, Harbin Technical University, Shanghai Jiao Tong University, and other institutes have made a lot of achievements in the field of quadruped robots, successfully realizing robot steady walking on the slope and gravel road surface [6–9].

When a quadruped robot walks according to the planned trajectory, it is difficult to obtain an ideal foot trajectory due to the constraints of robot structure and control mode. Therefore, trajectory generation and control of quadruped robot has always been an important subject in this research field. In literature [10] He and Ma raised a method to generate cycloid trajectory of the foot. In literature [11], Lei et al. studied the kinematics and dynamics of several common trajectories and analyzed the advantages and disadvantages of cycloidal trajectory. Wang et al. proposed an improved algorithm for zero-impact cycloid trajectory to generate a foot trajectory with section of continuous function in literature [12]. However, none of the above literatures has proposed a specific method to realize the cycloid trajectory of the quadruped robot through the controller. In this paper, we designed an electrically driven leg structure and proposed a method of generating the foot trajectory of quadruped robot for the purpose of the trajectory planning. Furthermore, the planned foot trajectory is also written into the PMAC controller to realize the foot movement.

## 2. Structure Design and Kinematics Analysis of Leg of Quadruped Robot

**2.1. Structural Design.** When a quadruped robot walks, it mainly depends on the reaction force (friction and support force) of the ground to the touching foot to drive the fuselage forward. As a result, the design of leg mechanism will directly affect the stability of the quadruped robot during walking.

There are two main factors to be considered in leg design: driving method and leg structure. The common leg structures of quadruped robots can be divided into four types: full elbow joints, full knee joints, front knee joints and back elbow joints, and front elbow joints and back knee joints (Figure 1). Through the simulation of virtual prototypes and the testing of physical prototypes, Zhang et al. believed that the quadruped robots in the form of front elbow joints and back knee joints have the characteristics of high speed, small lateral offset, low energy consumption, and small fluctuation. In addition, the four symmetrical leg structures can effectively eliminate the sway of the fuselage while walking and maintain the stability of the fuselage. Most domestic and foreign quadruped robots use this method to arrange the leg structure [13].

There are two driving modes of quadruped robot: hydraulic and servo. The hydraulic actuator changes the force mainly by changing the hydraulic pressure and has the advantages of simple structure, stable acceleration and deceleration, and good reliability. However, the liquid medium is easy to be polluted, and the cost of hydraulic components is high. The servo driver has the advantages of high standardization, simple structure, low cost, and high transmission efficiency. In this paper, from the perspective of structure and application, the servo motor with high transmission efficiency is selected as the main driving mode. In order to satisfy the three conditions of low inertia and quality of the legs and ensure good motion performance and quick recovery of the stability of the whole machine after the imbalance, the leg structure is designed according to the skeletal anatomy and bionics of German shepherd dog as is shown in Figure 2. The motors of the hip and knee joint are integrated into the side swing joint of the body. The driving moment of the knee joint is transmitted to the knee joint of the leg through parallelogram and contra-parallelogram mechanism. Four identical side swing motors are arranged symmetrically on the left and right sides. The electrically driven MQ (MCVN quadruped robot) as shown in Figure 3 is designed on the basis of the idea of front elbow joints and back knee joints.

**2.2. Kinematic Modeling.** The leg structure of quadruped robot has two degrees of freedom: hip joint and knee joint. Its structure includes parallelogram mechanism (ABCD), the contra-parallelogram mechanism (AEFG), thigh connecting rod  $l_{AG}$ , and crus connecting rod  $l_{GH}$ . The parallelogram mechanism is composed of two cranks ( $l_{BC}$  and  $l_{AD}$ ) and two connecting rods ( $l_{AB}$  and  $l_{DC}$ ), while the contra-parallelogram mechanism is composed of two cranks ( $l_{AE}$

and  $l_{FG}$ ) and one connecting rod  $l_{AG}$  (Figure 4). By driving the crank  $l_{BC}$  of parallelogram and the  $l_{AG}$  of connecting rod of thigh, the foot can perform specific movements in  $XY$  plane [14, 15].

In light of the geometric characteristics of parallelogram and contra-parallelogram mechanisms, the corresponding angle relationship can be calculated, where  $\text{lin } l_{FGH}$  is the same linkage with an angle of 170 degrees. Constructing auxiliary dotted lines as shown in Figure 4, the corresponding sides in triangle AEF and triangle AFG, triangle AEG, and triangle FGE are all equal, so they are congruent triangles. If  $\theta_1$  and  $\theta_2$  are known,  $\theta_3$  can be calculated through the cosine theorem (the length of each rod is known):

$$\alpha_1 = \theta_2 - 10^\circ, \quad (1)$$

$$l_{AF}^2 = l_{FG}^2 + l_{AG}^2 - 2l_{FG}l_{AG} \cos \alpha_1, \quad (2)$$

$$\cos \alpha_2 = \frac{l_{AF}^2 + l_{FG}^2 - l_{AG}^2}{2l_{AF}l_{FG}}, \quad (3)$$

$$\alpha_3 = 180^\circ - \alpha_1 - \alpha_2, \quad (4)$$

$$\theta_3 = 370^\circ - (\theta_1 + \theta_2 + 2\alpha_2). \quad (5)$$

Equations (1)–(5) can be sorted out as follows:

$$\theta_3 = 370^\circ - \left( \theta_2 + \theta_2 + 2a \cos \frac{l_{FG} - l_{AG}(\theta_2 - 10^\circ)}{\sqrt{l_{FG}^2 + l_{AG}^2 - 2l_{FG}l_{AG} \cos(\theta_2 - 10^\circ)}} \right), \quad (6)$$

where the parameters of each connecting rod of leg joint of quadruped robot are shown in Table 1:

Similarly, if the  $\theta_3$  and  $\theta_1$  are known, knee angle  $\theta_2$  can be calculated as follows:

$$\theta_2 = 10^\circ + 2a \cos \left( \frac{l_{AE} + l_{AG} \cos(\theta_1 + \theta_3)}{\sqrt{l_{AG}^2 + l_{AE}^2 + 2l_{AG}l_{AE} \cos(\theta_1 + \theta_3)}} \right) - (\theta_1 + \theta_3). \quad (7)$$

**2.3. Forward and Inverse Kinematics.** D-H (Denavit Hartenberg) coordinate method is used to analyze the kinematics of quadruped robot [16–19]. Due to the complexity of D-H coordinate and the characteristics of parallelogram and contra-parallelogram linkage mechanism, the leg model of the quadruped robot is simplified in kinematics analysis. According to the conversion relationship between equations (6) and (7), the actual rotation angle of the servo motor is mapped into the D-H coordinate system. In addition, on the basis of rules of D-H coordinate system, the fixed reference coordinates ( $X_0, Y_0, Z_0$ ) at hip joint A are first determined, then the common vertical lines of joint axes 1 and 2 are obtained. Their intersection points are the origin of the link coordinate system  $\{1\}$ . In line with the difficulty of calculation, the direction of axis  $Z_1$  is confirmed; meanwhile the positive direction of axis  $X_1$  as the direction of the common vertical line mentioned above is specified. Finally, the

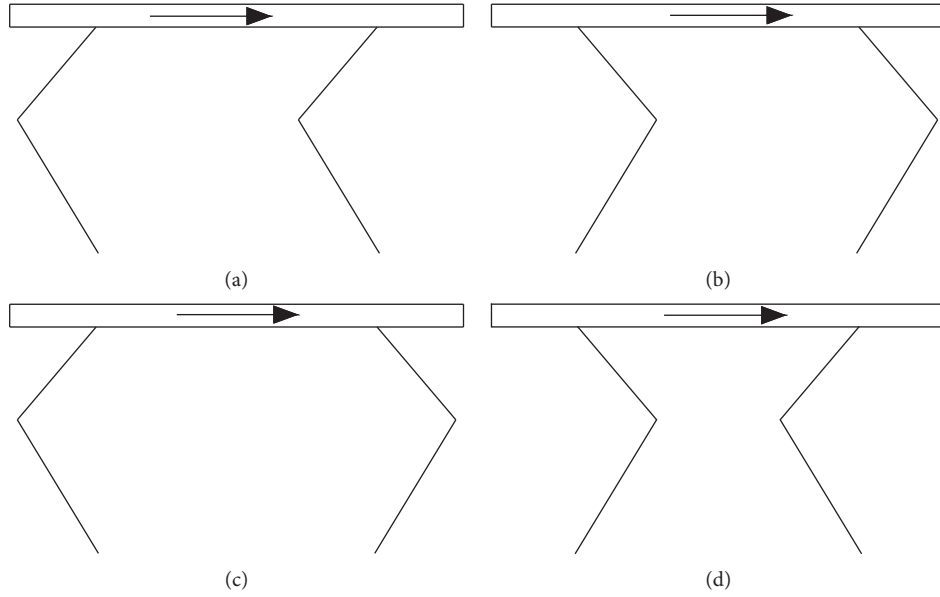


FIGURE 1: Leg structure of quadruped robot: (a) full elbow joints, (b) full knee joints, (c) front knee joints and back elbow joints, and (d) front elbow joints and back knee joints.

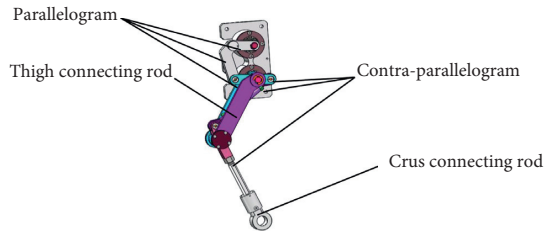


FIGURE 2: Single-leg 3d design model.

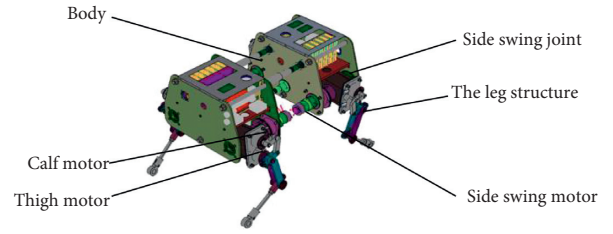


FIGURE 3: Three-dimensional design model of the whole machine.

direction of  $Y_1$  is determined by the right hand rule. Similarly, the linkage coordinate systems  $\{2\}$  and  $\{3\}$  can be established. The D-H coordinates of the swinging phase of the quadruped robot are shown in Figure 5.

D-H related parameters are shown in Table 2.

For the D-H coordinate system with  $n$  joints, the coordinate transformation of link  $i$  relative to link  $i-1$  is  ${}_{i-1}^{i}T$ :

$${}_{i-1}^{i}T = \begin{bmatrix} c\theta_i & -s\theta_i & 0 & a_{i-1} \\ s\theta_i c\alpha_{i-1} & c\theta_i c\alpha_{i-1} & -s\alpha_{i-1} & -s\alpha_{i-1}d_i \\ s\theta_i s\alpha_{i-1} & c\theta_i s\alpha_{i-1} & c\alpha_{i-1} & c\alpha_{i-1}d_i \\ 0 & 0 & 0 & 1 \end{bmatrix}, \quad (8)$$

where  $c\theta_i = \cos(\theta_i)$ ;  $s\theta_i = \sin(\theta_i)$ ;  $c\alpha_i = \cos(\alpha_i)$ ;  $s\alpha_i = \sin(\alpha_i)$ ;  $l_i$  is the length of connecting rod;  $\theta_i$  is the joint angle;  $\alpha_i$  is the connecting rod angle; and  $d_i$  is the offset of connecting rod.

According to the above D-H coordinate transformation, the attitude and position change of reference coordinate system  $\{3\}$  relative to base coordinate system  $\{0\}$  can be obtained as shown in the following equation:

$${}^0_3T = {}^0_1T_1{}^1_2T_2{}^2_3T_3 = \begin{bmatrix} c_{12} & -s_{12} & 0 & l_{AG}c_{12} + l_{GH}c_{12} \\ s_{12} & c_{12} & 1 & l_{AG}s_{12} + l_{GH}s_{12} \\ 0 & 0 & 1 & 0 \\ 0 & 0 & 0 & 1 \end{bmatrix}, \quad (9)$$

where  $c_{12} = \cos(\theta_1 + \theta_2)$  and  $s_{12} = \sin(\theta_1 + \theta_2)$ .

Through geometric analysis, the inverse kinematic solution of the leg linkage can be received as shown in the following equation:

$$\begin{cases} \theta_1 = A \tan 2(y, x) - A \cos\left(\frac{x^2 + y^2 + l_{AG}^2 - l_{GH}^2}{2l_{AG}\sqrt{x^2 + y^2}}\right), \\ \theta_2 = A \cos\left(\frac{x^2 + y^2 - l_{AG}^2 - l_{GH}^2}{2l_{AG}l_{GH}}\right), \end{cases} \quad (10)$$

where  $(x, y)$  is the position of the robot foot in the space coordinate  $\{0\}$ .

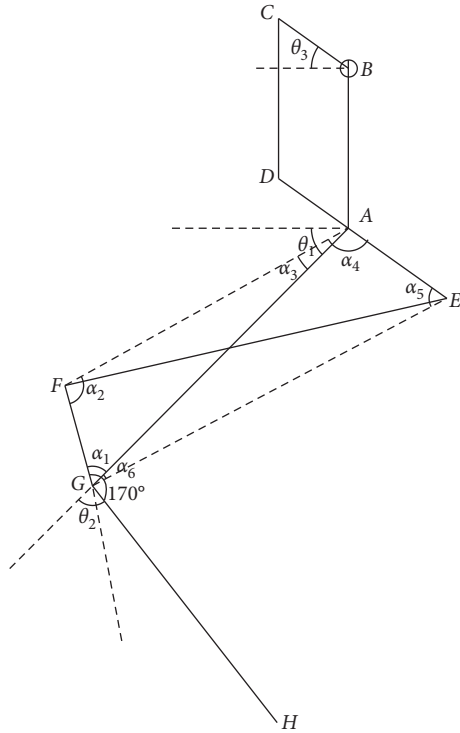


FIGURE 4: Schematic diagram of the motion model.

TABLE 1: Joint parameters of quadruped robot.

Joint	Size (mm)	Initial phase (°)
Thigh connecting rod $l_{AG}$	170	40
Crus connecting rod $l_{GH}$	250	80
Parallelogram $l_{AD}/l_{BC}$	50/84	
Contra-parallelogram $l_{AE}/l_{EF}$	34/170	

### 3. Foot Workspace Analysis and Trajectory Planning

**3.1. Foot Workspace Analysis.** The foot workspace of a quadruped robot, which is one of the important indexes to measure the motion performance, is a collection of points of spatial position that can be reached. However, the workspace of each robot is only related to its own characteristic parameters. At present, analytic, numerical, and graphical methods are usually used to solve the workspace. The analytic method usually solves the workspace boundary by linear or nonlinear function relationship between the joints. In addition, its expression is relatively complex and is not suitable for applications in practical engineering [20]. The graphical method is intuitive, but it is limited by the degree of freedom. When the degree of freedom exceeds three, graphical methods usually require grouping [21]. What is more, it only needs to select as many different joint variables as possible in the numerical method. It can use the forward kinematics of the robot to solve the foot coordinates. The boundary surface formed by the coordinate points is the working interval of the robot.

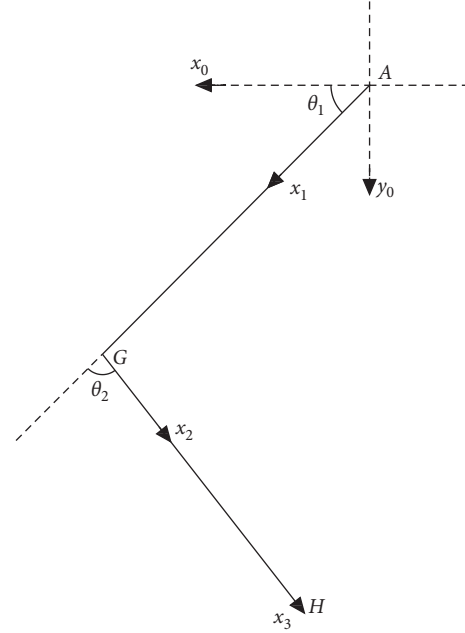


FIGURE 5: D-H coordinates of quadruped robot.

Typical numerical methods include search method, iteration method, and Monte Carlo method. In this paper, Monte Carlo method is adopted to calculate the working space of the robot foot. The specific steps are as follows:

- (1) The forward kinematics of the leg mechanism is calculated
- (2) The random variables of each joint of the robot are calculated, including the constraint relationship between the angles of each joint
- (3) The boundary surface of foot workspace is drawn by MATLAB

**3.2. Foot Trajectory Planning and Interpolation Control.** In this paper, PMAC programmable multi-axis motion controller from Delta-Tau-Data-System company is selected as the main controller to control the leg servo motor. The method of calculating other points between known points based on a particular algorithm is called interpolation control. Common interpolation algorithms include line, arc, and PVT (Position Velocity and Time). The curve velocity calculated by the linear algorithm is not smooth and has acceleration and deceleration errors and is not suitable for accurate control [22]. Arc algorithm is suitable for rough interpolation and is usually mixed with other algorithms [23]. The essence of PVT algorithm is Hermite interpolation, which can generate more intuitive control curves [24, 25]. According to the position and velocity of the initial point and the position and velocity of the end point, the position and velocity of any curve at any time in the curve section can be approximately solved under the PVT mode. Furthermore, the velocity variation received is relatively smooth.

TABLE 2: D-H coordinate parameters of four-legged robot with single leg.

Serial number $i$	Connecting rod rotation angle $\alpha_{i-1}$	Connecting rod length $a_{i-1}$	Joint angle $\theta$	Connecting rod offset $d_i$
1	0	0	$\theta_1$	0
2	0	$l_{AG}$	$\theta_2$	0
3	0	$l_{GH}$	0	0

**3.2.1. Foot Trajectory Planning.** The movement process of quadruped robot is divided into swing and support phase. In swing phase, the length and height step have an important impact on the performance of the whole machine. In supporting the phase, the foot of the robot is always in contact with the ground, and the trajectory formed is usually a simple straight line. Therefore, the movement of the swinging phase is only to be considered in the trajectory planning. In order to reduce the impact of the foot on the ground and prevent the foot from sliding with the ground, the lifting and landing speed of the swing stage are both zero. As the trajectory of the quadruped robot is relatively free, a variety of curves, which met the above requirements, can be designed.

In this paper, a piecewise interpolation method based on known points in the workspace is proposed. At the same time, in order to facilitate the writing of trajectory function into PMAC controller, a more intuitive PVT interpolation algorithm is selected. Because the PVT interpolation function of the controller itself does not make a specific study on the selection method of segment points, the segmented point selection and the foot track characteristics of the quadruped robot based on the original PVT interpolation function are studied in this paper. The Hermite interpolation (PVT) cubic polynomial of a curve segment can be expressed as follows:

$$p(t) = \left(1 + 2\frac{t-t_k}{h_k}\right)\left(\frac{t-t_{k+1}}{h_k}\right)^2 p_k + \left(1 - 2\frac{t-t_{k+1}}{h_k}\right)\left(\frac{t-t_k}{h_k}\right)^2 p_{k+1} \\ + (t-t_k)\left(\frac{t-t_{k+1}}{h_k}\right)^2 v_k + (t-t_{k+1})\left(\frac{t-t_k}{h_k}\right)^2 v_{k+1}, \quad (11)$$

where  $p_k$  and  $p_{k+1}$  are the track points at time  $t_k$  and  $t_{k+1}$ , respectively;  $v_k$  and  $v_{k+1}$  are the velocities at time  $v_k$  and  $v_{k+1}$  respectively;  $h_k = t_{k+1} - t_k$  represents the time interval within the current subsection.

At the same time, in order to get a relatively smooth curve of velocity change, the proportional coefficient  $C$  was introduced in literature [26]. As shown in equation (12), the relationship between velocity and position increment is adjusted by area method. Typical velocity variation curves that used Hermite interpolation are shown in Figure 6:

$$\Delta p = v_k h_k + c(v_{k+1} - v_k) h_k. \quad (12)$$

Here,  $\Delta p$  is the increment of position change.

The smoothness of the speed change of quadruped is related not only to the speed change within a certain

section, but also to the selection of segment points. A selection method of segment points is proposed in this paper. Referring to the characteristic of velocity smoothing of cycloid trajectory (equation (13)) proposed in reference [27], the swing phases in a cycle are evenly divided into four equal parts for Hermite interpolation. The velocity curve of cycloid trajectory can be approximately equivalent by choosing the appropriate proportional coefficient  $C$ .

Referring to the law of velocity variation shown in Figure 7, where the velocity at the beginning and end points of the  $X$ -axis direction is zero, a concave curve with a ratio coefficient  $C$  of  $1/3$  as shown in Figure 6(a) is selected (the velocity variation at  $V_k$  is relatively gentle). Meanwhile, in order to satisfy the smooth change of velocity at the transition points at  $T/2$  time, the convex curve with a proportionality coefficient  $C$  of  $2/3$  as shown in Figure 6(b) is chosen for the symmetric piecewise curves of the transition point (the velocity variation at  $V_{k+1}$  is relatively gentle). In the  $Y$ -axis direction, in order to meet the requirement that the velocity change at the transition point at  $T/2$  and  $T/4$  time is relatively smooth and the time velocity at  $2/T$  is zero, a convex curve with a proportionality coefficient  $C$  of  $2/3$  as shown in Figure 6(b) is selected. To sum up, the velocity change rate coefficient of  $X$ -axis is  $[1/3, 2/3, 2/3, 1/3]$ , and the velocity change rate coefficient of  $Y$ -axis is  $2/3$ . Finally, the change curve of foot track speed is obtained as shown in Figure 8:

$$x = S\left(\frac{t}{T} - \frac{1}{2\pi} \sin\left(\frac{2\pi t}{T}\right)\right), \\ y = H\left(\frac{1}{2} - \frac{1}{2} \cos\left(\frac{2\pi t}{T}\right)\right), \quad (13)$$

where  $S$  is the step length,  $H$  is the step height, and  $T$  is the period of oscillation phase.

Assuming that the period of the oscillating phase is two seconds, the maximum velocity in the  $X$ -axis direction is 80 mm/s, and the maximum velocity in the  $Y$ -axis direction is 16 mm/s. In the  $X$ -axis direction, at  $T/2$  time, the foot speed reaches the maximum value  $-V_{\max}$ ; at  $T/4$  and  $3 T/4$  time, the speed is one half of the maximum value. According to equation (13), the position increment of the four points is  $[-6.67, -33.33, -33.33, -6.77]$  mm. In the direction of  $Y$  axis, at  $T/4$  time, the foot velocity reaches the maximum value  $-V_{\max}$ ; at  $3 T/4$  time, the foot velocity is  $V_{\max}$ ; at  $T/2$  time, the foot velocity is zero. The position increments of the four points calculated by equation (13) are  $[-5.33, -5.33, 5.33, 5.33]$  mm. The foot trajectory function generated by interpolation is shown in the following equation:



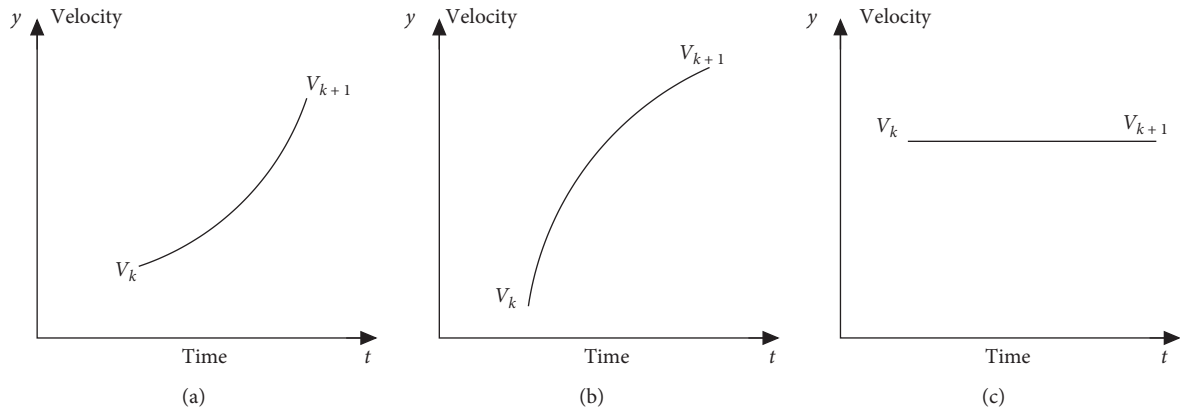


FIGURE 6: Variation curve of typical Hermite interpolation speed: (a)  $c = 1/3$ ; (b)  $c = 2/3$ , (c)  $c = 1$ .

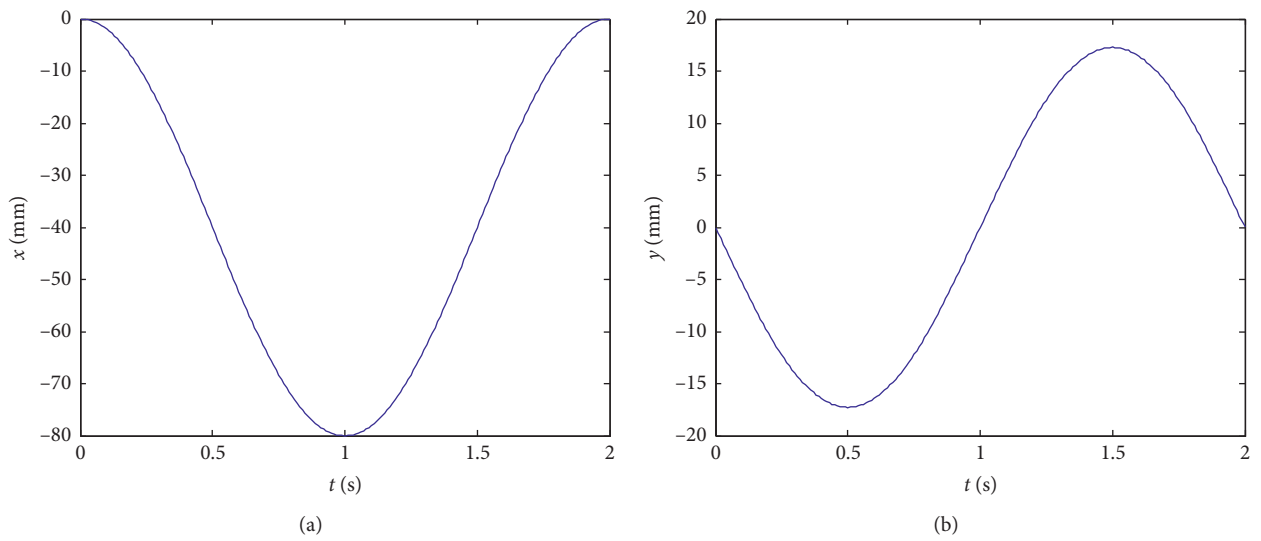


FIGURE 7: The velocity curve of the real cycloid track: (a) X-axis velocity curve (cycloid track); (b) Y-axis velocity curve (cycloid track).

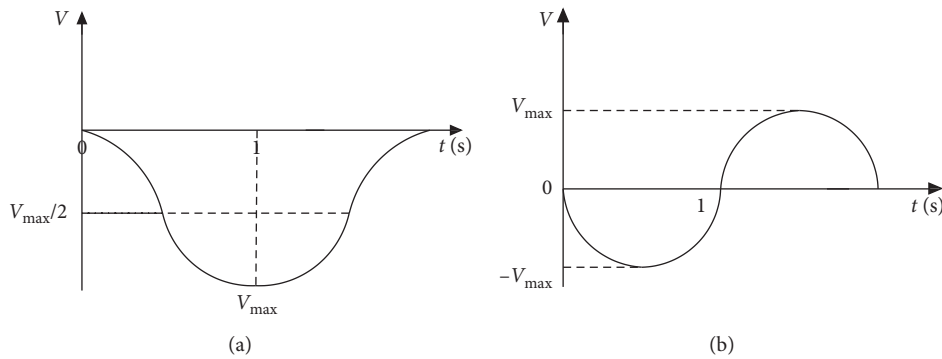


FIGURE 8: The velocity curve of interpolation track: (a) X-axis velocity curve (interpolation track); (b) Y-axis velocity curve (interpolation track).

$$\begin{aligned}
 x(t) &= \begin{cases} 4(1320t + 330)(t - 0.5)^2 - 4t^2(1298.4t - 973.8) - 4t^2(16t - 8) & 0 < t < 0.5 \\ 4(133.2t - 33.3)(t - 1)^2 - 4(80t - 80)(t - 0.5)^2 - 4(40t - 20)(t - 1)^2 & 0.5 < t < 1 \\ 4(133.2t - 233.1)(t - 1)^2 - 4(80t - 80)(t - 1.5)^2 - 4(40t - 60)(t - 1)^2 & 1 < t < 1.5 \\ 4(160t - 360)(t - 1.5)^2 - 4(40t - 60)(t - 2)^2 - 4(133.2t - 166.5)(t - 2)^2 & 1.5 < t < 2 \end{cases} \\
 y(t) &= \begin{cases} 4(1320t + 330)(t - 0.5)^2 - 4t^2(1298.4t - 973.8) - 4t^2(16t - 8) & 0 < t \leq 0.5 \\ 4(1298.4t - 324.6)(t - 1)^2 - 4(16t - 8)(t - 1)^2 - 4(1277.2t - 1596.5)(t - 0.5)^2 & 0.5 < t \leq 1 \\ 4(16t - 24)(t - 1)^2 + 4(1277.2t - 957.9)(t - 1.5)^2 - 4(1298.4t - 2272.2)(t - 1)^2 & 1 < t \leq 1.5 \\ 4(16t - 24)(t - 2)^2 - 4(1320t - 2970)(t - 1.5)^2 + 4(1298.4t - 1623)(t - 2)^2 & 1.5 < t \leq 2 \end{cases} \quad (14)
 \end{aligned}$$

The step length and lift height of the quadruped robot are shown in the following equation:

$$\begin{aligned}
 S &= \sum_{i=1}^4 \Delta P_i, \\
 H &= \sum_{j=1}^4 \Delta P_j,
 \end{aligned} \quad (15)$$

where  $i$  and  $j$  are the numbers of sections and  $\Delta P_i$  and  $\Delta P_j$  are the displacement increments of each section.

According to equation (15), the step length  $S$  is 80 mm and the leg lift height  $H$  is 10.66 mm. As can be seen from Figure 9, the foot trajectory formed by the step length and step height is within the working space of the leg of the quadruped robot. Considering the mechanical characteristics of parallelogram and contra-parallelogram, the foot trajectory is symmetrically distributed along the  $Y$ -axis with an initial position of (40 mm, 330 mm), when the robot's leg joint moves. Since the positive direction of D-H coordinate is located in the third quadrant of the rectangular coordinate system, when the robot's leg moves to the highest point, the  $Y$ -axis coordinate is 319.34 mm. The generated foot track is shown in Figure 10.

**3.2.2. Interpolation Control.** The speed of the segment points and the segment points of the planned trajectory are written into the controller by script language (Figure 11). The leg servo motor is controlled to move according to the planned trajectory. The trajectory interpolation procedure within 0.5 seconds is shown in the following equation:

$$\begin{aligned}
 &PVT 500, \\
 X 33.3: -40 Y 324.7: -16,
 \end{aligned} \quad (16)$$

where 500 milliseconds is the interval between segments;  $X$  33.33 mm and  $Y$  324.67 mm are the existing positions of  $P_0$  (the initial points) after  $\Delta P$  increment change;  $-40$  mm/s and  $-16$  mm/s are the velocities of the end points of the first segment.

## 4. Simulation and Experimental Analysis

**4.1. ADAMS Simulation.** In order to verify correctness of the quadruped robot foot trajectory and the smoothness of the

speed change in the direction of  $XY$  axis, the simulation is carried out by MATLAB and ADAMS in this paper [28, 29]. Firstly, SolidWorks is used to build the 3D model of the virtual prototype, and then the 3D model is imported into ADAMS to add constraints and drivers. The coordinate set on the foot track is mapped to the corresponding motor angle by MATLAB. Finally, the motor angle is imported into ADAMS to complete the simulation verification of the virtual model. The specific simulation process is shown in Figure 12.

In one cycle, the foot movement process is shown in Figure 13.

**4.2. Simulation Results Analysis.** When a quadruped robot travels along the foot trajectory formed by Hermite interpolation, the synthetic velocity curve along the  $XY$  axis is shown in Figure 14. According to the graph, the change of the foot speed of the robot in a single cycle is relatively smooth and can meet the requirements of the stable motion of the robot.

**4.3. Analysis of Experimental Results.** The quadruped robot designed in this paper uses steel processing leg structure. In order to verify the trajectory of one leg when the robot swings, and to avoid the friction caused by the contact between the other three legs and the ground affecting the trajectory of the foot, aluminum profiles are used to construct a support frame to support the entire body in the air. The standard laser tracker R-20 Radian of the automatic precision engineering company (API) is adopted in the measurement system. The spatial position of the measuring point relative to the measuring coordinate system is calculated by the laser interference principle [30]. The experimental platform is shown in Figure 15.

Due to the limited space of the body of the quadruped robot, in order to increase the reliability of the robot in the process of moving and the bearing capacity of the body of the robot, PMAC 16-axis ck3e controller with small size and good openness is selected as the main controller. The controller is equipped with the corresponding EtherCAT slave station module to realize the information interaction between switch and analog. The DB59M024035-KYAN brushless DC servo motor of Nanotec German is used as the servo motor. The specific models are shown in Table 3.

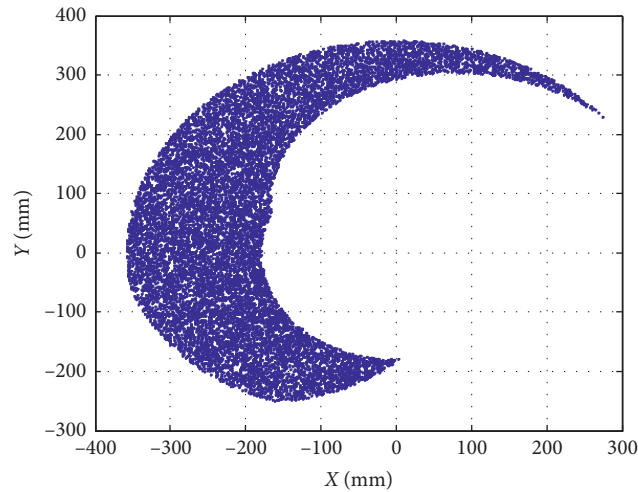


FIGURE 9: Workspace of the foot end of the quadruped robot.

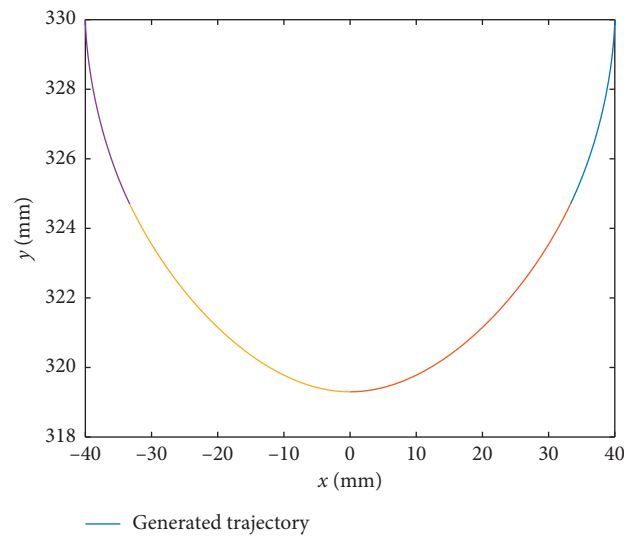


FIGURE 10: Displacement variation curve.

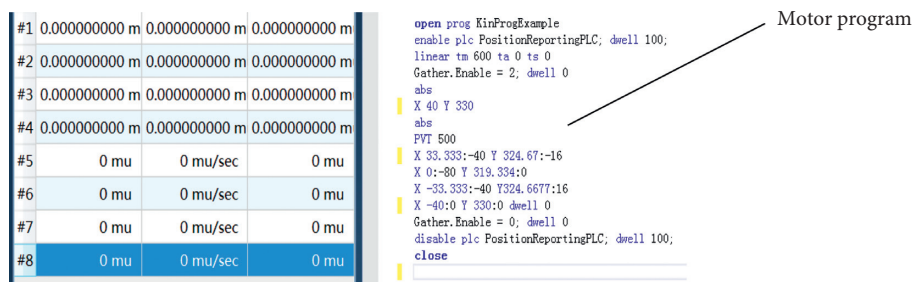


FIGURE 11: Interface of motion program software.

The control principle of the whole machine is shown in Figure 16.

The initial joint angle of the robot is set as  $40^\circ$  for the hip joint and  $80^\circ$  for the knee joint. According to the kinematics model, the initial angle of the calf motor is calculated as  $52.8^\circ$ . The trajectory drawing software embedded in PMAC

is used to draw the movement trajectory of the robot foot in the oscillating phase in a single cycle (Figure 17). Under the initial conditions, the program of fast return to zero is executed, then the foot moves to (40 mm, 330 mm), and the foot of the robot walks according to the preset trajectory. In one period, the displacement in the X-axis direction is

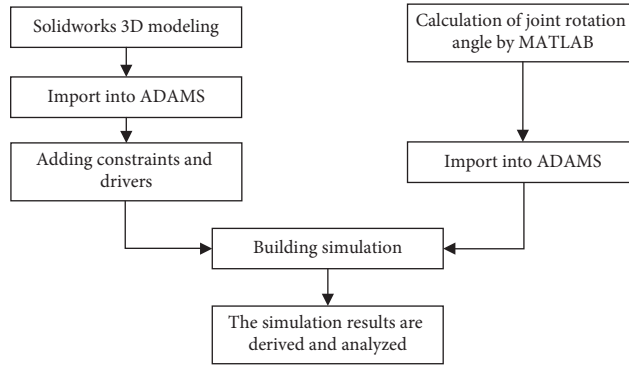


FIGURE 12: Virtual prototype simulation process.

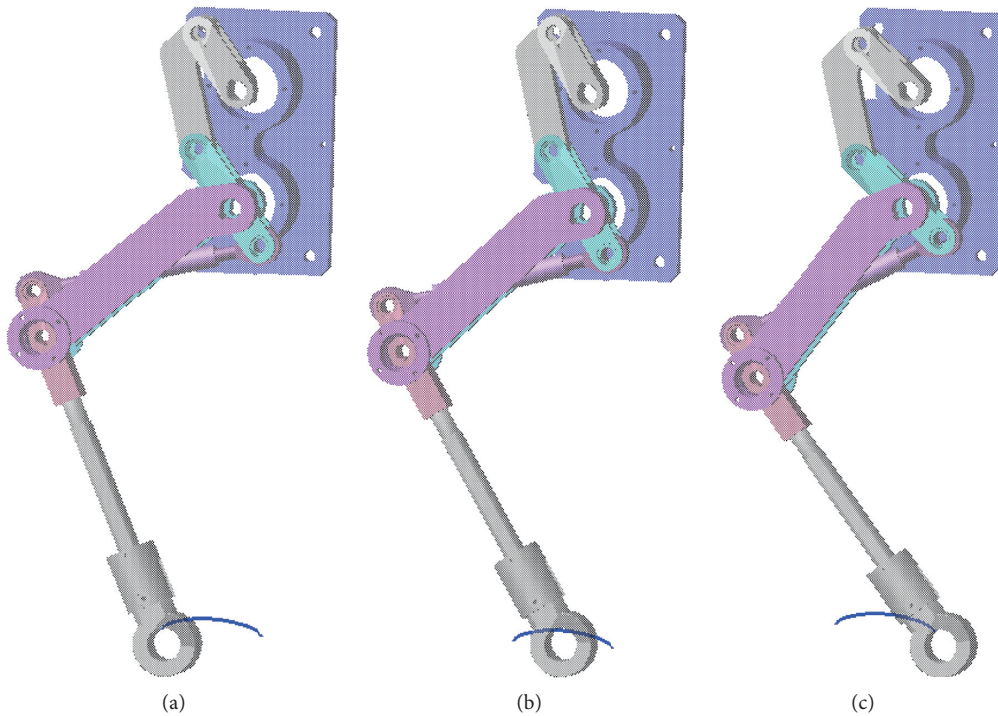


FIGURE 13: Schematic diagram of full cycle foot movement of quadruped robot: (a)  $t=0$ ; (b)  $t=1$  s; (c)  $t=2$  s.

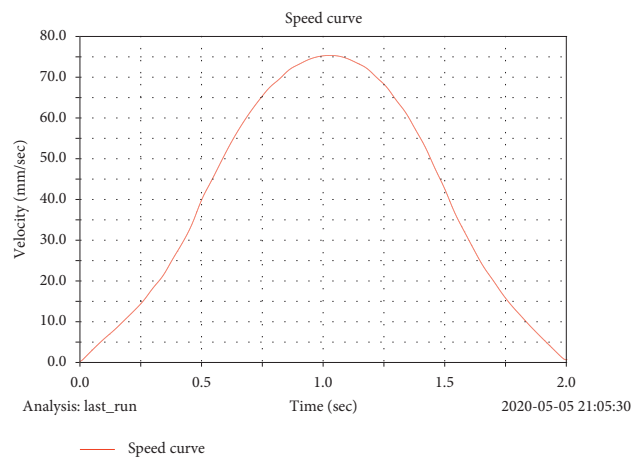


FIGURE 14: Full period speed variation curve of quadruped robot's foot.



FIGURE 15: Experimental platform.

TABLE 3: List of control system components.

Name	Model	Main parameter	Function
Controller	PMAC CK3E-1310	16 axis	EtherCAT bus controller
Servo amplifier	Nanotec C5-E-2-21		
Driver	DB59M024035-KYAN	3500 r/min	DC servo motor
Coupler	NX -ECC203		EtherCAT
Digital input module	NX-ID5342	16	Zero position signal and power supply under voltage signal input
Digital input module	NX-ID4342	8	Digital input standby module
Digital output module	NX-OD4121	8	Digital output standby module
Analog input module	NX-AD4603	8	Analog input standby module

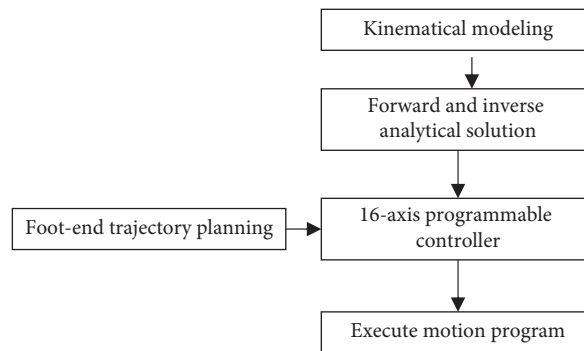


FIGURE 16: System control schematic diagram of the whole machine.

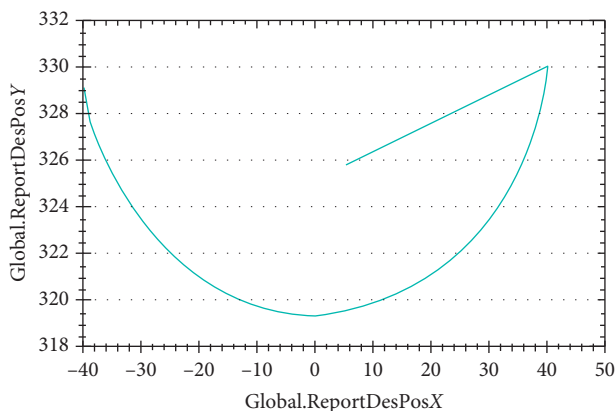


FIGURE 17: Trajectory curve of foot end of quadruped robot (x/mm, y/mm).

80 mm, and the displacement in the  $y$ -direction is about 10.66 mm. The sampling time is set by the laser tracker, and the foot motion track is measured as shown in Figure 18.

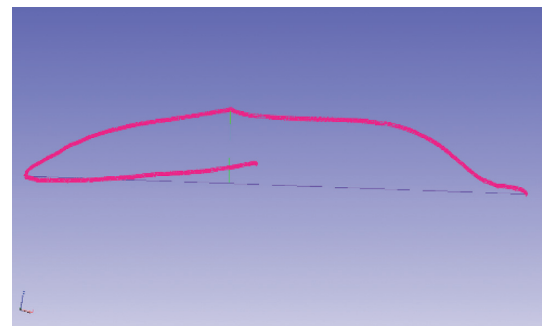


FIGURE 18: Testing trajectory of laser tracker (x/mm, y/mm).

Due to the gap in the leg structure during processing and assembly, the mechanical mechanism of the foot has a slight vibration in the actual movement process, which leads to the deviation between the fitted track and the actual track. The displacement in the  $X$ -axis direction is 81.3 mm with an error of 1.65%. The maximum displacement in the  $Y$ -axis direction is 10.3 mm with an error of 3.4%. The error is small and can fully meet the walking requirements.

## 5. Conclusion

- (1) In order to reduce the inertia of quadruped robot's legs, a leg structure is designed in this paper. The motor of hip joint and knee joint is reasonably arranged on the body, and the parallel quadrilateral and contra-parallel quadrilateral bar structures are used for power transmission.
- (2) For the quadruped robot with the goal of trajectory planning, MATLAB software is adopted, Hermit interpolation algorithm is applied, and the characteristic of smooth velocity change of cycloid trajectory is used for reference. Proportional coefficient  $C$  is reasonably selected to approximate the velocity change curve of the foot trajectory, so as to generate the movement trajectory of the foot of the quadruped robot. ADAMS software is used to simulate. According to the simulation results, the quadruped robot can move using the designed trajectory, and the speed changes in the process of movement are relatively smooth.
- (3) The PMAC bus controller with small volume and high integration is adopted as the main controller. The forward and inverse solution algorithm is written and the PVT interpolation library function is called to control the leg servo motor by writing the motion program through scripting language, so as to test the real prototype. The experimental results show that the trajectory generated by piecewise interpolation based on the cycloid velocity curve can be realized under the leg structure of the quadruped robot in this paper. At the same time, the velocity variation is relatively stable during the movement. This experiment offers a theoretical basis for the trajectory design, optimization, and overall debugging of the electrically driven quadruped robot.

## Data Availability

The data used to support the findings of this study are available from the corresponding author upon request.

## Conflicts of Interest

The authors declare that there are no conflicts of interest regarding the publication of this paper.

## Acknowledgments

This work was supported by the Kunming University of Science and Technology Talent Research Start-up Fund Project (No. KKZ3201601002), Major Science and Technology Project in Yunnan Province (No. 2017RA010), National Key Research and Development Plan Project (No. 2017YFC1702503), and the National Natural Science Foundation of China (Nos. 51965029, 61873115, and 51565021).

## References

- [1] S. Yi, "Reliable gait planning and control for miniaturized quadruped robot pet," *Mechatronics*, vol. 20, no. 4, pp. 485–495, 2010.
- [2] X. Chen, F. Gao, C. Qi, and X. Tian, "Gait planning for a quadruped robot with one faulty actuator," *Chinese Journal of Mechanical Engineering*, vol. 28, no. 1, pp. 11–19, 2015.
- [3] J. Meng, C. J. Liu, and X. W. Rong, "Current situation and prospect of quadruped robot development," *Tech Review*, vol. 33, no. 21, pp. 59–63, 2015.
- [4] M. Raibert, K. Blankespoor, G. Nelson et al., "BigDog, the rough-terrain quadruped robot," in *Proceedings of the International Federation of Automatic Control*, pp. 10822–10825, Seoul, Korea, July 2008.
- [5] L. Ding, R. Wang, F. Huashan, and J. Li, "Brief analysis of a BigDog quadruped robot," *China Mechanical Engineering*, vol. 23, no. 5, pp. 505–514, 2012.
- [6] Z. L. Ma, R. J. Lv, and Y. C. Li, "Design and analysis on the structure of imitating cheetah quadruped robot," *Transactions of Beijing University of Technology*, vol. 28, no. 1, pp. 33–39, 2018.
- [7] Z. L. Ma, P. Q. Zhang, and R. J. Lv, "Stability analysis of walking on the slope for a quadruped robot," *Journal of Northeastern University (Natural Science)*, vol. 39, no. 5, pp. 68–73, 2018.
- [8] B. L. Han, Y. Jia, and H. S. Li, "Posture adjustment for quadruped robot trotting on a slope," *Transactions of Beijing University of Technology*, vol. 36, no. 3, pp. 242–246, 2016.
- [9] B. W. Gao, S. K. Wang, and Y. F. Gao, "Single leg vertical hopping gait planning for hydraulic quadruped robot," *Chinese Journal of Scientific Instrument*, vol. 38, no. 5, pp. 1086–1092, 2017.
- [10] D. Q. He and P. S. Ma, "Simulation of dynamic walking of quadruped robot and analysis of walking stability," *Computer Simulation*, vol. 22, no. 2, pp. 146–149, 2005.
- [11] J. T. Lei, F. Wang, and H. Y. Yu, "Analysis on trajectory planning and energy consumption of quadruped robot," *Machine Design and Research*, vol. 30, no. 1, pp. 29–34, 2014.
- [12] L. Wang, J. Wang, S. Wang, and Y. He, "Strategy of foot trajectory generation for hydraulic quadruped robots gait planning," *Journal of Mechanical Engineering*, vol. 49, no. 1, pp. 39–44, 2013.
- [13] X. Zhang, H. Zheng, X. Guan, Z. Cheng, and L. Zhao, "A biological inspired quadruped robot: structure and control," in *Proceedings of the 2005 IEEE International Conference on Robotics & Biomimetics ROBIO*, Shatin, China, July 2005.
- [14] X. J. Han, W. J. Yang, and H. Y. Gao, "The kinematics analysis and footprint optimization of the four legged bionic robot based on linkage mechanism," *Forest Engineering*, vol. 33, no. 1, pp. 52–58, 2017.
- [15] P. F. Li, J. Sh, and J. P. Chen, "Analysis of inverse kinematics of quadruped robot based on closed vector method and D-H method," *Science Technology and Engineering*, vol. 19, no. 4, pp. 161–165, 2019.
- [16] H. Kimura, Y. Fukuoka, and A. H. Cohen, "Biologically inspired adaptive walking of a quadruped robot," *Philosophical Transactions of the Royal Society A: Mathematical, Physical and Engineering Sciences*, vol. 365, no. 1850, pp. 153–170, 2007.
- [17] S. C. Li, R. X. Xiong, and M. X. Li, "Kinematic analysis and simulation of quadruped robot leg structure," *Journal of Military Transportation University*, vol. 16, no. 8, pp. 91–94, 2014.
- [18] T. Zhao, Q. Peng, and J. Dai, "Mechanism design of a bio-mimetic quadruped robot," *Industrial Robot*, vol. 44, no. 4, 2017.



- [19] X. Rong, Y. Li, J. Ruan, and B. Li, "Design and simulation for a hydraulic actuated quadruped robot," *Journal of Mechanical Science and Technology*, vol. 26, no. 4, pp. 1171–1177, 2012.
- [20] W. T. Zhao and Z. Z. Liu, "The foot workspace analysis of quadruped bio-robot," *Machine Design and Manufacturing Engineering*, vol. 40, no. 13, pp. 19–22, 2011.
- [21] W. G. Tang, L. W. Wang, and C. P. Wang, "The calculation system development of the quadruped robot's workspace on fixed pose," *Applied Mechanics and Materials*, vol. 220–223, no. 1, pp. 1186–1189, 2012.
- [22] L. M. Deng, *Research on Real-Time Control System of the Baby Elephant*, Shanghai Jiao Tong University, Shanghai, China, 2014.
- [23] X.-D. Chen, W. Ma, and J.-C. Paul, "Cubic B-spline curve approximation by curve unclamping," *Computer-Aided Design*, vol. 42, no. 6, pp. 523–534, 2010.
- [24] W. S. Chi, S. J. Tang, and W. S. Chi, "Analysis and application of PVT motion mode of PMAC motion controller," *Machinery*, vol. 47, no. 7, pp. 35–37, 2009.
- [25] H. Yue, W. Chen, W. Chen, and X. Wu, "Spline-interpolation based PVT algorithm and application in a bionic cockroach robot," in *Proceedings of the 11th International Conference on Control Automation Robotics & Vision*, Singapore, December 2010.
- [26] X. S. Wang and M. Kang, "Cutting path planning of complex optical surface using Hermite interpolation," *Journal of Mechanical Engineering*, vol. 48, no. 11, pp. 195–220, 2012.
- [27] Y. B. Li, B. Li, and X. W. Rong, "Mechanical design and gait planning of a hydraulically actuated quadruped bionic robot," *Journal of Shandong University (Engineering Edition)*, vol. 41, no. 5, pp. 32–36, 2011.
- [28] F. Pop, E. C. Lovasz, V. Dolga, M. Ceccarelli, D. Mărgineanu, and C. Pop, "A dynamic analysis based on MBD ADAMS program for a variant of quadruped robot," *Applied Mechanics and Materials*, vol. 823, pp. 429–434, 2016.
- [29] B. Li, Y. Li, and X. Rong, "Locomotion planning and performance analysis of quadruped robot based on ADAMS and MATLAB co-simulation," in *Proceedings of the 32nd Chinese Control Conference*, Xi'an, China, July 2013.
- [30] F. Liu, *Kinematics Parameter Identification and Compensation of an Industrial Robot*, Kunming University of Science and Technology, Kunming, China, 2018.

## Research Article

# Trajectory Tracking Control of Robot Manipulators Based on U-Model

Xianghua Ma , Yang Zhao, and Yiqun Di

*School of Electrical and Electronic Engineering, Shanghai Institute of Technology, Shanghai 201418, China*

Correspondence should be addressed to Xianghua Ma; [xhuam@sit.edu.cn](mailto:xhuam@sit.edu.cn)

Received 6 April 2020; Accepted 20 April 2020; Published 12 May 2020

Guest Editor: Weicun Zhang

Copyright © 2020 Xianghua Ma et al. This is an open access article distributed under the Creative Commons Attribution License, which permits unrestricted use, distribution, and reproduction in any medium, provided the original work is properly cited.

A new trajectory tracking control method based on the U-model is proposed to improve the trajectory tracking speed of robot manipulators. The U-model method is introduced to relieve the requirement of the dynamic mathematical model and make the design of trajectory tracking controller of robot manipulators simpler. To further improve the trajectory tracking speed, an improved iterative learning control algorithm is used to suppress the influence of the initial state error with less computation time. Experimental results show that the proposed control method is effective and practical for the trajectory tracking control of robot manipulators, especially with a high real-time requirement.

## 1. Introduction

Nowadays, most robot manipulators need to possess the capacity of accurate and fast trajectory tracking. Trajectory tracking control is a key issue in the field of robot manipulator motion planning [1–3]. It aims to enable the joints or links of the robot manipulator to track the desired trajectory with ideal dynamic quality or to stabilize them in the specified position [4]. At present, there are two main ways to analyze and design the trajectory tracking control for robot manipulator [5]. The first one is with respect to a classical linear control method [6, 7]. This way is easy, and some classical control theory and methods can be used directly in some nonlinear properties which are approximated into a linear relationship or neglected. However, the trajectory tracking control of robot manipulators is a multi-input and multioutput (MIMO) control problem, and the motion equation of a robot manipulator with multiple degrees of freedom is highly coupled and complex [8]. If each joint is supposed to be independent and the inertia of each joint be constant, it may lead to inconsistent system damping and other unexpected situations in the entire workspace [9]. Therefore, there is the second way, which focuses on the nonlinear control method without the requirements of the above assumptions [10–12]. However, this nonlinear

method also has some limits; for example, it needs to get the exact data of the structure and precise parameters when modelling the manipulator so as to correctly describe all these uncertainties, for example, the interaction among robot joints and the change in centroid.

The initial state error has a great influence on the trajectory tracking speed. Iterative learning control method is used to rapidly suppress the influence of the initial state error. Hongfeng et al. [13] proposed an iterative learning trajectory tracking control algorithm for discrete nonlinear systems in which the initial states are not strictly identical to given expected values in track tracking. Jin [14] proposed a new iterative learning control method which can track the nonrepetitive motion trajectory without assuming that the initial state error of the system is unchanged. Hui et al. [15] proposed a data-driven iterative learning control method based on an extended state observer. The concept of ESO is introduced into the iteration direction. The random initial state and the disturbance are taken as the extended state of a whole. Theoretical analysis shows that the method is robust to initial displacements and perturbations of iterative changes.

A reasonable learning gain matrix can improve the trajectory tracking speed. In order to obtain the optimal learning gain, many researches have been done including

variable exponential gain method [16], fuzzy PID method [17], and the method combining neural network controller and compensation controller [18]. However, the complex control law and the learning law will bring a huge amount of computation time and affect the trajectory tracking speed.

According to the above analysis, both the classical linear control method and the nonlinear control method have their advantages and also some limitations, respectively. If there is a way to combine the benefits of the classical linear and the nonlinear control methods, not only the analysis and design of trajectory tracking control can be easier but also the speed and accuracy of trajectory tracking control may be improved as well. U-Model belongs to a generic systematic approach, which converts the nonlinear polynomial model into a controller output-based time-varying polynomial model [19–23]. Inspired by this idea, the U-model theory is introduced into the trajectory tracking control, which can help understand the inner structure and parameters of the robot manipulator better and reduce the structure complexity of control system. Iterative learning control method is used with a new iterative learning control law, which can greatly decrease the computation time and further improve the trajectory tracking speed.

The remainder of the paper is organized as follows. Section 2 describes trajectory tracking U-control system in detail. Section 3 analyzes the asymptotic convergence of the control law and the stability of the system. In Section 4, simulation experiment is carried out to prove the effectiveness of the proposed method. Conclusions are given in Section 5.

## 2. Trajectory Tracking U-Control System

In this paper, a trajectory tracking U-control method is proposed, and the control system mainly includes robot manipulator and a U-controller, as shown in Figure 1. The U-controller is composed with an iterative learning controller (ILC for abbreviation) and the U-model of a robot manipulator, where  $G_c$  is the mathematical model of the linear controller,  $G_p$  is the mathematical model of the robot manipulator, and  $G_p^{-1}$  is the dynamic inverse of robot manipulator model based on U-model theory. The desired output trajectory is denoted as  $y_d(t)$ , and the system output is denoted as  $y_k(t)$  at time  $t \in R^+$ .  $k$  is the number of iterations.

**2.1. Realization of U-Controller.** Consider a robot manipulator with  $n$  DOF; its general dynamic model can be represented as

$$M(q)\ddot{q} + C(q, \dot{q})\dot{q} + G(q) + u_a = u, \quad (1)$$

where  $q_{n \times 1} = [q_1, q_2, \dots, q_n]^T \in R^n$  is the angular displacement vector;  $\dot{q}_{n \times 1}$  and  $\ddot{q}_{n \times 1}$  are angular velocity and angular acceleration vectors of each joint, respectively;  $u \in R^{n \times 1}$  is the torque vector;  $M(q) \in R^{n \times n}$  represents the inertia term;  $C(q, \dot{q}) \in R^{n \times n}$  is the Coriolis and centrifugal terms;  $G(q) \in R^n$  is the gravitational term; and  $u_a \in R^{n \times n}$  is the unknown disturbance term.

Based on the U-model theory, the mathematical model  $G_p$  of the robot manipulator (1) can be converted into the following U-model expression:

$$\begin{aligned} \ddot{y}(t) = & -M^{-1}y(t)[C(y(t), \dot{y}(t))\dot{y}(t) + G(y(t), \dot{y}(t))] \\ & + M^{-1}y(t)u(t) - M^{-1}y(t)u_a, \end{aligned} \quad (2)$$

where  $y(t) = q(t)$ .

In order to consistent with the U-model theoretical expression, equation (2) can be transformed as follows:

$$v_k(t) = \alpha_0(t) + \alpha_1(t)u_k(t) + E(t), \quad (3)$$

where

$$\begin{cases} v_k(t) = \ddot{y}(t), \\ \alpha_0(t) = -M^{-1}y(t)[C(y(t), \dot{y}(t))\dot{y}(t) + G(y(t), \dot{y}(t))], \\ \alpha_1(t) = M^{-1}y(t), \\ E(t) = -M^{-1}y(t)u_a. \end{cases} \quad (4)$$

From the transformation of equation (2) to equation (3), it can be seen that the realization of the U-model is different from the general approximate linear transformation and the properties of the original robot manipulator dynamic model will not be changed.

As seen from Figure 1, the U-controller consists of ILC and the dynamic inverse controller  $G_p^{-1}$  based on the U-model. After the U-model expression  $G_p$  of the manipulator dynamic model (3) is obtained, the U-controller can be designed based on the U-model theory. The output of the ILC is shown as follows:

$$v_k(t) = v_{k-1}(t) + G_c e(t), \quad (5)$$

where trajectory error  $e(t) = y_d(t) - y_k(t)$ .

According to the definition of U-model theory, in this trajectory tracking U-control system, the general mathematical express of  $G_p$  can be obtained by

$$v_k^{(M)}(t) = \sum_{j=0}^M \alpha_j(t) u_k^{(N)}(t) + E(t), \quad M > N, \quad (6)$$

where  $v_k^{(M)}(t)$  and  $u_k^{(N)}(t)$  are the  $M$ th and  $N$ th orders of derivatives of  $v_k(t)$  and  $u_k(t)$ , respectively.  $\alpha_j(t)$  is a time-varying coefficient of  $u_k^{(N-1)}(t), \dots, u_k(t)$  and  $v_k^{(M-1)}(t), \dots, v_k(t)$ .

By solving the root of equation (6), the output  $u_k(t)$  of the U-controller can be obtained and expressed as

$$u_k(t) = F \left[ v_k^{(M)}(t) - \sum_{j=0}^M \alpha_j(t) u_k^{(N)}(t) - E(t) \right], \quad (7)$$

where  $F[*]$  is a root-solving algorithm. In order to improve the convergence speed of iterative algorithms, based on the Newton–Raphson iterative algorithm, the model of the U-controller is obtained as shown in equation (8), which can optimize the output of ILC so as to reduce the number of iterations and speed up the tracking convergence.

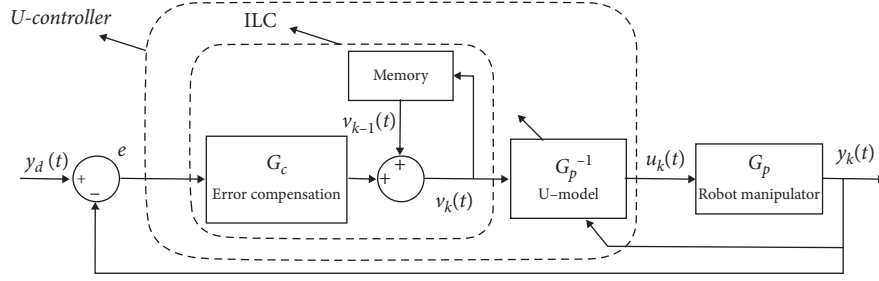


FIGURE 1: U-Control system framework.

The mathematical model of the U-controller can be expressed as

$$u_k(t) = \frac{v_k(t) - \alpha_0(t) - E(t)}{\alpha_1(t)}. \quad (8)$$

From the above equation, it can be seen that the output of the U-controller only needs to search a single value of  $u_k(t)$  and obtain the output of ILC through fewer iterations, which greatly reduces the complexity of operation.

**2.2. Iterative Learning Control Law.** Iterative learning control algorithm is a common method for trajectory tracking control of manipulator. In order to improve the trajectory tracking speed of the manipulator, it is necessary to reduce the number of iterations required for the convergence while ensuring the convergence of the iterative learning control law. Therefore, both the initial state error and the convergence speed of the error are considered when the iterative learning control law is designed.

Let  $x_k(t) = [q \ \dot{q}]^T$ , the robot manipulator (1) can be rewritten into the following expression (9), and the displacement and velocity of each joint of the manipulator are used as the system output:

$$\begin{cases} \dot{x}_k(t) = \begin{bmatrix} \dot{q} \\ \ddot{q} \end{bmatrix} = f(x_k(t), t) + B(t)u_k(t) + W_k(t), \\ y_k(t) = C(t)x_k(t) + V_k(t), \end{cases} \quad (9)$$

where  $W_k(t)$  and  $V_k(t)$  are state disturbance and output disturbance, respectively.  $k$  is the number of iterations.

$$\begin{aligned} f(x_k(t), t) &= \begin{bmatrix} \dot{q} \\ -M^{-1}(C(q, \dot{q})\dot{q} + G(q)) \end{bmatrix}, \\ B(t) &= \begin{bmatrix} 0 \\ M^{-1}(q) \end{bmatrix}, \\ W_k(t) &= \begin{bmatrix} 0 \\ -M^{-1}(q) \end{bmatrix} u_a, \\ C(t) &= I. \end{aligned} \quad (10)$$

It is assumed that the above robot manipulator system satisfies the following conditions.

**Assumption 1.**  $f(x_k(t), t)$  satisfies the Lipschitz condition; that is, there exists a constant  $L_f$  ( $L_f > 0$ ) that satisfies the following:

$$\|f(x_{k+1}(t), t) - f(x_k(t), t)\| \leq L_f \|x_{k+1}(t) - x_k(t)\|. \quad (11)$$

**Assumption 2.** The adjacent state disturbance variation and the output disturbance variation are bounded, expressed as follows:

$$\begin{cases} \|W_{k+1}(t) - W_k(t)\| \leq b_W, \\ \|V_{k+1}(t) - V_k(t)\| \leq b_V. \end{cases} \quad (12)$$

**Assumption 3.**  $B(t)$  and  $C(t)$  are bounded.

**Assumption 4.** Expected trajectory  $y_d(t)$  is continuous for all  $t \in [0, T]$ .

It is assumed that the system has a random initial error, which is denoted as  $e_k(t) = y_d(t) - y_k(t)$ , and the initial state of the  $k$ th iteration is  $x_k(0)$ . The control law is as follows:

$$v_k(t) = v_{k-1}(t) + \Gamma e_k(t) + \Gamma \dot{e}_k(t) + \phi_k(t)X_k(0), \quad t \in [0, T], \quad (13)$$

where  $\Gamma$  is the constant gain matrix and  $G_c = \Gamma(e_k(t) + \dot{e}_k(t) + \phi_k(t)X_k(0))$ .

The learning law for the initial state is

$$\phi(t) = \begin{cases} \frac{2a^k}{h} \left(1 - \frac{a^k}{h}t\right), & t \in \left[0, \frac{h}{a^k}\right], \\ 0, & t \in \left[\frac{h}{a^k}, T\right], \end{cases} \quad (14)$$

$$a > 1, 0 < h < T,$$

$$X_k(0) = B(0)\Gamma e_k(0) + x_k(0) - x_{k+1}(0), \quad (15)$$

where  $a > 1, 0 < h < T$ .

From equation (14), the initial state error can only affect the trajectory tracking speed within the time interval  $[0, (h/a^k)]$ . After  $t = h/a^k$ , the initial state error will be 0. With the increase in the number of iterations  $k$ , the time instant  $h/a^k$  will tend to 0 quickly, which means the time the initial state error affects the trajectory tracking speed will become very short as well. It means that the trajectory tracking speed can be improved by the use of the proposed iterative learning control law.

### 3. Convergence Analysis

The stability of the trajectory tracking system requires that the actual output trajectory of the system converges to the desired trajectory under the action of the proposed U-controller; that is, the error between expected and actual trajectory will converge to 0 or within a boundary finally.

**Lemma 1.** For the robot manipulator described in equation (9), if it satisfies the following conditions,

$$\rho = \sup_{t \in [0, T]} \|1 - M^{-1}(q)G\| < 1, \quad (16)$$

then the tracking error of the system will eventually converge to a boundary.

*Proof.* From equation (9), we can get

$$\begin{aligned} & x_{k+1}(t) - x_k(t) \\ &= \int_0^t [f(x_{k+1}(s), s) - f(x_k(s), s)] ds \\ &+ \int_0^t B(s)[u_{k+1}(s) - u_k(s)] ds + \int_0^t [W_{k+1}(s) \\ &- W_k(s)] ds + x_{k+1}(0) - x_k(0). \end{aligned} \quad (17)$$

According to equation (13), there is

$$\begin{aligned} & \int_0^t B(s)[v_{k+1}(s) - v_k(s)] ds \\ &= \int_0^t B(s)[\Gamma e_k(s) + \Gamma \dot{e}_k(s) + \phi_k(s)X_k(0)] ds \\ &= \int_0^t B(s)\Gamma e_k(s) ds + B(t)\Gamma e_k(t) - \int_0^t e_k(s)[\dot{B}(s)\Gamma + B(s)\dot{\Gamma}] ds \\ &+ X_k(0) \int_0^t [B(s)\phi_k(s) - 1] ds + x_k(0) - x_{k+1}(0). \end{aligned} \quad (18)$$

Then, equation (17) can turn into

$$\begin{aligned} & x_{k+1}(t) - x_k(t) \\ &= \int_0^t [f(x_{k+1}(s), s) - f(x_k(s), s)] ds + \int_0^t [W_{k+1}(s) - W_k(s)] ds \\ &+ \int_0^t B(s)\Gamma e_k(s) ds + B(t)\Gamma e_k(t) - \int_0^t e_k(s)[\dot{B}(s)\Gamma + B(s)\dot{\Gamma}] ds \\ &+ X_k(0) \int_0^t [B(s)\phi_k(s) - 1] ds. \end{aligned} \quad (19)$$

According to the tracking error definition  $e_k(t) = y_d(t) - y_k(t)$ ,

$$\begin{aligned} & e_{k+1}(t) - e_k(t) \\ &= y_d(t) - y_{k+1}(t) - y_d(t) + y_k(t) \\ &= -C(t)[x_{k+1}(t) - x_k(t)] - [V_{k+1}(t) - V_k(t)]. \end{aligned} \quad (20)$$

Substituting equation (19) into equation (20),

$$\begin{aligned} & e_{k+1}(t) \\ &= e_k(I - CB\Gamma) - C(t) \left[ \int_0^t [f(x_{k+1}(t), t) - f(x_k(t), t)] ds \right. \\ &+ \int_0^t B(s)\Gamma e_k(s) ds - \int_0^t e_k(s)[\dot{B}(s)\Gamma + B(s)\dot{\Gamma}] ds \left. \right] \\ &- C(t) \int_0^t [W_{k+1}(s) - W_k(s)] ds \\ &- C(t)X_k(0) \int_0^t [B(s)\phi_k(s) - 1] ds - [V_{k+1}(t) - V_k(t)]. \end{aligned} \quad (21)$$

According to equation (14), when  $t \in [(h/a^k), T]$ , we can get

$$\int_0^t (B(t)\phi_k(t) - 1) ds = 0. \quad (22)$$

According to Bellman–Gronwall lemma, equation (19), and assumptions (1) and (2), we have

$$\begin{aligned} & \|x_{k+1}(t) - x_k(t)\| \\ &\leq \int_0^t L_f \|x_{k+1}(s) - x_k(s)\| ds + b_W s|_0^t + \int_0^t \|B(s)\Gamma\| \|e_k(s)\| ds \\ &+ \|B(t)\Gamma\| \|e_k(t)\| + \int_0^t \|\dot{B}(s)\Gamma + B(s)\dot{\Gamma}\| \|e_k(s)\| ds. \end{aligned} \quad (23)$$

Multiply both sides of equation (23) by  $e^{-\lambda t}$ , where  $\lambda > 0$ , and take the maximum value of the right-hand side, and assume that  $t = t_{\max} \in [0, T]$ :

$$\begin{aligned} & \|x_{k+1}(t) - x_k(t)\|_\lambda \\ &\leq \frac{L_f}{\lambda} \|x_{k+1}(t) - x_k(t)\|_\lambda + b_W t + \frac{1 + \lambda}{\lambda} \sup_t \|B\Gamma\| \|e_k(t)\|_\lambda \\ &+ \frac{\sup_t \|\dot{B}\Gamma + B\dot{\Gamma}\|}{\lambda} \|e_k(t)\|_\lambda (t = t_{\max}). \end{aligned} \quad (24)$$

Let  $L_f < \lambda$ , and equation (24) can be simplified as

$$\begin{aligned} & \|x_{k+1}(t) - x_k(t)\|_\lambda \leq \frac{\lambda b_W t}{\lambda - L_f} \\ &+ \frac{(1 + \lambda) \sup_t \|B\Gamma\| + \sup_t \|\dot{B}\Gamma + B\dot{\Gamma}\|}{\lambda - L_f} \|e_k(t)\|_\lambda. \end{aligned} \quad (25)$$

In the same way, equation (21) can turn into

$$\begin{aligned} \|e_{k+1}(t)\|_{\lambda} &\leq \|e_k(t)\|_{\lambda} \rho + \frac{\sup_t \|C(t)\|_{L_f}}{\lambda} \|x_{k+1}(t) - x_k(t)\|_{\lambda} \\ &+ \frac{\sup_t \|C(t)\| (\sup_t \|B\Gamma\| + \sup_t \|\dot{B}\Gamma + B\dot{\Gamma}\|)}{\lambda} \|e_k(t)\|_{\lambda} \\ &+ \sup_t \|C(t)\| b_w t + b_v. \end{aligned} \quad (26)$$

Substituting equation (25) into (26),

$$\|e_{k+1}(t)\|_{\lambda} \leq P \|e_k(t)\|_{\lambda} + Q, \quad (27)$$

where

$$\begin{aligned} P &= \rho + \sup_t \|C(t)\| \frac{(L_f + 1) \sup_t \|B\Gamma\| + \sup_t \|\dot{B}\Gamma + B\dot{\Gamma}\|}{\lambda - L_f}, \\ Q &= \frac{\lambda \sup_t \|C(t)\| b_w t}{\lambda - L_f} + b_v. \end{aligned} \quad (28)$$

When the value of  $\lambda$  is big enough, according to equation (16), we can get  $P \approx \rho < 1$ . When  $\lambda$  is chosen,  $Q$  becomes a constant. Further deform equation (27) into

$$\|e_{k+1}(t)\|_{\lambda} \leq \rho^k \left( \|e_k(t)\|_{\lambda} - \frac{Q}{1-M} \right) + \frac{Q}{1-M}. \quad (29)$$

Therefore, we can have

$$\|e_k(t)\|_{\lambda} \leq \rho^{k-1} \left( \|e_{k-1}(t)\|_{\lambda} - \frac{Q}{1-M} \right) + \frac{Q}{1-M}. \quad (30)$$

With the number of iterations  $k \rightarrow \infty$ , we have  $\rho^{k-1} \rightarrow 0$  ( $\rho < 1$ ) and the following inequality:

$$\lim_{k \rightarrow \infty} \|e_k(t)\|_{\lambda} \leq \frac{\lambda \sup_t \|C(t)\| b_w t}{(1-\rho)(\lambda - L_f)} + \frac{b_v}{1-\rho}. \quad (31)$$

From equation (31), it can be seen that, after time  $t = h/a^k$ , the initial state error no longer affects the tracking error, and the tracking error is only determined by the degree of inaccuracy of the system model parameters and other external disturbances. For the value of the right part of inequality is constant, the tracking error of the system will eventually converge to a boundary.

#### 4. Simulations

A 2-DOF planar robot manipulator is used to prove the effectiveness of the proposed control method. As shown in Figure 2, the parameters are as follows: link 1: length  $l_1$  and mass  $m_1$ , the distance between the center of mass of link 1 and base joint is  $l_{c1}$ , and the inertia of link 1 is  $I_1$ . Link 2: length  $l_2$  and mass  $m_2$ ; the distance between the center of mass of link 2 and joint 1 is  $l_{c2}$ , and the inertia of link 2 is  $I_2$ .

The robot manipulator is modeled by the Lagrange method. The parameters of inertia matrix  $M(q)_{2 \times 2}$ , Coriolis and centrifugal matrix  $C(q, \dot{q})_{2 \times 2}$ , and gravity term matrix  $G(q)_{2 \times 1}$  are set as follows:

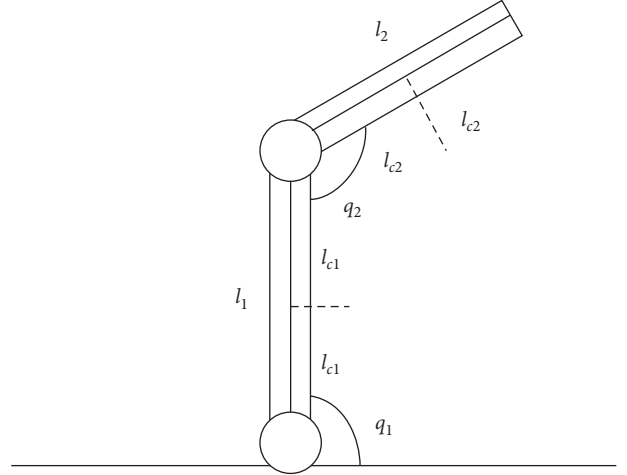


FIGURE 2: 2-DOF robot manipulator.

$$\begin{aligned} M &= [m_{ij}]_{2 \times 2}, \\ m_{11} &= m_1 l_{c1}^2 + m_2 (l_1^2 + l_{c2}^2 + 2l_1 l_2 \cos q_2) + I_1 + I_2, \\ m_{12} &= m_{21} = m_2 (l_{c2}^2 + l_1 l_{c2} \cos q_2) + l_2, \\ m_{22} &= m_2 l_{c2}^2 + I_2, \\ C &= [c_{ij}]_{2 \times 2}, \\ c_{11} &= h \dot{q}_2, \\ c_{12} &= h \dot{q}_1 + h \dot{q}_2, \\ c_{21} &= -h \dot{q}_1, \\ c_{22} &= 0, \\ h &= -m_2 l_1 l_{c2} \sin q_2, \\ G &= [G_1, G_2]^T, \\ G_1 &= (m_1 l_{c1} + m_2 l_1) g \cos q_1 + m_2 l_{c2} g \cos(q_1 + q_2), \\ G_2 &= m_2 l_{c2} g \cos(q_1 + q_2). \end{aligned} \quad (32)$$

The robot system parameters are

$$\begin{aligned} m_1 &= m_2 = 1, \\ l_1 &= l_2 = 0.5, \\ l_{c1} &= l_{c2} = 0.25, \\ I_1 &= I_2 = 0.1, \\ g &= 9.81. \end{aligned} \quad (33)$$

Set the expected trajectory of the system as

$$\begin{cases} y_{1d} = \sin(3t), \\ y_{2d} = \cos(3t). \end{cases} \quad (34)$$

The constant gain matrix of iterative learning control law is set as

$$\Gamma = \begin{bmatrix} 200 & 0 \\ 0 & 200 \end{bmatrix}. \quad (35)$$



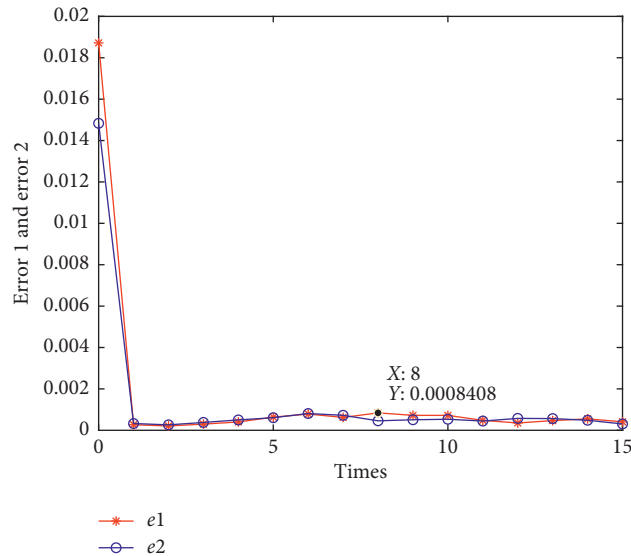


FIGURE 3: Error convergence curve with U-model.

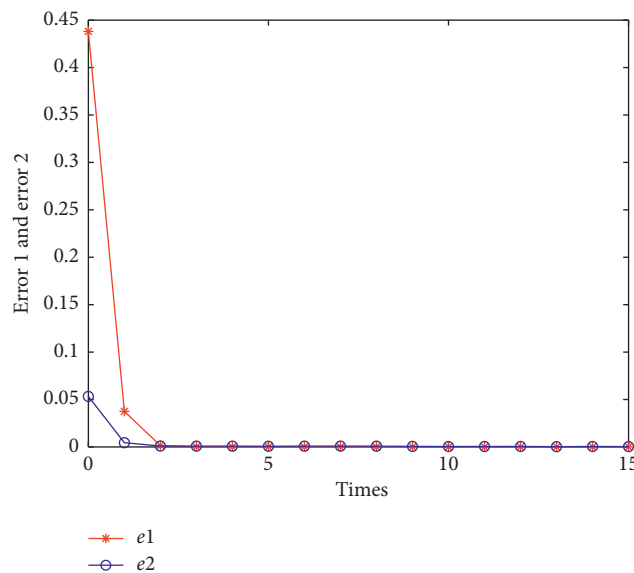


FIGURE 4: Error convergence curve without U-model.

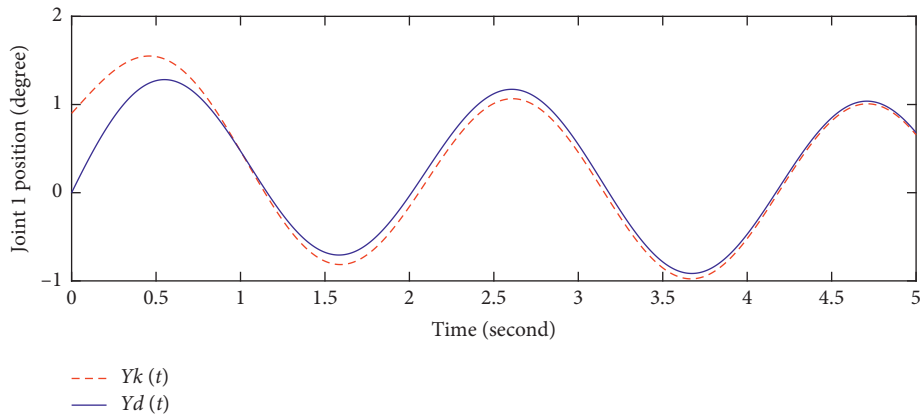
The remaining simulation parameters are initial input  $u_0(t) = \begin{bmatrix} 0 \\ 0 \end{bmatrix}$ ,  $h = 0.1$ , and  $a = 2$ . The initial state of the system is randomly generated by the random function.

In order to illustrate the valid of the proposed U-controller, two experiments are carried out to show the difference of displacement errors rates of the two joints of the robot manipulator with and without U-model, respectively, and the results are shown in Figures 3 and 4.  $x$  axle represents the number of iterations, and  $y$  axle represents the displacement errors of joint 1 and joint 2, respectively.

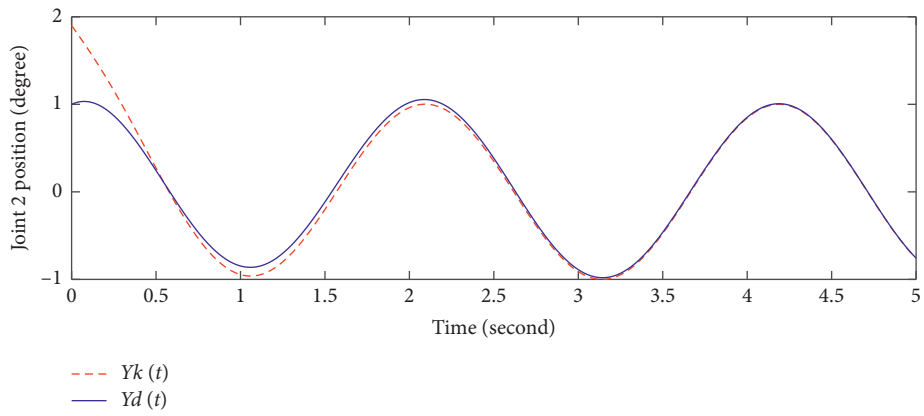
From Figure 3, we can see that when the U-model method is used, only one iteration is needed for each joint to make the displacement error converge to a boundary. However, at least

two iterations for each joint are needed without the use of U-model; from the Figure 4, we can see that the angular displacement errors of joint 1 and joint 2 converge to 0 after three iterations. It means that the U-model control framework can reduce the number of iterations and effectively improve the tracking speed. However, there are displacement errors caused by the U-model, but the loss of tracking accuracy can be acceptable for a robot manipulator, especially when it is used in the fields with high real-time requirement.

In order to show the valid of the proposed ILC law, two experiments are carried out using the U-controller with different ILC laws. The first ILC law is designed in this paper, and the other is the ILC only considering the initial state error. The number of iterations  $k$  is 5. The trajectory tracking

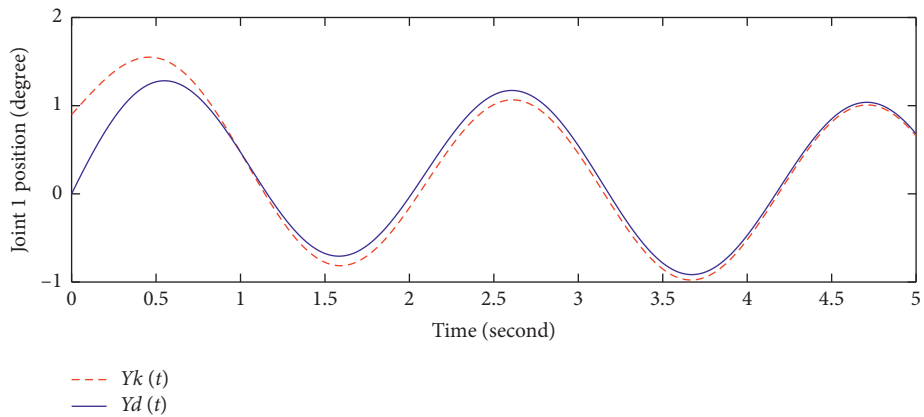


(a)



(b)

FIGURE 5: Trajectory tracking result with the proposed ILC law with 5 iterations.



(a)

FIGURE 6: Continued.

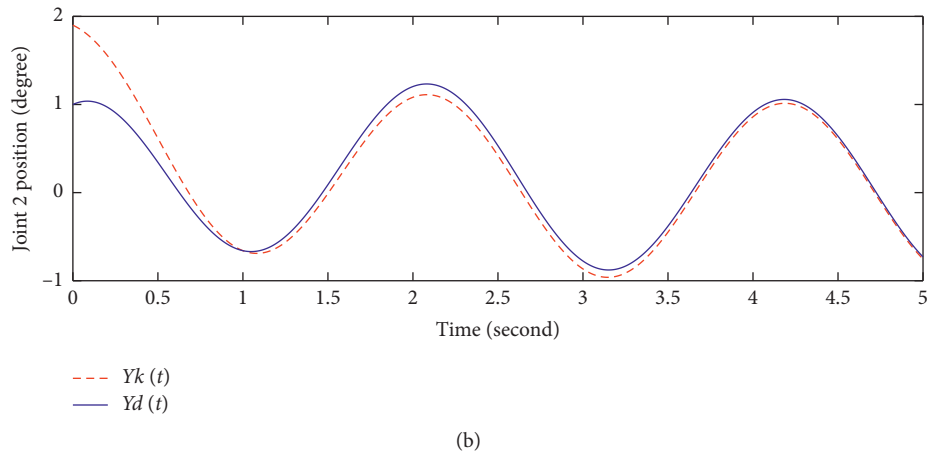


FIGURE 6: Trajectory tracking result with the other ILC law with 5 iterations.

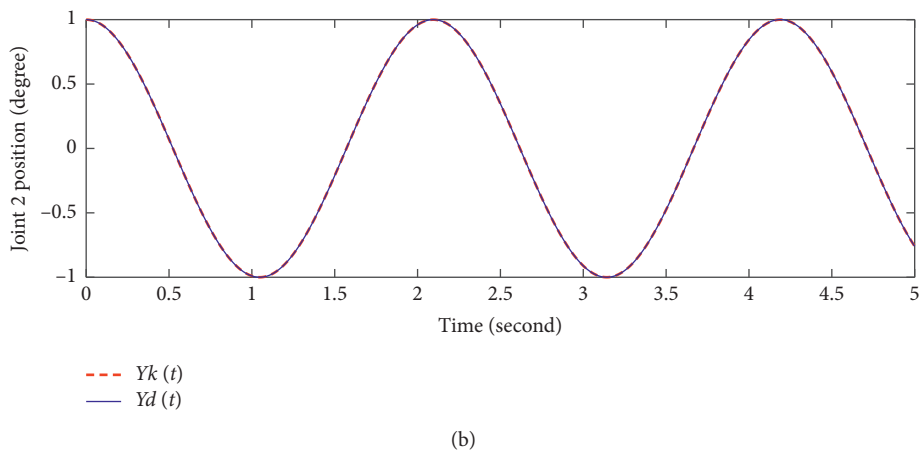
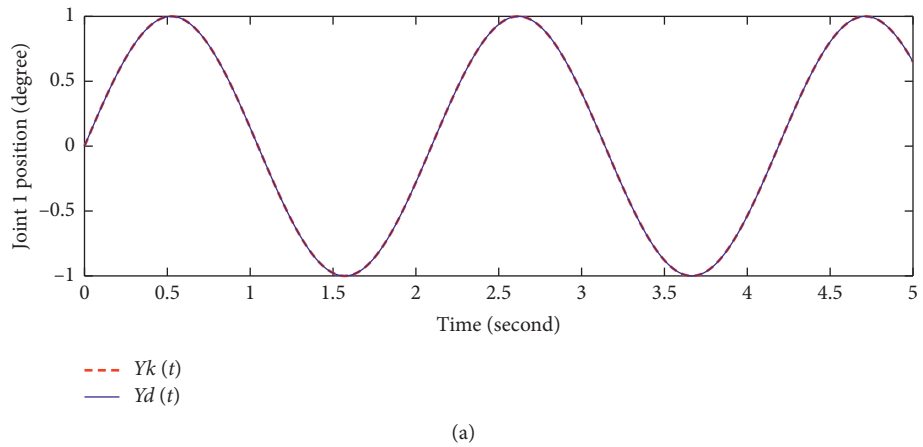


FIGURE 7: Trajectory tracking result with the proposed ILC law with 10 iterations.

curves are shown in Figures 5 and 6. The blue solid line stands for the expected trajectory, and the red dotted line stands for the actual trajectory of the robot manipulator.

From Figure 5, we can see that the actual output trajectory has totally tracked the desired trajectory after 2.5 seconds, while in Figure 6, it takes about 4.5 seconds for the

robot manipulator to track the desired trajectory. By the proposed ILC law, the speed of trajectory tracking is improved more obviously than other ILC law, which does not consider the convergence speed of the initial state error.

With the increasing  $k$ , the benefit of the proposed ILC law will be more obvious. We set  $k = 10$  and repeat the above

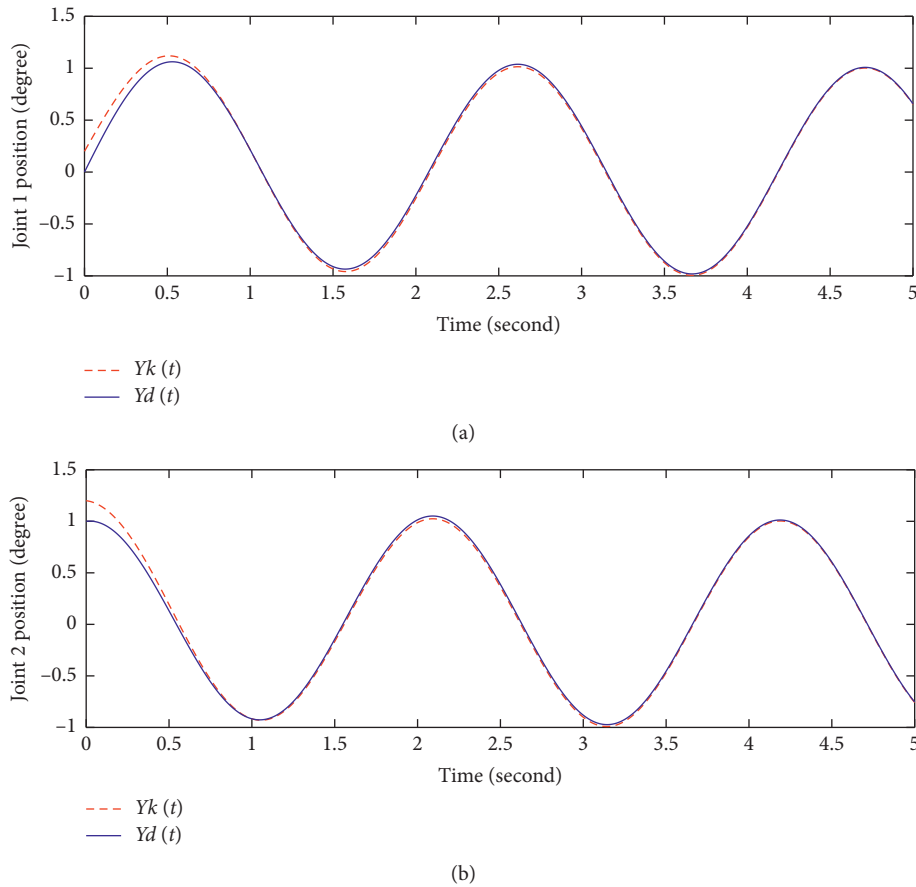


FIGURE 8: Trajectory tracking result with the other ILC law with 10 iterations.

experiment with the tracking results, as shown in Figures 7 and 8. In Figure 7, by using the proposed method, the actual trajectory output is totally tracking the desired trajectory even from the beginning, while in Figure 8, there is still tracking error until 0.5 seconds later.

## 5. Conclusions

The proposed trajectory tracking U-control method has a simple structure and does not need to change the original nonlinear characteristics of the manipulator system. The iterative learning algorithm based on the initial state errors and the speed of error convergence is designed to effectively suppress the influence made by the initial errors and fasten the trajectory tracking. The U-model control framework can reduce the number of iterations of ILC law and further improve the speed of the trajectory tracking. The proposed trajectory tracking the U-control method is particularly suitable for real-time applications.

## Data Availability

The detailed mechanism model and parameters of U-controller are given in the manuscript. The results are computed on the Matlab software with the model and given parameters, while the relevant results are also given in the manuscript.

## Conflicts of Interest

The authors declare that they have no conflicts of interest.

## References

- [1] C. Yang, Y. Jiang, W. He, J. Na, Z. Li, and B. Xu, "Adaptive parameter estimation and control design for robot manipulators with finite-time convergence," *IEEE Transactions on Industrial Electronics*, vol. 65, no. 10, pp. 8112–8123, 2018.
- [2] M. Mehdi Fateh, S. Azargoshasb, and S. Khorashadizadeh, "Model-free discrete control for robot manipulators using a fuzzy estimator," *COMPEL—The International Journal for Computation and Mathematics in Electrical and Electronic Engineering*, vol. 33, no. 3, pp. 1051–1067, 2014.
- [3] I. Koryakovskiy, M. Kudruss, R. Babuška et al., "Benchmarking model-free and model-based optimal control," *Robotics and Autonomous Systems*, vol. 92, pp. 81–90, 2017.
- [4] F. Wang, Z. Chao, L. Huang et al., "Trajectory tracking control of robot manipulator based on RBF neural network and fuzzy sliding mode," *Cluster Computing*, vol. 7, pp. 1–11, 2017.
- [5] L. Pan, T. Gao, F. Xu, and L. Zhang, "Enhanced robust motion tracking control for 6 degree-of-freedom industrial assembly robot with disturbance adaption," *International Journal of Control, Automation and Systems*, vol. 16, no. 2, pp. 921–928, 2018.
- [6] J. Li, Y. Zhang, and M. Mao, "Continuous and discrete zeroing neural network for different-level dynamic linear system with

- robot manipulator control," *IEEE Transactions on Systems, Man, and Cybernetics: Systems*, pp. 1–10, 2018.
- [7] Y. Wang, L. Gu, Y. Xu, and X. Cao, "Practical tracking control of robot manipulators with continuous fractional-order nonsingular terminal sliding mode," *IEEE Transactions on Industrial Electronics*, vol. 63, no. 10, pp. 6194–6204, 2016.
- [8] A. Dumlu and K. Erenturk, "Trajectory tracking control for a 3-DOF parallel manipulator using fractional-order  $PI^{\lambda}D^{\mu}$  control," *IEEE Transactions on Industrial Electronics*, vol. 61, no. 7, pp. 3417–3426, 2014.
- [9] A. Izadbakhsh and S. Khorashadizadeh, "Robust task-space control of robot manipulators using differential equations for uncertainty estimation," *Robotica*, vol. 35, no. 9, pp. 1923–1938, 2017.
- [10] R. S. Mohammad, H. Jafaar, and S. Mahmoodreza, "Robust nonlinear control of robot manipulator with uncertainties in Kinematics, Dynamics and actuator models," *International Journal of Innovative Computing, Information and Control*, vol. 8, no. 8, pp. 5487–5489, 2012.
- [11] A. Andreev and O. Peregudova, "Trajectory tracking control for robot manipulators using only position measurements," *International Journal of Control*, vol. 92, no. 7, pp. 1490–1496, 2017.
- [12] P. Farzin, M. Mina, S. Forouzan, N. Iman, and E. Sara, "Design baseline computed torque controller," *International Journal of Engineering (IJE)*, vol. 6, no. 3, pp. 129–141, 2012.
- [13] T. Hongfeng, D. Xiaoqi, and Y. Huizhong, "Robust optimization and application of iterative learning trajectory tracking algorithm for discrete nonlinear systems," *Information & Control*, vol. 45, no. 4, pp. 385–390, 2016.
- [14] X. Jin, "Iterative learning control for non-repetitive trajectory tracking of robot manipulators with joint position constraints and actuator faults," *International Journal of Adaptive Control and Signal Processing*, vol. 31, no. 6, pp. 859–875, 2017.
- [15] Y. Hui, R. Chi, B. Huang, and Z. Hou, "Extended state observer-based data-driven iterative learning control for permanent magnet linear motor with initial shifts and disturbances," *IEEE Transactions on Systems, Man, and Cybernetics: Systems*, pp. 1–11, 2019.
- [16] Y. Tian, Y. Wang, H. Liu, R. Miao, and Z. Hao, "Variable gain iterative learning control with initial error correction," in *Proceedings of the 2019 IEEE International Conference on Smart Internet of Things (SmartIoT)*, pp. 412–416, Tianjin, China, August 2019.
- [17] H. Reham, F. Bendary, and K. Elserafi, "Trajectory tracking control for robot manipulator using fractional order-fuzzy-PID controller," *International Journal of Computer Applications*, vol. 134, no. 15, pp. 22–29, 2016.
- [18] T. Ye, Z. Luo, and G. Wang, "Adaptive sliding mode control of robot based on fuzzy neural network," *Journal of Ambient Intelligence and Humanized Computing*, 2020.
- [19] Q. Zhu, S. Li, and D. Zhao, "A universal U-model based control system design," in *Proceedings of the 33rd Chinese Control Conference*, pp. 1839–1844, Nanjing, China, July 2014.
- [20] Q. M. Zhu and L. Z. Guo, "A pole placement controller for non-linear dynamic plants," *Proceedings of the Institution of Mechanical Engineers, Part I: Journal of Systems and Control Engineering*, vol. 216, no. 6, pp. 467–476, 2002.
- [21] S. S. A. Ali, M. A. Fouad, and S. Muhammad, "Learning feedforward control of MIMO nonlinear systems using U-model," in *Proceedings of the 9th IASTED International Conference on Control and Applications*, pp. 278–283, Innsbruck, Austria, February 2007.
- [22] S. S. A. Ali, F. M. Al-Sunni, M. Shafiq, and J. M. Bakhshwain, "U-model based learning feedforward control of MIMO nonlinear systems," *Electrical Engineering*, vol. 91, no. 8, pp. 405–415, 2010.
- [23] S. S. A. Ali, F. M. AL-Sunni, and M. Shafiq, "U-model based 2DoF multi-variable IMC for improved input-disturbance rejection: a case study on a 2-link robot manipulator," *International Journal of Advanced Robotic Systems*, vol. 8, no. 3, pp. 166–175, 2011.

## Research Article

# Adaptive Predefined Performance Neural Control for Robotic Manipulators with Unknown Dead Zone

Shifen Shao,<sup>1</sup> Kaisheng Zhang ,<sup>1</sup> Jun Li,<sup>2</sup> and Jirong Wang<sup>3</sup>

<sup>1</sup>College of Electrical and Control Engineering, Shaanxi University of Science and Technology, Xi'an 710021, China

<sup>2</sup>College of Computer Science and Technology, Qingdao University, Qingdao 266071, China

<sup>3</sup>College of Mechanical and Electronic Engineering, Qingdao University, Qingdao 266071, China

Correspondence should be addressed to Kaisheng Zhang; [qdhgysfwz@163.com](mailto:qdhgysfwz@163.com)

Received 6 January 2020; Accepted 3 February 2020; Published 12 May 2020

Guest Editor: Jing Na

Copyright © 2020 Shifen Shao et al. This is an open access article distributed under the Creative Commons Attribution License, which permits unrestricted use, distribution, and reproduction in any medium, provided the original work is properly cited.

This paper proposes an adaptive predefined performance neural control scheme for robotic manipulators in the presence of nonlinear dead zone. A neural network (NN) is utilized to estimate the model uncertainties and unknown dynamics. An improved funnel function is designed to guarantee the transient behavior of the tracking error. The proposed funnel function can release the assumption on the conventional funnel control. Then, an adaptive predefined performance neural controller is proposed for robotic manipulators, while the tracking errors fall within a prescribed funnel boundary. The closed-loop system stability is proved via Lyapunov function. Finally, the numerical simulation results based on a 2-DOF robotic manipulator illustrate the control effect of the presented approach.

## 1. Introduction

Robotic manipulators have been widely utilized in industrial applications such as manufacturing industry, aerospace, and military equipment [1–9]. Nevertheless, the nonlinear terms include the nonlinear friction, model uncertainties, and dead zone that can reduce the control accuracy. To address this problem, the conventional PID controller was designed for robotic manipulators, but PID cannot achieve the satisfactory control performance [9]. To improve the tracking performance of robotic manipulators, a variety of control strategies were proposed for robotic systems such as adaptive control [10, 11], nonlinear control [12], and backstepping control [13–15].

In fact, the difficulties in the control design for robotic systems mainly stem from nonlinear terms. To tackle these nonlinear terms, disturbance observer techniques were proposed to reject the unknown disturbance [1, 16, 17]. In [1], a new unknown dynamics estimator- (UDE-) based first-order filter is proposed for robotic manipulators, the UDE was incorporated into control design that can effectively reject the unknown dynamics. An unknown input observer

(UIO) was developed by introducing the first-order filter to estimate the unknown dynamics of servomechanisms, where the UIO had only one tuned parameter [18]. A novel nonlinear disturbance observer (NDO) was proposed for robotic manipulators in [17]. A disturbance observer (DOB) was devised for robot manipulators, where the external disturbance can be rejected by using the DOB [19]. Although the aforementioned disturbance observer-based control strategies can improve the performance of the robotic manipulator, the transient behavior is not considered in control design.

On the other hand, as neural networks (NNs) [1, 20–25] or fuzzy logic systems (FLS) [26–28] have been used to approximate the system uncertainties due to their approximation ability. In [25], an adaptive neural network control was proposed for robot manipulators, where the NN was utilized to approximate the unknown dead zone and system uncertainties. In [29], a contouring control method was proposed for robot manipulators and the NN was used to estimate the unknown dynamics. In [30], a NN-based terminal sliding mode control (TSMC) was designed for robot manipulators with actuator dynamics, where the NN was



used to estimate the unknown actuator dynamics. A neural-fuzzy control was used to estimate the inverse dynamics; then, the approximation was incorporated into an adaptive neural-fuzzy controller to compensate the unknown dynamics of robot systems [31]. Although the aforementioned approaches can improve the control performance, the transient behavior and steady-state performance are not considered in controller design.

Recently, it is well known that the prescribed performance control (PPC) method can be used to quantitatively analyse the transient behavior [32]. The main feature is that a prescribed function with maximum overshoot and convergence rate is used to transform the original tracking error into a new error. Then, the new error is used to design a controller in which the tracking error can be remained within a predefined boundary. This control method has been used to control some systems [33–38]. In [39], an adaptive prescribed performance control was proposed for servomechanisms to improve the control performance. In [40], a modified prescribed performance function was proposed and incorporated into control design to control piezo-actuated positioning systems. A PPC was developed to control a variable stiffness actuated robot in [34]. Moreover, a funnel control (FC) as a constraint control was also proposed to guarantee the transient response [41]. The concept of FC is to construct an adjustable proportional gain  $\tau$  to control the dynamics systems. The funnel control has been used to control some practice systems such as two-mass systems [42], air-breathing hypersonic vehicles [43], and nonlinear dynamics systems [44]. In [45], a funnel control based on the adaptive fuzzy control was proposed to control stochastic nonlinear systems, where the fuzzy logic is utilized to approximate the unknown nonlinear dynamics. A neural network based on the adaptive control was developed for two-mass systems with backlash, where the neural network was employed to estimate the unknown backlash [46]. If a control system is with high relative degree ( $r \geq 3$ ), the funnel control may not suit this kind of systems. Thus, the application of funnel control is limited. Moreover, the application of funnel control in robotic manipulators cannot be found.

This paper will propose a novel adaptive neural prescribed performance control method for robotic manipulators with unknown dead zone. A novel funnel variable is defined based on the tracking error. The modified funnel variable can release the assumption on the original funnel control. An echo state neural network (ESN) is adopted to estimate the unknown dynamics of robotic manipulators, and the approximation is used in control design to compensate the nonlinear dead zone. Then, an adaptive control scheme for a robotic manipulator is proposed to improve the control performance. Numerical simulation demonstrates the effectiveness of the proposed control approach.

The special contributions of this paper are as follows:

- (i) A novel funnel function is proposed based on the tracking error, and it can release the limitation on the original funnel function and is used in control design to improve the control performance

- (ii) A neural network is utilized to estimate the nonlinear dead zone, and the approximation is to design a controller, where the dead zone is compensated
- (iii) The effectiveness of the proposed control method is evaluated based on a robotic manipulator by using numerical simulations

The remainder of this paper is organized as follows. Section 2 presents system description, funnel control design, and echo state neural network structure. An adaptive neural funnel controller is shown in Section 3. Numerical simulation results are given in Section 4. Finally, the paper is concluded in Section 5.

## 2. Problem Formulation

*2.1. System Description.* This paper considers a  $n$ -degree-of-freedom (DOF) robotic manipulator, which can be modeled as

$$M(q)\ddot{q} + C(q, \dot{q})\dot{q} + G(q) + d_l = d(\tau), \quad (1)$$

where  $q$ ,  $\dot{q}$ , and  $\ddot{q}$  are the robot joint position, velocity, and acceleration, respectively;  $M(q)$  denotes the inertia matrix,  $C(q, \dot{q})$  represents the Coriolis/centrifugal torque, including the viscous friction and nonlinear damping,  $G(q)$  is the gravity torque,  $\tau$  is the control input, and  $d_l$  is the unknown disturbance.

For the matrices  $M(q)$  and  $C(q, \dot{q})$ , the following properties hold.

*Property 1.* The matrix  $\dot{M}(q) - 2C(q, \dot{q})$  is a skew-symmetric matrix.

*Property 2.* The matrix  $M(q)$  is bounded such that  $0 < M_a \leq \|M(q)\| \leq M_b$ , where  $M_a$  and  $M_b$  are positive constants.

*Assumption 1.* The dead-zone nonlinearity (see Figure 1) can be written as

$$d(\tau) = \begin{cases} d_r(\tau), & \text{if } \tau(t) \geq b_r, \\ 0, & \text{if } b_l < \tau(t) < b_r, \\ d_l(\tau), & \text{if } \tau(t) \leq b_l, \end{cases} \quad (2)$$

where  $\tau(t)$  is the control torque,  $d_l(v)$  and  $d_r(v)$  denote unknown smooth functions, and  $b_l < 0$  and  $b_r > 0$  denote constants.

$d_r(\tau(t))$  and  $d_l(\tau(t))$  can be written as

$$d_l(v) = d_l(v) - d_l(b_l)d'_l(\xi_l)(v - b_l), \quad (3)$$

$$\forall v \in (-\infty, b_l] \text{ with } \xi_l \in (-\infty, b_l),$$

$$d_r(v) = d_r(v) - d_r(b_r) = d'_r(\xi_r)(v - b_r), \quad (4)$$

$$\forall v \in [b_r, +\infty) \text{ with } \xi_r \in (b_r, +\infty),$$

where  $d'_i = d(D_i \xi) / d\xi|_{\xi=\xi_i}$ ,  $i = l, r$ , denotes the derivative of  $d_i(\xi)$ ,  $i = l, r$ .

Using (3) and (8), the dead zone is given as

$$d(\tau(t)) = (\chi_l(t) + \chi_r(t))\tau(t) + \rho(t) = d(t)\tau(t) + \rho(t), \quad (5)$$

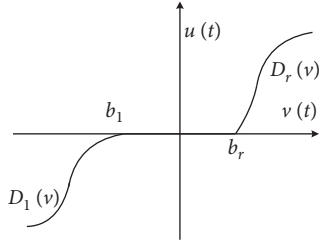


FIGURE 1: Nonlinear dead zone.

where  $d(t) = \chi_l(t) + \chi_r(t)$  with

$$\chi_l(t) = \begin{cases} d_l'(\xi_l), & \text{if } \tau(t) \leq b_r, \\ 0, & \text{if } \tau(t) > b_r, \end{cases} \quad (6)$$

$$\chi_r(t) = \begin{cases} d_r'(\xi_r), & \text{if } \tau(t) \leq b_l, \\ 0, & \text{if } \tau(t) > b_l. \end{cases} \quad (7)$$

**2.2. Echo State Neural Network Approximation.** The echo state neural network is a novel NN with superior capability to approximate the unknown dynamics. The basic architecture of the ESN is shown in Figure 2. The ESN is composed of three parts: (1)  $K$  input neurons,  $N$  reservoir neurons, and  $L$  output layer. The ESN model can be written as

$$\begin{aligned} \dot{X} &= C(-aX + f(W^{\text{in}}u + WX + W^{\text{back}}y)), \\ y &= G(W_0^T X), \end{aligned} \quad (8)$$

where  $X$  denotes the reservoir neuron state,  $C > 0$  is a time constant, and  $a$  represents the leaking decay rate.  $W^{\text{in}} \in R^{N \times K}$ ,  $W \in R^{N \times N}$ , and  $W^{\text{out}} \in R^{N \times L}$  denote the input weight matrix, the reservoir weight matrix, and the feedback weight matrix, respectively. The ESN can be used to approximate any continuous function  $f(x)$  over a compact domain  $\Omega \in R^m$ .

The function  $f(x)$  can be expressed as

$$f(x) = W^T \Phi(x) + \varepsilon, \quad \forall x \in \Omega \subset R^m, \quad (9)$$

where  $\varepsilon$  is the estimation error of the ESN,  $|\varepsilon| \leq \varepsilon_m$ , and  $W$  denotes the weight.

Therefore,

$$W^* = \arg \min_{W \in R^L} \left\{ \sup_{x \in \Omega} |f(x) - W^{*T} X(x)| \right\}. \quad (10)$$

**2.3. Funnel Control.** Funnel control [41] is a novel control strategy. By the error transformation, the original tracking error can be transformed into a new error dynamics. Then, the new errors are used to design a control that can guarantee the control error remaining within a predefined boundary. The system  $S$  has the following properties:

- (i) Relative degree  $r = 1$  or  $2$
- (ii) Minimum phase
- (iii) Known high frequency gain

The controller is given as

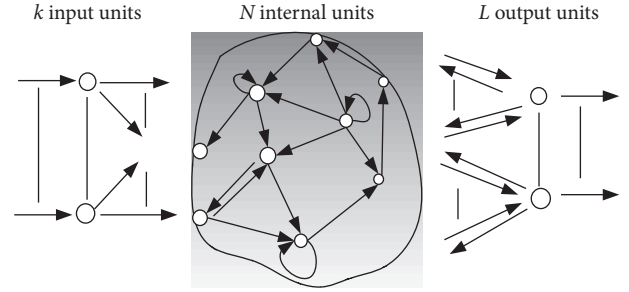


FIGURE 2: Basic architecture of the ESN.

$$u(t) = \tau(F_\varphi(t), \psi(t), \|e(t)\|) \cdot e(t), \quad (11)$$

where  $F_\varphi(t)$  is the funnel function and  $\psi(t)$  denotes the scaling factor. The distance  $d_v(t)$  is defined as

$$d_v(t) = F_\varphi(t) - \|e(t)\|, \quad (12)$$

where  $e(t)$  is the tracking error, which is defined as

$$e(t) = x_d - x(t). \quad (13)$$

Thus, the funnel itself is defined as the set

$$F'_\varphi := \{(t, e) \in R \times R^n \mid \varphi(t) \cdot \|e(t)\| < 1\}. \quad (14)$$

The gain  $\tau(\cdot)$  is

$$\tau(F_\varphi(t), \psi(t), \|e(t)\|) = \frac{\psi(t)}{F_\varphi(t) - \|e(t)\|}. \quad (15)$$

According to [41], the boundary (see Figure 3) is

$$F_\varphi(t) = \varphi_0 \cdot \exp(-at) + \varphi_\infty, \quad (16)$$

where  $\varphi_0$ ,  $\varphi_\infty$ , and  $a$  are design parameters and satisfy  $\varphi_0 \geq \varphi_\infty > 0$  and  $|e(0)| < F_\varphi(0) = \varphi_0 + \varphi_\infty$ .

A novel funnel variable can be given as

$$z(t) = \frac{e(t)}{F_\varphi(t) - \|e(t)\|}. \quad (17)$$

### 3. Adaptive Control Design

**3.1. Controller Design.** In this section, we consider the full state information,  $x_1$  and  $x_2$ , is measured, where  $x_1 = [q_1, q_2, \dots, q_n]^T$  and  $x_2 = [\dot{q}_1, \dot{q}_2, \dots, \dot{q}_n]^T$ . (Figure 4) Then, the system model can be expressed as

$$\begin{aligned} \dot{x}_1 &= x_2, \\ \dot{x}_2 &= M^{-1} [D(\tau) - C(x_1, x_2)x_2 - G(x-1) - d_1]. \end{aligned} \quad (18)$$

*Step 1.* The tracking error  $e_1$  is defined as

$$e_1 = x_1 - x_d, \quad (19)$$

where  $x_d$  is the desired trajectory. According to (15), the funnel error can be defined as

$$z_1 = \frac{e_1}{F_{\varphi_1} - |e_1|}. \quad (20)$$

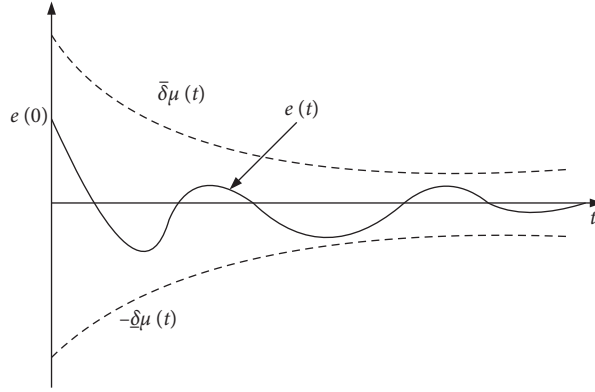


FIGURE 3: Funnel control.

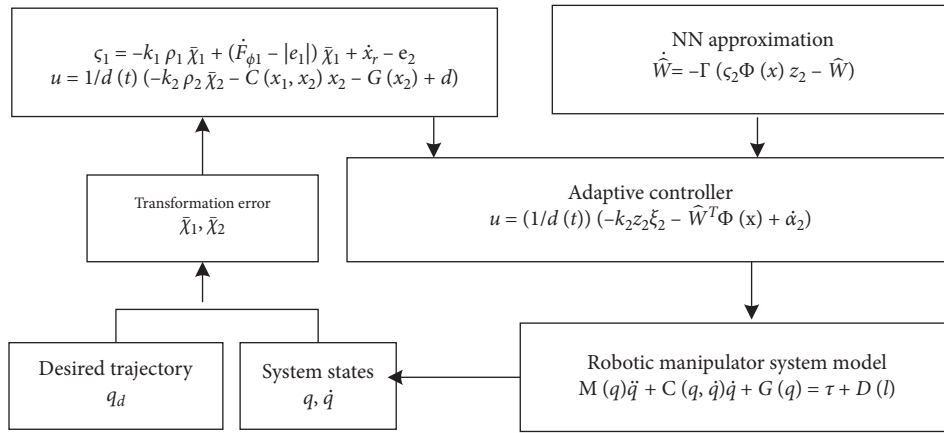


FIGURE 4: Controller architecture.

The time derivative of (20) is

$$\begin{aligned} \dot{z}_1 &= \frac{1}{(F_{\varphi_1} - |e_1|)^2} [\dot{e}_1(F_{\varphi_1} - |e_1|) - e_1(\dot{F}_{\varphi_1} - |\dot{e}_1|)] \\ &= \frac{1}{(F_{\varphi_1} - |e_1|)} [x_2 - (\dot{F}_{\varphi_1} - |\dot{e}_1|)z_1 - \dot{x}_d]. \end{aligned} \quad (21)$$

The Lyapunov function is defined as

$$V_1 = \frac{1}{2} z_1^2. \quad (22)$$

Its time derivative is

$$\dot{V}_1 = z_1 \dot{z}_1 = \frac{z_1}{(F_{\varphi_1} - |e_1|)} [x_2 - (\dot{F}_{\varphi_1} - |\dot{e}_1|)z_1 - \dot{x}_d]. \quad (23)$$

The second error variable is defined as

$$e_2 = x_2 - \alpha_2. \quad (24)$$

Substituting (24) into (23), one has

$$\begin{aligned} \dot{V}_1 &= z_1 \dot{z}_1 = \frac{z_1}{(F_{\varphi_1} - |e_1|)} [\alpha_2 + e_2 - (\dot{F}_{\varphi_1} - |\dot{e}_1|)z_1 - \dot{x}_d] \\ &= z_1 \zeta_1 [\alpha_2 + e_2 - (\dot{F}_{\varphi_1} - |\dot{e}_1|)z_1 - \dot{x}_d], \end{aligned} \quad (25)$$

where  $\zeta_1 = 1/(F_{\varphi_1} - |e_1|)$ .

An intermediate control signal is chosen as

$$\alpha_2 = -k_1 z_1 \zeta_1 + (\dot{F}_{\varphi_1} - |\dot{e}_1|)z_1 + \dot{x}_d - e_2, \quad (26)$$

where  $k_1$  is a design parameter.

Step 2. The time derivative of  $e_2$  is

$$\dot{e}_2 = \dot{x}_2 - \dot{\alpha}_2. \quad (27)$$

According to (17), the second funnel error variable can be defined as

$$z_2 = \frac{e_2}{F_{\varphi_2} - |e_2|}. \quad (28)$$

The time derivative of  $z_2$  is

$$\begin{aligned} \dot{z}_2 &= \frac{1}{(F_{\varphi_2} - |e_2|)^2} [\dot{e}_2(F_{\varphi_2} - |e_2|) - e_2(\dot{F}_{\varphi_2} - |\dot{e}_2|)] \\ &= \frac{1}{(F_{\varphi_2} - |e_2|)} [\dot{x}_2 - (\dot{F}_{\varphi_2} - |\dot{e}_2|)z_2 - \dot{\alpha}_2] \\ &= \zeta_2 z_2 [M^{-1}(D(\tau) - C(x_1, x_2)x_2 - G(x_1) \\ &\quad - d_1) - (\dot{F}_{\varphi_2} - |\dot{e}_2|)z_2 - \dot{\alpha}_2], \end{aligned} \quad (29)$$

where  $\zeta_2 = 1/(F_{\varphi_2} - |e_2|)$ .

The Lyapunov function is defined as

$$V_2 = \frac{1}{2}z_2^T M(x_1)z_2. \quad (30)$$

The derivative of (30) is

$$\begin{aligned} \dot{V}_2 &= z_2^T M(x_1)\dot{z}_2 + z_2^T \frac{1}{2}\dot{M}(x_1)z_2 \\ &= \zeta_2 z_2^T [(d(t)v(t) + \rho(t) - C(x_1, x_2)x_2 - G(x_1) - d_l) \\ &\quad - (\dot{F}_{\varphi_2} - |\dot{e}_2|)z_2 - \dot{\alpha}_2 + \frac{1}{2}\dot{M}(x_1)z_2] \\ &= \zeta_2 z_2^T [(d(t)v(t) + F(x) - \dot{\alpha}_2)]. \end{aligned} \quad (31)$$

where  $F(x) = \rho(t) - C(x_1, x_2)x_2 - G(x_1) - d_l - (\dot{F}_{\varphi_2} - |\dot{e}_2|) + z_2(1/2)\dot{M}(x_1)z_2$  denotes the unknown term, which can be approximated by using the NN.

The actual controller can be designed as

$$\tau(t) = \frac{1}{d(t)}(-k_2 z_2 \zeta_2 + \widehat{W}\Phi(X) + \dot{\alpha}_2), \quad (32)$$

where  $\widehat{W}$  denotes the estimation of  $W$ , which is defined as

$$\dot{\widehat{W}} = -\Gamma(\zeta_2 \Phi(X)z_2 - \sigma \widehat{W}), \quad (33)$$

where  $\Gamma$  and  $\sigma$  are design parameters.

**3.2. Stability Analysis.** In this section, we will employ the Lyapunov function to analyse the convergence of the closed-loop system.

**Theorem 1.** Consider the robotic manipulators (1) with the proposed controller (32), intermediate controller (26), and adaptive law (33), then all the signals of the closed-loop system are bounded, and the tracking error can converge to the prescribed zone.

*Proof.* A Lyapunov function is chosen as

$$V = V_1 + V_2. \quad (34)$$

The time derivative of (34) is

$$\dot{V} = \dot{V}_1 + \dot{V}_2. \quad (35)$$

Substituting (23) and (31) into (35), one has

$$\begin{aligned} \dot{V} &= z_1 \zeta_1 [\alpha_2 + e_2 - (\dot{F}_{\varphi_1} - |\dot{e}_1|)z_1 - \dot{x}_d] \\ &\quad + \zeta_2 z_2 [M^{-1}(D(\tau) - C(x_1, x_2)x_2 - G(x_1) - d_l) \\ &\quad - (\dot{F}_{\varphi_2} - |\dot{e}_2|)z_2 - \dot{\alpha}_2]. \end{aligned} \quad (36)$$

Based on (27), (33), and adaptive law (34), one has

$$\dot{V} = -k_1 \zeta_1 z_1 - k_2 \zeta_2 z_2 + \sigma \widehat{W}\widehat{W}. \quad (37)$$

Using Young's inequality, one has

$$\sigma \widehat{W}\widehat{W} \leq -\frac{\sigma}{2}\widehat{W}\widehat{W} + \frac{\sigma}{2}W^2. \quad (38)$$

Substituting (38) into (37), we have

$$\begin{aligned} \dot{V} &\leq -k_1 \zeta_1 z_1 - k_2 \zeta_2 z_2 - \frac{\sigma}{2}\widehat{W}\widehat{W} + \frac{\sigma}{2}W^2 \\ &\leq -\rho V + \delta, \end{aligned} \quad (39)$$

where  $\rho = \min\{2k_1 \zeta_1, 2k_2 \zeta_2, \sigma\}$  and  $\delta = (\sigma/2)W^2$  are positive constants.

From (39), we know that  $V$  is bounded by  $\delta/\rho$ . Therefore, all the signals of the closed-loop system are semiglobally uniformly and ultimately bounded.

The parameter tuning guidelines are given as follows:

- (1) Select the funnel variables  $\varphi_0$ ,  $\varphi_{\infty}$ , and  $a$ , and they should satisfy the initial conditions  $\varphi_0(0) > \varphi_{\infty}(0) > 0$ .
- (2) Choose the control gains  $k_1$  and  $k_2$ , and the adaptive law parameters are  $\Gamma$  and  $\sigma$ . In general, they can be set large for the ease of fast convergence. However, practical control systems do not allow using large gains because they may produce oscillations. Hence, they can be chosen based on a trial-and-error method.  $\square$

## 4. Numerical Simulation

In this section, we will employ an example to illustrate the control performance of the developed control method. A diagram of the robotic manipulator system with 2-DOF is shown in Figure 5. The robotic manipulator parameters are listed in Table 1.

The system matrices  $M(q)$ ,  $C(q, \dot{q})$ , and  $G(q)$  are defined as

$$M(q) = \begin{bmatrix} \alpha l_1^2 + \beta l_2^2 + 2\gamma l_1 l_2 c_2 & \beta l_2^2 + \gamma l_1 l_2 c_2 \\ \beta l_2^2 + \gamma l_1 l_2 c_2 & \beta l_2^2 \end{bmatrix}, \quad (40)$$

$$G(q) = 0,$$

$$C(q) = \begin{bmatrix} -2\gamma l_1 l_2 \dot{q}_2 s_2 & -\gamma l_1 l_2 \dot{q}_2 s_2 \\ \gamma l_1 l_2 \dot{q}_2 s_2 & 0 \end{bmatrix}, \quad (41)$$

where  $\alpha = 1/4m_1 + m_2 + m_3 + m_4$ ,  $\beta = 1/4m_3 + m_4$ , and  $\gamma = 1/2m_3 + m_4$ , respectively.

The controller parameters are given as  $k_1 = 5$  and  $k_2 = 10$ . The adaptive parameters are  $\Gamma = 10I$  and  $\sigma = 0.02$ . The initial weight  $\widehat{W} = 0$ . The initial position of robotic manipulator is chosen as  $q_0 = [0, 0]$  and  $\dot{q}_0 = [0, 0]$ . The friction term is  $F(q) = [15\dot{q}_1 + 6 \operatorname{sign}(\dot{q}_1); 15\dot{q}_2 + 6 \operatorname{sign}(\dot{q}_2)]$ . The funnel function is  $F_{\varphi_i}(t) = \varphi_{0i} \cdot \exp(-a_i t) + \varphi_{\infty i}$ ,  $i = 1, 2$ , with  $\varphi_{01} = \varphi_{02} = 0.18$ ,  $\varphi_{\infty 1} = \varphi_{\infty 2} = 0.01$ , and  $a_1 = a_2 = 2$ . The reference signals are given as  $q_{1d} = 0.3 \sin t$  and  $q_{2d} = 0.3 \sin t$ .

Figures 6–8 depict the simulation results, where the output tracking performance, control actions, and ESN estimation are given. From Figure 6, we can see that the developed control approach can achieve the satisfactory control performance. In addition, we can see that the

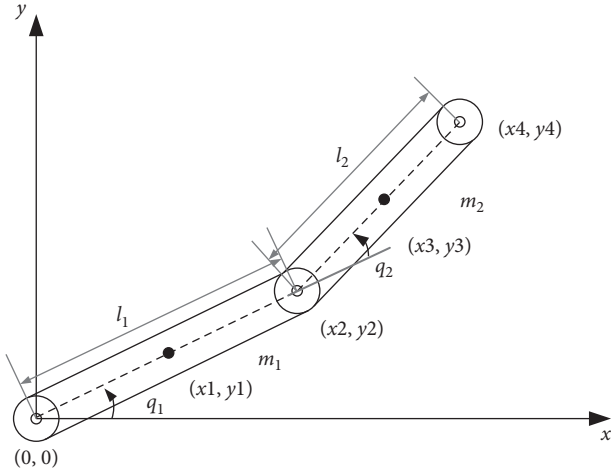


FIGURE 5: Diagram of the robotic manipulator.

TABLE 1: Parameters for the robotic manipulator.

Parameters	Description	Value	Unit
$l_1$	Length of link 1	1	m
$l_2$	Length of link 2	0.8	m
$m_1$	Mass of link 1	1	kg
$m_2$	Mass of joint 2	1.5	kg
$m_3$	Mass of link 2	2	kg
$m_3$	Mass of actuator	1.5	kg

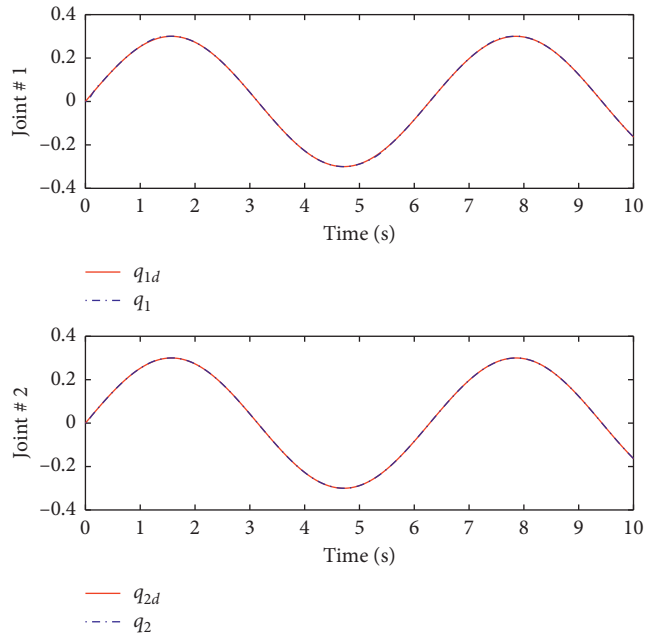


FIGURE 6: Output tracking.

nonlinear friction can be estimated by using the echo state neural network. From these results, we find that the proposed control method improves the tracking performance of the robotic manipulator.

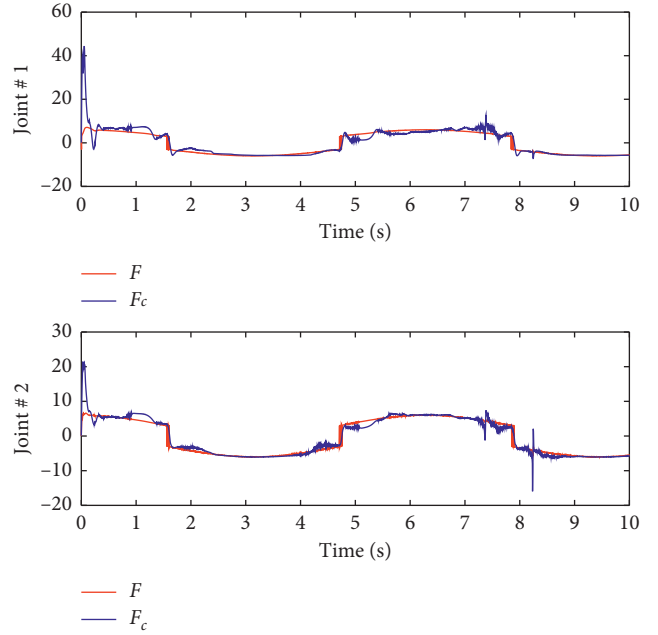


FIGURE 7: Friction compensation.

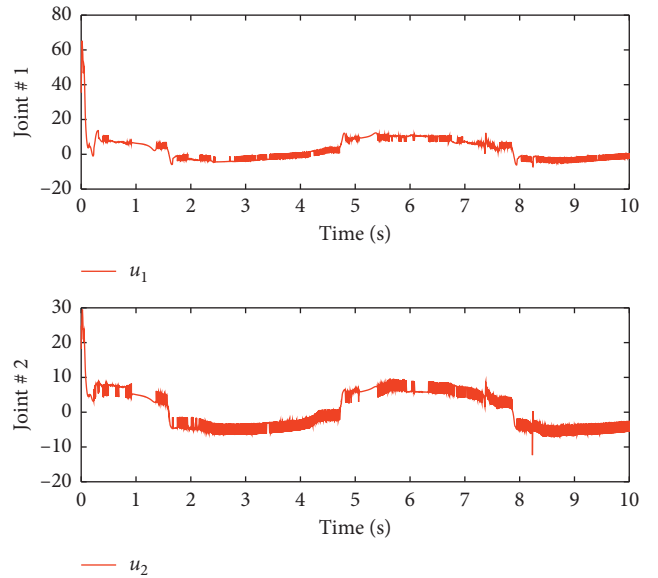


FIGURE 8: Control signals.

### 5. Conclusion

In this paper, an adaptive predefined performance control for robotic manipulators in the presence of nonlinear dead zone was proposed. A novel funnel variable was designed based on the tracking error. The new error variable was utilized to design a controller that can guarantee the transient response. A neural network was adopted to estimate the unknown dynamics (parameter uncertainties and nonlinear dead zone), and the approximation was utilized in controller design to compensate the unknown dynamics. An adaptive controller based on funnel control was designed for the robotic manipulator. Both the transient response and



steady-state performance of the tracking error are guaranteed.

## Data Availability

The data used to support the findings of this study are available from the corresponding author upon request.

## Conflicts of Interest

The authors declare that they have no conflicts of interest.

## Acknowledgments

This work was supported by the Project of Science and Technology Department of Shanxi Province (16JK1100).

## References

- [1] J. Na, J. Yang, S. Wang, G. Gao, and C. Yang, "Unknown dynamics estimator-based output-feedback control for nonlinear pure-feedback systems," *IEEE Transactions on Systems, Man, and Cybernetics: Systems*, pp. 1–12, 2019.
- [2] S. Wang, X. Ren, J. Na, and T. Zeng, "Extended-state-observer-based funnel control for nonlinear servomechanisms with prescribed tracking performance," *IEEE Transactions on Automation Science and Engineering*, vol. 14, no. 1, pp. 98–108, 2017.
- [3] T. Li, S. Duan, J. Liu, L. Wang, and T. Huang, "A spintronic memristor-based neural network with radial basis function for robotic manipulator control implementation," *IEEE Transactions on Systems, Man, and Cybernetics: Systems*, vol. 46, no. 4, pp. 582–588, 2016.
- [4] W. He, Y. Ouyang, and J. Hong, "Vibration control of a flexible robotic manipulator in the presence of input dead-zone," *IEEE Transactions on Industrial Informatics*, vol. 13, no. 1, pp. 48–59, 2017.
- [5] H. Gao, W. He, C. Zhou, and C. Sun, "Neural network control of a two-link flexible robotic manipulator using assumed mode method," *IEEE Transactions on Industrial Informatics*, vol. 15, no. 2, pp. 755–765, 2019.
- [6] M. Jafarinasab, S. Sirouspour, and E. Dyer, "Model-based motion control of a robotic manipulator with a flying multitor base," *IEEE/ASME Transactions on Mechatronics*, vol. 24, no. 5, pp. 2328–2340, 2019.
- [7] S. Wang, J. Na, and Y. Xing, "Adaptive optimal parameter estimation and control of servo mechanisms: theory and experiments," *IEEE Transactions on Industrial Electronics*, p. 1, 2020.
- [8] Q. Chen, S. Xie, M. Sun, and X. He, "Adaptive nonsingular fixed-time attitude stabilization of uncertain spacecraft," *IEEE Transactions on Aerospace and Electronic Systems*, vol. 54, no. 6, pp. 2937–2950, 2018.
- [9] Y. Jia, "Robust control with decoupling performance for steering and traction of 4WS vehicles under velocity-varying motion," *IEEE Transactions on Control Systems Technology*, vol. 8, no. 3, pp. 554–569, 2000.
- [10] C. Yang, Y. Jiang, W. He, J. Na, Z. Li, and B. Xu, "Adaptive parameter estimation and control design for robot manipulators with finite-time convergence," *IEEE Transactions on Industrial Electronics*, vol. 65, no. 10, pp. 8112–8123, 2018.
- [11] M. Tao, Q. Chen, X. He, and M. Sun, "Adaptive fixed-time fault-tolerant control for rigid spacecraft using a double power reaching law," *International Journal of Robust and Nonlinear Control*, vol. 29, no. 12, pp. 4022–4040, 2019.
- [12] R. M. Robinson, C. S. Kothera, R. M. Sanner, and N. M. Wereley, "Nonlinear control of robotic manipulators driven by pneumatic artificial muscles," *IEEE/ASME Transactions on Mechatronics*, vol. 21, no. 1, pp. 55–68, 2016.
- [13] N. Nikdel, M. Badamchizadeh, V. Azimirad, and M. A. Nazari, "Fractional-order adaptive backstepping control of robotic manipulators in the presence of model uncertainties and external disturbances," *IEEE Transactions on Industrial Electronics*, vol. 63, no. 10, pp. 6249–6256, 2016.
- [14] S. Wang, H. Yu, and J. Yu, "Robust adaptive tracking control for servo mechanisms with continuous friction compensation," *Control Engineering Practice*, vol. 87, pp. 76–82, 2019.
- [15] S. Wang, J. Na, H. Yu, and Q. Chen, "Finite time parameter estimation-based adaptive predefined performance control for servo mechanisms," *ISA Transactions*, vol. 87, pp. 174–186, 2019.
- [16] J. N. Yun, J. Su, Y. I. Kim, and Y. C. Kim, "Robust disturbance observer for two-inertia system," *IEEE Transactions on Industrial Electronics*, vol. 60, no. 7, pp. 2700–2710, 2013.
- [17] W.-H. Chen, D. J. Ballance, P. J. Gawthrop, and J. O'Reilly, "A nonlinear disturbance observer for robotic manipulators," *IEEE Transactions on Industrial Electronics*, vol. 47, no. 4, pp. 932–938, 2000.
- [18] S. Wang, J. Na, X. Ren, H. Yu, and J. Yu, "Unknown input observer-based robust adaptive funnel motion control for nonlinear servomechanisms," *International Journal of Robust and Nonlinear Control*, vol. 28, no. 18, pp. 6163–6179, 2018.
- [19] S. P. Chan, "A disturbance observer for robot manipulators with application to electronic components assembly," *IEEE Transactions on Industrial Electronics*, vol. 42, no. 5, pp. 487–493, 1995.
- [20] S. Wang, J. Na, and X. Ren, "Rise-based asymptotic prescribed performance tracking control of nonlinear servo mechanisms," *IEEE Transactions on Systems, Man, and Cybernetics: Systems*, vol. 48, no. 12, pp. 2359–2370, 2018.
- [21] S. Wang, H. Yu, J. Yu, J. Na, and X. Ren, "Neural-network-based adaptive funnel control for servo mechanisms with unknown dead-zone," *IEEE Transactions on Cybernetics*, vol. 50, no. 4, pp. 1383–1394, 2020.
- [22] J. Na, S. Wang, Y.-J. Liu, Y. Huang, and X. Ren, "Finite-time convergence adaptive neural network control for nonlinear servo systems," *IEEE Transactions on Cybernetics*, pp. 1–12, 2019.
- [23] Q. Chen, H. Shi, and M. Sun, "Echo state network-based backstepping adaptive iterative learning control for strict-feedback systems: an error-tracking approach," *IEEE Transactions on Cybernetics*, pp. 1–14, 2019.
- [24] S. Wang, Q. Chen, X. Ren, and H. Yu, "Neural network-based adaptive funnel sliding mode control for servo mechanisms with friction compensation," *Neurocomputing*, vol. 377, pp. 16–26, 2020.
- [25] W. He, A. O. David, Z. Yin, and C. Sun, "Neural network control of a robotic manipulator with input deadzone and output constraint," *IEEE Transactions on Systems, Man, and Cybernetics: Systems*, vol. 46, no. 6, pp. 759–770, 2016.
- [26] L. Cao, H. Li, N. Wang, and Q. Zhou, "Observer-based event-triggered adaptive decentralized fuzzy control for nonlinear large-scale systems," *IEEE Transactions on Fuzzy Systems*, vol. 27, no. 6, pp. 1201–1214, 2019.
- [27] T. Wang, S. Tong, J. Yi, and H. Li, "Adaptive inverse control of cable-driven parallel system based on type-2 fuzzy logic



- systems,” *IEEE Transactions on Fuzzy Systems*, vol. 23, no. 5, pp. 1803–1816, 2015.
- [28] Y. Li and S. Tong, “Adaptive fuzzy control with prescribed performance for block-triangular-structured nonlinear systems,” *IEEE Transactions on Fuzzy Systems*, vol. 26, no. 3, pp. 1153–1163, 2018.
- [29] L. Wang, T. Chai, and C. Yang, “Neural-network-based contouring control for robotic manipulators in operational space,” *IEEE Transactions on Control Systems Technology*, vol. 20, no. 4, pp. 1073–1080, 2012.
- [30] L. Wang, T. Chai, and L. Zhai, “Neural-network-based terminal sliding-mode control of robotic manipulators including actuator dynamics,” *IEEE Transactions on Industrial Electronics*, vol. 56, no. 9, pp. 3296–3304, 2009.
- [31] F. Sun, L. Li, H.-X. Li, and H. Liu, “Neuro-fuzzy dynamic-inversion-based adaptive control for robotic manipulators—discrete time case,” *IEEE Transactions on Industrial Electronics*, vol. 54, no. 3, pp. 1342–1351, 2007.
- [32] C. P. Bechlioulis and G. A. Rovithakis, “Prescribed performance adaptive control for multi-input multi-output affine in the control nonlinear systems,” *IEEE Transactions on Automatic Control*, vol. 55, no. 5, pp. 1220–1226, 2010.
- [33] Q. Hu, X. Shao, and L. Guo, “Adaptive fault-tolerant attitude tracking control of spacecraft with prescribed performance,” *IEEE/ASME Transactions on Mechatronics*, vol. 23, no. 1, pp. 331–341, 2018.
- [34] E. Psomopoulou, A. Theodorakopoulos, Z. Doulgeri, and G. A. Rovithakis, “Prescribed performance tracking of a variable stiffness actuated robot,” *IEEE Transactions on Control Systems Technology*, vol. 23, no. 5, pp. 1914–1926, 2015.
- [35] Y. Zhu, J. Qiao, and L. Guo, “Adaptive sliding mode disturbance observer-based composite control with prescribed performance of space manipulators for target capturing,” *IEEE Transactions on Industrial Electronics*, vol. 66, no. 3, pp. 1973–1983, 2019.
- [36] C. Hua, G. Liu, L. Li, and X. Guan, “Adaptive fuzzy prescribed performance control for nonlinear switched time-delay systems with unmodeled dynamics,” *IEEE Transactions on Fuzzy Systems*, vol. 26, no. 4, pp. 1934–1945, 2018.
- [37] J. Na, Y. Huang, Q. Pei, X. Wu, G. Gao, and G. Li, “Active suspension control of full-car systems without function approximation,” *IEEE/ASME Transactions on Mechatronics*, vol. 25, no. 2, pp. 779–791, 2020.
- [38] Y. Huang, J. Na, X. Wu, and G. Gao, “Approximation-free control for vehicle active suspensions with hydraulic actuator,” *IEEE Transactions on Industrial Electronics*, vol. 65, no. 9, pp. 7258–7267, 2018.
- [39] J. Na, Q. Chen, X. Ren, and Y. Guo, “Adaptive prescribed performance motion control of servo mechanisms with friction compensation,” *IEEE Transactions on Industrial Electronics*, vol. 61, no. 1, pp. 486–494, 2014.
- [40] M. L. Nguyen, X. Chen, and F. Yang, “Discrete-time quasi-sliding-mode control with prescribed performance function and its application to piezo-actuated positioning systems,” *IEEE Transactions on Industrial Electronics*, vol. 65, no. 1, pp. 942–950, 2018.
- [41] A. Ilchmann, E. P. Ryan, and C. J. Sangwin, “Tracking with prescribed transient behaviour,” *ESAIM: Control, Optimisation and Calculus of Variations*, vol. 7, Article ID 471493, 2002.
- [42] A. Ilchmann and H. Schuster, “Pi-funnel control for two mass systems,” *IEEE Transactions on Automatic Control*, vol. 54, no. 4, pp. 918–923, 2009.
- [43] X. Bu, “Air-breathing hypersonic vehicles funnel control using neural approximation of non-affine dynamics,” *IEEE/ASME Transactions on Mechatronics*, vol. 23, no. 5, pp. 2099–2108, 2018.
- [44] S. I. Han and J. M. Lee, “Fuzzy echo state neural networks and funnel dynamic surface control for prescribed performance of a nonlinear dynamic system,” *IEEE Transactions on Industrial Electronics*, vol. 61, no. 2, pp. 1099–1112, 2014.
- [45] C. Hua, K. Li, and X. Guan, “Event-based dynamic output feedback adaptive fuzzy control for stochastic nonlinear systems,” *IEEE Transactions on Fuzzy Systems*, vol. 26, no. 5, pp. 3004–3015, 2018.
- [46] S. Wang, H. Yu, J. Yu, and X. Gao, “Adaptive neural funnel control for nonlinear two-inertia servo mechanisms with backlash,” *IEEE Access*, vol. 7, pp. 33 338–33 345, 2019.

## Research Article

# A Genetic Optimization Algorithm Based on Adaptive Dimensionality Reduction

Tai Kuang <sup>1</sup>, Zhongyi Hu <sup>2</sup> and Minghai Xu<sup>2</sup>

<sup>1</sup>Department of Information Engineering, Zhejiang College of Security Technology, Wenzhou 325016, China

<sup>2</sup>Institute of Big Data and Information Technology, Wenzhou University, Wenzhou 325000, China

Correspondence should be addressed to Tai Kuang; [kuangtaikt@qq.com](mailto:kuangtaikt@qq.com)

Received 19 March 2020; Revised 17 April 2020; Accepted 20 April 2020; Published 11 May 2020

Guest Editor: Weicun Zhang

Copyright © 2020 Tai Kuang et al. This is an open access article distributed under the Creative Commons Attribution License, which permits unrestricted use, distribution, and reproduction in any medium, provided the original work is properly cited.

With the rise of big data in cloud computing, many optimization problems have gradually developed into high-dimensional large-scale optimization problems. In order to address the problem of dimensionality in optimization for genetic algorithms, an adaptive dimensionality reduction genetic optimization algorithm (ADRGGA) is proposed. An adaptive vector angle factor is introduced in the algorithm. When the angle of an individual's adjacent dimension is less than the angle factor, the value of the smaller dimension is marked as 0. Then, the angle between each individual dimension is calculated separately, and the number of zeros in the population is updated. When the number of zeros of all individuals in a population exceeds a given constant in a certain dimension, the dimension is considered to have no more information and deleted. Eight high-dimensional test functions are used to verify the proposed adaptive dimensionality reduction genetic optimization algorithm. The experimental results show that the convergence, accuracy, and speed of the proposed algorithm are better than those of the standard genetic algorithm (GA), the hybrid genetic and simulated annealing algorithm (HGSA), and the adaptive genetic algorithm (AGA).

## 1. Introduction

High-dimensional optimization problems have become increasingly prevalent in many fields, for example, radar waveform optimization [1, 2] and water quality monitoring [3]. Recently, major breakthroughs have been made with respect to solving such problems. Tuo et al. [4] proposed a global optimization algorithm that used the membrane calculation principle to solve high-dimensional functions in 2011. Their algorithm, by implementing high-dimensional segmentation, achieved the segmentation of a high-dimensional space into a low-dimensional one, thereby improving the performance. Also addressing the problem of high-dimensional space processing, Chen et al. [5] described an approach that established a sparse regression model by utilizing the geometric structural features of the approximate solution set, mapping the high-dimensional target space into a low-dimensional one. In 2015, Chen et al. [6] designed a congestion control strategy based on the concept of open angles and compared it against the indication-based

evolutionary algorithm (IBEA) [7], NSGA III (non-dominated sorting genetic algorithm III) [8], and the grid-based evolutionary algorithm (GrEA) [9]. The results indicated a significant improvement by the proposed algorithm. In the same year, Zheng et al. [10] proposed a high-dimensional multiobjective evolutionary algorithm based on information separation. Although this algorithm decomposed the high-dimensional space into a low-dimensional one, it did not remove the excess dimensions. In order to maintain a balance between the convergence and distributed features of the objective evolutionary algorithms, Bi and Wang [11] proposed a high-dimensional objective evolutionary algorithm based on an angle penalty. In 2018, He et al. [12] combined a dimensionality reduction and differential evolution algorithm to solve the knapsack problem. The experimental results showed that this algorithm achieved good accuracy and stability and is suited for solving large-scale problems. Liang et al. [13] first conducted an analysis of the features of large-scale high-dimensional problems and developed a coevolutionary dynamic particle

swarm optimization algorithm, dividing the whole swarm into different groups. Unlike the improvement targeting the number of dimensions, Xia et al. [14] proposed a fitness-based multiplayer swarm optimization algorithm (FMPSO), with the addition of a new component into the particle velocity update rules, called the “subspace learning” component. During the evolutionary process, two adjustment operators were introduced to adjust the roles and number of objective dimensions of the particles. Xu et al. [15] proposed a multidimensional learning strategy based on the experience of the best individuals, which was used to discover and integrate valuable information from the best swarm solution. In their experimentation, 16 classical benchmark functions, 30 CEC 2014 testing functions, and one actual optimization problem were used. This algorithm demonstrated higher convergence, accuracy, and speed. In 2015, Wu et al. [16] described a nondominated sorting genetic algorithm utilizing fractal dimensions and an elitist strategy for feature selection. This algorithm could successfully reduce the number of dimensions for the objective problems. This algorithm, however, only improved the classification accuracy as compared with the standard genetic algorithms to a limited extent. He and Yen [17] used the minimum included angle between two vectors to look for similar individuals, among which the individuals with poor convergence were deleted. However, it was still difficult to set the difference threshold. Xiang et al. [18] implemented priority selection based on the maximum included angle between two vectors, thereby ensuring the diversity of the swarm. However, a good strategy for determining the angle threshold was still not provided. Furthermore, the U-model methodology, which is a generic systematic approach to convert a nonlinear polynomial model into a controller output  $u(t-1)$ -based time-varying polynomial model, has been studied for facilitating a nonlinear control system design over the last decade [19–22]. Given the aforementioned, we define the concept of an adaptive vector angle factor, which changes with the swarm size and number of dimensions. In this paper, the adaptive vector angle factor is used for realizing dimensionality reduction with a GA. At the same time, it also provides a reference for U-model approaches in algorithm implementation.

## 2. The Proposed ADRGA Algorithm

**2.1. Vector Angle Factor.** Dimensionality reduction is a good approach for solving large-scale problems. However, most dimensionality reduction algorithms are random processes; those dimensions carrying important information or those crucial for objective problem solving may be deleted. Consider a 2D vector coordinate  $(a, b)$  in Figure 1. When the included angle  $\theta$  between this vector and the  $x$ -axis ( $y$ -axis) is infinitely small, the vector coordinate is approximated to  $(a, 0)$  or  $(0, b)$ . In this way, the 2D vector is approximately mapped into a one-dimensional one, as illustrated in Figure 2. Similarly, a 3D vector can be approximately mapped into a 2D or one-dimensional one, depending on the set threshold for the included angle between the two vectors.

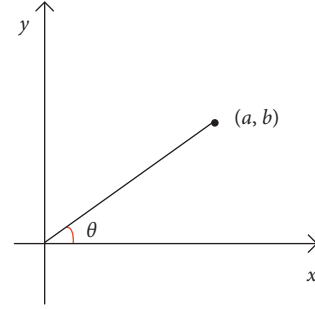


FIGURE 1: 2D vector representation.

Apparently, setting an appropriate threshold for the included angle between the two vectors is very important.

The dimension describes the precision of the required solution target characteristics. For example, when describing a pen in one dimension, only its length or width can be described, and so it is impossible to perform dimensionality reduction through mapping. In this case, the threshold for the included angle  $\theta$  between the two vectors must be close to 0. When a pen has two dimensions, both its length and width can be described. At this point, if the included angle between the two vectors is smaller than a certain threshold, the dimension where the smaller values are located can be neglected. In this case, the threshold for the included angle  $\theta$  between the two vectors may be close to a value above 0. The threshold range can be set according to an individual problem. When three dimensions are used for the description, not only the pen's length and width but also its cross-sectional radius can be described. Therefore, the threshold for the included angle  $\theta$  between the two vectors is larger than that for the 2D situation. As the number of dimensions increases, the threshold range of the included angle  $\theta$  between the two vectors increases as well. Experiments have shown that the threshold range cannot be infinitely large. Whatever the number of dimensions, the threshold must be maintained within the interval  $(0, \pi/4)$ . In this paper, the vector included angle factor is represented by the  $\sigma$  function in equation (1), which is a monotonically increasing function and also a bounded function:

$$\sigma(x) = \frac{1}{1 + e^{-x}}, \quad (1)$$

where  $x \in (-\infty, +\infty)$ ,  $\sigma \in (0, 1)$ .

The vector included angle factor proposed in this study must be within the interval  $(0, \pi/4)$ . An adaptive vector angle factor can be obtained by transformation of the  $\sigma$  function, as shown in equation (2), where  $a$  is the control parameter,  $a = 4.3926$ ,  $b$  is the adjustment parameter,  $b = 3.6072$ , and  $D$  is the number of dimensions. When the tangent of the included angle between the two vectors in adjacent dimensions  $\tan \theta < \tan \sigma_*$ , the dimension where the smaller value is located is denoted as 0 ( $\theta = x_{mi}/x_{mj}$ ,  $x_{mi}$  is the  $i$ -th dimension of the  $m$ -th individual;  $x_{mj}$  is the  $j$ -th dimension of the  $m$ -th individual).

$$\sigma_*(D) = a * \frac{1}{1 + e^{-D}} - b. \quad (2)$$

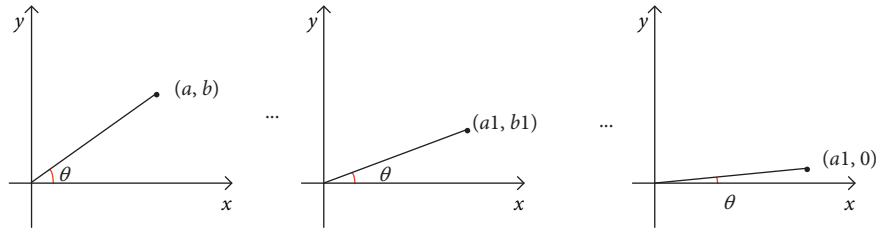


FIGURE 2: Changes of the included angle between the two vectors.

**2.2. ADRGA Workflow.** ADRGA targets high-dimensional swarms. First, the tangent value of the included angle between the two vectors in adjacent dimensions is calculated for each individual and is compared against the adaptive vector angle factor  $\sigma_*$ . If it is smaller than the latter, the dimension where the smaller value of the individual is located is denoted as 0. Then, using the same method, the tangent values of the included angle between the two vectors in adjacent dimensions for all individuals are compared against  $\sigma_*$ . Finally, the number of 0 elements in each dimension in the updated swarm *pop* is determined; if it is above the critical value  $Q$ , then this dimension is deleted.

Adaptive dimensionality reduction is feasible following the principle mentioned above. The pseudocode for ADRGA is shown in Algorithm 1 ( $P_c$  is the probability of crossover,  $P_m$  is the probability of mutation,  $N$  is the swarm size,  $G$  is the number of generations upon termination of evolution,  $T$  is the number of tests,  $Q$  is the critical value).

### 3. Experimental Results

Simulation was carried out using MATLAB 2014b under Windows 7 (also applicable to a higher version). A comparison was made between ADRGA, the standard GA [1], the hybrid genetic and simulated annealing algorithm (HGSA) [23], and the adaptive genetic algorithm (AGA) [24].

In this study, 8 standard composite testing functions were used, namely,  $F_1 \sim F_8$ , as shown in Table 1.  $F_1 \sim F_3$  are high-dimensional unimodal functions, which only have one global best solution;  $F_4 \sim F_8$  are high-dimensional multimodal functions, which have several local best solutions, but only one global best solution. The latter are generally hard to optimize. The global best solutions of all testing functions were 0. Since some testing functions have several optimal solutions, the algorithm is very likely to be trapped in a local optimum. This aspect may be challenging for the proposed ADRGA algorithm.

In the experimentation, the value of the fitness function  $f$  was the function value at the current position. The parameters of the GA were configured as follows: crossover probability  $P_c = 0.70$ , mutation probability  $P_m = 0.05$ , number of iterations  $FEs = 1000$ , swarm size  $size\ pop = 50$ , number of dimensions  $D = 1000$ , and the critical value  $Q = 1$ .

Each of the four algorithms was run 20 times on the 8 testing functions, and the means and standard deviations are shown in Table 2. Table 3 presents the improvement percentages of the optimal solutions using ADRGA as

compared with the other three algorithms, calculated as follows: (mean of other algorithm - mean of ADRGA) / (mean of other algorithm). When optimizing these 8 classical testing functions, ADRGA could obtain a solution closer to the global best solution compared to the other algorithms, as shown in Table 2. This was especially true for the testing functions  $F_3$ ,  $F_4$ , and  $F_6$ . But on the other testing functions, although a better solution was obtained using ADRGA, it failed to find the global optimum and was still far from achieving this goal. As shown in Table 3, the higher the improvement percentage, the greater the amplitude of performance improvement of ADRGA would be, and vice versa. Although a solution closer to the global optimum was obtained for  $F_4$  in Table 2, its improvement percentage was smaller than for the other 7 functions, indicating that  $F_4$  was less influenced by the number of dimensions.

The number of dimensions after dimensionality reduction and the average number of dimensions after running each algorithm 20 times are shown in Table 4. The number of residual dimensions varied after each run, indicating that the dimensionality reduction with the proposed algorithm changed with the initialized swarm in each run. Therefore, valuable information could be preserved when reducing the number of dimensions. Under the similar minimum included angle between the two vectors, the larger the included angle for the newly generated swarm, the smaller the number of dimensions deleted would be, and vice versa. As shown in Table 3, the maximum number of dimensions deleted was 40%, and the minimum was 34%. The maximum number of dimensions deleted was not above 50%, but it was ensured that the dimensions were not deleted randomly. Table 4 provides a better proof of the adaptive features of the proposed algorithm.

Figure 3 shows the comparison of convergence for the eight testing functions  $F_1 \sim F_8$ . The  $x$ -axis is the number of fitness calculations, and the  $y$ -axis is the mean fitness value. As shown in Figure 3, ADRGA had a faster convergence speed and accuracy on the functions  $F_1$ ,  $F_2$ ,  $F_5$ ,  $F_6$ , and  $F_7$ , though it was more likely to be trapped in a local optimum. For the testing function  $F_3$ , the convergence curves of ADRGA and GA nearly coincided. This was because the value range of the independent variable in function  $F_3$  was  $[-1, 1]$ . Therefore, when the numbers of dimensions were 600 and 1000, the difference was negligibly small. This also demonstrated that the impact on  $F_3$  was small if the number of dimensions did not change significantly. For the multimodal function  $F_4$ , the convergence curve of ADRGA not only had a faster convergence speed but also showed a more

Step 1: initialize parameters  $P_c$ ,  $P_m$ ,  $N$ ,  $G$ ,  $T$ , and  $Q$  and randomly generate the first swarm  $pop$

Step 2: for  $i < popsize$

Step 3: calculate the tangent value  $\tan(x_{in}/x_{in+1})$  of the included angle between the two vectors in adjacent dimensions for each individual  $pop(i)$

Step 4: if  $\tan(x_{in}/x_{in+1}) < 4.3926(1/(1 + e^{-D})) - 3.6072$ , then update the value of the  $n$ -th dimension of the  $i$ -th individual to 0; otherwise, do not update the value

Step 5: return to step 2

Step 6: calculate the number of 0 elements in each dimension for the updated swarm  $pop$ ; if it is above the critical value  $Q$ , then delete this dimension

Step 7: obtain the updated swarm  $pop$

Step 8: calculate the fitness value  $F(i)$  of each individual in the swarm  $pop$

Step 9: initialize the new swarm  $newpop$

Step 10: select two individuals from the swarm  $pop$  according to the fitness using the proportional selection algorithm

Step 11: if  $random(0, 1) < P_c$ , then move on to step 12; otherwise, implement step 13

Step 12: apply the crossover operator according to the crossover probability  $P_c$  on the two individuals

Step 13: if  $random(0, 1) < P_m$ , then move on to step 14

Step 14: apply the mutation operator according to the mutation probability  $P_m$  on the two individuals

Step 15: add the two new individuals into the swarm  $newpop$

Step 16: repeat this process until the  $N$ -th generation is produced; otherwise, return to step 4

Step 17: replace  $pop$  with  $newpop$

Step 18: repeat this process until the number of generations exceeds  $G$ ; otherwise, return to step 8

Step 19: end

ALGORITHM 1: ADRGA.

TABLE 1: Benchmark testing functions.

Testing function	Number of dimensions	Feasible solution space
$F_1 = \sum_{i=1}^D x_i^2$	1000	$[-100, 100]$
$F_2 = (x_1 - 1)^2 + \sum_{i=1}^D i * (2x_i^2 - x_{i-1})^2$	1000	$[-10, 10]$
$F_3 = \sum_{i=1}^D  x_i ^{i+1}$	1000	$[-1, 1]$
$F_4 = -a * \exp(-b\sqrt{(1/D)\sum_{i=1}^D x_i^2}) - \exp((1/D)\sum_{i=1}^D \cos(cx_i)) + a + \exp(1)$ $a = 20, b = 0.2, c = 2\pi$	1000	$[-32.768, 32.768]$
$F_5 = \sum_{i=1}^D (x_i^2 - 10 * \cos(2*\pi*x_i) + 10)$	1000	$[-5.12, 5.12]$
$F_6 = \sum_{i=1}^D (x_i^2/4000) - \prod_{i=1}^D \cos(x_i/\sqrt{i}) + 1$	1000	$[-600, 600]$
$F_7 = \sin^2(\pi\omega_1) + \sum_{i=1}^{D-1} (\omega_i - 1)^2 [1 + 10 \sin^2(\pi\omega_i + 1)] + (\omega_D - 1)^2 [1 + \sin^2(2\pi\omega_D)]$ $\omega_i = 1 + ((x_i - 1)/4)$	1000	$[-10, 10]$
$F_8 = 418.9829 D - \sum_{i=1}^D x_i \sin(\sqrt{ x_i })$	1000	$[-500, 500]$

TABLE 2: Optimization results of the different algorithms on 8 standard composite testing functions.

Function	Mean and standard deviation			
	GA	HGSA	AGA	ADPGA
$F_1$	$1.78e + 05 \pm 6.12e + 03$	$8.44e + 05 \pm 2.02e + 05$	$1.30e + 06 \pm 2.07e + 05$	$9.46e + 04 \pm 2.65e + 03$
$F_2$	$3.65e + 07 \pm 1.85e + 06$	$4.08e + 08 \pm 1.10e + 08$	$8.04e + 08 \pm 2.36e + 08$	$9.97e + 06 \pm 8.74e + 05$
$F_3$	$1.11e - 07 \pm 1.84e - 07$	$0.1793 \pm 0.0885$	$3.95e - 06 \pm 5.84e - 06$	$7.22e - 08 \pm 1.77e - 07$
$F_4$	$13.2492 \pm 0.1323$	$18.3028 \pm 0.7001$	$19.9960 \pm 0.0226$	$12.6016 \pm 0.2194$
$F_5$	$9.68e + 03 \pm 86.5390$	$1.21e + 04 \pm 512.6435$	$1.31e + 04 \pm 369.5460$	$5.84e + 03 \pm 147.5333$
$F_6$	$1.61e + 03 \pm 64.0915$	$7.37e + 03 \pm 1.56e + 03$	$1.17e + 04 \pm 1.76e + 03$	$874.5617 \pm 40.2598$
$F_7$	$8.62e + 03 \pm 366.1671$	$2.83e + 04 \pm 4.72e + 03$	$4.01e + 04 \pm 5.71e + 03$	$4.52e + 03 \pm 280.3275$
$F_8$	$3.70e + 05 \pm 2.42e + 03$	$4.17e + 05 \pm 757.5530$	$3.98e + 05 \pm 2.56e + 03$	$2.27e + 05 \pm 5.62e + 03$

apparent decreasing trend as compared with the other six testing functions (except for  $F_8$ ). This suggested that ADRGA was not trapped in the local optimum on  $F_4$ . For

the testing function  $F_8$ , ADRGA outperformed all the other algorithms. There was a dramatic improvement in the convergence accuracy and speed with ADRGA, and the

TABLE 3: Improvement percentage of optimal solutions for ADRGA.

Function	Algorithm		
	GA (%)	HGSA (%)	AGA (%)
$F_1$	46.85	88.79	92.72
$F_2$	72.68	97.56	98.76
$F_3$	34.95	100.00	98.17
$F_4$	4.89	31.15	36.98
$F_5$	39.67	51.74	55.42
$F_6$	45.68	88.13	92.53
$F_7$	47.56	84.03	88.73
$F_8$	38.65	45.56	42.96

TABLE 4: Number of residual dimensions and means after each cycle of dimensionality reduction using each algorithm.

Function	Experiment													
	1	2	3	4	...	10	11	...	16	17	18	19	20	Mean
$F_1$	642	637	635	631	...	614	656	...	621	633	625	631	641	636.65
$F_2$	620	638	654	622	...	656	641	...	634	635	649	660	634	639.25
$F_3$	635	657	652	646	...	633	637	...	620	633	643	612	649	638.45
$F_4$	642	637	635	631	...	614	656	...	621	633	625	631	641	636.65
$F_5$	620	638	654	622	...	656	641	...	634	635	649	660	634	639.25
$F_6$	635	657	652	646	...	633	637	...	620	633	643	612	649	638.45
$F_7$	653	632	638	648	...	650	639	...	612	661	641	647	619	639.05
$F_8$	646	625	619	641	...	649	641	...	638	660	647	600	631	638

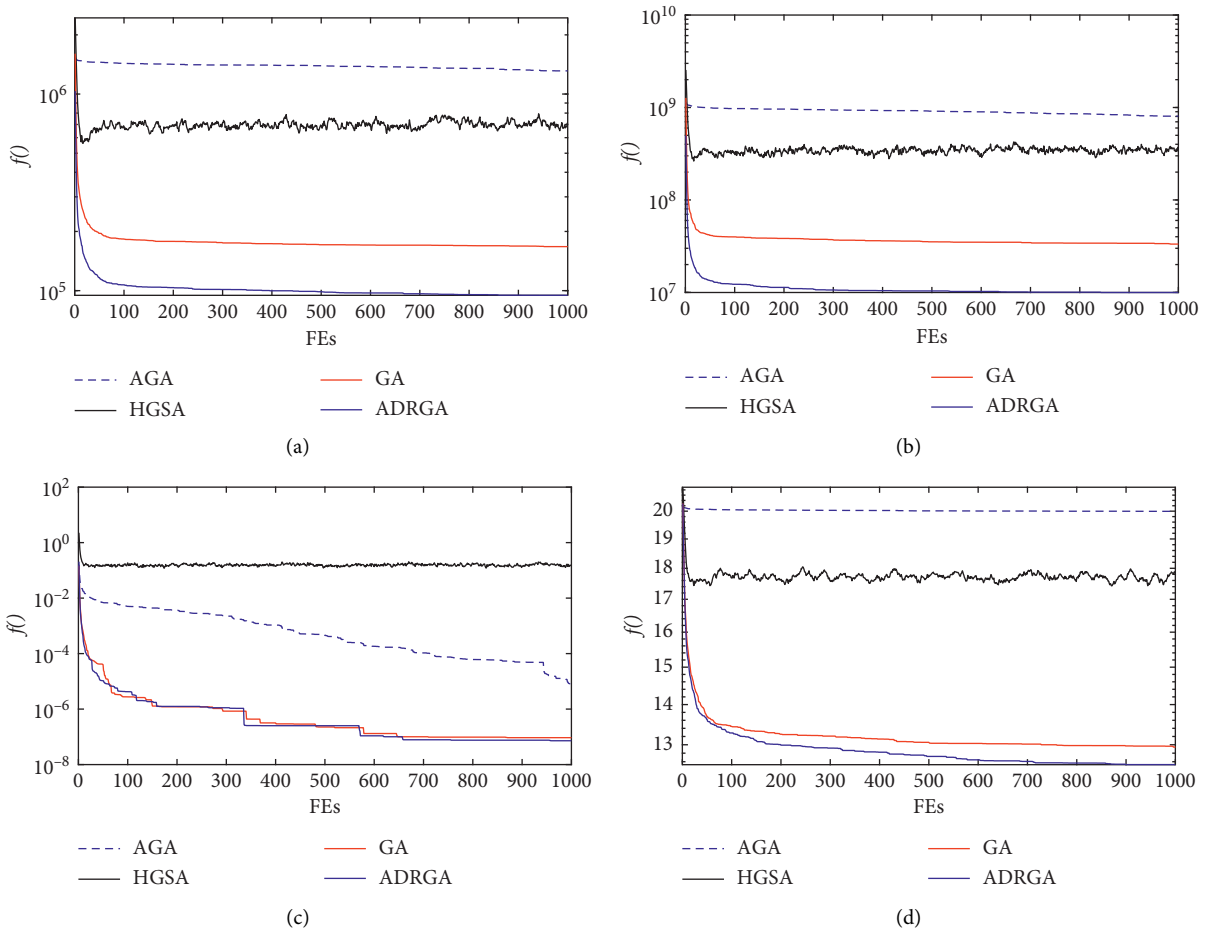


FIGURE 3: Continued.



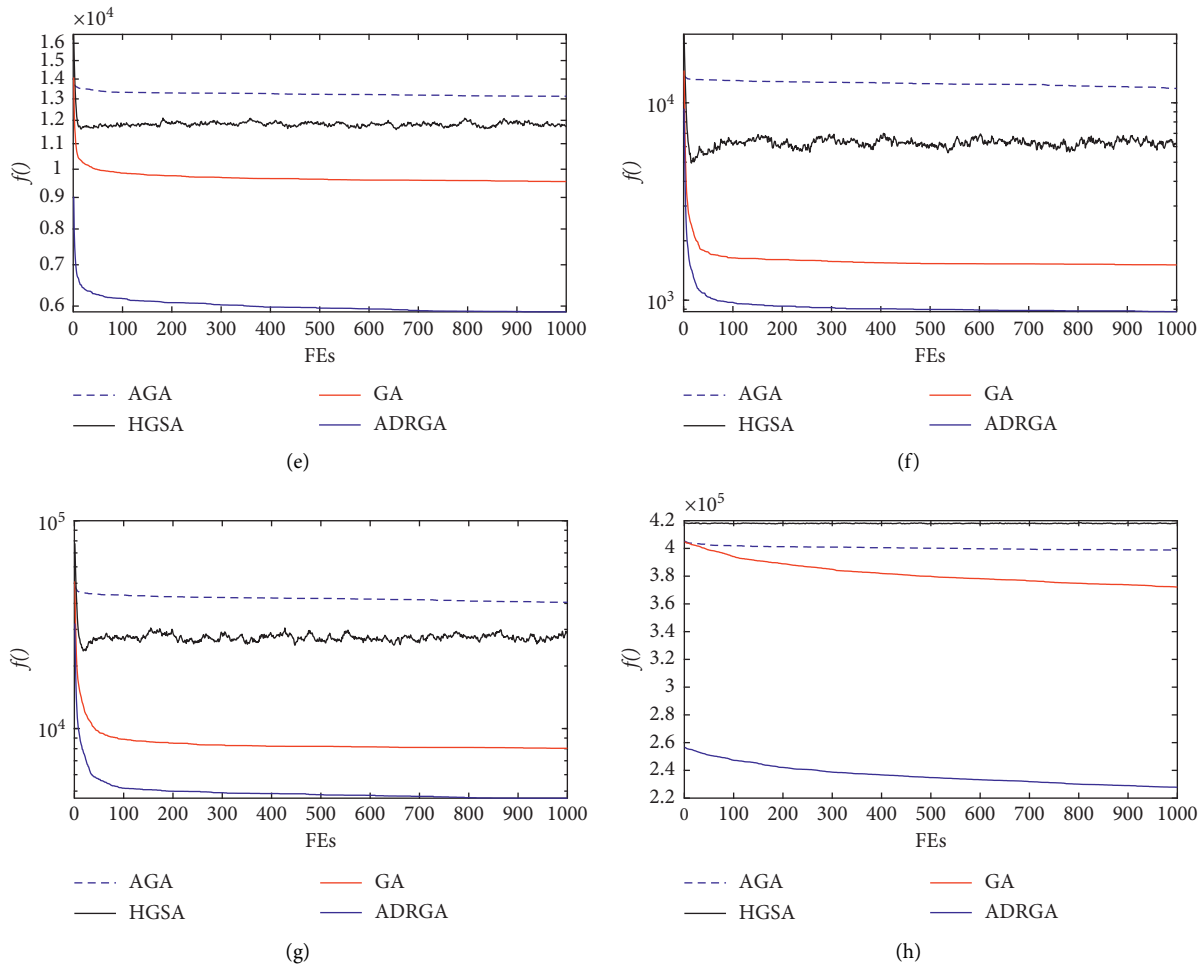


FIGURE 3: Convergence curve of different algorithms compared with the standard composite test function (including AGA, GA, HGSA, and ADRGA proposed in this paper). (a) Function  $F_1$ . (b) Function  $F_2$ . (c) Function  $F_3$ . (d) Function  $F_4$ . (e) Function  $F_5$ . (f) Function  $F_6$ . (g) Function  $F_7$ . (h) Function  $F_8$ .

convergence curve displayed a more apparent decreasing trend. For the five high-dimensional multimodal functions, ADRGA achieved better results on two testing functions, indicating that this algorithm was more appropriate for solving high-dimensional multimodal targets.

#### 4. Conclusion

This paper aims to find the optimal solutions for high-dimensional testing functions based on GAs. Similarity, the minimum included angle between the two vectors is utilized, and a GA approach for adaptive dimensionality reduction is proposed. The specific steps for dimensionality reduction are provided. The critical value  $Q$  is defined to ensure the diversity of the swarm information. It was then demonstrated via eight testing functions that ADRGA displays faster convergence speed and higher accuracy than other algorithms. However, a major problem with ADRGA is that the critical value  $Q$  is prespecified instead of changing with the swarm size and number of dimensions in real-time. In the

future, the critical value  $Q$  will be the focus in order to achieve better control of the number of dimensions in the swarm and more accurate dimensionality reduction.

#### Data Availability

The data used to support the study are available from the corresponding author upon request.

#### Conflicts of Interest

The authors declare that they have no conflicts of interest.

#### Acknowledgments

This work was supported in part by the National Natural Science Foundation of China under Grant U1809209 and the Zhejiang Provincial Natural Science Foundation (LZ15F030002) and the Zhejiang Provincial Natural Science Foundation under Grant LY16F020022.

## References

- [1] J. D. Bagley, "The behavior of adaptive systems which employ genetic and correlation algorithms," *Dissertation Abstracts International*, vol. 28, no. 12, 1967.
- [2] E. J. Hughes, "Radar waveform optimisation as a many objective application benchmark," in *International Conference on Evolutionary Multi-Criterion Optimization*, pp. 700–714, Springer-Verlag, Berlin, Germany, 2007.
- [3] P. M. Reed and J. B. Kollat, "Save now, pay later? Multi-period many-objective groundwater monitoring design given systematic model errors and uncertainty," *Advances in Water Resources*, vol. 35, pp. 55–68, 2012.
- [4] S. H. Tuo, F. A. Deng, and T. Zhou, "A global optimization algorithm using membrane calculation to solve high-dimensional functions," *Computer Engineering and Applications*, vol. 47, no. 19, pp. 27–30, 2011.
- [5] X. H. Chen, X. Li, and N. Wang, "Objective dimension reduction with sparse feature selection for multi-objective optimization problem," *Chinese Journal of Electronics*, vol. 43, no. 7, pp. 1300–1307, 2015.
- [6] Z. X. Chen, X. H. Yan, K. A. Wu et al., "Multi-objective optimization integrating open angle -based congestion control strategy," *Acta Automatica Sinica*, vol. 41, no. 6, pp. 1145–1158, 2015.
- [7] E. Zitzler and S. Künzli, "Indicator-based selection in multiobjective search," in *Proceedings of the 8th International Conference. Parallel Problem Solving from Nature-PPSN VIII*, pp. 832–842, Springer, Birmingham, UK, 2004.
- [8] K. Deb and H. Jain, "An evolutionary many-objective optimization algorithm using reference-point-based non-dominated sorting approach, Part I: solving problems with box constraints," *IEEE Transactions on Evolutionary Computation*, vol. 18, no. 4, pp. 577–601, 2014.
- [9] S. Yang, M. Li, X. Liu, and J. Zheng, "A grid-based evolutionary algorithm for many-objective optimization," *IEEE Transactions on Evolutionary Computation*, vol. 17, no. 5, pp. 721–736, 2013.
- [10] J. H. Zheng, R. M. Shen, M. Q. Li, and J. Zou, "Evolutionary algorithm based on information separation for multi-objective optimization," *Journal of Software*, vol. 26, no. 5, pp. 1013–1036, 2015.
- [11] X. J. Bi and C. Wang, "A multi-objective evolutionary algorithm based on angle penalized distance," *Journal of Electronics & Information Technology*, vol. 40, no. 02, pp. 314–322, 2018.
- [12] Y. C. He, X. Z. Wang, X. L. Zhang, and H. Z. Li, "Modeling and solving by dimensionality reduction of KPC problem based on discrete differential evolution," *Chinese Journal of Computers*, vol. 41, no. 116, pp. 1–15, 2018.
- [13] J. Liang, R. Liu, K. J. Yu et al., "Dynamic multi-swarm particle swarm optimization with cooperative coevolution for large scale global optimization," *Journal of Software*, vol. 29, no. 9, pp. 2595–2605, 2018.
- [14] X. Xia, Y. Xing, B. Wei et al., "A fitness-based multi-role particle swarm optimization," *Swarm and Evolutionary Computation*, vol. 44, pp. 349–364, 2019.
- [15] G. Xu, Q. Cui, X. Shi et al., "Particle swarm optimization based on dimensional learning strategy," *Swarm and Evolutionary Computation*, vol. 45, pp. 33–51, 2019.
- [16] M. Wu, G. R. Zhang, and H. Liu, "Feature selection based on fractal dimension and multi-objective genetic algorithm," *Computer Engineering and Applications*, vol. 51, no. 11, pp. 109–113, 2015.
- [17] Z. He and G. G. Yen, "Many-objective evolutionary algorithms based on coordinated selection strategy," *IEEE Transactions on Evolutionary Computation*, vol. 21, no. 2, pp. 220–233, 2017.
- [18] Y. Xiang, Y. Zhou, M. Li, and Z. Chen, "A vector angle-based evolutionary algorithm for unconstrained many-objective optimization," *IEEE Transactions on Evolutionary Computation*, vol. 21, no. 1, pp. 131–152, 2017.
- [19] Q. M. Zhu, D. Y. Zhao, and J. H. Zhang, "A general U-Block model-based design procedure for nonlinear polynomial control systems," *International Journal of Systems Science*, vol. 47, no. 14, pp. 3465–3475, 2016.
- [20] X. Geng, Q. Zhu, T. Liu, and J. Na, "U-model based predictive control for nonlinear processes with input delay," *Journal of Process Control*, vol. 75, pp. 156–170, 2019.
- [21] Q. Zhu, W. Zhang, J. Zhang, and B. Sun, "U-neural network-enhanced control of nonlinear dynamic systems," *Neurocomputing*, vol. 352, pp. 12–21, 2019.
- [22] Q. M. Zhu, L. Liu, W. C. Zhang, and S. Y. Li, "Control of complex nonlinear dynamic rational systems," *Complexity*, vol. 2018, Article ID 8953035, 12 pages, 2018.
- [23] C. F. Meng, D. H. Chu, K. Q. Liu et al., "Solving SaaS components optimization placement problem with hybrid genetic and simulated annealing algorithm," *Journal of Software*, vol. 27, no. 4, pp. 916–932, 2016.
- [24] S. G. Zhao, G. X. Liu, J. N. Wang, and W.-H. Yang, "Automated design approach for analog circuits based on a multi-stage adaptive genetic algorithm," *Chinese Journal of Electronics*, vol. 32, no. 4, pp. 680–683, 2004.

## Research Article

# Single-Phase Reactive Power Compensation Control for STATCOMs via Unknown System Dynamics Estimation

Cheng Guo <sup>1</sup>, Linzhen Zhong <sup>2</sup>, Jun Zhao <sup>2</sup> and Guanbin Gao <sup>2</sup>

<sup>1</sup>Yunnan Electrical Power Experiment Institute Co., Kunming 650217, Yunnan, China

<sup>2</sup>Faculty of Mechanical and Electrical Engineering, Kunming University of Science and Technology, Kunming 650500, China

Correspondence should be addressed to Guanbin Gao; [gbgao@163.com](mailto:gbgao@163.com)

Received 20 March 2020; Accepted 22 April 2020; Published 9 May 2020

Guest Editor: Jian Huang

Copyright © 2020 Cheng Guo et al. This is an open access article distributed under the Creative Commons Attribution License, which permits unrestricted use, distribution, and reproduction in any medium, provided the original work is properly cited.

In this paper, a single-phase reactive power compensation control for static compensator (STATCOM) is developed. The primary novelty lies in that the reactive power compensation of STATCOM is reformulated as an equivalent tracking control for the reactive current, and a novel unknown system dynamics estimator (USDE) is also investigated to address the unknown system dynamics. A modeling phase based on a basic structure of single-phase STATCOM and the principle of STATCOM is first carried out to describe its behavior. To address the unknown dynamics and external disturbances, a new USDE is then developed, so that the modeling uncertainties and external disturbances can be accommodated without using a function approximator, where the demanding computational costs and tedious parameter tuning in the other control schemes are remedied. Finally, based on the proposed estimator, we design a composite control with a proportional integral (PI) feedback controller and the proposed estimator to achieve precise current tracking. The convergence analysis of both the estimation error and the control error is also given. Simulation results using a realistic simulator are presented to show the efficiency of the suggested strategy.

## 1. Introduction

To improve the power quality in the power systems, it is necessary to provide users with pollution-free power and make the voltage stable. However, the stability of voltage is usually affected by many factors, e.g., generation, transmission and distribution links, and nonlinear components in the power grids, all of which cause fluctuations in the grid voltage [1–3]. In addition, the low-voltage single-phase inductive loads are widely used in the modern power systems, such as electric vehicle charging pile and electric locomotive, etc., which will in turn increase the loss of reactive power in the power systems [4]. Therefore, it is important to study the single-phase dynamic reactive power compensation to improve the stability of power systems [5].

Reactive static compensator (STATCOM), shunt capacitor, synchronous condenser, and saturation reactor (SR) are all widely used in the reactive compensation devices. Compared with the traditional compensation devices, the STATCOM has the advantages of wide operational range,

fast response speed, small capacity of energy storage elements, and control flexibility, and it can also compensate the reactive power in two directions [6]. Hence, it has become a modern reactive power compensation technology, which is attracting much research interest. STATCOM is usually connected in parallel with a 10 kV power grid system, so that the multilevel technology becomes a key scheme of these types of devices applied in the high-voltage power grid system [7]. In the multilevel technology [8], the chain topology has become the mainstream structure because of its high degree of modularity, high equivalent switching frequency, redundant operation, and other advantages [9–13]. Direct-current (DC) side voltage balance is the premise of safe and reliable operation of chain STATCOM. Otherwise, the overvoltage of DC bus caused by imbalance will lead to the damage of the capacitor, burning of insulated gate bipolar transistor, and other serious faults, which will lead to the shutdown of the device, and seriously affect the safety and stability of the parallel grid. Therefore, many researchers [14–17] have proposed DC-side voltage balance control

strategies for STATCOM with chain structure, photovoltaic grid connected inverter, power electronic transformer, and other devices.

In fact, the existing control methods for STATCOM include indirect current control [18], direct current control [19], sliding film variable structure control [20], and beat control [21], which use fully known system dynamics (i.e., nonlinear or linear dynamics). However, when we consider systems with unknown dynamics, nonlinearities, modeling errors, or disturbances, which are common in the power systems, it is not easy to design a controller to achieve satisfactory performance. Recently, U-model is proposed to address nonlinear system dynamics [22–25], which was originally developed by Zhu and Guo [26]. However, an accurate system model is again required in this framework. In the literature, the requirements on the system dynamics can be relaxed in terms of some disturbance estimation and rejection methods, e.g., high-gain observers [27, 28] and sliding mode observers [29, 30]. Another efficient method to deal with the unknown system dynamics is the disturbance observer (DOB), which was originally reported in [31]. However, the early developed DOB is mainly suitable for linear systems only. In the subsequent studies, various advanced DOBs have been developed, such as nonlinear disturbance observer (NDO) [32], extended state observer (ESO) [33], and unknown input observer (UIO) [34]. However, the aforementioned observers require designing an observer, and they impose many parameters to be tuned, which may not be an easy task for practitioners. In this respect, it is worth to further investigate a new estimator with less tuning parameters and guaranteed convergence to address the unknown system nonlinearities for STATCOM control systems.

Based on the above discussion, this paper will develop a novel reactive power compensation method for STATCOM with fully unknown nonlinear dynamics and external disturbances. The reactive power compensation of STATCOM is reformulated as an equivalent tracking control for the required reactive current. Then, we construct a model of a single-phase STATCOM based on its physical structure and the principle of STATCOM. Moreover, a new constructive unknown system dynamic estimator (USDE) is developed to address the unknown disturbances and model uncertainties, so that the function approximator is not needed, and the demanding computational costs and tedious parameter tuning are remedied. Finally, a proportional integral (PI) controller is combined with the proposed estimator as a feedforward compensation to achieve satisfactory tracking control response, such that improved operation performance can be achieved. The convergence analysis of both the estimation error and control error is also given, which is also verified in terms of simulations based on a realistic STATCOM plant.

The major contributions of this paper include the following:

- (1) The reactive power compensation of STATCOM is reformulated as an equivalent tracking control for the required reactive current. This allows developing

advanced control strategies to achieve improved control performance.

- (2) A novel USDE is developed to address the unknown system dynamics, modeling uncertainties, and external disturbances, where the function approximator is not needed, and thus, the demanding computational costs and complex parameter tuning are remedied. Different from the conventional DOB and other observers, this USDE has only one tuning parameter (the filter gain), and thus, it is easy to be implemented.

This paper is organized as follows: In Section 2, based on the structure of single-phase STATCOM and the principle of STATCOM, we construct a model to describe the behavior of the single-phase STATCOM. In Section 3, the proposed USDE, composite controller design and stability analysis are provided. Simulation results are given in Section 4, and some conclusions are drawn in Section 5.

## 2. Preliminaries and Problem Formulation

*2.1. Structure of Single-Phase STATCOM.* The main circuit structure of STATCOM can be generally divided into two types (i.e., voltage bridge circuit and current bridge circuit). In this paper, the STATCOM of single-phase voltage bridge circuit is considered as the research object to complete the reactive power compensation, since it has been used in many power system applications. Figure 1 shows the basic structure of single-phase STATCOM [7], which mainly includes the following three parts.

*2.1.1. Voltage Source Converter (VSC).* In the voltage source converter, the AC-side output is connected to the power grid, which is also composed of two pairs for bridge arms in parallel, where each pair of bridge arms is connected with two insulated gate bipolar transistors (IGBTs) power switches in series, and each IGBT is connected with one fast recovery diode in reverse parallel. The main purpose of the VSC is to produce an AC voltage from a DC voltage. Therefore, it is commonly referred to a DC-AC converter.

*2.1.2. Capacitor.* The direct-current (DC) capacitor is used to store energy and provide voltage for the VSC.

*2.1.3. Coupling Reactor.* Besides filtering out the possible high-order harmonics in the inverter output voltage, the reactor can be used to connect the voltage source between the converter side and the grid side.

*2.2. Principle of STATCOM.* According to the reactor dynamics, the self-commutating bridge circuit is connected with the power grid. Therefore, the circuit can generate or absorb the current by adjusting the phase or amplitude of the output voltage on the AC side of the bridge circuit properly or directly controlling the current on the AC side of the bridge circuit, so as to realize dynamic reactive power

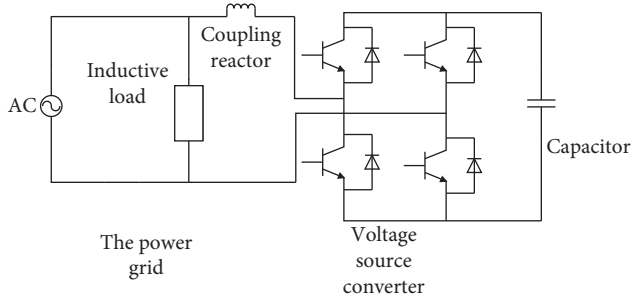


FIGURE 1: Structure of single-phase STATCOM.

compensation [9–13]. Moreover, the working principle of STATCOM can be represented by the equivalent circuit given in Figure 2.

In Figure 2,  $\vec{U}_s$  is the power grid voltage and  $\vec{U}_I$  is the output AC voltage of STATCOM. The voltage  $\vec{U}_L$  of reactor is the difference between  $\vec{U}_s$  and  $\vec{U}_I$ , and  $\vec{I}$  is the current absorbed by STATCOM from the power grid. It should be noted that  $\vec{U}_s$ ,  $\vec{U}_I$ , and  $\vec{U}_L$  are the vectors of  $U_s$ ,  $U_I$ , and  $U_L$ , respectively.

As shown in Figure 3, when  $\vec{U}_I$  is larger than  $\vec{U}_s$ , the current is  $90^\circ$  ahead of the power grid voltage, and the STATCOM provides reactive power to the system. When  $\vec{U}_I$  is less than  $\vec{U}_s$ , the current lags behind the power grid voltage  $90^\circ$ , and the STATCOM absorbs reactive power from the system.

**2.3. Modeling of Single-Phase STATCOM.** From Figure 2, we can obtain the voltage current equation as

$$U_s - U_I = RI + L \frac{dI}{dt}. \quad (1)$$

Then, the system quickly detects the reactive current. Through appropriate control, the STATCOM output corresponds to the reactive compensation current. To detect the reactive current in the load, the instantaneous reactive power theory [35] is used to construct the single-phase system into a three-phase system.

By taking  $I$  as  $I_a$ , delaying  $I$  by  $\pi/(3\omega)$  and reversing it, we have the c-phase load current  $I_c$ . Using the sum of three-phase current as 0, we can obtain the b-phase load current  $I_b$  as

$$I_b = -I_a - I_c. \quad (2)$$

The equivalent  $d$ - $q$  transformation is used for the three-phase current. Without loss of generality, we assume that  $d$ -axis coincide with the grid voltage vector. We can get the following equation:

$$\begin{bmatrix} I_d \\ I_q \end{bmatrix} = C_{abc2dq} [I_a \ I_b \ I_c]^T, \quad (3)$$

where  $I_d$  and  $I_q$  are the active and reactive components of three-phase current,  $C_{abc2dq}$  is the transformation matrix:

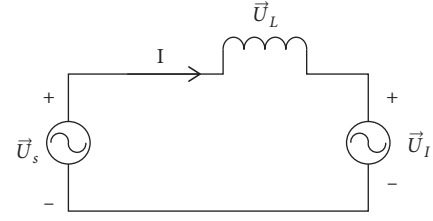


FIGURE 2: Equivalent circuit of single-phase STATCOM with the system.

$$C_{abc2dq} = \frac{2}{3} \begin{bmatrix} \sin(\omega t) & \sin\left(\frac{\omega t - 2\pi}{3}\right) & \sin\left(\frac{\omega t - 2\pi}{3}\right) \\ \cos(\omega t) & \cos\left(\frac{\omega t - 2\pi}{3}\right) & \cos\left(\frac{\omega t - 2\pi}{3}\right) \end{bmatrix}. \quad (4)$$

After obtaining the reactive current  $I_q$  of the load, we can take it as the reference value of STATCOM to compensate the reactive current. Furthermore, model (1) can be rewritten as follows:

$$\dot{i} = -\frac{R}{L}I - \frac{U_s}{L} + \frac{U_I}{L} = bU_I - d, \quad (5)$$

where  $b = (1/L)$  and  $d = (R/L)I + (U_s/L)$  are the control gain and the lumped disturbances. In addition,  $U_I$  is the control signal in (5). It is noted that  $d$  includes the system dynamics stemming from the unavoidable disturbances and load variations in the power systems. Without loss of generality, we assume that the derivative of  $d$  is bounded, i.e.,  $\sup_{t \geq 0} |\dot{d}| \leq \zeta$  holds for a constant  $\zeta > 0$ . Hence, the aim is to design a proper control such that the current  $I$  can track the reference  $I_q$ .

**Remark 1.** In some existing results for STATCOM control designs, the system dynamics are assumed to be fully known. Since  $U_s$  and  $I$  in equation (5) are the dynamic variables, we can consider this part (i.e., variable  $d$ ) as a total disturbance to be compensated in the control design, which will greatly reduce the modeling effort and improve the current tracking effect. In this line, the classical methods to handle unknown dynamics, such as high-gain observers [27, 28] and sliding mode observers [29, 30], may impose heavy computational costs and achieve poor convergence (e.g., chattering), leading to difficulties in practical applications. Another efficient method to deal with the uncertainties is the disturbance observer (DOB) [31]. However, the early developed DOB is mainly suitable for linear systems only. Although various advanced DOBs have been developed, such as nonlinear disturbance observer (NDO) [32], extended state observer (ESO) [33], and unknown input observer (UIO) [34], the aforementioned observers require to design an observer, and they impose many parameters to be tuned, which may not be an easy task for practitioners. To remedy this issue, this paper provides an alternative USDE, which has the same function as DOB, but a simpler structure and one tuning parameter only.



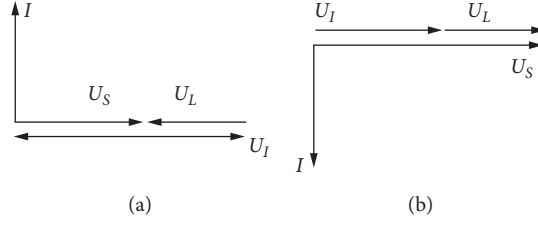


FIGURE 3: Single-phase STATCOM work vector diagram. (a) Current lead. (b) Current hysteresis.

### 3. Composite Current Control with Unknown System Dynamics Estimator

**3.1. Unknown System Dynamics Estimator.** In order to handle the lumped unknown dynamics in system (5), we will propose a novel USDE, which can estimate  $d$  by using the measured input and output. For this purpose, we define  $I_f$  and  $U_{I_f}$  as the filtered variables of  $I$  and  $U_I$  as

$$\begin{cases} k\dot{I}_f + I_f = I, & I_f(0) = 0, \\ k\dot{U}_{I_f} + U_{I_f} = U_I, & U_{I_f}(0) = 0, \end{cases} \quad (6)$$

where  $k > 0$  is a constant parameter denoting the bandwidth of the adopted low-pass filter.

The principle of invariant manifold will be explored to design the estimator. In this line, we first introduce the following result.

**Lemma 1** (see [36, 37]). *Consider system (5) and filter operation (6), a variable is defined as*

$$\beta = \frac{I - I_f}{k} - (bU_{I_f} - d). \quad (7)$$

Then, this variable is bounded for any finite constant  $k > 0$  and converges to zero exponentially, that is,

$$\lim_{k \rightarrow 0} \left[ \lim_{t \rightarrow \infty} \left\{ \left( \frac{I - I_f}{k} \right) - (bU_{I_f} - d) \right\} \right] = 0. \quad (8)$$

*Proof.* From (6) and (7), the time derivative of  $\beta$  is given by

$$\dot{\beta} = \frac{\dot{I} - \dot{I}_f}{k} - (b\dot{U}_{I_f} - \dot{d}) = \frac{1}{k} (\beta - k\dot{d}). \quad (9)$$

Select a Lyapunov function as  $V_\beta = (1/2)\beta^2$  such that

$$\dot{V}_\beta = -\frac{1}{k}\beta^2 + \beta\dot{d}. \quad (10)$$

According to Young's inequality, we have

$$\beta\dot{d} \leq \frac{1}{2k}\beta^2 + \frac{k}{2}\dot{d}^2. \quad (11)$$

Substituting (11) into (10), we can get the following inequality:

$$\begin{aligned} \dot{V}_\beta &\leq -\frac{1}{k}\beta^2 + \frac{1}{2k}\beta^2 + \frac{k}{2}\dot{d}^2 \\ &\leq -\frac{1}{k}V_\beta + \frac{k}{2}\zeta^2. \end{aligned} \quad (12)$$

By solving inequality (12), one can easily verify that  $V_\beta(t) \leq e^{-t/k}V_\beta(0) + k^2\zeta^2/2$ . Thus,  $\beta(t)$  will converge to a small compact set bounded by  $|\beta(t)| = \sqrt{2V_\beta(t)} \leq \sqrt{e^{-t/k}\beta^2(0) + k^2\zeta^2}$ , where its size is determined by the filter parameter  $k$  and the upper bound  $\zeta$  of  $d$ , i.e.,  $\lim_{t \rightarrow \infty} \beta(t) = k\zeta$ , which vanishes for sufficiently small  $k$  and/or  $d$  (i.e.,  $d = 0$ ). This completes the proof.  $\square$

The above ideal invariant manifold provides a mapping from the measured variable  $I_f$  and  $U_{I_f}$  to the unknown system dynamics  $d$ . Thus, it can be used to design an estimator for  $d$ , which is given by

$$\hat{d} = bU_{I_f} - \frac{I - I_f}{k}. \quad (13)$$

Clearly, only the scalar constant  $k > 0$  used in the filter should be selected by the designer, which is a trivial task in comparison to the existing ESO and DOB methods.

Now, we have the following results:

**Theorem 1.** (see [36, 37]). *For system (5) with unknown system dynamics estimator (13), the estimation error  $e_F = d - \hat{d}$  is bounded by  $|e_F(t)| \leq \sqrt{e_F^2(0)e^{-t/k} + k^2\zeta^2}$  and thus  $d \rightarrow \hat{d}$  holds for  $k \rightarrow 0$  and/or  $\zeta = 0$ .*

*Proof.* After applying the filter operation  $1/(ks + 1)$  on the both sides of (5), we can get

$$\dot{I}_f = bU_{I_f} - d_f, \quad (14)$$

Substituting the first equation of (6) into (14), we get

$$d_f = bU_{I_f} - \frac{I - I_f}{k}. \quad (15)$$

Comparing (13) with (15), it is easy to find  $\hat{d} = d_f$ . Therefore, the estimation error can be derived as

$$e_F = d - \hat{d} = d - d_f. \quad (16)$$

To facilitate the proof, we further derive the derivative of the estimation error in (13) as

$$\dot{e}_F = \dot{d} - \dot{\hat{d}} = \dot{d} - \frac{1}{k}(d - d_f) = \dot{d} - \frac{1}{k}e_F. \quad (17)$$



Obviously, the estimation error can be very small, when a sufficiently small  $k$  is used. To show this point, a Lyapunov function can be selected as  $V = e_F^2/2$ , and its derivative can be calculated as

$$\dot{V} = e_F \dot{e}_F = -\frac{1}{k} e_F^2 + e_F \dot{d}. \quad (18)$$

According to Young's inequality, we have

$$e_F \dot{d} \leq \frac{e_F^2}{2k} + \frac{k\dot{d}^2}{2}. \quad (19)$$

Substituting (19) into (18), we can get the following inequality:

$$\dot{V} = e_F \dot{e}_F = -\frac{1}{k} e_F^2 + e_F \dot{d} \leq -\frac{1}{k} V + \frac{k}{2} \zeta^2. \quad (20)$$

Hence, one can calculate the solution of inequality (20) as  $V(t) \leq e^{-t/k} V(0) + k^2 \zeta^2 / 2$ , which further implies that the estimation error is bounded by  $|e_F(t)| \leq \sqrt{e^{-t/k} V(0) + k^2 \zeta^2}$ , and thus, we can claim  $e_F(t) \rightarrow 0$  for  $k \rightarrow 0$  and/or  $\zeta = 0$ . This completes the proof.  $\square$

*Remark 2.* From the above analysis, we know that the unknown system dynamics can be estimated accurately by constructed USDE (13). It is noted that the proposed USDE only imposes the filter operations given in (6) and algebraic calculation given in (13). Moreover, only the filter gain  $k$  in (6) needs to be set by the designers. Hence, the structure of USDE is simple and its implementation is straightforward.

**3.2. Composite Control Design Based on USDE.** In this section, the aforementioned estimator will be introduced into the control design for system (5) to achieve current tracking. Furthermore, we will use the estimated term  $\hat{d}$  in (13) as an extracompensator superimposed on the PI control to design a new composite current control for the STATCOM plant. The composite control with the proposed USDE together with a PI control [38] is shown in Figure 4.

Let  $I_q$  denote the reference current signal  $I_{ref}$ . The current tracking error is defined as follows:

$$e = I_{ref} - I. \quad (21)$$

To reduce the tracking error  $e$ , the controller can be designed as

$$U_I = b \left[ k_p e + k_i \int_0^t e(\tau) d\tau + \hat{d} \right]. \quad (22)$$

where  $U_I$  is the output AC voltage of STATCOM,  $k_p > 0$  and  $k_i > 0$  denote the effect of the proportional and integral gains.  $\hat{d}$  is a newly added compensation in addition to the feedback control part given in (13).

It is clear that the first part is the PI control, which is used to retain the stability of the controlled system, while the second term is the estimate of unknown dynamics to achieve satisfactory tracking response. Hence, the stability of the proposed control system with the estimator and composite

control and the convergence of estimation and control errors can be summarized in the following.

**Theorem 2.** If composite control (22) with estimator (13) is applied for STATCOM system (2), the current tracking error  $e$  and the estimation error  $e_F$  will converge to a small compact set around zero, and  $I$  can track the desired reference  $I_{ref}$  detected by the system.

*Proof.* By deriving (21) and substituting (22) into (5), the following equation can be obtained:

$$\begin{aligned} \dot{e} &= d - \hat{d} - k_p e - k_i \int_0^t e(\tau) d\tau \\ &= e_F - k_p e - k_i \int_0^t e(\tau) d\tau, \end{aligned} \quad (23)$$

which can be rewritten as

$$\dot{e} = e_F - k_p e - k_i e_i, \quad (24)$$

where  $e_i = \int_0^t e(\tau) d\tau$ . To cope with the integral term  $e_i$ , we define the augmented error vector as  $E = [e_i \ e]^T$  and select an augmented Lyapunov function as  $V = (1/2)E^T P E + (1/2)e_F^2$  for a positive symmetric matrix  $P$ . Then, (24) can be written as

$$\dot{E} = \begin{bmatrix} 0 & 1 \\ -k_i & -k_p \end{bmatrix} E + \begin{bmatrix} 0 \\ 1 \end{bmatrix} e_F = A E + B e_F. \quad (25)$$

The preconfigured PI control gains  $k_p$  and  $k_i$  are set to retain the stability of the control system, such that the matrix  $A$  can guarantee that the error system  $\dot{E} = A E$  is exponentially stable. Then, based on the Lyapunov theory, there exist positive definite symmetric matrices  $P > 0$  and  $Q > 0$  such that  $\dot{P} + A^T P + P A = -Q$  holds, and thus  $E^T P E$  can be taken as a Lyapunov function for the error system. In this case, we calculate the time derivative of the augmented Lyapunov function along (17) and (25) as

$$\begin{aligned} \dot{V} &= \frac{1}{2} E^T P \dot{E} + \frac{1}{2} E^T P E + \frac{1}{2} E^T \dot{P} E + e_F \dot{e}_F \\ &= -\frac{1}{2} E^T Q E + E^T P B e_F - \frac{1}{k} e_F^2 + e_F \dot{d} \\ &\leq -\frac{1}{2} \left( \lambda_{\min}(Q) - \frac{\eta}{2} \right) \|E\|^2 - \left( \frac{1}{k} - \frac{1 + \|PB\|^2}{2\eta} \right) e_F^2 + \frac{\eta \zeta^2}{2} \\ &\leq -\alpha V + \beta, \end{aligned} \quad (26)$$

where  $\eta > 0$  is a positive constant from Young's inequality,  $\alpha = \min\{(\lambda_{\min}(Q) - \eta/2)/\lambda_{\max}(P), 2(1/k - (1 + \|PB\|^2)/2\eta)\}$ , and  $\beta = \eta \zeta^2 / 2$  are positive constants for appropriately selected parameters  $\eta \leq 2\lambda_{\min}(Q)$  and  $k \leq 2\eta / (1 + \|PB\|^2)$ . This implies that  $V(t) \leq e^{-\alpha t} V(0) + \eta^2 \zeta^2 / 2$ ; thus, the control errors  $e$ ,  $e_i$  and the estimator error  $e_F$  will exponentially converge to a compact small set  $\Omega := \{e, e_F \mid |e| \leq \eta \zeta, |e_i| \leq \eta \zeta, |e_F| \leq \eta \zeta\}$ . It is clear that  $\lim_{t \rightarrow \infty} e(t) = 0$ ,  $\lim_{t \rightarrow \infty} e_i(t) = 0$ , and  $\lim_{t \rightarrow \infty} e_F(t) = 0$  hold for  $\eta \rightarrow 0$

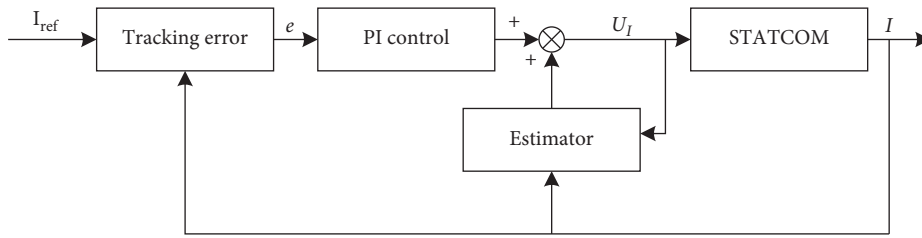


FIGURE 4: Control scheme of PI + USDE.

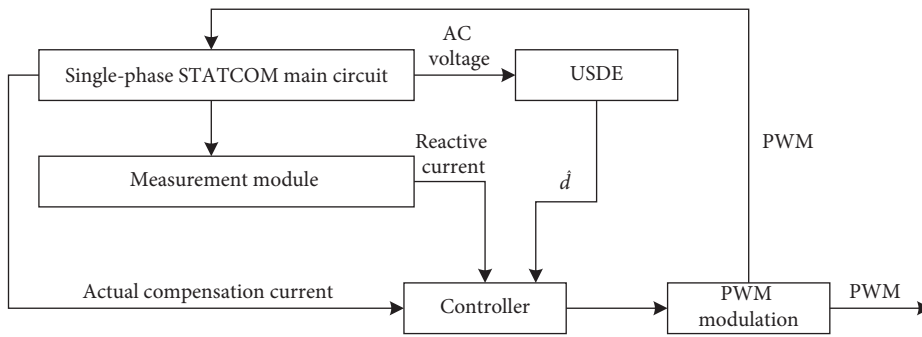


FIGURE 5: The proposed control block diagram for simulation.

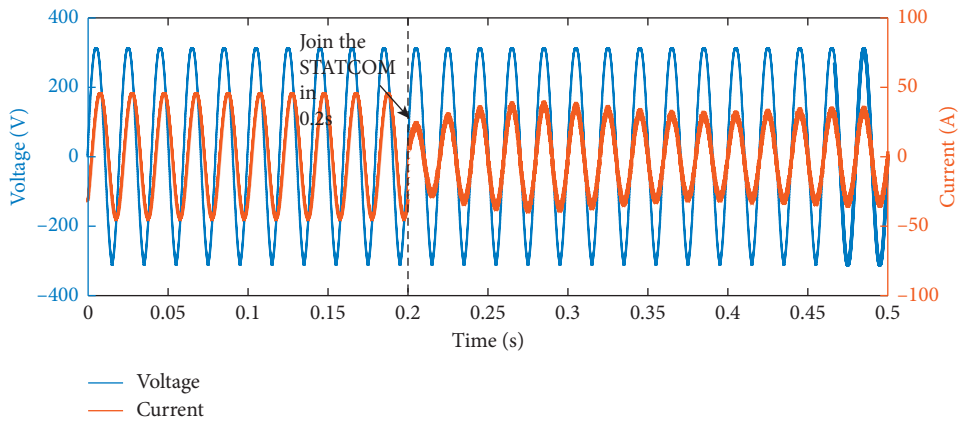


FIGURE 6: The waveforms of voltage and current on the grid side.

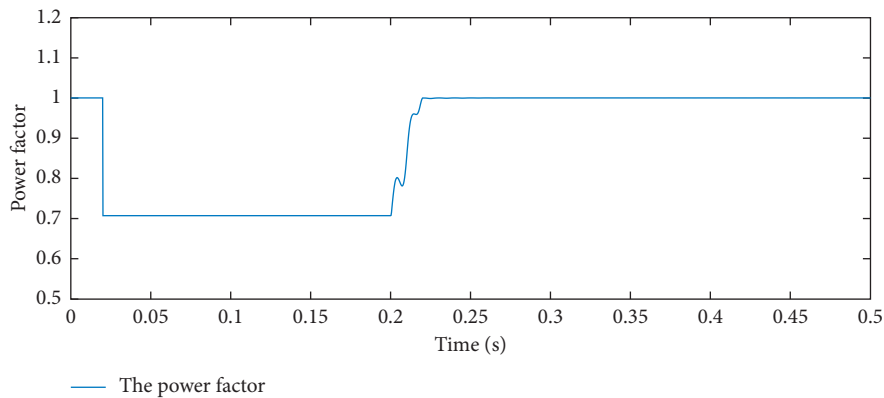


FIGURE 7: The power factor.

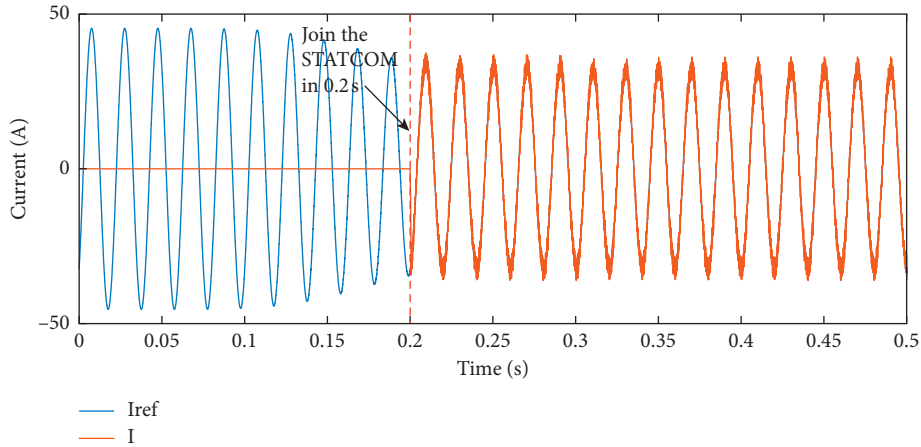


FIGURE 8: Current profile with composite control (PI + USDE).

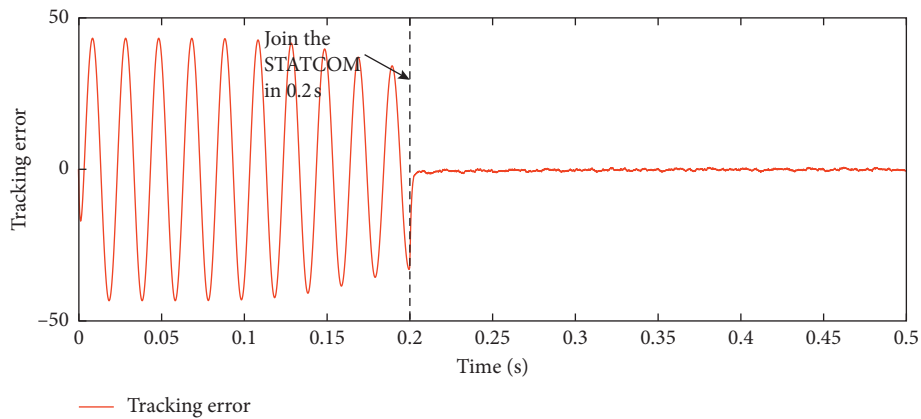


FIGURE 9: Current tracking error with composite control (PI + USDE).

and/or  $\zeta \rightarrow 0$ , for which  $k$  is adequately small and/or  $d$  is a constant and thus the bound of  $|d|$  is  $\zeta = 0$ . This completes the proof.  $\square$

As shown in the above proof, PI control is used to guarantee the stability of the STATCOM current control system. Then, the estimation  $\hat{d}$  is taken as an extra-feed-forward compensation to achieve disturbance rejection and thus better performance. In this respect, this idea brings a two-degree-of-freedom control structure in which the design of the USDE is independent of the PI control, and thus, even in the worst case without the compensator, the controlled system is still stable. Hence, the proposed estimator can be combined with other STATCOM controllers to achieve better control response.

#### 4. Simulation Results and Analysis

Recently, STATCOM has been extended to the compensation of distribution systems. The purpose of this paper is to design a controller, which can control the current of STATCOM, so as to complete the compensation of the distribution system. To verify the effectiveness of the system model and the control method proposed in this paper, we

build a simulation model based on Matlab/Simulink. In the systems, the electric locomotive load is a typical single-phase load, so that we use the resistance and inductance load to simulate the inductive load of electric locomotive. The whole simulation model consists of three parts: main circuit, controller, and measurement module. The function of the measurement module is to detect the reactive current in the load. The parameters of the system used in the simulation are given as follows: the effective value of grid phase voltage  $U_s = 220$  V, the frequency is 50 Hz, the connected inductance  $L = 9$  mH, the inductive reactive power of the load is 5000 Var, the DC side capacitance  $C = 350 \mu\text{F}$ , and the capacitor voltage  $U_{dc} = 700$  V. To show the structure of the proposed STATCOM control system, the diagram of the built Simulink model is given in Figure 5.

The PI controller parameters are set as follows: the proportional gain  $k_p = 300$  and the integral gain  $k_i = 13$ . Furthermore, the filter constant of USDE is  $k = 0.001$ . In order to test the effectiveness of STATCOM reactive power compensation with/without the proposed control method, we take STATCOM into the load circuit at 0.2 s through a breaker. Moreover, to further show the efficacy of the proposed approach, a sliding mode observer used in [39] is also tested for comparison in terms of estimating the

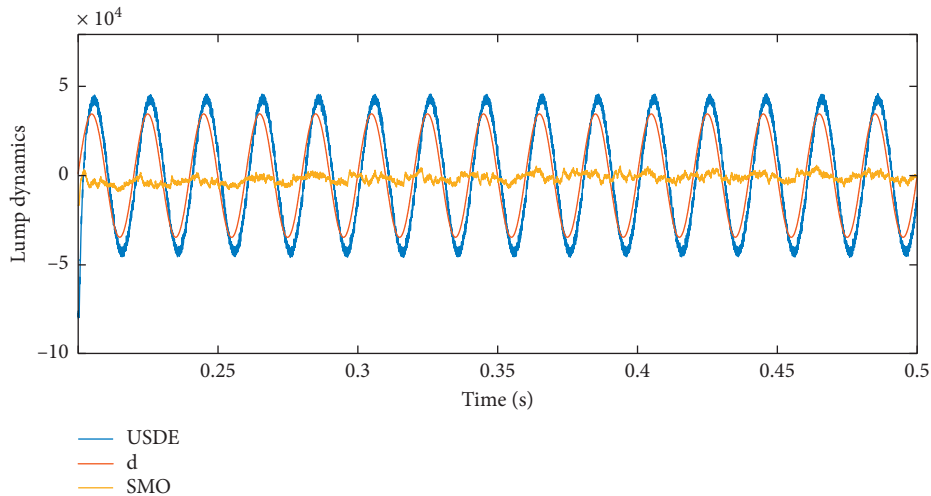


FIGURE 10: Estimation performance of USDE and SMO.

unknown dynamics  $d$ , and the parameters used in the sliding mode observer are set as  $k = 0.01$  and  $\lambda = 150$ .

When the inductive load is set to 5000 Var, the waveforms of voltage and current on the grid side are shown in Figure 6. By comparing the waveforms before and after 0.2 s, we can find that before putting the device into the operation as the load, the systems are inductive, and the inductive reactive power needs to be absorbed from the grid side. It is clear that the system current lags behind the system voltage, such that the power factor is very low. Nevertheless, after completing the reactive current compensation for the STATCOM, the voltage and current are in the same phase and thus the power factor also increases. Hence, we can find in Figure 7 that the power factor increases from about 0.7 to almost ideal value of 1. The current tracking result is shown in Figure 8, where the proposed composite control with the PI control and USDE can achieve satisfactory tracking response. The current tracking error is given in Figure 9, which shows that the steady-state error converges to 0 after putting the STATCOM into operation. Finally, the profiles of the estimated dynamics with the USDE and the SMO are given in Figure 10, which indicate that better estimation performance can be achieved by using USDE than that of SMO.

From the above simulation results, we can claim that for the electric locomotive system, the proposed composite control strategy with the USDE and PI controller can reduce the error of current fluctuations and realize more efficient reactive power compensation.

## 5. Conclusion

In this paper, the reactive power compensation of STATCOM is reformulated as an equivalent tracking control for the required reactive current. We first construct a model of a single-phase STATCOM based on its structure and the operation principle of STATCOM. Then, a new USDE is proposed to address the lumped unknown dynamics in the STATCOM model. With the suggested USDE superimposed on a standard PI control, a composite control structure can

be derived. This brings a two-degree-of-freedom control structure in which the design of the USDE is independent of the PI control, and thus even in the worst case without the compensator, the controlled system is still stable. The convergence analysis of both the estimation error and control error is rigorously studied. Finally, numerical simulations are given to support the theoretical claims and show the effectiveness of the proposed method.

## Data Availability

Data were curated by the authors and are available upon request.

## Conflicts of Interest

The authors declare that there are no conflicts of interest regarding the publication of this paper.

## References

- [1] C. Mu, Y. Tang, and H. He, "Improved sliding mode design for load frequency control of power system integrated an adaptive learning strategy," *IEEE Transactions on Industrial Electronics*, vol. 64, no. 8, pp. 6742–6751, 2017.
- [2] Y. Tang, H. He, J. Wen, and J. Liu, "Power system stability control for a wind farm based on adaptive dynamic programming," *IEEE Transactions on Smart Grid*, vol. 6, no. 1, pp. 166–177, 2015.
- [3] H. A. Soodi and A. M. Vural, "Single phase nine-level converter based STATCOM for reactive power compensation and power factor correlation," in *Proceedings of the 2018 International Conference on Engineering Technology and Their Applications (IICETA)*, pp. 19–24, Al-Najaf, Iraq, May 2018.
- [4] B. Singh, B. N. Singh, A. Chandra, K. Al-Haddad, A. Pandey, and D. P. Kothari, "A review of single-phase improved power quality ac-dc converters," *IEEE Transactions on Industrial Electronics*, vol. 50, no. 5, pp. 962–981, 2003.
- [5] S. Mariethoz and A. C. Rufer, "Open loop and closed loop spectral frequency active filtering," *IEEE Transactions on Power Electronics*, vol. 17, no. 4, pp. 564–573, 2002.

- [6] J. Yang and Z. Wang, *Harmonic Suppression and Reactive Power Compensation*, China Machine Press, Beijing, China, 1998, in Chinese.
- [7] J. A. Barrena, L. Marroyo, M. Á. Rodríguez Vidal, and J. R. Torrealday Apraiz, "Individual voltage balancing strategy for PWM cascaded H-bridge converter-based STATCOM," *IEEE Transactions on Industrial Electronics*, vol. 55, no. 1, pp. 21–29, 2008.
- [8] E. Babaei, "A cascade multilevel converter topology with reduced number of switches," *IEEE Transactions on Power Electronics*, vol. 23, no. 6, pp. 2657–2664, 2008.
- [9] W.-H. Liu, Q. Song, L.-T. Teng, W. Wang, W.-H. WEI, and J.-C. GENG, "Balancing control of DC voltages of 50MVA STATCOM based on cascade multilevel inverters," *Proceedings of the CSEE*, vol. 24, pp. 145–150, 2004.
- [10] Q. Song, W. Liu, and Z. Yuan, "Multilevel optimal modulation and dynamic control strategies for STATCOMs using cascaded multilevel inverters," *IEEE Transactions on Power Delivery*, vol. 22, no. 3, pp. 1937–1946, 2007.
- [11] D. Jiang and Z. Zhang, "Control scheme of decoupled state feedback linearization of single-phase H-bridge cascaded STATCOM," *Power System Technology*, vol. 11, pp. 1–14, 2011.
- [12] X. Wang, J. Lin, L. Teng, and K. Wang, "Current control strategy of chain circuit STATCOM in d-q-0 coordinates," *Zhongguo Dianji Gongcheng Xuebao(Proceedings of the Chinese Society of Electrical Engineering)*, vol. 32, no. 15, pp. 48–54, 2012.
- [13] H. Akagi, S. Inoue, and T. Yoshii, "Control and performance of a transformerless cascade PWM STATCOM with star configuration," *IEEE Transactions on Industry Applications*, vol. 43, no. 4, pp. 1041–1049, 2007.
- [14] J. Shi, W. Gou, H. Yuan, T. Zhao, and A. Q. Huang, "Research on voltage and power balance control for cascaded modular solid-state transformer," *IEEE Transactions on Power Electronics*, vol. 26, no. 4, pp. 1154–1166, 2011.
- [15] X. She, A. Q. Huang, and G. Wang, "3-D space modulation with voltage balancing capability for a cascaded seven-level converter in a solid-state transformer," *IEEE Transactions on Power Electronics*, vol. 26, no. 12, pp. 3778–3789, 2011.
- [16] L. Wang, D. Zhang, Y. Wang, B. Wu, and H. S. Athab, "Power and voltage balance control of a novel three-phase solid-state transformer using multilevel cascaded H-bridge inverters for microgrid applications," *IEEE Transactions on Power Electronics*, vol. 31, no. 4, pp. 3289–3301, 2016.
- [17] C. Zhao, D. Dujic, A. Mester et al., "Power electronic traction transformer—medium voltage prototype," *IEEE Transactions on Industrial Electronics*, vol. 61, no. 7, pp. 3257–3268, 2014.
- [18] D.-H. Lee, "Design and direct field current control scheme of a synchronous generator with PM exciter based on the reference frequency," *IET Electric Power Applications*, vol. 13, no. 8, pp. 1150–1156, 2019.
- [19] S. K. Dash, G. Panda, P. K. Ray, and S. S. Pujari, "Realization of active power filter based on indirect current control algorithm using Xilinx system generator for harmonic elimination," *International Journal of Electrical Power & Energy Systems*, vol. 74, pp. 420–428, 2016.
- [20] K. D. E. Kerrouche, L. Wang, A. Mezouar, L. Boumediene, and A. Van Den Bossche, "Fractional-order sliding mode control for D-STATCOM connected wind farm based DFIG under voltage unbalanced," *Arabian Journal for Science and Engineering*, vol. 44, no. 3, pp. 2265–2280, 2019.
- [21] G. Farivar, C. D. Townsend, B. Hredzak, J. Pou, and V. G. Agelidis, "Passive reactor compensated cascaded H-bridge multilevel LC-StatCom," *IEEE Transactions on Power Electronics*, vol. 32, no. 11, pp. 8338–8348, 2017.
- [22] Q. M. Zhu, D. Y. Zhao, and J. Zhang, "A general U-block model-based design procedure for nonlinear polynomial control systems," *International Journal of Systems Science*, vol. 47, no. 14, pp. 3465–3475, 2016.
- [23] X. Geng, Q. Zhu, T. Liu, and J. Na, "U-model based predictive control for nonlinear processes with input delay," *Journal of Process Control*, vol. 75, pp. 156–170, 2019.
- [24] Q. Zhu, W. Zhang, J. Zhang, and B. Sun, "U-neural network-enhanced control of nonlinear dynamic systems," *Neurocomputing*, vol. 352, pp. 12–21, 2019.
- [25] Q. Zhu, L. Liu, W. Zhang, and S. Li, "Control of complex nonlinear dynamic rational systems," *Complexity*, vol. 2018, Article ID 8953035, 12 pages, 2018.
- [26] Q. M. Zhu and L. Z. Guo, "A pole placement controller for non-linear dynamic plants," *Proceedings of the Institution of Mechanical Engineers, Part I: Journal of Systems and Control Engineering*, vol. 216, no. 6, pp. 467–476, 2002.
- [27] H. K. Khalil, "Cascade high-gain observers in output feedback control," *Automatica*, vol. 80, pp. 110–118, 2017.
- [28] F. Smida, S. Hadj Saïd, and F. M'sahli, "Robust high-gain observers based liquid levels and leakage flow rate estimation," *Journal of Control Science and Engineering*, vol. 2018, Article ID 8793284, 8 pages, 2018.
- [29] F. Allahverdi, A. Ramezani, and M. Forouzanfar, "Sensor fault detection and isolation for a class of uncertain nonlinear system using sliding mode observers," *Automatika*, vol. 61, no. 2, pp. 219–228, 2020.
- [30] H. Wang, B. Su, Y. Wang, and J. Gao, "Adaptive sliding mode fixed-time tracking control based on fixed-time sliding mode disturbance observer with dead-zone input," *Complexity*, vol. 2019, Article ID 8951382, 14 pages, 2019.
- [31] K. Ohishi, M. Nakao, K. Ohnishi, and K. Miyachi, "Microprocessor-controlled DC motor for load-insensitive position servo system," *IEEE Transactions on Industrial Electronics*, vol. IE-34, no. 1, pp. 44–49, 1987.
- [32] W.-H. Chen, D. J. Ballance, P. J. Gawthrop, and J. O'Reilly, "A nonlinear disturbance observer for robotic manipulators," *IEEE Transactions on Industrial Electronics*, vol. 47, no. 4, pp. 932–938, 2000.
- [33] J. Han, "From PID to active disturbance rejection control," *IEEE Transactions on Industrial Electronics*, vol. 56, no. 3, pp. 900–906, 2009.
- [34] Y. Guan and M. Saif, "A novel approach to the design of unknown input observers," *IEEE Transactions on Automatic Control*, vol. 36, no. 5, pp. 632–635, 1991.
- [35] J. Y. Zhaoan Wang, *Harmonic Suppression and Reactive Power Compensation*, China Machine Press, Beijing, China, 1998.
- [36] J. Na, J. Yang, S. Wang, G. Gao, and C. Yang, "Unknown dynamics estimator-based output-feedback control for nonlinear pure-feedback systems," *IEEE Transactions on Systems, Man, and Cybernetics: Systems*, pp. 1–12, 2019.
- [37] J. Na, A. S. Chen, Y. Huang et al., "Air-fuel ratio control of spark ignition engines with unknown system dynamics estimator: theory and experiments," *IEEE Transactions on Control Systems Technology*, pp. 1–8, 2019.
- [38] G.-J. Wang, C.-T. Fong, and K. J. Chang, "Neural-network-based self-tuning PI controller for precise motion control of PMAC motors," *IEEE Transactions on Industrial Electronics*, vol. 48, no. 2, pp. 408–415, 2001.
- [39] J. Na, A. S. Chen, G. Herrmann, R. Burke, and C. Brace, "Vehicle engine torque estimation via unknown input observer and adaptive parameter estimation," *IEEE Transactions on Vehicular Technology*, vol. 67, no. 1, pp. 409–422, 2018.



## Research Article

# U-Model-Based Sliding Mode Controller Design for Quadrotor UAV Control Systems

Rui Wang <sup>1</sup>, Lei Gao,<sup>1</sup> Chengrui Bai,<sup>1</sup> and Hui Sun <sup>1,2</sup>

<sup>1</sup>College of Information Engineering and Automation, Haihang Building, South Campus, Civil Aviation University of China, Tianjin 300300, China

<sup>2</sup>Department of Engineering Design and Mathematics, University of the West of England, Frenchy Campus, Coldharbour Lane, Bristol BS16 1QY, UK

Correspondence should be addressed to Hui Sun; shhappy1@hotmail.com

Received 2 January 2020; Accepted 28 February 2020; Published 28 April 2020

Guest Editor: Weicun Zhang

Copyright © 2020 Rui Wang et al. This is an open access article distributed under the Creative Commons Attribution License, which permits unrestricted use, distribution, and reproduction in any medium, provided the original work is properly cited.

This paper proposes a U-model-based fault-tolerant controller design method in order to ensure the unmanned aerial vehicle (UAV) flight performance when subject to the actuator failures. Depending on the decoupled quadrotor model, this paper presents a sliding mode control method based on U-model in detail and realizes fault-tolerant control for the quadrotor UAV with the stability theory and simulation experiment verifications. The results show that the new controller designed by using the U-model method can simplify the controller design process which has good fault-tolerant characteristics when actuator faults occur compared with the traditional method.

## 1. Introduction

Quadrotor vehicle is a typical UAV and has been widely used in reconnaissance, damage assessment, agricultural inspection, express delivery, formation performance, and other multiple different functions by carrying corresponding task equipment [1, 2]. To meet the vast missions quadrotor vehicles can perform, different types of vehicles spring up and the corresponding various controllers are required to meet performance requirements and demands. In addition, quadrotor UAV may suffer various problems such as gust disturbance, mechanical vibration, and actuator failures during flight. These problems may reduce the flight performance and bring greater difficulties for controller design. Therefore, the controller design method compensating among different models will improve the development process of quadrotor UAV while ensuring the control system performance.

The U-model was first proposed in 2002, and this method considers the controlled object as a unit when designing the controller and then designs a universal controller that meets the requirements of the controlled object [3]. The core process is to calculate the inverse of the object plant and integrate with the already designed universal

controller to form a new controller. This universal controller is not necessary to be redesigned when fixed because of the performance requirements which are almost the same for different quadrotors. Under normal circumstances, aerial vehicle actuator failures include damage, stuck, floats, and saturation failures. These failures will affect system dynamics performances, even damage aerial vehicles [4]. In order to guarantee the safety for quadrotors, the fault-tolerant control technology has been widely employed in control system designs. Hao proposed an adaptive fault-tolerant control method for the quadrotor attitude system with portion of actuator failures [5–7]. Zhang developed the active fault-tolerant quadrotor UAV flight experiments based on sliding mode control and demonstrated that robustness of the active fault-tolerant is better than that of the passive one [8, 9]. Liu studied an improved fault-tolerant tracking controller for the quadrotor UAV which is able to compensate the efficiency loss due to actuator failures [10]. Meanwhile, multiple studies focus on generating observers to realize fault diagnosis and reconstruction. For example, Yang conducted system linear transformation and reconstructed faults by using sliding mode observers and the equivalent output injection method [11]. Gong proposed a



fault diagnosis method based on the state observer technology and theoretically analyzed its robustness and fastness [12].

So far, a large amount of in-depth research on controller design and system construction methods for quadrotor UAVs are improving better and better. However, in specific design process, it is still necessary to spend a lot of time to design different controllers for different models. The main contribution of this paper is to develop a general controller design method for UAVs by combining U-model and the fault-tolerant control methods. The proposed method can simplify the design process, and the designed universal controller can be reused in the design of controllers for

different UAV plants as well as guarantee the great control performances.

## 2. U-Model-Based Quadrotor UAV Model

*2.1. Preliminary about Quadrotor UAV Dynamics.* First, two basic coordinate systems are mentioned to obtain the mathematical model for the quadrotor, the inertial system  $E$  ( $OXYZ$ ), and the airframe coordinate system  $B$  ( $oxyz$ ), as shown in Figure 1.

The transformation matrix for converting coordinate systems is described as follows:

$$Q = Q_x Q_y Q_z = \begin{bmatrix} \cos \psi \cos \phi & \cos \psi \sin \theta \sin \psi & \cos \psi \sin \theta \cos \phi + \sin \psi \sin \phi \\ \sin \psi \cos \theta & \sin \psi \sin \theta \sin \phi & \sin \psi \sin \theta \cos \phi - \sin \phi \cos \psi \\ -\sin \theta & \cos \theta \sin \phi & \cos \theta \cos \phi \end{bmatrix}, \quad (1)$$

where  $\Phi$ ,  $\theta$ , and  $\psi$  are the roll angle, pitch angle, and yaw angle of the three axes of the inertial coordinate system, respectively.  $F_x$ ,  $F_y$ , and  $F_z$  are defined as components of  $F$  in three coordinate axes of the airframe coordinate system.  $F$  is the external force applied on the quadrotor,  $m$  is the mass of the quadrotor,  $V$  is the speed of the aircraft, and  $M$  is the sum of the torques experienced by the quadrotor. According to the physical equation,

$$\begin{aligned} F &= m \frac{dV}{dt}, \\ M &= \frac{dH}{dt}. \end{aligned} \quad (2)$$

Gravity  $G$ , drag  $D_i$ , lift of a single rotor  $T_i$  are defined as follows

$$\begin{aligned} G &= mg, \\ D_i &= \frac{\rho C_d \omega_i^2}{2} = k_d \omega_i^2, \\ T_i &= \frac{\rho C_t \omega_i^2}{2} = k_t \omega_i^2. \end{aligned} \quad (3)$$

According to the force analysis, Newton's second law, and the dynamics and coordinate transformation (1), the linear motion equation can be obtained as follows:

$$\begin{cases} \ddot{x} = \frac{(F_x - K_1 \dot{x})}{m} = \frac{(k_t \sum_{i=1}^4 \omega_i^2 (\cos \psi \sin \theta \cos \phi + \sin \psi \sin \phi) - K_1 \dot{x})}{m}, \\ \ddot{y} = \frac{(F_y - K_2 \dot{y})}{m} = \frac{(k_t \sum_{i=1}^4 \omega_i^2 (\sin \psi \sin \theta \sin \phi \cos \phi - \cos \psi \sin \phi) - K_2 \dot{y}) - K_2 \dot{x}}{m}, \\ \ddot{z} = \frac{(F_z - K_3 \dot{z} - mg)}{m} = \frac{(k_t \sum_{i=1}^4 \omega_i^2 (\cos \phi \cos \phi) - K_3 \dot{z})}{m} - g. \end{cases} \quad (4)$$

Furthermore,

$$\begin{bmatrix} \dot{\phi} \\ \dot{\theta} \\ \dot{\psi} \end{bmatrix} = \begin{bmatrix} \frac{(p \cos \theta + q \sin \phi \sin \theta + r \cos \phi \sin \theta)}{\cos \theta} \\ q \cos \phi + r \sin \phi \\ \frac{(q \sin \phi + r \cos \phi)}{\cos \theta} \end{bmatrix}, \quad (5)$$

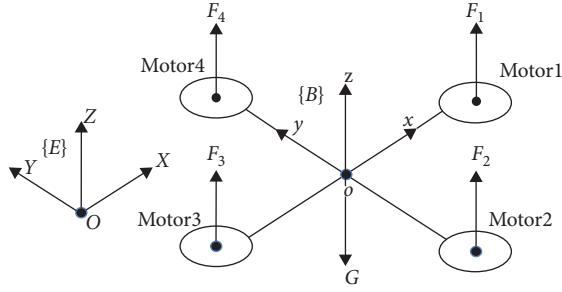


FIGURE 1: Rigid body force diagram of a quadrotor.

The angular motion equations can be derived by calculating angular momentum as follows:

$$\begin{bmatrix} \ddot{\phi} \\ \ddot{\theta} \\ \ddot{\psi} \end{bmatrix} = \begin{bmatrix} \frac{[M_x + (I_x - I_z)\dot{\theta}\dot{\psi}]}{I_x} \\ \frac{[M_y + (I_z - I_x)\dot{\psi}\dot{\phi}]}{I_y} \\ \frac{[M_z + (I_x - I_y)\dot{\phi}\dot{\theta}]}{I_z} \end{bmatrix}, \quad (6)$$

where  $M_x$ ,  $M_y$ , and  $M_z$  are three-axial angular motion and  $I_x$ ,  $I_y$ , and  $I_z$  are the moments of inertia.

Define  $u_1$ ,  $u_2$ ,  $u_3$ , and  $u_4$  as control inputs for four independent channels of the quadrotor, respectively:

$$\begin{bmatrix} u_1 \\ u_2 \\ u_3 \\ u_4 \end{bmatrix} = \begin{bmatrix} F_1 + F_2 + F_3 + F_4 \\ F_4 - F_2 \\ F_3 - F_1 \\ F_2 + F_4 - F_3 - F_1 \end{bmatrix} = \begin{bmatrix} k_t \sum_{i=1}^4 \omega_i^2 \\ k_t (\omega_4^2 - \omega_2^2) \\ k_t (\omega_3^2 - \omega_1^2) \\ k_d (\omega_1^2 - \omega_2^2 + \omega_3^2 - \omega_4^2) \end{bmatrix}, \quad (7)$$

where  $u_1$  is the vertical speed control amount,  $u_2$  is the roll input control amount,  $u_3$  is the pitch control amount,  $u_4$  is the yaw control amount, and  $\omega$  is the rotor speed.

The linear motion equation and the angular motion equation can be combined to obtain the nonlinear motion equation of the quadrotor. The mathematical model is described as follows:

$$\begin{aligned} \ddot{x} &= \frac{(\cos \psi \sin \theta \cos \phi + \sin \psi \sin \phi)u_1}{m}, \\ \ddot{y} &= \frac{(\sin \psi \sin \phi \cos \phi - \cos \psi \sin \phi)u_1}{m}, \\ \ddot{z} &= \frac{(\cos \phi \cos \theta)u_1}{m} - g, \\ \ddot{\phi} &= \frac{[lu_2 + \dot{\theta}\dot{\psi}(I_y - I_z)]}{I_x}, \\ \ddot{\theta} &= \frac{[lu_3 + \dot{\phi}\dot{\psi}(I_z - I_x)]}{I_y}, \\ \ddot{\psi} &= \frac{[u_4 + \dot{\phi}\dot{\theta}(I_x - I_y)]}{I_z}, \end{aligned} \quad (8)$$

where  $l$  is the distance from the center of the rotor to the origin of the airframe coordinate system and  $k_i$  is the wind resistance coefficient. In the case of no wind and slow flight, the resistance coefficient is neglected [13, 14].

The system can be decoupled into independent sub-systems including linear motion and angular motion. Furthermore, angular motion is not affected by linear motion. However, linear motion is affected by angular motion. When ignoring the additional small perturbations, the equation of motion of the quadrotor (8) can be obtained as follows [14]:

$$m\dot{\mathbf{x}} = A\mathbf{x} + B\mathbf{u},$$

$$\mathbf{x} = [\dot{x} \ \dot{y} \ \dot{z} \ \dot{\theta} \ \dot{\phi} \ \dot{\psi} \ \theta \ \phi \ \psi]^T, \quad (9)$$

$$\mathbf{u} = [u_1 \ u_2 \ u_3 \ u_4]^T.$$

According to the literature [14], the parameters about the quadrotor is demonstrated in Table 1 and the corresponding continuous transfer functions for each control channel of the quadrotor system is listed in Table 2. The calculated discretized transfer functions for each control channel of the quadrotor system are listed in Table 3.

TABLE 1: Quadrotor parameters [14].

Parameters	Values
$m$ (kg)	1.2
$l$ (m)	0.2
$k_t \times 10^{-5}$ (N·s <sup>2</sup> )	3.13
$k_d \times 10^{-7}$ (N·s <sup>2</sup> )	7.5
$I_x \times 10^{-3}$ (kg·m <sup>2</sup> )	2.353
$I_y \times 10^{-7}$ (kg·m <sup>2</sup> )	2.353
$I_z \times 10^{-7}$ (kg·m <sup>2</sup> )	5.262

TABLE 2: Continuous transfer function of each channel [14].

Channels	Transfer functions
Pitch channel	$G_1 = (\theta/u_1) = (56.95s + 4391/s^3 + 105s^2 + 870s + 4430)$
Roll channel	$G_2 = (\phi/u_2) = (65s + 4560/s^3 + 109s^2 + 1023s + 2935)$
Yaw channel	$G_3 = (\psi/u_3) = (105/s^2 + 413s)$
Z-axis motion	$G_4 = (z/u_4) = (1.63/s^2 + 5s)$

## 2.2. U-Model-Based Quadrotor UAV Model

**2.2.1. Preliminary about U-Model.** It is known that the controlled plant is considered as a unit when using the U-model to design a new controller. Then, according to the performance requirements for the plant, the new controller is formed by multiplication between the general controller and the inverse of the plant. Furthermore, the U-model is an expression for a class of smooth nonlinear objects. The nonlinear model for the system output can be expressed as a polynomial with  $u(k-1)$ [3]:

$$y(k) = \sum_{j=0}^M \alpha_j(k) u^j(k-1) + e(k), \quad (10)$$

where  $k$  is the time,  $k \in N^+$ , and  $M$  is the order of the model input  $u(k-1)$ . Parameter  $\alpha_j(k)$  is a function of inputs  $u(k-2), \dots, u(k-n)$  and outputs. The errors,  $e(k), \dots, e(k-n)$ , are unknown and unmeasured quantities. The control portion can be expressed as a power series of inputs  $u(k-1)$  with time-varying parameter  $\alpha_j(k)$ . In order to apply the linear control design method to obtain the controller outputs, it can be further converted into the current form, that is,

$$\begin{aligned} u_{\lambda+1}(k-1) &= u_{\lambda}(k-1) - \frac{\Theta[U_{\lambda}(k-1)] - U(k)}{d\Theta[u(k-1)]/du(k-1)} \\ &= u_{\lambda}(k-1) - \frac{\sum_{j=0}^M \alpha_j(k) u_{\lambda}^j(k-1) - U(k)}{d[\sum_{j=0}^M \alpha_j(k) u_{\lambda}^j(k-1)]/du(k-1)} \Big|_{u^j(k-1)=u_{\lambda}^j(k-1)}. \end{aligned} \quad (16)$$

$$U(k) = \sum_{j=0}^M \alpha_j(k) u^j(k-1) + e(k). \quad (11)$$

Because the U-model still keeps the characteristics of the controlled plant during inversion processes, it can improve the controller design efficiency.

Combining the U-model as mentioned in equation (10) with the pole placement described in the literature [15, 16] in detail, the method of designing the U-model-based pole placement controller is presented below according to each part of Figure 2.

*Step 1.* Regard the controlled plant as a unit.  $U(k) = y(k) = y_d(k)$ ,

$$Ry_d(k) = Ow(k) - Sy(k),$$

$$y_d(k) = \frac{O}{R+S} w(k) = \frac{O}{A_c} w(k), \quad (12)$$

$$R + S = A_c, \quad (13)$$

$$O = A_c(1), \quad (14)$$

$$R = h^a + r_1 h^{a-1} + \dots + r_a,$$

$$O = o_0 h^b + o_1 h^{b-1} + \dots + o_b, \quad (15)$$

$$S = s_0 h^d + s_1 h^{d-1} + \dots + s_d,$$

where  $w(k)$  is the reference input of the system.  $R$ ,  $O$ , and  $T$  are polynomials about the forward operator  $h$ .  $a$ ,  $b$ , and  $d$  are the highest powers in the forward operator in  $R$ ,  $O$ , and  $S$ , respectively, and should satisfy  $d < a$  and  $b \leq a$ . Parameters  $r_{p1}, r_{p2}, r_{p3} \in R$ , where  $p1 = 1, \dots, a$ ,  $p2 = 1, \dots, b$ , and  $p3 = 1, \dots, c$ .  $A_c$  is the characteristic equation polynomial of the closed-loop system, and  $y_d$  is the expected output of the system.  $A_c$  needs to be set during the design process according to the performance requirements of the actual controlled object.

*Step 2.* Calculate the general controller output,  $U(k)$ , and use the Newton–Raphson algorithm to solve the output  $u(k-1)$  of the actual controller:

TABLE 3: Discrete transfer function of each channel.

Channels	Transfer functions
Pitch channel	$G'_1 = (0.1753z^2 + 0.1199z - 5.78 \times 10^{-4}/z^3 - 1.128z^2 + 0.4256z - 2.754 \times 10^{-5})$
Roll channel	$G'_2 = (0.1763z^2 + 0.1083z - 7.907 \times 10^{-4}/z^3 - 1.184z^2 + 0.3666z - 1.846 \times 10^{-5})$
Yaw channel	$G'_3 = (0.2481z + 0.006/z^2 + z - 1.158 \times 10^{-18})$
Z-axis motion	$G'_4 = (0.006946z - 5.881 \times 10^{-3}/z^2 - 1.607z + 0.6065)$

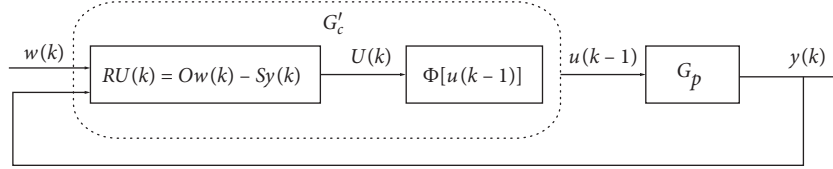


FIGURE 2: Design flow of the pole configuration controller [3].

Step 3. Regard  $G_c G_p^{-1} = G'_c$  as the new controller of  $G_p$ . Now,  $u(k-1)$  is the input of  $G_p$  which has been converted to U-model form.

2.2.2. *Quadrotor UAV Controller Design.* For the above-mentioned quadrotor flight control system, a controller with a natural frequency of 1 rad/s and a damping ratio of 0.7 is designed to achieve zero steady-state error. The closed-loop characteristic equation is designed as

$$A_c = h^2 - 1.3205h + 0.4966. \quad (17)$$

Therefore, substitute  $h=1$  into (17), and then it is obtained from (14) that

$$O = A_c(1) = 1 - 1.3205 + 0.4966 = 0.1761. \quad (18)$$

So, the polynomials  $R$  and  $S$  can be expressed as

$$\begin{aligned} R &= h^2 + r_1 h + r_2, \\ S &= s_0 h + s_1. \end{aligned} \quad (19)$$

Substituting the characteristic equations (17) and (19) into (13), equation (12) can be derived:

$$\begin{aligned} r_2 + s_1 &= 0.4966, \\ r_1 + s_0 &= -1.3205. \end{aligned} \quad (20)$$

To ensure the convergence of  $U(k)$ , let  $r_1 = -0.9$  and  $r_2 = 0.009$ , and then obtain  $s_0 = -0.4205$  and  $s_1 = 0.4876$ . Therefore, the output of the universal controller is

$$\begin{aligned} U(k+1) &= 0.9U(k) - 0.009U(k-1) + 0.1761w(k-1) \\ &\quad + 0.4205y(k) - 0.4876y(k-1). \end{aligned} \quad (21)$$

Design controllers for each of the four channels with the above-mentioned universal controller, respectively.

- (1) Convert the discretized transfer function of the pitch channel to a polynomial form as

$$\begin{aligned} y_1(k) &= 1.128y(k-1) - 0.4256y(k-2) + 2.754 \times 10^{-5}y(k-3) \\ &\quad + 0.1753u(k-1) + 0.1199u(k-2) - 5.78 \times 10^{-4}u(k-3). \end{aligned} \quad (22)$$

The corresponding U-model form is

$$\begin{aligned} \alpha_{10} &= 1.128y(k-1) - 0.4256y(k-2) \\ &\quad + 2.754 \times 10^{-5}y(k-3) + 0.1199u(k-2) - 5.78 \\ &\quad \times 10^{-4}u(k-3), \\ \alpha_{11} &= 0.1753. \end{aligned} \quad (23)$$

The sample time is set 0.001s in this paper. The U-model-based pole placement method is used to design the output and the input responses of the pitch channel as shown in Figures 3(a) and 3(b). It can be seen from Figure 3(a) that the system has a small overshoot, almost zero steady-state error, and a fast response speed, which meet the performance requirements of a quadrotor during flight. It can be seen from Figure 3(b) that the controller designed according to the idea of U-model simplifies the design process of the controller while ensuring the uniqueness of the controller.

- (2) Convert the discretized transfer function of the rollover channel to a polynomial form as

$$\begin{aligned} y_2(k) &= 1.184y(k-1) - 0.3666y(k-2) + 1.846 \\ &\quad \times 10^{-5}y(k-3) + 0.1763u(k-1) + 0.1083u(k-2) \\ &\quad - 7.907 \times 10^{-4}u(k-3). \end{aligned} \quad (24)$$

The corresponding U-model form is

$$\begin{aligned} \alpha_{20}(k) &= 1.184y(k-1) - 0.3666y(k-2) + 1.846 \\ &\quad \times 10^{-5}y(k-3) + 0.1083u(k-2) - 7.907 \\ &\quad \times 10^{-4}u(k-3), \\ \alpha_{21} &= 0.1763. \end{aligned} \quad (25)$$

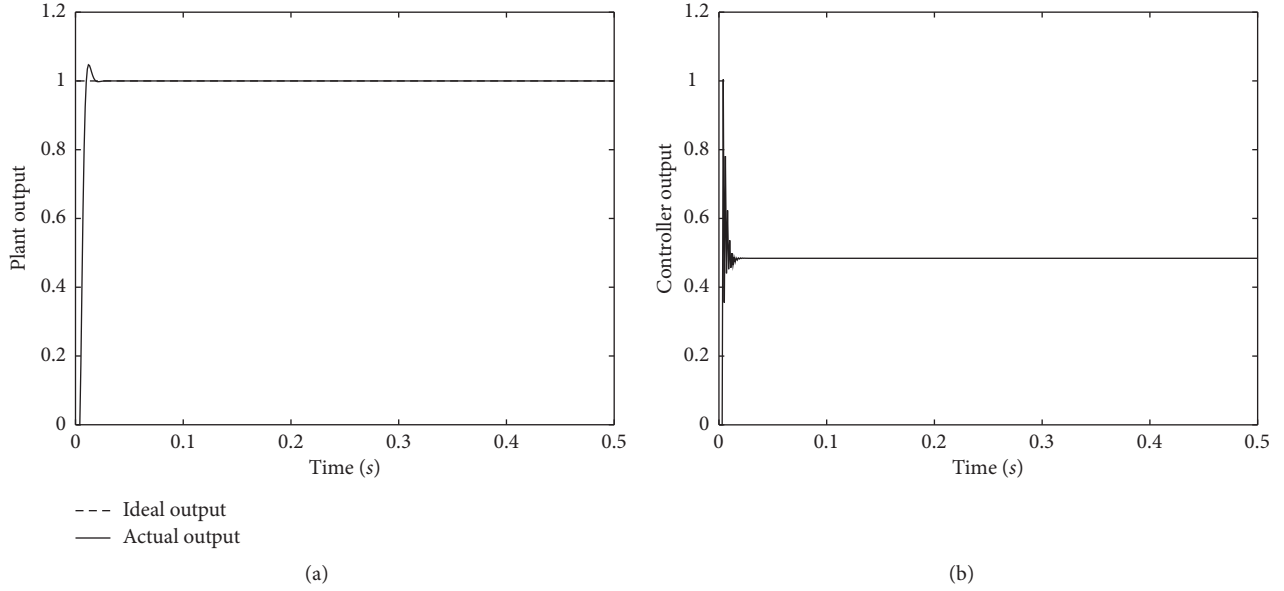


FIGURE 3: (a) Output of the pitch channel. (b) Input of the pitch channel.

The output and the input responses of the roll channel are designed using the U-model-based pole placement method as shown in Figures 4(a) and 4(b). The comparison between Figures 4(a) and 3(a) shows that the output performance of the controlled object is the same. At the same time, it is found that the input of the controlled object is different, which proves that the designed controller is unique when comparing Figure 4(b) to Figure 3(b).

- (3) Convert the discretized transfer function of the yaw channel to a polynomial form as

$$y_3(k) = -y(k-1) + 1.158 \times 10^{-18} y(k-2) + 0.2481u(k-1) + 0.006u(k-2). \quad (26)$$

The corresponding U-model form is

$$\begin{aligned} \alpha_{30}(k) &= -y(k-1) + 1.158 \times 10^{-18} y(k-2) + 0.006u(k-2), \\ \alpha_{31}(k) &= 0.2481. \end{aligned} \quad (27)$$

The U-model-based pole placement method is used to design the output and the input responses of the yaw channel as shown in Figures 5(a) and 5(b). The output of the controlled object is also the same as those in Figures 3(a) and 4(a); however, the output of the controller is different from those in Figures 3(b) and 4(b).

- (4) Convert the discretized transfer function of the motion in the Z-axis direction into a polynomial form as

$$y_4(k) = 1.607y(k-1) - 0.6065y(k-2) + 6.946u(k-1) - 5.881 \times 10^{-3}u(k-2). \quad (28)$$

The corresponding U-model form is

$$\begin{aligned} \alpha_{40} &= 1.607y(k-1) - 0.6065y(k-2) - 5.881 \times 10^{-3}u(k-2), \\ \alpha_{41} &= 6.946. \end{aligned} \quad (29)$$

The U-model-based pole placement method is used to design the output and the input responses of the Z-axis motion as shown in Figures 6(a) and 6(b). The output of the controlled object is also the same as those in Figures 3(a), 4(a), and 5(a), and the inputs of the controlled objects are different.

By comparing Figures 3(a)–6(a) for simulation results, it can be seen that the output responses of the controlled object are the same when the U-model controller is used to control the controlled object. Comparing Figures 3(b)–6(b), it can be seen that the designed controller outputs are different. The newly designed controller developed by using the U-model of the object is formed by  $G_c G_p^{-1}$ . Because  $G_p^{-1}$  varies depending upon the different plants, the newly designed controller issue is converted into calculating the inverse of the plant which simplifies the design process, meanwhile ensuring the performance requirements. Therefore, each newly designed controller works for the specific object.

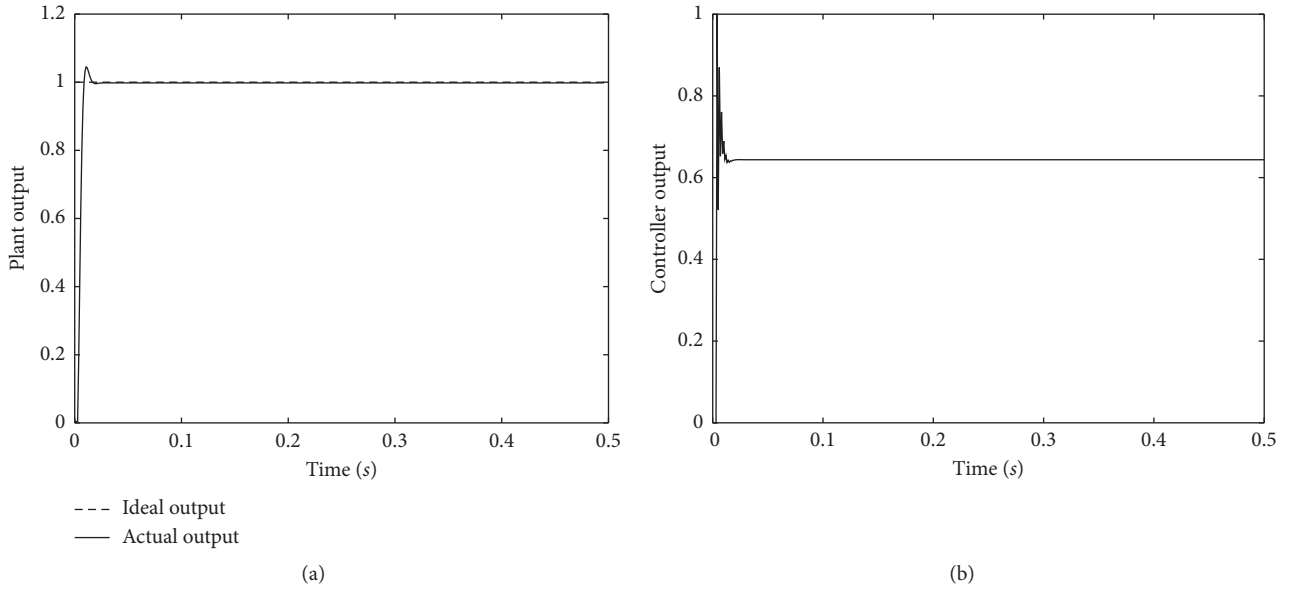


FIGURE 4: (a) Output of the roll channel. (b) Input of the roll channel.

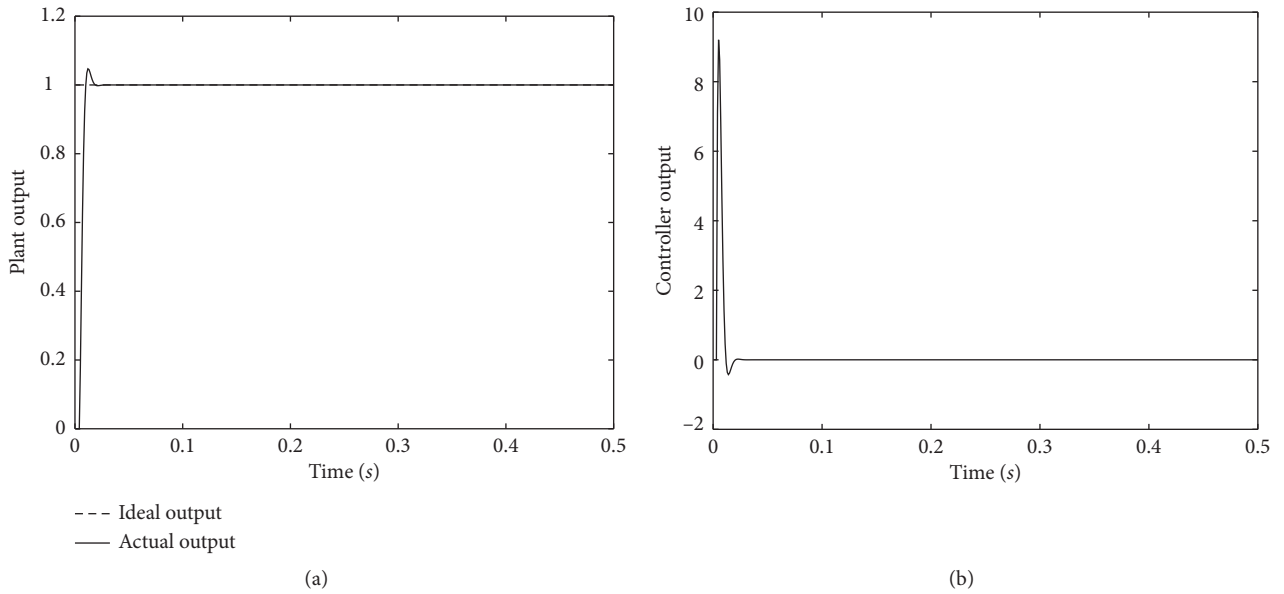


FIGURE 5: (a) Output of the yaw channel. (b) Input of yaw channel.

### 3. U-Block-Based Fault-Tolerant Control

The abovementioned U-model method also works in state space form by using the method proposed in the literature [17]. This section discusses a U-model-based fault-tolerant control method employed in state space.

According to the specified characteristic equation  $A_c$  proposed in the U-model and the performance requirements of different controlled objects,  $A_c$  can be derived by placing reasonable poles:

$$A_c = (h - \vartheta_1) \cdots (h - \vartheta_t) = h^t + a_{c1}h^{t-1} + \cdots + a_{ct} = 0,$$

$$\frac{Y(h)}{w(h)} = \frac{A_c(1)}{h^t + a_{c1}h^{t-1} + \cdots + a_{ct}}. \tag{30}$$

Therefore, the corresponding state equation form in a controllable implementation is

$$\begin{aligned} x(k+1) &= Ax(k) + Bw(k), \\ y(k) &= Cx(k). \end{aligned} \tag{31}$$



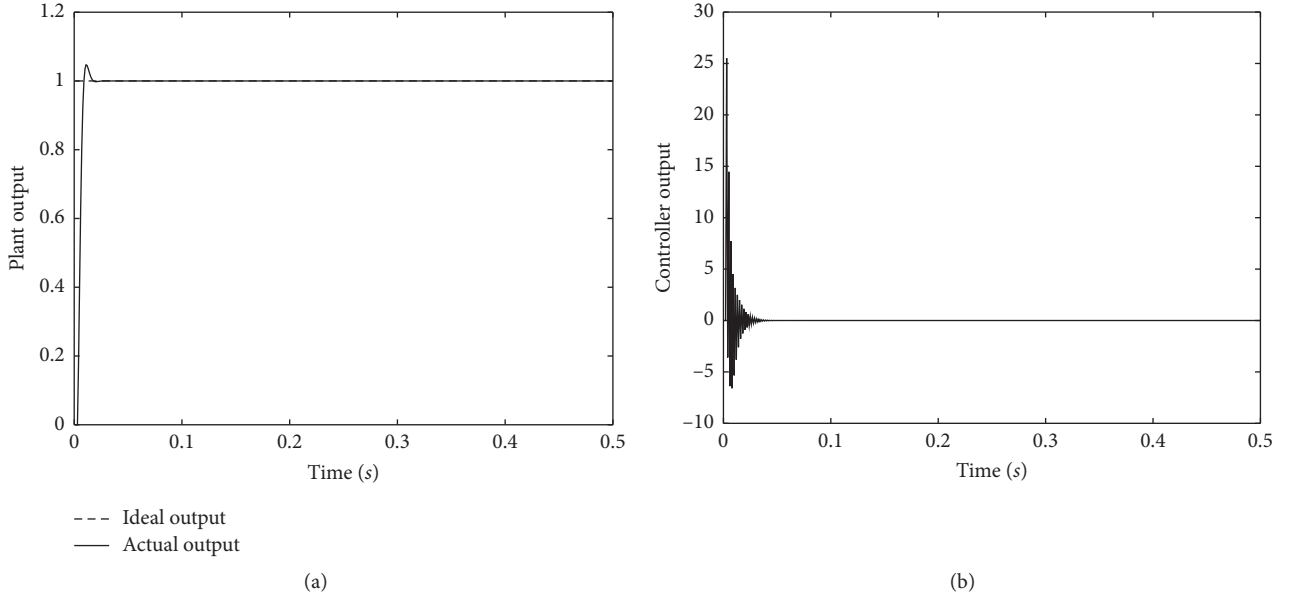


FIGURE 6: (a) Z-axis motion output. (b) Z-axis motion input.

Furthermore,

$$\begin{bmatrix} x_1(k+1) \\ x_2(k+1) \\ \vdots \\ x_{t-1}(k+1) \\ x_t(k+1) \end{bmatrix} = \begin{bmatrix} 0 & 1 & 0 & \cdots & 0 \\ 0 & 0 & 1 & \cdots & 0 \\ \vdots & & & & \\ 0 & 0 & 0 & \cdots & 1 \\ -a_{ct} & -a_{c(t-1)} & -a_{c(t-2)} & \cdots & -a_{c1} \end{bmatrix} \begin{bmatrix} x_1(k) \\ x_2(k) \\ \vdots \\ x_{t-1}(k) \\ x_t(k) \end{bmatrix} + \begin{bmatrix} 0 \\ 0 \\ \vdots \\ 0 \\ A_c(1) \end{bmatrix} w(k) \quad (32)$$

$$y(k) = [1 \ 0 \ 0 \ 0 \ 0] \begin{bmatrix} x_1(k) \\ x_2(k) \\ \vdots \\ x_{t-1}(k) \\ x_t(k) \end{bmatrix}.$$

When an unmanned aerial vehicle drone fails, the controlled object model can be expressed as

$$\begin{cases} \dot{x}(k) = Ax(k) + Bu(k) + f(k, x, u), \\ y(k) = Cx(k). \end{cases} \quad (33)$$

The function  $f(k, x, u)$  indicates that the actuator fails and is defined as

$$f(k, x, u) = B\xi(k, x, u), \quad (34)$$

where  $\xi(k, x, u)$  is an unknown and bounded function:

$$\|\xi(k, x, u)\| \leq \gamma \|u\| + \zeta(k, x), \quad (35)$$

in which  $\zeta(k, x)$  indicates disturbances and  $0 \leq \gamma < 1$  indicates the damage degree of actuator failure [18]. So, system (33) can be further described as

$$\begin{cases} \dot{x}(k) = Ax(k) + B(I - \Gamma)u(k) + B\alpha(k, x), \\ y(k) = Cx(k), \end{cases} \quad (36)$$

where  $\Gamma = \text{diag}(\gamma_1, \gamma_2, \dots, \gamma_m)$  and  $\gamma_i$  is a scalar and satisfies

$$\begin{cases} \gamma_i = 0, & \text{no fault,} \\ 0 < \gamma_i < 1, & \text{fault on } i \text{ th operation surface,} \end{cases} \quad (37)$$

$i = 1, 2, \dots, m.$

It is known that sliding mode control can realize the insensitivity and robustness of sliding mode for a kind of uncertainty and interference. Therefore, this paper employs the sliding mode control (SMC) method to design a U-model-based controller to improve the robustness of control systems subject to faults. For the second-order discrete system, let the position command be  $w(k)$  and  $dw(k)$  is the derivative of  $w(k)$ . Take  $W = [w(k) \ dw(k)]^T$

and  $W_1 = [w(k+1) \ dw(k+1)]^T$ , and use linear extrapolation to predict  $w(k+1)$  and  $dw(k+1)$ , *s.t.*

$$\begin{aligned} w(k+1) &= 2w(k) - w(k-1), \\ dw(k+1) &= 2dw(k) - dw(k-1). \end{aligned} \quad (38)$$

Design a sliding mode surface function as

$$s(k) = C_e(W(k) - x(k)), \quad (39)$$

where  $C_e = [c \ 1]$ .

$$\begin{aligned} s(k+1) &= C_e(W(k+1) - x(k+1)) = C_e(W(k+1) \\ &\quad - Ax(k) - Bu(k)) \\ &= C_e(W(k+1) - C_eAx(k) - C_eBu(k)). \end{aligned} \quad (40)$$

Therefore, the designed control law is

$$u(k) = (C_eB)^{-1}(C_eW(k+1) - C_eAx(k) - s(k+1)). \quad (41)$$

For continuous sliding mode variable structure control, the commonly used approach is the exponential approach law:

$$\dot{s}(t) = -\varepsilon \operatorname{sgn}(s(t)) - \sigma s(t), \quad \varepsilon > 0, \sigma > 0. \quad (42)$$

Correspondingly, the discrete exponential approach law can be derived as

$$\frac{s(k+1) - s(k)}{T_s} = -\varepsilon \operatorname{sgn}(s(k)) - \sigma s(k), \quad (43)$$

$$s(k+1) - s(k) = -\sigma T_s s(k) - \varepsilon T_s \operatorname{sgn}(s(k)),$$

where  $\varepsilon > 0$ ,  $\sigma > 0$ ,  $1 - \sigma T_s > 0$ , and  $T_s$  is the sampling period. So, the discrete approach law is

$$s(k+1) = s(k) + T_s(-\varepsilon \operatorname{sgn}(s(k)) - \sigma s(k)). \quad (44)$$

Substituting (44) into equation (40), the discrete control law,  $u(k)$ , based on the exponential approach is obtained:

$$u(k) = (C_eB)^{-1}(C_eW(k+1) - C_eAx(k) - s(k) - ds(k)), \quad (45)$$

where  $ds(k) = -\varepsilon T_s \operatorname{sgn}(s(k)) - \sigma T_s s(k)$ , and  $C_e = [c \ 1]$ .

*Proof.* To verify the stability of the selected sliding surface, the Lyapunov function is designed as

$$V(k) = \frac{1}{2}s(k)^2. \quad (46)$$

When the condition  $\dot{V}(k) \leq 0$  is satisfied, the conclusion that the system is stable can be drawn:

$$\begin{aligned} \dot{V}(k) &= s(k)\dot{s}(k) \\ &= s(k)\left(\frac{s(k+1) - s(k)}{T_s}\right) \\ &= \frac{1}{T_s}s(k)[- \sigma T_s s(k) - \varepsilon T_s \operatorname{sgn}(s(k))] \\ &= -\sigma s^2(k) - \varepsilon s(k)\operatorname{sgn}(s(k)) \\ &\leq -\sigma s^2(k) - \varepsilon |s(k)|. \end{aligned} \quad (47)$$

Since  $\varepsilon > 0$  and  $\sigma > 0$ , then  $\dot{V}(k) \leq 0$  is obtained.

#### 4. Analysis of Simulation Results

When partial actuator failures occur in the yaw channel, the discrete sliding mode control law is applied for designing a fault-tolerant controller for each channel, respectively. The discrete yaw channel model is transformed into a U-block form using the pole placement method. According to equations (26), (44), and (45), the corresponding state space equations are derived and the corresponding model matrices are

$$\begin{aligned} A &= \begin{bmatrix} 0 & 1 \\ -0.4966 & 1.3205 \end{bmatrix}, \\ B &= \begin{bmatrix} 0 \\ 0.1761 \end{bmatrix}, \\ C &= [1 \ 0]. \end{aligned} \quad (48)$$

The parameters of the controller according to (44) are  $c = 50$ ,  $\varepsilon = 5$ , and  $\sigma = 150$ .

This paper conducts simulations when faults are inserted at time 2 s demonstrated in Figures 7(a)-7(b). The simulation selects the sampling period, 0.001 s. That is, the control system operates in normal conditions from 0 s to 2 s. However, at time 2 s, the actuator experienced a 50% performance failure. Meanwhile, the designed controller brings about a great tracking performance.

As illustrated in Figures 7(a) and 7(b), it can be seen that the design controller works properly to track the desired output of the system. Even though the actuator loses 50% operation efficiency at 2 s, it still maintains good tracking performance. Figure 7(b) illustrates the control error between the actual and expected outputs and obviously shows that the error falls within 5% and satisfies the performance requirements. The simulation results verify the feasibility of the designed controller by using the U-model and, furthermore, demonstrate that the U-model-based controller can simplify the controller design process. When combining the sliding mode control method, the proposed controller presents good fault-tolerance performance, good stability, and tracking performance.

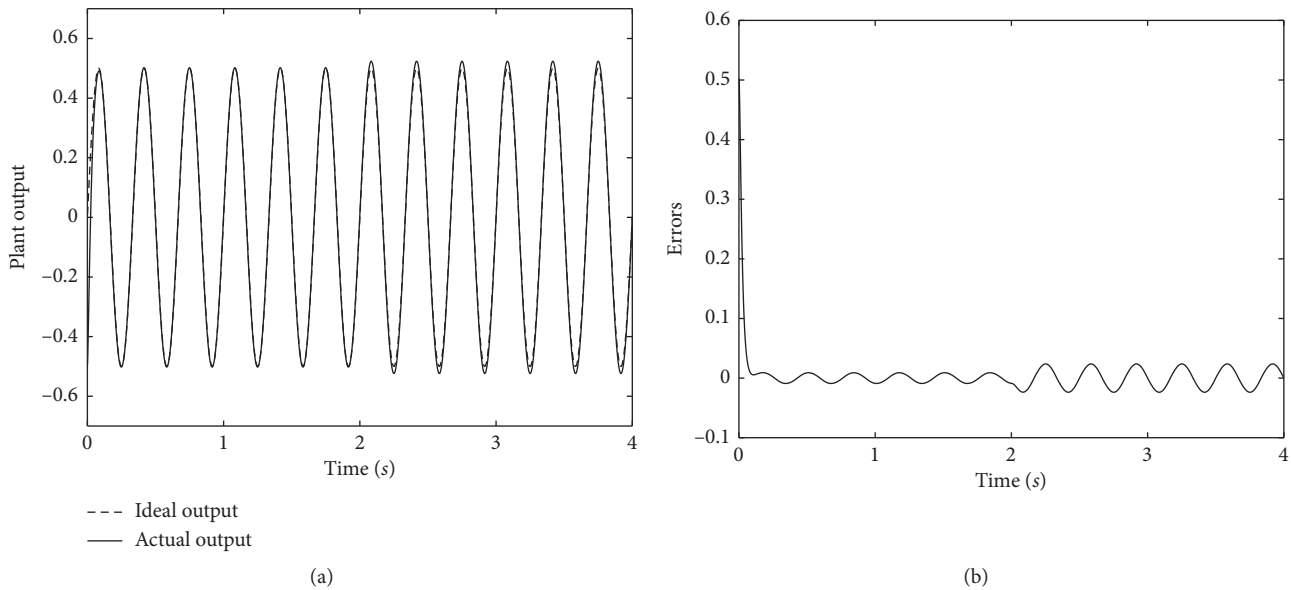


FIGURE 7: (a) Comparison between the actual output and the expected output when a fault occurs at 2 s. (b) Error between actual output and expected output.

## 5. Conclusions and Future Works

In this paper, the transfer function of each channel of the quadrotor control system is decoupled and converted into the U-block form by using the pole placement method. Furthermore, the actuator failure along with partial performance loss is considered and U-model-based sliding mode controller is designed and applied to a four-rotor flight control system in this paper. The simulations verify that the designed controller provides great fault-tolerant performance for quadrotor systems. The method proposed in this paper not only guarantees the performance requirements and simplifies the controller design process but also can be extended to other plants with the same performance requirements. This method can be mixed with other controller design methods to improve the stability of the system when suffering a fault as well in the future. The physical verification of this method will also be considered and conducted in the near future.

## Data Availability

The data used to support the findings of this study are available from the corresponding author upon request.

## Conflicts of Interest

The authors declare that there are no conflicts of interest regarding the publication of this paper.

## Acknowledgments

This work was supported by the Fundamental Research Funds for the Central Universities-Civil Aviation University of China (3122019044).

## References

- [1] F. Kendoul, "Survey of advances in guidance, navigation, and control of unmanned rotorcraft systems," *Journal of Field Robotics*, vol. 29, no. 2, pp. 315–378, 2012.
- [2] L. Zhou, J. Zhang, H. She, and H. Jin, "Quadrotor UAV flight control via a novel saturation integral backstepping controller," *Automatika*, vol. 60, no. 2, pp. 193–206, 2019.
- [3] Q. M. Zhu and L. Z. Guo, "A pole placement controller for non-linear dynamic plants," *Proceedings of the Institution of Mechanical Engineers, Part I: Journal of Systems and Control Engineering*, vol. 216, no. 6, pp. 467–476, 2002.
- [4] F. Chen, D. Lu, and X. Li, "Robust observer based fault-tolerant control for one-sided lipschitz markovian jump systems with general uncertain transition rates," *International Journal of Control, Automation and Systems*, vol. 17, no. 7, pp. 1614–1625, 2019.
- [5] H. Castañeda and J. Gordillo, "Spatial modeling and robust flight control based on adaptive sliding mode approach for a quadrotor MAV," *Journal of Intelligent & Robotic Systems: Theory & Applications*, vol. 93, no. 1-2, pp. 101–111, 2019.
- [6] A.-R. Merheb, H. Noura, and F. Bateman, "Design of passive fault-tolerant controllers of a quadrotor based on sliding mode theory," *International Journal of Applied Mathematics and Computer Science*, vol. 25, no. 3, pp. 561–576, 2015.
- [7] D.-T. Nguyen, D. Saussié, and L. Saydy, "Robust self-scheduled fault-tolerant control of a quadrotor UAV," *IFAC-PapersOnLine*, vol. 50, no. 1, pp. 5761–5767, 2017.
- [8] T. Li, Y. Zhang, and B. W. Gordon, "Nonlinear fault-tolerant control of a quadrotor UAV based on sliding mode control technique," *IFAC Proceedings Volumes*, vol. 45, no. 20, pp. 1317–1322, 2012.
- [9] Y. Zhang, X. Yu, B. Wang, and D. Liu, "Design and implementation of fault-tolerant control algorithms for an unmanned quadrotor system," *Control Engineering*, vol. 23, no. 12, pp. 1874–1882, 2016, in Chinese.
- [10] Z. Liu, C. Yuan, X. Yu, and Y. Zhang, "Retrofit fault-tolerant tracking control design of an unmanned quadrotor helicopter considering actuator dynamics," *International Journal of*

- Robust and Nonlinear Control*, vol. 29, no. 16, pp. 5293–5313, 2017.
- [11] Y. Dong, P. Yang, W. Ma, and B. Ma, “Sliding mode robust adaptive fault-tolerant control design for uncertain time-delay systems,” in *Proceedings of the 2016 IEEE Chinese Guidance, Navigation and Control Conference (CGNCC)*, pp. 2143–2147, IEEE, Nanjing, China, August 2016.
  - [12] X. Gong and L. Wang, “Fault-tolerant attitude stabilization control of four rotor aircraft,” *Electro-Optic and Control*, vol. 21, no. 7, pp. 14–18, 2014, in Chinese.
  - [13] C. Wu, H. Wang, Y. Zhang, J. Tan, and X. Ni, “Trajectory tracking of unmanned helicopter based on LADRC,” *Journal of Aeronautics*, vol. 36, no. 2, pp. 473–483, 2014, in Chinese.
  - [14] J. Li and Y. Li, “Dynamic modeling and PID control of quadrotor,” *Journal of Liaoning Technical University (Natural Science Edition)*, vol. 31, no. 1, pp. 116–119, 2012, in Chinese.
  - [15] Q. Zhu, S. Li, and D. Zhao, “A universal U-model based control system design,” in *Proceedings of the 33rd Chinese Control Conference*, pp. 1839–1844, IEEE, Nanjing, China, July 2014.
  - [16] M. Paluszek and S. Thomas, *Adaptive Control*, Apress, New York, NY, USA, 2017.
  - [17] Q. M. Zhu, D. Y. Zhao, and J. Zhang, “A general U-block model-based design procedure for nonlinear polynomial control systems,” *International Journal of Systems Science*, vol. 47, no. 14, pp. 3465–3475, 2016.
  - [18] H. Alwi and C. Edwards, “Fault detection and fault-tolerant control of a civil aircraft using a sliding-mode-based scheme,” *IEEE Transactions on Control Systems Technology*, vol. 16, no. 3, pp. 499–510, 2008.

## Research Article

# An Output Force Control for Robotic Manipulator by Changing the Spring Stiffness

Jirong Wang,<sup>1</sup> Yuhang Zheng ,<sup>1</sup> Jun Li,<sup>2</sup> Cheng Liu,<sup>1</sup> Youliang Huang,<sup>1</sup> and Yu Liu<sup>1</sup>

<sup>1</sup>College of Mechanical and Electronic Engineering, Qingdao University, Qingdao 266300, China

<sup>2</sup>College of Computer Science and Technology, Qingdao University, Qingdao 266300, China

Correspondence should be addressed to Yuhang Zheng; 2498365119@qq.com

Received 4 December 2019; Revised 10 January 2020; Accepted 3 February 2020; Published 24 April 2020

Guest Editor: Jing Na

Copyright © 2020 Jirong Wang et al. This is an open access article distributed under the Creative Commons Attribution License, which permits unrestricted use, distribution, and reproduction in any medium, provided the original work is properly cited.

This paper presents an output control for a manipulator by changing the spring stiffness. Through the modeling and analysis of the nonlinear stiffness characteristics of the crank-rocker mechanism, and using the zero stiffness domain search method to select the appropriate spring stiffness, using different spring stiffness to establish different mechanism models, the robot can finally control the output of ideal constant force, and at the same time, the analysis results are applied to the improved design of the tyre grabbing manipulator. Through this method, the tyre grabbing manipulator becomes a constant grabbing force mechanism, and the mechanism is transformed from a rigid-body mechanism to a pseudo-rigid-body mechanism. The accuracy and stability of the whole system are greatly improved. In this study, the method of adding spring to each joint of the linkage mechanism is applied to the improvement design of the linkage mechanism, and the four-bar constant force mechanism is designed for the first time, which expands the application field of the nonlinear stiffness characteristics of the linkage mechanism, and has great application value to the improvement design of the mechanical system with the linkage mechanism and the control of the output force.

## 1. Introduction

Handling robots are widely used in machine tool loading and unloading, stamping machine automatic production line, automatic assembly line, palletizing, and container and other automatic handling. In the tyre industry, the tyre handling robot can not only make full use of the space of the environment but also can improve the material handling capacity, save the working time in the process of loading and unloading, and improve the efficiency of loading and unloading. The weight of all-steel radial tyres is generally heavy. According to the size parameters of the all-steel radial tyre, the overall design of the triple-speed truss manipulator is carried out.

The designed manipulator can realize the technological actions of grabbing tyres for the assembly line and completing tyre vulcanization, loading pot, and storage and stacking. But in the actual operation process, because of the inadequate motion accuracy and the excessive grasping force of the manipulator, it is easy to cause the appearance defects

of the tyre bead when the manipulator grasps the tyre, which not only affects the safety of the tyre but also affects the installation of the tyre and other processes. If the gripping force of the manipulator is too large, the deformation of the tyre blank and ellipticity of the tyre will increase during storage and stacking, which will cause the chuck to gnaw the steel ring in the vulcanization process and lead to the extrusion of the rubber and the outcrop of the tyre rim. The vibration of the manipulator in the process of operation can easily lead to the accumulation of errors, which will eventually lead to a large deviation of the tyre stacking position. At the same time, because the grasping mechanism of the manipulator is a rigid-body mechanism, there is a large friction and clearance itself, which will also lead to the problem of tyre stacking position. When the tyre is stored in a vertical tyre storage truck, once there is a problem in the storage location, there are also some problems such as the deformation of the blank and the ellipticity of the tyre, which will also lead to extrusion of the compound and the appearance of the bead. The appearance defect of the tyre bead

will seriously affect the qualified rate of the tyre, reduce production efficiency, and increase production cost.

In view of the problem that the grasping force of the manipulator is too large, the traditional solution is to calculate the theoretical diameter of the tyre bead according to the product design and component size and, at the same time, to measure the actual diameter of the tyre bead after forming. Based on the minimum diameter, determination of the maximum distance between the claws after the manipulator is closed was performed. Then, comparing the distance between the claw pieces after closing of the current manipulator, cutting and grinding the excess parts of the claw pieces, testing the safety of different quality tyres after lifting, ensuring that the tyre will not squeeze the bead when the manipulator grabs the tyre, and that the bead will not fall off after lifting, and solving the problem of the upper bead crack caused by the extrusion of the mechanical claw pieces on the bead were performed. However, this improvement method is too cumbersome and unsuitable for tyre production with different inner diameters. Therefore, in order to solve the problem of excessive grasping force and tyre production with different inner diameters, the constant force grasping mechanism manipulator is used to solve the aforementioned problems.

Using the characteristics of the mechanical structure, the constant force of mechanisms can provide approximately constant force output. Constant force of mechanisms is widely used in overload protection, biomedical applications, and robotic end effectors to provide friendly interaction with the environment, as well as to protect micro-objects from damage to micro-operations [1]. Because of its many advantages, many scholars have carried out a lot of research on it. Guimin Chen optimized the parameters of the constant force mechanism by using the nonlinear stiffness characteristics [2]. Chia-Wenhou proposed a functional joint mechanism with constant torque output, studied the torque speed curves of different materials, and compared their resistance to hysteresis and stress relaxation [3]. Patrice Lambert proposed a new type of constant force mechanism of pin shaft connection and analyzed the influence of friction produced by pin shaft connection on output force by using the establishment of nonlinear stiffness [4]. Piyu Wang designed a XY precision positioning platform with constant force output parallel kinematics based on a compact flexible mechanism, which can generate constant output force without using a force controller [5]. Tolman proposed a fully flexible constant force mechanism with the initial angle parallel guiding mechanism. Using the finite element model and the experimental prototype test, the pseudo-rigid-body model of the mechanism was established and verified [6]. Liu introduces the design and control of a new passive flexible constant force fixture. The positive stiffness mechanism and negative stiffness mechanism are combined to realize the constant force output function, and the validity of the fixture system is verified through the experimental study of the microcopper wire grip release operation [7]. For the application of the constant force mechanism in industry, the most representative is the constant force compression mechanism. Constant force compression mechanism

(CFCM) is a kind of slider mechanism with large deflection beam. Midha et al. first introduced this mechanism and weight and proposed the selection method of this mechanism [8]. Later, Boyle [9] developed a dynamic model of the flexible constant force compression mechanism. It is necessary to establish the nonlinear stiffness characteristics when the constant force of mechanism is designed. The research and application of the nonlinear stiffness characteristics of compliant mechanisms are also very extensive. Zheng constructed high-static and low-dynamic-stiffness (HSLD) pillars with negative stiffness magnetic spring (NSMS), established a Stewart isolation platform model with high strength steel braces, and studied the stiffness characteristics of the isolation platform [10]. Zongwei Yang improved the weight balance mechanism by synthesizing the required nonlinear torque curve with two linear springs (one tension spring and one compression spring) [11]. Andò presented a low-cost vibration energy acquisition method based on the nonlinear stiffness design of springs [12]. Lucas studied the effect of replacing the main spring with a nonlinear cubic spring. It is proved that if the stiffness is softened, the use of cubic stiffness can improve the frequency transfer rate around and above the resonance [13]. Through static analysis of the nonlinear stiffness system, Wu proved that the nonlinear stiffness system can improve the efficiency of wave energy collection and increase the average power by improving the inherent period and expanding resonance [14]. Ivana Koavcic studied a vibration isolator consisting of a vertical linear spring and two nonlinear prestressing oblique springs [15]. Based on a free vibration test, Bin Tang simply estimated the performance of the absorber by connecting the nonlinear absorber with the vibrating screen [16]. Pellegrini studied an alternative method of obtaining mechanical vibration by using two kinds of energy collectors with stable structures. According to the feasibility of miniaturization, different designs and classifications of existing bistable energy collectors were made [17]. Xiuting Sun studied an N-story shear structure (SLS) vibration isolation platform, focusing on the analysis and design of its nonlinear stiffness, friction, and damping characteristics, and obtained good vibration isolation performance [18]. The constant force grasping mechanism manipulator can achieve the function of grasping tyre well, and because the grasping force is constant, there will be no case of extrusion of the bead or tyre deformation.

## 2. Grasping Mechanism of Tyre Grabbing Manipulator

The grabbing mechanism of the triple-speed truss manipulator adopts crank-rocker mechanism (as shown in Figure 1). The lengths of the four connecting rods are  $AB = 100$  mm,  $BC = 110$  mm,  $CD = 130$  mm, and  $AD = 180$  mm. The angle between CD and DE is  $50^\circ$ . The whole manipulator is composed of three identical crank-rocker mechanisms (as shown in Figure 2). The power source is the motor. In practical use, the connecting rod AB of the three linkage mechanisms is simplified as a whole



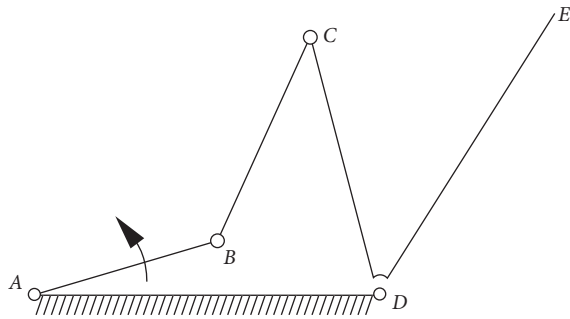


FIGURE 1: Motion sketch of the mechanism.

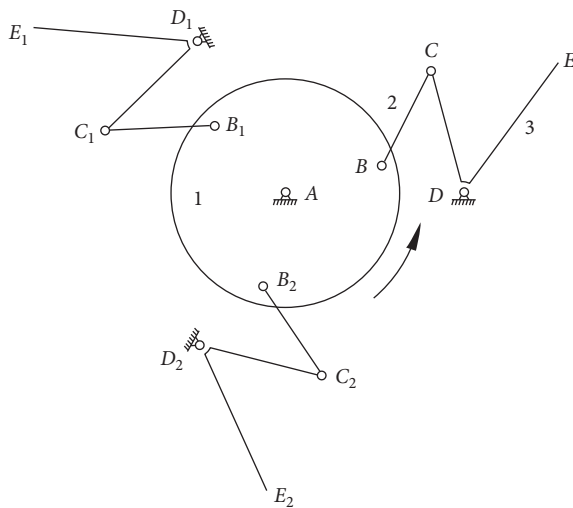


FIGURE 2: Motion and structure sketch of the manipulator.

into a disc. After the motor passes through the reducer, it is connected with the disc through the coupling and then drives the connecting rod 2 and 3 to rotate. By adjusting the rotation angle of the motor, the crank rotates at the corresponding angle and finally drives the rocker to rotate. The end of point E contacts the tyre, and the tyre is grasped by three-point positioning.

The three-dimensional structure of the manipulator is shown in Figure 3. Structures 1, 2, and 3 are exactly the same three crank-rocker mechanisms. After calculation, the maximum inner diameter of the tyre grasped by the manipulator is as follows:  $\varphi_d = 609.6 \text{ mm}$ . At this time, the maximum output torque of the motor after passing through the reducer is  $T_1 = 55.3779 \text{ N} \cdot \text{m}$ . The minimum inner diameter of the tyre grasped by the manipulator is  $\varphi_d = 406.4 \text{ mm}$ , and the maximum output torque of the motor after passing through the reducer is  $T_2 = 104.4972 \text{ N} \cdot \text{m}$ . Because the crank-rocker mechanism is a rigid-body mechanism, there are still large clearances and friction, which are prone to errors in the operation of the mechanism. When the equipment decelerates to the left or accelerates to the right, mechanism 3 will be impacted by inertia. When the equipment decelerates to the right or accelerates to the left, mechanism 1 and mechanism 2 will be impacted by inertia, which will also affect the accuracy of the equipment.

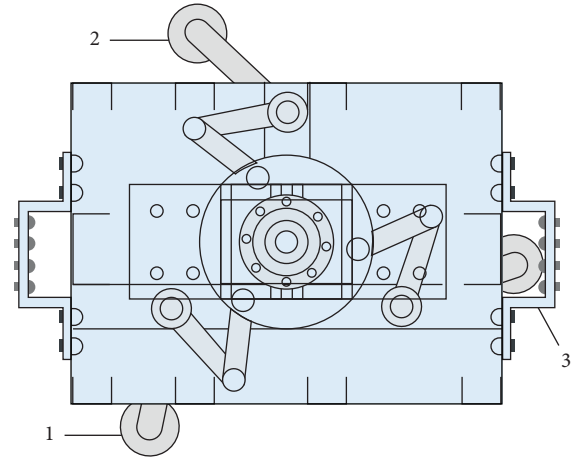


FIGURE 3: Three-dimensional structure of the manipulator.

### 3. Tyre Constant Force Grabbing Manipulator

To solve the problem of tyre deformation, the tyre grasping mechanism can be improved into a constant force mechanism. There are two ways to improve the mechanism into a constant force mechanism, namely, adding force sensors and controllers to the force control technology and transforming the mechanism into a constant force clamping mechanism. At present, many experts are also actively studying new controllers. Shubo Wang proposed an adaptive funnel control (FC) scheme for the unknown dead zone servo mechanism [19] and proposed an unknown input observer for the servo mechanism with unknown dynamics (such as nonlinear friction, parameter uncertainty, and external interference) [20] and designed a new adaptive controller to compensate nonlinear friction and bounded interference [21]. Although the force control technology of adding force sensors and controllers is stable and reliable, the algorithm design is complex and the cost is high. The mechanism improvement is used to transform the mechanism into a constant force mechanism with low cost and simpler improvement. Therefore, the tyre grasping mechanism is improved to a constant force mechanism with the improvement of the mechanical structure. Through consulting the data, it is found that, in the books of Alabuzhev et al. [22], the constant force mechanism (or quasizero stiffness mechanism) can be divided into four categories according to its stiffness characteristics. Through comparison, it is found that the curve beam constant force mechanism is the closest to the crank-rocker mechanism. The pseudo-rigid-body model method is adopted in the establishment of the kinematics model. The research method provides a way to design the constant force mechanism with crank-rocker mechanism as the model. The pseudo-rigid-body model method is to transform the constant force mechanism of curved beam into a pseudo-rigid-body mechanism for analysis, as shown in Figure 4. It can be seen from the figure that the transformed mechanism is a pseudo-rigid-body mechanism with spring installed at the node of the mechanism.

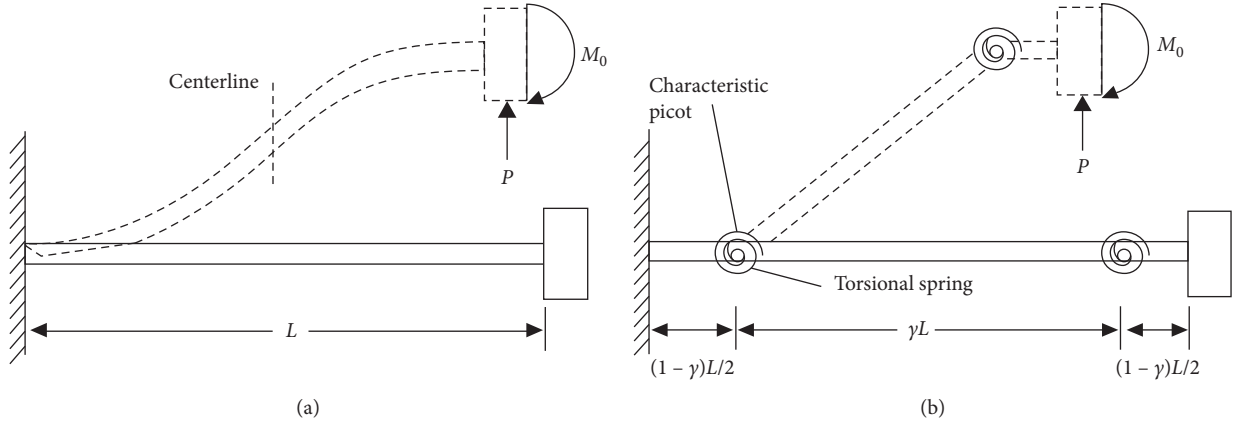


FIGURE 4: Schematic diagram of (a) fixed-guided beam and (b) the corresponding pseudo-rigid-body method [23].

Through the aforementioned ideas, the joints of crank-rocker mechanism can also be installed with springs. Through the stiffness design of the springs, a new constant force mechanism can be designed. A new type of double-slider mechanism proposed by Baokun Li [24] was very similar to the crank-rocker mechanism, but if the double-slider mechanism was applied to the improvement of the tyre grasping manipulator, it is necessary to change the length of the connecting rod and to increase the slider. Not only the calculation is difficult but also the improved structure is too large, and the three mechanical structures will interfere. Therefore, the torsion spring can be installed on the node of the crank-rocker mechanism to design the local constant force mechanism. The constant force mechanism designed by this method can not only keep constant grasping force to avoid tyre deformation but also can greatly reduce friction and clearance and extend the life of the machine as the grasping mechanism transforms from a rigid-body mechanism to a pseudo-rigid-body mechanism after the node is installed with spring.

#### 4. Dynamic and Static Models of Mechanisms

Figure 5 shows the mechanism motion sketch of the manipulator. The crank AB rotates counterclockwise around point A and drives the rocker CDE to rotate. Crank AB and rocker CDE are connected by coupler BC. The torsional stiffness of four joints are  $K_{RA}$ ,  $K_{RB}$ ,  $K_{RC}$ , and  $K_{RD}$ , respectively. The stiffness of E-point compression spring is set to  $K_{PE}$ .

The Cartesian coordinate system  $O$ -XYZ is fixed to point A. The origin  $O$  coincides with point A. The positive direction of the  $x$ -axis points to the right side of the horizontal plane. The positive direction of the  $y$ -axis is vertical. The  $z$ -axis is determined by the right manipulation.

Vectors AB, BC, CD, and DE are defined by  $r_1$ ,  $r_2$ ,  $r_3$ , and  $r_5$ , respectively. The position  $D$  on the  $x$ -axis is represented by  $r_4 \cdot r_1 = 100$  mm,  $r_2 = 110$  mm,  $r_3 = 130$  mm,

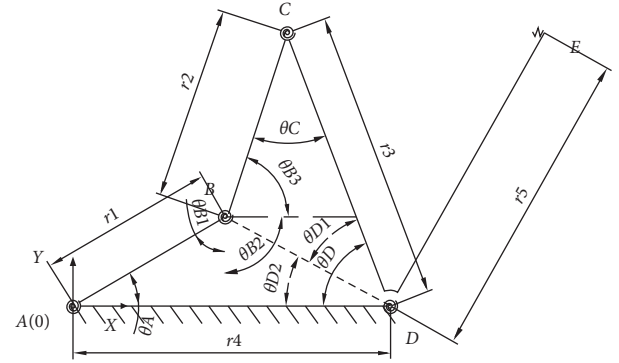


FIGURE 5: Motion sketch of the manipulator mechanism.

$r_5 = 165$  mm, and  $r_4 = 180$  mm. The angle between CD and DE is  $50^\circ$ .

In order to show the correct limit position of the mechanism, we assume that there is no friction and clearance between two connecting rods connected by the kinematic pair. In addition, we only discuss the static model of the mechanism in motion, without considering any inertial force (torque) and gravity.

In order to compute the static relationship among the components of the mechanism, it is necessary to first calculate the relationship among the angles. Figure 5 shows that

$$\theta_A + \theta_B + \theta_C + \theta_D = 2\pi, \quad (1)$$

$$\theta_D = \theta_{D1} + \theta_{D2}. \quad (2)$$

Connect BD and suppose the length is  $a$ . According to the cosine theorem,

$$\begin{aligned} a^2 &= r_1^2 + r_4^2 - 2r_1r_4 \cos \theta_A, \\ r_2^2 &= a^2 + r_3^2 - 2ar_3 \cos \theta_{D1}, \end{aligned} \quad (3)$$

$$r_1 \sin \theta_A = a \cdot \sin \theta_D.$$

Therefore, it can be obtained that

$$\theta_{D1} = \arccos \frac{a^2 + r_3^2 - r_2^2}{2ar_3} = \arccos \frac{r_1^2 + r_4^2 - 2r_1r_4 \cos \theta_A + r_3^2 - r_2^2}{2r_3 \sqrt{r_1^2 + r_4^2 - 2r_1r_4 \cos \theta_A}}, \quad (4)$$

$$\theta_{D2} = \arcsin \frac{r_1 \sin \theta_A}{\sqrt{r_1^2 + r_4^2 - 2r_1r_4 \cos \theta_A}}, \quad (5)$$

$$\theta_D = \theta_{D1} + \theta_{D2} = \arccos \frac{r_1^2 + r_4^2 - 2r_1r_4 \cos \theta_A + r_3^2 - r_2^2}{2r_3 \sqrt{r_1^2 + r_4^2 - 2r_1r_4 \cos \theta_A}} + \arcsin \frac{r_1 \sin \theta_A}{\sqrt{r_1^2 + r_4^2 - 2r_1r_4 \cos \theta_A}}, \quad (6)$$

$$\theta_B = \pi - \theta_A + \arcsin \frac{r_3 \sin \theta_D - r_1 \sin \theta_A}{r_2}, \quad (7)$$

$$\theta_C = \arccos \frac{r_1^2 + r_4^2 - r_2^2 - r_3^2 - 2r_1r_2 \cos \theta_A}{-2r_2r_3}.$$

## 5. Using the Principle of Virtual Work to Calculate the Output Force $F$

At present, there are two methods to establish the dynamic model of the linkage mechanism, that is, to establish the relationship between generalized force and generalized coordinates by the Lagrange equation and to establish the dynamic and static model of the linkage mechanism by virtual work principle. For the general four-bar mechanism, especially the constant-force compressor mechanism, the Lagrange equation method is generally adopted. But there are two problems for the four-bar mechanism: first, the establishment of the Lagrange equation needs to involve velocity calculation. There are kinematic singularities in the linkage mechanism. When the mechanism reaches the dead point or change point, so-called singular positions, the linear velocity equations of mechanism cannot be derived. The angular velocity of the follower bar other than the original bar can be obtained directly. At this time, the motion of the mechanism is usually considered to be uncertain. The motion analysis of the mechanism in singular position is also rare [25]. Second, in the process of establishing the Lagrange equation, it is necessary to define the mass of the link and other moving parts, while in the kinematic analysis of the linkage mechanism, the mass of the link should be determined. Most of the quality is neglected. Therefore, virtual work principle is used to build the dynamic model.

It can be seen from the four sections that the relationship between the angles of the four-bar mechanism is complex, so the calculation of the joint moment and virtual work of the four-bar mechanism by using the principle of virtual work is seldom used. Although the kinematic equation of the double-slider four-bar mechanism is analyzed by Li [26], because the angle analysis of the double-slider four-bar mechanism is different from that of the crank-rocker mechanism, the kinematic equation analysis

of the double-slider four-bar mechanism cannot be used. However, the method of nonlinear stiffness analysis can be used for reference, and the moment and virtual work of each joint of the four-bar mechanism can also be calculated.

*5.1. Utilizing the Principle of Virtual Work to Calculate the Torque and Virtual Work of Joints.* The formula of virtual work principle is

$$\delta W = \sum_i F_i \cdot \delta r_i + \sum_i C_i \cdot \delta r_i = 0, \quad (8)$$

where  $F_i$  is the external force and  $C_i$  is the binding force. In this model, the formula becomes

$$\delta W = \sum_i T_i \cdot \delta \theta_i + F \cdot \delta r = 0. \quad (9)$$

Among them,  $T_i$  is the driving torque applied to the bar  $AB$  after the motor is decelerated by the reducer and the torque caused by the springs at each node.  $F$  is the clamping force needed to clamp the tyre. The driving torque applied on the rod  $AB$  is set to

$$T_d = T_d K. \quad (10)$$

Among them, vector  $K$  is the unit vector of  $z$ -axis (vector  $i$  and  $j$  are the unit vectors of  $x$ -axis and  $y$ -axis, respectively). The orbital vector  $T_d$  is along the  $z$ -axis. Scalar  $\|T_d\|$  is the magnitude of the driving torque, where  $T_d > 0$  represents the positive direction of  $T_d$  along the  $z$ -axis and  $T_d < 0$  corresponds to the negative direction of  $T_d$  to  $z$ -axis.

Torque caused by springs on each node can be expressed as

$$T_i = K_{Ri} \cdot \psi_i, \quad (11)$$

where  $K_{Ri}$  is the stiffness of the spring added to each node and  $\varphi_i$  is the angular displacement produced by each node. Since the mechanism has four nodes, formula (17) can be expressed as a fourth-order system:

$$\begin{bmatrix} K_{RA} & 0 & 0 & 0 \\ 0 & K_{RB} & 0 & 0 \\ 0 & 0 & K_{RC} & 0 \\ 0 & 0 & 0 & K_{RD} \end{bmatrix} \begin{bmatrix} \psi_A \\ \psi_B \\ \psi_C \\ \psi_D \end{bmatrix} = \begin{bmatrix} T_A \\ T_B \\ T_C \\ T_D \end{bmatrix}. \quad (12)$$

Angular displacement at joint  $A$

$$\psi_A = (\theta_A - \theta_{A0})K. \quad (13)$$

Among them,  $\theta_{A0}$  is the rotation angle from  $x$ -axis to connecting rod  $AB$ , indicating the input position angle of connecting rod  $AB$ , and  $\theta_A$  corresponds to the initial angle. Here, we consider  $\theta_A$  as a general coordinate mechanism. Similarly, the virtual angular displacements relative to joint  $B$ ,  $C$ , and  $D$  are  $\psi_B = (\theta_B - \theta_{B0})K$ ,  $\psi_C = (\theta_C - \theta_{C0})K$ , and  $\psi_D = (\theta_D - \theta_{D0})K$ .

Therefore, it can be expressed as

$$\begin{bmatrix} K_{RA} & 0 & 0 & 0 \\ 0 & K_{RB} & 0 & 0 \\ 0 & 0 & K_{RC} & 0 \\ 0 & 0 & 0 & K_{RD} \end{bmatrix} \begin{bmatrix} \theta_A - \theta_{A0} \\ \theta_B - \theta_{B0} \\ \theta_C - \theta_{C0} \\ \theta_D - \theta_{D0} \end{bmatrix} K = \begin{bmatrix} T_A \\ T_B \\ T_C \\ T_D \end{bmatrix}. \quad (14)$$

The virtual angular displacement relative to joint A is

$$\delta\psi_A = \frac{d\psi_A}{d\theta_A} \delta\theta_A. \quad (15)$$

The virtual angular displacement relative to joint B is

$$\begin{aligned} \delta\psi_B &= \frac{d\psi_B}{d\theta_A} \delta\theta_A = \frac{d(\theta_B - \theta_{B0})}{d\theta_A} \delta\theta_A K = \frac{d\theta_B}{d\theta_A} \delta\theta_A K \\ &= \frac{d(\pi - \theta_A + \arcsin(r_3 \sin \theta_D - r_1 \sin \theta_A / r_2))}{d\theta_A} \delta\theta_A K. \end{aligned} \quad (16)$$

The virtual angular displacement relative to joint C is

$$\begin{aligned} \delta\psi_B &= \frac{d\psi_B}{d\theta_A} \delta\theta_A = \frac{d(\theta_B - \theta_{B0})}{d\theta_A} \delta\theta_A K = \frac{d\theta_B}{d\theta_A} \delta\theta_A K \\ &= \frac{d(\pi - \theta_A + \arcsin(r_3 \sin \theta_D - r_1 \sin \theta_A / r_2))}{d\theta_A} \delta\theta_A K. \end{aligned} \quad (17)$$

The virtual angular displacement relative to joint D is

$$\delta\psi_D = \frac{d\psi_D}{d\theta_A} = \frac{d(\theta_D - \theta_{D0})}{d\theta_A} \delta\theta_A = \frac{d\theta_D}{d\theta_A} \delta\theta_A K. \quad (18)$$

The virtual displacement at E is

$$\delta\psi_E = r_5 \sin(100^\circ - \theta_D) \frac{d\theta_D}{d\theta_A} \delta\theta_A K. \quad (19)$$

By combining formulas (11)–(19) and substituting formula (9), we can get

$$\delta W = [\delta\psi_A \quad \delta\psi_A \quad \delta\psi_B \quad \delta\psi_C \quad \delta\psi_D] \begin{bmatrix} T_d \\ -T_A \\ -T_B \\ -T_C \\ -T_D \end{bmatrix} + F \cdot \delta\psi_E = 0. \quad (20)$$

After sorting out, we can get

$$F = [\delta\psi_A \quad \delta\psi_A \quad \delta\psi_B \quad \delta\psi_C \quad \delta\psi_D] \begin{bmatrix} -T_d \\ T_A \\ T_B \\ T_C \\ T_D \end{bmatrix} \frac{1}{\delta\psi_E} \quad (21)$$

$$= \frac{T_d - K_{RA}(\theta_A - \theta_{A0}) - K_{RB}(\theta_B - \theta_{B0})(d\theta_B/d\theta_A) - K_{RC}(\theta_C - \theta_{C0})(d\theta_C/d\theta_A) - K_{RD}(\theta_D - \theta_{D0})(d\theta_D/d\theta_A)}{r_5 \sin(100^\circ - \theta_D)(d\theta_D/d\theta_A)}$$

It can be seen from formula (21) that the change trend of grasping force  $F$  curve with  $\theta_A$  is related to the driving moment  $T_d$  and the torsional stiffness of each torsion spring. In order to set appropriate parameters to obtain constant grasping force, it is necessary to analyze

the influence of each parameter on  $F$ . To analyze the influence of each parameter, one of the torques can be set to nonzero and the other to zero and the grasping force can be used as the output to obtain a fifth-order system:

$$F = \begin{bmatrix} F_d \\ F_A \\ F_B \\ F_C \\ F_D \end{bmatrix} = \begin{bmatrix} \frac{d\psi_A}{d\theta_A} \\ \frac{d\psi_A}{d\theta_A} \\ \frac{d\theta_B}{d\theta_A} \\ \frac{d\theta_C}{d\theta_A} \\ \frac{d\theta_D}{d\theta_A} \end{bmatrix} [T_d \ T_A \ T_B \ T_C \ T_D] \quad (22)$$

$$\cdot \frac{1}{r_5 \sin(100^\circ - \theta_D) (d\theta_D/d\theta_A)},$$

where  $F_d$  is the grasping force  $F$  when the driving moment  $T_d \neq 0$  and the stiffness of other joint torsion springs is set to  $K_{RA} = K_{RB} = K_{RC} = K_{RD} = 0$ . At this time, the grasping force is

$$F = F_d = \frac{T_d}{r_5 \sin(100^\circ - \theta_D) (d\theta_D/d\theta_A)}. \quad (23)$$

Through calculation, it can be concluded that when  $\theta_A = 42.1^\circ$ , the grasping force  $F$  tends to infinity, which is located in the singular position of the linkage. Because it is difficult to analyze the singular position of motion, the position is abandoned. By analyzing other position curves, there is a bistable curve between  $-100^\circ$  and  $-10^\circ$ , as shown in Figure 6. The analysis shows that the bistable curve is easy to fit other curves. Therefore, we chose this curve to fit.

When the driving torque is  $T_d = 0$ , the stiffness of one torsion spring is set as nonzero and that of other joints is set as zero, and

$$F = F_i = \frac{K_{Ri}(\theta_i - \theta_{i0})}{r_5 \sin(100^\circ - \theta_D) (d\theta_D/d\theta_A)}. \quad (24)$$

In the aforementioned formula,  $i = A, B, C, D$ .

Set  $K_{RA} = 1 \text{ N} \cdot \text{m}^\circ$ ,  $K_{RA} = 3 \text{ N} \cdot \text{m}^\circ$ ,  $K_{RA} = 5 \text{ N} \cdot \text{m}^\circ$ , and  $\theta_{A0} = 30^\circ$ , and the stiffness of torsion spring of other joints is set to zero. With MATLAB, the image of grasping force  $F_A$  changing with input position angle  $\theta_A$  can be obtained. Similarly, we can get the image of force  $F_B$ ,  $F_C$ , and  $F_D$ , changing with input position angle  $\theta_A$  (as shown in Figure 7). Because the fitting range is selected above,  $-100^\circ$  to  $10^\circ$ , the curve of  $-100^\circ$  to  $10^\circ$  is also selected for fitting. Note that when  $\theta_A \leq 0$ , then  $\theta_B = 2\pi + \theta_A - \theta_C - \theta_D$ , which is different from equation (7).

As can be seen from Figure 7(a), in the region of  $-100^\circ$  to  $10^\circ$ , the grabbing force  $F$  shows a monotonous decreasing characteristic when only  $K_{RA} \neq 0$ . As can be seen from Figure 7(b), the grabbing force  $F$  is only monotonically decreasing in the  $-100^\circ$  to  $10^\circ$  region, but the calculation method of  $\theta_B$  is different when  $\theta_A \leq 0$  and  $\theta_A \geq 0$ .

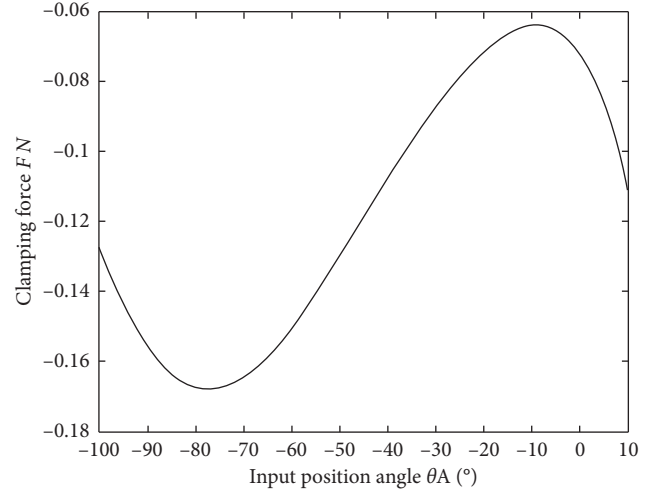


FIGURE 6: Grasping force  $F$  changes with position angle  $\theta_A$ .

Therefore, the torsion spring at joint  $B$  is discarded. From Figure 7(c), it can be seen that, in this region, the grasping force  $F$  shows a monotonic decreasing characteristic when only  $-100^\circ - 10^\circ$ . From Figure 7(d), it can be seen that the grabbing force  $F$  increases monotonously when the grabbing force is only  $-100^\circ$  to  $10^\circ$  in this region, and it can be found that with the increase of the stiffness of each spring, the image features will be more obvious. Therefore, the desired image features can be obtained by adjusting the spring stiffness properly.

**5.2. Determining the Parameters of Each Part and Establishing the Constant Force Interval.** According to the curve trend in the previous section, the expected constant force range can be established by designing appropriate spring stiffness. The process of designing the constant force interval is as follows:

- (1) Establishing the relationship between spring stiffness: substituting  $\theta_A = -100^\circ$  and other given parameters to solve the differential of equation (22) with respect to  $\theta_A$  and then obtaining the following expression:

$$\left. \frac{dF}{d\theta_A} \right|_{\theta_A = -100^\circ} = f(T_d, K_{RA}, K_{RB}, K_{RC}, K_{RD}) = 0. \quad (25)$$

- (2) Searching constant force interval: when the grasping force satisfies  $|F - F|_{\theta_A = -100^\circ} / F|_{\theta_A = -100^\circ}| \leq 2\%$ , it is considered to be a constant force interval. When the geometric parameters are given as  $r_1 = 100 \text{ mm}$ ,  $r_2 = 110 \text{ mm}$ ,  $r_3 = 130 \text{ mm}$ ,  $r_4 = 180 \text{ mm}$ , and  $r_5 = 165 \text{ mm}$  and the initial input position angle is assembled as  $\theta_{A0} = 30^\circ$ , equation (25) is obtained:

$$0.2347T_d + 0.4066K_{RA} + 0.0204K_{RC} + 0.0445K_{RD} = 0. \quad (26)$$

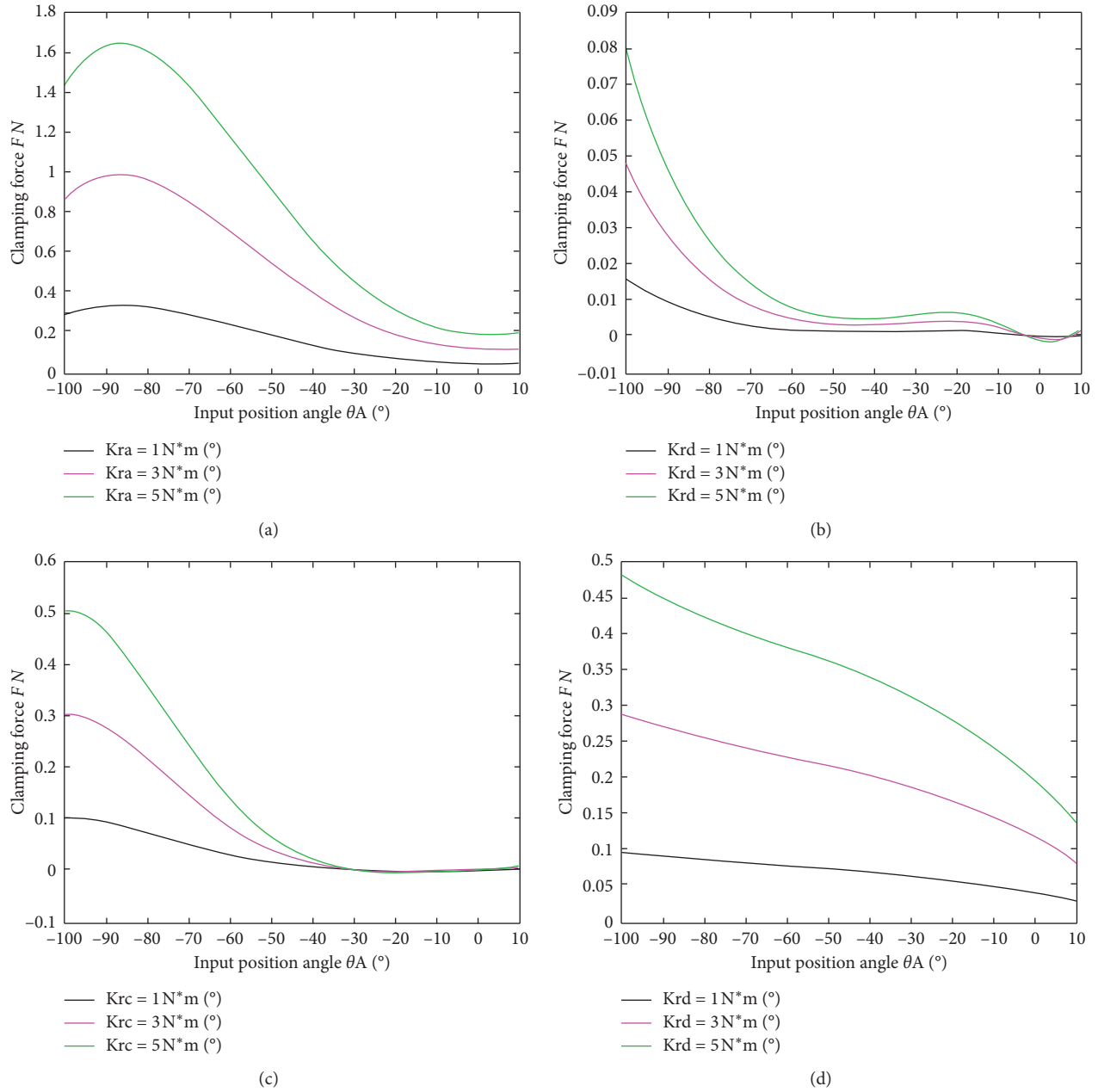


FIGURE 7: Grasping force  $F$  changes with position angle  $\theta_A$ .

Using this optimization method, the appropriate spring stiffness can be found.

It can be seen from the previous section that,  $K_{RA}$ ,  $K_{RC}$ , and  $K_{RD}$  all produce monotonic increasing curve, and  $T_d$  generates bistable curve. Based on image analysis, if a constant force is required, it can be assumed that  $K_{RA} = K_{RC} = 0$  and  $T_d = 1 \text{ N}\cdot\text{m}$ , then  $K_{RD} = 5.2741 \text{ N}\cdot\text{cm}/^\circ$ . At this time, the grasping force is

$$F = \frac{1 - 5.2741(\theta_D - \theta_{D0})(d\theta_D/d\theta_A)}{r_5 \sin(100^\circ - \theta_D)(d\theta_D/d\theta_A)}. \quad (27)$$

This is shown in Figure 8.

It can be seen from the image that  $\theta_A = -50^\circ$  is in the constant force range. Because the actual gripping force is  $167 \text{ N}$ , the gripping force is set to  $180 \text{ N}$  for safety reasons. According to formula (27), the required torque  $T_d$  can be obtained as follows:

$$T_d = \frac{180 \cdot r_5 \sin(100^\circ - \theta_D)(d\theta_D/d\theta_A)}{1 + 5.2741(\theta_D - 1.4415)(d\theta_D/d\theta_A)} \quad (28)$$

$$= 720.5607 \text{ N}\cdot\text{m} \approx 720 \text{ N}\cdot\text{m}.$$

At this time, we can get  $K_{RD} = 37.97352 \text{ N}\cdot\text{m}/^\circ$ . At this time, the grasping force is



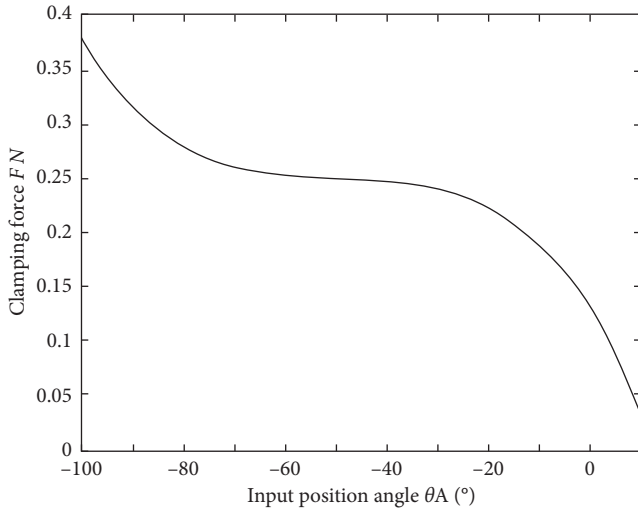


FIGURE 8: Grasping force  $F$  changes with position angle  $\theta_A$ .

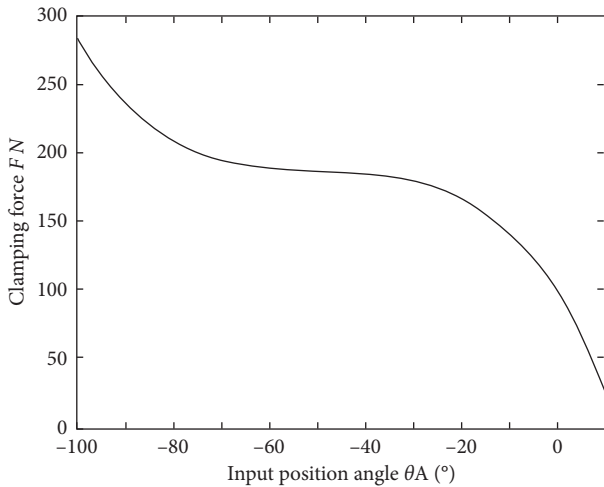


FIGURE 9: Grasping force  $F$  changes with position angle  $\theta_A$ .

$$F = \frac{T_d - K_{RD}(\theta_D - \theta_{D0})(d\theta_D/d\theta_A)}{r_5 \sin(100^\circ - \theta_D)(d\theta_D/d\theta_A)}. \quad (29)$$

This is shown in Figure 9.

According to the equation, the search constant force interval is  $[-64.2317, -34.99948]$ . In this interval, grasping force  $F$  can be regarded as constant force. Through the calculation and analysis of the mechanism, the range of constant force interval can fully meet the requirement of grasping tyres with inner diameter ranging from 404.9 mm to 606.4 mm. As long as the position of the mechanism is properly adjusted, the tyres with different inner diameters can be grasped with constant force.

The grabbing force of the improved mechanism changes with the angle is as shown in Figure 10.

As can be seen from Figure 10, the grip force of the improved mechanism is very unstable. With the change of the inner diameter of the tyre, it is easy to appear that the grip force is too strong to cause the deformation of the tyre. As can be seen from the previous section, the improved grip

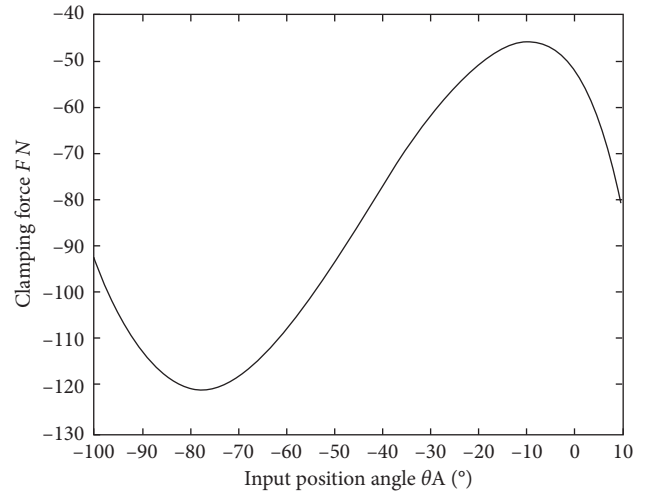


FIGURE 10: Grasping force  $F$  changes with position angle  $\theta_A$ .

force has little change and can be regarded as constant grip force.

## 6. Conclusion

In this paper, a manipulator of tyre constant force grasping mechanism is designed by using a spring stiffness design, and the nonlinear stiffness characteristics of crank-rocker mechanism are modeled and analyzed. The following conclusions can be drawn: (1) By designing the spring stiffness of the connecting rod mechanism nodes, the connecting rod mechanism can be transformed from a rigid-body mechanism to a pseudorigid-body mechanism, which greatly reduces the clearance and friction of the mechanism and increases the accuracy and stability of the mechanism. (2) By modeling and analyzing the nonlinear stiffness characteristics of the mechanism, the expected nonlinear stiffness can be obtained, and the clamping mechanism of the manipulator can be improved into a constant force clamping mechanism. (3) Compared with the general constant force mechanism, the design and calculation of the four-bar constant force mechanism are more complicated. Because of the problems of multiple dead points, the virtual work principle should be used to analyze the mechanism rather than the Lagrange equation. (4) Because of the more complex structure of the four-bar mechanism, it is difficult to achieve constant force in the process of motion. It can only design a constant force interval of one or several segments, and the range of the constant force interval is also affected by the length of each link. Therefore, the scope of adaptation will be affected.

## Data Availability

The data used to support the findings of this study are available from the corresponding author upon request.

## Conflicts of Interest

The authors declare that they have no conflicts of interest.

## Acknowledgments

This work was supported by the Natural Science Foundation of China (Grant no. 51705268).

## References

- [1] P. Wang and Q. Xu, "Design and modeling of constant-force mechanisms: a survey," *Mechanism and Machine Theory*, vol. 119, pp. 1–21, 2018.
- [2] G. Chen, H. Chang, and L. Geng, "Design of constant-force compliant Sarrus mechanism considering stiffness nonlinearity of compliant joints," in *Advances in Reconfigurable Mechanisms and Robots II*, vol. 36, pp. 107–116, Springer, Cham, Switzerland, 2016.
- [3] C.-W. Hou and C.-C. Lan, "Functional joint mechanisms with constant-torque outputs," *Mechanism and Machine Theory*, vol. 62, pp. 166–181, 2013.
- [4] L. Patrice and J. L. Herder, "An adjustable constant force mechanism using pin joints and springs," *New Trends in Mechanism and Machine Science*, vol. 43, pp. 453–461, Springer, Cham, Switzerland, 2017.
- [5] P. Wang and Q. Xu, "Design of a compact compliant constant-force XY precision positioning stage," in *Proceedings of the 2016 12th IEEE/ASME International Conference on Mechatronic and Embedded Systems and Applications (MESA)*, Auckland, New Zealand, 2016.
- [6] K. A. Tolman, E. G. Merriam, and L. L. Howell, "Compliant constant-force linear-motion mechanism," *Mechanism and Machine Theory*, vol. 106, pp. 68–79, 2016.
- [7] Y. Liu, Y. Zhang, and Q. Xu, "Design and control of a novel compliant constant-force gripper based on buckled fixed-guided beams," *IEEE/ASME Transactions on Mechatronics*, vol. 22, no. 1, pp. 476–486, 2016.
- [8] A. Midha, L. L. Howell, and T. W. Norton, "Limit positions of compliant mechanisms using the pseudo-rigid-body model concept," *Mechanism and Machine Theory*, vol. 35, no. 1, pp. 99–115, 2000.
- [9] C. Boyle, L. L. Howell, S. P. Magleby, and M. S. Evans, "Dynamic modeling of compliant constant-force compression mechanisms," *Mechanism and Machine Theory*, vol. 38, no. 12, pp. 1469–1487, 2003.
- [10] Y. Zheng, Q. Li, B. Yan, Y. Luo, and X. Zhang, "A Stewart isolator with high-static-low-dynamic stiffness struts based on negative stiffness magnetic springs," *Journal of Sound and Vibration*, vol. 422, pp. 390–408, 2018.
- [11] Z.-W. Yang and C.-C. Lan, "An adjustable gravity-balancing mechanism using planar extension and compression springs," *Mechanism and Machine Theory*, vol. 92, pp. 314–329, 2015.
- [12] B. Andò, S. Baglio, A. R. Bulsara, and V. Marletta, "A bistable buckled beam based approach for vibrational energy harvesting," *Sensors and Actuators A: Physical*, vol. 211, pp. 153–161, 2014.
- [13] L. de Haro Silva, P. J. Paupitz Gonçalves, D. Wagg, and W. David, "On the dynamic behavior of the Zener model with nonlinear stiffness for harmonic vibration isolation," *Mechanical Systems and Signal Processing*, vol. 112, pp. 343–358, 2018.
- [14] Z. Wu, C. Levi, and S. F. Estefen, "Wave energy harvesting using nonlinear stiffness system," *Applied Ocean Research*, vol. 74, pp. 102–116, 2018.
- [15] I. Kovacic, M. J. Brennan, and T. P. Waters, "A study of a nonlinear vibration isolator with a quasi-zero stiffness characteristic," *Journal of Sound and Vibration*, vol. 315, no. 3, pp. 700–711, 2008.
- [16] B. Tang, M. J. Brennan, G. Gatti, and N. S. Ferguson, "Experimental characterization of a nonlinear vibration absorber using free vibration," *Journal of Sound and Vibration*, vol. 367, pp. 159–169, 2016.
- [17] S. P. Pellegrini, N. Sergio, M. Schenk, and J. L. Herder, "Bistable vibration energy harvesters: a review," *Journal of Intelligent Material Systems and Structures*, vol. 24, no. 11, pp. 1303–1312, 2013.
- [18] X. Tolou and X. Jing, "Analysis and design of a nonlinear stiffness and damping system with a scissor-like structure," *Mechanical Systems and Signal Processing*, vol. 66–67, pp. 723–742, 2016.
- [19] S. Wang et al., "Neural-network-based adaptive funnel control for servo mechanisms with unknown dead-zone," *IEEE transactions on cybernetics*, vol. 50, no. 4, pp. 1383–1394, 2018.
- [20] S. Wang, J. Na, X. Ren, H. Yu, and J. Yu, "Unknown input observer-based robust adaptive funnel motion control for nonlinear servomechanisms," *International Journal of Robust and Nonlinear Control*, vol. 28, no. 18, pp. 6163–6179, 2018.
- [21] S. Wang, H. Yu, and J. Yu, "Robust adaptive tracking control for servo mechanisms with continuous friction compensation," *Control Engineering Practice*, vol. 87, pp. 76–82, 2019.
- [22] P. Alabuzhev, A. Gritchin, and L. Kim, *Vibration Protecting and Measuring Systems with Quasi-Zero Stiffness*, Hemisphere Publishing Corp, New York, NY, USA, 1989.
- [23] W. B. Lewis, "Development and Design of Constant-Force Mechanisms," *Doctoral Dissertation*, Brigham Young University, Provo, UT, USA, 2002.
- [24] B. Li and G. Hao, "Nonlinear behaviour design using the kinematic singularity of a general type of double-slider four-bar linkage," *Mechanism and Machine Theory*, vol. 129, pp. 106–130, 2018.
- [25] X.-B. Chen, N. Iwatsuki, and I. Hayashi, "Kinematic analysis at singular points of linkages based on L'hospital's theorem," *Journal of Tongji University*, vol. 30, no. 8, pp. 973–978, 2002.
- [26] B. Li and G. Hao, "On generating expected kinetostatic nonlinear stiffness characteristics by the kinematic limb-singularity of a crank-slider linkage with springs," *Chinese Journal of Mechanical Engineering*, vol. 32, no. 1, pp. 32–54, 2019.

## Research Article

# A Stochastic Differential Equation Driven by Poisson Random Measure and Its Application in a Duopoly Market

Tong Wang  and Hao Liang

*The School of Economic Mathematics, Southwestern University of Finance and Economics, Wenjiang, Chengdu 611130, China*

Correspondence should be addressed to Tong Wang; wangt@smail.swufe.edu.cn

Received 23 November 2019; Accepted 26 February 2020; Published 20 April 2020

Academic Editor: Magdi S. Mahmoud

Copyright © 2020 Tong Wang and Hao Liang. This is an open access article distributed under the Creative Commons Attribution License, which permits unrestricted use, distribution, and reproduction in any medium, provided the original work is properly cited.

We investigate a stochastic differential equation driven by Poisson random measure and its application in a duopoly market for a finite number of consumers with two unknown preferences. The scopes of pricing for two monopolistic vendors are illustrated when the prices of items are determined by the number of buyers in the market. The quantity of buyers is proved to obey a stochastic differential equation (SDE) driven by Poisson random measure which exists a unique solution. We derive the Hamilton-Jacobi-Bellman (HJB) about vendors' profits and provide a verification theorem about the problem. When all consumers believe a vendor's guidance about their preferences, the conditions that the other vendor's profit is zero are obtained. We give an example of this problem and acquire approximate solutions about the profits of the two vendors.

## 1. Introduction

Consider two vendors that provide different goods for different types of consumers in a duopoly market. For instance, in the pharmaceutical market, two vendors provide different drugs for different patients with different diseases. As the commodity price is proportional to the number of consumers, pricing strategies are especially important for vendors. We study this problem in a nondurable goods duopoly market.

Consumers' preferences or types take key roles in the market and affect the pricing strategies determined by vendors. Eeckhout and Weng [1] assume that there are  $N \geq 2$  consumers who have the same type either  $H$  or  $L$ . Two vendors provide two different kinds of goods for the two types, respectively. In this article, we assume that consumers' types are diverse. This assumption is different from the assumption that all consumers' types are identical in [1]. In general, there exist different types of consumers who need to buy the same kind of goods in the market, just like people with high and low fever who need antipyretics simultaneously. Thus, it is reasonable to assume that all consumers' preferences are different in the market. In this situation, some consumers choose one vendor and others choose the

other vendor, i.e., all consumers do not choose the same vendor at the first time.

Furthermore, we assume that the price of goods is a function of the number of consumers instead of the consumers' posterior beliefs in [1] as the price of goods is affected by the quantity of supply and demand. Since technological content of nondurable goods is lower than that of other goods in general, prices of nondurable goods fluctuate more obviously with the number of consumers. Therefore, the assumption that price of goods depends on the number of consumers is logical.

Vendors need to know how many consumers choose their own goods at each time  $t \in [0, +\infty)$  in order to implement pricing strategies. Whether a consumer changes his decision is related to the judgment of his type and the prices of two goods. We find ranges of commodity prices and prove that the quantity of buyers who purchase one of the vendor's goods obeys a SDE and verifies existence and uniqueness of its solutions, which is a main contribution in this article.

Generally speaking, consumers do not know their own types whereas the vendors recognize. Under the setting of asymmetric information, consumers who are informed of their own types tend to buy commodity, which brings benefits for vendors. Consumers need to make choices of the

types based on the guidance given by the two vendors. In certain cases, consumers are willing to follow the authoritative vendor's guidance. We call this vendor as the type-leader vendor and the other as the following vendor, which is a new setting evolved from the Stackelberg leadership model [2]. The type-leader model contains only one type-leader vendor. In the type-leader model, the vendor directly leads to consumers' preferences rather than the prices of goods. In some markets, such as the pharmaceutical market, consumers are more concerned about the efficacy of goods than its price. This makes it important for vendors to guide consumers' types. Thus, the type-leader model is more reasonable than the Stackelberg leadership model. Pricing rules for goods are obtained in the type-leader model. Moreover, we derive the conditions to ensure that the following vendor's profit is zero.

The main contributions of this paper are mentioned as follows. Compared with the assumption in [1] where there exists only one type of consumers, the situation that there exist two different types of consumers in the market is explored. Considering the impact of commodity prices, we assume that the price of goods is decided by the number of consumers. As a comparison, Eeckhout and Weng [1] define that the price is a function of consumers' posterior beliefs. Observing that the effectiveness of goods is more important than its price in our model, we use the type-leader model instead of the Stackelberg leadership model to study vendors' optimal strategies. An example of this problem is given and approximate solutions about the profit of the two vendors are acquired.

Several literatures investigate multiarmed bandit problems. Robbins [3] describes the problem as a decision-maker facing  $M$  slot machines (called arms), and the participator has to choose one of the arms at each instantaneous time. The value of pulling an arm in discrete time is calculated by Gittins and Jones [4] and Michael et al. [5]. Comparing the value to the Gittins index of all other arms, Michael et al. [5] present that the value pulling each arm itself does not depend on the cutoff. This problem is transformed into a standard optimal stopping problem in [6, 7]. Bolton and Harris [8] and Bergemann and Valimaki [9] show that choosing the products from the same vendor is the optimal strategy of consumers when there are  $K \geq 2$  vendors who offer different products and  $M$  consumers whose preferences are the same (but unknown) in the market. The necessary and sufficient conditions for the existence of only two vendors in the market are obtained by Gao et al. [10]. Two-armed bandit problems in the continuous time with the property of Lévy processes are studied by Cohen and Solan [11] (Lévy process is described in [12, 13]). Cohen and Solan [11] conclude that the optimal strategy is a cutoff strategy when the arms have two types. The problem that multiple arms can be chosen by the decision-maker is studied by Kuksov et al. [14] and Doval [15]. It is discovered that the decision-maker is indifferent to search an alternative arm which does not have the highest reservation price. When a Bayesian decision-maker makes a selection from multiple arms with uncertain payoffs and an outside arm with known payoff, maximizing his expected profit is studied in Ke et al.

[16]. For other optimal strategies and control approaches, the reader is referred to [17, 18] and the references therein.

The remainder of the paper is organized as follows. In Section 2, we introduce a two-period example and show the scopes of prices. In Section 3, the definition of the Poisson integral is used to prove that the quantity of buyers obeys an SDE and verifies the existence and uniqueness of the solutions for the SDE in global space. In Section 4, based on the dynamic programming principle, we derive HJB equations for the vendors' utility functions and give the verification theorem for the type-leader model. Using solutions of HJB equations, we obtain the optimal strategy for the type-leader vendor. In Section 5, we give an example of this problem and acquire approximate solutions about the profit of the two vendors.

## 2. A Two Period Example

There are two vendors who offer different nondurable goods, indexed by  $j = 1, 2$ , and  $M$  consumers whose preferences are high or low in the market, where  $M$  is positive integer. However, consumers do not know their preferences. If the type is high, a consumer gets expected value  $\zeta_{1H}$  from buying goods 1 and  $\zeta_{2H}$  from buying goods 2. Otherwise, a consumer gets expected value  $\zeta_{1L}$  from buying goods 1 and  $\zeta_{2L}$  from buying goods 2. We assume that  $\zeta_{1H} > \zeta_{2H}$  and  $\zeta_{1L} < \zeta_{2L}$ , where  $\zeta_{jH}$  and  $\zeta_{jL}$  belong to  $(0, +\infty)$ .

At any time, all market participants observe all previous outcomes. Because of the influence caused by uncertain external factors, the flow utility  $u_{ji}(t)$  ( $i \in \{H, L\}$ ) has a noisy signal of the true value (for detailed discussion, refer to [1]).

$$du_{ji}(t) = \zeta_{ji}dt + \sigma_j d\bar{B}_j(t), \quad (1)$$

where  $\bar{B}_1(t)$  and  $\bar{B}_2(t)$  are independent Brownian motions. In the market, besides the types of consumers, there are many uncertain factors affecting the effectiveness of products to consumers. For example, there exist some subtle and unavoidable differences in the quality of the goods and these differences affect consumers' utilities. The noisy signal of the true value is used to characterize the effects of these factors on consumers' utilities.

Assume that  $x_t \in [0, 1]$  is the belief that the type is high if consumers choose the first vendor and  $y_t \in [0, 1]$  is the belief that the type is high if consumers choose the other vendor; that is to say,  $x_t := \Pr(i = H | u_{1i}^t)$  and  $y_t := \Pr(i = H | u_{2i}^t)$ , where  $u_{ji}^t := \{u_{ji}(\tau)\}_{\tau=0}^t$  is a realized path. From [19], we have

$$\begin{aligned} dx_t &= x_t(1-x_t)s_1 \frac{du_{1i}(t) - \zeta_{1H}dt - \zeta_{1L}dt}{\sigma_1} \\ &:= x_t(1-x_t)s_1 dB_1(t), \\ dy_t &= y_t(1-y_t)s_2 \frac{du_{2i}(t) - \zeta_{2H}dt - \zeta_{2L}dt}{\sigma_2} \\ &:= y_t(1-y_t)s_2 dB_2(t), \end{aligned} \quad (2)$$

where  $s_j = (\zeta_{jH} - \zeta_{jL})/\sigma_j$ ,  $j = 1, 2$ ,  $B_1(t)$  and  $B_2(t)$  are independent Brownian motions.



If a consumer chooses the first vendor, his expected utility is  $f_1(x_t) := x_t\zeta_{1H} + (1 - x_t)\zeta_{1L}$ . Letting  $a_1 := \zeta_{1H} - \zeta_{1L}$  and  $b_1 := \zeta_{1L}$ , the utility is represented by

$$f_1(x) = a_1x_t + b_1. \quad (3)$$

Similarly, if a consumer chooses the second vendor, his expected utility is represented by

$$f_2(x) = a_2y_t + b_2, \quad (4)$$

where  $a_2 := \zeta_{2H} - \zeta_{2L}$  and  $b_2 := \zeta_{2L}$ . The definitions of  $a_j$  and  $b_j$  imply  $a_1 + b_1 > a_2 + b_2$ ,  $b_1 < b_2$  and  $a_1 > a_2$ .

Let  $n_t$  be the number of consumers who choose the first vendor and  $M - n_t$  be the number of consumers who choose the second vendor,  $n_t \in \{0, 1, \dots, M\}$ .  $P_1(n_t)$  is the price of goods from the first vendor and  $P_2(n_t)$  is the price of goods from the second one. Formally, the price of goods is a measurable function  $P_j: \{0, 1, \dots, M\} \rightarrow \mathbb{R}^+ \cup \{0\}$ . We assume that the change of price has hysteresis (the product price of the second vendor is a function with respect to  $n_t$  when  $M$  fixed).

As consumers' beliefs change, the lower the beliefs they have, the lower the profits they earn if they choose the first vendor. For a consumer who chooses the first vendor, if his belief is low enough at certain time, he gives up the vendor to choose the second one. Denote  $\alpha_t \in [0, 1]$  as the belief, i.e., if  $x_t < \alpha_t$ , a consumer transforms his choice from the first to the second vendor. Similarly, the consumer gives up buying goods from the second vendor and chooses to buy goods from the first vendor if  $y_t > \beta_t \in [0, 1]$ .

For nondurable goods, if a consumer chooses the first vendor at first time, the common belief for high type is  $x_t$  at time  $t$ . The utility of the consumer is  $x_t\zeta_{1H} + (1 - x_t)\zeta_{1L} - P_1(n_t)$ . If the consumer gives up the first vendor to choose second one, the prices for the vendors do not change due to the hysteresis of the change of price. The utility of the consumer is  $x_t\zeta_{2H} + (1 - x_t)\zeta_{2L} - P_2(n_t)$ . If the consumer voluntarily gives up the first vendor to choose the second vendor, it has

$$x_t\zeta_{1H} + (1 - x_t)\zeta_{1L} - P_1(n_t) < x_t\zeta_{2H} + (1 - x_t)\zeta_{2L} - P_2(n_t). \quad (5)$$

Inequality (5) is rewritten as

$$x_t < \frac{b_2 - b_1 + P_1(n_t) - P_2(n_t)}{a_1 - a_2}. \quad (6)$$

From the definition of  $\alpha_t$ , it has  $\alpha_t = ((b_2 - b_1 + P_1(n_t) - P_2(n_t))/(a_1 - a_2))$ . In the same way, we obtain  $\beta_t = ((b_2 - b_1 + P_1(n_t) - P_2(n_t))/(a_1 - a_2))$ . After the above discussion,  $\alpha_t$  and  $\beta_t$  satisfy

$$\alpha_t = \beta_t = \frac{b_2 - b_1 + P_1(n_t) - P_2(n_t)}{a_1 - a_2}. \quad (7)$$

Equation (7) shows that the common belief which makes a consumer change his choice from the first vendor to the second one is equal to that which makes the changes from the second vendor to the first one. It is called cutoff in [1]. The cutoff increases as  $P_1(n_t)$  increases and decreases as

$P_2(n_t)$  increases. The cutoff is linear with both  $P_1(n_t)$  and  $P_2(n_t)$ . In a market, as  $P_1(n_t)$  increases, the utility of the consumer who chooses the first vendor is smaller. The consumers who have the same common belief tend to choose the second vendor. Thus, the cutoff cuts down. If  $P_2(n_t)$  decreases, the relative price for the second vendor increases. Similarly, the cutoff reduces. In the following, we use  $\alpha_t$  to denote the cutoff. The ranges of pricing for two vendors obtained from equation (7) are shown in Proposition 1.

**Proposition 1.** *Suppose that  $P_1(\cdot)$  and  $P_2(\cdot)$  are the prices of goods from the first and second vendors, respectively. Then  $P_1(\cdot)$  and  $P_2(\cdot)$  satisfy*

$$0 \leq P_1(n_t) \leq (a_1 + b_1) - (a_2 + b_2) + P_2(n_t), \quad (8)$$

$$0 \leq P_2(n_t) \leq b_2 - b_1 + P_1(n_t), \quad (9)$$

where one of the second signs of inequalities (8) or (9) is sign of strict inequality.

*Proof.*  $P_1(n_t)$  and  $P_2(n_t)$  are greater than zero as the vendors' costs of goods are zero. In the following, we prove  $P_1(n_t) \leq (a_1 + b_1) - (a_2 + b_2) + P_2(n_t)$  and  $P_2(n_t) \leq b_2 - b_1 + P_1(n_t)$ .

If  $\alpha_t > 1$ , i.e.,  $x_t < \alpha_t$ , all consumers give up the first vendor to choose the second one. For the first vendor, the price of his goods satisfies  $\alpha_t \leq 1$ . It has

$$\frac{b_2 - b_1 + P_1(n_t) - P_2(n_t)}{a_1 - a_2} \leq 1, \quad (10)$$

i.e.,

$$P_1(n_t) \leq (a_1 + b_1) - (a_2 + b_2) + P_2(n_t). \quad (11)$$

In the same way, the second vendor makes the price of goods satisfy  $\alpha_t \geq 0$ . We have

$$P_2(n_t) \leq b_2 - b_1 + P_1(n_t). \quad (12)$$

Inequalities (8) and (9) are proved.

From inequalities (8) and (9), we obtain

$$\begin{aligned} P_1(n_t) &\leq (a_1 + b_1) - (a_2 + b_2) + P_2(n_t) \\ &\leq (a_1 + b_1) - (a_2 + b_2) + b_2 - b_1 + P_1(n_t) \\ &= a_1 - a_2 + P_1(n_t). \end{aligned} \quad (13)$$

From inequality (13), we obtain  $a_2 \leq a_1$  which contradicts the assumption  $a_2 < a_1$ . Thus, one of the second signs of inequalities in (8) and (9) is sign of strict inequality.

Proposition 1 shows the scopes of commodity prices which are decided by two monopolistic vendors. We find that the supremum of the price for a vendor increases as the price for the other vendor increases. The supremum of the price for a vendor and the price for the other vendor are linear dependence. In the duopoly market, an increase in the price of goods means a decrease of benefit to the number of consumers. Due to the substitution effect between goods, the benefit to someone who chooses the other vendor increases.

The supremum of the price for the other vendor aggrandizes.  $\square$

**Corollary 1.**  $P_1(n_t) < +\infty$  if and only if  $P_2(n_t) < +\infty$  while  $P_1(n_t) = \infty$  if and only if  $P_2(n_t) = \infty$ .

Corollary 1 is easily proved from Proposition 1 and reveals the commodity prices under periods of economic prosperity and economic crisis. During periods of economic prosperity, the commodity prices are bounded while the

prices are infinite on account of discontinued sale of goods during the economic crisis. In next discussion, we ignore the situation of economic crisis.

### 3. Duopoly Market

If there exists  $\{t_\Theta\}_{0 \leq \Theta \leq d}$  such that  $0 = t_0 < t_1 < \dots < t_d = t$ , a consumer chooses a vendor, denoted by  $j$ ,  $t \in (t_{2k}, t_{2k+1})$  and chooses the other vendor, denoted by  $-j$ ,  $t \in (t_{2k+1}, t_{2k+2})$ ,  $k = 0, 1, \dots, (d/2) - 1$ . Let

$$p_t := \Pr\left\{i = H \mid u_{ji}^{(t_0, t_1)}, u_{-ji}^{(t_1, t_2)}, \dots, u_{ji}^{(t_{2k}, t_{2k+1})}, u_{-ji}^{(t_{2k+1}, t_{2k+2})}, \dots, u_{ji}^{(t_{d-2}, t_{d-1})}, u_{-ji}^{(t_{d-1}, t)}\right\}, \quad (14)$$

where  $u_{ji}^{(\pi_1, \pi_2)} := \left\{u_{ji}(\tau)\right\}_{\tau=\pi_1}^{\pi_2}$ . Using the arguments in [8, 9], we know that  $p_t$  satisfies

$$\begin{aligned} dp_t &= \sqrt{n_t} p_t (1 - p_t) s_1 dW_1(t) \\ &+ \sqrt{M - n_t} p_t (1 - p_t) s_2 dW_2(t), \end{aligned} \quad (15)$$

where  $W_1(t)$  and  $W_2(t)$  are independent Winner processes.

For any time  $l$  and small  $\varepsilon > 0$ , a consumer gives up the second vendor and chooses the first vendor when

$$\begin{aligned} l &\in \{s > 0 \mid p_s = \alpha_s, \alpha_{s-\varepsilon} - p_{s-\varepsilon} \in A_2, \alpha_{s+\varepsilon} - p_{s+\varepsilon} \in A_1\} \\ &\subseteq \{s > 0 \mid p_s = \alpha_s, \Delta(\alpha_s - p_s) \in A_1\} \\ &\subseteq \{s > 0 \mid \Delta(\alpha_s - p_s) \in A_1\}, \end{aligned} \quad (16)$$

where  $A_1 := \{x \leq 0\} / \{0\}$ ,  $A_2 := \{x \geq 0\} / \{0\}$  and  $\Delta(X_s) := X_s - X_{s-}$  with  $X_{s-} := \lim_{t \rightarrow s-} X_t$ . Similarly, a consumer replaces

the goods of the first vendor with the goods of the second vendor if

$$\begin{aligned} l &\in \{s > 0 \mid p_s = \alpha_s, \alpha_{s-\varepsilon} - p_{s-\varepsilon} \in A_1, \alpha_{s+\varepsilon} - p_{s+\varepsilon} \in A_2\} \\ &\subseteq \{s > 0 \mid p_s = \alpha_s, \Delta(\alpha_s - p_s) \in A_2\} \\ &\subseteq \{s > 0 \mid \Delta(\alpha_s - p_s) \in A_2\}. \end{aligned} \quad (17)$$

We assume that the number of consumers who choose one vendor to replace the other one is related to  $\Delta(\alpha_l - p_l)$ ,  $p_l$  and  $n_l$  at time  $l$ . All of them reflect the relationship between  $\alpha_t$  and  $p_t$  at  $t \in (l - \varepsilon, l + \varepsilon)$ . Let  $G_j(\Delta(\alpha_l - p_l), p_l, n_l)$  ( $\in \{0, 1, \dots, M\}$ ) be the number of consumers who give up the other vendor to choose the vendor  $j$ ,  $j = 1, 2$ . If  $n_t$  is known, the number of consumers who choose the first vendor at  $(t + dt)$  is expressed by

$$\begin{aligned} n_{t+dt} &= n_t \\ &+ \sum_{0 \leq u \leq dt} G_1(\Delta(\alpha_u - p_u), p_u, n_u) \#\{0 \leq s \leq u \mid p_s = \alpha_s, \alpha_{s-\varepsilon} - p_{s-\varepsilon} \in A_2, \alpha_{s+\varepsilon} - p_{s+\varepsilon} \in A_1\} \\ &- \sum_{0 \leq u \leq dt} G_2(\Delta(\alpha_u - p_u), p_u, n_u) \#\{0 \leq s \leq u \mid p_s = \alpha_s, \alpha_{s-\varepsilon} - p_{s-\varepsilon} \in A_1, \alpha_{s+\varepsilon} - p_{s+\varepsilon} \in A_2\}, \end{aligned} \quad (18)$$

where  $\#$  represents the number of elements in a set. Let

$$\begin{aligned} \bar{\omega}_1(\Delta(\alpha_u - p_u), p_u) &= \frac{\#\{0 \leq s \leq u \mid p_s = \alpha_s, \alpha_{s-\varepsilon} - p_{s-\varepsilon} \in A_2, \alpha_{s+\varepsilon} - p_{s+\varepsilon} \in A_1\}}{\#\{0 \leq s \leq u \mid \Delta(\alpha_u - p_u) \in A_1\}}, \\ \bar{\omega}_2(\Delta(\alpha_u - p_u), p_u) &= \frac{\#\{0 \leq s \leq u \mid p_s = \alpha_s, \alpha_{s-\varepsilon} - p_{s-\varepsilon} \in A_1, \alpha_{s+\varepsilon} - p_{s+\varepsilon} \in A_2\}}{\#\{0 \leq s \leq u \mid \Delta(\alpha_u - p_u) \in A_2\}}. \end{aligned} \quad (19)$$

If  $\{0 \leq s \leq u \mid p_s = \alpha_s, \alpha_{s-\varepsilon} - p_{s-\varepsilon} \in A_2, \alpha_{s+\varepsilon} - p_{s+\varepsilon} \in A_1\} \neq \emptyset$ , we require that  $\gamma_1(\Delta(\alpha_u - p_u), p_u)$  equals to  $\bar{\omega}_1(\Delta(\alpha_u - p_u), p_u)$  while  $\gamma_1(\Delta(\alpha_u - p_u), p_u) := 0$  for another case.

Similarly, if  $\{0 \leq s \leq u \mid p_s = \alpha_s, \alpha_{s-\varepsilon} - p_{s-\varepsilon} \in A_1, \alpha_{s+\varepsilon} - p_{s+\varepsilon} \in A_2\}$  is not empty, let  $\gamma_2(\Delta(\alpha_u - p_u), p_u)$  be equal to  $\bar{\omega}_2(\Delta(\alpha_u - p_u), p_u)$  and zero otherwise. Defining



$$g_1(\Delta(\alpha_u - p_u), p_u, n_u) = G_1(\Delta(\alpha_u - p_u), p_u, n_u) \gamma_1 \cdot (\Delta(\alpha_u - p_u), p_u), \quad (20)$$

$$g_2(\Delta(\alpha_u - p_u), p_u, n_u) = G_2(\Delta(\alpha_u - p_u), p_u, n_u) \gamma_2 \cdot (\Delta(\alpha_u - p_u), p_u), \quad (21)$$

we have

$$n_{t+dt} = n_t + \sum_{0 \leq u \leq dt} g_1(\Delta(\alpha_u - p_u), p_u, n_u) \#\{0 \leq s \leq u \mid \Delta(\alpha_u - p_u) \in A_1\} - \sum_{0 \leq u \leq dt} g_2(\Delta(\alpha_u - p_u), p_u, n_u) \#\{0 \leq s \leq u \mid \Delta(\alpha_u - p_u) \in A_2\}, \quad (22)$$

where  $g_j(\Delta(\alpha_u - p_u), p_u, n_u) \leq G_j(\Delta(\alpha_u - p_u), p_u, n_u)$  due to  $\gamma_j(\cdot, \cdot) \in [0, 1]$ , i.e.,  $g_j(\Delta(\alpha_u - p_u), p_u, n_u)$  is bounded. Proposition 2 can be obtained by using the definition of Poisson stochastic integral as  $dt \rightarrow 0$  and  $s \rightarrow u$ .

**Proposition 2.** *If  $(\alpha_t - p_t)$  is a stochastic process which has independent and stationary increments with càdlàg paths (paths are continuous on the right and have limits on the left [20, 21]), then*

$$dn_t = \int_{A_1} g_1(h, p_{t-}, n_{t-}) N(dt, dh) - \int_{A_2} g_2(h, p_{t-}, n_{t-}) N(dt, dh), \quad (23)$$

where  $g_1(h, p_{t-}, n_{t-})$  and  $g_2(h, p_{t-}, n_{t-})$  are defined in Equations (20) and (21). Moreover, SDE (23) has a unique solution.

*Proof.* As  $g_1(\cdot, \cdot, \cdot)$  and  $g_2(\cdot, \cdot, \cdot)$  are bounded,  $A_1$  and  $A_2$  are bounded below, from [22], we obtain that  $n_t$  is convergent in  $L^2$  for any measurable random variable  $n_0$ . Besides,  $g_1(\cdot, \cdot, \cdot)$  and  $g_2(\cdot, \cdot, \cdot)$  can be verified to satisfy

- (i) Lipschitz condition: There exists  $K_1 > 0$ , for any  $y_1, y_2 \in \{0, 1, \dots, M\}$  and  $x \in [0, 1]$  such that

$$\left| \int_{A_1} |g_1(h, x, y_1) - g_1(h, x, y_2)|^2 \nu(dh) \right| \leq K_1 |y_1 - y_2|^2, \\ \left| \int_{A_2} |g_2(h, x, y_1) - g_2(h, x, y_2)|^2 \nu(dh) \right| \leq K_1 |y_1 - y_2|^2. \quad (24)$$

- (ii) Growth condition: there exists  $K_2 > 0$ , for any  $y \in \{0, 1, \dots, M\}$  and  $x \in [0, 1]$ , such that

$$2y \int_{A_1} g_1(h, x, y) \nu(dh) + \int_{A_1} |g_1(h, x, y)|^2 \nu(dh) \leq K_2 (1 + |y|^2), \\ 2y \int_{A_2} g_2(h, x, y) \nu(dh) + \int_{A_2} |g_2(h, x, y)|^2 \nu(dh) \leq K_2 (1 + |y|^2). \quad (25)$$

Equation (23) is proved to exist a unique solution by using the results in [23, 24].

Proposition 2 shows the existence and uniqueness of global solutions for the SDE (23) which describes the quantity of buyers who choose the first vendor in the duopoly market. It is presented as a pure jump process.  $g_j(\cdot, \cdot, \cdot)$  is defined as the rate of change of the number of consumers who give up the other vendor and choose the  $j$ th one.  $\square$

#### 4. The Optimal Strategy for Vendors

As consumers do not know their types, they choose one of two vendors referred by the prices of goods at initial time. We assume that there are  $n$  consumers who choose the first vendor, i.e.,  $n_0 = n$ . After that, vendors inform consumers' types, denoted by  $p := p_0$ , to guide consumers to make subsequent choices. Ignoring the interaction between the two vendors, denoting  $V_j(\cdot)$  as the  $j$ th vendor's optimal utility and  $r$  as risk-free interest rate, for the first vendor, we have

$$V_1(n) = \max_{p \in [0, 1]} \mathbb{E} \left[ \int_0^{+\infty} e^{-rt} n_t P_1(n_t) dt \right] \\ s.t. \, dn_t = \int_{A_1} g_1(h, p_{t-}, n_{t-}) N(dt, dh) - \int_{A_2} g_2(h, p_{t-}, n_{t-}) N(dt, dh). \quad (26)$$

The HJB equation is obtained as follows:

$$rV_1(n) = nP_1(n) + \max_{p \in [0, 1]} \left\{ \int_{A_1} [V_1(n + g_1(h, p, n)) - V_1(n)] \nu(dh) - \int_{A_2} [V_1(n + g_2(h, p, n)) - V_1(n)] \nu(dh) \right\}, \quad (27)$$

where  $\nu$ , the intensity measure of  $N$ , is the finite intensity measure as  $A_1$  and  $A_2$  are bounded below. Suppose that  $w(n)$  is a solution of equation (27), the verification result is obtained as follows.

**Proposition 3.** *If there exists an integrable function  $\phi(\cdot)$  such that  $|w(\cdot)| \leq \phi(\cdot)$ .*

(i) *Suppose that*

$$rw(n) - nP_1(n) - \max_{p \in [0,1]} \left\{ \int_{A_1} [w(n + g_1(h, p, n)) - w(n)] \nu(dh) - \int_{A_2} [w(n + g_2(h, p, n)) - w(n)] \nu(dh) \right\} \geq 0, \quad (28)$$

$$\limsup_{T \rightarrow +\infty} e^{-rT} \mathbb{E}[w(n_T)] \geq 0. \quad (29)$$

Then  $w(n) \geq v(n)$  if  $n \in \{1, 2, \dots, M\}$ .

(ii) *Suppose that for all  $n \in \{1, 2, \dots, M\}$ , there exists a  $p^*$  such that*

$$rw(n) - nP_1(n) - \left\{ \int_{A_1} [w[n + g_1[h, p^*, n]] - w[n]] \nu(dh) - \int_{A_2} [w[n + g_2[h, p^*, n]] - w[n]] \nu(dh) \right\} = 0, \quad (30)$$

the stochastic differential equation

$$\begin{aligned} dn_t = & \int_{A_1} g_1(h, p_{t-}^*, n_{t-}) N(dt, dh) \\ & - \int_{A_2} g_2(h, p_{t-}^*, n_{t-}) N(dt, dh), \end{aligned} \quad (31)$$

admits a unique solution and

$$\liminf_{t \rightarrow \infty} e^{-rt} \mathbb{E}[w(n_T)] \leq 0, \quad (32)$$

then

$$w(n) = v(n), \quad n \in \{1, 2, \dots, M\}. \quad (33)$$

*Proof.* Three steps are divided to prove Proposition 3.  $\square$

*Step 1.* We prove  $\mathbb{E}[\int_0^{+\infty} e^{-rt} n_t P_1(n_t) dt] < +\infty$ . From the assumptions, it has

$$\mathbb{E} \left[ \int_0^{+\infty} e^{-rt} n_t P_1(n_t) dt \right] \leq M \mathbb{E} \left[ \int_0^{+\infty} e^{-rt} P_1(n_t) dt \right]. \quad (34)$$

Hence, from  $\int_0^{+\infty} e^{-rt} dt < +\infty$  and  $P_1(n_t)$  which is a monotone bounded function, we derive

$$\mathbb{E} \left[ \int_0^{+\infty} e^{-rt} P_1(n_t) dt \right] < +\infty. \quad (35)$$

Thus,  $\mathbb{E}[\int_0^{+\infty} e^{-rt} n_t P_1(n_t) dt] < +\infty$  as  $M < +\infty$ .

*Step 2.* The proof of (i) in Proposition 3. Let

$$\begin{aligned} \tau_k := & \inf \left\{ t \geq 0 \mid \int_{A_1} e^{-rt} [w(n_{t-} + g_1(h, p_t, n_t)) - w(n_{t-})] \nu(dh) \geq k \right. \\ & \left. \text{or } \int_{A_2} e^{-rt} [w(n_{t-} + g_2(h, p_t, n_t)) - w(n_{t-})] \nu(dh) \geq k \right\}. \end{aligned} \quad (36)$$

Using Itô's lemma for  $e^{-r(T \wedge \tau_k)} w(n_{T \wedge \tau_k})$ , where  $T \wedge \tau_k := \min\{T, \tau_k\}$ , we obtain

$$\begin{aligned}
 & e^{-r(T \wedge \tau_k)} w(n_{T \wedge \tau_k}) \\
 &= w(n) - \int_0^{T \wedge \tau_k} r e^{-rs} w(n_s) ds \\
 &+ \int_0^{T \wedge \tau_k} \int_{A_1} e^{-rs} [w(n_{s-} + g_1(h, p_s, n_s)) - w(n_{s-})] N(ds, dh) \\
 &- \int_0^{T \wedge \tau_k} \int_{A_2} e^{-rs} [w(n_{s-} + g_2(h, p_s, n_s)) - w(n_{s-})] N(ds, dh).
 \end{aligned} \tag{37}$$

Introducing compensation Poisson random measure, equation (37) is rewritten as

$$\begin{aligned}
 & e^{-r(T \wedge \tau_k)} w(n_{T \wedge \tau_k}) \\
 &= w(n) - \int_0^{T \wedge \tau_k} r e^{-rs} w(n_s) ds \\
 &+ \int_0^{T \wedge \tau_k} \int_{A_1} e^{-rs} [w(n_{s-} + g_1(h, p_s, n_s)) - w(n_{s-})] \tilde{N}(ds, dh) \\
 &- \int_0^{T \wedge \tau_k} \int_{A_2} e^{-rs} [w(n_{s-} + g_2(h, p_s, n_s)) - w(n_{s-})] \tilde{N}(ds, dh) \\
 &+ \int_0^{T \wedge \tau_k} ds \int_{A_1} e^{-rs} [w(n_{s-} + g_1(h, p_s, n_s)) - w(n_{s-})] \nu(dh) \\
 &- \int_0^{T \wedge \tau_k} \int_{A_2} e^{-rs} [w(n_{s-} + g_2(h, p_s, n_s)) - w(n_{s-})] \nu(dh),
 \end{aligned} \tag{38}$$

where the compensation Poisson random measure  $\tilde{N}(s, dh) := N(s, dh) - s \cdot \nu(dh)$  is a martingale. Taking expectation for both sides of equation (38) yields

$$\begin{aligned}
 & \mathbb{E} \left[ e^{-r(T \wedge \tau_k)} w(n_{T \wedge \tau_k}) \right] \\
 &= w(n) - \mathbb{E} \left[ \int_0^{T \wedge \tau_k} r e^{-rs} w(n_s) ds \right] \\
 &+ \mathbb{E} \left[ \int_0^{T \wedge \tau_k} ds \int_{A_1} e^{-rs} [w(n_{s-} + g_1(h, p_s, n_s)) - w(n_{s-})] \nu(dh) \right] \\
 &- \mathbb{E} \left[ \int_0^{T \wedge \tau_k} \int_{A_2} e^{-rs} [w(n_{s-} + g_2(h, p_s, n_s)) - w(n_{s-})] \nu(dh) \right].
 \end{aligned} \tag{39}$$

From inequality (28), we obtain

$$\mathbb{E} \left[ e^{-r(T \wedge \tau_k)} w(n_{T \wedge \tau_k}) \right] \leq w(n) - \mathbb{E} \left[ \int_0^{T \wedge \tau_k} e^{-rs} n_s P_1(n_s) ds \right]. \tag{40}$$

Letting  $k \rightarrow +\infty$ , using the dominated convergence theorem, inequality (40) becomes

$$\mathbb{E} \left[ e^{-rT} w(n_T) \right] \leq w(n) - \mathbb{E} \left[ \int_0^T e^{-rs} n_s P_1(n_s) ds \right]. \tag{41}$$

As  $T \rightarrow +\infty$ , in accordance with inequality (29), for any  $p \in [0, 1]$ , the inequality

$$w(n) \geq \mathbb{E} \left[ \int_0^T e^{-rs} n_s P_1(n_s) ds \right], \tag{42}$$

is obtained. Hence,

$$w(n) \geq \max_{p \in [0,1]} \mathbb{E} \left[ \int_0^T e^{-rs} n_s P_1(n_s) ds \right] = V(n). \quad (43)$$

The (i) in Proposition 3 is proved by Steps 1 and 2.

*Step 3.* The proof of (ii) in Proposition 3. As  $p^*$  is the optimal choice for the vendor, we obtain

$$\mathbb{E} \left[ e^{-rT} w(n_T) \right] = w(n) - \mathbb{E} \left[ \int_0^T e^{-rs} n_s P_1(n_s) ds \right], \quad (44)$$

where

$$\begin{aligned} dn_t = & \int_{A_1} g_1(h, p_{t-}^*, n_{t-}) N(dt, dh) \\ & - \int_{A_2} g_2(h, p_{t-}^*, n_{t-}) N(dt, dh), \end{aligned} \quad (45)$$

$$\begin{aligned} rV_2(n) = & (M - n)P_2(n) + \max_{p \in [0,1]} \left\{ \int_{A_1} [V_2(n + g_1(h, p, n)) - V_2(n)] \nu(dh) \right. \\ & \left. - \int_{A_2} [V_2(n + g_2(h, p, n)) - V_2(n)] \nu(dh) \right\}. \end{aligned} \quad (47)$$

We assume that one of the two vendors is a type-leader vendor. Without loss of generality, denote the first vendor as the type-leader vendor. In this situation, we acquire

$$\begin{aligned} \kappa V_1(n) = & nP_1(n) + \int_{A_1} V_1(n + g_1(h, p^*, n)) \nu(dh) \\ & - \int_{A_2} V_1(n + g_2(h, p^*, n)) \nu(dh). \end{aligned} \quad (48)$$

For the second vendor, his payoff function satisfies

$$\begin{aligned} \kappa V_2(n) = & (M - n)P_2(n) + \int_{A_1} V_2(n + g_1(h, p^*, n)) \nu(dh) \\ & - \int_{A_2} V_2(n + g_2(h, p^*, n)) \nu(dh), \end{aligned} \quad (49)$$

where  $\kappa := r - [\int_{A_1} \nu(dh) - \int_{A_2} \nu(dh)] < \infty$ .

As the second vendor considers that the first vendor informs all consumers whose types are  $H$  and consumers tend to buy goods from the first vendor, the second vendor's goods are not sold. From Corollary 2.1, if the vendor wants more consumers to buy his goods, he prices his goods  $P_2(n_t)$ , based on the price  $P_1(n_t)$  of the first vendor, such that  $P_1(n_t) = (a_1 + b_1) - (a_2 + b_2) + P_2(n_t)$ , i.e.,

$$P_2(n_t) = (a_2 + b_2) - (a_1 + b_1) + P_1(n_t). \quad (50)$$

From equation (50), we find that  $P_2(n_t) < 0$  if  $P_1(n_t) < (a_1 + b_1) - (a_2 + b_2)$ . Thus, the price of the second vendor's goods is zero. For the type-leader vendor, the price of their goods is

has a unique solution. Letting  $T \rightarrow +\infty$ , from inequality (32), we have

$$w(n) \leq \mathbb{E} \left[ \int_0^T e^{-rs} n_s P_1(n_s) ds \right] = V(n). \quad (46)$$

From inequalities (43) and (46), we have  $w(n) = V(n)$ . The proof is completed.

Proposition 3 shows that the solution of HJB equation (27) is  $V_1(n)$ .

Similarly, for the second vendor, it has

$$P_1(n) = (a_1 + b_1) - (a_2 + b_2) - \varepsilon, \quad (51)$$

where  $\varepsilon > 0$  is an arbitrary small number. Denoted by  $P_1^\varepsilon$  as  $(a_1 + b_1) - (a_2 + b_2) - \varepsilon$ , then  $P_1^\varepsilon < (a_1 + b_1) - (a_2 + b_2) + 0$  and  $0 = P_2(n_t) \leq a_1 - a_2 - \varepsilon$  satisfy pricing ranges for both vendors in Proposition 1. Equations (48) and (49) are equivalent to

$$\begin{aligned} \kappa V_1(n) = & nP_1^\varepsilon + \int_{A_1} V_1(n + g_1(h, p^*, n)) \nu(dh) \\ & - \int_{A_2} V_1(n + g_2(h, p^*, n)) \nu(dh), \end{aligned} \quad (52)$$

$$\begin{aligned} \kappa V_2(n) = & \int_{A_1} V_2(n + g_1(h, p^*, n)) \nu(dh) \\ & - \int_{A_2} V_2(n + g_2(h, p^*, n)) \nu(dh), \end{aligned} \quad (53)$$

respectively. In this situation, the payoffs of the leader and the following vendors are shown in Proposition 4.

**Proposition 4.** *If there exist  $P_1^\varepsilon$ , the rate of change  $g_j(\cdot, \cdot, \cdot)$ , a finite intensity measure  $\nu$  and  $p^* \in [0, 1]$  such that the equation*

$$\begin{aligned} \kappa V_1(n) = & nP_1^\varepsilon + \int_{A_1} V_1(n + g_1(h, p^*, n)) \nu(dh) \\ & - \int_{A_2} V_1(n + g_2(h, p^*, n)) \nu(dh), \end{aligned} \quad (54)$$

*has solutions; then its solution is unique if and only if  $V_2(n) \equiv 0$ , i.e., the type-leader vendor makes the other vendor's profit be zero with pricing strategy.*

*Proof.* Firstly, we prove that if there exists  $P_1^e$ , the rate of change  $g_j(\cdot, \cdot, \cdot)$ , a finite intensity measure  $\nu$  and  $p^* \in [0, 1]$  such that the equation

$$\begin{aligned} \kappa V_1(n) &= nP_1^e + \int_{A_1} V_1(n + g_1(h, p^*, n))\nu(dh) \\ &\quad - \int_{A_2} V_1(n + g_2(h, p^*, n))\nu(dh), \end{aligned} \quad (55)$$

has a unique solution, then  $V_2(n) \equiv 0$ .

As  $V_1(n)$  and  $V_2(n)$  are the maximum utilities of the first and second vendor, we have  $V_1(n) \geq 0$  and  $V_2(n) \geq 0$ . Denote  $V(\cdot) = V_1(\cdot) + V_2(\cdot)$ , where  $V(\cdot)$  represents the sum of two vendors' profits. It is straightforward to verify  $V(n) \geq V_1(n)$  and  $V(n) \geq V_2(n)$ . From equations (52) and (53), we have

$$\begin{aligned} \kappa V(n) &= nP_1^e + \int_{A_1} V_1(n + g_1(h, p^*, n))\nu(dh) - \int_{A_2} V_1(n + g_2(h, p^*, n))\nu(dh) \\ &\quad + \int_{A_1} V_2(n + g_1(h, p^*, n))\nu(dh) - \int_{A_2} V_2(n + g_2(h, p^*, n))\nu(dh) \\ &= nP_1^e + \int_{A_1} [V_1(n + g_1(h, p^*, n)) + V_2(n + g_1(h, p^*, n))]\nu(dh) \\ &\quad - \int_{A_2} [V_1(n + g_2(h, p^*, n)) + V_2(n + g_2(h, p^*, n))]\nu(dh). \end{aligned} \quad (56)$$

From the definition of  $V(\cdot)$ , we derive that

$$\begin{aligned} \kappa V(n) &= nP_1^e + \int_{A_1} V(n + g_1(h, p^*, n))\nu(dh) \\ &\quad - \int_{A_2} V(n + g_2(h, p^*, n))\nu(dh). \end{aligned} \quad (57)$$

Comparing Eqs. (54) and (57) finds that  $V_1(\cdot)$  and  $V(\cdot)$  have the same structure. If there exists a unique solution to equation (57), we have  $V(\cdot) \equiv V_1(\cdot)$ . Therefore,  $V_2(\cdot) \equiv 0$ . The necessity of Proposition 3 is proved.

Now, we prove the sufficiency. If  $V_2(\cdot) \equiv 0$  and the solution of equation (54) exists, then it is unique. Assume that there exist two solutions  $v_1$  and  $v_2$ ,  $v_1 \equiv v_2$ , i.e., there exists  $m \in \{0, 1, \dots, M\}$  such that  $v_1(m) \neq v_2(m)$ . Without loss of generality, we assume that  $v_1(m) < v_2(m)$ . From  $V(\cdot) > V_1(\cdot)$ ,  $v_2(m) = V(m)$  and  $v_1(m) = V_1(m)$  are obtained. Moreover,  $V_2(m) = V(m) - V_1(m) \neq 0$ , contradictory with  $V_2 \equiv 0$ . Therefore, if the solution of equation (54) exists, its solution is unique when  $V_2(\cdot) \equiv 0$ . The sufficiency of Proposition 3 is proved.

Proposition 4 shows the condition that the type-leader vendor obtains surplus of all producers. In this case, the following vendor is unprofitable and gradually withdraws from the market. Eventually, the market will be monopolized by the type-leader vendor.  $\square$

## 5. Example

For the convenience of explanation, we add two assumptions.

*Assumption 1.* Let  $g_j(h, p, n) := \psi_j(h)\phi_j(p, n)$  where  $\psi_j(\cdot)$  and  $\phi_j(\cdot, \cdot)$  are bounded and  $\phi_j(\cdot, \cdot)$  is twice continuously differentiable for the first variable.

Let  $\xi_j := \int_{A_j} \nu(dh)$ ,  $\omega_j := \int_{A_j} \psi_j(h)\nu(dh)$  and  $\eta_j := \int_{A_j} \psi_j^2(h)\nu(dh)$ .  $\xi_j$ ,  $\omega_j$  and  $\eta_j$  are finite as  $A_1$  and  $A_2$  are bounded below. The first order condition for  $p$  from HJB equation (27) is

$$\begin{aligned} \int_{A_1} V_1'(n + \psi_1(h)\phi_1(p, n)) \frac{\partial \phi_1(p, n)}{\partial p} \psi_1(h)\nu(dh) \\ - \int_{A_2} V_2'(n + \psi_2(h)\phi_2(p, n)) \frac{\partial \phi_2(p, n)}{\partial p} \psi_2(h)\nu(dh) = 0. \end{aligned} \quad (58)$$

As the exact analytic solution of HJB equation (27) is difficult to be obtained, we consider the approximate solution of equation (27). Let  $V_j(n + \psi_1(h)\phi_1(p, n))$  be approximately equal to  $V_j(n) + V_j'(n)\psi_j(h)\phi_j(p, n) + 1/2V_j''(n)\psi_j^2(h)\phi_j^2(p, n)$  and  $V_j'(n + \psi_1(h)\phi_1(p, n))$  be approximately equal to  $V_j'(n) + V_j''(n)\psi_j(h)\phi_j(p, n)$ . Substituting them into (58) yields

$$\tilde{V}_1'(n) \left[ \omega_1 \frac{\partial \phi_1(p, n)}{\partial p} - \omega_2 \frac{\partial \phi_2(p, n)}{\partial p} \right] + \tilde{V}_1''(n) \left[ \eta_1 \phi_1(p, n) \frac{\partial \phi_1(p, n)}{\partial p} - \eta_2 \phi_2(p, n) \frac{\partial \phi_2(p, n)}{\partial p} \right] = 0, \quad (59)$$

where  $\tilde{V}_j(\cdot)$  is an approximate solution of  $V_j(\cdot)$ . For acquiring the type-leader vendor's optimal strategy, Assumption 2 is given.

*Assumption 2.* There exist  $\omega_j, \eta_j, p^*, \phi_j(p, n)$  to satisfy Assumption 1, for any  $p \in [0, 1]$ , such that

$$\begin{aligned} & \tilde{V}'_1(n) \left[ \omega_1 \frac{\partial^2 \phi_1(p, n)}{\partial p^2} - \omega_2 \frac{\partial^2 \phi_2(p, n)}{\partial p^2} \right] + \tilde{V}''_1(n) \left[ \eta_1 \phi_1(p, n) \frac{\partial^2 \phi_1(p, n)}{\partial p^2} \right. \\ & \left. + \eta_1 \left( \frac{\partial \phi_1(p, n)}{\partial p} \right)^2 - \eta_2 \phi_2(p, n) \frac{\partial \phi_2(p, n)}{\partial p} - \eta_2 \left( \frac{\partial \phi_2(p, n)}{\partial p} \right)^2 \right] < 0 \\ & \left. \frac{\partial \phi_1(p, n)}{\partial p} \right|_{p=p^*} = \left. \frac{\partial \phi_2(p, n)}{\partial p} \right|_{p=p^*} = 0. \end{aligned} \tag{60}$$

Assumption 2 implies that  $p^*$  is a unique optimal strategy for the type-leader vendor. Combining with pricing strategy, HJB equation (27) can be approximately written by

$$q_1 \tilde{V}''_1(n) + q_2 \tilde{V}'_1(n) + q_3 \tilde{V}_1(n) + nP_1^\epsilon = 0, \tag{61}$$

where  $q_1 := 1/2(\eta_1 \phi_1^2(p^*, n) - \eta_2 \phi_2^2(p^*, n))$ ,  $q_2 := \omega_1 \phi_1(p^*, n) - \omega_2 \phi_2(p^*, n)$ , and  $q_3 := \xi_1 - \xi_2 - \kappa$ . Similarly,

$$q_1 \tilde{V}''_2(n) + q_2 \tilde{V}'_2(n) + q_3 \tilde{V}_2(n) = 0. \tag{62}$$

In order to simplify the analytical solution of equations (61) and (62), we assume that  $q_1$  and  $q_2$  are independent to  $n$ . Denote  $C_Y$  as constants which do not depend on  $n$  ( $Y = 1, 2, \dots, 11$ ). Four cases are divided to solve equations (61) and (62).

*Case 1.* Consider  $q_1 \neq 0$  and  $q_2^2 - 4q_1q_3 > 0$ . If  $q_3 \neq 0$ , Solving equations (61) and (62) yields

$$\begin{aligned} \tilde{V}_1(n) &= -\frac{nP_1^\epsilon}{q_3} + \frac{q_2 P_1^\epsilon}{q_3^2} + C_1 e^{((-q_2 + \sqrt{q_2^2 - 4q_1q_3})/2q_1)n} + C_2 e^{((-q_2 - \sqrt{q_2^2 - 4q_1q_3})/2q_1)n}, \\ \tilde{V}_2(n) &= C_1 e^{((-q_2 + \sqrt{q_2^2 - 4q_1q_3})/2q_1)n} + C_2 e^{((-q_2 - \sqrt{q_2^2 - 4q_1q_3})/2q_1)n}. \end{aligned} \tag{63}$$

If  $q_3 = 0$ , the solutions of  $\tilde{V}_1(n)$  and  $\tilde{V}_2(n)$  are

$$\tilde{V}_1(n) = C_3 e^{-(q_2/q_1)n} + C_4 - \frac{nP_1^\epsilon}{q_2} \tag{64}$$

$$\tilde{V}_2(n) = C_3 e^{-(q_2/q_1)n} + C_4,$$

respectively.

*Case 2.* Consider  $q_1 \neq 0$  and  $q_2^2 - 4q_1q_3 = 0$ . If  $q_2 \neq 0$ , solving equations (61) and (62), we have

$$\tilde{V}_1(n) = -\frac{nP_1^\epsilon}{q_3} + \frac{q_2 P_1^\epsilon}{q_3^2} + (C_5 + nC_6) e^{-(q_2/q_1)n}, \tag{65}$$

$$\tilde{V}_2(n) = (C_5 + nC_6) e^{-(q_2/q_1)n}.$$

If  $q_2 = 0$ ,  $\tilde{V}_1(n)$  and  $\tilde{V}_2(n)$  are verified to satisfy

$$\tilde{V}_1(n) = -\frac{n^3 P_1^\epsilon}{6q_1} + C_7 n + C_8, \tag{66}$$

$$\tilde{V}_2(n) = C_7 n + C_8.$$

*Case 3.* Consider  $q_1 \neq 0$  and  $q_2^2 - 4q_1q_3 < 0$ . In this case, we solve equations (61) and (62) to obtain

$$\begin{aligned} \tilde{V}_1(n) &= -\frac{nP_1^\epsilon}{q_3} + \frac{q_2 P_1^\epsilon}{q_3^2} + e^{-(q_2/2q_1)n} \left( C_9 \cos \frac{\sqrt{4q_1q_3 - q_2^2}}{2q_1} n + C_{10} \sin \frac{\sqrt{4q_1q_3 - q_2^2}}{2q_1} n \right), \\ \tilde{V}_2(n) &= e^{-(q_2/2q_1)n} \left( C_9 \cos \frac{\sqrt{4q_1q_3 - q_2^2}}{2q_1} n + C_{10} \sin \frac{\sqrt{4q_1q_3 - q_2^2}}{2q_1} n \right). \end{aligned} \tag{67}$$



Case 4. Consider  $q_1 = 0$ . If  $q_2 \neq 0$ , Solving equations (61) and (62) yields

$$\tilde{V}_1(n) = C_{11}e^{-(q_3/q_2)n} - \frac{P_1^\varepsilon}{q_3} \left( n - \frac{q_2}{q_3} \right), \quad (68)$$

$$\tilde{V}_2(n) = C_{11}e^{-(q_3/q_2)n}.$$

If  $q_2 = 0$ ,  $\tilde{V}_1(n)$  and  $\tilde{V}_2(n)$  satisfy

$$\tilde{V}_1(n) = -\frac{n}{q_3}P_1^\varepsilon, \quad (69)$$

$$\tilde{V}_2(n) \equiv 0. \quad (70)$$

It is easy to verify that the solutions in the four cases satisfy the verification theorem in Proposition 3. In particular, from equations (69) and (70),  $\tilde{V}_1(\cdot)$  has a unique solution and  $\tilde{V}_2(n) \equiv 0$  in this situation, which satisfies the conclusion in Proposition 4.

## 6. Conclusion

This paper explores a stochastic differential equation driven by Poisson random measure and its application in a duopoly market which exists two different types of consumers. We assume that prices of goods are decided by the number of consumers. To study vendors' optimal pricing strategies, scopes of goods prices are obtained from the cutoff. In addition, we prove that the quantity of buyers obeys a SDE resorting to the definition of Poisson stochastic measure and maximizing the vendor payoff. We also verify that the SDE exists a unique solution. Given the SDE, the corresponding HJB equation reflecting the profits of vendor is derived by using the dynamic programming principle.

In certain markets where the effectiveness of goods is more important than its price, we introduce the type-leader model. In the type-leader model, we find vendors' price strategies and verify that the commodity prices are in the price ranges in Proposition 1. The conditions that the type-leader vendor obtains surplus of all producers are acquired by existence and uniqueness of solutions of HJB equations. An example of this problem is given and approximate solutions for the profit of the two vendors are obtained.

## Data Availability

No data were used in this manuscript.

## Conflicts of Interest

The authors declare that they have no conflicts of interests.

## Authors' Contributions

The article is a joint work of two authors who contributed equally to the final version of the paper. Both authors read and approved the final manuscript.

## Acknowledgments

This work was supported by the Fundamental Research Funds for the Central Universities (JBK120504). Thanks are given to the reviewers for their valuable comments.





## References

- [1] J. Eeckhout and X. Weng, "Common value experimentation," *Journal of Economic Theory*, vol. 160, pp. 317–339, 2015.
- [2] M. V. Stackelberg, "Die bauprinzipien der carbide, silicide, nitride and phosphide elektropositiver metalle," *Zeitschrift Fu'r Physikalische Chemie*, vol. 27, pp. 53–57, 1934.
- [3] H. Robbins, "Some aspects of the sequential design of experiments," *Bulletin of the American Mathematical Society*, vol. 58, no. 5, pp. 527–536, 1952.
- [4] J. C. Gittins and D. M. Jones, "A dynamic allocation index in the sequential design of experiments," in *Progress in Statistics*, pp. 241–266, North Holland, Amsterdam, Netherlands, 1974.
- [5] N. K. Michale, F. Arthur, and J. R. Veinott, "The multi-armed bandit problem: decomposition and computation," *Mathematics of Operations Research*, vol. 12, no. 2, pp. 262–268, 1987.
- [6] I. Karatzas, "Gittins indices in the dynamic allocation problem for diffusion processes," *The Annals of Probability*, vol. 12, no. 1, pp. 173–192, 1984.
- [7] H. Kaspi and A. Mandelbaum, "Levy bandits: multi-armed bandits driven by Levy processes," *The Annals of Applied Probability*, vol. 5, no. 2, pp. 541–565, 1995.
- [8] P. Bolton and C. Harris, "Strategic experimentation," *Econometrica*, vol. 67, no. 2, pp. 349–374, 1999.
- [9] D. Bergemann and J. Valimaki, "Experimentation in markets," *Review of Economic Studies*, vol. 67, no. 2, pp. 213–234, 2000.
- [10] X. Gao, H. Liang, and T. Wang, "A common value experimentation with multiarmed bandits," *Mathematical Problems in Engineering*, vol. 2018, Article ID 4791590, 8 pages, 2018.
- [11] A. Cohen and E. Solan, "Bandit problems with Lévy processes," *Mathematics of Operations Research*, vol. 38, no. 1, pp. 92–107, 2013.
- [12] Y. Y. Zheng, L. Serdukova, J. Q. Duan, and J. G. Kurths, "Transitions in a genetic transcriptional regulatory system under Lévy motion," *Scientific Reports*, vol. 6, p. 29274, 2016.
- [13] F. Y. Wu, X. L. Chen, Y. Y. Zheng, J. Q. Duan, J. Kurths, and X. F. Li, "Lévy noise induced transition and enhanced stability in a gene regulatory network," *Chaos: An Interdisciplinary Journal of Nonlinear Science*, vol. 28, no. 7, Article ID 075510, 2018.
- [14] D. Kuksov and J. M. Villas-Boas, "When more alternatives lead to less choice," *Marketing Science*, vol. 29, no. 3, pp. 507–524, 2010.
- [15] L. Doval, "Whether or not to open Pandora's box," *Journal of Economic Theory*, vol. 175, pp. 127–158, 2018.
- [16] T. T. Ke, J. M. Villas-Boas, and J. Miguel, "Optimal learning before choice," *Journal of Economic Theory*, vol. 180, pp. 383–437, 2019.
- [17] Q. Li, Y. M. Fang, J. X. Li, and Z. Ma, "Nonlinear compound control for nonsinusoidal vibration of the mold driven by servo motor with variable speed," *Mathematical Problems in Engineering*, vol. 2019, Article ID 1728768, 9 pages, 2019.
- [18] Y. F. Xin, T. Z. Zhang, H. X. Zhang, Q. H. Zhao, J. Zheng, and C. C. Wang, "Fuzzy logic optimization of composite brake control strategy for load-isolated electric bus," *Mathematical*

- Problems in Engineering*, vol. 2019, Article ID 9735368, 14 pages, 2019.
- [19] R. S. Liptser and A. N. Shiryaev, *Statistics of Random Processes II: Applications*, Springer, Berlin, Germany, 2001.
  - [20] D. Applebaum, *Lévy Processes and Stochastic Calculus*, Cambridge University Press, New York, NY, USA, 2nd edition, 2009.
  - [21] J. Duan, *An Introduction to Stochastic Dynamics*, Cambridge University Press, New York, NY, USA, 2015.
  - [22] Z. Liu and K. Sun, “Almost automorphic solutions for stochastic differential equations driven by Lévy noise,” *Journal of Functional Analysis*, vol. 266, no. 3, pp. 1115–1149, 2014.
  - [23] N. Ikeda and S. Watanabe, *Stochastic Differential Equations and Diffusion Processes*, Kodansha, Tokyo, Japan, 2nd edition, 1989.
  - [24] S. Albeverio, Z. Brzeźniak, and J.-L. Wu, “Existence of global solutions and invariant measures for stochastic differential equations driven by Poisson type noise with non-Lipschitz coefficients,” *Journal of Mathematical Analysis and Applications*, vol. 371, no. 1, pp. 309–322, 2010.

## Research Article

# Adaptive Vector Nonsingular Terminal Sliding Mode Control for a Class of n-Order Nonlinear Dynamical Systems with Uncertainty

Nannan Shi <sup>1</sup>, Zhikuan Kang <sup>1</sup>, Zhuo Zhao <sup>1</sup> and Qiang Meng <sup>2</sup>

<sup>1</sup>Seismic Engineering and Structure Key Laboratory of Beijing, Beijing University of Technology, Beijing 100124, China

<sup>2</sup>Beijing RULEBIT Intelligent Robot Technology Co., Ltd., Beijing 100000, China

Correspondence should be addressed to Qiang Meng; [qiang.meng@rulebittech.com](mailto:qiang.meng@rulebittech.com)

Received 28 November 2019; Revised 7 February 2020; Accepted 19 February 2020; Published 30 March 2020

Guest Editor: Jing Na

Copyright © 2020 Nannan Shi et al. This is an open access article distributed under the Creative Commons Attribution License, which permits unrestricted use, distribution, and reproduction in any medium, provided the original work is properly cited.

This paper proposed an adaptive vector nonsingular terminal sliding mode control (NTSMC) algorithm for the finite-time tracking control of a class of n-order nonlinear dynamical systems with uncertainty. The adaptive vector NTSMC incorporates a vector design idea and novel adaptive updating laws based on the commonly used NTSMC, which consider the common existence of the degree-of-freedom (DOF) directional differences and eliminate the chattering problem. The closed-loop stability of the n-order nonlinear dynamical systems under the adaptive vector NTSMC is demonstrated using Lyapunov direct method. Simulations performed on a two-degree-of-freedom (DOF) manipulator are provided to illustrate the effectiveness and advantages of the proposed adaptive vector NTSMC by comparing with the common NTSMC.

## 1. Introduction

Sliding mode control (SMC), which provides invariance to uncertainty, is one of the effective and efficient nonlinear robust control schemes [1, 2]. It has been successfully implemented in many systems, such as induction motor [3], Stewart platform [4], car-like mobile robots [5], and PMSM speed regulation system [6, 7]. Essentially, two basic components cause the characteristics of the SMC: a driving effort that forces the system states to reach and stay on a stable hyperplane, and a sliding surface achieves the desired error dynamics [8]. Commonly, the linear sliding hyperplane assures asymptotic stability of the system in the sliding mode but cannot make the system state errors converge to zero at a finite time.

To achieve the finite-time convergence of the system state errors, terminal SMC (TSMC) has been derived by introducing a nonlinear sliding mode to provide faster convergence than the linear hyperplane-based sliding mode [8, 9]. However, TSMC has a singularity problem [10]; accordingly, nonsingular TSMC (NTSMC) has been successfully developed to avoid the singularity [10, 11]. Thus, owing to its advantages of insensitive to uncertainty, finite-

time convergence, TSMC, and NTSMC, as variant schemes of SMC, have attracted great attention [12–14] and have also been widely adopted in both linear and nonlinear uncertain systems [15–19].

In the past decade, the appropriate selection of the uncertainty upper bound of the TSMC/NTSMC has been a hot topic, which may cause serious chattering problem as a large one or existence of tracking errors as a low one. To tackle the problem of upper bound design, the adaptive algorithms have been widely investigated in recent years [20–29]. Since the fuzzy logic and neural networks are universal function approximators, the adaptive TSMC/NTSMC schemes which integrated the unknown dynamic-learning algorithms using the function approximators have developed quickly [20–23]. Moreover, other adaptive updating laws have also been proposed to improve the control performances and have been adopted in the multiple motion axis systems [24], DC-DC buck converters [25], uncertain nonlinear SISO systems [26], nonlinear differential inclusion systems [27], and the electromechanical actuator [28], and so on. However, the uncertainty upper bound of the previous adaptive schemes without the function approximators is designed as a constant, which

cannot analyze the common existence of the DOF directional different characteristics. Fortunately, few available control schemes without the finite-convergence performance, whose upper bounds of the uncertainty are designed as vector numbers, have been proposed for spacecraft formation flying [29], a class of MIMO nonlinear systems [30].

Motivated by the above discussion, this paper considers the finite-time stabilization for a class of n-order nonlinear dynamical systems with unknown uncertainty upper bound. The main contributions of this work can be summarized as follows: (i) the upper bound of the uncertainty is designed as a vector, which can analyze the DOF directional different characteristics; (ii) novel adaptive updating laws for the vector upper bound of the uncertainty are derived to improve the performance of usually NTSMC; and (iii) the closed-loop stability of the n-order nonlinear dynamical systems under the proposed adaptive vector NTSMC is demonstrated using Lyapunov direct method.

## 2. Preliminaries

The kinematic and dynamic equations of a class of n-order nonlinear dynamical systems can be described as follows:

$$\dot{\mathbf{x}}_1 = \mathbf{f}_1(\mathbf{x}_1, \mathbf{x}_2), \quad (1)$$

$$\dot{\mathbf{x}}_2 = \mathbf{f}_2(\mathbf{x}_1, \mathbf{x}_2) + \mathbf{G}(\mathbf{x}_1, \mathbf{x}_2)\mathbf{u}, \quad (2)$$

where  $\mathbf{x}_1 \in \mathcal{R}^n$  and  $\mathbf{x}_2 \in \mathcal{R}^n$  represent the system states;  $\mathbf{u} \in \mathcal{R}^n$  is the control vector;  $\mathbf{f}_1(\mathbf{x}_1, \mathbf{x}_2) \in \mathcal{R}^n$  and  $\mathbf{f}_2(\mathbf{x}_1, \mathbf{x}_2) \in \mathcal{R}^n$  are smooth vector functions; and  $\mathbf{G}(\mathbf{x}_1, \mathbf{x}_2) \in \mathcal{R}^{n \times n}$  denotes a nonsingular matrix. The class of n-order nonlinear dynamical system model can be used to describe many physical systems, such as robot manipulators, spacecraft [31], and conventional mechanical systems.

Considering the uncertainty, such as unmodeled dynamics, parameter variation, and external disturbances, the dynamics of the n-order uncertain nonlinear dynamical system can be rewritten as

$$\dot{\mathbf{x}}_2 = \mathbf{f}_{2,0} + \Delta \mathbf{f}_2 + (\mathbf{G}_0 + \Delta \mathbf{g})\mathbf{u}, \quad (3)$$

where  $\mathbf{f}_{2,0}$  and  $\mathbf{G}_0$  denote the estimated terms and  $\Delta \mathbf{f}_2$  and  $\Delta \mathbf{G}$  are the uncertain terms.

(3) can be further rearranged as

$$\dot{\mathbf{x}}_2 = \mathbf{f}_{2,0} + \mathbf{G}_0\mathbf{u} + \boldsymbol{\delta}_{\text{total},n}, \quad (4)$$

$$\boldsymbol{\delta}_{\text{total},n} = \Delta \mathbf{f}_2 + \Delta \mathbf{g}\mathbf{u}. \quad (5)$$

By recalling that the n-order uncertain nonlinear dynamical system is considered (described by (1), (4), and (5)), the following properties can be obtained.

*Assumption 1.*  $\boldsymbol{\delta}_{\text{total},n}$  denotes the uncertainties and disturbances satisfying

$$\|\boldsymbol{\delta}_{\text{total},n}\| \leq b_{1,n} + b_{2,n}\|\mathbf{x}_1\| + b_{3,n}\|\mathbf{x}_2\|^2, \quad (6)$$

where  $b_{1,n}$ ,  $b_{2,n}$ , and  $b_{3,n}$  are the positive numbers and  $\|\cdot\|$  denotes the norm operation.

*Remark 1.* The mathematics model to describe the physical systems is simplified, which is hard to employ the accuracy parameters to consider the uncertainties such as the unmodeled dynamics, parameter variation, and external disturbances. Generally, the boundary of the total uncertainty is assumed to be a constant [12, 14], which is usually enlarged to satisfy the assumption. In practice, the uncertainty is related to the state of the physical systems, such as the motion command of the robots. Therefore, Assumption 1 proposed a more feasible uncertainty boundary considering the influence of the system states, which includes the general constant total uncertainty boundary assumption.

*Remark 2.* In practice, it is probably the existence of the following conditions: (i) there are serious discrepancies between the dynamical characteristics of the different DOF directions; (ii) some DOF directions have special tracking performance demands. Besides, the system state elements ( $x_{1,i}$  and  $x_{2,i}$ ) commonly represent special physical meanings, such as the DOF directional values and control command directional values, which can be directly or indirectly transformed as the DOF directional values. For instance, the DOF directional dynamical performances of the typical Stewart platform are different, especially for the heave direction. Therefore, it is an urgent work to propose a vector NTSMC scheme to consider different design demands or dynamical characteristics corresponding to the special DOF directions.

In this paper, we aim to design a control scheme to obtain the satisfactory tracking performances of the n-order uncertain nonlinear dynamical systems with uncertainty (described by (1), (4), and (5)) and make the tracking error of the nonlinear systems converge to zero in finite time.

## 3. Control Development

In this section, two trajectory tracking controllers are proposed for the n-order uncertain nonlinear dynamical systems with uncertainty (described by (1), (4), and (5)), which can achieve the finite-time convergence of the system state errors.

*3.1. NTSMC for Nonlinear Systems.* The commonly utilized NTSMC algorithm proposed by Feng et al. has been successfully employed in the rigid manipulators and also been extended to the n-order nonlinear dynamical systems [11]. However, in [11], the stability analysis of the NTSMC for the n-order nonlinear dynamical systems has not been mentioned, and the controller is available for the trajectory stabilization of the n-order nonlinear dynamical systems. To overcome this problem, the corresponding NTSMC scheme for the tracking control of the n-order nonlinear dynamical systems is introduced in this section.

To aid the subsequent control development, we define the vector  $\mathbf{V}_{\text{vec}}(\cdot) \in \mathfrak{R}^{n \times 1}$  and matrix  $\mathbf{D}_{\text{diag}}(\cdot) \in \mathfrak{R}^{n \times n}$  as follows:

$$\mathbf{V}_{\text{vec}}(z_i) = [z_1, \dots, z_n]^T, \quad (7)$$

$$\mathbf{D}_{\text{diag}}(z_i) = \text{diag}(z_1, \dots, z_n), \quad (8)$$

where  $\text{diag}(\cdot)$  represents the diagonal matrix function.

Based on the definition of (7) and (8), the sliding surface considered different DOF directional design demands which can be formulated as

$$\mathbf{s} = \boldsymbol{\varepsilon}_1 + \boldsymbol{\Lambda} \mathbf{V}_{\text{vec}}(\dot{\boldsymbol{\varepsilon}}_{1,i}^{p_i/q_i}), \quad (9)$$

$$\boldsymbol{\varepsilon}_1 = \mathbf{x}_1 - \mathbf{x}_{1,d}, \quad (10)$$

$$\boldsymbol{\Lambda} = \mathbf{D}_{\text{diag}}(\lambda_i), \quad (11)$$

where  $\mathbf{x}_{1,d}$  is the desired system state;  $(\cdot)_i$  means the  $i$ th element of  $(\cdot)$ ;  $p_i$ ,  $q_i$ , and  $\lambda_i$  ( $i = 1, \dots, n$ ) are positive numbers; and the condition ( $1 < p_i/q_i < 2$ ) must be satisfied to achieve the nonsingularity of the NTSMC control [11].

The proposed NTSMC scheme can be formulated as

$$\begin{aligned} \mathbf{u}_{\text{antsmc},n} = & - \left( \frac{\partial \mathbf{f}_1}{\partial \mathbf{x}_2} \mathbf{G}_0 \right)^+ \left( \boldsymbol{\Psi} \|\mathbf{s}\| \left\| \mathbf{D}_{\text{diag}}(\dot{\boldsymbol{\varepsilon}}_{1,i}^{p_i/q_i-1}) \frac{\partial \mathbf{f}_1}{\partial \mathbf{x}_2} \right\| \left( b_{1,n} + b_{2,n} \|\mathbf{x}_1\| + b_{3,n} \|\mathbf{x}_2\|^2 \right) \right. \\ & \left. + \frac{\partial \mathbf{f}_1}{\partial \mathbf{x}_1} \mathbf{f}_1 + \frac{\partial \mathbf{f}_1}{\partial \mathbf{x}_2} \mathbf{f}_{2,0} + \Upsilon^{-1} \boldsymbol{\Lambda}^{-1} \mathbf{V}_{\text{vec}}(\dot{\boldsymbol{\varepsilon}}_{1,i}^{2-p_i/q_i}) - \ddot{\mathbf{x}}_{1,d} \right), \end{aligned} \quad (12)$$

where

$$\Upsilon = \mathbf{D}_{\text{diag}}\left(\frac{p_i}{q_i}\right), \quad (13)$$

$$\boldsymbol{\Psi} = \mathbf{V}_{\text{vec}}\left(\frac{\begin{bmatrix} s_i \dot{\boldsymbol{\varepsilon}}_{1,i}^{p_i/q_i-1} \end{bmatrix}^T}{|s_i \dot{\boldsymbol{\varepsilon}}_{1,i}^{p_i/q_i-1}|^2}\right). \quad (14)$$

Now, we are in a position to state the NTSMC control scheme for  $n$ -order nonlinear dynamical systems.

**Theorem 1.** *Given the  $n$ -order uncertain nonlinear dynamical systems of (1) and (4), the system tracking error  $\boldsymbol{\varepsilon}_1$  will converge to zero in finite time under the NTSMC scheme (designed as (9) and (14)) if Assumption 1 holds.*

*Proof of Theorem 1.* The proof proceeding is divided into two parts: firstly, the finite-time convergence of the sliding surface of NTSMC (9) is proved based on Lyapunov

method; secondly, the convergence time of the tracking error is calculated.

*Step 1.* To this end, the following Lyapunov-like function candidate is adopted:

$$V_{\text{ntsmc},n,i} = \frac{1}{2} s_i^T s_i. \quad (15)$$

Differentiating  $V_{\text{ntsmc},n,i}$  with respect to time and substituting (9) and (10), we have

$$\begin{aligned} \dot{V}_{\text{ntsmc},n,i} &= s_i^T \dot{s}_i = s_i^T \left( \dot{\boldsymbol{\varepsilon}}_1 + \Upsilon \boldsymbol{\Lambda} \mathbf{D}_{\text{diag}}(\dot{\boldsymbol{\varepsilon}}_{1,i}^{p_i/q_i-1}) \boldsymbol{\varepsilon}_1 \right)_i \\ &= s_i^T \left( \dot{\boldsymbol{\varepsilon}}_1 + \Upsilon \boldsymbol{\Lambda} \mathbf{D}_{\text{diag}}(\dot{\boldsymbol{\varepsilon}}_{1,i}^{p_i/q_i-1}) (\mathbf{x}_1 - \ddot{\mathbf{x}}_{1,d}) \right)_i; \end{aligned} \quad (16)$$

According to system models (1) and (4), (16) can be further formulated as

$$\dot{V}_{\text{ntsmc},n,i} = s_i^T \left( \dot{\boldsymbol{\varepsilon}}_1 + \Upsilon \boldsymbol{\Lambda} \mathbf{D}_{\text{diag}}(\dot{\boldsymbol{\varepsilon}}_{1,i}^{p_i/q_i-1}) \left( \frac{\partial \mathbf{f}_1}{\partial \mathbf{x}_1} \mathbf{f}_1 + \frac{\partial \mathbf{f}_1}{\partial \mathbf{x}_2} (\mathbf{f}_{2,0} + \mathbf{G}_0 \mathbf{u} + \boldsymbol{\delta}_{\text{total},n}) - \mathbf{x}_{1,d} \right) \right)_i. \quad (17)$$





$$\frac{1}{2} \frac{d}{dt} s_i^T s_i < -\frac{p_i \lambda_i \|s\|}{q_i} \left\| \mathbf{D}_{\text{diag}}(\dot{\varepsilon}_{1,i}^{p_i/q_i-1}) \frac{\partial \mathbf{f}_1}{\partial \mathbf{x}_2} \right\| \cdot \left( b_{1,n} + b_{2,n} \|\mathbf{x}_1\| + b_{3,n} \|\mathbf{x}_2\|^2 - \|\boldsymbol{\delta}_{\text{total},n}\| \right). \quad (22)$$

Then, we define the following equation when  $s_i \neq 0$ :

$$\min \left( \frac{p_i \lambda_i}{q_i} \left\| \mathbf{D}_{\text{diag}}(\dot{\varepsilon}_{1,i}^{p_i/q_i-1}) \frac{\partial \mathbf{f}_1}{\partial \mathbf{x}_2} \right\| \left( b_{1,n} + b_{2,n} \|\mathbf{x}_1\| + b_{3,n} \|\mathbf{x}_2\|^2 - \|\boldsymbol{\delta}_{\text{total},n}\| \right) \right) = \eta_{1,i} > 0, \quad (23)$$

where  $\eta_{1,i}$  is a positive number and  $\min(\cdot)$  is the minimum of  $(\cdot)$ .

Based on (23), (22) can be rewritten as

$$\frac{1}{2} \frac{d}{dt} s_i^T s_i < -\eta_{1,i} \|s\| < -\eta_{1,i} |s_i|. \quad (24)$$

So, if  $s_i \neq 0$ , the system states will reach the sliding mode  $s_i = 0$  within the finite time  $t_{r,i}$ , which satisfies

$$t_{r,i} \leq -\frac{|s_i(0)|}{\eta_{1,i}}. \quad (25)$$

When the sliding mode  $s_i = 0$  is achieved, the convergence time  $t_{s,i}$  that is taken to travel from  $\varepsilon_{1,i}(t_{r,i}) \neq 0$  to  $\varepsilon_{1,i}(t_{r,i} + t_{s,i}) = 0$  is calculated by

$$t_{s,i} = -\lambda_i^{q_i/p_i} \int_{\varepsilon_{1,i}(t_{r,i})}^0 \varepsilon_{1,i}^{-q_i/p_i} d\varepsilon_{1,i} = \lambda_i^{q_i/p_i} \left( \frac{p_i}{p_i - q_i} \right) |\varepsilon_{1,i}^{1-q_i/p_i}(t_{r,i})|. \quad (26)$$

Therefore, the total finite time  $t_{f,i}$  of the system states can be formulated by

$$t_{f,i} = t_{r,i} + t_{s,i}. \quad (27)$$

Moreover, the total finite time  $t_f$  for all of the system state elements can be given by

$$t_f = \max(t_{f,i}) = \max(t_{r,i} + t_{s,i}). \quad (28)$$

Hence, the asymptotic stability in finite time of the nonlinear dynamical systems under NTSMC has been proved.

**Remark 3.** The improved NTSMC in the previous section solves the following problems: (i) available for the trajectory tracking and trajectory stabilization; (ii) the asymptotic stability in finite time of the nonlinear dynamical systems under NTSMC has been proved. However, there are still some conservatisms of the proposed NTSMC: (i) the upper bound of the uncertainty is chosen as a constant value, but the actual uncertain upper boundary is unknown; (ii) the discrepancies between the dynamical characteristics of different DOF directions cannot be considered owing to the constant number designing of the upper bound.

Thus, an adaptive vector NTSMC algorithm for the  $n$ -order nonlinear dynamical systems is derived in the following section.

### 3.2. Adaptive Vector NTSMC for Nonlinear Systems

**Assumption 2.** To further consider the influences of different dynamical characteristics corresponding to the DOF directions, the total uncertainty is assumed to be bounded as (29), where  $b_{1,n,i}$ ,  $b_{2,n,i}$ , and  $b_{3,n,i}$  are positive numbers, and  $|\cdot|$  means the absolute operation.

$$\left\| \frac{\partial \mathbf{f}_1}{\partial \mathbf{x}_2} \right\| \left( b_{1,n,i} + b_{2,n,i} \|\mathbf{x}_1\| + b_{3,n,i} \|\mathbf{x}_2\|^2 \right) > \left| \left( \frac{\partial \mathbf{f}_1}{\partial \mathbf{x}_2} \boldsymbol{\delta}_{\text{total},n} \right)_i \right|. \quad (29)$$

**Remark 4.** Assumption 1 considers the influence of the system states to induce the uncertainty boundary, which is beneficial to reduce the chattering of the SMC controller. For MIMO systems, the uncertainty boundary can be further reduced by considering different dynamical characteristics corresponding to the DOF directions, which is verified in the literature [4] to propose a novel sliding mode controller for the Stewart platform.

Then, the adaptive vector NTSMC can be formulated by

$$\mathbf{u}_{\text{avntsmc},n} = -\left( \frac{\partial \mathbf{f}_1}{\partial \mathbf{x}_2} \mathbf{G}_0 \right)^+ \left( \boldsymbol{\kappa} \|s\| \left\| \mathbf{D}_{\text{diag}}(\dot{\varepsilon}_{1,i}^{p_i/q_i-1}) \right\| \left\| \frac{\partial \mathbf{f}_1}{\partial \mathbf{x}_2} \right\| \hat{\Gamma}_{\text{adaptive},n} + \frac{\partial \mathbf{f}_1}{\partial \mathbf{x}_1} \mathbf{f}_1 + \frac{\partial \mathbf{f}_1}{\partial \mathbf{x}_2} \mathbf{f}_{2,0} + \mathbf{Y}^{-1} \mathbf{\Lambda}^{-1} \mathbf{V}_{\text{vec}}(\dot{\varepsilon}_{1,i}^{2-p_i/q_i}) - \ddot{\mathbf{x}}_{1,d} \right), \quad (30)$$

$$\boldsymbol{\kappa} = \mathbf{D}_{\text{diag}} \left( \begin{bmatrix} |s_i \dot{\varepsilon}_{1,i}^{p_i/q_i-1}|^T \\ |s_i \dot{\varepsilon}_{1,i}^{p_i/q_i-1}|^2 \end{bmatrix} \right), \quad (31)$$

where  $\hat{\Gamma}_{\text{adaptive},n} \in \mathfrak{R}^{n \times 1}$  represents the estimated upper bound, which is designed as a time-varying vector.

Moreover, the updating laws are chosen as

$$\hat{\Gamma}_{\text{adaptive},n,i} = \hat{b}_{1,n,i} + \hat{b}_{2,n,i} \|\mathbf{x}_1\| + \hat{b}_{3,n,i} \|\mathbf{x}_2\|^2, \quad (32)$$

$$\dot{\hat{b}}_{1,n,i} = d_{1,n,i} \frac{p_i \lambda_i \|s\|}{q_i} \left\| \mathbf{D}_{\text{diag}}(\dot{\varepsilon}_{1,i}^{p_i/q_i-1}) \right\| \left\| \frac{\partial \mathbf{f}_1}{\partial \mathbf{x}_2} \right\|, \quad (33)$$

$$\dot{\hat{b}}_{2,n,i} = d_{2,n,i} \frac{p_i \lambda_i \|s\|}{q_i} \left\| \mathbf{D}_{\text{diag}}(\dot{\varepsilon}_{1,i}^{p_i/q_i-1}) \right\| \left\| \frac{\partial \mathbf{f}_1}{\partial \mathbf{x}_2} \right\| \|\mathbf{x}_1\|, \quad (34)$$

$$\dot{\hat{b}}_{3,n,i} = d_{3,n,i} \frac{p_i \lambda_i \|s\|}{q_i} \left\| \mathbf{D}_{\text{diag}}(\dot{\varepsilon}_{1,i}^{p_i/q_i-1}) \right\| \left\| \frac{\partial \mathbf{f}_1}{\partial \mathbf{x}_2} \right\| \|\mathbf{x}_2\|^2. \quad (35)$$

Therefore, the adaptive vector NTSMC scheme for the  $n$ -order nonlinear dynamical systems can be summarized as follows.

**Theorem 2.** Given the  $n$ -order uncertain nonlinear dynamical systems of (1) and (4), the system tracking error  $\boldsymbol{\varepsilon}_1$  will converge to zero in finite time under the adaptive vector NTSMC scheme (designed as (9) and (30)–(35)) if Assumption 2 holds.

*Proof of Theorem 2.* The proof proceeding is divided into two parts: firstly, the finite-time convergence of the sliding surface of adaptive vector NTSMC (30) is proved based on Lyapunov method; secondly, the convergence time of the tracking error is calculated.

*Step 1.* Consider the following Lyapunov function:

$$V_{\text{avntsmc},n,i} = \frac{1}{2} \left( s_i^T s_i + \frac{1}{d_{1,n,i}} \tilde{b}_{1,n,i}^T \tilde{b}_{1,n,i} + \frac{1}{d_{2,n,i}} \tilde{b}_{2,n,i}^T \tilde{b}_{2,n,i} + \frac{1}{d_{3,n,i}} \tilde{b}_{3,n,i}^T \tilde{b}_{3,n,i} \right), \quad (36)$$

and the mismatch between the actual and estimated value of  $b_{1,n,i}$ ,  $b_{2,n,i}$ , and  $b_{3,n,i}$  can be given by

$$\tilde{b}_{1,n,i} = b_{1,n,i} - \hat{b}_{1,n,i}, \quad (37)$$

$$\tilde{b}_{2,n,i} = b_{2,n,i} - \hat{b}_{2,n,i}, \quad (38)$$

$$\tilde{b}_{3,n,i} = b_{3,n,i} - \hat{b}_{3,n,i}. \quad (39)$$

Taking the time derivative of (36) and substituting (37)–(39), we can obtain

$$\dot{V}_{\text{avntsmc},n,i} = s_i^T \dot{s}_i - \frac{1}{d_{1,n,i}} \tilde{b}_{1,n,i}^T \dot{\hat{b}}_{1,n,i} - \frac{1}{d_{2,n,i}} \tilde{b}_{2,n,i}^T \dot{\hat{b}}_{2,n,i} - \frac{1}{d_{3,n,i}} \tilde{b}_{3,n,i}^T \dot{\hat{b}}_{3,n,i}. \quad (40)$$

Similar to the proof process of Theorem 1, (40) can be further rearranged by substituting (9), (11), (13), (19), and (30):

$$\begin{aligned} \dot{V}_{\text{avntsmc},n,i} &= s_i^T \left( \dot{\mathbf{x}}_1 + \mathbf{Y} \mathbf{A} \mathbf{D}_{\text{diag}}(\dot{\hat{\epsilon}}_{1,i}^{p_i/q_i-1}) \left( \frac{\partial \mathbf{f}_1}{\partial \mathbf{x}_1} \mathbf{f}_1 + \frac{\partial \mathbf{f}_1}{\partial \mathbf{x}_2} (\mathbf{f}_{2,0} + \mathbf{G}_0 \mathbf{u}_{\text{avntsmc},n} + \boldsymbol{\delta}_{\text{total},n}) - \ddot{\mathbf{x}}_{1,d} \right) \right)_i \\ &\quad - \frac{1}{d_{1,n,i}} \tilde{b}_{1,n,i}^T \dot{\hat{b}}_{1,n,i} - \frac{1}{d_{2,n,i}} \tilde{b}_{2,n,i}^T \dot{\hat{b}}_{2,n,i} - \frac{1}{d_{3,n,i}} \tilde{b}_{3,n,i}^T \dot{\hat{b}}_{3,n,i} \\ &= \frac{p_i}{q_i} \lambda_i s_i^T \left( \mathbf{D}_{\text{diag}}(\dot{\hat{\epsilon}}_{1,i}^{p_i/q_i-1}) \frac{\partial \mathbf{f}_1}{\partial \mathbf{x}_2} \boldsymbol{\delta}_{\text{total},n} \right)_i - \frac{p_i}{q_i} \lambda_i s_i^T \left( \mathbf{D}_{\text{diag}}(\dot{\hat{\epsilon}}_{1,i}^{p_i/q_i-1}) \boldsymbol{\kappa} \|\mathbf{s}\| \left\| \mathbf{D}_{\text{diag}}(\dot{\hat{\epsilon}}_{1,i}^{p_i/q_i-1}) \right\| \left\| \frac{\partial \mathbf{f}_1}{\partial \mathbf{x}_2} \right\| \hat{\Gamma}_{\text{adaptive},n} \right)_i \\ &\quad - \frac{1}{d_{1,n,i}} \tilde{b}_{1,n,i}^T \dot{\hat{b}}_{1,n,i} - \frac{1}{d_{2,n,i}} \tilde{b}_{2,n,i}^T \dot{\hat{b}}_{2,n,i} - \frac{1}{d_{3,n,i}} \tilde{b}_{3,n,i}^T \dot{\hat{b}}_{3,n,i}. \end{aligned} \quad (41)$$

Then, (41) can be rewritten as

$$\begin{aligned} \dot{V}_{\text{avntsmc},n,i} &< \frac{p_i}{q_i} \lambda_i \|\mathbf{s}\| \left\| \mathbf{D}_{\text{diag}}(\dot{\hat{\epsilon}}_{1,i}^{p_i/q_i-1}) \right\| \left\| \left( \frac{\partial \mathbf{f}_1}{\partial \mathbf{x}_2} \boldsymbol{\delta}_{\text{total},n} \right)_i \right\| - \frac{p_i}{q_i} \lambda_i s_i^T \left( \mathbf{D}_{\text{diag}}(\dot{\hat{\epsilon}}_{1,i}^{p_i/q_i-1}) \boldsymbol{\kappa} \|\mathbf{s}\| \left\| \mathbf{D}_{\text{diag}}(\dot{\hat{\epsilon}}_{1,i}^{p_i/q_i-1}) \right\| \left\| \frac{\partial \mathbf{f}_1}{\partial \mathbf{x}_2} \right\| \hat{\Gamma}_{\text{adaptive},n} \right)_i \\ &\quad - \frac{1}{d_{1,n,i}} \tilde{b}_{1,n,i}^T \dot{\hat{b}}_{1,n,i} - \frac{1}{d_{2,n,i}} \tilde{b}_{2,n,i}^T \dot{\hat{b}}_{2,n,i} - \frac{1}{d_{3,n,i}} \tilde{b}_{3,n,i}^T \dot{\hat{b}}_{3,n,i}. \end{aligned} \quad (42)$$

Substituting (31) into (42) gives

$$\begin{aligned} \dot{V}_{\text{avntsmc},n,i} &< - \frac{p_i}{q_i} \lambda_i \|\mathbf{s}\| \left\| \mathbf{D}_{\text{diag}}(\dot{\hat{\epsilon}}_{1,i}^{p_i/q_i-1}) \right\| \left( \left\| \frac{\partial \mathbf{f}_1}{\partial \mathbf{x}_2} \right\| \hat{\Gamma}_{\text{adaptive},n,i} - \left\| \left( \frac{\partial \mathbf{f}_1}{\partial \mathbf{x}_2} \boldsymbol{\delta}_{\text{total},n} \right)_i \right\| \right) \\ &\quad - \frac{1}{d_{1,n,i}} \tilde{b}_{1,n,i}^T \dot{\hat{b}}_{1,n,i} - \frac{1}{d_{2,n,i}} \tilde{b}_{2,n,i}^T \dot{\hat{b}}_{2,n,i} - \frac{1}{d_{3,n,i}} \tilde{b}_{3,n,i}^T \dot{\hat{b}}_{3,n,i}. \end{aligned} \quad (43)$$

Substituting (32)–(35) and (37)–(39) into (43) yields

$$\begin{aligned}
& \dot{V}_{\text{avntsmc},n,i} \\
&= -\frac{p_i}{q_i} \lambda_i \|\mathbf{s}\| \left\| \mathbf{D}_{\text{diag}} \left( \dot{\varepsilon}_{1,i}^{p_i/q_i-1} \right) \left( \left\| \frac{\partial \mathbf{f}_1}{\partial \mathbf{x}_2} \right\| \left( \widehat{b}_{1,n,i} + \widehat{b}_{2,n,i} \|\mathbf{x}_1\| + \widehat{b}_{3,n,i} \|\mathbf{x}_2\|^2 \right) - \left| \left( \frac{\partial \mathbf{f}_1}{\partial \mathbf{x}_2} \boldsymbol{\delta}_{\text{total},n} \right)_i \right| \right) \right\| \\
&\quad - \frac{p_i}{q_i} \lambda_i \|\mathbf{s}\| \left\| \mathbf{D}_{\text{diag}} \left( \dot{\varepsilon}_{1,i}^{p_i/q_i-1} \right) \left\| \frac{\partial \mathbf{f}_1}{\partial \mathbf{x}_2} \right\| \left( \widetilde{b}_{1,n,i} + \widetilde{b}_{2,n,i} \|\mathbf{x}_1\| + \widetilde{b}_{3,n,i} \|\mathbf{x}_2\|^2 \right) \right\| \\
&= -\frac{p_i}{q_i} \lambda_i \|\mathbf{s}\| \left\| \mathbf{D}_{\text{diag}} \left( \dot{\varepsilon}_{1,i}^{p_i/q_i-1} \right) \left( \left\| \frac{\partial \mathbf{f}_1}{\partial \mathbf{x}_2} \right\| \left( b_{1,n,i} + b_{2,n,i} \|\mathbf{x}_1\| + b_{3,n,i} \|\mathbf{x}_2\|^2 \right) - \left| \left( \frac{\partial \mathbf{f}_1}{\partial \mathbf{x}_2} \boldsymbol{\delta}_{\text{total},n} \right)_i \right| \right) \right\|.
\end{aligned} \tag{44}$$

Based on (44) and LaSalle's invariant principle [9], we have  $s_i(t) \rightarrow 0$  for any initial state  $(\mathbf{x}_{1,0}, \mathbf{x}_{2,0})$  if Assumption 2 holds.

*Step 2.* We define the following equation when  $s_i \neq 0$ :

$$\begin{aligned}
& \min \left( \frac{p_i}{q_i} \lambda_i \|\mathbf{s}\| \left\| \mathbf{D}_{\text{diag}} \left( \dot{\varepsilon}_{1,i}^{p_i/q_i-1} \right) \left( \left\| \frac{\partial \mathbf{f}_1}{\partial \mathbf{x}_2} \right\| \left( b_{1,n,i} + b_{2,n,i} \|\mathbf{x}_1\| \right. \right. \right. \\
& \quad \left. \left. \left. + b_{3,n,i} \|\mathbf{x}_2\|^2 \right) - \left| \left( \frac{\partial \mathbf{f}_1}{\partial \mathbf{x}_2} \boldsymbol{\delta}_{\text{total},n} \right)_i \right| \right) \right\| \right) = \eta_{2,i} > 0,
\end{aligned} \tag{45}$$

where  $\eta_{2,i}$  is a positive number.

Therefore, the finite time for the  $i$ th system state element  $t_{f,i}$  and total system states  $t_f$  under the adaptive vector NTSMC can be calculated by

$$\begin{aligned}
t_{s,i} &= -\lambda_i^{q_i/p_i} \int_{\varepsilon_{1,i}(t_{r,i})}^0 \varepsilon_{1,i}^{-q_i/p_i} d\varepsilon_{1,i} \\
&= \lambda_i^{q_i/p_i} \left( \frac{p_i}{p_i - q_i} \right) \left| \varepsilon_{1,i}^{1-q_i/p_i}(t_{r,i}) \right|, \\
t_{r,i} &\leq -\frac{|s_i(0)|}{\eta_{2,i}}, \\
t_{f,i} &= t_{r,i} + t_{s,i}, \\
t_f &= \max(t_{f,i}) = \max(t_{r,i} + t_{s,i}).
\end{aligned} \tag{46}$$

Hence, the asymptotic stability in finite time of the nonlinear dynamical systems under adaptive vector NTSMC has been proved.

*Remark 5.* The advantages of the proposed adaptive vector NTSMC can be summarized as follows: (i) the vector design idea of the uncertain upper bound can analyze the DOF directional different characteristics; (ii) novel adaptive updating laws can online adjust the upper bound of the uncertainty, which can extensively eliminate the chattering problem of the SMC schemes.

*Remark 6.* To eliminate the chattering problem of the SMC, the following equations are adopted to replace  $\Psi$  (14) and  $\kappa$  (31) in Theorem 1 and Theorem 2:

$$\begin{aligned}
\Psi &= \mathbf{V}_{\text{vec}} \left( \frac{\begin{bmatrix} s_i \dot{\varepsilon}_{1,i}^{p_i/q_i-1} \end{bmatrix}^T}{\left( |s_i \dot{\varepsilon}_{1,i}^{p_i/q_i-1}| + \varsigma_i \right)^2} \right), \\
\kappa &= \mathbf{D}_{\text{diag}} \left( \frac{\begin{bmatrix} s_i \dot{\varepsilon}_{1,i}^{p_i/q_i-1} \end{bmatrix}^T}{\left( |s_i \dot{\varepsilon}_{1,i}^{p_i/q_i-1}| + \varsigma_i \right)^2} \right),
\end{aligned} \tag{47}$$

where  $\varsigma_i$  is a positive number.

#### 4. Application to the 2-DOF Manipulator

This section presents a comparison study of performance between the adaptive vector NTSMC and the NTSMC with the application to a 2-DOF robot manipulator.

The dynamics of a 2-DOF robot manipulator can be formulated using the Euler–Lagrange equations as follows [32, 33]:

$$\begin{aligned}
& \mathbf{M}(\mathbf{q})\ddot{\mathbf{q}} + \mathbf{C}(\mathbf{q}, \dot{\mathbf{q}})\dot{\mathbf{q}} + \mathbf{D}\dot{\mathbf{q}} + \mathbf{g}(\mathbf{q}) = \boldsymbol{\tau}, \\
\mathbf{M}(\mathbf{q}) &= \begin{bmatrix} k_1 + 2k_2 \cos(q_{\text{rob},2}) & k_3 + k_2 \cos(q_{\text{rob},2}) \\ k_3 + k_2 \cos(q_{\text{rob},2}) & k_3 \end{bmatrix}, \\
\mathbf{C}(\mathbf{q}, \dot{\mathbf{q}}) &= \begin{bmatrix} -k_2 \sin(q_{\text{rob},2}) \dot{q}_{\text{rob},2} & -k_2 \sin(q_{\text{rob},2}) \dot{q}_{\text{rob},2} \\ k_2 \sin(q_{\text{rob},2}) \dot{q}_{\text{rob},1} & 0 \end{bmatrix}, \\
\mathbf{D} &= \mathbf{D}_{\text{diag}}(0, \dots, 0), \\
\mathbf{g}(\mathbf{q}) &= \begin{bmatrix} k_4 \sin(q_{\text{rob},1}) + k_5 \sin(q_{\text{rob},1} + q_{\text{rob},2}) \\ k_5 \sin(q_{\text{rob},1} + q_{\text{rob},2}) \end{bmatrix},
\end{aligned} \tag{48}$$

where  $k_1, k_2, k_3, k_4$ , and  $k_5$  (SI units) are 8.77, 0.51, 0.76, 74.48, and 6.174, respectively.

Based on the previous description, the NTSMC and adaptive vector NTSMC available for the two-DOF robot manipulator can be formulated as follows:

Sliding surface:

$$\mathbf{s}_{\text{rob}} = \boldsymbol{\varepsilon}_{\text{rob}} + \mathbf{D}_{\text{diag}}(\lambda_i) \mathbf{V}_{\text{vec}}(\dot{\boldsymbol{\varepsilon}}_{\text{rob},i}^{p_i/q_i}). \quad (49)$$

NTSMC:

$$\boldsymbol{\tau}_{\text{ntsmc,rob}} = -\mathbf{M}_0 \left( \begin{array}{l} \mathbf{V}_{\text{vec}} \left( \frac{\left[ \begin{array}{c} s_{\text{rob},i} \dot{\boldsymbol{\varepsilon}}_{\text{rob},i}^{p_i/q_i-1} \\ |s_{\text{rob},i} \dot{\boldsymbol{\varepsilon}}_{\text{rob},i}^{p_i/q_i-1}|^2 \end{array} \right]^T}{|s_{\text{rob},i} \dot{\boldsymbol{\varepsilon}}_{\text{rob},i}^{p_i/q_i-1}|^2} \right) \|\mathbf{s}_{\text{rob}}\| \|\mathbf{D}_{\text{diag}}(\dot{\boldsymbol{\varepsilon}}_{\text{rob},i}^{p_i/q_i-1})\| (b_{1,\text{rob}} + b_{2,\text{rob}} \|\mathbf{q}\| + b_{3,\text{rob}} \|\dot{\mathbf{q}}\|^2) + \mathbf{M}_0^{-1} (-\mathbf{C}_0(\mathbf{q}, \dot{\mathbf{q}}) \dot{\mathbf{q}}_d - \mathbf{D}_0 \dot{\mathbf{q}}_d - \mathbf{g}_0(\mathbf{q})) \\ + \mathbf{D}_{\text{diag}}^{-1} \left( \frac{p_i}{q_i} \right) \mathbf{D}_{\text{diag}}^{-1}(\lambda_i) \mathbf{V}_{\text{vec}}(\dot{\boldsymbol{\varepsilon}}_{\text{rob},i}^{2-p_i/q_i}) - \ddot{\mathbf{q}}_d \end{array} \right). \quad (50)$$

Adaptive vector NTSMC:

$$\boldsymbol{\tau}_{\text{avntsmc,rob}} = -\mathbf{M}_0 \left( \begin{array}{l} \mathbf{D}_{\text{diag}} \left( \frac{\left[ \begin{array}{c} s_{\text{rob},i} \dot{\boldsymbol{\varepsilon}}_{\text{rob},i}^{p_i/q_i-1} \\ |s_{\text{rob},i} \dot{\boldsymbol{\varepsilon}}_{\text{rob},i}^{p_i/q_i-1}|^2 \end{array} \right]^T}{|s_{\text{rob},i} \dot{\boldsymbol{\varepsilon}}_{\text{rob},i}^{p_i/q_i-1}|^2} \right) \|\mathbf{s}_{\text{rob}}\| \|\mathbf{D}_{\text{diag}}(\dot{\boldsymbol{\varepsilon}}_{\text{rob},i}^{p_i/q_i-1})\| \hat{\Gamma}_{\text{adaptive,rob}} + \mathbf{M}_0^{-1} (-\mathbf{C}_0(\mathbf{q}, \dot{\mathbf{q}}) \dot{\mathbf{q}}_d - \mathbf{D}_0 \dot{\mathbf{q}}_d - \mathbf{g}_0(\mathbf{q})) \\ + \mathbf{D}_{\text{diag}}^{-1} \left( \frac{p_i}{q_i} \right) \mathbf{D}_{\text{diag}}^{-1}(\lambda_i) \mathbf{V}_{\text{vec}}(\dot{\boldsymbol{\varepsilon}}_{\text{rob},i}^{2-p_i/q_i}) - \ddot{\mathbf{q}}_d \end{array} \right), \quad (51)$$

$$\hat{\Gamma}_{\text{adaptive,rob},i} = \hat{b}_{1,\text{rob},i} + \hat{b}_{2,\text{rob},i} \|\mathbf{q}\| + \hat{b}_{3,\text{rob},i} \|\dot{\mathbf{q}}\|^2,$$

$$\dot{\hat{b}}_{1,\text{rob},i} = d_{1,\text{rob},i} \frac{p_i}{q_i} \lambda_i \|\mathbf{s}_{\text{rob}}\| \|\mathbf{D}_{\text{diag}}(\dot{\boldsymbol{\varepsilon}}_{\text{rob},i}^{p_i/q_i-1})\|,$$

$$\dot{\hat{b}}_{2,\text{rob},i} = d_{2,\text{rob},i} \frac{p_i}{q_i} \lambda_i \|\mathbf{s}_{\text{rob}}\| \|\mathbf{D}_{\text{diag}}(\dot{\boldsymbol{\varepsilon}}_{\text{rob},i}^{p_i/q_i-1})\| \|\mathbf{q}\|,$$

$$\dot{\hat{b}}_{3,\text{rob},i} = d_{3,\text{rob},i} \frac{p_i}{q_i} \lambda_i \|\mathbf{s}_{\text{rob}}\| \|\mathbf{D}_{\text{diag}}(\dot{\boldsymbol{\varepsilon}}_{\text{rob},i}^{p_i/q_i-1})\| \|\dot{\mathbf{q}}\|^2.$$

The desired and the initial position trajectories ( $\mathbf{q}_d$ ,  $\mathbf{q}_0$ , and  $\dot{\mathbf{q}}_0$ ) for links 1 and 2 are selected as

$$\begin{aligned} \mathbf{q}_d &= [\sin(\pi t), \sin(\pi t)]^T, \\ \mathbf{q}_0 &= [0.5, 0.5]^T, \\ \dot{\mathbf{q}}_0 &= [2.2, 0]^T. \end{aligned} \quad (52)$$

Considering the influences of the uncertainty and disturbance, the estimated parameters  $k_{1,0}$ ,  $k_{2,0}$ ,  $k_{3,0}$ ,  $k_{4,0}$ , and  $k_{5,0}$  of  $k_1$ ,  $k_2$ ,  $k_3$ ,  $k_4$ , and  $k_5$  are assumed to be 8.77, 0.51, 0.76, 97, and 6.174. Besides, the sampling period is set as 0.5 ms, and the saturation value of torque is set as 80 Nm. For fair comparison, the control parameters (except the uncertainty upper bound designing) of NTSMC and adaptive vector NTSMC are chosen as the same:  $\lambda_1 = \lambda_2 = 1$ ,  $p_1 = p_2 = 9$ ,  $q_1 = q_2 = 5$ , and  $\varsigma_1 = \varsigma_2 = 0.001$ . Moreover, to illustrate the

effectiveness and advantages of the proposed adaptive vector NTSMC, three NTSMC with different upper bounds are given as follows:

NTSMC1:

$$0.8 + 1.8 \|\mathbf{q}\| + 0.09 \|\dot{\mathbf{q}}\|^2. \quad (53)$$

NTSMC2:

$$2.4 + 5.4 \|\mathbf{q}\| + 0.27 \|\dot{\mathbf{q}}\|^2. \quad (54)$$

NTSMC3:

$$7.2 + 16.2 \|\mathbf{q}\| + 0.8 \|\dot{\mathbf{q}}\|^2. \quad (55)$$

Adaptive vector NTSMC:

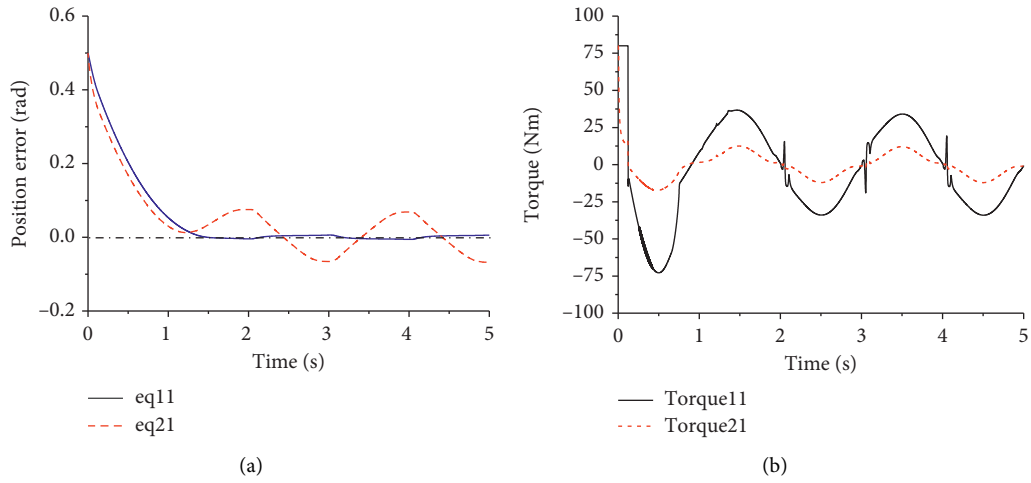


FIGURE 1: Position tracking errors and input torque of the n-order nonlinear dynamical systems under NTSMC1.

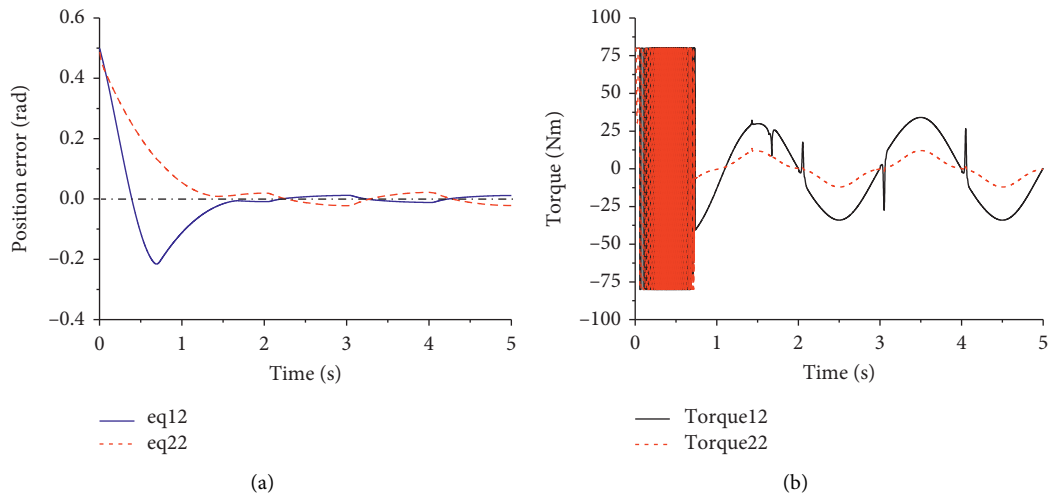


FIGURE 2: Position tracking errors and input torque of n-order nonlinear dynamical systems under NTSMC2.

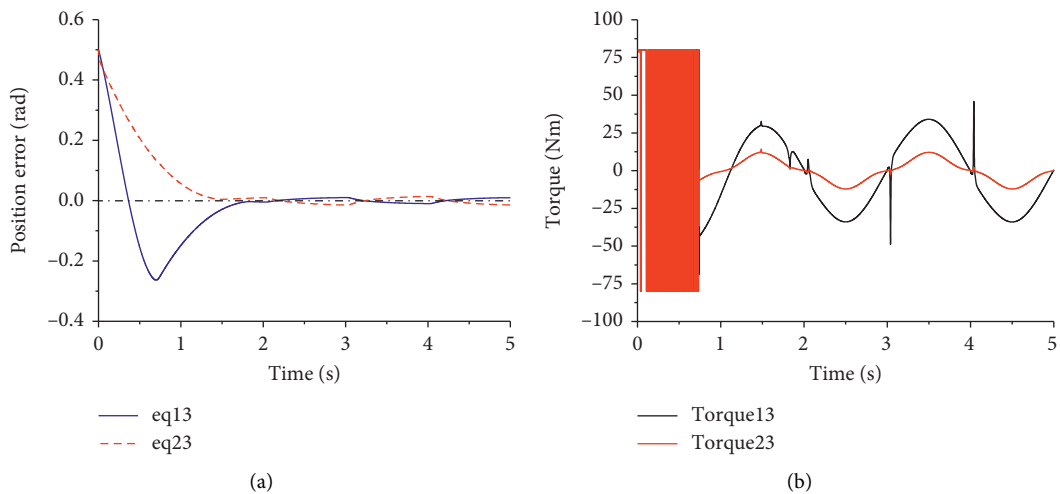


FIGURE 3: Position tracking errors and input torque of n-order nonlinear dynamical systems under NTSMC3.

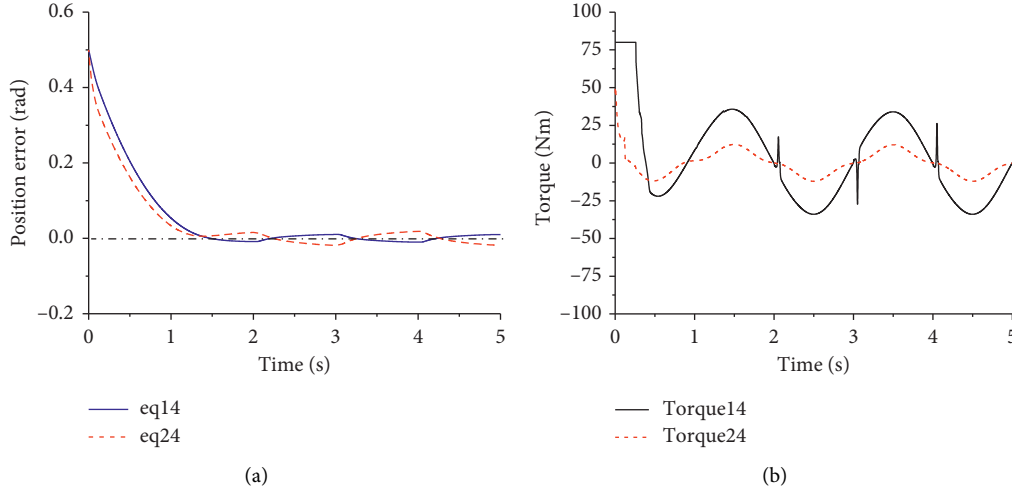


FIGURE 4: Position tracking errors and input torque of n-order nonlinear dynamical systems under NTSMC4.

$$\begin{aligned}
 d_{1,rob,1} &= 10, \\
 d_{1,rob,2} &= 1.8, \\
 d_{2,rob,1} &= 17, \\
 d_{2,rob,2} &= 2, \\
 d_{3,rob,1} &= 0.001, \\
 d_{3,rob,2} &= 0.001, \\
 \hat{b}_{1,rob,1,0} &= 1, \\
 \hat{b}_{1,rob,2,0} &= 0.1, \\
 \hat{b}_{2,rob,1,0} &= 1, \\
 \hat{b}_{2,rob,2,0} &= 0.1, \\
 \hat{b}_{3,rob,1,0} &= 0.1, \\
 \hat{b}_{3,rob,2,0} &= 0.1,
 \end{aligned} \tag{56}$$

where  $\hat{b}_{1,rob,1,0}$ ,  $\hat{b}_{1,rob,2,0}$ ,  $\hat{b}_{2,rob,1,0}$ ,  $\hat{b}_{2,rob,2,0}$ ,  $\hat{b}_{3,rob,1,0}$ , and  $\hat{b}_{3,rob,2,0}$  are the initial values of  $\hat{b}_{1,rob,1}$ ,  $\hat{b}_{1,rob,2}$ ,  $\hat{b}_{2,rob,1}$ ,  $\hat{b}_{2,rob,2}$ ,  $\hat{b}_{3,rob,1}$ , and  $\hat{b}_{3,rob,2}$ .

Figures 1–4 illustrate the tracking errors and input torque under the NTSMC1, NTSMC2, NTSMC3, and adaptive vector NTSMC, where “eq $ij$ ” and “torque $ij$ ” mean the tracking error and input torque of the  $i$ th link under the  $j$ th control scheme, respectively. NTSMC1, NTSMC2, NTSMC3, and adaptive vector NTSMC represent the 1st, 2nd, 3rd, and 4th control schemes.

It can be seen that the tracking errors of the nonlinear system under the NTSMC2, NTSMC3, and the adaptive vector NTSMC can be converged to the acceptable level in finite time (about 1.5 s), but the tracking error of the second link under NTSMC1 is obvious even in the stabilization period (about 0.07 rad after 1.5 s). Besides, the tracking errors of the first link have amplitude overshoot (0.22 rad for NTSMC2 and 0.26 rad for NTSMC3) under NTSMC2 and NTSMC3 in the initial 1.5 s. From the comparison, it can be clearly seen that the proposed adaptive vector NTSMC can

obtain a much faster transient and better tracking performance in comparison with the NTSMC. Moreover, considering the input torque of the controllers, the chattering problems under NTSMC2 and NTSMC3 are serious, and the input commands of NTSMC1 and adaptive vector NTSMC are smooth. As a result, from the simulations, we can conclude that the proposed adaptive vector NTSMC can solve the problem of finite-time tracking without chattering phenomenon.

To clearly show the effectiveness and advantages of the proposed adaptive vector NTSMC, we simply explain the results illustrated in Figures 1–4. Firstly, the vector upper bound analyzes different dynamical characteristics of the two-DOF manipulator (the peak torque of the first link and the second link is about 36 Nm and 12 Nm, respectively). Secondly, the initial position errors of the dynamical system usually cause serious chattering in the initial time for the SMC schemes, which also was resolved by introducing of novel adaptive updating laws for the upper bound.

## 5. Conclusions

In this paper, we considered the finite-time tracking problem of n-link nonlinear dynamical systems with uncertainty. The well-known NTSMC for the robot manipulator was extended to the general n-link nonlinear dynamical systems, and the corresponding rigorous stability analysis of the NTSMC for the nonlinear systems was also established based on the Lyapunov method. Moreover, a novel adaptive vector NTSMC is further proposed by replacing the constant upper bound with an adaptive vector bound, and its asymptotic stability has also been analyzed. Furthermore, the convergence times of the NTSMC and adaptive vector NTSMC are calculated for the nonlinear system. Finally, simulations performed on a two-DOF manipulator demonstrate the effectiveness and advantages of the proposed adaptive vector NTSMC in comparison with the NTSMC. The developed controller offers an alternative approach to a large class of nonlinear systems, which considers different dynamical



characteristics and special design demands and eliminates the chattering problem existing in the common SMC schemes.

### Data Availability

The data used to support the findings of this study are included within the article.

### Conflicts of Interest

The authors declare that they have no conflicts of interest.

### Acknowledgments

The authors are grateful for the financial support of this work by the National Natural Science Foundation of China (no. 51708008).



### References

- [1] V. Utkin, "Variable structure systems with sliding modes," *IEEE Transactions on Automatic Control*, vol. 22, no. 2, pp. 212–222, 1977.
- [2] J. Yang, S. Li, and X. Yu, "Sliding-mode control for systems with mismatched uncertainties via a disturbance observer," *IEEE Transactions on Industrial Electronics*, vol. 60, no. 1, pp. 160–169, 2013.
- [3] O. Barambones and P. Alkorta, "Position control of the induction motor using an adaptive sliding-mode controller and observers," *IEEE Transactions on Industrial Electronics*, vol. 61, no. 12, pp. 6556–6565, 2014.
- [4] Q. Meng, T. Zhang, X. Gao, and J.-Y. Song, "Adaptive sliding mode fault-tolerant control of the uncertain Stewart platform based on offline multibody dynamics," *IEEE/ASME Transactions on Mechatronics*, vol. 19, no. 3, pp. 882–894, 2014.
- [5] C.-L. Hwang, L.-J. Chang, and Y.-S. Yu, "Network-based fuzzy decentralized sliding-mode control for car-like mobile robots," *IEEE Transactions on Industrial Electronics*, vol. 54, no. 1, pp. 574–585, 2007.
- [6] S. Li, M. Zhou, and X. Yu, "Design and implementation of terminal sliding mode control method for PMSM speed regulation system," *IEEE Transactions on Industrial Informatics*, vol. 9, no. 4, pp. 1879–1891, 2013.
- [7] Y. Wang, Y. Feng, X. Zhang, and J. Liang, "A new reaching law for antidisturbance sliding-mode control of PMSM speed regulation system," *IEEE Transactions on Power Electronics*, vol. 35, no. 4, pp. 4117–4126, 2020.
- [8] M. Jin, J. Lee, P. Chang, and C. Choi, "Practical nonsingular terminal sliding-mode control of robot manipulators for high-accuracy tracking control," *IEEE Transactions on Industrial Electronics*, vol. 56, no. 9, pp. 3593–3601, 2009.
- [9] J. J. E. Sloine and W. Li, *Applied Nonlinear Control*, Prentice-Hall, Enlewood Cliffs, NJ, USA, 1991.
- [10] Y. Wu, X. Yu, and Z. Man, "Terminal sliding mode control design for uncertain dynamic systems," *Systems & Control Letters*, vol. 34, no. 5, pp. 281–287, 1998.
- [11] Y. Feng, X. Yu, and Z. Man, "Non-singular terminal sliding mode control of rigid manipulators," *Automatica*, vol. 38, no. 12, pp. 2159–2167, 2002.
- [12] S. Li, H. Du, and X. Yu, "Discrete-time terminal sliding mode control systems based on euler's discretization," *IEEE Transactions on Automatic Control*, vol. 59, no. 2, pp. 546–552, 2014.
- [13] C. Mu, W. Xu, and C. Sun, "On switching manifold design for terminal sliding mode control," *Journal of the Franklin Institute*, vol. 353, no. 7, pp. 1553–1572, 2016.
- [14] C. Mu and H. He, "Dynamic behavior of terminal sliding mode control," *IEEE Transactions on Industrial Electronics*, vol. 65, no. 4, pp. 3480–3490, 2018.
- [15] H. Wang, Z.-Z. Han, Q.-Y. Xie, and W. Zhang, "Finite-time chaos control via nonsingular terminal sliding mode control," *Communications in Nonlinear Science and Numerical Simulation*, vol. 14, no. 6, pp. 2728–2733, 2009.
- [16] S.-Y. Chen and F.-J. Lin, "Robust nonsingular terminal sliding-mode control for nonlinear magnetic bearing system," *IEEE Transactions on Control Systems Technology*, vol. 19, no. 3, pp. 636–643, 2011.
- [17] J. Yang, S. Li, J. Su, and X. Yu, "Continuous nonsingular terminal sliding mode control for systems with mismatched disturbances," *Automatica*, vol. 49, no. 7, pp. 2287–2291, 2013.
- [18] Y. Feng, S. Bao, and X. Yu, "Inverse dynamics nonsingular terminal sliding mode control of two-link flexible manipulators," *International Journal of Robotics & Automation*, vol. 19, no. 2, pp. 91–102, 2004.
- [19] Y. Feng, X. Yu, and F. Han, "On nonsingular terminal sliding-mode control of nonlinear systems," *Automatica*, vol. 49, no. 6, pp. 1715–1722, 2013.
- [20] D. Z. Xu, B. Jiang, M. S. Qian, and J. Zhao, "Terminal sliding mode control using adaptive fuzzy-neural observer," *Mathematical Problems in Engineering*, vol. 2013, Article ID 958958, 8 pages, 2013.
- [21] L. Cao, X. Chen, and T. Sheng, "Fault tolerant small satellite attitude control using adaptive non-singular terminal sliding mode," *Advances in Space Research*, vol. 51, no. 12, pp. 2374–2393, 2013.
- [22] V. Nekoukar and A. Erfanian, "Adaptive fuzzy terminal sliding mode control for a class of MIMO uncertain nonlinear systems," *Fuzzy Sets and Systems*, vol. 179, no. 1, pp. 34–49, 2011.
- [23] C.-K. Lin, "Nonsingular terminal sliding mode control of robot manipulators using fuzzy wavelet networks," *IEEE Transactions on Fuzzy Systems*, vol. 14, no. 6, pp. 849–859, 2006.
- [24] D. Zhao, S. Li, Q. Zhu, and F. Gao, "Robust adaptive terminal sliding mode-based synchronised position control for multiple motion axes systems," *IET Control Theory & Applications*, vol. 3, no. 1, pp. 136–150, 2009.
- [25] H. Komurcugil, "Adaptive terminal sliding-mode control strategy for DC-DC buck converters," *ISA Transactions*, vol. 51, no. 6, pp. 673–681, 2012.
- [26] W. Q. Tang and Y. L. Cai, "High-order sliding mode control design based on adaptive terminal sliding mode," *International Journal of Robust and Nonlinear Control*, vol. 23, no. 2, pp. 149–166, 2013.
- [27] J. Huang, L. N. Sun, and Z. Z. Han, "Adaptive terminal sliding mode control for nonlinear differential inclusion systems with disturbance," *Nonlinear Dynamics*, vol. 72, no. 1–2, pp. 221–228, 2013.
- [28] H. Li, L. Dou, and Z. Su, "Adaptive nonsingular fast terminal sliding mode control for electromechanical actuator," *International Journal of Systems Science*, vol. 44, no. 3, pp. 401–415, 2013.
- [29] J. Wang and Z. Sun, "6-DOF robust adaptive terminal sliding mode control for spacecraft formation flying," *ACTA Astronautica*, vol. 73, pp. 76–87, 2012.

- [30] A. Nasiri, S. Kiong Nguang, and A. Swain, "Adaptive sliding mode control for a class of MIMO nonlinear systems with uncertainties," *Journal of the Franklin Institute*, vol. 351, no. 4, pp. 2048–2061, 2014.
- [31] G. Shen, Z.-C. Zhu, X. Li et al., "Robust fault-tolerant tracking control for a class of nonlinear systems based on position measurements only," *Proceedings of the Institution of Mechanical Engineers, Part E: Journal of Process Mechanical Engineering*, vol. 230, no. 6, pp. 486–497, 2016.
- [32] A. Loria and H. Nijmeijer, "Bounded output feedback tracking control of fully actuated Euler-Lagrange systems," *Systems & Control Letters*, vol. 33, no. 3, pp. 151–161, 1998.
- [33] Y. Su, "Global continuous finite-time tracking of robot manipulators," *International Journal of Robust and Nonlinear Control*, vol. 19, no. 17, pp. 1871–1885, 2009.

## Research Article

# U-Model Based Adaptive Neural Networks Fixed-Time Backstepping Control for Uncertain Nonlinear System

Jianhua Zhang <sup>1,2,3</sup>, Yang Li <sup>1,3</sup>, Wenbo Fei <sup>1,2</sup> and Xueli Wu <sup>1,2</sup>

<sup>1</sup>Hebei University of Science and Technology, Shijiazhuang, Hebei 050018, China

<sup>2</sup>Hebei Provincial Research Center for Technologies in Process Engineering Automation, Shijiazhuang, Hebei 050018, China

<sup>3</sup>School of Information and Control Engineering, Qingdao University of Technology, Qingdao, Shandong 266520, China

Correspondence should be addressed to Jianhua Zhang; [jianhuazhang@aliyun.com](mailto:jianhuazhang@aliyun.com)

Received 21 January 2020; Accepted 20 February 2020; Published 23 March 2020

Guest Editor: Jing Na

Copyright © 2020 Jianhua Zhang et al. This is an open access article distributed under the Creative Commons Attribution License, which permits unrestricted use, distribution, and reproduction in any medium, provided the original work is properly cited.

Under U-model control design framework, a fixed-time neural networks adaptive backstepping control is proposed. The majority of the previously described adaptive neural controllers were based on uniformly ultimately bounded (UUB) or practical finite stable (PFS) theory. For neural networks control, it makes the control law as well as stability analysis highly lengthy and complicated because of the unknown ideal weight and unknown approximation error. Moreover, there has been very limited research focus on adaptive law for neural networks adaptive control in finite time. Based on fixed-time stability theory, a fixed-time bounded theory is proposed for fixed-time neural networks adaptive backstepping control. The most outstanding novelty is that fixed-time adaptive law for training weights of neural networks is proposed for fixed-time neural networks adaptive control. Furthermore, by combining fixed-time adaptive law and Lyapunov-based arguments, a valid fixed-time controller design algorithm is presented with universal approximation property of neural networks to ensure the system is fixed-time bounded, rather than PFS or UUB. The controller guarantees closed-loop system fixed-time bounded in the Lyapunov sense. The benchmark simulation demonstrated effectiveness and efficiency of the proposed approach.

## 1. Introduction

Recently, neural networks control has increasingly attracted attention and intensive research has been performed in adaptive law for training neural networks weights and application in different fields [1–3]. Neural network technique is a typical data-driven modelling method [4–6], which used measured data to find proper control in reversion of some expected closed-loop performance [7–9]. U-model control [10, 11] played an important role in some complex systems. U-model control, due to its capability to solve some complex problems as model separated design, provides a general way to separate system design process and control design process. U model control method makes control process explicitness and is easy to control. It provides a control direction to design the system controller. U model NNs control makes system control easy and clear based on the approximation ability of NNs.

The majority of the neural networks controllers previously used for nonlinear systems [12] are based on UUB theory and sliding mode schemes [13–15]. The conventional adaptive law for training neural networks and feedback control is linear feedback which makes the system exponential stable [16, 17] or exponentially bounded [18–20]. Finite time [21, 22] and fixed-time [14] stable results are more meaningful for uncertain nonlinear systems.

Motivated by the above critical analyses, fixed-time adaptive neural networks controller for uncertain nonlinear systems is proposed. We extend the prior works [23, 24] to the fixed-time case in which closed-loop systems are global bounded with fixed time. Fixed-time neural networks control is proposed in order to deal with convergence time of the neural networks control. The main contributions of this paper can be summarized as follows:

- (1) Fixed-time adaptive neural networks for uncertain nonlinear systems are proposed. As mentioned, this paper is the first study to propose convergence time as the fixed time for neural networks control.
- (2) For training neural networks weights, a new adaptive law is proposed to realize the fixed-time neural networks adaptive control for training neural network weights based on Lyapunov bounded theory.
- (3) U-model control technology, which is a model-independent design technology, is used to realize the model-independent control system design.

The rest of this paper is organized as follows. Section 2 gives problem formulation and preliminaries, including necessary inequality and some lemmas with necessary proof. In Section 3, a fixed-time bounded theory is proposed for fixed-time neural networks adaptive backstepping control based on U-model control. Based on fixed-time theory, a new fixed-time adaptive law is developed for training neural networks to control the the nonlinear system, and Lyapunov fixed-time bounded theory is used to guaranteeing the closed-loop system signals bounded in fixed time in Section 4. In Section 5, a bench test is proposed to indicate efficiency and effectiveness of the procedure. The conclusion is provided in Section 6.

## 2. Problem Description and Preliminaries

In this paper, a general dynamic system can be described as follows:

$$y^{(n)} + f_1(y)y^{(n-1)} + \dots + f_i(y)y^{(n-i)} + \dots + f_n(y)y = u, \quad (1)$$

where  $y \in R$  and  $u \in R$  are state variable and control input, respectively, and  $f_i(\cdot)$  is nonlinear with system state. This model is generally used in some areas, such as mechanical dynamic of the PMSM servo system.

To design the neural networks control, radial basis function (RBF) NN is adopted in order to approximate the continuous function  $F(x): \mathfrak{R}^n \rightarrow \mathfrak{R}$  over a compact set

$$F_{\text{NN}}(x, W) = W^T \Psi(x), \quad (2)$$

where  $x \in \Omega \subset \mathfrak{R}^n$  is neural networks input,  $W = [w_1, \dots, w_l]^T \in \mathfrak{R}^l$  is weight vector,  $\Psi(x) = [\psi_1(x), \dots, \psi_l(x)]^T$  is node vector, and element  $\psi_i(x)$  is Gaussian function in form of

$$\psi_i(x) = \exp\left[\frac{-(x - \mu_i)^T(x - \mu_i)}{\eta_i^2}\right], \quad i = 1, 2, \dots, l, \quad (3)$$

where  $\mu_i = [\mu_{i1}, \dots, \mu_{in}]^T$  is the center of the basis function and  $\eta_i$  is the scalar width of the Gaussian function.

The RBF NNs can be used to approximate any continuous function over a compact set  $\Omega_x \subset \mathfrak{R}^n$  as

$$F(x) = W^{*T} \Psi(x) + \varepsilon(x), \quad (4)$$

where  $\varepsilon(x)$  is the NN approximation error and  $W^*$  is the ideal NN weight which is given as

$$W^* = \arg \min_{W \in \mathfrak{R}^l} \left\{ \sup |F(x) - W^T \Psi(x)| \right\}, \quad (5)$$

where  $\widehat{W}$  is estimated weight and  $\widetilde{W} = \widehat{W} - W^*$ .

To design the fixed-time bounded theory, some lemmas are proposed based on a general nonlinear system:

$$\dot{x} = f(x), \quad (6)$$

where  $x$  is system state.

**Lemma 1** (see [25]). *Suppose that  $V(\cdot): R^n \rightarrow R_+ \cup \{0\}$  is a continuous radically unbounded function and the following two conditions hold:*

- (1)  $V(x) = 0 \iff x = 0$
- (2) Any solution  $x(t)$  of system (6) satisfies

$$\dot{V}(x(t)) \leq -aV^p(x(t)) - bV^q(x(t)), \quad (7)$$

for some  $a, b > 0$ ,  $0 \leq p < 1$ , and  $q > 1$ .

Then, the origin of system (6) can achieve fixed-time stability, and  $T_{\text{max}} = (1/(a(1-p))) + (1/(b(q-1)))$ .

*Remark 1.* In Lemma 1, if  $p = 1 - (1/(2\mu))$  and  $q = 1 + (1/(2\mu))$ , where  $\mu \geq (1/2)$ , then the origin of system (6) can achieve fixed-time stability, and  $T_{\text{max}} = ((\pi\mu)/\sqrt{ab})$ .

**Lemma 2.** For  $x_i \in R$ ,  $i = 1, 2, \dots, n$ ,  $q > 1$ ,  $0 < p < 1$ , then

$$\begin{aligned} \left( \sum_{i=1}^n |x_i| \right)^p &\leq \sum_{i=1}^n |x_i|^p \leq n^{1-p} \left( \sum_{i=1}^n |x_i| \right)^p, \\ n^{1-q} \left( \sum_{i=1}^n |x_i| \right)^q &\leq \sum_{i=1}^n |x_i|^q \leq \left( \sum_{i=1}^n |x_i| \right)^q. \end{aligned} \quad (8)$$

**Lemma 3** (Young's inequality). For any constant  $a, b \in \mathfrak{R}$ , the following inequality holds:

$$ab \leq \frac{1}{p} a^p + \frac{1}{q} b^q, \quad (9)$$

where  $p > 1$ ,  $q > 1$ , and  $(1/p) + (1/q) = 1$ .

## 3. Fixed-Time U-Model Control

In this section, a fixed-time bounded theory is proposed for fixed-time neural networks adaptive control based on U-model control.

**Theorem 1.** *Suppose that  $V(\cdot): R^n \rightarrow R_+ \cup \{0\}$  is a continuous radically unbounded function and the following two conditions hold:*

- (1)  $V(x) = 0 \iff x = 0$
- (2) Any solution  $x(t)$  of system (6) satisfies

$$\dot{V}(x(t)) \leq -aV^p(x(t)) - bV^q(x(t)) + c, \quad (10)$$

for some  $a, b > 0$ ,  $0 \leq p < 1$ ,  $q > 1$ , and  $p, q$  are odd rational number, which means numerator and denominator are both odd numbers.

Then states of system (6) can achieve fixed-time bounded, and the bound  $\xi$  is roots of the equation.

$$2^{p-1}a\xi^p + b\xi^q = c, \text{ fixed-time } T_{\max} = (1/2^{p-1}a(1-p)) + (1/b(q-1)).$$

*Proof.* Assume that  $V > \xi$ ; based on Lemma 2, we have

$$\begin{aligned} \dot{V} &\leq -aV^p - bV^q + c, \\ 2^{p-1}a\xi^p + b\xi^q &= c, \end{aligned} \quad (11)$$

and

$$-aV^p - bV^q + c = -aV^p - bV^q + 2^{p-1}a\xi^p + b\xi^q, \quad (12)$$

because

$$\begin{aligned} -aV^p + 2^{p-1}a\xi^p &\leq -2^{p-1}a(V - \xi)^p, \\ -bV^q + b\xi^q &\leq -b(V - \xi)^q. \end{aligned} \quad (13)$$

Therefore,

$$\dot{V} \leq -2^{p-1}a(V - \xi)^p - b(V - \xi)^q. \quad (14)$$

Let

$$V_\xi = V - \xi. \quad (15)$$

Then,

$$\dot{V}_\xi \leq -2^{p-1}aV_\xi^p - bV_\xi^q. \quad (16)$$

Based on Lemma 1,  $V_\xi$  is fixed-time stable and fixed time; therefore,  $V$  is fixed-time bounded with  $\xi$  and  $T_{\max} = (1/(2^{p-1}a(1-p))) + (1/(b(q-1)))$ , and if  $p = 1 - (1/(2\mu))$  and  $q = 1 + (1/(2\mu))$ , where  $\mu \geq (1/2)$ ,  $T_{\max} = ((\pi\mu)/\sqrt{2^{p-1}ab})$ .

The proof is completed.

For system (1), based on U-model technology, let

$$\begin{cases} x_1 = y - y_d, \\ x_i = y^{(i-1)} - y_d^{(i-1)}, \quad 2 \leq i \leq n. \end{cases} \quad (17)$$

Then, the system can be changed as

$$\begin{cases} \dot{x}_1 = x_2, \\ \dot{x}_i = x_{i+1}, \quad 2 \leq i \leq n-1, \\ \dot{x}_n = -f_1(x_1)x_n - \dots - f_i(x_1)x_{n-i+1} - f_n(x_1)x_1 + u, \\ y = x_1, \end{cases} \quad (18)$$

and then the system can be changed as

$$\begin{cases} \dot{x}_1 = x_2, \\ \dot{x}_i = x_{i+1}, \quad 2 \leq i \leq n-1, \\ \dot{x}_n = U, \\ y = x_1, \end{cases} \quad (19)$$

where

$$U = -f_1(x_1)x_n - \dots - f_i(x_1)x_{n-i+1} - f_n(x_1)x_1 + u, \quad (20)$$

which is a single-input single-output nonlinear system; U-model is used to design the control procedure.

In the first step,

$$z_1 = x_1, \quad (21)$$

and then we have

$$\dot{z}_1 = x_2, \quad (22)$$

and to design fixed-time control, choose the virtual control law

$$\alpha_1 = -a_1z_1^p - b_1z_1^q, \quad (23)$$

where for some  $a_1, b_1 > 0$ ,  $0 \leq p < 1$ ,  $q > 1$ , and  $p, q$  are odd rational numbers, which means numerator and denominator are both odd numbers; then,

$$\dot{z}_1 = -a_1z_1^p - b_1z_1^q + z_2, \quad (24)$$

where

$$z_2 = x_2 - \alpha_1. \quad (25)$$

Therefore, in the  $i$ th step ( $2 \leq i \leq n-1$ ),

$$\dot{z}_i = x_{i+1} - \dot{\alpha}_{i-1}, \quad (26)$$

and to design fixed-time control, choose the virtual control law

$$\alpha_i = -z_{i-1} - a_iz_i^p - b_iz_i^q + \dot{\alpha}_{i-1}, \quad (27)$$

where for some  $a_i, b_i > 0$ ,  $0 \leq p < 1$ ,  $q > 1$ , and  $p, q$  are odd rational numbers, which means numerator and denominator are both odd numbers; then,

$$\dot{z}_i = -z_{i-1} - a_iz_i^p - b_iz_i^q + z_{i+1}, \quad (28)$$

where

$$z_{i+1} = x_{i+1} - \alpha_i. \quad (29)$$

In the last stage, because

$$z_n = x_n - \alpha_{n-1}, \quad (30)$$

we have

$$\dot{z}_n = U - \dot{\alpha}_{n-1}, \quad (31)$$

and to design fixed-time control, choose the U-model control

$$U = -z_{n-1} - a_nz_n^p - b_nz_n^q + \dot{\alpha}_{n-1}, \quad (32)$$

where for some  $a_n, b_n > 0$ ,  $0 \leq p < 1$ ,  $q > 1$ , and  $p, q$  are odd rational numbers, which means numerator and denominator are both odd numbers; then,

$$\dot{z}_n = -z_{n-1} - a_n z_n^p - b_n z_n^q. \quad (33)$$

Under U-model control design framework and fixed-time theory, choose Lyapunov candidate functional

$$V = \frac{1}{2} \sum_{i=1}^n z_i^2, \quad (34)$$

and take time derivative of function (34) along with (24) and (28); (33) is derived as

$$\begin{aligned} \dot{V} &= -\sum_{i=1}^n a_i z_i^{p+1} - \sum_{i=1}^n b_i z_i^{q+1} \\ &\leq -\underline{a} \sum_{i=1}^n z_i^{p+1} - \underline{b} \sum_{i=1}^n z_i^{q+1}, \end{aligned} \quad (35)$$

where  $\underline{a} = \min(a_i)$ ,  $\underline{b} = \min(b_i)$ ,  $i = 1, 2, \dots, n$ ; based on Lemma 2,

$$\begin{aligned} -\sum_{i=1}^n (z_i^2)^{(1+p)/2} &\leq -\left(\sum_{i=1}^n z_i^2\right)^{(1+p)/2} \\ -\sum_{i=1}^n (z_i^2)^{(1+q)/2} &\leq -n^{(1-q)/2} \left(\sum_{i=1}^n z_i^2\right)^{(1+q)/2}. \end{aligned} \quad (36)$$

Therefore,

$$\dot{V} \leq -2^{p_1} \underline{a} V^{p_1} - 2^{q_1} n^{1-q_1} \underline{b} V^{q_1}, \quad (37)$$

where  $p_1 = ((1+p)/2)$ ,  $q_1 = ((1+q)/2)$ , and  $0 \leq p_1 < 1$ ,  $q_1 > 1$ .  $\square$

#### 4. Neural Networks Fixed-Time Control

In the last step of backstepping in equation (32), neural networks are used to approximate the nonlinear system

$$\dot{z}_n = -f_1(x_1)x_n - \dots - f_i(x_1)x_{n-i+1} - f_n(x_1)x_1 - \dot{\alpha}_{n-1} + u, \quad (38)$$

$$u^* = -z_{n-1} + f_1(x_1)x_n + \dots + f_i(x_1)x_{n-i+1} + f_n(x_1)x_1 + \dot{\alpha}_{n-1}, \quad (39)$$

$$-f_1(x_1)x_n - \dots - f_i(x_1)x_{n-i+1} - f_n(x_1)x_1 - \dot{\alpha}_{n-1} = W^{*T} \Psi(\bar{x}_n) + \varepsilon. \quad (40)$$

Choose adaptive law

$$\dot{\hat{W}} = \Gamma [z_n \Psi_n(\bar{x}_n) - a_\sigma \hat{W}^p - b_\sigma \hat{W}^q], \quad (41)$$

where  $\Gamma = \Gamma^T > 0$ , and  $a_\sigma > 0$ ,  $b_\sigma > 0$  are positive constant design parameters.

Finally, choose the controller as

$$u = -\hat{W}^T \Psi(\bar{x}_n) - z_{n-1} - \left(a_n + \frac{\zeta}{p+1}\right) z_n^p - \left(b_n + \frac{1-\zeta}{q+1}\right) z_n^q, \quad (42)$$

where  $0 \leq \zeta \leq 1$ ; then, the system

$$\dot{z}_n = -\tilde{W}^T \Psi(\bar{x}_n) - z_{n-1} - \left(a_n + \frac{\xi}{p+1}\right) z_n^p - \left(b_n + \frac{1-\xi}{q+1}\right) z_n^q + \varepsilon, \quad (43)$$

where  $\tilde{W} = \hat{W} - W^*$ .

**Theorem 2.** With regard to nonlinear system (1), the model dynamic is approximated by neural networks (40), with fixed-time adaptive law (41), with virtual control (23), (27), with controller (42), then the closed loop signal converge to a compact set with fixed-time

$$T_{\max} = \frac{1}{2^{p_2-1} a (1-p_2)} + \frac{1}{b (q_2-1)}. \quad (44)$$

*Proof.* Consider system (1) and Lemmas 1-3.

In  $i$ th ( $1 \leq i \leq n-1$ ) step, choose Lyapunov candidate functional

$$V_i = \frac{1}{2} z_i^2. \quad (45)$$

In the last step, choose Lyapunov candidate functional

$$V_n = \frac{1}{2} z_n^2 + \frac{1}{2} \tilde{W} \Gamma^{-1} \tilde{W}^T, \quad (46)$$

and then take time derivative of function (46) along with trajectory (41), and (43) is derived as

$$\begin{aligned} \dot{V}_n &= z_n \dot{z}_n + \tilde{W} \Gamma^{-1} \dot{\hat{W}}^T \\ &= -z_n \tilde{W}^T \Psi(\bar{x}_n) - z_{n-1} z_n - \left(a_n + \frac{\xi}{p+1}\right) z_n^p \\ &\quad - \left(b_n + \frac{1-\xi}{q+1}\right) z_n^q + z_n \varepsilon \\ &\quad + z_n \tilde{W} \Psi_n(\bar{x}_n) - a_\sigma \tilde{W} \hat{W}^p - b_\sigma \tilde{W} \hat{W}^q. \end{aligned} \quad (47)$$

Based on Lemma 3,



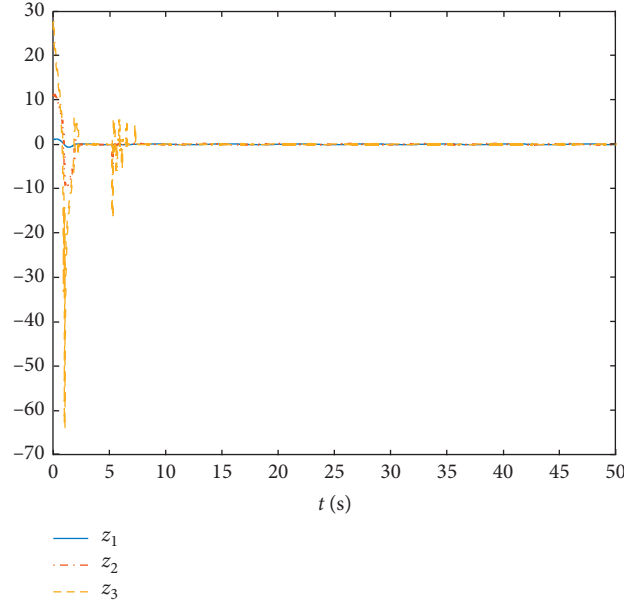


FIGURE 1: Trajectories of error system.

$$\begin{aligned}
 z_n \varepsilon &\leq \zeta \left( \frac{1}{p+1} z_n^{p+1} + \frac{p}{p+1} \varepsilon^{(p+1)/p} \right) + (1-\zeta) \left( \frac{1}{q+1} z_n^{q+1} + \frac{q}{q+1} \varepsilon^{(q+1)/q} \right) \\
 &\quad - a_\sigma \tilde{W} \hat{W}^p \leq -c_p \tilde{W}^{(1+p)/2} \Gamma^{-1} \tilde{W}^{((1+p)/2)T} + a_p W^{*((1+p)/2)} W^{*((1+p)/2)T} \\
 &\quad - b_\sigma \tilde{W} \hat{W}^q \leq -c_q \tilde{W}^{(1+q)/2} \Gamma^{-1} \tilde{W}^{((1+q)/2)T} + b_q W^{*((1+q)/2)} W^{*((1+q)/2)T},
 \end{aligned} \tag{48}$$

where  $0 \leq \zeta \leq 1$ ,  $c_p > 0$ ,  $c_q > 0$ ,  $a_p > 0$ ,  $b_q > 0$  exist.

$$\begin{aligned}
 \dot{V}_n &\leq -z_{n-1} z_n - \left( a_n + \frac{\zeta}{p+1} \right) z_n^p - \left( b_n + \frac{1-\zeta}{q+1} \right) z_n^q \\
 &\quad + \zeta \left( \frac{1}{p+1} z_n^{p+1} + \frac{p}{p+1} \varepsilon^{(p+1)/p} \right) + (1-\zeta) \\
 &\quad \cdot \left( \frac{1}{q+1} z_n^{q+1} + \frac{q}{q+1} \varepsilon^{(q+1)/q} \right) \\
 &\quad - c_p \tilde{W}^{(1+p)/2} \Gamma^{-1} \tilde{W}^{((1+p)/2)T} + a_p W^{*((1+p)/2)} W^{*((1+p)/2)T} \\
 &\quad - c_q \tilde{W}^{(1+q)/2} \Gamma^{-1} \tilde{W}^{((1+q)/2)T} + b_q W^{*((1+q)/2)} W^{*((1+q)/2)T}.
 \end{aligned} \tag{49}$$

Therefore,

$$\begin{aligned}
 V &= \sum_{i=1}^n V_i, \\
 \dot{V} &\leq -\sum_{i=1}^n a_i z_i^{p+1} - \sum_{i=1}^n b_i z_i^{q+1} + \frac{p\zeta}{p+1} \varepsilon^{(p+1)/p} + \frac{q(1-\zeta)}{q+1} \varepsilon^{(q+1)/q} \\
 &\quad - c_p \tilde{W}^{(1+p)/2} \Gamma^{-1} \tilde{W}^{((1+p)/2)T} + a_p W^{*((1+p)/2)} W^{*((1+p)/2)T} \\
 &\quad - c_q \tilde{W}^{(1+q)/2} \Gamma^{-1} \tilde{W}^{((1+q)/2)T} + b_q W^{*((1+q)/2)} W^{*((1+q)/2)T} \\
 &\leq -aV^{p_2} - bV^{q_2} + c,
 \end{aligned} \tag{50}$$

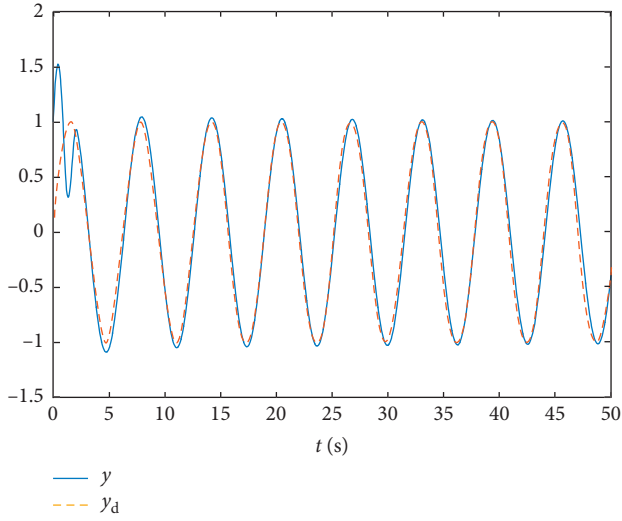
where

$$\begin{aligned}
 a &= 2^{(p+1)/2} \min(c_p, a_i, \quad i = 1, 2, \dots, n), \\
 b &= 2^{(q+1)/2} (n+1)^{(1-q)/2} \min(c_q, b_i, \quad i = 1, 2, \dots, n), \\
 c &= \frac{p\zeta}{p+1} \varepsilon^{\frac{p+1}{p}} + \frac{q(1-\zeta)}{q+1} \varepsilon^{(q+1)/q} + a_p W^{*((1+p)/2)} W^{*((1+p)/2)T} \\
 &\quad + b_q W^{*((1+q)/2)} W^{*((1+q)/2)T}, \\
 p_2 &= \frac{1+p}{2}, \\
 q_2 &= \frac{1+q}{2},
 \end{aligned} \tag{51}$$

and based on Lemma 3,  $V$  is bounded with fixed time. Therefore, it can be concluded that for all  $1 \leq i \leq n$ , the error signals  $z_i$ ,  $\tilde{W}_i$  are bounded with fixed time  $T_{\max} = (1/(2^{p_2-1}a(1-p_2))) + (1/(b(q_2-1)))$ . If  $p = 1 - (1/(2\mu))$  and  $q = 1 + (1/(2\mu))$ , where  $\mu \geq (1/2)$ , fixed-time  $T_{\max} = ((\pi\mu)/\sqrt{2^{p-1}ab})$ .

The proof is completed.  $\square$

*Remark 2.* For the virtual control in equation (26), to avoid singularity problem, we assume that  $|z_i| > \varepsilon$ , otherwise  $\dot{\alpha}_{i-1} = 0$ . Because this is bounded theory, the motivation is control  $|z_i| < \varepsilon$ .

FIGURE 2: Trajectories of  $y, y_d$ .

## 5. Simulation Example

A simulation has been performed for the nonlinear system in order to show the effectiveness and efficiency of the proposed approach.

$$y^{(3)} + (1 + y)y^{(2)} + (2 - y^2)y^{(1)} + y = u. \quad (52)$$

Based on U-model and neural networks technology, design the controller; the initial state is  $y(0) = 1$  and the reference output is  $y_d = \sin(t)$ ; then, based on U-model technology,

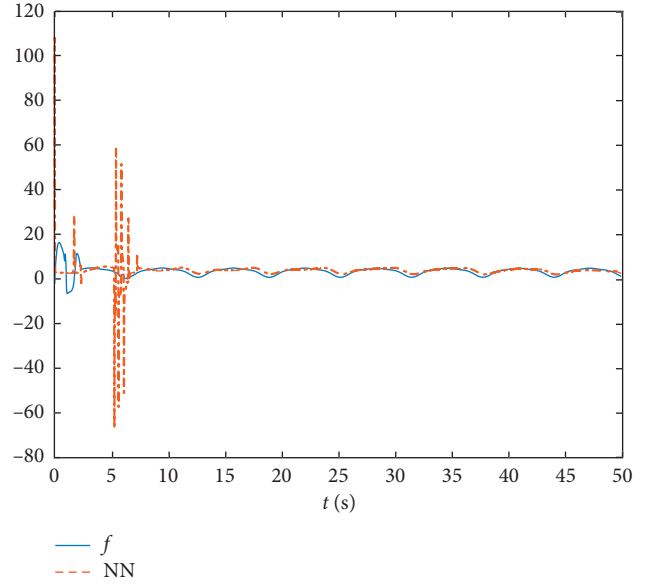
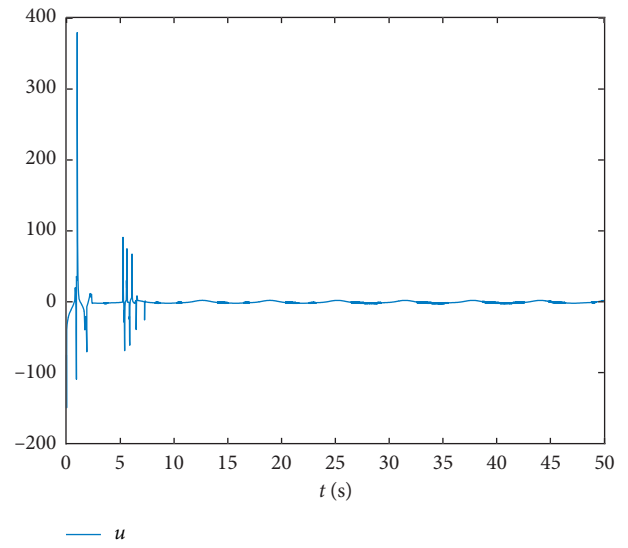
$$\begin{cases} x_1 = y - y_d, \\ x_2 = y^{(1)} - y_d^{(1)}, \\ x_3 = y^{(2)} - y_d^{(2)}, \end{cases} \quad (53)$$

and the system can be changed as

$$\begin{cases} \dot{x}_1 = x_2, \\ \dot{x}_2 = x_3, \\ \dot{x}_3 = f + u, \\ y = x_1, \end{cases} \quad (54)$$

where  $f = -(1 + x_1 + y_d)(x_3 + y_d^{(2)}) - (2 - (x_1 + y_d)^2)(x_2 + y_d^{(1)}) - x_1 - y_d$ .

The initial conditions of NN weights are chosen as zero and  $p = (1/3), q = 3$ . The motivation is to design the adaptive finite time neural tracking controller for a system such that all the system outputs follow the given reference signal  $y_d$  with finite time. To illustrate the ability of controller, Figures 1–4 show the better tracking performance. Figure 1 shows the states of error system convergence to origin point in finite time. Figure 2 shows the system output  $y$  and system reference output  $y_d$  and output tracked reference output quickly. Figure 3 shows the approximation of NNs, and Figure 4 shows the controller.

FIGURE 3: Trajectories of  $f, NN$ .FIGURE 4: Trajectory of control input  $u$ .

## 6. Conclusion

A fixed-time neural networks adaptive backstepping control is proposed under U-model control design framework. The proposed controller guarantees closed-loop system fixed-time bounded and not only uniformly ultimately bounded UUB or PFS. The benchmark simulation has well demonstrated effectiveness and efficiency of the proposed approach.

## Data Availability

No data were used to support this study.

## Conflicts of Interest

The authors declare that they have no conflicts of interest.

## Acknowledgments

This study was partially supported by the National Natural Science Foundation of China (grant nos. 61273188 and 61473312) and Taishan Scholar Construction Engineering Special Funding, Shandong, China. This study was also supported by the Hebei Province Nature Fund (grant no. F2015208128) and Project in Hebei Province Department of Education (grant nos. QN20140157 and BJ2016020).

## References

- [1] Q. Chen, H. Shi, and M. Sun, "Echo state network-based backstepping adaptive iterative learning control for strict-feedback system: an error-tracking approach," *IEEE Transactions on Cybernetics*, pp. 1–14, 2019.
- [2] F. Cheng, L. Qu, W. Qiao, C. Wei, and L. Hao, "Fault diagnosis of wind turbine gearboxes based on DFIG stator current envelope analysis," *IEEE Transactions on Sustainable Energy*, vol. 10, no. 3, pp. 1044–1053, 2019.
- [3] R. Liu and X. Gao, "Neural network identification and sliding mode control for hysteresis nonlinear system with backlash-like model," *Complexity*, vol. 2019, Article ID 4949265, 10 pages, 2019.
- [4] C. Wei, M. Benosman, and T. Kim, "Online parameter identification for state of power prediction of lithium-ion batteries in electric vehicles using extremum seeking," *International Journal of Control, Automation and System*, vol. 17, no. 11, pp. 2906–2916, 2019.
- [5] Y. Yin, J. Liu, J. A. Sanchez et al., "Observer-based adaptive sliding mode control of NPC converters: an RBF neural network approach," *IEEE Transactions on Power Electronics*, vol. 34, no. 4, pp. 3831–3841, 2019.
- [6] Q. Chen, Y. Wang, and Z. Hu, "Finite time synergetic control for quadrotor UAV with disturbance compensation," *International Journal of Applied Mathematics in Control Engineering*, vol. 1, no. 1, pp. 31–38, 2018.
- [7] X. Luo, S. Ge, J. Wang, and X. Guan, "Time delay estimation-based adaptive sliding-mode control for nonholonomic mobile robots," *International Journal of Applied Mathematics in Control Engineering*, vol. 1, no. 1, pp. 1–8, 2018.
- [8] R. Portillo, S. Vazquez, J. I. Leon, M. M. Prats, and L. G. Franquelo, "Model based adaptive direct power control for three-level NPC converters," *IEEE Transactions on Industrial Informatics*, vol. 9, no. 2, pp. 1148–1157, 2013.
- [9] M. Tan, J. Li, X. Chen, and X. Cheng, "Power grid fault diagnosis method using intuitionistic fuzzy petri nets based on time series matching," *Complexity*, vol. 2019, Article ID 7890652, 14 pages, 2019.
- [10] Q. M. Zhu and L. Z. Guo, "A pole placement controller for non-linear dynamic plants," *Proceedings of the Institution of Mechanical Engineers, Part I: Journal of Systems and Control Engineering*, vol. 216, no. 6, pp. 467–476, 2002.
- [11] Q. Zhu, W. Zhang, J. Zhang, and B. Sun, "U-neural network-enhanced control of nonlinear dynamic systems," *Neurocomputing*, vol. 352, pp. 12–21, 2019.
- [12] X.-J. Xie, J. H. Park, H. Mukaidani, and W. Zhang, "Mathematical theories and applications for nonlinear control systems," *Mathematical Problems in Engineering*, vol. 2019, Article ID 2065786, 6 pages, 2019.
- [13] Q. Chen, T. Liang, Y. Nan, and X. Ren, "Adaptive nonlinear sliding mode control of mechanical servo system with LuGre friction compensation," *Journal of Dynamic Systems Measurement & Control*, vol. 138, no. 2, Article ID 021003, 2016.
- [14] L. Tao, Q. Chen, and Y. Nan, "Disturbance-observer based adaptive control for second-order nonlinear systems using chattering-free reaching law," *International Journal of Control, Automation and Systems*, vol. 17, no. 2, pp. 356–369, 2019.
- [15] W. Zhang, X. Gao, B. Sun, X. Hu, and K. Zhu, "Echo state network for extended state observer and sliding mode control of vehicle drive motor with unknown hysteresis nonlinearity," *Mathematical Problems in Engineering*, vol. 2020, Article ID 2534038, 13 pages, 2020.
- [16] X. Li, C. Qin, and Q. Zhu, "Exponential stability of anti-periodic solution for BAM neural networks with time-varying delays," *Mathematical Problems in Engineering*, vol. 2018, Article ID 3034794, 13 pages, 2018.
- [17] S. Shi, M. Liu, and J. Ma, "Fractional-order sliding mode control for a class of nonlinear systems via nonlinear disturbance observer," *International Journal of Applied Mathematics in Control Engineering*, vol. 1, no. 1, pp. 103–110, 2018.
- [18] Q. Chen, S. Xie, M. Sun, and X. He, "Adaptive nonsingular fixed-time attitude stabilization of uncertain spacecraft," *IEEE Transactions on Aerospace & Electronic Systems*, vol. 54, no. 6, pp. 2937–2950, 2018.
- [19] M. Tao, Q. Chen, X. He, and M. Sun, "Adaptive fixed-time fault-tolerant control for rigid spacecraft using a double power reaching law," *International Journal of Robust and Nonlinear Control*, vol. 29, no. 12, pp. 4022–4040, 2019.
- [20] Q. Chen, L. Shi, N. Jing, X. Ren, and Y. Nan, "Adaptive echo state network control for a class of pure-feedback systems with input and output constraints," *Neurocomputing*, vol. 275, pp. 1370–1382, 2017.
- [21] Q. Chen, X. Ren, N. Jing, and D. Zheng, "Adaptive robust finite-time neural control of uncertain PMSM servo system with nonlinear dead zone," *Neural Computing & Applications*, vol. 28, no. 12, pp. 3725–3736, 2016.
- [22] J. Zhang, Q. Zhu, and L. Yang, "Convergence time calculation for super-twisting algorithm and application for nonaffine nonlinear systems," *Complexity*, vol. 2019, Article ID 6235190, 15 pages, 2019.
- [23] J. Zhang, Q. Zhu, L. Yang, and X. Wu, "Homeomorphism mapping based neural networks for finite time constraint control of a class of nonaffine pure-feedback nonlinear systems," *Complexity*, vol. 2019, Article ID 9053858, 11 pages, 2019.
- [24] X. Wu, J. Zhang, and Q. Zhu, "A generalized procedure in designing recurrent neural network identification and control of time-varying-delayed nonlinear dynamic systems," *Neurocomputing*, vol. 73, no. 7–9, pp. 1376–1383, 2010.
- [25] C. Chen, L. Li, H. Peng, and Y. Yang, "Fixed-time synchronization of inertial memristor-based neural networks with discrete delay," *Neural Networks*, vol. 109, pp. 81–89, 2019.

## Research Article

# Mathematical Modeling and Dynamic Analysis of Planetary Gears System with Time-Varying Parameters

Zhengming Xiao , Jinxin Cao, and Yinxin Yu

*Faculty of Mechanical and Electrical Engineering, Kunming University of Science and Technology, Kunming, Yunnan, China*

Correspondence should be addressed to Zhengming Xiao; [suzem@sina.com](mailto:suzem@sina.com)

Received 14 January 2020; Accepted 20 February 2020; Published 16 March 2020

Guest Editor: Jian Huang

Copyright © 2020 Zhengming Xiao et al. This is an open access article distributed under the Creative Commons Attribution License, which permits unrestricted use, distribution, and reproduction in any medium, provided the original work is properly cited.

Planetary gears are widely used in automobiles, helicopters, heavy machinery, etc., due to the high speed reductions in compact spaces; however, the gear fault and early damage induced by the vibration of planetary gears remains a key concern. The time-varying parameters have a vital influence on dynamic performance and reliability of the gearbox. An analytical model is proposed to investigate the effect of gear tooth crack on the gear mesh stiffness, and then the dynamical model of the planetary gears with time-varying parameters is established. The natural characteristics of the transmission system are calculated, and the dynamic responses of transmission components, as well as dynamic meshing force of each pair of gear are investigated based on varying internal excitations induced by time-varying parameters and tooth root crack. The effects of gear tooth root crack size on the planetary gear dynamics are simulated, and the mapping rules between damage degree and gear dynamics are revealed. In order to verify the theoretical model and simulation results, the planetary gear test rig was built by assembling faulty and healthy gear separately. The failure mechanism and dynamic characteristics of the planetary gears with tooth root crack are clarified by comparing the analytical results and experimental data.

## 1. Introduction

Planetary transmissions are an important form of mechanical transmission. Because of its advantages of high transmission ratio, high bearing capacity, and compact structure, it is widely used in complex mechanical equipment such as aerospace, wind power generation equipment, and mining machinery. Due to the influence of time-varying parameters, the planetary gear system always has the problem of nonlinear dynamics and excessive vibration. The planetary transmission system has a high failure rate, and the root crack is one of the most important forms of gear failure, due to complicated internal structure and large load during operation. When the root of the transmission system is cracked, the vibration of the system will be intensified and, in serious cases, the equipment will be damaged. Therefore, the dynamic study of the planetary gear transmission system with tooth root crack failure and analysis of the fault

mechanism has an important theoretical significance and engineering application value for improving the reliability and service life of the gear. Mathematical modeling and analysis are important methods to solve the nonlinear dynamics of planetary gear transmission systems. The control of nonlinear dynamic systems is a widely recognized challenging issue. It is promising to develop vibration reduction design of the planetary gear system based on U-model, because of the unique advantages of U-model in nonlinear control [1, 2]. Some scholars have carried out a lot of work on the dynamics of gear systems by mathematical modeling. Bonori and Pellicano [3] presented a dynamic model of a single pair of gear transmission systems and analyzed the effects of random manufacturing errors on the dynamic response of the system. Chaari et al. [4] established an analytical model of time-varying gear meshing stiffness based on the analytical method and analyzed the variation of crack to gear stiffness under two different parameters. Guo and



$$\begin{cases}
\text{Ring:} & \begin{cases} m_r (\ddot{x}_r - 2\omega_c \dot{y}_r - \omega_c^2 x_r) - \sum_{n=1}^N (c_{rn} \dot{\delta}_{rn} + k_{rn} \delta_{rn}) \sin \psi_{rn} + c_{rx} \dot{x}_r + k_{rx} x_r = 0, \\ m_r (\ddot{y}_r + 2\omega_c \dot{x}_r - \omega_c^2 y_r) + \sum_{n=1}^N (c_{rn} \dot{\delta}_{rn} + k_{rn} \delta_{rn}) \cos \psi_{rn} + c_{ry} \dot{y}_r + k_{ry} y_r = 0, \\ \left( \frac{I_r}{r_r^2} \right) \ddot{u}_r + \sum_{n=1}^N (c_{rn} \dot{\delta}_{rn} + k_{rn} \delta_{rn}) + c_{ru} \dot{u}_c + k_{ru} u_c = \frac{T_r}{r_r}, \end{cases} \\
\text{Sun:} & \begin{cases} m_s (\ddot{x}_s - 2\omega_c \dot{y}_s - \omega_c^2 x_s) - \sum_{n=1}^N (c_{sn} \dot{\delta}_{sn} + k_{sn} \delta_{sn}) \sin \psi_{sn} + c_{sx} \dot{x}_s + k_{sxt} x_s = 0, \\ m_s (\ddot{y}_s + 2\omega_c \dot{x}_s - \omega_c^2 y_s) + \sum_{n=1}^N (c_{sn} \dot{\delta}_{sn} + k_{sn} \delta_{sn}) \cos \psi_{sn} + c_{sy} \dot{y}_s + k_{syt} y_s = 0, \\ \left( \frac{I_s}{r_s^2} \right) \ddot{u}_s + \sum_{n=1}^N (k_{sn} \delta_{sn} + c_{sn} \dot{\delta}_{sn}) + c_{su} \dot{u}_s + k_{su} u_s = \frac{T_s}{r_s}, \end{cases} \\
\text{Carrier:} & \begin{cases} \sum_{n=1}^N [k_{pn} (\delta_{nr} \cos \psi_n - \delta_{nt} \sin \psi_n) + c_{pn} (\dot{\delta}_{nr} \cos \psi_n - \dot{\delta}_{nt} \sin \psi_n)] + m_c (\ddot{x}_c - 2\omega_c \dot{y}_c - \omega_c^2 x_c) + c_{cx} \dot{x}_c \\ + k_{cx} x_c = 0, \\ \sum_{n=1}^N [k_{pn} (\delta_{nr} \sin \psi_n + \delta_{nt} \cos \psi_n) + c_{pn} (\dot{\delta}_{nr} \sin \psi_n + \dot{\delta}_{nt} \cos \psi_n)] + m_c (\ddot{y}_c + 2\omega_c \dot{x}_c - \omega_c^2 y_c) \\ + c_{cy} \dot{y}_c + k_{cy} y_c = 0, \\ \left( \frac{I_c}{r_c^2} \right) \ddot{u}_c + \sum_{n=1}^N (k_{pn} \delta_{nt} + c_{pn} \dot{\delta}_{nt}) + c_{cu} \dot{u}_c + k_{cu} u_c = \frac{T_c}{r_c}, \end{cases} \\
\text{Planet:} & \begin{cases} m_{pn} (\ddot{\zeta}_n - 2\omega_c \dot{\eta}_n - \omega_c^2 \zeta_n) - (c_{sn} \dot{\delta}_{sn} + k_{sn} \delta_{sn}) \cos \alpha_s - (c_{rn} \dot{\delta}_{rn} + k_{rn} \delta_{rn}) \cos \alpha_r - c_{pn} \dot{\delta}_{nr} - k_{pn} \delta_{nr} = 0, \\ m_{pn} (\ddot{\eta}_n + 2\omega_c \dot{\zeta}_n - \omega_c^2 \eta_n) - (c_{sn} \dot{\delta}_{sn} + k_{sn} \delta_{sn}) \sin \alpha_s + (c_{rn} \dot{\delta}_{rn} + k_{rn} \delta_{rn}) \sin \alpha_r - c_{pn} \dot{\delta}_{nt} - k_{pn} \delta_{nt} = 0, \\ \left( \frac{I_{pn}}{r_{pn}^2} \right) \ddot{u}_n + c_{sn} \dot{\delta}_{sn} + k_{sn} \delta_{sn} - c_{rn} \dot{\delta}_{rn} - k_{rn} \delta_{rn} = 0, \end{cases}
\end{cases} \quad (1)$$

where  $\delta_{sn}$  is the elastic deformation of the sun gear and the  $n$ th planet gear on the meshing line:

$$\delta_{sn} = -x_s \sin \psi_{sn} + y_s \cos \psi_{sn} - \zeta_n \sin \alpha_s - \eta_n \cos \alpha_s + u_s + u_n + e_{sn}, \quad (2)$$

where  $\delta_{rn}$  is the elastic deformation of the ring and the  $n$ th planet gear on the meshing line:

$$\delta_{rn} = y_r \cos \psi_{rn} - x_r \sin \psi_{rn} - \zeta_n \sin \alpha_r - \eta_n \cos \alpha_r + u_r - u_n + e_{rn}, \quad (3)$$

where  $\delta_{nr}$  is the projection of the planet carrier in the  $\zeta$  direction relative to the  $n$ th planet gear:

$$\delta_{nr} = x_c \cos \psi_n + y_c \sin \psi_n - \zeta_n, \quad (4)$$



where  $\delta_{nt}$  is the projection of the planet carrier in the  $\eta$  direction with respect to the  $n$ th planet gear:

$$\delta_{nt} = -x_c \sin \psi_n + y_c \cos \psi_n + u_c - \eta_n, \quad (5)$$

where  $\psi_{sn} = \psi_n - \alpha_s$ ,  $\psi_{rn} = \psi_n + \alpha_r$ ,  $\psi_n$  is the position angle of the  $n$ th planet gear,  $\alpha_r$  is the meshing angle between the ring and the planet gear, and  $\alpha_s$  is the meshing angle between the sun gear and the planet gear.

The dynamic equations of the various components established above are collated. The dynamic equations of the planetary transmission system can be expressed in the form of a matrix. The dynamic equation of the transmission system can be expressed as follows:

$$M\ddot{x} + \omega_c G\dot{x} + [K_b + K_m - \omega_c^2 K_\omega]x = F + T, \quad (6)$$

where  $G$  is the gyromatrix;  $K_m$  is the meshing stiffness matrix;  $K_\omega$  is the centripetal stiffness matrix;  $x$  is the generalized displacement matrix of the system;  $M$  is the generalized mass matrix of the system;  $K_b$  is the bearing support stiffness matrix;  $K_m$  is the meshing stiffness matrix;  $T$  is the external load of the system; and  $F$  is the internal excitation.

### 3. Time-Varying Stiffness Model of Bearing

In order to simplify the calculation, it is assumed that the steel ball rotates at a constant speed and the movement between the inner and outer rings of the bearing is pure rolling. Regardless of the oil film stiffness under bearing lubrication, the bearing stiffness of the bearing can be analyzed according to Hertz contact theory.

As shown in Figure 2, during the movement of the bearing, the inner and outer rings of the bearing are subjected to the weight of the roller and the centrifugal force. Therefore, the forces of the contact between the roller and the inner and outer rings of the bearing are different. The contact force  $Q_o$  between the roller and the outer ring is as follows:

$$Q_o = Q - mg \sin \varphi_k + mR_p \omega_c^2, \quad (7)$$

$$\omega_c = \frac{\pi(1 - (D_b/D_p)\cos\beta)n_s}{60},$$

where  $\omega_c$  is the angular velocity of the cage,  $Q$  is the load on the inner ring of the bearing,  $m$  is the mass of the steel ball. The radius of the circle where the geometric center of the roller is located is  $R_p$ ,  $D_b$  is the diameter of the roller,  $n_s$  is the rotational speed of the shaft, and  $\beta$  is the contact angle.

According to Hertz contact theory, the relationship between the contact force  $Q$  of the rolling bearing steel ball and the elastic approaching amount  $\delta$  can be expressed as follows:

$$Q = K_c \delta^{3/2}, \quad (8)$$

where  $Q$  is the contact load of the steel ball and  $K_c$  is the Hertz contact stiffness.

According to the force balance condition, the component forces  $f_x$  and  $f_y$  of the bearing  $x$  and  $y$  directions are equal to the sum of the component forces of the load  $Q_k$  of

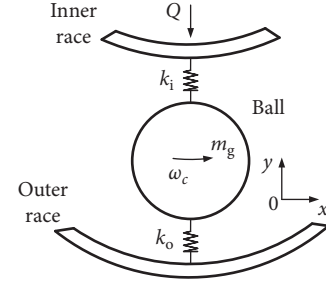


FIGURE 2: Bearing rolling element-ring model.

each roller in the  $x$  and  $y$  directions, and  $f_x$  and  $f_y$  can be expressed by the following formulas:

$$\begin{cases} f_x = \sum_{k=1}^N Q_k \cos(\varphi_k), \\ f_y = \sum_{k=1}^N Q_k \sin(\varphi_k). \end{cases} \quad (9)$$

The radial stiffness  $k_b$  of the bearing is

$$k_b = \sum_{k=1}^N [K_k \cos \varphi_k], \quad (10)$$

where  $K_k$  is the contact stiffness of the  $k$ th roller.

The relevant parameters of the rolling bearing in the planetary transmission system are shown in Table 1. The bearing material is bearing steel, which is solved according to the time-varying bearing stiffness model of the rolling bearing. Figure 3 shows the variation of the radial stiffness of the bearing with the angle of the steel ball as the position angle changes.

### 4. Effect of Crack on Gear Meshing Stiffness

During the movement of the gear, the root position will produce a bending stress greater than other positions due to the periodicity of the load, which will easily lead to the occurrence of fatigue cracks in the gear teeth. When calculating the gear meshing stiffness, the gear teeth are generally considered be cantilever beams. There are five kinds of stiffness in the gear meshing pair: Hertz contact stiffness  $k_h$ , bending stiffness  $k_b$ , shear stiffness  $k_a$ , and radial compression stiffness  $k_s$  [12]. In addition to the above stiffness, there is also a matrix flexible stiffness  $k_f$  of the gear. When the gear is cracked, the surface contact area and radial force of the gear are constant, so the Hertz contact stiffness, radial compression stiffness, and matrix flexibility of the gear are unchanged. The gear meshing stiffness of the crack mainly considers the bending stiffness and shears stiffness.

In this paper, the planetary gearbox with tooth root crack fault is taken as the research object. The relevant parameters of the planetary box are shown in Table 2. When the crack tooth enters the meshing state, the meshing stiffness of the cracked gear is calculated. Figure 4 shows the comparison of the stiffness of a simulated crack occurrence (the tooth crack

TABLE 1: Geometric parameters of the bearing.

Outer diameter $D$ (mm)	Inner diameter $d$ (mm)	Bearing width $B$ (mm)	Ball diameter $D_b$ (mm)	Number of rolling elements $n_b$
80	40	18	12	9

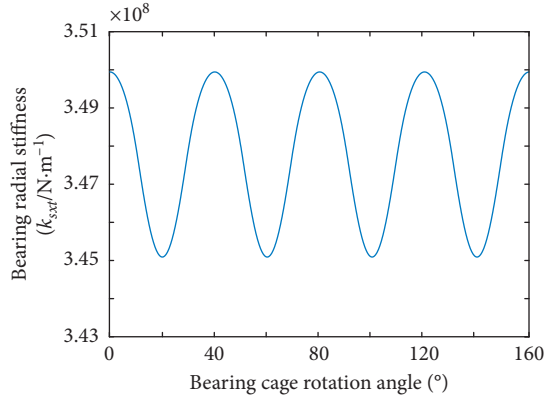


FIGURE 3: Time-varying bearing stiffness.

TABLE 2: Parameters of planetary gearbox.

Parameter	Ring	Carrier	Planet gear	Sun gear
Mass (kg)	10.12	2.7	0.45	0.8
Number of teeth	71		42.29	28
Base circle diameter (mm)	150.12	112	20	59.2
Modulus (mm)			2.25	
Engagement angle (°)			20°	

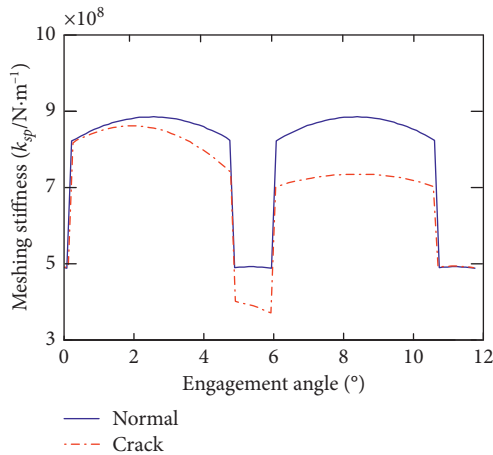


FIGURE 4: Time-varying meshing stiffness.

has an expansion angle  $\alpha_c$  of  $60^\circ$  and a crack depth  $q$  of 1.8 mm.) when engaged with a healthy gear pair.

## 5. Dynamic Response and Analysis

**5.1. Modal Analysis of Planetary Gears.** The modal analysis of the gear-bearing coupling dynamics model of the above mentioned planetary transmission system is carried out.

Regardless of the effect of damping, the average stiffness is used instead of the time-varying stiffness, and the dynamic equation is expressed as follows:

$$M\ddot{x} + \omega_c G\dot{x} + [K_b + K_m - \omega_c^2 K_\omega]x = 0. \quad (11)$$

Thus, the  $n$  positive real roots  $\omega_i$ , which are the natural frequencies of the system, could be determined. The main mode equation is

$$\omega_i^2 M\phi_i = [K_b + K_m]\phi_i. \quad (12)$$

The planetary gears system has 18 degrees of freedom. The natural frequencies of the system are calculated, as shown in Table 3, and the corresponding vibration modes are shown in Figure 5. There are three kinds of vibration mode: rigid mode, rotational modes (no repetitive frequency, no translation only torsion), and translational modes (there is a repetitive frequency, no torsion only translation). The phenomenon of 5 equivalent natural frequencies (repetitive frequency) occurs in the system because the geometrical and physical parameters of the planetary gears in the transmission system are assumed to be the same, resulting in a symmetrical type of the planetary transmission stage. The occurrence of repetitive frequencies causes different types of vibration to be induced at one frequency.

**5.2. Dynamic Response Analysis of Planetary System.** In order to deeply study the influence of sun gear root crack failure on the dynamic characteristics of the planetary gear transmission system. This paper selects the fault model and fault-free model of the sun gear crack 1.8 mm. Considering the time-varying meshing stiffness of healthy and tooth cracked gears, the directional parameter method is used to establish the translation-torsion dynamics modeling of the planetary transmission system. The dynamic equation is solved by Runge-Kutta method. The input torque of the system is 30 Nm, and the dynamic response of the planetary transmission system at 1000 r/min is analyzed. The meshing frequency of the transmission system is 334.68 Hz, and the bearing ball revolution frequency is 118.1 Hz.

Figures 6–8 shows the vibration velocity response of a healthy and root-cracked gear transmission system. As shown in Figure 6, the peak velocity of the sun gear of the healthy system is 5.25 mm/s, and the peak velocity of the sun gear with root crack fault transmission system is 8.77 mm/s. As shown in Figure 7, the peak velocity of the planet gear of the healthy system is 2.83 mm/s, and the peak velocity of the sun gear with root crack fault transmission system is 3.95 mm/s. As shown in Figure 8, the peak velocity of the ring gear of the healthy system is 0.295 mm/s, and the peak velocity of the ring gear with the root crack fault transmission system is 0.362 mm/s.

Through the comparison of the time domain waveform of the healthy and faulty transmission systems, it can be seen

TABLE 3: Natural frequencies of the system.

Vibration mode	Natural frequencies (Hz)
Rigid mode	$f_1 = 0$
Rotational modes	$f_2 = f_3 = 1104, f_5 = f_6 = 4595, f_{10} = f_{11} = 9286, f_{13} = f_{14} = 15111, f_{16} = f_{17} = 21544$
Translational modes	$f_4 = 1207, f_7 = 4930, f_8 = 5967, f_9 = 6467, f_{12} = 10421, f_{15} = 17898, f_{18} = 23060$

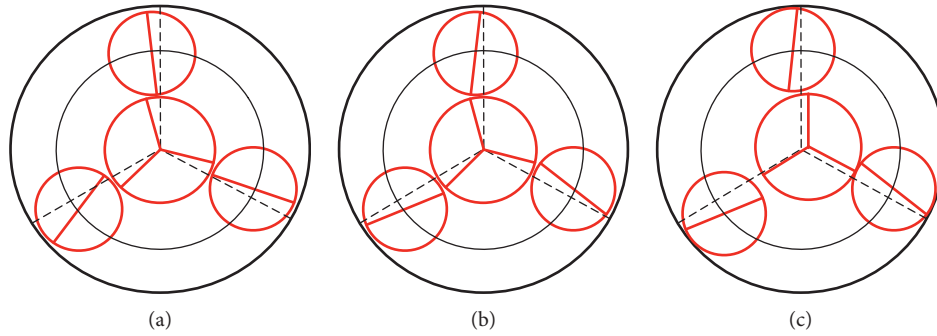


FIGURE 5: Vibration modes of planetary transmission system: (a) rigid mode, (b) rotational mode, and (c) translational mode.

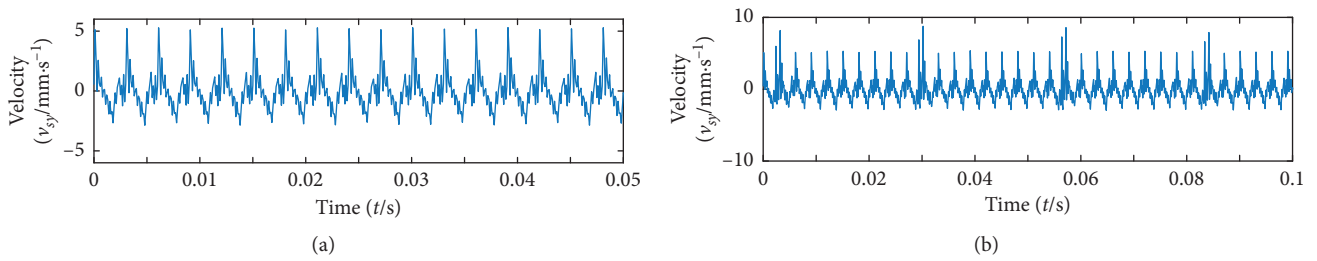


FIGURE 6: Vibration velocity response of the sun gear. (a) Healthy planetary transmission system. (b) Faulty planetary transmission system.

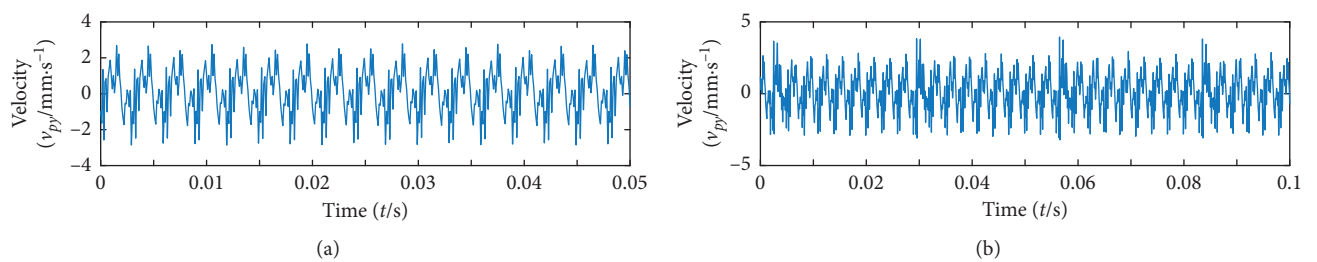


FIGURE 7: Vibration velocity response of planet gear. (a) Healthy planetary transmission system. (b) Faulty planetary transmission system.

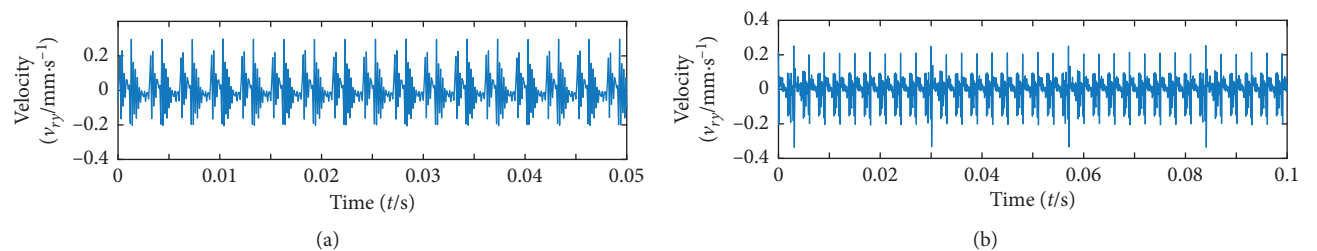


FIGURE 8: Vibration velocity of ring. (a) Healthy planetary transmission system. (b) Faulty planetary transmission system.

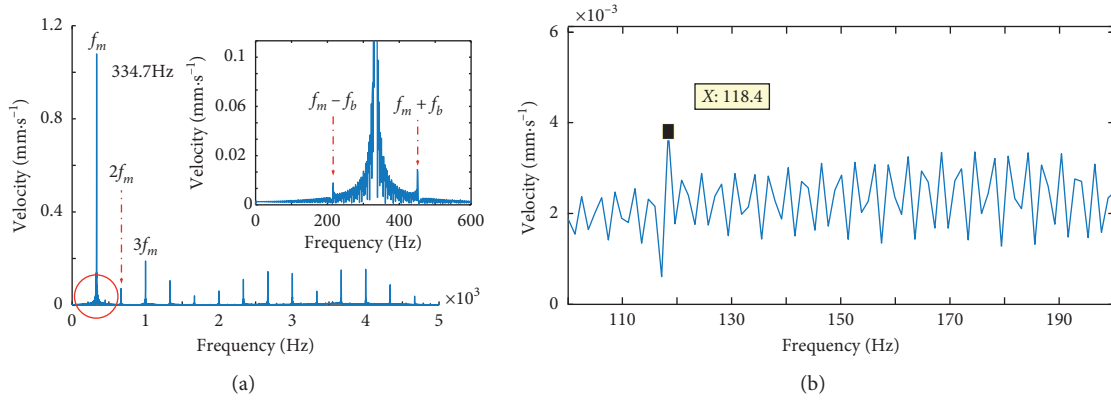


FIGURE 9: Spectrum diagram of sun gear. (a) Spectrum of healthy signal. (b) Spectrum refinement of healthy signals.

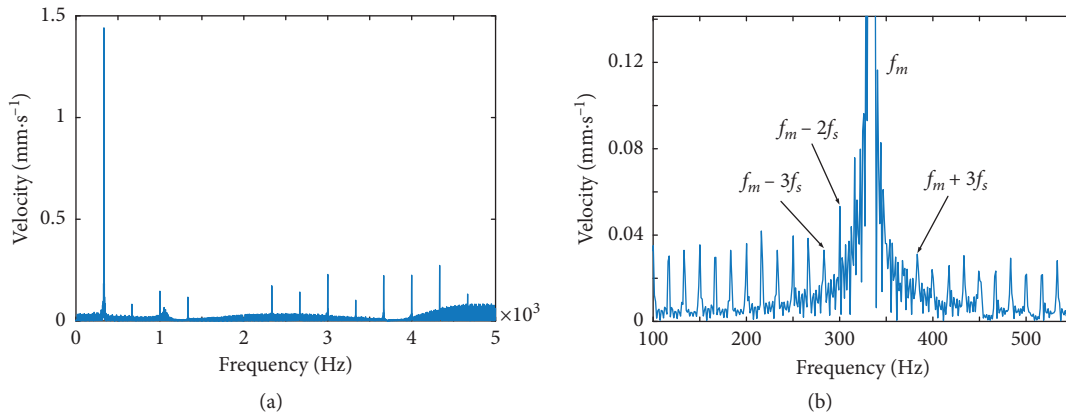


FIGURE 10: Spectrum diagram of sun gear with root crack. (a) Spectrum of fault signal. (b) Spectrum refinement of fault signal.

that a periodic shock signal appears in the time domain waveform diagram of the faulty system compared to the healthy transmission system. The occurrence of sun gear cracks causes the gear teeth of the cracks to reduce the meshing stiffness, which makes the vibration velocity the sun gear, the planet gears, and the ring in the system increase significantly, which aggravates the vibration of the planetary transmission system.

The spectrum analysis of the vibration velocity response of the sun gear in the  $y$  direction of the transmission system is performed. Figures 9 and 10 are the spectrum diagrams of the vibration velocity response of the healthy and the tooth root crack faulty transmission system. As shown in Figure 9, in the spectrum diagram of the healthy transmission system, the meshing frequency of the transmission system is 334.7 Hz, and the bearing ball revolution frequency is 118.4 Hz, and the meshing frequency  $f_m$  is mainly dominant, and the peak of the first frequency is relatively high. At the same time, a sideband appears on both sides of the meshing frequency, and the distance of the sideband from the meshing frequency is the frequency at which the ball revolves.

Compared with healthy gears, sidebands appear around the meshing frequency in the spectrum of root crack failure,

as shown in Figure 10. This is because the sun gear shaft frequency  $f_s$  produces a frequency modulation effect on the meshing frequency. The distance between the sideband and the meshing frequency is  $nf_s$  ( $n = 1, 2, 3, \dots$ ). At the same time, the amplitude of the meshing frequency of the system increases.

## 6. Experimental Analysis

Taking the planetary transmission gearbox as the experimental object, the test was carried out on the planetary gearbox with the sun gear root crack failure. The test bench and measurement points are shown in Figure 11. Measuring points 1–3 are set on the output bearing, ring gear, and input bearing, respectively. The vibration acceleration signals of the healthy and faulty transmission systems are acquired and the vibration signal in the  $z$  direction of the measuring point 1 are shown in Figure 12.

The spectrum of the vibration acceleration signals are shown in Figure 13. In the spectrum diagram of the healthy transmission system, the meshing frequency  $f_m$  and its multiplication are mainly dominant; the meshing frequency of the system is 334.6 Hz, and the frequency of the bearing

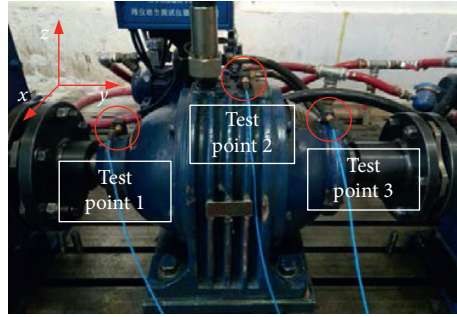


FIGURE 11: Test setup.

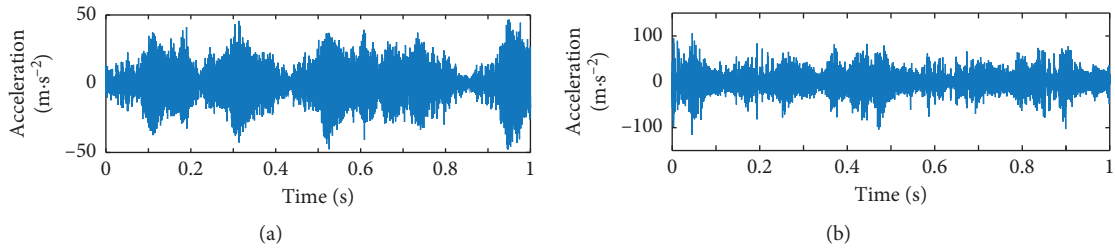


FIGURE 12: Vibration acceleration of test point 1. (a) Healthy system. (b) Fault system.

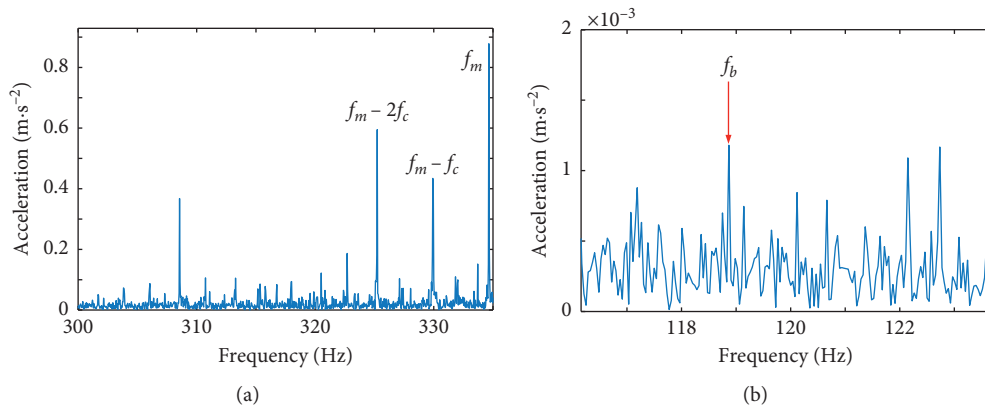


FIGURE 13: Spectrum diagram of the healthy system. (a) System meshing frequency. (b) Frequency conversion bearing steel ball.

steel ball is 118.9 Hz. At the same time, a sideband having a carrier frequency  $f_c$  as a modulation signal appears around the meshing frequency.

Because the influence of the vibration signal transmission path is not considered, there is no sideband caused by the frequency  $f_c$  modulation of the carrier around the meshing frequency, and the spectrum of the actual vibration signal is slightly different.

As shown in Figure 14, the spectrum of the vibration response of the fault-containing system is obtained. The amplitude of the faulty system spectrum is larger than that of the healthy system. The meshing frequency of the system is 334.6 Hz. The sideband of the sun frequency  $f_s$  is modulated around the meshing frequency. The correctness of the simulation model is verified.

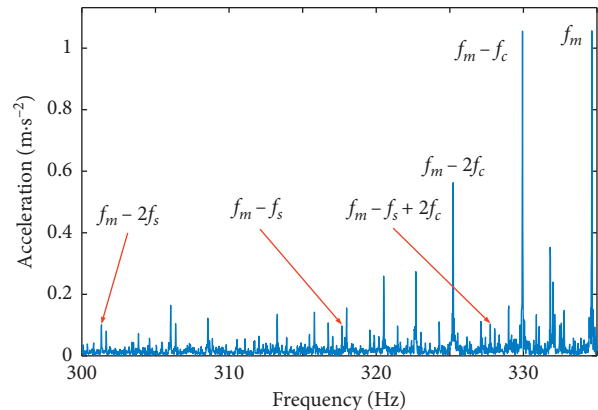


FIGURE 14: Spectrum diagram of the faulty system.



## 7. Conclusions

The gear-bearing coupling dynamics model of the planetary transmission system is established by using the lumped parameter method. The natural characteristics analysis of the system is carried out, and the influencing factors such as the time-varying parameters of the meshing stiffness and the bearing stiffness are considered. The dynamic characteristics of the planetary transmission system are calculated and simulated. The system dynamic response and frequency domain characteristics are obtained by theoretical analysis and bench test. The next work is to analyze the influence of design and operation parameters on system dynamics, so as to propose effective methods for controlling system vibration. The specific conclusions are as follows:

- (1) Based on the analytical method, the natural frequency and modal characteristics of the gear transmission system are obtained. The natural frequencies of the system are mainly concentrated in the 1104 to 23060 Hz.
- (2) By solving the dynamic model and comparing and analyzing the vibration response of the transmission system, it is shown that the vibration of the transmission system increases due to the influence of the root crack. In the frequency domain, in the middle of the spectrum of the faulty transmission system, a sideband occurs around the meshing frequency. This is because the frequency shift  $f_s$  of the sun gear has a modulation effect on the meshing frequency  $f_m$ .
- (3) Through the bench experiment, we can find the sidebands generated by the modulation of the carrier frequency  $f_c$ , in the spectrogram of the vibration acceleration of the faulty system, and also there are sidebands generated by the frequency  $f_s$  modulation of the sun gear. The experimental results verify the correctness of the mathematical model. It also guides the future direction to control nonlinear dynamics of the planetary gear system.

## Data Availability

The data used to support the findings of this study are available from the corresponding author upon request.

## Conflicts of Interest

The authors declare that they have no conflicts of interest.

## Acknowledgments

This work was supported by the National Natural Science Foundation of China (Grant no. 51965025).

## References

- [1] Q. Zhu, L. Liu, S. Li, and W. Zhang, "Control of complex nonlinear dynamic rational systems," *Complexity*, vol. 2018, Article ID 8953035, 12 pages, 2018.
- [2] Q. M. Zhu, D. Y. Zhao, and J. Zhang, "A general U-block model-based design procedure for nonlinear polynomial control systems," *International Journal of Systems Science*, vol. 47, no. 14, pp. 1–10, 2016.
- [3] G. Bonori and F. Pellicano, "Non-smooth dynamics of spur gears with manufacturing errors," *Journal of Sound and Vibration*, vol. 306, no. 1-2, pp. 271–283, 2007.
- [4] F. Chaari, T. Fakhfakh, and M. Haddar, "Analytical modelling of spur gear tooth crack and influence on gearmesh stiffness," *European Journal of Mechanics—A/Solids*, vol. 28, no. 3, pp. 461–468, 2009.
- [5] Y. Guo and R. G. Parker, "Dynamic modeling and analysis of a spur planetary gear involving tooth wedging and bearing clearance nonlinearity," *European Journal of Mechanics—A/Solids*, vol. 29, no. 6, pp. 1022–1033, 2010.
- [6] Z. Chen and Y. Shao, "Dynamic simulation of planetary gear with tooth root crack in ring gear," *Engineering Failure Analysis*, vol. 31, no. 9, pp. 8–18, 2013.
- [7] Q. Zhou, *A Dynamic Analysis and Numerical Simulation of Cylindrical Spur Gear and Crack Fault*, Ph.D thesis, Taiyuan University of Technology, Taiyuan, China, 2008.
- [8] Z. Wan, "Time-varying mesh stiffness algorithm correction and tooth crack dynamic modeling," *Journal of Mechanical Engineering*, vol. 49, no. 11, p. 153, 2013.
- [9] C. T. Walters, "The dynamics of ball bearings," *Journal of Tribology*, vol. 93, no. 1, pp. 1–10, 1970.
- [10] T. A. Harris and M. N. Kotzalas, *Advanced Concepts of Bearing Technology: Rolling Bearing Analysis*, CRC Press, Boca Raton, FL, USA, 5th edition, 2007.
- [11] Z. G. Zhou, *Study on Dynamics and Time-dependent Reliability of Gear Transmission System of Wind Turbine under Random Wind Conditions*, Ph.D thesis, Chongqing University, Chongqing, China, 2012.
- [12] O. D. Mohammed, M. Rantatalo, J. O. Aidanpää, and U. Kumar, "Vibration signal analysis for gear fault diagnosis with various crack progression scenarios," *Mechanical Systems & Signal Processing*, vol. 41, no. 1-2, pp. 176–195, 2013.
- [13] J. Park, Y. Kim, K. Na, and B. D. Youn, "Variance of energy residual (VER): an efficient method for planetary gear fault detection under variable-speed conditions," *Journal of Sound and Vibration*, vol. 453, no. 4, pp. 253–267, 2019.



## Research Article

# Modeling of Coupling Mechanism between Ballast Bed and Track Structure of High-Speed Railway

Xuejun Wang, Jianghua Pu, Peng Wu, and Mingfang Chen 

*Faculty of Mechanical and Electrical Engineering, Kunming University of Science and Technology, Kunming 650500, China*

Correspondence should be addressed to Mingfang Chen; [mfchen111@sina.com](mailto:mfchen111@sina.com)

Received 18 December 2019; Accepted 20 January 2020; Published 21 February 2020

Guest Editor: Weicun Zhang

Copyright © 2020 Xuejun Wang et al. This is an open access article distributed under the Creative Commons Attribution License, which permits unrestricted use, distribution, and reproduction in any medium, provided the original work is properly cited.

In this paper, a discrete and continuous body coupling algorithm is used to study the dynamic contact characteristics between ballasts and between ballasts and track structures. Firstly, the three-dimensional fine modeling of ballast particles is realized based on the three-dimensional laser scanning method, and then through the discrete and continuum coupling algorithm from the micro-macro point of view, a multiscale and unified particle-track structure coupling model is established. Based on the coupling model, the macro- and microdynamic characteristics of the ballast bed and the mechanical characteristics of the track structure under the dynamic load of high-speed trains with different driving speeds are studied. It is shown that the cumulative settlement of the ballast bed is directly proportional to the contact force and rotation speed of the ballast, and the faster the driving speed is, the greater the cumulative deposition speed and cumulative settlement of the ballast are. The contact force between the ballast and sleeper mainly comes from the bottom of the sleeper, and its contact force and contact strength increase with the increase of driving speed.

## 1. Introduction

Ballasted track is an important part of the track structure of high-speed railway, which has the advantages of good elasticity, easy maintenance, and fine noise absorption. As a key part of the ballast track structure, the ballast bed is mainly composed of crushed stone ballast, which directly suffers the train load transmitted by sleepers. With the increase of train speed, the train load and frequency of track structure expand, which accelerates the accumulated deformation and uneven settlement of the ballast bed [1]. The deterioration of the ballasted track bed increases the track irregularity and enhances the wheel rail power. The vicious cycle formed by the two will directly affect the service status of the track structure and the safety and ride comfort of train operation. Therefore, many studies have been carried out on the interaction between the ballast bed and track structure.

In terms of experimental research, Kaynia et al. [2] studied the test results of ground and subgrade vibration response when high-speed trains pass on the southern line of Sweden and proposed the evaluation model of ground and

subgrade vibration at different positions. Shaer et al. [3] built a 1:3 scale track model to study the deformation and settlement characteristics of the ballasted track under repeated load and pointed out the correlation between track settlement and sleeper vibration acceleration. Ishikawa et al. [4] studied the distribution characteristics of internal stress of subgrade and the development law of track settlement under changeable load through an 1:5 indoor model test of the ballasted track. Koike et al. [5] used the 1:5 shrinking test model to test the lateral resistance of six different types of sleepers. Kennedy [6] established a full-scale test model system (GRAFT) for ballasted track and subgrade, studied the influence of subgrade deformation modulus on the subsidence of the ballasted track, and proposed a prediction method for the subsidence of the ballasted track with load amplitude, subgrade deformation modulus, and other factors. Jing et al. [7] carried out field tests to compare and analyze the lateral resistance of type III sleepers under different geometric sections of the ballast bed and the lateral resistance of ladder sleepers under different ballast shoulder widths of the ballast bed. In addition to the track model, the

loading system is also important for the test. Among them, Faghihi Kashani et al. [8], Momoya et al. [9], and Yu et al. [10] use the actuator controlled by hydraulic servocontrol system to load. The hydraulic servosystem is a nonlinear system; in order to achieve the accuracy and stability of dynamic wheel load simulation, it is necessary to adopt efficient control methods. As a new control method, U-model is an effective method for the nonlinear control system design [11]. For U-model research, by Zhu et al. [12], the first and second feedback adaptive control platforms of the nonlinear system are established based on U-model. At the same time, a U-neural network (U-NN) structure is proposed to facilitate the design and control of all dynamic systems modeled by linear/nonlinear polynomials/state space equations [13]. In addition, Geng et al. [14] proposed a predictive control scheme based on U-model, which solves the problem of input delay in nonlinear systems.

As it is difficult to analyze the microcosmic contact characteristics between multilayer heterostructures by experiments, numerical simulation is also used to perform the research work. Based on the discrete element method, Lobo Guerrero and Vallejo [15] established a two-dimensional discrete element model of the sleeper track bed to study the impact of ballast breaking on track settlement and analyze the change of force chain distribution of the granular track bed and the process of ballast breaking under cyclic load. Based on the finite element analysis method, Shaer et al. [3] studied the relationship between the ballast deformation and the track settlement from the overall structure. In [16], based on the Bernoulli-Euler beam theory in the finite element method, the meshless method is used to analyze the deformation of the beam element. Kabo [17] used the finite element method to establish an overall model of the ballast bed and studied the influence of the ballast shoulder form on the lateral resistance of the ballast bed. In [18], based on dynamic theory and finite element method, five different track models are established to study the mechanical properties of the ballasted track under high-frequency load. Gao et al. [19] established the three-dimensional model of the ballast bed and sleeper by the discrete element method and studied the influence of important factors such as ballast slope, thickness, top width, and shoulder height on the cross-section size of the ballast bed.

The ballast bed is of discrete material, but the track structure is of continuous medium. When analyzing the interaction between the ballast bed and track structure, it is impossible to use a single discrete element method or finite element method to analyze the interaction between the track structure and the track structure. Therefore, to address the coupling dynamics, many scholars, e.g., Gao and Xu [20] and Ngo et al. [21], built the numerical model of the granular ballast soil subgrade based on the coupling algorithm of discrete element and finite difference, analyzed the interface stress of its interaction, and verified the correctness of the model through the field measurement results. Dowding and Gilbert [22], Michael et al. [23], and Nishiura et al. [24] established the coupling models of the bulk track bed and track structure by means of the coupling method of discrete element and finite element to study the mechanical characteristics of the ballasted track. The coupling of the discrete

element, the finite element, and the finite difference method provides a new method for studying the interaction between the ballast and the track structure. However, these above-mentioned results are still far from the mature one. Specifically, in viewing the current research results, they mainly suffer from the following problems: (1) the numerical model is mostly based on two-dimensional dynamics and some three-dimensional calculation models are all scaled models; (2) the major objective is on the interaction between the ballast bed and the lower subgrade foundation, while only few of them focus on the interaction between the ballast bed and the upper track; and (3) the calculation process does not consider the adjacent sleepers, such that it cannot fully simulate the high-speed moving train load.

In view of the abovementioned deficiencies, this work first utilizes the laser scanning method to form the ballast model, and then based on the discrete and continuum coupling algorithm, we establish the coupling solution model of the ballast bed and upper track structure with three sleepers in the contact layer between the track bed and the track structure, and the contact force of the discrete element and the displacement information of the nodes of the finite element mesh are transmitted continuously. Thus, the mechanical coupling of the multilayer medium structure can be realized. On this basis, the distributed control loading mode is adopted to load the cyclic load with a certain phase difference on the three sleepers to simulate the moving load of the high-speed train. The mechanical characteristics and micromechanism of the ballast bed and continuous track structure under the dynamic load of high-speed train are studied, and the rationality of the model is verified by comparing with the existing research results. The relevant conclusions can provide scientific basis for the design and regulation of the ballasted track, and the model can also provide a reference for the further design of the test model and the design of the corresponding loading control system.

## 2. The Principle of Discrete-Continuous Medium Coupling Algorithm

In this paper, the coupling simulation model of the track structure and bulk track bed is established to simulate the interaction between the track structure and track structure under the cyclic load of train. In the process of analysis, the key point is the transfer of mechanical parameters between the discrete track bed and the continuous track structure on the coupling contact surface. Figure 1 shows the transfer mode of mechanical parameters in the coupling process.

The basic kinetic equation of particles in the figure is [25]

$$\begin{cases} m^i \ddot{r}^i = \sum_{j=1}^{N_i} F^{ij} + R^i, & i = 1, \dots, N, \\ J^i \ddot{\theta}^i = \sum_{j=1}^{N_i} q^{ij} \times F^{ij} + K_e^i, & i = 1, \dots, N, \end{cases} \quad (1)$$

where  $m^i$  is the mass of particles,  $J_i$  is the moment of inertia of particles,  $r^i$  and  $\theta^i$  are the center position and angle vector of particles,  $F^{ij}$  is the force exerted on particle  $i$  by contacting

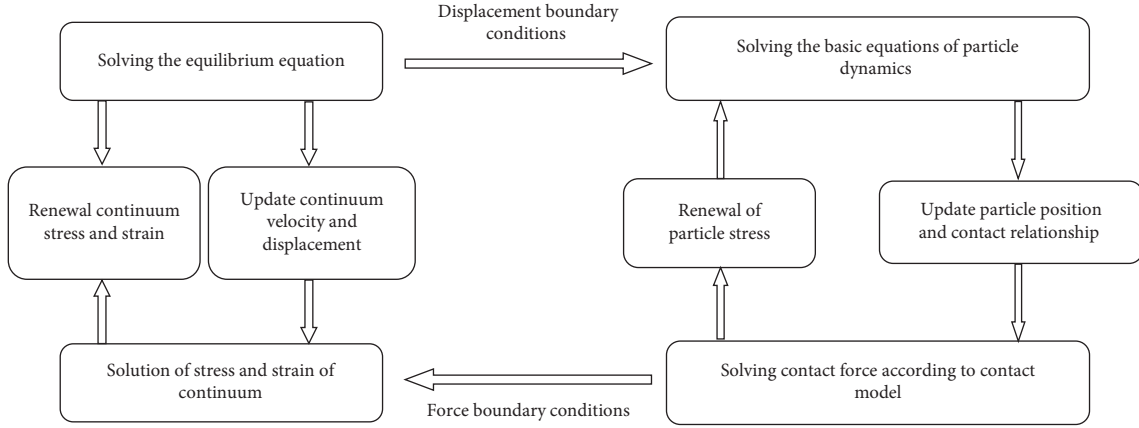


FIGURE 1: Coupled solution process of discrete-continuous medium.

particle  $j$ ,  $q^{ij}$  is the moment from force  $F^{ij}$  to the particle centroid  $i$ ,  $R^i$  and  $K_e^i$  are the external forces and moments on particle  $i$ , respectively,  $N_i$  is the number of particles in contact with  $i$ , and  $N$  is the total number of particles in the system.

The equilibrium equation of continuum is as follows:

$$M\ddot{u} = -(C\dot{u} + Ku) + F_e, \quad (2)$$

where  $\ddot{u}$ ,  $\dot{u}$ , and  $u$  represent, respectively, acceleration, velocity, and displacement of continuum nodes,  $M$ ,  $C$ , and  $K$  are the mass, damping, and stiffness matrices, respectively, and  $F_e$  is the node load.

Since the contact force on the coupling surface is usually not located on the nodes of the finite element mesh, the difference method of type row number is used to transfer the contact force from the discrete element domain to the finite element domain. In the finite element analysis of the track mechanism, the 8-node hexahedron isoperimetric element is used to mesh, and the virtual work of the contact force on the contact surface is

$$\delta W = \delta U^T P, \quad (3)$$

where  $P$  is the contact force on the coupling contact surface and  $U$  is the displacement vector at the contact point, which is obtained by interpolation of node displacement and type function as follows:

$$U = N_i^8 u_i, \quad i = 1 \sim 8, \quad (4)$$

where  $N_i^8$  is the shape function of the 8-node parameter element at the contact point and  $u_i$  is the node displacement of element.

The virtual work of the equivalent node force at the node is

$$\delta W_e = \delta u_i F_e, \quad (5)$$

where  $F_e$  is the equivalent joint force and  $\delta W = \delta W_e$  can be obtained from the principle of virtual work so that the equivalent nodal force is given as follows:

$$F_e = [N_i^8]^T P, \quad i = 1 \sim 8, \quad (6)$$

with

$$N_i(\xi, \eta, \zeta) = \frac{1}{8} (1 + \xi\xi_i)(1 + \eta\eta_i)(1 + \zeta\zeta_i), \quad i = 1, 2, 3, \dots, 8, \quad (7)$$

where  $\xi_i$ ,  $\eta_i$ , and  $\zeta_i$  are the coordinate values of the node  $(\xi_i, \eta_i, \zeta_i)$ ,  $(i = 1, 2, 3, \dots, 8)$  in the local coordinate system, which can be taken as 1 or -1.

### 3. Coupling Model of Ballast Bed and Track Structure of High-Speed Railway

**3.1. Establishment of Three-Dimensional Model of Fine Ballast Particles.** The shape of ballast particles affects the mechanical properties of the particles. The reasonable description of the shape of ballast particles is the key to realize the numerical simulation of the ballast bed. In order to establish a discrete element model that can simulate the real shape of the ballast, a three-dimensional laser scanning platform composed of a computer, a laser scanner, and a rotating platform is built to obtain the real shape of the ballast, as shown in Figure 2. The scanning range of the laser scanner is  $200 \times 320 \times 180$  mm, the scanning accuracy is higher than 0.05 mm, and the average point distance is 0.075 mm. Previous studies have shown that when the number of selected typical ballast particles is more than 10, the impact of increasing the number of particle shape samples on the simulation accuracy can be ignored [26]. Therefore, in this paper, 12 kinds of typical ballast particles are selected from a batch of high-speed railway ballast particle samples for fine modeling, and Figure 3 shows one of the typical ballast particle modeling process.

According to Figure 3, the modeling process of ballast particles is as follows. Firstly, the particle surface point cloud image is obtained through the three-dimensional laser scanning platform for ballast particles shown in Figure 2. Then, according to the point cloud of the particle surface obtained by scanning, the closed grid of the particle surface is constructed to realize the reconstruction of ballast geometry. Finally, the geometric profile of ballast particles is filled. At present, there are two forms of three-dimensional ballast particles: spherical cluster particles and bonded particles. The bonding particles can consider ballast

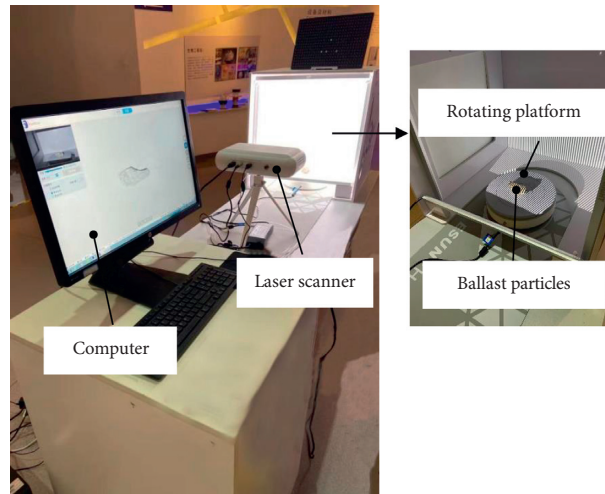


FIGURE 2: Three-dimensional laser scanning platform for ballast particles.

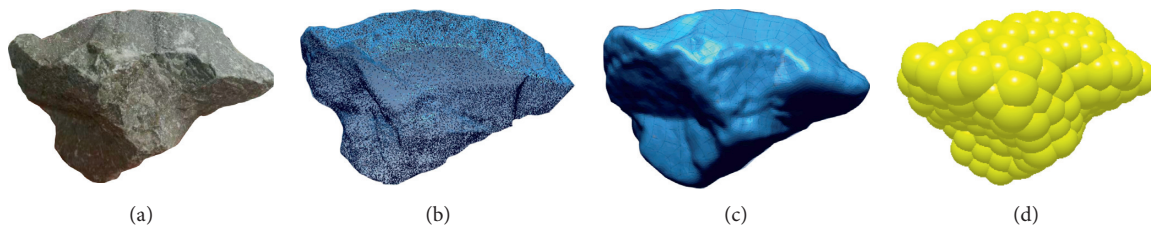


FIGURE 3: Modeling process of ballast particles: (a) true shape of ballast particles, (b) point cloud image of the ballast particle surface, (c) outer boundary of ballast particles, and (d) model of ballast particle cluster.

crushing, but for the full-scale simulation model, the amount of calculation is too large. Therefore, this paper uses multiball cluster particles to simulate the ballast. When the spherical cluster model is established, the grid coordinate information is obtained by meshing, and the appropriate spherical element radius for filling is selected according to the grid size, and then the ballast particle spherical cluster model is established by API program based on the grid coordinates and spherical element radius. The other 11 kinds of typical ballasts are finely modeled according to the modeling method shown in Figure 3, and the ballast particle geometric profile and ball cluster model are obtained, as shown in Figure 4.

In addition, the model of ballast sphere cluster can be simplified by increasing the mesh size and the radius of sphere element used for filling. It reduces the number of spheres that make up the ballast particles, reduces the number of contact search and judgment of particles in the calculation process, and improves the calculation efficiency. Figure 5 shows the comparison before and after simplification of the ballast particle cluster model.

**3.2. Coupling Model of Ballast Bed and Track Structure of High-Speed Railway.** The number of spheres in the spherical cluster model in Figure 4 is reduced without affecting the geometric shape of the particles. According to the special ballast particle gradation curve shown in Figure 6, typical

shape particles are randomly generated into ball cluster models with different particle sizes, and the coupling model of high-speed railway ballast track and track structure is established, as shown in Figure 7. When the train passes, the area of vertical dynamic wheel load is mainly concentrated in the area covered by three sleepers under the axle, which bears more than 85% of the load [27]. Therefore, in order to simulate the force effect of adjacent sleepers and eliminate the influence of displacement boundary, the simulation analysis model established includes at least three sleepers. The fixed wall boundary is set at the bottom and side of the ballast bed, respectively, while the top surface and slope of the ballast bed are free boundary. In addition, in order to truly represent the shape and corner features of the sleeper, the wall is used to simulate the sleeper.

High-speed railway requires that the ballast should be made of super granite and the sleeper should be type III concrete sleeper. The physical parameters of the ballast and sleeper are shown in Table 1.

Due to the ball cluster model used to simulate ballast particles, there is no sticky spherical surface in ballast particles and the simulated ballast bed is in a state of no dirt. Therefore, the contact between ballast particles and between ballast and geometry is a general contact. Therefore, in this paper, the Hertz–Mindlin (no-slip) contact model is used to simulate the contact between ballast particles, as well as between the ballast and sleeper and boundary. The specific contact parameters are shown in Table 2.



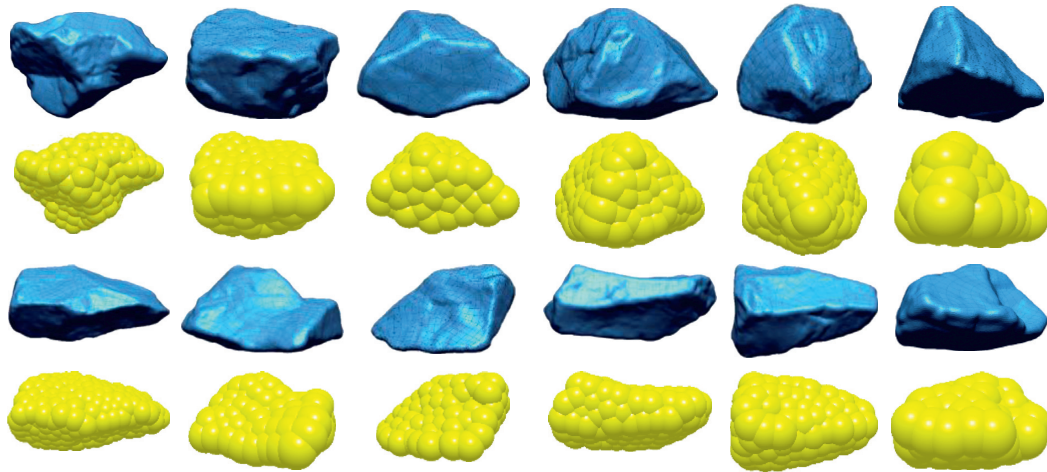


FIGURE 4: Geometric profile and ball cluster model of typical ballast particles.

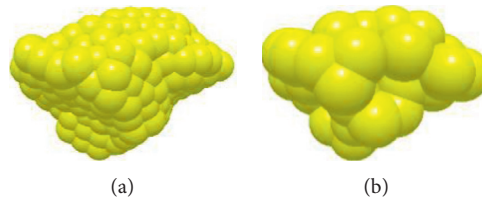


FIGURE 5: Comparison of the ballast ball cluster model before and after simplification: (a) particle cluster model and (b) simplified particle cluster model.

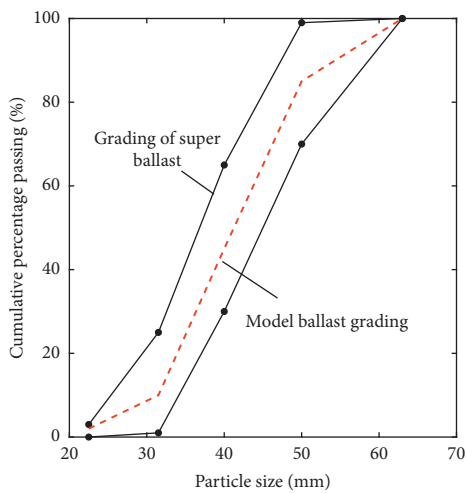


FIGURE 6: Grading curve of ballast particles.

#### 4. Moving Load Simulation and Control Loading Mode of High-Speed Vehicle with Ballast Bed

In this paper, the CHR2 type high-speed train in China is taken as the research plant, the track irregularity of Qinhuangdao Shenyang passenger dedicated line is taken as the excitation, and the vertical coupling dynamic model of the high-speed train ballasted track described in reference [28] is used to calculate the fulcrum force acting on the rail

when the EMU operates at speed of 160 km/h, 200 km/h, 250 km/h, 300 km/h, and 350 km/h, respectively. Through the abovementioned calculation, the rail fulcrum amplitudes corresponding to different speeds are 24.8 kN, 25 kN, 25.4 kN, 26 kN, and 28.8 kN, respectively. Figure 8 is the schematic diagram of the middle car body of the CHR2 high-speed train set. It can be seen from Figure 8 that the distance between the two bogies in the middle car is 17500 mm, and the distance between the bogie and both ends of the car is 3500 mm. In order to accurately simulate the train load, the distance between the two bogies is used as the train load interval. Therefore, the train passing frequencies corresponding to the abovementioned speeds are obtained by equation  $f = v/L$ , which are 2.54 Hz, 3.17 Hz, 3.97 Hz, 4.76 Hz, and 5.56 Hz. In the formula,  $f$  is the passing frequency,  $v$  is the driving speed, and  $L$  is the distance between the bogies. Given the amplitude of rail fulcrum force and train passing frequency, the curve of train cyclic load can be obtained, considering the load phase difference of adjacent sleepers, and the train cyclic load curve of three sleepers in 1 s under the speed of 250 km/h is shown in Figure 9.

The controlled loading mode of the moving load of the high-speed vehicle is shown in Figure 10. As can be seen from Figure 10, when the vertical wheel load of the train acts directly above the middle sleeper, the loading forces shared by the three sleepers are  $F_1$ ,  $F_2$ , and  $F_3$ , respectively.  $G_1$ ,  $G_2$ , and  $G_3$  in the picture represent the weight of the three sleepers, respectively. When the high-speed train passes

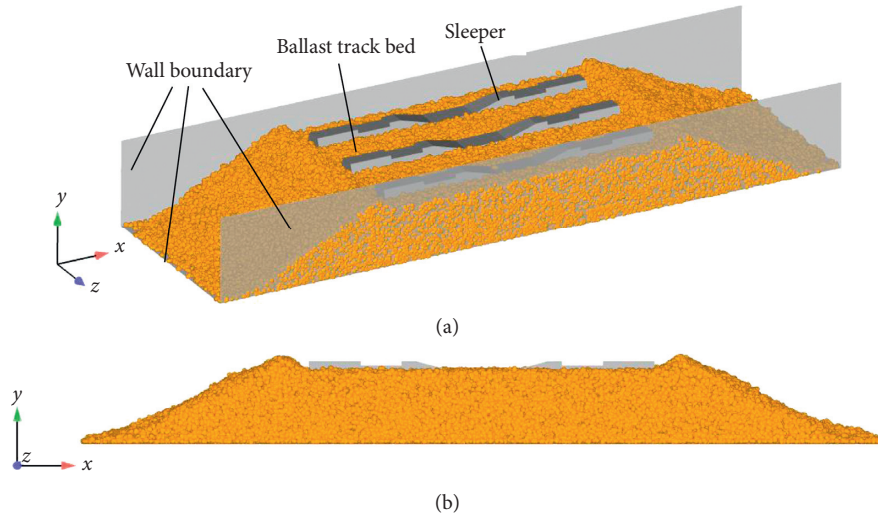


FIGURE 7: Coupling model of the ballasted bed and track structure of high-speed railway: (a) general view and (b) main view.

TABLE 1: Physical parameters of the ballast and sleeper.

Physical parameters	Ballast	Type III concrete sleeper
Density ( $\text{kg}\cdot\text{m}^{-3}$ )	2700	2000
Poisson's ratio	0.25	0.25
Shear modulus (Pa)	$1.0 \times 10^{10}$	$1.44 \times 10^{10}$

TABLE 2: Contact parameters of the discrete element model.

Contact parameter	Between ballast particles	Between ballast particles and sleeper and side boundary
Restitution coefficient	0.6	0.6
Coefficient of static friction	0.8	0.86
Dynamic friction coefficient	0.1	0.03

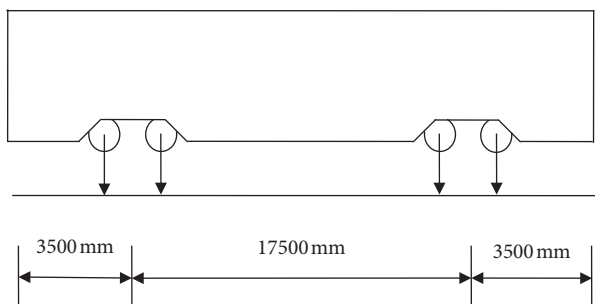


FIGURE 8: Cyclic load curve of train with speed of 250 km/h.

through the ballast bed, the moving wheel load acting on the sleeper through the rail is the moving load. The distributed control loading mode is adopted to realize the independent control of the loading force, and the phase difference of the loading forces  $F_1$ ,  $F_2$ , and  $F_3$  of the adjacent sleepers is controlled by writing the loading program so that the moving loading of trains with different speeds can be completed. In addition to the moving load transmitted by the sleeper, the ballasted bed also bears the weight of the sleeper, so a servo is introduced to apply gravity to the wall sleeper in the process of calculation.

## 5. Mechanical Characteristics of Ballasted Bed of High-Speed Railway

### 5.1. Dynamic Characteristics and Settlement of Loose Ballast Bed

5.1.1. *Dynamic Characteristics of Ballast Contact Force under Dynamic Load of High-Speed Train.* In order to study the change of ballast contact force in the ballast bed when the high-speed train passes, Figure 11 shows the spatial distribution of ballast contact force vector before the train passes and when the train passes at 200 km/h, 250 km/h, and 300 km/h. Figure 11(a) shows the spatial distribution of the ballast contact force vector in the track bed before the train passes. Figures 11(b)–11(d), respectively, show the spatial distribution of the ballast contact force vector when the train passes at 200 km/h, 250 km/h, and 300 km/h. In the figure, the direction of the solid line segment indicates the contact force direction of the ballast, and the color of the solid line segment indicates the contact force. It can be seen from Figure 11(a) that the contact force of the ballast in the ballast bed is evenly distributed before the train passes through, only a small amount of large contact force appears under the sleeper, and the contact force of the ballast before loading is



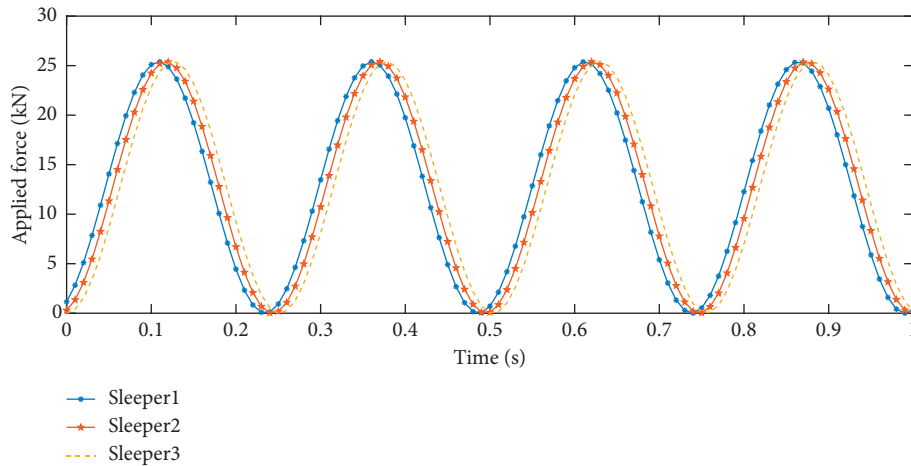


FIGURE 9: Cyclic load curve of train with speed of 250 km/h.

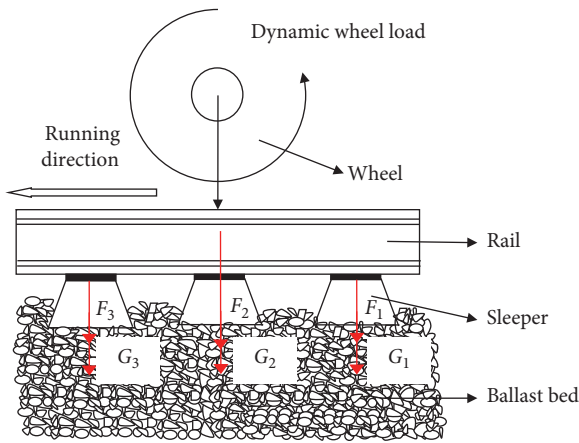


FIGURE 10: Control loading mode of moving load of high-speed vehicle.

very small because the ballast bed is not compacted before loading. It can be seen from Figures 11(b)–11(d) that the train passes at a certain speed, the ballast contact force inside the ballast bed is not evenly distributed, and the contact force is mainly distributed on the bottom of the sleeper, and the direction is spread in the form of trapezoid downward, which is basically consistent with the previous research [29]. The contact around the sleeper is relatively large, but the contact force is mainly distributed in the shallower position directly below the sleeper. With the increase of the depth of the ballast bed, the contact force of the ballast decreases continuously, which shows that the ballast bed can disperse and reduce the train load. The higher the driving speed, the more uneven the spatial distribution of the contact force vector of the ballast in the track bed, and the contact force increases with the increase of speed.

At different speeds, the maximum and average contact force of ballast in the ballast bed is shown in Figure 12. As it can be seen from Figure 12, there is a significant difference between the maximum contact force and the average contact force between ballasts, mainly because the ballast particles of the ballast shoulder are generally at rest when the train

passes. The results show that the maximum contact force and average contact force of the ballast increase with the increase of speed. When the driving speed is 160 km/h, the maximum contact force of ballast is 7372.1 N, and the average contact force is 3.13 N. When the driving speed is 250 km/h, the maximum contact force of the ballast is 7425.3 N, and the average contact force is 3.20 N, increasing by 0.72% and 2.2%, respectively. When the driving speed increases to 350 km/h, the maximum contact force of the ballast is 7647.0 N, the average contact force is 10.0 N, the maximum contact force increases by 3.73%, and the average contact force increases by 3.2 times. The abovementioned analysis shows that the higher the driving speed is, the greater the contact force of ballast will be. When the driving speed reaches 250 km/h, the growth rate of contact force will be high rapidly.

*5.1.2. The Change of Ballast Angular Velocity under Dynamic Load of High-Speed Train.* The rearrangement of ballast particles is the main factor affecting the stability of the ballast bed and also the direct factor causing the settlement of the ballast bed. The rearrangement of ballast particles is mainly due to the contact sliding and rotation between ballast particles, in which the relative rotation angular velocity of ballast particles describes the overall rotation angle of ballast particles. Figure 13 shows the change of ballast rotation angle speed under different driving speeds when the load reaches the peak value. It can be seen from the figure that the greater the train speed, the greater the average speed of the ballast. When the running speed varies from 160 km/h to 300 km/h, the average speed of the ballast changes slowly. When the speed is 350 km/h, the ballast speed increases significantly. From the figure, due to the discreteness of the ballast bed, the maximum velocity of ballast particles has no obvious rule.

*5.1.3. Effect of Driving Speed on Cumulative Settlement of Ballast Bed.* The ballast will produce movement and deformation during the train load cycle, which will lead to the settlement of the ballast bed. The uneven settlement of track

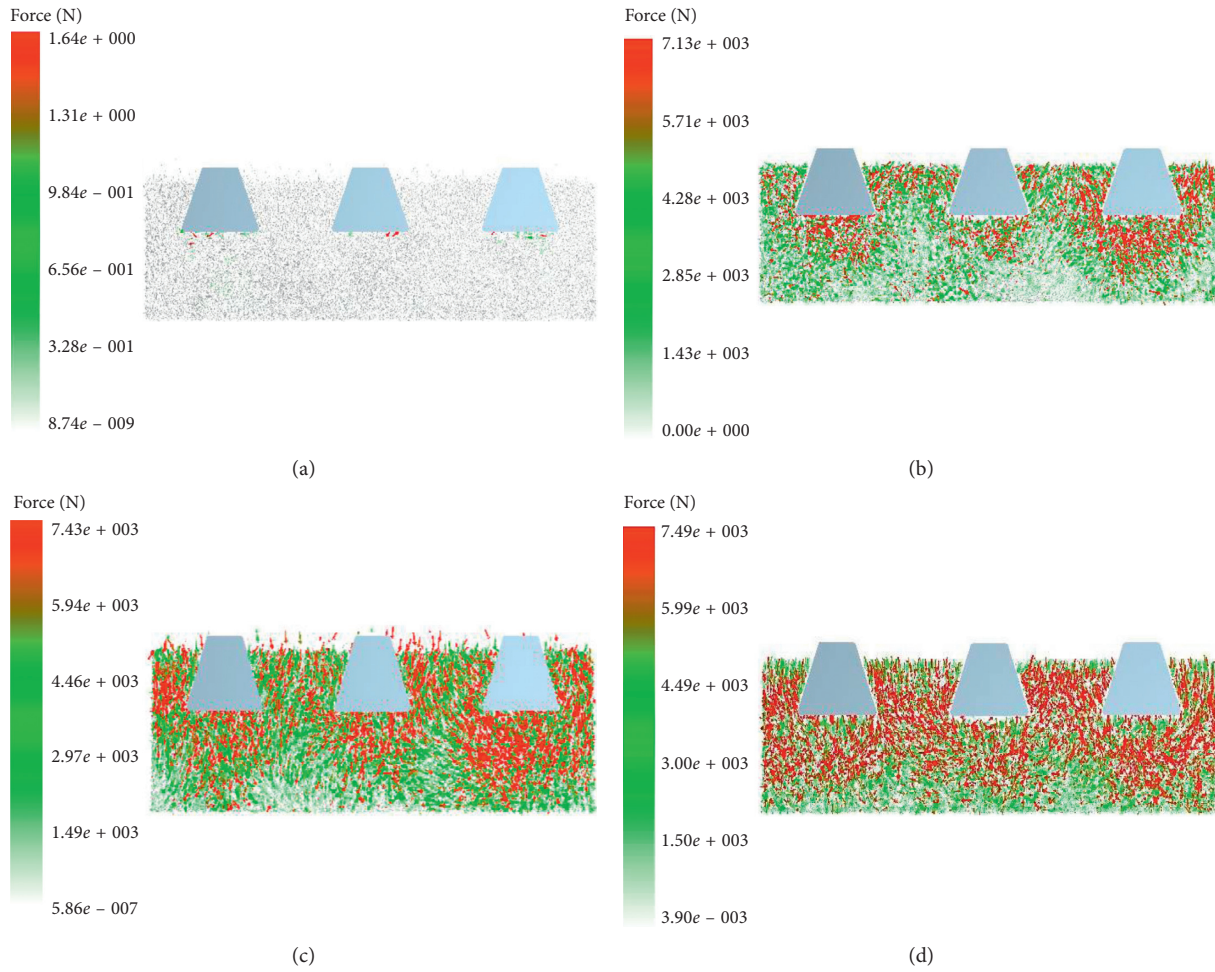


FIGURE 11: Spatial distribution of ballast contact force: (a) before train passing, (b) when the train passes at 200 km/h, (c) when the train passes at 250 km/h, and (d) when the train passes at 300 km/h.

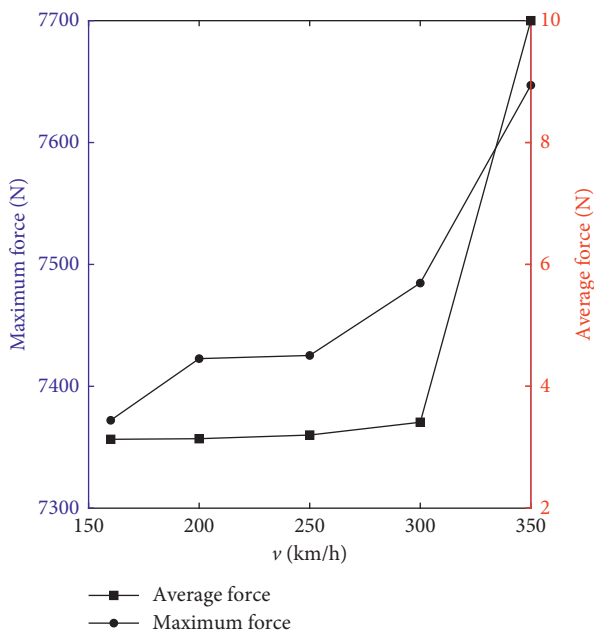


FIGURE 12: Maximum and average contact force of the ballast at different speeds.

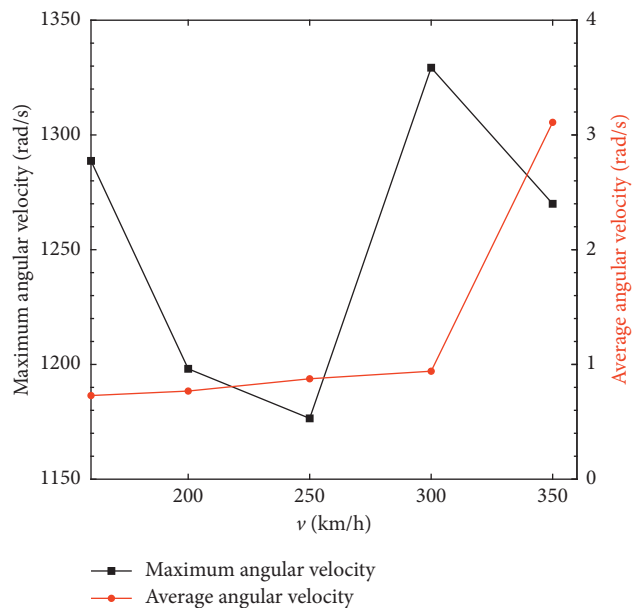


FIGURE 13: Maximum and average value of ballast angular speed at different speeds.

bed leads to track irregularity, which directly threatens the safety of train operation. The running speed of high-speed train is one of the main factors affecting the stability of the ballasted track so that it is necessary to study the settlement characteristics of their ballast bed from the aspect of train running speed. In the coupling model established in this paper, the wall is used to simulate the sleeper and endow the sleeper with weight so that the sleeper is in the direct contact with the ballast, and the settlement of the track bed can be expressed by the vertical settlement of the sleeper. In order to ensure the reliability of the results, the settlement of the middle sleeper in the vertical direction is selected to represent the ballast settlement, and the relationship between driving speed and ballast cumulative settlement is obtained, as shown in Figure 14. It can be seen from Figure 14 that the larger the driving speed is, the faster the accumulated settlement and settlement speed of the ballast bed will be. As the ballast bed is not compacted in the layers, the settlement of the ballast bed is large at the initial stage of loading. With the increase of loading times, the settlement speed of the ballast bed becomes slow.

To sum up, the running speed of high-speed trains directly affects the force chain distribution, the contact force size, and the relative rotation speed of ballast particles in the ballast bed, and the greater the running speed, the greater the contact force and rotation speed between the ballast. However, the mutual movement of ballast particles leads to the settlement of the ballast bed so that the larger the driving speed is, the greater the accumulated deposition speed and the accumulated settlement of ballast bed are.

5.2. The Force Acting on the Track Structure and the Settlement Characteristics of the Track Bed

5.2.1. Analysis of Contact Characteristics between Sleeper and Ballast. When the high-speed train is running, there will be interaction between the sleeper and ballast under the action of train load. The coupling model of the ballast bed and track structure was established to analyze the contact between the sleeper and ballast at different running speeds.

Figure 15 shows the contact between the ballast and the sleeper when the load reaches the peak. In Figure 15, the direction of the solid line segment indicates the direction of contact force, and the color and thickness of the solid line segment indicate the contact size. As it can be seen from the figure, the number of contacts between the ballast and the end face of the sleeper is the least, and the contact force is also relatively small. Although there are many contacts on the side of sleeper, the contribution to the resistance of the ballast bed is relatively small. The contact force between the sleeper and ballast bed mainly comes from the bottom of the sleeper, which is consistent with previous research results [7].

Figure 16 shows the relationship between the number of contacts and between the ballast and sleeper when the driving speed is 250 km/h. It can be seen from the figure that when the train passes, the ballast particles in the track bed will rotate, slide, and rearrange continuously, which will lead to the continuous fluctuation of the number of contacts

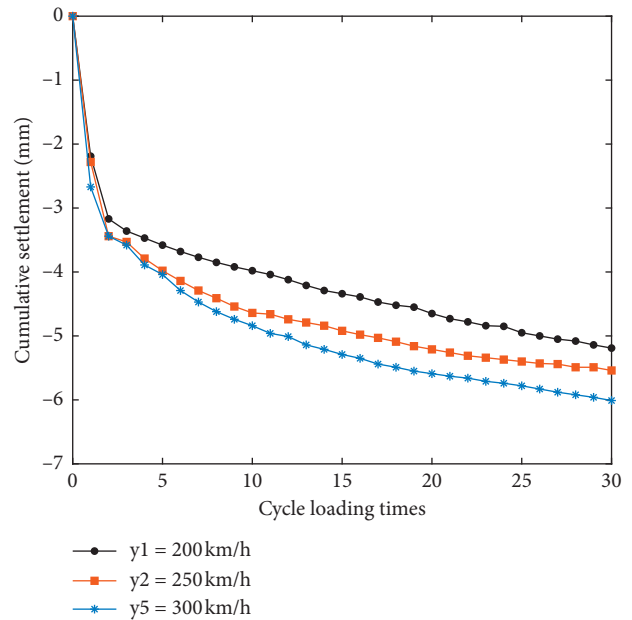


FIGURE 14: Driving speed and ballast bed settlement.

between the ballast and the sleeper. The number of contacts between the middle sleeper and the ballast is relatively low, indicating that the resistance of the middle sleeper is less than that of the other two sleepers. It shows that the wall boundary has a significant influence on the sleeper, and the scale model considering only one sleeper has limitations in the process of calculation.

Figure 17 shows the relationship between the number of contacts and between the ballast and intermediate sleeper with time at different driving speeds. As it can be seen from the figure, due to the lack of layered compaction of the ballast, the number of contacts between the sleeper and the ballast increases rapidly at the beginning of loading. When the driving speed is 160 km/h, 200 km/h, 250 km/h, and 300 km/h, the contact number between the sleeper and ballast is similar, and the change trend of the contact number with time is stable. When the driving speed is 350 km/h, the number of contacts between the sleeper and ballast is relatively large, and the number of contacts changes greatly. Due to the discrete characteristics of ballast bed, the number of contacts between the ballast and sleeper has no obvious rule under different driving speeds, and it proves the discreteness of contact between the sleeper and ballast bed.

5.2.2. Analysis of Contact Strength between Sleeper and Ballast Bed. The contact strength between the sleeper and ballast bed is the ratio of contact force and contact area between the bottom of the sleeper and ballast bed, where the contact area is 7228.56 cm<sup>2</sup>. Since the contact area is constant, the change trend of contact force and contact strength is consistent. Figure 18 shows the contact strength between the bottom of the sleeper and the ballast at different driving speeds. It can be seen from the figure that the change trend of contact strength is close to the change trend of contact force and rotation speed of ballast particles in Figures 7 and 13.

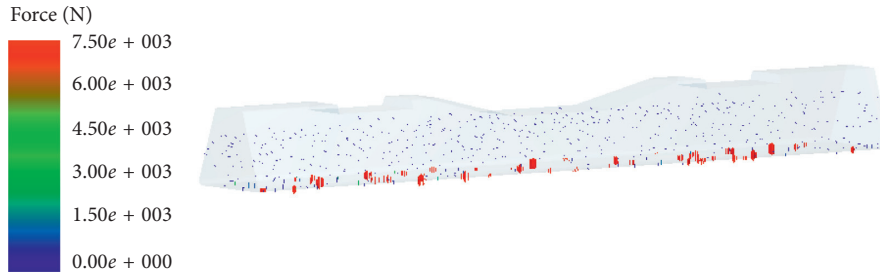


FIGURE 15: Contact distribution between the ballast and sleeper.

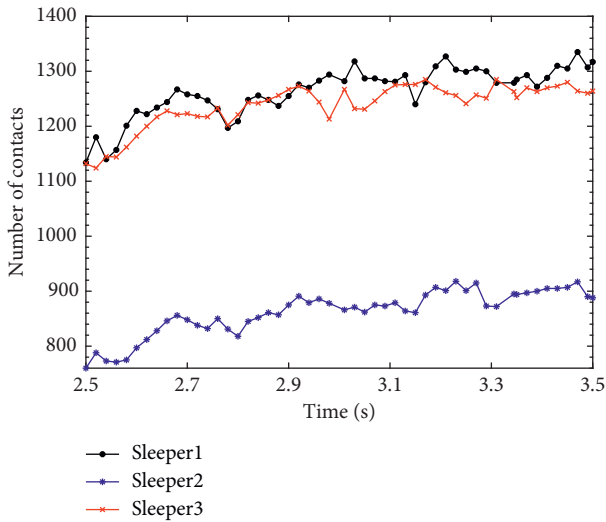


FIGURE 16: Number of contacts between the ballast and sleeper.

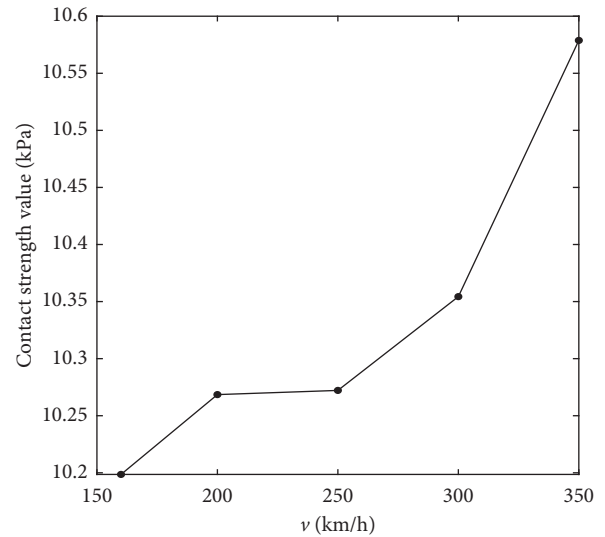


FIGURE 18: Contact strength between the sleeper and ballast.

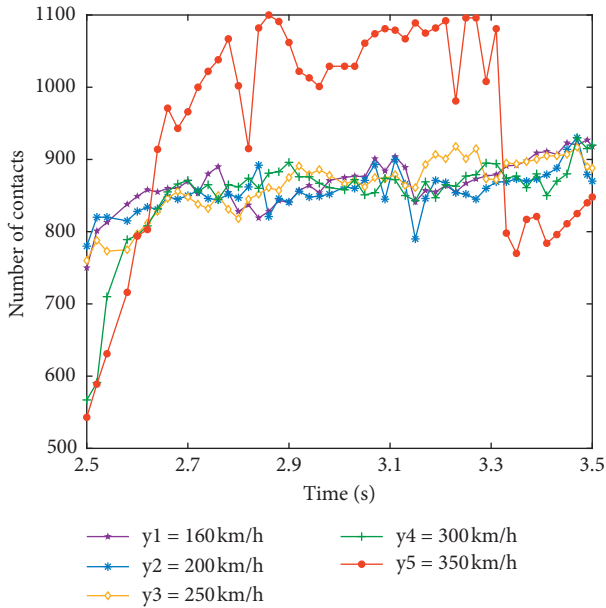


FIGURE 17: The relationship between the number of contacts between the ballast and sleeper with time.

And with the increase of driving speed, the value of contact strength increases, which means that the contact force increases with the increase of driving speed. Compared with

Figure 14, the greater the contact strength between the sleeper and the ballast is, the faster the settlement speed of the ballast bed is and the greater the settlement is.

## 6. Conclusion

- (1) In this paper, the three-dimensional laser scanning method is used to establish the real model of the ballast, and then the coupling model of the ballast bed and upper track structure with three sleepers is established based on the coupling method of the discrete body and continuous body. The analysis of the contact between three sleepers and ballast shows that the wall boundary has a significant impact on the sleepers, and the coupling model considering only one sleeper has limitations in the calculation process. The conclusion can provide a reference for further research on the coupling modeling of the ballast bed and track structure.
- (2) Based on the coupling model of the ballast bed and track structure, the macro- and microdynamic characteristics of the ballast bed under the dynamic load of high-speed trains with different speeds are studied. The results show that the running speed of the high-speed train directly affects the force chain



distribution of the ballast in the ballast bed, the contact force between ballast particles and the relative rotation speed of ballast particles. The larger the driving speed is, the larger the contact force and rotation speed between the ballasts will be, which will eventually lead to the increase of the accumulated deposition speed and the accumulated settlement amount of the ballast bed with the increase of the driving speed. This conclusion provides a reference for the study of macroscopic and mesoscopic characteristics of the ballast bed settlement.

- (3) The coupling contact between the ballast bed and track structure is studied. The results show that the ballast has contact with the end, side, and bottom of the sleeper. Although there are a large number of contacts between the ballast and the side of the sleeper, the contact force here is relatively small, and the contact force between the sleeper and the ballast bed mainly comes from the bottom of the sleeper. In addition, the contact strength and contact force between the sleeper and the track bed are directly proportional to the driving speed. The conclusion provides a reference for the study of the coupling contact between the ballast bed and the track structure.
- (4) The distributed control method is used to simulate the moving load of the high-speed train. The research results provide reference for the further design of the test model and the design of the corresponding loading control system.

## Data Availability

The data used to support the findings of this study are available from the corresponding author upon request.

## Conflicts of Interest

The authors declare that they have no conflicts of interest.

## Acknowledgments

This work was supported by the Natural Science Foundation of China (NSFC) under Grant nos. 51565021 and 51965029.

## References

- [1] Y. Guo, V. Markine, X. Zhang, W. Qiang, and G. Jing, "Image analysis for morphology, rheology and degradation study of railway ballast: a review," *Transportation Geotechnics*, vol. 18, pp. 173–211, 2019.
- [2] A. M. Kaynia, C. Madshus, and P. Zackrisson, "Ground vibration from high-speed trains: prediction and countermeasure," *Journal of Geotechnical and Geoenvironmental Engineering*, vol. 126, no. 6, pp. 531–537, 2000.
- [3] A. A. Shaer, D. Duhamel, K. Sab, G. Foret, and L. Schmitt, "Experimental settlement and dynamic behavior of a portion of ballasted railway track under high speed trains," *Journal of Sound & Vibration*, vol. 316, no. 1–5, pp. 211–233, 2008.
- [4] T. Ishikawa, E. Sekine, and S. Miura, "Cyclic deformation of granular material subjected to moving-wheel loads," *Canadian Geotechnical Journal*, vol. 48, no. 5, pp. 691–703, 2011.
- [5] Y. Koike, T. Nakamura, K. Hayano, and Y. Momoya, "Numerical method for evaluating the lateral resistance of sleepers in ballasted tracks," *Soils and Foundations*, vol. 54, no. 3, pp. 502–514, 2014.
- [6] J. Kennedy, *A full-scale laboratory investigation into railway track substructure performance and ballast reinforcement*, Ph.D. dissertation, Heriot-Watt University, Edinburgh, UK, 2011.
- [7] G. Q. Jing, H. Fu, W. L. Jia et al., "Macro-micro analysis of lateral resistance for high speed railway ballasted track," *Journal of Railway Engineering Society*, vol. 35, no. 9, pp. 24–28, 2018, in Chinese.
- [8] H. Faghihi Kashani, J. P. Hyslip, and C. L. Ho, "Laboratory evaluation of railroad ballast behavior under heavy axle load and high traffic conditions," *Transportation Geotechnics*, vol. 11, pp. 69–81, 2017.
- [9] Y. Momoya, T. Takahashi, and T. Nakamura, "A study on the deformation characteristics of ballasted track at structural transition zone by multi-actuator moving loading test apparatus," *Transportation Geotechnics*, vol. 6, pp. 123–134, 2016.
- [10] Z. Yu, D. P. Connolly, P. K. Woodward, and O. Laghrouche, "Settlement behaviour of hybrid asphalt-ballast railway tracks," *Construction and Building Materials*, vol. 208, pp. 808–817, 2019.
- [11] Q. M. Zhu, D. Y. Zhao, and J. H. Zhang, "A general U-block model based design procedure for nonlinear polynomial control systems," *International Journal of Systems Science*, vol. 47, no. 17, pp. 3465–3475, 2016.
- [12] Q. Zhu, W. Zhang, J. Zhang, and B. Sun, "U-neural network-enhanced control of nonlinear dynamic systems," *Neurocomputing*, vol. 352, pp. 12–21, 2019.
- [13] Q. Zhu, L. Liu, W. Zhang, and S. Li, "Control of complex nonlinear dynamic rational systems," *Complexity*, vol. 2018, Article ID 8953035, 12 pages, 2018.
- [14] X. Geng, Q. Zhu, T. Liu, and J. Na, "U-model based predictive control for nonlinear processes with input delay," *Journal of Process Control*, vol. 75, pp. 156–170, 2019.
- [15] S. Lobo-Guerrero and L. E. Vallejo, "Discrete element method analysis of railtrack ballast degradation during cyclic loading," *Granular Matter*, vol. 8, no. 3–4, pp. 195–204, 2006.
- [16] Y. Tian, C. Zhang, and Y. Z. Sun, "The application of mesh-free method in the numerical simulation of beams with the size effect," *Mathematical Problems in Engineering*, vol. 2014, Article ID 590271, 6 pages, 2014.
- [17] E. Kabo, "A numerical study of the lateral ballast resistance in railway tracks," *Proceedings of the Institution of Mechanical Engineers, Part F: Journal of Rail and Rapid Transit*, vol. 220, no. 4, pp. 425–433, 2006.
- [18] J. Y. Shih, D. Kostovasilis, Y. Bezin et al., "Modelling options for ballast track dynamics," in *Proceedings of the 24th International Congress on Sound and Vibration*, London, UK, July 2017.
- [19] L. Gao, Q. Luo, Y. Xu et al., "Effects of ballast bed section dimension on its lateral resistance," *Journal of Southwest Jiaotong University*, vol. 49, no. 6, pp. 954–960, 2014.
- [20] L. Gao and Y. Xu, "Application of coupled discrete element-finite difference method in railway ballast bed research," *Journal of Beijing Jiaotong University*, vol. 40, no. 4, pp. 37–44, 2016, in Chinese.

- [21] N. T. Ngo, B. Indraratna, and C. Rujikiatkamjorn, "Simulation ballasted track behavior: numerical treatment and field application," *International Journal of Geomechanics*, vol. 17, no. 6, pp. 04016130-1-04016130-12, 2017.
- [22] C. H. Dowding and C. Gilbert, "Dynamic stability of rock slopes and high frequency traveling waves," *Journal of Geotechnical Engineering*, vol. 114, no. 10, pp. 1069-1088, 2016.
- [23] M. Michael, F. Vogel, and B. Peters, "DEM-FEM coupling simulations of the interactions between a tire tread and granular terrain," *Computer Methods in Applied Mechanics and Engineering*, vol. 289, pp. 227-248, 2015.
- [24] D. Nishiura, H. Sakai, A. Aikawa, S. Tsuzuki, and H. Sakaguchi, "Novel discrete element modeling coupled with finite element method for investigating ballasted railway track dynamics," *Computers and Geotechnics*, vol. 96, pp. 40-54, 2018.
- [25] Z. P. Tang, "Three-dimensional DEM theory and its application to impact mechanics," *Science in China (Series E)*, vol. 44, no. 6, pp. 561-571, 2001.
- [26] H. Huang, *Discrete element modeling of railroad ballast using imaging based aggregate morphology characterization*, Ph.D. dissertation, University of Illinois, Urbana, IL, USA, 2010.
- [27] V. A. Profillidis, *Railway Engineering*, Ashgate Publishing Limited, Aldershot, UK, 2000.
- [28] X. Zhang, *Numerical Simulation and Experiment Study on Macro-Micro Mechanical Behaviors of High-Speed Railway Ballast*, Southwest Jiaotong University, Chengdu, China, 2017, in Chinese.
- [29] D. R. Ahlbeck, H. C. Meacham, and R. H. Prause, "The development of analytical models for railroad track dynamics," in *Proceedings of the Symposium on Railroad Track Mechanics & Technology*, pp. 239-263, Princeton, NJ, USA, January 1978.



## Research Article

# U-Model-Based Finite-Time Control for Nonlinear Valve-Controlled Hydraulic Servosystem

Hao Yan <sup>1,2</sup>, Jiafeng Li <sup>1</sup>, Hassan Nouri,<sup>3</sup> and Lingling Xu<sup>1</sup>

<sup>1</sup>School of Mechanical, Electronic and Control Engineering, Beijing Jiaotong University, Beijing 100044, China

<sup>2</sup>Key Laboratory of Vehicle Advanced Manufacturing, Measuring and Control Technology, Beijing Jiaotong University, Ministry of Education, Beijing 100044, China

<sup>3</sup>Power System and Control Research Laboratory, University of the West of England, Bristol BS16 1QY, UK

Correspondence should be addressed to Hao Yan; [hyan@bjtu.edu.cn](mailto:hyan@bjtu.edu.cn)

Received 25 November 2019; Accepted 4 January 2020; Published 10 February 2020

Guest Editor: Weicun Zhang

Copyright © 2020 Hao Yan et al. This is an open access article distributed under the Creative Commons Attribution License, which permits unrestricted use, distribution, and reproduction in any medium, provided the original work is properly cited.

Valve-controlled servosystems are widely used in dynamic tracking, but, not properly studied, nonlinearity, perturbation of internal parameters, and external disturbance have significant impacts on the control performance and challenge in the controller design. This study, with consideration of the finite pressure gain of actual servovalves, proposes a new unified nonlinear model of the valve-controlled servosystem. Based on a U-control platform, this study makes the control strategy design independent from the nonlinear plant, and a virtual nominal plant is presented to eliminate the unmodeled high-frequency characteristics, acquire the desired control performance, and enable the control variable to be explicitly expressed. Then, there follows, designing the U-model-based finite-time control in the valve-controlled systems. Simulation demonstrations show the consistency with theoretical development that the valve-controlled system can smoothly track the command signal within the specified time, and the phase lag is eliminated. Moreover, U-model's application effectively copes with the system chattering, and with the maximum of 1 m/s the dynamic position error caused by discretization of the controller is reduced to less than 0.15%, which can satisfy the demand of general valve-controlled servosystems.

## 1. Introduction

With the advantages of fast response and high stiffness, valve-controlled servosystems have been widely applied in machinery manufacturing, ship maneuvering, and industrial control. The traditional valve-controlled system often adopts output feedback and the PID control method to achieve dynamic tracking. However, almost all the valve-controlled systems work based on the throttle mechanism and the working pressure produced by closed chambers. Therefore, inherent nonlinear elements exist. With the increase of the spool deviation and the movement of the actuator, not only the nonlinear throttling effect becomes remarkable but also the structural parameters of the hydraulic actuator vary. Particularly, the orifices exhibit different directional properties in valve forward and reverse. Actually, for strongly dynamic signals, the tracking effect of the valve-controlled

system is often unsatisfactory, involving phenomena of lag and attenuation. In addition, parameter uncertainties and external disturbances also play a complicated role in degrading the valve-controlled system operation. Consequently, for improving control performance, new research and development should expand those developed from linear model-based approaches that treat the valve-controlled systems as a linear system and simplify it into a second-order oscillating element.

The traditional controller design of the valve-controlled servosystem is based on the linearization of the hydraulic drive mechanism and frequency domain analyses [1–3], forming a set of linear theoretical methods and focusing on the valve control system's applications in engineering. To adapt to the advanced control algorithm and enhance the dynamic performance further, building up a nonlinear state space model and pursuing the finite transitional time

become important research topics. Although the finite-time control has been developed in some tracking applications in recent years [4–8], it is seldom appeared in valve-controlled systems due to the difficulty of constructing a reasonable model for this nonlinear system. Ye [9] established different nonlinear state space models for different directions of the orifice and linearized them, respectively. Based on nonlinear models of the valve-controlled system, Li et al. [10] built an adaptive sliding mode controller. In this system, the fuzzy algorithm is used to estimate the equivalent control and the genetic algorithm is used to realize the adaptive switching control. And Li et al. [11] applied the second-order sliding mode control method in the valve-controlled system and scheduled the reaching speed with the optimization objective of time, which is substantially a finite-time controller. Schmidt et al. [12] clearly presented a finite-time controller for the linearized valve-controlled system by utilizing a modified super-twisting controller. Moreover, adopting the terminal sliding mode control method, Yao et al. [13] proposed a finite-time controller for the nonlinear valve-controlled system. In a critical comment of these aforementioned studies, the nonlinear models are all variable structure models depending on the polarity of the valve's control variable, which is only an ideal situation and inconsistent with the actual system. And since the control variable cannot be expressed explicitly, the discontinuity and mismatching caused by the control variable could only be treated as uncertainty, and the global robustness to initial states was not considered. These factors have restricted further improvement of the finite-time controller for valve-controlled systems.

In fact, to reduce the complexity of the model-based control system design, particularly for those nonlinear dynamic plants, Zhu [14–16] proposed a systematical universal transform to convert classical nonlinear polynomial models into  $U$ -models with time-varying parameters and controller output  $u(t-1)$ . This  $U$ -model-based control design framework,  $U$ -control in short, and it stands for <model independent design> against conventional <model based design> and <model free (data driven) design>. In the design, no matter what kind of the plant model structure is, like linear/nonlinear or polynomial/state space,  $U$ -control separates the closed-loop control system design from controller output determination, accordingly a linear control performance with dynamic and steady state requests can be specified with damping ratio and undamped natural frequency. For determining the controller output, the plant  $U$ -model is referred facilitating dynamic inversion in root solving. It should be noted that  $U$ -control is not aiming at increasing control accuracy; it is, indeed, for improving design feasibility and efficiency in concise formulation. As it is a supplement to the classical model-based control framework,  $U$ -control can integrate well-developed linear control system design approaches with nonlinear dynamic plants.

The major contributions of the study include

- (1) Deriving a proper principle model to accommodate dynamic and nonlinearities for a typical valve-controlled servosystem

- (2) Using  $U$ -control to separate control system design and controller output determination
- (3) Developing a global robust sliding mode control scheme for valve-controlled systems
- (4) Providing computational experiments to validate the control scheme and to guide the potential users in their potential ad hoc applications

The rest of the study is organised into five sections. Section 1 establishes the nonlinear model of a typical valve-controlled system. After analysis on the model variable structure, it reformulates a more practical and unified nonlinear model. Section 2 derives the  $U$ -model realization of the principle model developed in Section 1, which is used for the dynamic inversion of the valve-controlled system and proposes a virtual nominal plant model to eliminate the unmodeled high-frequency dynamics and achieve the performance objective. Section 3 derives a global robust finite-time controller based on  $U$ -control platform. Section 4 provides simulation studies to demonstrate the feasibility of the proposed controller procedure, in addition to provide guidance for potential users for their ad hoc expansions/applications. Finally, Section 5 concludes the study.

## 2. Modeling of Valve-Controlled Servosystems

Figure 1 shows a typical valve-controlled system consists of four-way spool valves and a symmetrical hydraulic actuator. The hydraulic oil is throttled twice from the inlet and outlet, and then the pressure is formed in the left and right chambers of the cylinder. The pressure difference between the two chambers is the working pressure, which drives the piston for load motion. Generally, the load includes inertia, elastic and viscous components, and other arbitrary components can be thought of as external disturbances.

Assuming that the fluid is incompressible, it can formulate the valve-controlled system as [2]

$$Q_L = C_d w_x x_v \sqrt{\frac{1}{\rho} (P_s - \text{sgn}(x_v) P_L)}, \quad (1)$$

$$Q_L = A \dot{y} + C_{te} P_L + \frac{V_t}{4\beta_e} \dot{P}_L, \quad (2)$$

$$A P_L = m \ddot{y} + B_c \dot{y} + K y + F, \quad (3)$$

where  $x_v$ : the displacement of the spool,  $P_L$ : the working pressure,  $A$ : the effective area of the piston,  $y$ : the displacement of the piston,  $\beta_e$ : the elastic modulus of oil,  $V_t$ : the total volume of the two chambers of the cylinder,  $m$ : the total mass of the piston,  $B_c$ : the damping coefficient of the load,  $K$ : the spring stiffness of the load,  $F$ : the arbitrary external load acting on the piston,  $C_d$ : the flow coefficient of the throttle,  $w_x$ : the area gradient of the orifice,  $P_s$ : the supply pressure of the oil,  $\rho$ : the density of the oil, and  $C_{te}$ : the total leaking coefficient calculated by  $C_{te} = C_{ic} + C_{ec}$  in which  $C_{ic}$  and  $C_{ec}$  are the internal leaking coefficient and external leaking coefficient, respectively.

From equations (1) and (2), it gives

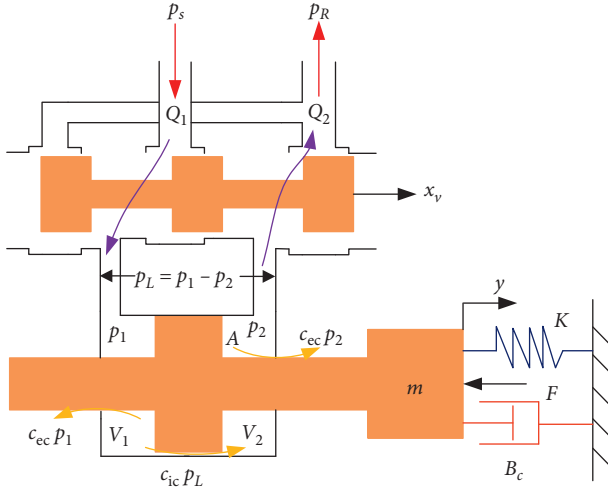


FIGURE 1: Valve-controlled system's structure.

$$A\dot{y} + C_{te}P_L + \frac{V_t}{4\beta_e}\dot{P}_L = C_d w_x x_v \left( \frac{1}{\rho} (P_s - \text{sgn}(x_v)P_L) \right)^{1/2}. \quad (4)$$

(3) and its derivative give the following set equations:

$$P_L = \frac{1}{A} (m\ddot{y} + B_c\dot{y} + Ky + F), \quad (5)$$

$$\dot{P}_L = \frac{1}{A} (m\ddot{\dot{y}} + B_c\dot{\dot{y}} + K\dot{y} + \dot{F}). \quad (6)$$

Substituting equations (5) and (6) into equation (4) yields

$$\ddot{y} = -\left(\frac{C_{te}}{b} + \frac{B_c}{m}\right)\dot{y} - \frac{A^2 + C_{te}B_c + bK}{bm}\dot{y} - \frac{C_{te}K}{bm}y - \left(\frac{C_{te}}{bm}F + \frac{1}{m}\dot{F}\right) + \Psi(x_v, y, F), \quad (7)$$

where  $\Psi(x_v, y, F) = ((AC_d w_x \sqrt{(1/\rho)})/bm) (P_s - \text{sgn}(x_v) (1/A)(m\dot{y} + B_c\dot{y} + Ky + F))^{1/2} x_v$ , and  $b = (V_t/4\beta_e)$ .

Choosing the state variables as

$$\begin{cases} x_1 = y, \\ x_2 = \dot{x}_1 = \dot{y}, \\ x_3 = \dot{x}_2 = \ddot{y}, \end{cases} \quad (8)$$

and assigning the control variable  $u = x_v$ , it gives the state space representation of the nonlinear dynamic model, which will facilitate the following control system designs:

$$\begin{cases} \dot{x}_1 = x_2, \\ \dot{x}_2 = x_3, \\ \dot{x}_3 = \left(\frac{c_{te}}{b} + \frac{B_c}{m}\right)x_3 - \frac{A^2 + c_{te}B_c + bK}{bm}x_2 - \frac{c_{te}K}{bm}x_1 - \left(\frac{c_{te}}{bm}F + \frac{1}{m}\dot{F}\right) + \Psi(u, \mathbf{x}, F), \end{cases} \quad (9)$$

$$y = x_1,$$

where

$$\Psi(u, \mathbf{x}, F) = \frac{AC_d w_x \sqrt{(1/\rho)}}{bm} \left( P_s - \text{sgn}(u) \frac{1}{A} (mx_3 + B_c x_2 + Kx_1 + F) \right)^{1/2} u, \quad (10)$$

and  $\mathbf{x} = [x_1, x_2, x_3]^T$ .

The state space model (9) can be abbreviated as

$$\begin{cases} \dot{x}_1 = x_2, \\ \dot{x}_2 = x_3, \\ \dot{x}_3 = f(\mathbf{x}) + \Psi(u, \mathbf{x}, F) + d(F), \end{cases} \quad (11)$$

$$y = x_1,$$

where  $f(\mathbf{x}) = -(C_{te}/b + B_c/m)x_3 - ((A^2 + C_{te}B_c + bK)/bm)x_2 - (C_{te}K/bm)x_1$  is the linear item of the system,  $\Psi(u, \mathbf{x}, F)$  is a nonlinear function augmented with the control variable, the external force, and the state vector, and  $d(F) = -((C_{te}/bm)F + (1/m)\dot{F})$  is the disturbance related to the external force.

Inspection of equation (10), there exists a sign function in  $\Psi(u, \mathbf{x}, F)$  and the load pressure difference is  $\text{sgn}(u)(1/A)(mx_3 + B_c x_2 + Kx_1 + F)$ , which means that the pressure gain is infinity while  $u$  tends to zero displacement of the spool. This is just an ideal and extreme condition. However, this assumption is not consistent with the actual scenarios and it has led to a variable structure and noncontinuous feature for different polarities of the control variable. In fact, because the radial clearance between the spool and the sleeve always exists, the actual pressure gain is a finite value. The experimental pressure gain curve of the servovalve is given by Reference [2]. Alternatively, it can be deduced that when the servovalve's control variable changes polarity, the load pressure will change along the pressure gain curve, not a step function. Then, according to the characteristics of the experimental curve, this study proposes replacing the sign function with a hyperbolic tangent function to describe the pressure difference state, as depicted in Figure 2, which can bring the same motion pattern as the experimental pressure.

Then, equation (10) becomes

$$\Psi(u, x, F) = \frac{AC_d w_x \sqrt{(1/\rho)}}{bm} \left( P_s - \tanh(\lambda u) \frac{1}{A} (mx_3 + B_c x_2 + Kx_1 + F) \right)^{1/2} u, \quad (12)$$

where  $\tanh(\lambda u) = (e^{\lambda u} - e^{-\lambda u})/(e^{\lambda u} + e^{-\lambda u})$  and  $\lambda$  is a real constant greater than 1. The value of  $\lambda$  should make the pressure gain consistent with the experimental value. Consequently, equations (11) and (12) constitute a unified smooth nonlinear model for valve-controlled systems.

### 3. Using U-Control to Separate Control System Design and Controller Output Determination

**3.1. U-Model Realization of Valve-Controlled Servosystem.** Usually, the continuous smooth system, including linear and nonlinear systems, can be formulated as a polynomial

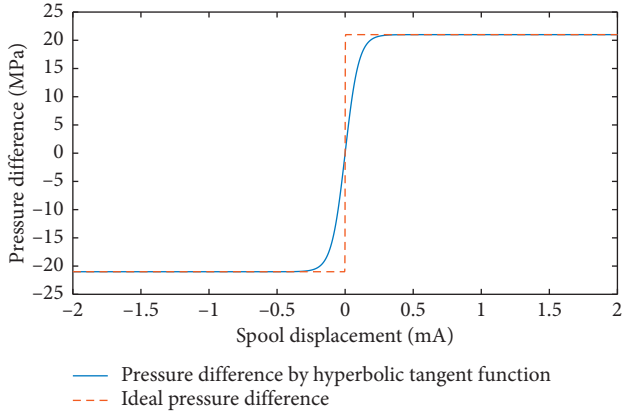


FIGURE 2: Load pressure difference near the zero displacement of the spool.

function with time-varying parameters, i.e., NARMAX (Nonlinear Autoregressive Moving Average with Exogenous input) model [17]. Without losing generality, consider a Single Input Single Output (SISO)  $U$ -model for a general discrete time nonlinear system with respect to output  $y(k)$  and control input  $u(k-1)$  [15]:

$$y(k) = \sum_{j=0}^M \lambda_j(k) u^j(k-1), \quad (13)$$

where  $u \in \mathbb{R}^1$  is the input,  $y \in \mathbb{R}^1$  is the output,  $M$  is the degree of the input, the time-varying parameter vector  $\lambda(k) = [\lambda_0(k), \dots, \lambda_M(k)] \in \mathbb{R}^{M+1}$  is a function of past inputs and outputs  $(u(k-2), \dots, u(k-n), y(k-1), \dots, y(k-n))$ , and  $k$  is the sampling instance.

The input and output dynamic relationship of equation (13) can be expressed as a map of

$$U: u(k-1) \longrightarrow y(k). \quad (14)$$

Customarily, this map is called  $U$ -model realization of the system. If the inverse of the map exists, it has

$$U^{-1}: y(k) \longrightarrow u(k-1). \quad (15)$$

On this basis, a  $U$ -model-based controller framework can be established as

$$\sum_{U \text{ Framework}} = (\Phi \ U^{-1}), \quad (16)$$

$$\begin{cases} x_1(k) = x_1(k-1) + hx_2(k), \\ x_2(k) = x_2(k-1) + hx_3(k), \\ x_3(k) = x_3(k-1) + h\{f[x(k)] + d[F(k)] + \Psi[u(k), x(k), F(k)]\}, \\ y(k) = x_1(k), \end{cases} \quad (17)$$

where  $h$  is the sampling period. Equation (17) can be seen as a generalized  $U$ -model in the form of state equations. When  $x_1(k)$  is given, the solutions of  $x_2(k)$  and  $x_3(k)$  can be

derived by backstepping routines, and finally the control variables  $u(k)$  can be obtained by solving the nonlinear equation. For a valve-controlled system described by

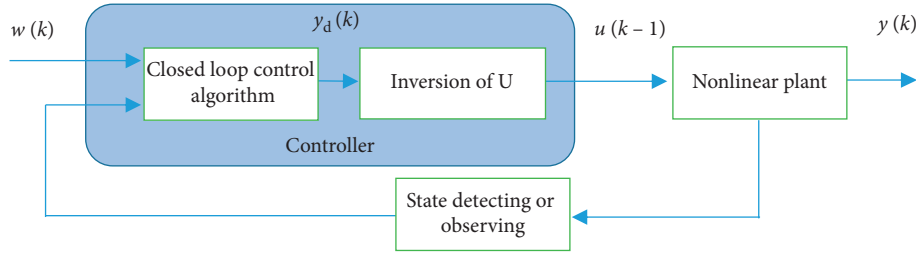
where  $\Phi$  is the closed-loop control algorithm and it can be any linear time-invariant control method. For example, for PID control, it includes error calculation and a PID module.  $U^{-1}$  represents the inversion operation for the  $U$ -model. Figure 3 illustrates this framework.

Because the plant amounts to the map  $U$ , if the inversion of the  $U$ -model is accurate, the output of the controller  $u(k-1)$  will ensure that the actual output  $y(k)$  is equal to the desirable output  $y_d(k)$ . Thus, the effect of the nonlinear characteristics on the controller design can be cancelled ideally and the design of control algorithm is made independent from the nonlinear system. Accordingly, all off-the-shelf and advanced control strategies for linear systems can be applied to a variety of nonlinear systems.

The  $U$ -model control method brings the following advantages. Firstly, this is a model-independent controller design framework, which can polish the complex plant model and freely give the system the required closed-loop dynamic performance by various control strategies. Secondly, the traditional design of the nonlinear control system is decomposed into control algorithm design and real-time dynamic inversion. These processes can be carried out in parallel, which greatly improves the design efficiency and reduces the design difficulty. Thirdly, this method has versatility, that is, it is suitable for not only nonlinear systems but also complex linear systems, and almost all known control strategies can be applied in the closed-loop control algorithm. At last, the interchangeability of the controller design is realized. For the satisfactory control algorithm, when the plant changes only the  $U$ -model needs to be updated to ensure the invariant performance of the system.

However, for most nonlinear systems, it is difficult to obtain the analytical solution by  $U$ -model. Therefore, the realization of  $U$ -model method depends on solving the inverse of the  $U$ -model numerically for each sampling period, which is naturally discrete and practical for engineering. So the discretization of the nonlinear plant's model is needed firstly. According to the characteristics of equation (11), the first-order backward difference method is used to discretize the system as follows:

derived by backstepping routines, and finally the control variables  $u(k)$  can be obtained by solving the nonlinear equation. For a valve-controlled system described by


 FIGURE 3:  $U$ -model method frame.

equation (17), the solution will be  $u(k)$  rather than  $u(k-1)$  because the function  $\Psi$  is a complex nonlinear function with respect to  $u(k)$ . Meanwhile, the  $U$ -model cannot be written as a time-varying coefficient polynomial such as the classical  $U$ -model. Consequently equation (17) can be regarded as an extension of  $U$ -model, and  $u(k)$  can still be solved numerically by the Newton-Raphson method as

$$u_{n+1}(k) = u_n(k) - \frac{x_3(k) - x_3[u_n(k)]}{(d[x_3(k)]/du(k))}, \quad (18)$$

where  $n$  is the number of iterations. According to equation (14), in order to realize the inversion of the nonlinear model,  $d[x_3(k)]/du(k)$  is needed to be updated continuously, which requires that the function  $x_3(k)$  is first-order differentiable with respect to  $u(k)$ . According to equations (12) and (17), this requirement can be satisfied. Because the parameters in the expression of  $x_3(k)$  are time-varying, we can firstly take a derivative of its symbolic expression in the computer for each sampling period and then calculate current  $d[x_3(k)]/du(k)$  and  $u_{n+1}(k)$ . For example, giving a sinusoidal signal to a valve-controlled hydraulic system as the desirable output  $y_d(k)$ , we can perform simulation according to equations (17) and (18) with the parameters specified by Table 1. The output of controller  $u(k)$  and the system response  $y(k)$  are shown in Figures 4 and 5, respectively. The simulation shows that under ideal conditions the output of the controller  $u$  is stable and smooth after an initial transient vibration, and the dynamic performance of the valve-controlled system is perfectly compensated by solving the inverse numerically.

**3.2. Design of Fundamental Performance of Valve-Controlled System.** Ideally, the inverse of the nonlinear system can accurately to eliminate the influence of the nonlinear plant on the design of controllers. However, in reality, it is impossible to obtain perfect results over the full frequency band, since there always exist high-frequency external disturbance and unmodeled dynamics. Therefore, besides the introduction of a closed-loop algorithm, it is necessary to design a suitable filter to inhibit these unfavorable conditions in the high-frequency range. In addition, it can also cancel undesirable high-frequency excitations and noises. In fact, this filter can be regarded as a virtual nominal plant, which will assist in the design of the closed-loop controller and determine the fundamental performance of the system. Figure 6 shows the structure of  $U$ -control based on the output feedback and the virtual nominal system.

The virtual nominal plant is separated from the control algorithm, which enables to specify an open-loop performance  $G_V$  for the plant within a certain range, and any ready-made controller  $G_c$  can be adopted. Consequently, for different nonlinear plants, an identical control strategy and the same performance can be achieved conveniently, and the repeated controller design process can be omitted so that the design efficiency is greatly enhanced. Therefore, different from the traditional model-based or model free controller design methods, the  $U$ -model method including a virtual nominal plant is a model-independent design scheme and provides an interface for various algorithms and various performances developed from model classical approaches.

Moreover, if the specified closed-loop performance is  $W_b$  and  $G = G_c G_V$  is defined as the open-loop characteristic of the entire system, we can obtain  $G$  by

$$G = \frac{W_b}{1 - W_b}. \quad (19)$$

Then, applying  $G$  to the digital controller, the expected dynamic performance can be achieved. Typically, valve-controlled servosystems [2] can be considered as a third-order linear system with the closed-loop transfer function:

$$W_b(s) = \frac{1}{((1/\omega_b)s + 1)((1/\omega_{nc}^2)s^2 + (2\xi_{nc}/\omega_{nc})s + 1)}, \quad (20)$$

where  $\omega_b$  is the bandwidth of the system,  $\omega_{nc}$  is the resonance frequency, and  $\xi_{nc}$  is the damping ratio. Assuming that the closed-loop performance  $W_b$  is the design objective, according to equation (19) the open-loop performance  $G$  can be expressed by

$$G = \frac{1}{\beta_3 s^3 + \beta_2 s^2 + \beta_1 s}, \quad (21)$$

where  $\beta_3 = 1/(\omega_b \omega_{nc}^2)$ ,  $\beta_2 = 2\xi_{nc}/(\omega_b \omega_{nc}^2) + 1/\omega_{nc}^2$ , and  $\beta_1 = 1/\omega_b + 2\xi_{nc}/\omega_{nc}$ . Thus, in the controller, the relationship between  $y_d$  and the control error  $e_r$  can be expressed as

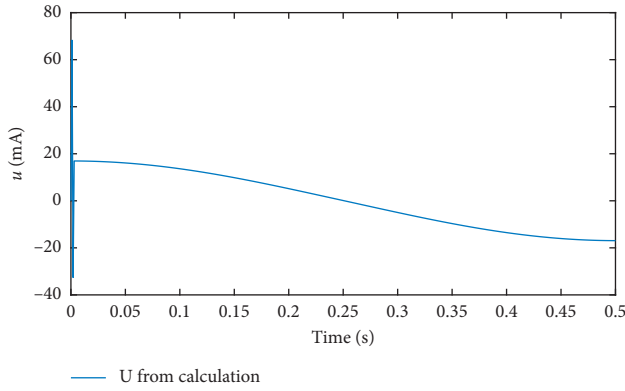
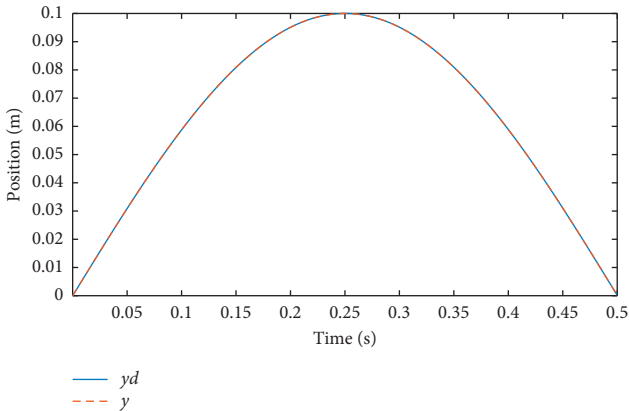
$$\sum_{i=1}^3 \beta_i y_d^{(i)}(t) = e_r(t). \quad (22)$$

After discretizing equation (22) by a certain method, the digital controller in Figure 6 can be determined, and the nonlinear valve-controlled servosystem will obtain the performance of the specified three-order linear system, that can be considered as a fundamental performance for further



TABLE 1: Parameters of simulated valve-controlled system.

Parameters	Symbol	Value
Total leakage coefficient	$C_{le}$	$2 \times 10^{-13}$ (m <sup>3</sup> /s/Pa)
Total volume of cylinder	$V_t$	$1.72 \times 10^{-3}$ (m <sup>3</sup> )
Total mass of piston	$m$	80 (Kg)
Effective area of piston	$A$	$3.44 \times 10^{-3}$ (m <sup>2</sup> )
Elastic modulus of oil	$\beta_e$	$6.9 \times 10^8$ (Pa)
Flow coefficient of throttle	$C_d$	0.69
Density of the oil	$\rho$	880 (Kg/m <sup>3</sup> )
Oil supply's pressure	$P_s$	21 (MPa)
Damping coefficient	$B_c$	1000 (N/(m/s))
Parameters of switching surface	$c_1$	4
	$c_2$	4
	$c_3$	1
Resonance frequency	$\omega_{nc}$	20 (Hz)
Bandwidth of the system	$\omega_b$	8 (Hz)
Damping ratio	$\xi_{nc}$	0.7
Coefficient of hyperbolic tangent	$\lambda$	12
Error limit	$D_1$	0.01
Error limit	$D_2$	0.1
Specified finite time	$T$	3 (s)

FIGURE 4: Output of controller  $u(k)$ .FIGURE 5: Desirable output  $y_d(k)$  and the system response  $y(k)$ .

processing. In fact,  $W_b$  can be the model of any simpler systems, even other types of transmission mechanisms, and this flexibility will enable the valve-controlled system to replace the other types of actuators conveniently.

#### 4. U-Model-Based Finite-Time Controller

For the nonlinear valve-controlled servosystem represented by equations (11) and (12), the control variable cannot be expressed explicitly, leading to difficulty for applying general control strategies. However, by the  $U$ -model method, the nonlinearity of the system is removed by its inversion, which makes it possible to further improve the performance of the system. For valve-controlled hydraulic servosystems, the general requirement is fast response and perfect tracking, but the initial state is usually arbitrary, which often leads to violent vibration caused by excessive control variable. Therefore, the  $U$ -model-based finite-time control with global robustness is proposed for valve-controlled systems.

As mentioned above, transform the nonlinear valve-controlled servosystem into a new equivalent linear system with dynamic performance  $W_b$ , as shown in Figure 7.

The state variables of the new system are still defined by equation (8), and then the state equations are

$$\begin{cases} \dot{x}_1 = x_2, \\ \dot{x}_2 = x_3, \\ \dot{x}_3 = -\frac{\beta_2}{\beta_3}x_3 - \frac{\beta_1}{\beta_3}x_2 - x_1 + \frac{1}{\beta_3}w(t), \\ y = x_1. \end{cases} \quad (23)$$

Assuming that the state vector  $\mathbf{x} = [x_1, x_2, x_3]^T$  and the given desirable state vector  $\mathbf{x}_d = [x_{1d}, x_{2d}, x_{3d}]^T$ , where  $x_{2d} = \dot{x}_{1d}$  and  $x_{3d} = \ddot{x}_{1d}$ , and the error vector can be calculated by

$$\mathbf{e}(t) = \mathbf{x} - \mathbf{x}_d = [e_1, e_2, e_3]^T, \quad (24)$$

where  $e_1$  is the displacement error,  $e_2 = \dot{e}_1$  and  $e_3 = \ddot{e}_1$ .

For the valve-controlled system, the error  $\mathbf{e}$  is taken as the state vector to design the switching function. According to a definition [18] and extending the method to third-order case, the global sliding mode surface has a general form as

$$s = c_1 e_1 + c_2 e_2 + c_3 e_3 - p_f(t), \quad (25)$$

where  $c_i$  ( $i = 1, 2, 3$ ) is the positive real constant ensuring that  $c_3 \tau^2 + c_2 \tau + c_1$  is a stable Hurwitz polynomial, in which  $\tau$  is the Laplace operator, and  $p_f(t)$  is a forcing function, determining the dynamic of the switching surface. For the existence of the switching surface,  $p_f(t)$  must be first-order differentiable. Assuming that

$$p_f(t) = c_1 p_1(t) + c_2 p_2(t) + c_3 p_3(t), \quad (26)$$

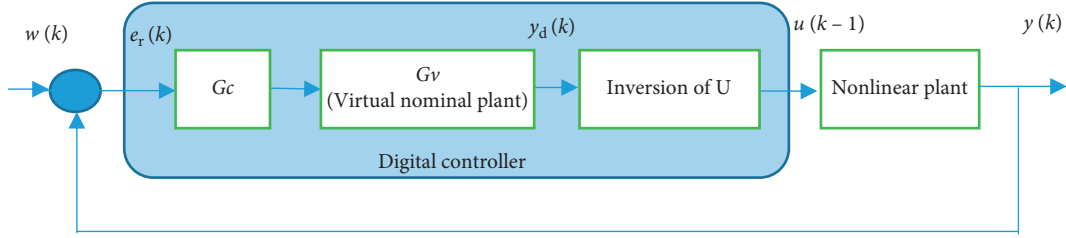
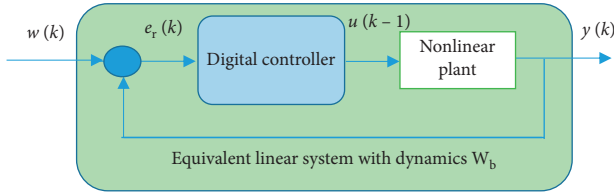
when the system works on the switching surface,

$$s = c_1(e_1 - p_1) + c_2(e_2 - p_2) + c_3(e_3 - p_3) = 0. \quad (27)$$

That is,

$$s = \mathbf{c} \cdot [\mathbf{e}(t) - \mathbf{p}(t)] = 0, \quad (28)$$




 FIGURE 6:  $U$ -model method including virtual nominal plant.

 FIGURE 7:  $U$ -model-based equivalent system.

where  $\mathbf{c} = [c_1, c_2, c_3]^T$ ,  $\mathbf{p}(t) = [p_1(t), p_2(t), p_3(t)]^T$ , and  $p_f(t) = \mathbf{c} \cdot \mathbf{p}(t)$ .

$$p_1(t) = \begin{cases} a_0 + a_1 t + a_2 t^2 + a_3 t^3 + a_4 t^4 + a_5 t^5 + a_6 t^6 + a_7 t^7, & 0 \leq t < T, \\ 0, & t \geq T. \end{cases} \quad (29)$$

Substituting the boundary conditions into equation (29),  $p_1(t)$  can be obtained as

$$\begin{cases} e_1(0) + \dot{e}_1(0) + \frac{1}{2}\ddot{e}_1(0)t^2 + \frac{1}{6}\dddot{e}_1(0)t^3 + \left[ \frac{-35}{T^4}e_1(0) + \frac{-20}{T^3}\dot{e}_1(0) + \frac{-5}{T^2}\ddot{e}_1(0) + \frac{-2}{3T}\dddot{e}_1(0) \right] t^4 \\ + \left[ \frac{84}{T^5}e_1(0) + \frac{-20}{T^4}\dot{e}_1(0) + \frac{10}{T^3}\ddot{e}_1(0) + \frac{1}{T^2}\dddot{e}_1(0) \right] t^5 + \left[ \frac{-70}{T^6}e_1(0) + \frac{-20}{T^5}\dot{e}_1(0) + \frac{-7.5}{T^4}\ddot{e}_1(0) + \frac{-2}{T^3}\dddot{e}_1(0) \right] t^6 \\ + \left[ \frac{20}{T^7}e_1(0) + \frac{-20}{T^6}\dot{e}_1(0) + \frac{2}{T^5}\ddot{e}_1(0) + \frac{1}{6T^4}\dddot{e}_1(0) \right] t^7, & 0 \leq t \leq T, \\ 0, & t \geq T. \end{cases} \quad (30)$$

So, the forcing function can be calculated as

$$p_f(t) = c_1 p_1(t) + c_2 \dot{p}_1(t) + c_3 \ddot{p}_1(t). \quad (31)$$

The system described by equation (23) is reconstructed by the  $U$ -model method, which is influenced by the fluctuation of parameters and external disturbance. Considering the uncertainty of the model, equation (23) can be written as

$$\begin{cases} \dot{x}_1 = x_2, \\ \dot{x}_2 = x_3, \\ \dot{x}_3 = f'(\mathbf{x}) + d'(t) + g'(t)w(t), \\ y = x_1, \end{cases} \quad (32)$$

Because  $e_2 = \dot{e}_1$  and  $e_3 = \ddot{e}_1$ , it should be ensured that  $p_2 = \dot{p}_1$  and  $p_3 = \ddot{p}_1$  in order to satisfy equation (27). Then, if the state vector  $\mathbf{e}$  is needed to converge to zero in the finite time  $T$ , equation (23) must be satisfied with the following boundary conditions. That is, if  $t = 0$ ,  $p_1(0) = e_1(0)$ ,  $p_2(0) = \dot{p}_1(0) = \dot{e}_1(0)$ ,  $p_3(0) = \ddot{p}_1(0) = \ddot{e}_1(0)$ , and  $\dot{p}_3(0) = \dot{\ddot{p}}_1(0) = \dot{\ddot{e}}_1(0)$ . And if  $t = T$ ,  $p_1(T) = e_1(T) = 0$ ,  $p_2(T) = \dot{p}_1(T) = 0$ ,  $p_3(T) = \ddot{p}_1(T) = 0$ , and  $\dot{p}_3(T) = \dot{\ddot{p}}_1(T) = 0$ . For these eight equations, a sever-order polynomial can be designed to construct  $p_1(t)$

where  $f'(\mathbf{x}) = -(\beta_2/\beta_3)x_3 - (\beta_1/\beta_3)x_2 - x_1$ ,  $g'(t) = (1/\beta_3)[1 + \Delta(t)]$ ,  $d'(t)$  represents the uncertainty caused by the perturbations of  $\beta_1$ ,  $\beta_2$ , and  $\beta_3$ , and  $\Delta(t)$  is the uncertainty of the input function, related to  $\beta_3$ . Assume these uncertainties bounded, i.e.,  $\|\Delta\| \leq D_1$  and  $\|d'(t)\| \leq D_2$ , where  $D_1$  and  $D_2$  are positive real numbers. Then, the controller can be designed as follows:

$$w(t) = -\beta_3 \left[ \frac{c_1}{c_3} (\dot{e}_1 - \dot{p}_1) + \frac{c_2}{c_3} (\ddot{e}_1 - \ddot{p}_1) + f'(\mathbf{x}) - \ddot{x}_{1d} - \ddot{p}_1 + \zeta \text{sgn}(s) \right]. \quad (33)$$

Differentiating equation (27) and substituting equations (23) and (24) into it gives

$$\dot{s} = c_1(\dot{e}_1 - \dot{p}_1) + c_2(\ddot{e}_1 - \ddot{p}_1) + c_3 \cdot [f'(\mathbf{x}) + g'(t)w + d'(t) - \ddot{x}_{1d} - \ddot{p}_1]. \quad (34)$$

Then,

$$s\dot{s} = s\{c_1(\dot{e}_1 - \dot{p}_1) + c_2(\ddot{e}_1 - \ddot{p}_1) + c_3 \cdot [f'(\mathbf{x}) + g'(t)w + d'(t) - \ddot{x}_{1d} - \ddot{p}_1]\}. \quad (35)$$

Substituting  $g'(t)$  and equation (33) into (35) yields

$$\begin{aligned} s\dot{s} &= s\left\{c_3d'(t) + \Delta\left[c_3\ddot{x}_{1d} + c_3\ddot{p}_1 - c_1(\dot{e}_1 - \dot{p}_1) - c_2(\ddot{e}_1 - \ddot{p}_1) - c_3f'(\mathbf{x})\right] - (1 + \Delta)c_3\zeta\text{sgn}(s)\right\} \\ &\leq \|s\left\|c_3D_2 + D_1\left\|c_3\ddot{x}_{1d} + c_3\ddot{p}_1 - c_1(\dot{e}_1 - \dot{p}_1) - c_2(\ddot{e}_1 - \ddot{p}_1) - c_3f'(\mathbf{x})\right\| - (1 + \Delta)c_3\zeta\right\| \\ &\leq \|s\left\|c_3D_2 + D_1\left\|c_3\ddot{x}_{1d} + c_3\ddot{p}_1 - c_1(\dot{e}_1 - \dot{p}_1) - c_2(\ddot{e}_1 - \ddot{p}_1) - c_3f'(\mathbf{x})\right\| - (1 - D_1)c_3\zeta\right\|. \end{aligned} \quad (36)$$

According to equation (36), when the switching control coefficient

$$\zeta \geq (1 - D_1)^{-1} \left[ D_2 + D_1 \left\| \ddot{x}_{1d} + \ddot{p}_1 - \frac{c_1}{c_3}(\dot{e}_1 - \dot{p}_1) - \frac{c_2}{c_3}(\ddot{e}_1 - \ddot{p}_1) - f'(\mathbf{x}) \right\| \right]. \quad (37)$$

the reaching condition  $s\dot{s} \leq 0$  can be satisfied, which means that the switching surface exists and the system will be stable. Therefore, utilizing equations (33) and (37), a global robust finite-time controller for the valve-controlled system can be determined.

In order to inhibit chattering, a boundary layer with thickness  $\delta = 0.02$  for the quasi-sliding mode is specified, and a saturation function used for replacing the sign function is defined as

$$\text{sat}(s) = \begin{cases} \text{sgn}(s), & \|s\| > \delta, \\ \frac{s}{\delta}, & \|s\| < \delta. \end{cases} \quad (38)$$

Therefore, the nonlinear model controller from equation (33) can be rewritten as

$$w(t) = -\beta_3 \left[ \frac{c_1}{c_3}(\dot{e}_1 - \dot{p}_1) + \frac{c_2}{c_3}(\ddot{e}_1 - \ddot{p}_1) + f'(\mathbf{x}) - \ddot{x}_{1d} - \ddot{p}_1 + \zeta \text{sat}(s) \right]. \quad (39)$$

## 5. Simulation Studies

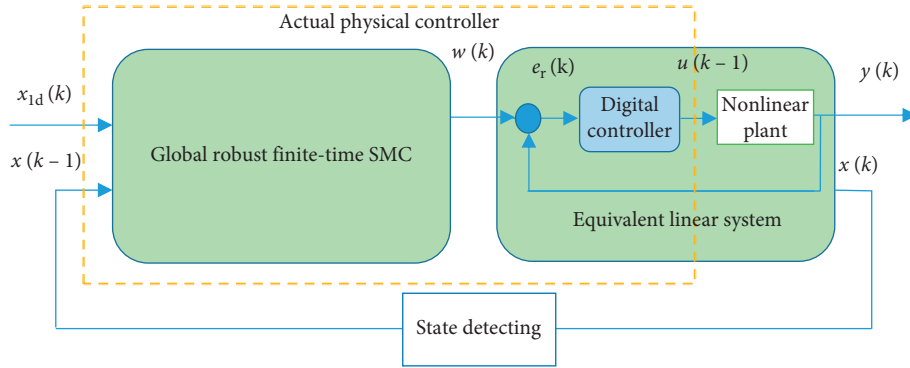
According to the above analyses, controller (39) can guarantee the reachability of the switching surface. If there is no disturbance and perturbation, the states of the system will follow (27) all the time, since the initial state is just on the switching surface. As the forcing function converges to zero in the time  $T$ , the valve-controlled system will become an error-free tracking system, which is a desirable result. However, for valve-controlled hydraulic systems, uncertainties always exist, such as fluctuation of external force, variation of elastic modulus with temperature, and inaccuracy of hydraulic oil density, which will firstly act on the solution of  $U$ -model and then affect the dynamic

performance of the actual system. In addition, since digital controllers are widely applied now, the discretization of the control strategy will have an impact on the ultimate effect. In order to investigate these problems, the framework of the  $U$ -model-based finite-time control system and its simulation scheme are established, as shown in Figure 8.

Logically, the system includes an equivalent linear system and a global robust finite-time controller, and the connections between the two sections are a virtual control variable  $w(k)$  and the state feedback  $\mathbf{x}(k)$ , while the actual physical controller should consist of the finite-time controller and the digital controller within the equivalent linear system. Therefore, this structure still embodies the  $U$ -model's thought of dealing with the nonlinear system in the controller.

In the simulation, assuming that the state vector  $\mathbf{x}(k)$  is available in real time, the virtual control variable  $w(k)$  can be calculated according to equation (39) and the digital controller in the equivalent linear system can be calculated according to equations (22) and (18). Exerting a standard sinusoidal signal  $x_{1d} = \sin(t)$  as the command input on the system, the simulation is performed based on Simulink platform with the sampling period of 1 ms, as depicted in Figure 9. The parameters of the valve-controlled system are given by Table 1, and the simulation results are shown in Figure 10.

Simulation results show that the controller can track the position of the accurate nonlinear model of the valve-controlled cylinder hydraulic servosystem, and a  $U$ -model-based global robust finite-time controller described by Figure 8 is feasible. The valve-controlled system under the zero initial state can track the command signal within a specified time, and the transient process is quite smooth. Compared with the traditional PID controller, this method can eliminate the phase lag, as shown in Figure 11, which is


 FIGURE 8:  $U$ -model-based global robust finite-time controller and simulation principle.

very important for some phase sensitive systems. In addition, this method effectively reduces the impact on the valve-controlled system at the beginning of the movement, as depicted in Figure 12.

On the basis of the  $U$ -model method and the proposed virtual nominal system, the nonlinear valve-controlled system has been redesigned as a linear system, so its controllability and performance are significantly improved. For example, the chattering of the switching function is greatly suppressed. Simulations show that if direct global robust finite-time control on this nonlinear valve-controlled system without  $U$ -model method is exerted, the chattering amplitude will be two orders of magnitude larger than that of the  $U$ -model-based control system, as shown in Figure 13. Moreover, when the  $U$ -model is adopted, the control error is greatly reduced after reaching the specified finite time, as shown in Figure 14.

Even so, the control error still exists in a small range and has the same periodicity as the command signal, indicating that the system is in a quasi-sliding mode state and the system itself is not strictly asymptotically stable. When the speed of the command signal increases, the phenomenon of the state, escaping from the sliding mode surface, is more obvious. In order to explore the essence of this issue, the simulation assumed that the valve-controlled system is ideal and there is no uncertainty. According to equation (34) and supposing that

$$\begin{aligned} \dot{s} &= c_1(\dot{e}_1 - \dot{p}_1) + c_2(\ddot{e}_1 - \ddot{p}_1) + c_3 \\ &\cdot [f'(x) + g'(t)w_{eq} + d'(t) - \ddot{x}_{1d} - \ddot{p}_1] = 0, \end{aligned} \quad (40)$$

where  $w_{eq}$  is the equivalent control variable, then it gives

$$w_{eq} = -\beta_3 \left[ \frac{c_1}{c_3}(\dot{e}_1 - \dot{p}_1) + \frac{c_2}{c_3}(\ddot{e}_1 - \ddot{p}_1) + f'(x) - \ddot{x}_{1d} - \ddot{p}_1 \right]. \quad (41)$$

After replacing  $w$  with  $w_{eq}$  to drive the ideal system in Figure 8, run a simulation again, and the result, as shown in Figure 15(a), shows that although the system has fulfilled the tracking task, the value of the switching function still fluctuates with the command signal, which means that even if the system is under ideal conditions, its state cannot be

always maintained on the switching surface. However, since  $w_{eq}$  is derived from equation (40), it should ensure that  $\dot{s} \equiv 0$ , but the actual  $\dot{s}$  in the simulation is not constant, as depicted in Figure 15(b).

The analysis shows that the discretization of the controller brings the derivatives of  $x_{1d}$ ,  $\dot{x}_{1d}$ ,  $\ddot{x}_{1d}$ ,  $p_1$ ,  $\dot{p}_1$ , and  $\ddot{p}_1$  different calculation errors, resulting in a minor mismatch with ideal equation (40). As  $w_{eq}$  is just calculated by (40), this mismatch can lead to the fluctuation of  $s$  and make the system unable to be asymptotically stable as expected. Therefore, this is an inherent error for the global robust sliding mode controller. However, for the specific application scenario of the valve-controlled hydraulic system, the maximum dynamic error has been restrained below 0.15% of the amplitude with the maximum speed of 1 m/s, which usually meets the requirements.

## 6. Conclusions

- (1) Contrast to the traditional model of the valve-controlled hydraulic system, the new model structure has accommodated the nonlinear dynamics and the polarity effect of the control variable. Another insight on the nonlinear dynamic model is to use hyperbolic tangent function to approximate sign function for the relationship between pressure difference and spool displacement. Accordingly, these contributed make the theoretical model more consistent with the actual situation and provide a universal model structure for such system analysis and control design.
- (2) By  $U$ -control design, the dynamic inversion of the controlled valve-controlled system can be achieved in real time, which makes the design of the control algorithm independent from the nonlinear characteristics of the system. On this basis, the proposed virtual nominal plant can not only eliminate the effect of the unfavorable high-frequency unmodeled dynamics and noise but also make it possible to adopt a ready-made control algorithm and obtain the same performance for different nonlinear plants.

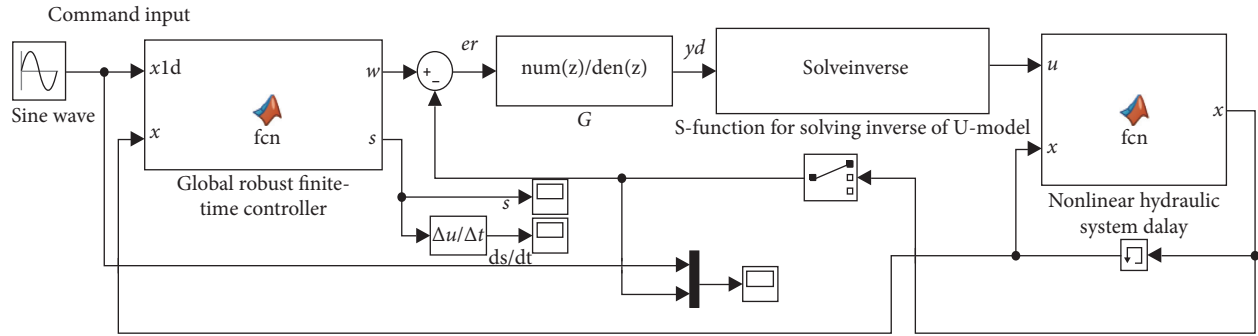


FIGURE 9: Simulation diagram by Simulink.

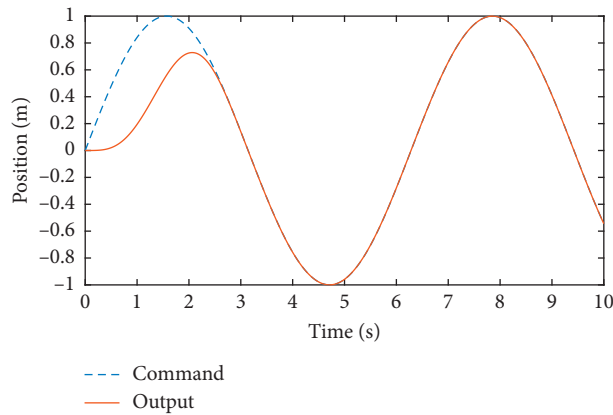


FIGURE 10: Simulation result of position tracking.

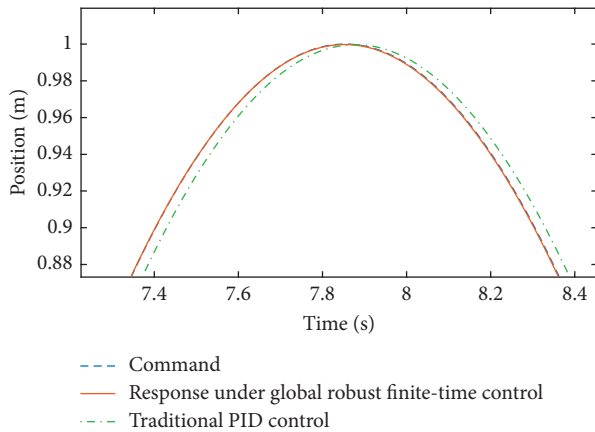


FIGURE 11: Comparison of different controllers.

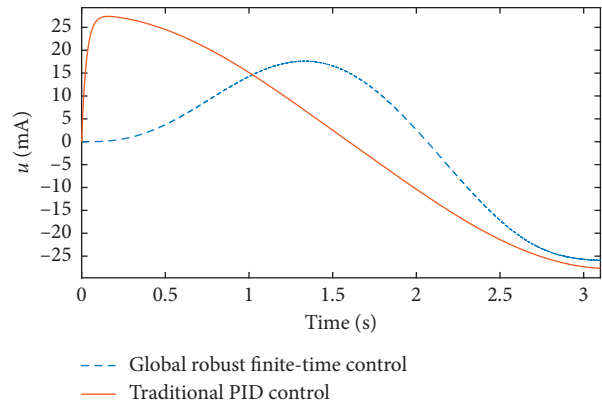


FIGURE 12: Impact of valve when motion starts.

Since the repeated design process can be omitted, the design efficiency is greatly enhanced.

- (3) Meanwhile, the application of the virtual nominal plant changes the situation that the control variable cannot be expressed explicitly in the valve-controlled servosystem. Thus, the control variable is no longer considered as part of the uncertainty and the controlled plant is more regular; consequently, the

control strategy can get better effect. With the *U*-model-based finite-time control method, the valve-controlled system can smoothly track the command signal within the specified time and the phase lag is eliminated, which is important for phase sensitive systems. Moreover, because of *U*-model's application, the chattering of the system effectively relieved and the control error greatly reduced.

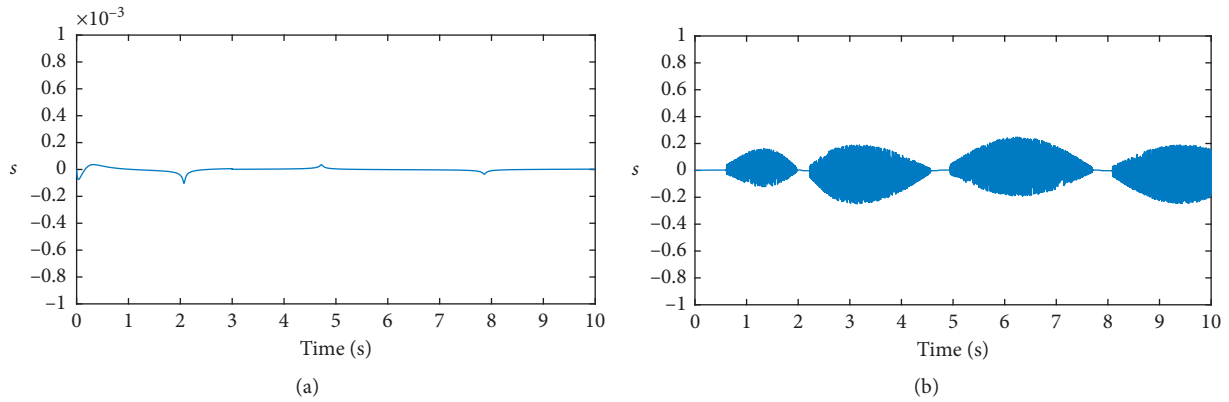


FIGURE 13: Smoothness of the switching function for global robust finite-time control: (a)  $U$ -model-based control and (b) direct control without  $U$ -model.

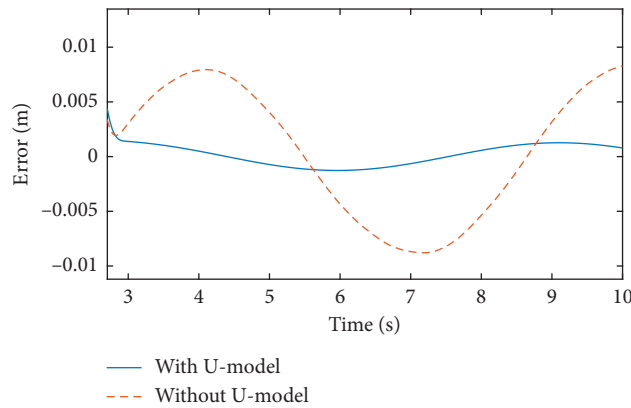


FIGURE 14: Dynamic control error.

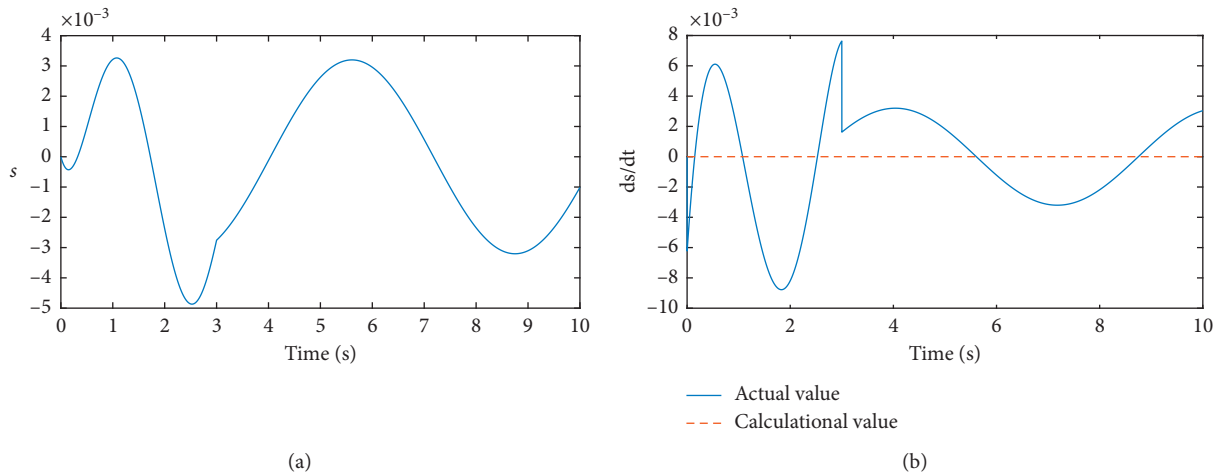


FIGURE 15: Simulated switching function value for ideal valve-controlled system under equivalent control. (a) Value of  $s$ . (b) Value of  $\dot{s}$ .

(4) The discretization will cause the system state to fluctuate near the switching surface with the speed's variation, resulting in a certain dynamic error. However, for the specific application scenario of the

valve-controlled system, the dynamic error can be maintained below 0.15% of the amplitude with the maximum speed of 1 m/s, which usually can meet the requirements.

## Data Availability

The data used to support the findings of this study are available from the corresponding author upon request.

## Disclosure

This work was completed when the first author was an academic visitor at the University of the West of England.

## Conflicts of Interest

The authors declare that they have no conflicts of interest.

## Acknowledgments

This work was funded by the National Natural Science Foundation of China (Grant no. 51775032), Foundation of Key Laboratory of Vehicle Advanced Manufacturing, Measuring and Control Technology, Beijing Jiaotong University, Ministry of Education, China, and China Scholarship Council.

## References

- [1] H. E. Merritt, *Hydraulic Control Systems*, Wiley, New York, NY, USA, 1991.
- [2] H. R. Li, *Hydraulic Control System*, National Defense Industry Press, Beijing, China, 1991.
- [3] C. X. Wang, *Hydraulic Control System*, China Machine Press, Beijing, China, 2011.
- [4] M. Galicki, "Finite-time control of robotic manipulators," *Automatica*, vol. 51, pp. 49–54, 2015.
- [5] M. Galicki, "Constraint finite-time control of redundant manipulators," *International Journal of Robust and Nonlinear Control*, vol. 27, no. 4, pp. 639–660, 2016.
- [6] J. Zhang, Q. Hu, and D. Wang, "Bounded finite-time attitude tracking control for rigid spacecraft via output feedback," *Aerospace Science and Technology*, vol. 64, pp. 75–84, 2017.
- [7] J.-G. Sun, S.-L. Xu, S.-M. Song, and X.-J. Dong, "Finite-time tracking control of hypersonic vehicle with input saturation," *Aerospace Science and Technology*, vol. 71, pp. 272–284, 2017.
- [8] H. Pan, X. Jing, and W. Sun, "Robust finite-time tracking control for nonlinear suspension systems via disturbance compensation," *Mechanical Systems and Signal Processing*, vol. 88, pp. 49–61, 2017.
- [9] X. H. Ye, *Research on Modelling and Control Method of Valve-Controlled Asymmetrical Cylinder System*, Hefei University of Technology, Hefei, China, 2015.
- [10] L. Li, F. Li, Y. B. Feng et al., "Research on control strategy of large hydraulic erecting system based on adaptive fuzzy sliding mode," *Acta Armamentarii*, vol. 37, no. 1, pp. 71–76, 2016.
- [11] Y. Li, L. M. Yang, and Z. H. Zhang, "Study on second-order sliding mode control law for electro-hydraulic servo system," *Chinese Journal of Mechanical Engineering*, vol. 41, no. 3, pp. 72–75, 2005.
- [12] L. Schmidt, T. O. Andersen, and H. C. Pedersen, "An approach for second order control with finite time convergence for electro-hydraulic drives," in *Proceedings of the ASME/BATH 2013 Symposium on Fluid Power & Motion Control*, American Society of Mechanical Engineers (ASME), Sarasota, FL, USA, October 2013.
- [13] J. Y. Yao, L. Liu, H. Jian et al., "Finite time continuous sliding mode control method for electro-hydraulic position servo system," Chinese Patent CN105093936A, 2015.
- [14] Q. M. Zhu and L. Z. Guo, "A pole placement controller for non-linear dynamic plants," *Proceedings of the Institution of Mechanical Engineers, Part I: Journal of Systems and Control Engineering*, vol. 216, no. 6, pp. 467–476, 2002.
- [15] Q. M. Zhu, D. Y. Zhao, and J. Zhang, "A general U-block model-based design procedure for nonlinear polynomial control systems," *International Journal of Systems Science*, vol. 47, no. 14, pp. 3465–3475, 2016.
- [16] F. X. Xu, Q. M. Zhu, D. Y. Zhao et al., "U-model based design methods for nonlinear control systems: a survey of the development in the 1st decade," *Control and Decision*, vol. 28, no. 7, pp. 961–971, 2013.
- [17] S. A. Billings, *Nonlinear System Identification: NARMAX Methods in the Time, Frequency, and Spatio-Temporal Domains*, Wiley, New York, NY, USA, 2013.
- [18] Y.-S. Lu and J.-S. Chen, "Design of a global sliding-mode controller for a motor drive with bounded control," *International Journal of Control*, vol. 62, no. 5, pp. 1001–1019, 1995.



## Research Article

# Echo State Network for Extended State Observer and Sliding Mode Control of Vehicle Drive Motor with Unknown Hysteresis Nonlinearity

Xuehui Gao <sup>1</sup>, Bo Sun <sup>1</sup>, Xinyan Hu,<sup>1</sup> and Kun Zhu<sup>2</sup>

<sup>1</sup>The Department of Mechanical and Electrical Engineering, Shandong University of Science and Technology, Tai'an 271019, China

<sup>2</sup>Traffic Control Technology Co. Ltd., Beijing 100071, China

Correspondence should be addressed to Bo Sun; [bo\\_sun@sdust.edu.cn](mailto:bo_sun@sdust.edu.cn)

Received 27 November 2019; Accepted 12 December 2019; Published 4 January 2020

Guest Editor: Weicun Zhang

Copyright © 2020 Xuehui Gao et al. This is an open access article distributed under the Creative Commons Attribution License, which permits unrestricted use, distribution, and reproduction in any medium, provided the original work is properly cited.

An echo state network (ESN) for extended state observer (ESO) and sliding mode control (SMC) of permanent magnet synchronous motor (PMSM) in an electric vehicle system is investigated in this paper. For the PMSM model, most researches neglect the hysteresis loss and other nonlinear factors, which reduces the accuracy of the PMSM model. We present a modified PMSM model considering the hysteresis loss and then transform the new PMSM model to a canonical form to simplify the controller design. In order to deal with the hysteresis loss, an ESN is utilized to estimate the nonlinearity. Considering that some states cannot be directly obtained, an ESO with ESN is proposed to estimate unknown system states of the electric vehicle PMSM system. Afterwards, an SMC is adopted to control the closed-loop system based on the ESO with ESN, and a double hyperbolic function instead of the sign function is used to suppress the chattering of the SMC. The stabilities of the observer and the controller are all guaranteed by Lyapunov functions. Finally, simulations are presented to verify the validity of the echo state network for extended state observer and the neural network sliding mode control.

## 1. Introduction

Electric vehicles are the most important new energy resource vehicles that attract much attention in these years. Many researchers and factories have investigated the electric vehicles and got some well results. Different electric vehicles have been produced, and some have been accepted in the market. Even though the electric vehicles already appeared in the market, they also have a lot of problems that need to be investigated. For example, an accurate electric vehicle motor model is one of the important issues that needs to be investigated more such that it can improve the precision of the control system and the automation for electric vehicles.

Most of the electric vehicles adopt permanent magnet synchronous motor (PMSM), and their models have been

investigated for many years. But the electric vehicles not only include the PMSM but also have many other subsystems such as torque production dynamics and crankshaft dynamics. Na et al. [1] discussed the different models of vehicle and designed an input observer and adaptive estimations to approximate the unknown parameters. In order to precisely control the tracking errors, Na et al. [2] utilized the prescribed performance function to control the vehicles suspensions. Wang et al. [3, 4] designed an adaptive controller to precisely control the model of PMSM with funnel motion control that is similar to that in literature [2]. Huang et al. [5] proposed an approximation-free control strategy which does not need function approximators (e.g., neural networks and fuzzy logic systems) for the vehicles suspension [2]. Furthermore, Na et al. [6] investigated the nonlinear active suspension systems of vehicles with adaptive finite time

fuzzy control strategy considering the input delay since the input delay commonly appears in the suspension systems of vehicle. And in literature [7], the autonomous vehicles were researched with extended Kalman filter designing minimum model error tracking control that considers the input saturation in real vehicle systems that always contains the issue of the input saturation. Compared with many other literatures that utilized linear tyre model, Li et al. [8] had investigated the nonlinear tyre model with vehicle MP algorithm. Sun et al. [9, 10] investigated the variable stiffness and damping model of magnetorheological (MR) vehicle suspension system. The MR damper is described by two Bouc–Wen hysteretic models, and TS fuzzy approach was used to model the quarter car system.

All the above studies investigated the vehicles' model or part of vehicles' model (submodel), but these vehicle systems are not just pure electric vehicle systems, which also include hybrid electric vehicle systems. In pure electric vehicle systems, the motor model is the most important model such that it draws much attention. Many kinds of motor can be utilized for electric vehicles, and the permanent magnet synchronous motors (PMSMs) are the common motors in the vehicle systems. The PMSM model has been investigated for many years, and different approaches were applied for different conditions. Luo et al. [11] proposed a field-circuit-coupled parameter adaptive modeling method for PMSM which combined the merits of a mathematical model and a magnetic field model. Since the permanent magnet materials in the electric vehicles have hysteresis losses in practice, it has been investigated in different applications and many results were acquired. Egorov et al. [12] investigated the hysteresis loss of the permanent magnet using static history-dependent hysteresis model (HDHM) for PMSM with ferrite magnets of a rotor surface magnet. But in literature [13], a zero-sequence current hysteresis controller with space vector pulse-width modulation was presented to solve the system loss of the open-end winding permanent magnet synchronous motor, where the loss was caused by the limited maximum output power. Notwithstanding the hysteresis of the PMSM is widely researched [14, 15], and it also has much issues to be further researched such as using mathematical hysteresis models or intelligent models to describe the hysteresis or using an observer to estimate the unable direct measurement hysteresis parameters. Considering the U model theory [16–19], the structure of the model and the observer is presented under the inspiration of the model-independent framework for the U model. Therefore, the observer and the controller will be investigated based on the U model model-independent framework.

Many real electric vehicle systems cannot obtain all the model states directly, and then the observer will be utilized to estimate the unknown states or parameters. In general, the observer is utilized to estimate two categories of unknowns in controlled systems: disturbances and states [4, 20–24]. Many different observers have been applied to approximate the states or disturbances for many years. In these observers,

the extended state observer (ESO) is one of the excellent observers and has achieved well results. ESO is firstly proposed by Han [25], and it has been further researched by many excellent scholars. Xue et al. [26] proposed an ESO-based active disturbance rejection control (ADRC) to deal with the uncertainties of the system, where the ESO gain could automatically timely be adjusted for reducing the estimation errors. Xue et al. [27] proved that a certain ESO could serve as estimation through the augmented gain. Chen et al. [28] proposed an ESO to estimate both the high-order nonlinear system unknown states and uncertainties in order to facilitate the controller design. Sun et al. [29] focused on the multimotor servomechanism systems, using the ESO to approximate the unmeasured velocity of servo motors, and Wang et al. [30] also investigated the motor servomechanism systems, but it is different to [29]. The ESO was utilized to estimate the unknown dynamics in the control system (e.g., friction and disturbances) for its easy design on account of the system bandwidth. On the whole, most ESOs are utilized to estimate the “total disturbance,” which is regarded as the disturbance observer for the control systems. But in this paper, we will adjust the structure of the ESO to approximate the system states. The adjusted structure of ESO has designed high gain parameters that can fastly estimate the unknown system states and higher accuracy. In order to simplify the ESO design and guarantee the ESO convergence, the hysteresis nonlinearity of the PMSM model and other unknown sections as “general disturbance” will be handled by a proposed echo state network (ESN).

ESN has been utilized for many nonlinear systems for its fewer nodes and computational requirements. Chen et al. [31] designed an adaptive ESN control for a class of constrained pure-feedback nonlinear systems, but Sun et al. [32] investigated a modified ESN dynamic surface controller for multi-input and multioutput nonlinear systems. These ESNs all have acquired well results. In additions, Wang et al. [33, 34] investigated the prescribed performance tracking control of nonlinear servo mechanisms with ESN, one chose robust adaptive control and the other selected dynamic surface control and verified by experiments. Different from the above literatures, Wang et al. [35] researched the two-inertia servo mechanisms using ESN and designed a prescribed performance function dynamic surface control. Wang et al. [34] considered the influence of the backlash for the servo mechanisms. Different from [34] that utilized ESN to dispose the backlash nonlinearities, we will adopt ESN to deal with the unknown hysteresis nonlinear sections using the ESO simplifying the ESO design in this paper.

Sliding mode control (SMC) is one of the excellent control strategies which can be frequently used in practice. We have utilized a composite control which consists of a discrete inverse model-based control and a discrete adaptive sliding mode control to deal with a Hammerstein system in literature [36]. The Hammerstein system was composed of a linear dynamics connecting a hysteresis nonlinearity, where the order of linear dynamics was unknown and the hysteresis modeled by Preisach operator. Then, the effectiveness of the sliding mode control was verified by servo motor system experiments. In order to restrain the chattering of the sliding

mode control, Gao et al. and Tao et al. [36, 37] adopted double hyperbolic function  $\tanh(\cdot)$  instead of the  $\text{sign}(\cdot)$ , which can obtain favourable reduced chattering. The sliding mode control is applied for many real systems. Zhao et al. [38] applied the SMC to the multimotor driving servo systems, and Chen et al. [39] utilized the SMC for an uncertain spacecraft system. In the literature [7], the sliding mode control was used for the autonomous vehicles. In this paper, the SMC will be designed to precisely control the proposed PMSM model system where the unknown states are estimated by the adjusted ESO with ESN.

In this paper, we firstly consider the influence of the hysteresis nonlinearity for the PMSM model that mostly is neglected in the former models. Therefore, a new modified PMSM model including the hysteresis nonlinearities is established. Secondly, the modified PMSM model will be transformed to a canonical form to simplify the controller design. Then, the ESN is applied, and a new ESO will be proposed to estimate all the states whether that can be directly measured or not. A Lyapunov function guarantees the effectiveness of the observer results. Finally, an SMC with the ESN and the ESO is designed for this new modified PMSM model, and another Lyapunov function guarantees all the closed-loop signals bounded. In order to restrain the chattering of the SMC, we chose the continuous function  $\tanh(\cdot)$  replacing the discontinuous function  $\text{sign}(\cdot)$  and the simulations will verify the effectiveness of the proposed approaches. The contributions are listed as follows:

- (i) The PMSM model is improved for suiting the electric vehicle system which considers the hysteretic losses. Besides, the modified PMSM model is transformed to a canonical form that can simplify the ESO and controller design.
- (ii) Different from most ESOs of the disturbance observer, the structure of an ESO is adjusted to estimate the states of the modified PMSM model as well as the ESN is adopted to approximate the unknown hysteretic losses. That not only guarantees the convergence of ESO fastly but also simplifies the observer design.
- (iii) An SMC is designed with the designed ESO for this transformed PMSM model in electric vehicle systems and utilizes the continuous function  $\tanh(\cdot)$  replacing the discontinuous function  $\text{sign}(\cdot)$  to restrain the SMC chatting.

The rest of the paper is organized as follows: Section 2 discusses the problem formulations that give the new PMSM model and the transformation of the canonical form. The introduction of ESN is provided in Section 3, and Section 4 gives the ESO design, which includes the ESN, and the observer effectiveness is guaranteed. The neural network sliding mode control design is discussed in Section 5, and Section 6 shows simulations. Section 7 concludes this paper.

## 2. Problem Formulations

The electric vehicle model includes different sections, which is composed of vehicle derive, engine, motor,

battery, rear and front wheels, and other electrical and mechanical accessory models. In this paper, we discuss the motor model of the vehicle with hysteresis nonlinearity. According to reference [40], the permanent magnet synchronous motor (PMSM)  $d-q$  model can be described as follows:

$$\begin{cases} \frac{di_q}{dt} = \frac{R}{L_q}i_q + \frac{\omega L_d}{L_q}i_d - \frac{K_l}{L_q}\omega + \frac{1}{L_q}v_q, \\ \frac{di_d}{dt} = -\frac{R}{L_d}i_d - \frac{\omega L_q}{L_d}i_q + \frac{1}{L_d}v_d, \\ T = K_t i_q + K_l(L_d - L_q)i_d i_q, \end{cases} \quad (1)$$

where  $i_d, i_q, v_d$ , and  $v_q$  represent the motor  $d-q$ -axes currents and voltages, respectively;  $R$  and  $L_d$  and  $L_q$  mean the motor resistance and  $d-q$ -axes inductances, respectively;  $K_l$  and  $K_t$  are the motor-induced voltage constant and motor torque constant, respectively;  $T$  is the transmit torque; and  $\omega$  represents the motor speed.

From (1), it is obviously shown that the motor model parameters are viewed as constants. But it neglects hysteresis loss, cross coupling, eddy current loss, etc. In addition, according to the discussion of reference [40], since the number of rotor teeth is sufficiently high, one can assume that  $L_d \approx L_q$ . Then, considering the effect of the neglected factors in former models, especially the hysteresis loss, the model (1) is modified as

$$\begin{cases} \frac{di_q}{dt} = -\frac{R}{L_q}i_q + \frac{\omega L_d}{L_q}i_d - \frac{K_l}{L_q}\omega + \frac{1}{L_q}v_q + f_1(i_q, i_d), \\ \frac{di_d}{dt} = -\frac{R}{L_d}i_d - \frac{\omega L_q}{L_d}i_q + \frac{1}{L_d}v_d + f_2(i_q, i_d), \\ T \approx K_t i_q, \end{cases} \quad (2)$$

where  $f_1(i_q, i_d)$ ,  $f_2(i_q, i_d)$ , and  $g_1(i_q, i_d)$  are the unknown nonlinear smooth functions which represent the neglected factors such as hysteresis loss in (1). We rewrite the model (2) to the state-space form as follows:

$$\begin{cases} \frac{d}{dt} \begin{bmatrix} i_q \\ i_d \\ x \end{bmatrix} = \underbrace{\begin{bmatrix} \frac{R}{L_q} & \frac{\omega L_d}{L_q} \\ \frac{\omega L_q}{L_d} & -\frac{R}{L_d} \end{bmatrix}}_A \begin{bmatrix} i_q \\ i_d \end{bmatrix} + \underbrace{\begin{bmatrix} \frac{1}{L_q} \\ \frac{1}{L_d} \end{bmatrix}}_B \begin{bmatrix} v_q \\ v_d \end{bmatrix} + \underbrace{\begin{bmatrix} f_1(i_q, i_d) \\ f_2(i_q, i_d) \\ f(x) \end{bmatrix}}_{f(x)}, \\ \frac{T}{K_t} = i_q, \end{cases} \quad (3)$$

where

$$x = \begin{bmatrix} x_1 \\ x_2 \end{bmatrix} = \begin{bmatrix} i_q \\ i_d \end{bmatrix},$$

$$A = \begin{bmatrix} a_{11} & a_{12} \\ a_{21} & a_{22} \end{bmatrix} = \begin{bmatrix} \frac{R}{L_q} & \frac{\omega L_d}{L_q} \\ \frac{\omega L_q}{L_d} & \frac{R}{L_d} \end{bmatrix}, \quad (4)$$

$$B = \begin{bmatrix} b_1 \\ b_2 \end{bmatrix} = \begin{bmatrix} \frac{1}{L_q} \\ \frac{1}{L_d} \end{bmatrix} f(x) = \begin{bmatrix} f_1(x) \\ f_2(x) \end{bmatrix} = \begin{bmatrix} f_1(i_q, i_d) \\ f_2(i_q, i_d) \end{bmatrix}.$$

Many observers and controllers require that the system model should be in canonical form. To facilitate the observer and control design in this paper, a set of new state variables will be employed to transform the system model (2) into a canonical form. Define the new system states as

$$\begin{cases} z_1 = x_1, \\ z_2 = \dot{z}_1. \end{cases} \quad (5)$$

Then, according to the equation  $z_2 = \dot{z}_1 = \dot{x}_1 = -(R/L_q)i_q + (\omega L_d/L_q)i_d - (K_1/L_q)\omega + (1/L_q)v_q + f_1(i_q, i_d)$ , we have

$$\begin{aligned} \dot{z}_2 &= \bar{a}_1 z_1 + \bar{a}_2 z_2 + \tilde{b}u - \frac{\omega R}{L_q}i_d + \frac{\omega L_d}{L_q}(\varsigma_{12}u + \varsigma_{22}\chi_2) + \varsigma_{11}\dot{u} + \varsigma_{21}\dot{\chi}_1 \\ &= \bar{a}_1 z_1 + \bar{a}_2 z_2 + \underbrace{\left(\tilde{b} + \frac{\omega L_d \varsigma_{12}}{L_q}\right)}_{\tilde{b}} u - \underbrace{\frac{\omega R}{L_q}i_d + \frac{\omega L_d}{L_q}\varsigma_{22}\chi_2 + \varsigma_{11}\dot{u} + \varsigma_{21}\dot{\chi}_1}_{F(x)}, \end{aligned} \quad (8)$$

where  $\chi_1$  and  $\chi_2$  are defined in (7).

*Remark 2.* The Bouc–Wen model is a mathematical model for hysteresis nonlinearity, where the parameters  $\varsigma_1$  and  $\varsigma_2$  decide the direction of the hysteresis nonlinearity. If  $\omega_0 = 2$ ,  $\omega_1 = 4$ ,  $\omega_2 = 0.5$ ,  $h = 3$ ,  $\varsigma_1 = 3$ , and  $\varsigma_2 = 5$ , the input signal  $u = 2.5 \sin(1.5\pi)$ ; then, the curve of the Bouc–Wen model is illustrated in Figure 1. If the parameters  $\varsigma_1 = -3$  and  $\varsigma_2 = -5$  and other parameters are not changed, the curve is illustrated in Figure 2. It is obviously shown that the parameters  $\varsigma_1$  and  $\varsigma_2$  decide the direction of the Bouc–Wen model.

Then, the system model is transformed into the canonical form as

$$\begin{cases} \dot{z}_1 = z_2, \\ \dot{z}_2 = \bar{a}_1 z_1 + \bar{a}_2 z_2 + \tilde{b}u + F(x), \\ y = z_1. \end{cases} \quad (9)$$

$$\begin{aligned} \dot{z}_2 &= \ddot{z}_1 \\ &= \frac{R}{L_q}z_2 + \frac{\omega L_d}{L_q} \left( \frac{R}{L_d}i_d - \frac{\omega L_q}{L_d}i_q + \frac{1}{L_d}v_d + f_2(x) \right) + \dot{f}_1(x) \\ &= \underbrace{\frac{-\omega^2}{\bar{a}_1}}_{\tilde{a}_1} z_1 + \underbrace{\frac{R}{L_q}}_{\tilde{a}_2} z_2 + \underbrace{\frac{\omega}{L_q} \frac{v_d}{u} - \frac{\omega R}{L_q}i_d + \frac{\omega L_d}{L_q} f_2(x)}_{\tilde{F}(x)} + \dot{f}_1(x). \end{aligned} \quad (6)$$

In this paper, we adopt the Bouc–Wen hysteresis model to describe the hysteresis loss of the vehicle PMSM  $d-q$  model. The Bouc–Wen model is given as follows:

$$\begin{aligned} f(x) &= \varsigma_1 u + \varsigma_2 \chi, \\ \dot{\chi} &= \omega_0 \dot{u} - \omega_1 |\dot{u}| \chi^{h-1} \chi - \omega_2 \dot{u} |\chi|^h, \end{aligned} \quad (7)$$

where  $\omega_0 > 0$ ,  $\omega_1 > |\omega_2|$ ,  $h > 1$ ,  $\chi(0) = 0$ , and  $\chi = [\chi_1, \chi_2]^T \in \mathbb{R}^2$ .

*Remark 1.* At three-phase motor system, we have  $v_d = \sqrt{(3/2)}U_m$ ,  $v_q = 0$ , where  $U_m$  represents the root-mean-square (RMS) value of the input voltage by coordinate transform. Then, without loss of generality, we assume  $v_q = 0$  during the control process.

Then, equation (6) can be deduced as

### 3. Echo State Network

The echo state network (ESN) is relatively a new recurrent neural network (RNN) structure for complex dynamical systems. The structure of ESN is composed of a dynamical recursive hidden layer and a memoryless output layer. Because of the feedback recursive hidden layers like the echoes, the structure of the neural network is named ESN.

ESN has easily supervised training. Compared with some other NNs, the ESN can fastly, simply, and constructively realize the supervised learning. In addition, without changing all the weights between the input layer and hidden layer, only by changing the weights from the reservoir to the output layer, ESN can fastly obtain higher precision.

The continuous-time leaky integrator ESN can be defined as

$$\dot{\Omega} = \alpha(-\gamma\Omega + \psi(W_{in}\gamma + W_{it}\Omega + W_{ba}\xi)), \quad (10)$$

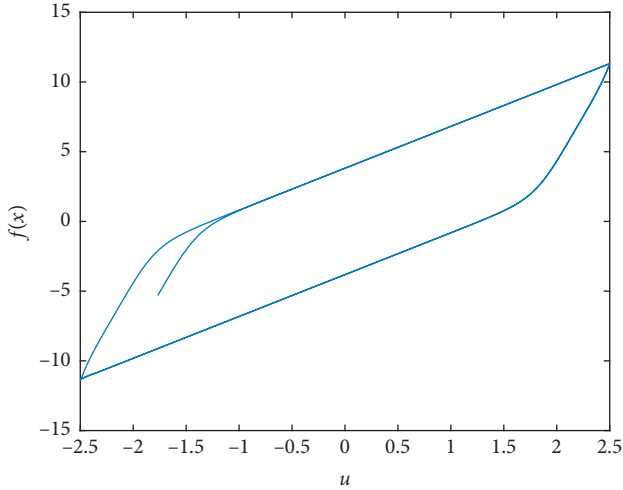


FIGURE 1: The curve of the Bouc-Wen model with  $\varsigma_1 = 3$  and  $\varsigma_2 = 5$ .

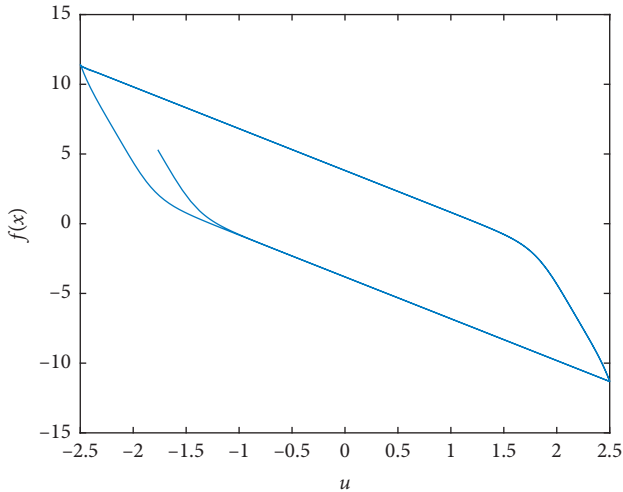


FIGURE 2: The curve of the Bouc-Wen model with  $\varsigma_1 = -3$  and  $\varsigma_2 = -5$ .

where  $\Omega$  represents the  $n$ -dimensional dynamic state;  $\alpha > 0$  is a time constant;  $\gamma$  is the leaking decay rate of the neuron's set  $\Omega$ ;  $\psi$  represents a given real continuous function, in this paper, we chose the Gaussian function; and  $W_{in} \in \mathbb{R}^{n \times m}$ ,  $W_{it} \in \mathbb{R}^{n \times n}$ , and  $W_{ba} \in \mathbb{R}^{n \times m}$  are the input, internal, and feedback weight matrices, respectively.

As suggested in [29], by choosing  $\alpha = 1$  and  $\gamma = 1$ , equation (10) is rewritten as

$$\dot{\Omega} = -\Omega + \psi(W_{in}\nu + W_{it}\Omega + W_{ba}\xi). \quad (11)$$

Then, the kernel function is chosen as the Gaussian function and  $\Omega$  is defined as  $\Omega(x) = [s_1(x), s_2(x), \dots, s_l(x)]$  with  $l$  the neuron node number of the ESN output layer. The function is

$$s_i(x) = \exp\left\{-\frac{(x - q_i)^T(x - q_i)}{\rho^2}\right\}, \quad (12)$$

where  $q_i = [q_{i1}, q_{i2}, \dots, q_{iq}]^T$ ,  $i = 1, 2, \dots, l$ ;  $q$  means the input number; and  $\rho$  represents the width of the Gaussian function.

Defining the output activation function  $\Theta$  is chosen as, the output of ESN is defined as

$$\Gamma = \Theta(W\Omega). \quad (13)$$

According to the literature [29], the output activation function  $\Theta$  units had no memory so that their values at time  $i + 1$  depended only fractionally and indirectly on their previous values. Thus, those networks are best suited for modeling intrinsically discrete-time systems with a computational and jumpy flavor. It is difficult to use networks with continuous dynamics. But we can define the ESNs with continuous function so that the dynamics can be approximated by this continuous function.

For any given real continuous function  $G(\cdot): \mathbb{R}^n \rightarrow \mathbb{R}$  on a sufficiently large compact set  $\Xi$  and arbitrary  $\varepsilon_M$ , the ESN system  $\Gamma$  satisfies

$$\sup_{\Omega \in \Xi} \|G - \Gamma\| \leq \varepsilon_M, \quad (14)$$

where  $G$  is a given real continuous function on a sufficiently large compact set  $\Xi \subset \mathbb{R}$  with the supremum  $\varepsilon_M > 0$ .

Then, the function  $G$  can be expressed as

$$G = W^*\Omega(x) + \varepsilon^*, \quad (15)$$

where  $\varepsilon^* \leq \varepsilon_M$  is the ESN error.

#### 4. Extended State Observer Design

Since the nonlinearities including hysteresis loss are considered, the controller cannot be directly designed, and the system states need an observer. Considering the normalized form (9), we will design an extended state observer (ESO) to approximate the system states. Before designing the ESO, an extended state  $z_3$  will be defined and the extended state system model is expressed as follows:

$$\begin{cases} \dot{z}_1 = z_2, \\ \dot{z}_2 = z_3 + \bar{b}u, \\ \dot{z}_3 = \bar{a}_1 z_1 + \bar{a}_2 z_2 + F(x). \end{cases} \quad (16)$$

Then, the ESO is designed as

$$\begin{cases} \dot{\hat{z}}_1 = \hat{z}_2 + \beta_1(y - \hat{z}_1), \\ \dot{\hat{z}}_2 = \hat{z}_3 + \bar{b}u + \beta_2(y - \hat{z}_1), \\ \dot{\hat{z}}_3 = \bar{a}_1 \hat{z}_1 + \bar{a}_2 \hat{z}_2 + \hat{F}(x) + \beta_3(y - \hat{z}_1), \end{cases} \quad (17)$$

where  $\hat{z}_1, \hat{z}_2, \hat{z}_3$ , and  $\hat{F}(x)$  are the estimations of  $z_1, z_2, z_3$ , and  $F(x)$ , respectively, and  $\beta_1, \beta_2$ , and  $\beta_3$  are the designed high gain parameters, respectively.

Define the errors

$$\begin{cases} \tilde{z}_i = z_i - \hat{z}_i, \quad i = 1, 2, 3, \\ \tilde{y} = y - \hat{y}, \\ \tilde{F}(x) = F(x) - \hat{F}(x), \end{cases} \quad (18)$$



where  $F(x)$  is described by the ESN. Therefore, it has  $F(x) = W\Omega(x) + \varepsilon$  and  $\widehat{F}(x) = \widehat{W}\Omega(x)$ . Then, we have  $\widehat{F}(x) = \widehat{W}\Omega(x) + \varepsilon = W\Omega(x) + \varepsilon - \widehat{W}\Omega(x)$ , and define the update law of  $\widehat{W}$  as

$$\dot{\widehat{W}} = \dot{W} = U(\widehat{\varepsilon}\Omega(x) - \varepsilon|\widehat{\varepsilon}|\widehat{W}), \quad (19)$$

where  $U = U^T$  is a constant matrix,  $\varepsilon$  is a designed positive constant, and  $\widehat{\varepsilon}$  is defined in (36).

**Lemma 1.** [41] *The ESN weights  $\widehat{W}$  in equation (19) are bounded by  $\|\widehat{W}\| \leq \|\omega\|_M/\varepsilon$ , where  $\|\omega\|_M$  is the bound of the ESN basis function vector, i.e.,  $\|\Omega\| \leq \|\omega\|_M$ .*

*Proof.* From the previous discussion, the ESN basis function vector  $\Omega$  are Gaussian functions so that it is bounded obviously, i.e.,  $\|\Omega\| \leq \|\omega\|_M$ . We choose the Lyapunov function candidate as

$$V_N = \frac{1}{2U}\widehat{W}^T\widehat{W}, \quad (20)$$

and then, considering equation (19), the time derivative of  $V_N$  can be deduced as

$$\begin{aligned} \dot{V}_N &= \frac{1}{U}\widehat{W}^T\dot{\widehat{W}} \\ &= \widehat{W}^T(\widehat{\varepsilon}\Omega(x) - \varepsilon|\widehat{\varepsilon}|\widehat{W}) \\ &\leq -\|\widehat{W}\|\|\widehat{\varepsilon}\|(\varepsilon\|\widehat{W}\| - \|\omega\|_M). \end{aligned} \quad (21)$$

According to reference [41],  $\widehat{W}$  is bounded by  $\|\widehat{W}\| \leq \|\omega\|_M/\varepsilon$  and thus  $\widehat{W} = W^* - \widehat{W}$  is also bounded as  $\|\widehat{W}\| \leq \|\omega\|_M$ , where  $\|\omega\|_M = W_N + (\|\omega\|_M/\varepsilon)$ .

Then, considering (16) and (17) yields

$$\begin{cases} \dot{\tilde{z}}_1 = -\beta_1\tilde{z}_1 + \tilde{z}_2, \\ \dot{\tilde{z}}_2 = -\beta_2\tilde{z}_1 + \tilde{z}_3, \\ \dot{\tilde{z}}_3 = (\bar{a}_1 - \beta_2)\tilde{z}_1 + \bar{a}_2\tilde{z}_2 + \widehat{F}(x). \end{cases} \quad (22)$$

Equation (22) can be rewritten as

$$\dot{\tilde{z}} = \bar{A}\tilde{z} + \zeta\widehat{F}(x), \quad (23)$$

where

$$\begin{aligned} \bar{A} &= \begin{bmatrix} -\beta_1 & 1 & 0 \\ -\beta_2 & 0 & 1 \\ \bar{a}_1 - \beta_3 & \bar{a}_2 & 0 \end{bmatrix}, \\ \zeta &= \begin{bmatrix} 0 \\ 0 \\ 1 \end{bmatrix}. \end{aligned} \quad (24)$$

Considering that the high gain parameters  $\beta_1, \beta_2$ , and  $\beta_3$  are designed, the characteristic polynomial of  $\bar{A}$  is Hurwitz. Then, given a positive definite symmetric matrix  $P = P^T > 0$ , the existing positive definite symmetric matrix  $Q = Q^T > 0$  satisfies

$$\bar{A}^T P + P\bar{A} \leq -Q. \quad (25)$$

□

*Remark 3.* In most cases, ESO has been utilized to estimate the generalized disturbance. But in this paper, the structure of the ESO has been adjusted to approximate the system states. If appropriate high gains  $\beta_1, \beta_2$ , and  $\beta_3$  are chosen, the ESO can fastly and precisely estimate the states. Besides, adjusting ESO can easily guarantee the convergence of the observer.

Therefore, the following theorem holds.

**Theorem 1.** *Considering the vehicle drive PMSM model (2), which is transformed into canonical form (9), the unknown nonlinearity  $F(x)$  is approximated by an ESN (15), the normalized system (9) is extended to (16), and then, all the signals are bounded and the states can be observed by an ESO (17).*

*Proof.* Considering the ESO (17) and equation (22), the Lyapunov function candidate  $V_o$  for the state observer errors can be designed as

$$V_o = \tilde{z}^T P \tilde{z}. \quad (26)$$

Considering (15), the derivative of  $V_o$  is deduced as

$$\begin{aligned} \dot{V}_o &= \tilde{z}^T \left( \bar{A}^T P + P\bar{A} \right) \tilde{z} + 2\widehat{F}(x)\zeta^T P \tilde{z} \\ &\leq -\tilde{z}^T Q \tilde{z} + 2\widehat{W}\Omega(x)P\tilde{z} + 2\varepsilon, \end{aligned} \quad (27)$$

where  $\widehat{W} = W - \widehat{W}$  and  $\widehat{W}$  is the estimation of the ESN weight, and the unknown nonlinearity  $F(x)$  is approximated by ESN  $F(x) = W\Omega(x) + \varepsilon$ ; therefore, the estimation  $\widehat{F}(x) = \widehat{W}\Omega(x)$ .

According to Lemma 1 and reference [31], the error weight of ESN satisfies  $\widehat{W} \leq \|\omega\|_M$ , and  $\Omega(x)$  is bounded, it has  $\Omega(x) \leq \|\omega\|_M$ . Considering  $\varepsilon \leq \varepsilon_M$ , equation (27) is expressed as

$$\begin{aligned} \dot{V}_o &\leq -\tilde{z}^T Q \tilde{z} + 2\|\omega_M\varphi_M\|\lambda_{\max}(P)\tilde{z} + 2\varepsilon_M \\ &\leq -\tilde{z}^T Q \tilde{z} + 2\|\omega_M\|\|\varphi_M\|\lambda_{\max}(P)\tilde{z} + 2\varepsilon_M, \end{aligned} \quad (28)$$

where  $\lambda_{\max}(P)$  represents the biggest norm of the matrix  $P$ . From Young's inequality  $ab \leq ((a^2 + b^2)/2)$ , it has  $2\|\omega_M\|\|\varphi_M\|\lambda_{\max}(P)\tilde{z} \leq \|\omega_M\|^2 + \|\varphi\|^2 + \lambda_{\max}^2(P) + \tilde{z}^2$ . Then, we have

$$\dot{V}_o \leq -\tilde{z}^T Q \tilde{z} + \|\omega_M\|^2 + \|\varphi\|^2 + \lambda_{\max}^2(P) + \tilde{z}^2 + 2\varepsilon_M. \quad (29)$$

We rewrite (29) as

$$\dot{V}_o \leq -\tilde{a}_1 V_o + \tilde{a}_2, \quad (30)$$

where  $\tilde{a}$  can be deduced by  $\bar{A}^T P + P\bar{A} \leq -Q$ ;  $\tilde{a}_2 = \|\omega_M\|^2 + \|\varphi\|^2 + \lambda_{\max}^2(P) + \tilde{z}^2 + 2\varepsilon_M$ . By integrating both sides of (30), the following equation can be obtained:

$$|\tilde{z}| \leq \sqrt{\frac{V_o(0)e^{-\tilde{a}_1 t} + (\tilde{a}_2/\tilde{a}_1)}{\lambda_{\max}(P)}}, \quad (31)$$



and that indicates all the signals are bounded and the observer error  $\tilde{z}$  is converged into a compact set around the zero. Therefore, according to the Lyapunov theory, the proposed ESO can estimate the system states.  $\square$

## 5. Sliding Mode Control Design

This section will design a sliding mode control for the new vehicle drive PMSM model that the hysteresis loss is described by ESN. The control structure of the sliding mode control with the ESO and ESN is illustrated in Figure 3. We firstly define a sliding mode manifold and then design the sliding mode controller. The stability of the control strategy finally is demonstrated.

To design the sliding mode control, the tracking error is defined as

$$e = y - y_d = z_1 - y_d, \quad (32)$$

and the sliding manifold is adopted as

$$s = \eta e + \dot{e}, \quad (33)$$

where the designed parameters  $\eta > 0$  and the reference signal  $y_d$  has continual derivative.

From (32), the derivative of  $s$  can be deduced as

$$\dot{s} = \eta \dot{e} + \ddot{e}. \quad (34)$$

Because the tracking error is defined in (32), we have

$$\begin{aligned} \dot{e} &= \dot{z}_1 - \dot{y}_d = z_2 - \dot{y}_d, \\ \ddot{e} &= \dot{z}_2 - \ddot{y}_d. \end{aligned} \quad (35)$$

We define the functions as

$$\begin{aligned} \hat{e} &= \hat{y} - y_d = \hat{z}_1 - y_d, \\ \hat{s} &= \eta \hat{e} + \dot{\hat{e}}, \\ \hat{\tau} &= s - \hat{s}, \\ \hat{e} &= e - \hat{e}. \end{aligned} \quad (36)$$

The sliding mode controller is designed as

$$u = \frac{1}{b} \left( -\eta_t \hat{s} - \hat{z}_3 - \eta \dot{\hat{e}} + \dot{y}_d - \tau \text{sign}(s) \right), \quad (37)$$

where the designed parameters  $\eta_t > 0$  and  $\hat{s}$  and  $\hat{e}$  represent the estimation of  $s$  and  $e$ , respectively. In order to decrease the influence of the chattering, we choose  $0 < \tau < 1$ .

Then, the following theorem can be obtained:

**Theorem 2.** For the vehicle drive PMSM model considering the hysteresis loss (9), which extends the state to (16), the states

are observed by ESO (17); defining the sliding mode manifold in (33) and designing the controller in (37), then, all signals in the closed-loop are uniformly ultimately bounded (UUB).

*Proof.* To verify the stability of the closed loop, the Lyapunov function is selected as

$$V = \frac{1}{2} s^2. \quad (38)$$

Considering the sliding manifold (33)–(35), the derivative of  $V$  is

$$\begin{aligned} \dot{V} &= s \dot{s} \\ &= s(\eta \dot{e} + \ddot{e}) \\ &= s(\eta \dot{e} + (\dot{z}_2 - \ddot{y}_d)). \end{aligned} \quad (39)$$

Substituting  $\dot{z}_2 = z_3 + \bar{b}u$  in (16) into (39) yields

$$\dot{V} = s(\eta \dot{e} + (z_3 + \bar{b}u - \ddot{y}_d)). \quad (40)$$

By the substitution of sliding mode controller (37) into (40), the derivative of  $V$  can be deduced as

$$\dot{V} = s(\eta \dot{e} + (z_3 - \eta_t \hat{s} - \hat{z}_3 - \eta \dot{\hat{e}} + \dot{y}_d - \tau \text{sign}(s) - \ddot{y}_d)). \quad (41)$$

Considering (36), the derivative of  $V$  can be deduced as

$$\begin{aligned} \dot{V} &= s(\eta \dot{\hat{e}} + \dot{\hat{z}}_3 - \eta_t \hat{s} - \tau \text{sign}(s)) \\ &= s(\eta \dot{\hat{e}} + \dot{\hat{z}}_3 - \eta_t (s - \hat{s}) - \tau \text{sign}(s)) \\ &= -\eta_t s^2 + s(\eta \dot{\hat{e}} + \dot{\hat{z}}_3 + \eta_t \hat{s} - \tau \text{sign}(s)). \end{aligned} \quad (42)$$

Substituting the sliding manifold (33) and  $\hat{s} = \eta \hat{e} + \dot{\hat{e}}$  in (36) into  $\hat{s}$  yields

$$\hat{s} = \eta \hat{e} + \dot{\hat{e}}. \quad (43)$$

By the substitution of (43) into (42), we get

$$\begin{aligned} \dot{V} &= -\eta_t s^2 + s(\eta \dot{\hat{e}} + \dot{\hat{z}}_3 + \eta \eta_t \hat{e} + \eta_t \dot{\hat{e}} - \tau \text{sign}(s)) \\ &= -\eta_t s^2 + s((\eta + \eta_t) \dot{\hat{e}} + \dot{\hat{z}}_3 + \eta \eta_t \hat{e} - \tau \text{sign}(s)). \end{aligned} \quad (44)$$

According to  $e = z_1 - y_d$  in (32), we have

$$\begin{aligned} \hat{e} &= \hat{z}_1 - y_d, \\ \dot{\hat{e}} &= \hat{z}_2 - \dot{y}_d. \end{aligned} \quad (45)$$

Substituting (22) and (45) into (44) yields

$$\begin{aligned} \dot{V} &= -\eta_t s^2 + s((\eta + \eta_t) \hat{z}_2 - (\eta + \eta_t) \dot{y}_d + \bar{a}_1 \hat{z}_1 + \bar{a}_2 \hat{z}_2 + \bar{F}(x) + \eta \eta_t \hat{z}_1 - \eta \eta_t y_d - \tau \text{sign}(s)) \\ &= -\eta_t s^2 + s((\bar{a}_1 + \eta \eta_t) \hat{z}_1 + (\bar{a}_2 + \eta + \eta_t) \hat{z}_2 - \eta \eta_t y_d - (\eta + \eta_t) \dot{y}_d + \bar{F}(x) - \tau \text{sign}(s)). \end{aligned} \quad (46)$$

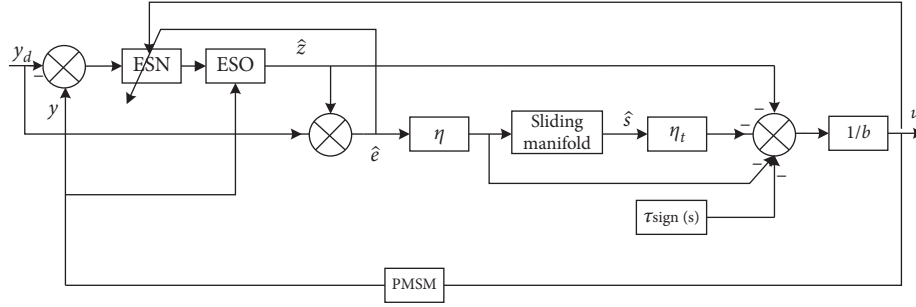


FIGURE 3: The structure of the controller.

Considering Theorem 1, the unknown bounded function  $\tilde{F}(x)$  can be approximated by the ESN  $\tilde{F}(x) = \tilde{W}\Omega(x) \leq \|\omega_M\| \|\varphi_M\|$  and  $\tilde{z}_1, \tilde{z}_2, y_d$ , and  $\dot{y}_d$  are all bounded, respectively. Then, defining  $\|(\bar{a}_1 + \eta\eta_t)\tilde{z}_1 + (\bar{a}_2 + \eta + \eta_t)\tilde{z}_2 - \eta\eta_t y_d - (\eta + \eta_t)\dot{y}_d + \tilde{W}\Omega(x)\| \leq \Delta_{\max}$ , where  $\Delta_{\max} \geq 0$ , equation (46) satisfies

$$\begin{aligned} \dot{V} &\leq -\eta_t s^2 + s\Delta_{\max} - \tau \text{sign}(s) \\ &\leq -\eta_t s^2 + s\Delta_{\max} - \tau |s|. \end{aligned} \quad (47)$$

If  $\tau |s| > 1$ , equation (47) can be rewritten as

$$\begin{aligned} \dot{V} &\leq -\eta_t s^2 + s\Delta_{\max} \\ &= -\mu + s\Delta_{\max}, \end{aligned} \quad (48)$$

where  $\mu = \eta_t > 0$ .

If  $0 \leq \tau |s| \leq 1$ , it has

$$\begin{aligned} \dot{V} &\leq -\eta_t s^2 + s\Delta_{\max} - \tau s^2 \\ &= -(\eta_t + \tau) s^2 + s\Delta_{\max} \\ &= -\mu s^2 + s\Delta_{\max}, \end{aligned} \quad (49)$$

where  $\mu = \eta_t + \tau > 0$ .

According to Young's inequality,  $s\Delta_{\max}$  has  $s\Delta_{\max} \leq (s^2/2) + (\Delta_{\max}^2/2)$ ; then, equation (47) can be rewritten as

$$\begin{aligned} \dot{V} &\leq -\mu s^2 + \frac{s^2}{2} + \frac{\Delta_{\max}^2}{2} \\ &= \left(-\mu + \frac{1}{2}\right) s^2 + \frac{\Delta_{\max}^2}{2}. \end{aligned} \quad (50)$$

When  $\mu > 0.5$ , according to the definition of the Lyapunov function  $V$  in (38), equation (50) can be solved

$$|s| \leq \sqrt{\frac{(2\mu - 1)V(0) + \Delta_{\max}^2}{(2\mu - 1)\Delta_{\max}}}. \quad (51)$$

Considering the definition of  $s$  in (33) and the bounded (51), the margin of error  $e$  is obtained:

$$|e| \leq \sqrt{\frac{s(0) + (\eta/\vartheta)}{\vartheta}}, \quad (52)$$

where  $\vartheta = \sqrt{((2\mu - 1)V(0) + \Delta_{\max}^2)/((2\mu - 1)\Delta_{\max})}$ .

Therefore, according to the Lyapunov theory, all the signals of the closed loop are uniformly ultimately bounded.  $\square$

*Remark 4.* In this controller design, we chose the robust function  $\text{sign}(\cdot)$  to design the sliding mode control. But the function  $\text{sign}(\cdot)$  is a discontinuous function which can deduce the strong chattering for the sliding mode manifold. In order to restrain the chattering, many approaches are utilized. In this paper, we select the continuous function  $\tanh(\cdot)$  instead of the discontinuous function  $\text{sign}(\cdot)$ , which can substantially restrain the chattering of the SMC. The simulations are demonstrated for this approach.

## 6. Simulations

We design the simulations with Simulink of Matlab to verify the effectiveness of the proposed ESO and ESNSMC for the vehicle drive motor with hysteresis nonlinearity. The PMSM, the ESO, and the ESNSMC parameters are selected as follows:  $d$ -axis inductance  $L_d$  and  $q$ -axis inductance  $L_q$  are 0.47 mH; torque  $T$  is 96.5 N · m; angular speed  $\omega$  is 3000 rpm; resistance  $R$  is 0.033  $\Omega$ ; motor-induced voltage constant  $K_1$  is 0.147; and motor torque constant  $K_t$  is 0.72. The high gain parameters  $\beta_1, \beta_2$ , and  $\beta_3$  are selected as  $\beta_1 = 360$ ,  $\beta_2 = 5000$ , and  $\beta_3 = 28500$ .  $\eta$  is chosen as 5.  $\tau$  can be selected as 0.3. In order to verify the proposed approaches, we restrain the errors in  $[-0.5, 0.5]$  in the simulations.

In the section, we design two series of simulations with different values of  $\tau \text{sign}(s)$ . One is  $\tau \text{sign}(s) = 0.3 \text{sign}(s)$ , and the other is selected as  $\tau \text{sign}(s) = 0.3 \tanh(s)$ . The reason of the design is to contrast the results of the ESNSMC to show the effect of the chattering in the sliding mode control.

*6.1. Case 1.* In this section, we select  $\tau \text{sign}(s) = 0.3 \text{sign}(s)$  in the controller of (37) to verify the proposed ESNSMC and ESO of this paper. The output tracking results of  $y, \dot{y}$ , and  $\ddot{y}$  are illustrated in Figure 4, and the tracking errors are shown in Figure 5. The observer results of  $z_1, z_2$ , and  $z_3$  of the proposed ESO are shown in Figure 6, and the observer errors are illustrated in Figure 7. Figure 8 is the proposed ESNSMC controller trajectory.

From Figures 4 and 6, it is obviously shown that both the proposed ESO and the ESNSMC are well tracking the reference signals. Based on the structure of the control strategy, the adjusting of the observer is in the closed loop and that follow the adjustment of the controller. Then, if the gains of ESO  $\beta_1, \beta_2$ , and  $\beta_3$  are chosen enough higher, it can quickly approximate the states  $z_1, z_2$ , and  $z_3$ . From Figure 6, one can clearly find that the proposed ESO worked well, and from

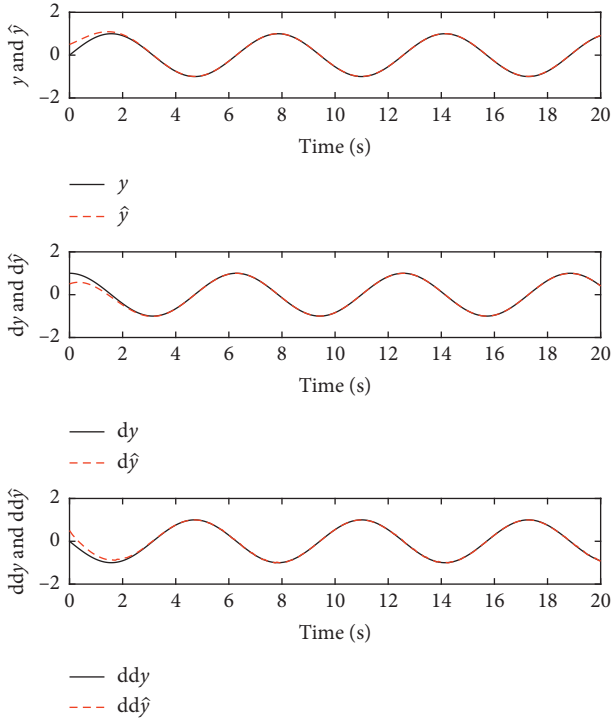


FIGURE 4: The output results  $y, dy,$  and  $ddy$  of the ESNSMC with ESO  $\tau\text{sign}(s) = 0.3\text{sign}(s)$ .

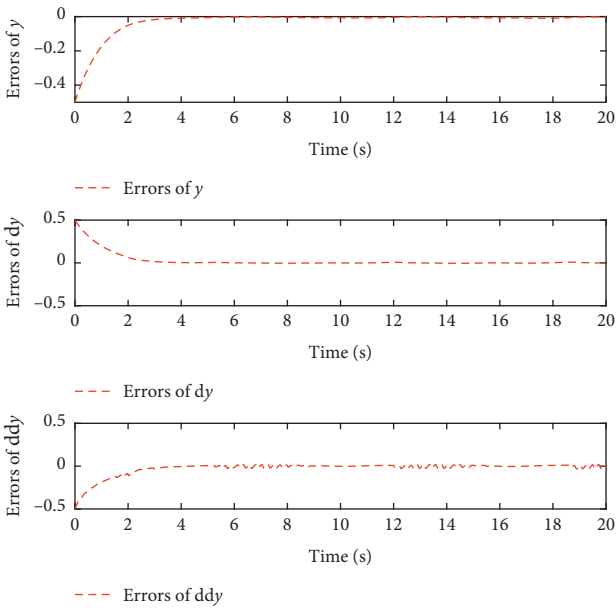


FIGURE 5: The errors of  $y, dy,$  and  $ddy$  of the ESNSMC with ESO  $\tau\text{sign}(s) = 0.3\text{sign}(s)$ .

Figure 4, one can also find that the output quickly tracks the reference signal. But from Figures 5 and 7, due to the existence of the chattering in the sliding mode control, it has been obviously shaking when the PMSM is veered. If we survey Figure 8, it can be seen that the trajectory of the proposed ESNSMC controller also has the same characteristics as well as the errors of ESNSMC control results and the ESO observer.

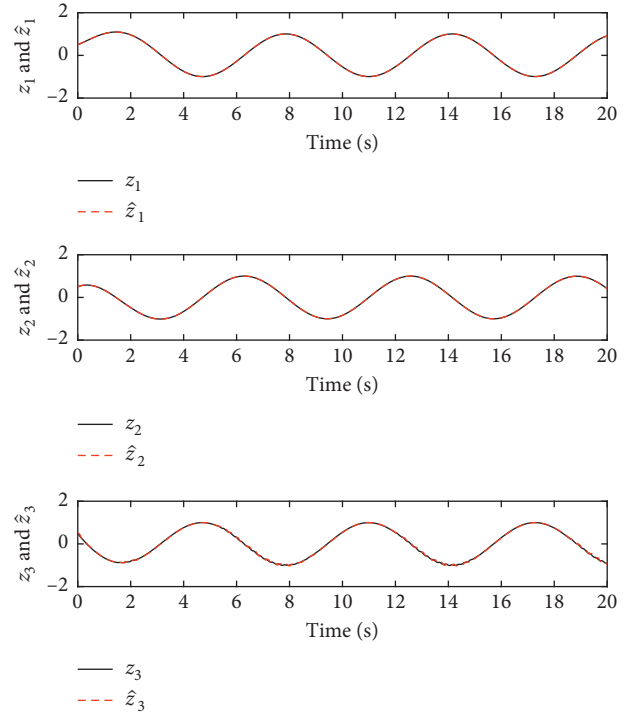


FIGURE 6: The observer results of  $z_1, z_2,$  and  $z_3$  with ESO  $\tau\text{sign}(s) = 0.3\text{sign}(s)$ .

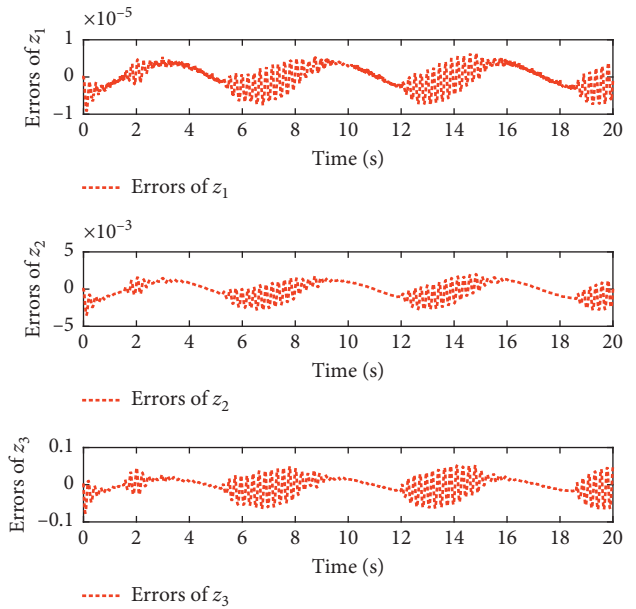


FIGURE 7: The observer errors of  $z_1, z_2,$  and  $z_3$  with ESO  $\tau\text{sign}(s) = 0.3\text{sign}(s)$ .

From Figures 4–8, one can easily find the influence of the chattering in the proposed ESNSMC, even though the ESN compensates the hysteresis nonlinearity. The chattering of the sliding mode control really degrades the precision of the control strategy. In order to alleviate the influence of the chattering of the ESNSMC, we chose continuous  $\tanh(\cdot)$  function to take the place of the discontinuous  $\text{sign}(\cdot)$  function in the next case.

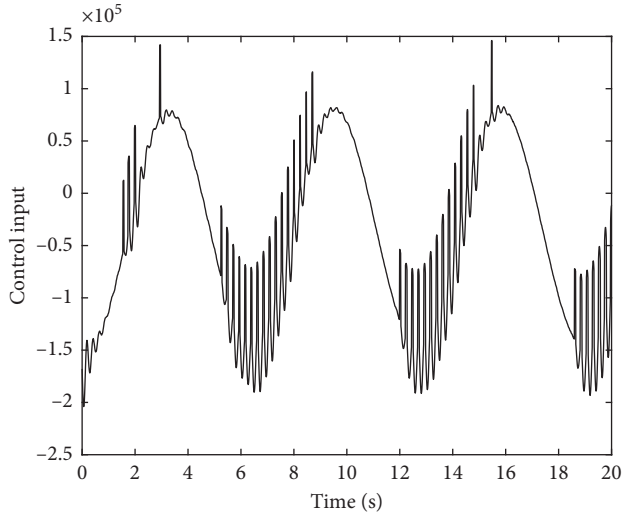


FIGURE 8: The trajectory of the ESNSMC controller  $\tau\text{sign}(s) = 0.3\text{sign}(s)$ .

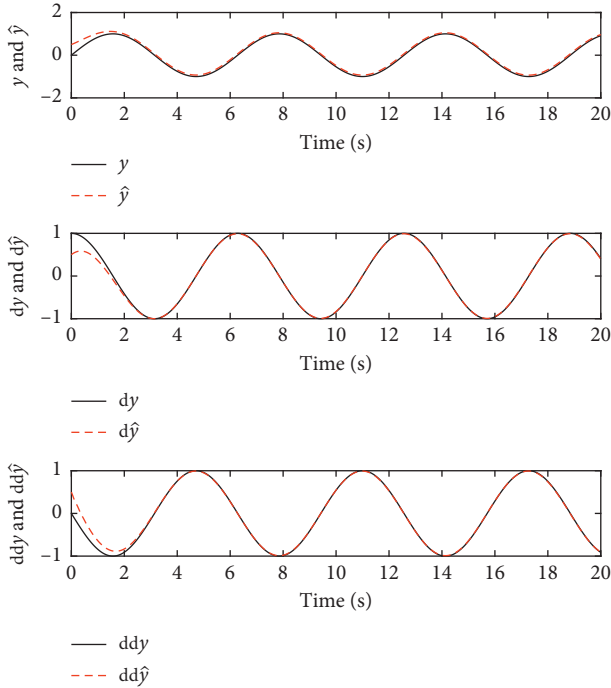


FIGURE 9: The output results  $y, dy$ , and  $ddy$  of the ESNSMC with ESO  $\tau\text{sign}(s)$  is replaced by  $0.3 \tanh(s)$ .

6.2. Case 2. In this section, the robust  $\tau\text{sign}(s)$  is chosen as  $\tau\text{sign}(s) = 0.3 \tanh(s)$ . Then, Figures 9 and 10 illustrate the output results  $y, \dot{y}$ , and  $\ddot{y}$  of the proposed ESNSMC with ESO for  $\tau\text{sign}(s) = 0.3 \tanh(s)$ , and the ESO estimates the states  $z_1, z_2$ , and  $z_3$  are shown in Figure 11. Figure 12 is the estimate errors of  $z_1, z_2$ , and  $z_3$  with the ESO observer. The controller input is illustrated in Figure 13 for the robust  $\tau\text{sign}(s) = 0.3 \tanh(s)$ .

Compared with the control tracking results Figures 4 and 9 and the controller errors Figures 5 and 10, one can obtain that the continuous function  $\tanh(\cdot)$  can substantially restrain

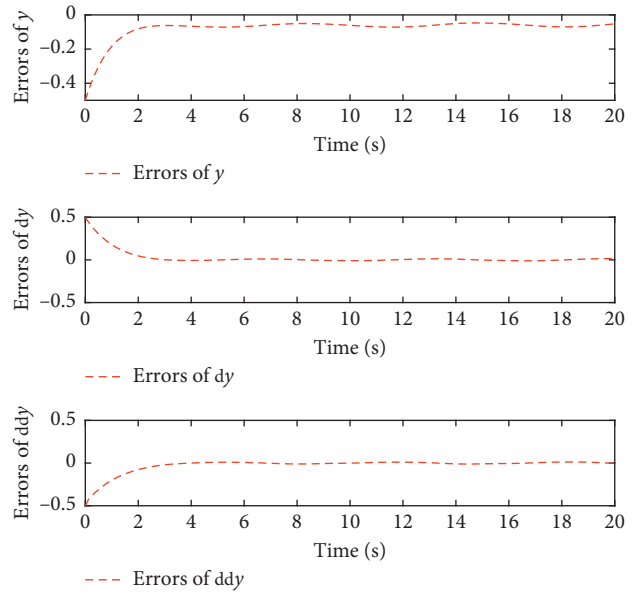


FIGURE 10: The errors of  $y, dy$ , and  $ddy$  of the ESNSMC with ESO  $\tau\text{sign}(s)$  is replaced by  $0.3 \tanh(s)$ .

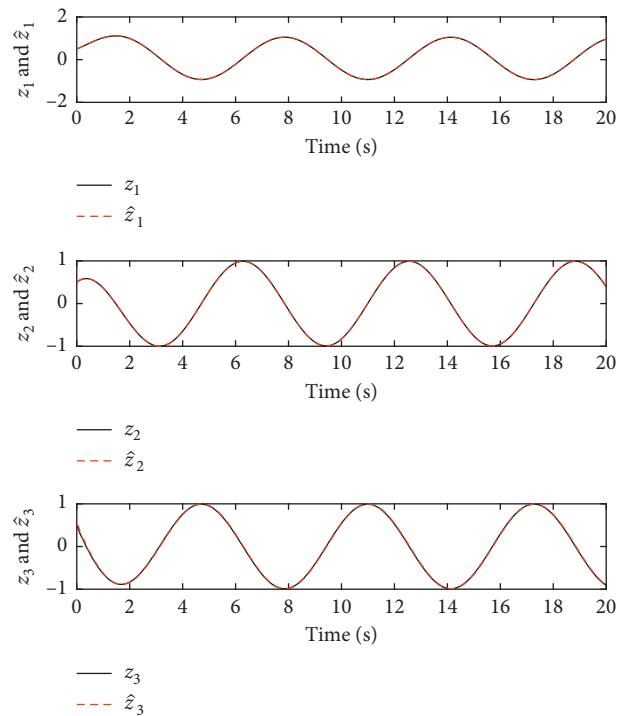


FIGURE 11: The observer results of  $z_1, z_2$ , and  $z_3$  with ESO  $\tau\text{sign}(s)$  is replaced by  $0.3 \tanh(s)$ .

the chattering of the sliding mode control. Especially in contrast with the tracking errors Figures 5 and 10, the influence of the chattering at the reversing processes almost is not caught in Figure 10 with the continuous robust function  $\tau\text{sign}(s) = 0.3 \tanh(s)$ . The same conclusions can also be deduced by the observer results and errors in Figures 11 and 12. Especially in contrast with Figures 7 and 12, one can find that the maximum of the error of  $z_3$  is about 0.08 at the

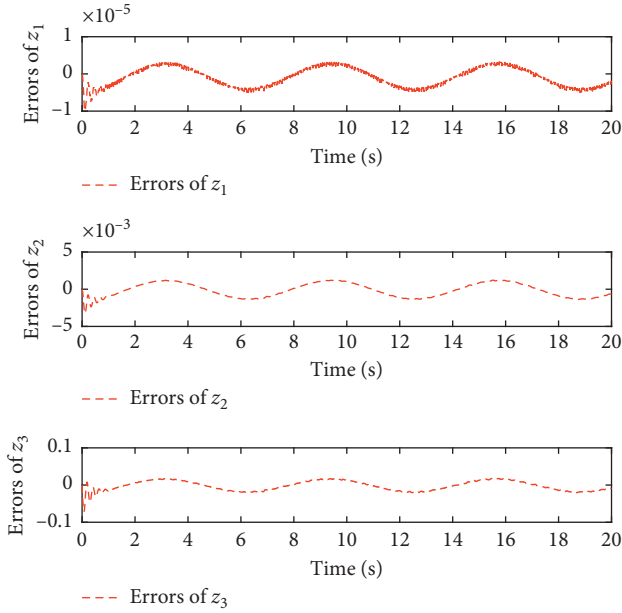


FIGURE 12: The observer errors of  $z_1, z_2$ , and  $z_3$  with ESO  $\tau\text{sign}(s)$  is replaced by  $0.3 \tanh(s)$ .

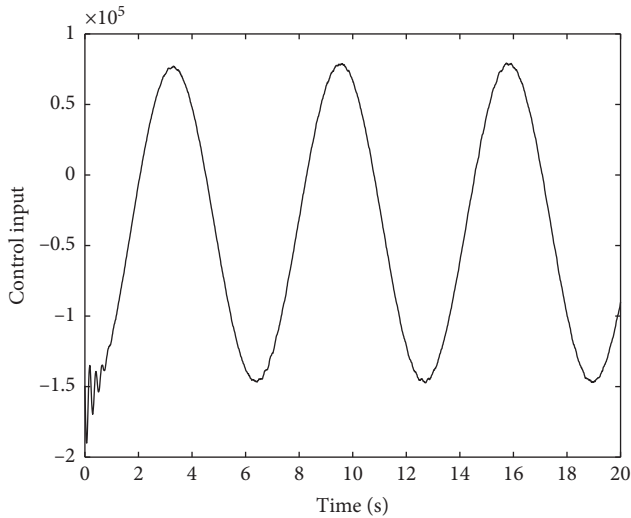


FIGURE 13: The trajectory of the ESNSMC controller  $\tau\text{sign}(s)$  is replaced by  $0.3 \tanh(s)$ .

reversing processes in Figure 7 and the maximum of the error of  $z_3$  is about 0.02 at the reversing processes in Figure 12. One can also obtain that, in Figure 12, the maximum of errors of  $z_1, z_2$ , and  $z_3$  appears at the dynamic processes with the continuous robust function  $\tau\text{sign}(s) = 0.3 \tanh(s)$ , which are caused by the ESN, but in Figure 8, the maximum of errors of  $z_1, z_2$ , and  $z_3$  appears at the reversing processes with discontinuous robust function  $\tau\text{sign}(s) = 0.3\text{sign}(s)$ , which are caused by the chattering of the SMC.

Table 1 illustrates the tracking errors and the observer errors with the discontinuous robust function  $\tau\text{sign}(s) = 0.3\text{sign}(s)$ , and the tracking errors and the observer errors with the continuous robust function  $\tau\text{sign}(s) =$

TABLE 1: The tracking errors and the observer errors with the robust  $\tau\text{sign}(s) = 0.3\text{sign}(s)$

Variables	MAE	Max	Min
$\tilde{y}$	0.0276	0.5	0.0014
$\dot{\tilde{y}}$	0.0269	0.5	$1.8734e^{-6}$
$\ddot{\tilde{y}}$	0.0317	0.5	$1.3852e^{-6}$
$\tilde{z}_1$	$2.702e^{-6}$	$9.9556e^{-6}$	0
$\tilde{z}_2$	$9.5797e^{-4}$	0.0035	0
$\tilde{z}_3$	0.0187	0.0763	0

TABLE 2: The tracking errors and the observer errors with the robust  $\tau\text{sign}(s) = 0.3 \tanh(s)$ .

Variables	MAE	Max	Min
$\tilde{y}$	0.0775	0.5	0.047
$\dot{\tilde{y}}$	0.0281	0.5	$7.9464e^{-6}$
$\ddot{\tilde{y}}$	0.0312	0.5	$1.473e^{-5}$
$\tilde{z}_1$	$2.2891e^{-6}$	$8.3371e^{-6}$	0
$\tilde{z}_2$	$8.3078e^{-4}$	0.0032	0
$\tilde{z}_3$	0.0116	0.0698	0

$0.3 \tanh(s)$  are shown in Table 2. From Tables 1 and 2, the MAEs of  $[\tilde{z}_1, \tilde{z}_2, \tilde{z}_3]^T$  are  $[2.702e^{-6}, 9.5797e^{-4}, 0.0187]^T$  and  $[2.289e^{-6}, 8.3078e^{-4}, 0.0116]^T$ , respectively. It is illustrated that the continuous robust function  $\tanh(\cdot)$  can substantially restrain the chattering of the SMC. But considering the MAE tracking errors  $[\tilde{y}, \dot{\tilde{y}}, \ddot{\tilde{y}}]^T$  are  $[0.0276, 0.0269, 0.0317]^T$  and  $[0.0775, 0.0281, 0.0312]^T$ , respectively, the MIN tracking errors are  $[0.0014, 1.8734e^{-6}, 1.3852e^{-5}]$  and  $[0.047, 7.9464e^{-6}, 1.473e^{-5}]$ , respectively. That means the continuous robust function  $\tanh(\cdot)$  can substantially restrain the chattering but degrade the tracking precision.

Compared with Figures 8 and 13, one can obviously find that the dynamic processes is influenced by the ESN in Figure 13 with the continuous robust function  $\tanh(\cdot)$  which can well restrain the chattering of the SMC, but the discontinuous robust function  $\text{sign}(\cdot)$  will result in strong chattering and difficult to achieve stable process from Figure 8.

## 7. Conclusion

A new neural network sliding mode control strategy was designed for PMSM of electric vehicles in this research. Firstly, a modified PMSM model considering hysteresis losses was proposed. Since the existence of the hysteresis nonlinearity complicated the PMSM model, a transformed canonical form was deduced to simplify the controller. Because most electric vehicle system states could not be measured directly, an ESO was adopted to estimate all the states including the indirectly obtained states, and the hysteresis nonlinearity was approximated by an ESN. Finally, we designed a sliding mode control based on the ESO results with the ESN in the closed loop to precisely control the electric vehicle PMSM systems, and the chattering of the SMC was restrained by  $\tanh(\cdot)$ . Two different Lyapunov



functions guaranteed the observer validity and the controller effectiveness. The simulations demonstrated that the proposed observer and controller can achieve a good performance and all the signals were uniformly ultimately bounded.

## Data Availability

The data used to support the findings of this study are available from the corresponding author upon request.

## Conflicts of Interest

The authors declare that they have no conflicts of interest.

## Acknowledgments

This work was supported by the Shandong Provincial Natural Science Foundation of China (ZR2017MF048), Shandong Provincial Key Research and Development Project (2019GGX101005 and 2016GGX105013), National Natural Science Foundation of China (61803216), and Shandong University Science and Technology Plan (J17KA214).

## References

- [1] J. Na, A. S. Chen, G. Herrmann, R. Burke, and C. Brace, "Vehicle engine torque estimation via unknown input observer and adaptive parameter estimation," *IEEE Transactions on Vehicular Technology*, vol. 67, no. 1, pp. 409–422, 2018.
- [2] J. Na, Y. Huang, X. Wu, G. Gao, G. Herrmann, and J. Z. Jiang, "Active adaptive estimation and control for vehicle suspensions with prescribed performance," *IEEE Transactions on Control Systems Technology*, vol. 26, no. 6, pp. 2063–2077, 2018.
- [3] S. Wang, H. Yu, J. Yu, J. Na, and X. Ren, "Neural-network-based adaptive funnel control for servo mechanisms with unknown dead-zone," *IEEE Transactions on Cybernetics*, pp. 1–12, 2018.
- [4] S. Wang, J. Na, X. Ren, H. Yu, and J. Yu, "Unknown input observer-based robust adaptive funnel motion control for nonlinear servomechanisms," *International Journal of Robust and Nonlinear Control*, vol. 28, no. 18, pp. 6163–6179, 2018.
- [5] Y. Huang, J. Na, X. Wu, and G. Gao, "Approximation-free control for vehicle active suspensions with hydraulic actuator," *IEEE Transactions on Industrial Electronics*, vol. 65, no. 9, pp. 7258–7267, 2018.
- [6] J. Na, Y. Huang, X. Wu, S.-F. Su, and G. Li, "Adaptive finite-time fuzzy control of nonlinear active suspension systems with input delay," *IEEE Transactions on Cybernetics*, pp. 1–12, 2019.
- [7] C. Hu, H. Gao, J. Guo et al., "MME-EKF-based path-tracking control of autonomous vehicles considering input saturation," *IEEE Transactions on Vehicular Technology*, vol. 68, no. 6, pp. 5246–5259, 2019.
- [8] B. Li, H. Du, W. Li, and B. Zhang, "Integrated trajectory planning and control for obstacle avoidance manoeuvre using non-linear vehicle mp algorithm," *IET Intelligent Transport Systems*, vol. 13, no. 2, pp. 385–397, 2019.
- [9] S. Sun, H. Deng, H. Du et al., "A compact variable stiffness and damping shock absorber for vehicle suspension," *IEEE/ASME Transactions on Mechatronics*, vol. 20, no. 5, pp. 2621–2629, 2015.
- [10] S. Sun, X. Tang, J. Yang et al., "A new generation of magnetorheological vehicle suspension system with tunable stiffness and damping characteristics," *IEEE Transactions on Industrial Informatics*, vol. 15, no. 8, pp. 4696–4708, 2019.
- [11] G. Luo, R. Zhang, Z. Chen, W. Tu, S. Zhang, and R. Kennel, "A novel nonlinear modeling method for permanent-magnet synchronous motors," *IEEE Transactions on Industrial Electronics*, vol. 63, no. 10, pp. 6490–6498, 2016.
- [12] D. Egorov, I. Petrov, J. Link, R. Stern, and J. J. Pyrhonen, "Model-based hysteresis loss assessment in PMSMs with ferrite magnets," *IEEE Transactions on Industrial Electronics*, vol. 65, no. 1, pp. 179–188, 2018.
- [13] X. Lin, W. Huang, and L. Wang, "SVPWM strategy based on the hysteresis controller of zero-sequence current for three-phase open-end winding PMSM," *IEEE Transactions on Power Electronics*, vol. 34, no. 4, pp. 3474–3486, 2019.
- [14] X. Gao, "Adaptive neural control for hysteresis motor driving servo system with Bouc-Wen model," *Complexity*, vol. 2018, Article ID 9765861, 9 pages, 2018.
- [15] X. Gao and R. Liu, "Multiscale Chebyshev neural network identification and adaptive control for backlash-like hysteresis system," *Complexity*, vol. 2018, Article ID 1872493, 9 pages, 2018.
- [16] Q. Zhu, W. Zhang, J. Na, and B. Sun, "U-model based control design framework for continuous-time systems," in *Proceedings of the 2019 Chinese Control Conference (CCC)*, pp. 106–111, Guangzhou, China, July 2019.
- [17] J. Zhang, Q. Zhu, Y. Li, X. Wu, and R. Zhen, "A general U-model based super twisting design procedure for nonlinear polynomial systems," in *Proceedings of the 2017 36th Chinese Control Conference (CCC)*, pp. 3641–3645, Dalian, China, July 2017.
- [18] Q. Zhu and L. Guo, "Stable adaptive neurocontrol for nonlinear discrete-time systems," *IEEE Transactions on Neural Networks*, vol. 15, no. 3, pp. 653–662, 2004.
- [19] Q. Zhu, D. Zhao, S. Zhang, and P. Narayan, "U-model enhanced dynamic control of a heavy oil pyrolysis/cracking furnace," *IEEE/CAA Journal of Automatica Sinica*, vol. 5, no. 2, pp. 577–586, 2018.
- [20] W. Wei, M. Wang, D. Li, M. Zuo, and X. Wang, "Disturbance observer based active and adaptive synchronization of energy resource chaotic system," *ISA Transactions*, vol. 65, pp. 164–173, 2016.
- [21] W. He, T. Meng, X. He, and C. Sun, "Iterative learning control for a flapping wing micro aerial vehicle under distributed disturbances," *IEEE Transactions on Cybernetics*, vol. 49, no. 4, pp. 1524–1535, 2019.
- [22] Y. Zhu and W. X. Zheng, "Observer-based control for cyber-physical systems with periodic dos attacks via a cyclic switching strategy," *IEEE Transactions on Automatic Control*, p. 1, 2019.
- [23] Y. Zhu, W. X. Zheng, and D. Zhou, "Quasi-synchronization of discrete-time Lur'e-type switched systems with parameter mismatches and relaxed PDT constraints," *IEEE Transactions on Automatic Control*, pp. 1–12, 2019.
- [24] Y. Zhu and W. X. Zheng, "Multiple lyapunov functions analysis approach for discrete-time switched piecewise-affine systems under dwell-time constraints," *IEEE Transactions on Automatic Control*, p. 1, 2019.
- [25] J. Q. Han, "The extended state observer for a class of uncertain systems," *Control and Decision*, vol. 10, no. 1, pp. 85–88, 1995, in Chinese.



- [26] W. Xue, W. Bai, S. Yang, K. Song, Y. Huang, and H. Xie, "ADRC with adaptive extended state observer and its application to air-fuel ratio control in gasoline engines," *IEEE Transactions on Industrial Electronics*, vol. 62, no. 9, pp. 5847–5857, 2015.
- [27] W. Xue, R. Madonski, K. Lakomy, Z. Gao, and Y. Huang, "Add-on module of active disturbance rejection for set-point tracking of motion control systems," *IEEE Transactions on Industry Applications*, vol. 53, no. 4, pp. 4028–4040, 2017.
- [28] Q. Chen, L. Tao, and Y. Nan, "Full-order sliding mode control for high-order nonlinear system based on extended state observer," *Journal of Systems Science and Complexity*, vol. 29, no. 4, pp. 978–990, 2016.
- [29] G. Sun, X. Ren, and D. Li, "Neural active disturbance rejection output control of multimotor servomechanism," *IEEE Transactions on Control Systems Technology*, vol. 23, no. 2, pp. 746–753, 2015.
- [30] S. Wang, X. Ren, J. Na, and T. Zeng, "Extended-state-observer-based funnel control for nonlinear servomechanisms with prescribed tracking performance," *IEEE Transactions on Automation Science and Engineering*, vol. 14, no. 1, pp. 98–108, 2017.
- [31] Q. Chen, L. Shi, J. Na, X. Ren, and Y. Nan, "Adaptive echo state network control for a class of pure-feedback systems with input and output constraints," *Neurocomputing*, vol. 275, pp. 1370–1382, 2018.
- [32] G. Sun, D. Li, and X. Ren, "Modified neural dynamic surface approach to output feedback of MIMO nonlinear systems," *IEEE Transactions on Neural Networks and Learning Systems*, vol. 26, no. 2, pp. 224–236, 2015.
- [33] S. Wang, J. Na, and X. Ren, "Rise-based asymptotic prescribed performance tracking control of nonlinear servo mechanisms," *IEEE Transactions on Systems, Man, and Cybernetics: Systems*, vol. 48, no. 12, pp. 2359–2370, 2018.
- [34] M. Wang, X. Ren, Q. Chen, S. Wang, and X. Gao, "Modified dynamic surface approach with bias torque for multi-motor servomechanism," *Control Engineering Practice*, vol. 50, pp. 57–68, 2016.
- [35] S. Wang, X. Ren, J. Na, and X. Gao, "Robust tracking and vibration suppression for nonlinear two-inertia system via modified dynamic surface control with error constraint," *Neurocomputing*, vol. 203, pp. 73–85, 2016.
- [36] X. Gao, C. Zhang, C. Zhu, and X. Ren, "Identification and control for hammerstein systems with hysteresis non-linearity," *IET Control Theory & Applications*, vol. 9, no. 13, pp. 1935–1947, 2015.
- [37] L. Tao, Q. Chen, Y. Nan, and C. Wu, "Double hyperbolic reaching law with chattering-free and fast convergence," *IEEE Access*, vol. 6, pp. 27717–27725, 2018.
- [38] W. Zhao, X. Ren, and S. Wang, "Parameter estimation-based time-varying sliding mode control for multimotor driving servo systems," *IEEE/ASME Transactions on Mechatronics*, vol. 22, no. 5, pp. 2330–2341, 2017.
- [39] Q. Chen, S. Xie, M. Sun, and X. He, "Adaptive nonsingular fixed-time attitude stabilization of uncertain spacecraft," *IEEE Transactions on Aerospace and Electronic Systems*, vol. 54, no. 6, pp. 2937–2950, 2018.
- [40] S. Bogosyan, M. Gokasan, and D. J. Goering, "A novel model validation and estimation approach for hybrid serial electric vehicles," *IEEE Transactions on Vehicular Technology*, vol. 56, no. 4, pp. 1485–1497, 2007.
- [41] J. Na, X. Ren, and D. Zheng, "Adaptive control for nonlinear pure-feedback systems with high-order sliding mode observer," *IEEE Transactions on Neural Networks and Learning Systems*, vol. 24, no. 3, pp. 370–382, 2013.